

**A metabolomics and biochemical
investigation of selected brain regions
from *Ndufs4* knockout mice**

J Coetzer

 **orcid.org 0000-0002-9269-3777**

Dissertation accepted in partial fulfilment of the requirements for
the degree *Master of Science in Biochemistry* at the North-West
University

Supervisor: Prof R Louw
Co-supervisor: Dr JZ Lindeque

Graduation May 2020
23509805

PREFACE AND ACKNOWLEDGEMENTS

Roughly one in every 5 000 people face the hard reality of mitochondrial disease. This dissertation marks the culmination of a journey that was set out to advance the knowledge on mitochondrial disease. Although only a small step forward, the hope is that the research of this study will pave the way for developing more effective therapeutic strategies. My heart goes out to the patients and families that are affected by this debilitating disease.

This study is the result of many minds (pardon the pun) and many hearts that deserve special mention. To Prof Roan Louw and Dr Zander Lindeque, thank you for your guidance, suggestions, practical assistance, answering my numerous questions and providing the balance that I needed for this study.

Prof Francois van der Westhuizen, thank you for supporting me and including me in the Mitochondrial-family. Thanks to Prof Albert Quintana (Universitat Autònoma De Barcelona, Catalonia, Spain), for your input in this study. I am sincerely grateful towards Peet Jansen van Rensburg and Mr Lardus Erasmus for your invaluable and constant assistance and support. Thanks also to Mari van Reenen, for your assistance with the statistical analyses and to Elmari Snoer, for language and grammar editing. My colleagues at the Mitochondria Research Laboratory for your friendship and support, thanks so much, especially to Jaundrie Fourie, Maryke Schoonen and Liesel Mienie. A special thanks also to Karin Terburgh, Hayley Miller, Wessel Horak and Michelle Mereis for always being willing to help with advice, practical assistance or just emotional support. I would also like to thank the National Research Foundation (NRF), North-West University (NWU) and the Technological Innovation Agency (TIA) for financial support. A general thank you to the team of the Preclinical Drug Development Platform (PCDDP, NWU, Potchefstroom Campus).

My sincere gratitude to my parents, Anita and Deon Coetzer, for your unfailing love, patience, prayers, encouragement and support in every area of my life. Though you only understand a little of Biochemistry jargon, you certainly understand me. Thank you for always believing in me. I love you. Thanks to the Boontjies-family (Devan, Andri, Aiden and Dian) for your love and upliftment. I also would like to thank my extended family and my second family (de Lecas) for their support. Thanks to all my other friends for your support: Laurencia van Deventer, Carien van der Berg, Leonie Venter, Megan Mcgee, the Hamman-family and Steiner-family. To Nadia van der Walt, I am grateful for your guidance and support which helped me tremendously in this “journey” (wink-wink). To my “Bestie”, Karl Steiner, I can never thank you enough for your patience, love, wisdom, support, encouragement and practical help. For your prayers, for understanding my heart and for defusing situations with your sense of humour. One day closer, one day stronger, I love you.

Above all, I want to thank the glorious Father of our Lord Jesus Christ for Your grace and Your everlasting love. You are my refuge, my strength and my dearest Friend. I am forever indebted to you for saving my soul and for giving me the gift to know You, Your Son and Your Holy Spirit. This journey has been challenging but rewarding. Thank you for all the opportunities and for taking care of me. You have created an intricately wonderful world. *“Great are the works of the Lord, studied by all who delight in them”* (Psalm 111:2). I love You so much.

“And God will wipe away every tear from their eyes; there shall be no more death, nor sorrow, nor crying. There shall be no more pain, for the former things have passed away.” (Revelation 21:4).

ABSTRACT

Mitochondria, the organelles found throughout the cytoplasm of most eukaryotic cells, have essential functions which have been implicated in the etiology of numerous metabolic and degenerative diseases. The mitochondrial oxidative phosphorylation (OXPHOS) system produces up to 90% of cellular energy. It comprises the respiratory chain (RC) of four enzyme complexes and the ATP synthase complex. Genetic mutations that affect the OXPHOS system cause a clinically heterogeneous group of disorders which fall under the umbrella term, primary mitochondrial disease (MD). Collectively, MDs are the most common among the inborn errors of metabolism in humans. These diseases generally present with severe, detrimental clinical phenotypes and primarily affect tissues with a high energy demand. An isolated OXPHOS complex I (CI) deficiency is the most commonly observed childhood-onset MD. It is often caused by a mutation in the nuclear coded NADH dehydrogenase (ubiquinone) iron-sulfur protein 4 (*Ndufs4*) gene. The resulting phenotype, known as Leigh syndrome, is characterised by progressive neurodegeneration in specific brain regions that drives disease progression and premature death. Currently, the mechanisms governing the brain's regional susceptibility to a CI deficiency are unclear and therapeutic strategies are lacking.

Using the *Ndufs4* knockout (KO) mouse, an accurate model of Leigh syndrome, this study aimed to determine whether brain regional differences in RC enzyme activities or metabolic profiles could be correlated with neurodegeneration. A combination of spectrophotometric enzyme activity assays and multi-platform metabolomics techniques were applied to investigate four selected brain regions: three neurodegeneration-prone regions (brainstem, cerebellum and olfactory bulbs) and a neurodegeneration-resilient region (anterior cortex). These were obtained from male *Ndufs4* KO and wild-type mice.

The enzyme assays (biochemical investigation) confirmed that CI activity was significantly reduced (60% to 80%) in the KO brain regions. Additionally, the findings suggested that lower residual CI activity, as well as higher OXPHOS requirements, or differential OXPHOS organisation, could underlie region-specific neurodegeneration. In accordance, a global disturbance in cellular metabolism distinguished the metabolic profiles (metabolomics investigation) of the KO brain regions. These global disturbances seemed to reflect a compensatory response in classic and non-classic metabolic pathways to alleviate the consequences of a CI deficiency. However, these adaptive responses seemed sub-optimal since they are susceptible to the detrimental effects of a CI deficiency and entail maladaptive features. Furthermore, the global metabolic perturbations had a gradient of severity across the brain regions which correlated with neurodegeneration and lower residual CI activity. It therefore seemed that the neurodegeneration-prone brain regions had greater requirements of the sub-

optimal compensatory pathways which ultimately reached a detrimental threshold. This then triggered neurodegenerative processes. The impairment of various redox-sensitive reactions also suggested that a lower cellular NAD⁺/NADH ratio in the neurodegeneration-prone brain regions might augment neurodegenerative processes. In addition, a few discriminatory metabolites unique to the anterior cortex suggested that inherent regional differences in metabolism might play a role in regional neurodegeneration. Conclusively, the results enabled a better understanding of the regional neurodegeneration in *Ndufs4* KO mice. The potential metabolic targets for treatment and for monitoring disease progression or therapeutic interventions revealed in this study, warrant further investigation.

Keywords: mitochondrial disease, OXPHOS, complex I deficiency, Leigh syndrome, brain regions, neurodegeneration, *Ndufs4* knockout, mouse model, metabolism, metabolomics.

TABLE OF CONTENTS

PREFACE AND ACKNOWLEDGEMENTS.....	I
ABSTRACT	III
LIST OF TABLES	XV
LIST OF FIGURES.....	XVII
LIST OF EQUATIONS	XXII
LIST OF SYMBOLS, UNITS, ABBREVIATIONS & LATIN TERMS.....	XXIII
CHAPTER 1 INTRODUCTION.....	1
1.1 Background and rationale for the study	1
1.2 Structure of the dissertation.....	2
1.3 Image disclaimer	2
1.4 Research output of the study	2
1.5 Financial support.....	2
CHAPTER 2 LITERATURE REVIEW.....	3
2.1 Introduction	3
2.2 Mitochondria.....	3
2.2.1 Mitochondrial structure and organisation	3
2.2.2 Mitochondrial genetics	5
2.2.3 Mitochondrial function and the OXPHOS system.....	5
2.3 Mitochondrial dysfunction and disease.....	8
2.3.1 Mitochondrial complex I deficiency	10
2.3.1.1 Complex I structure and function	10

2.3.1.2	Genetics and clinical presentation	12
2.3.1.3	Cellular consequences of complex I deficiency due to <i>Ndufs4</i> mutations.....	13
2.3.2	The complexity of the brain and its vulnerability to OXPHOS deficiencies	14
2.3.3	The <i>Ndufs4</i> knockout mouse model of complex I deficiency	18
2.3.4	Summary and problem statement	24
 CHAPTER 3: AIM, OBJECTIVES AND EXPERIMENTAL STRATEGY		25
3.1	Introduction	25
3.2	Aim	25
3.3	Objectives	25
3.4	Experimental strategy	26
 CHAPTER 4: MATERIALS AND METHODS.....		29
4.1	Introduction	29
4.2	Ethics statement.....	30
4.3	Animals and housing	30
4.4	Euthanasia and sample collection.....	31
4.5	Genotyping	32
4.5.1	Introduction.....	32
4.5.2	Materials and instrumentation.....	32
4.5.3	Methods.....	33
4.5.3.1	DNA isolation and quantification	33
4.5.3.2	DNA amplification and characterisation	34
4.6	Biochemical investigation.....	36

4.6.1	Introduction.....	36
4.6.2	Materials and instrumentation.....	37
4.6.3	Preparation of buffers and reagents.....	38
4.6.4	Methods.....	38
4.6.4.1	Samples and experimental groups.....	38
4.6.4.2	Preparation of homogenates and supernatants	39
4.6.4.3	Bicinchoninic acid (BCA) assay	40
4.6.4.4	Citrate synthase (CS) activity assay	41
4.6.4.5	Complex I (CI) activity assay	42
4.6.4.6	Complex II (CII) activity assay	44
4.6.4.7	Complex III (CIII) activity assay	45
4.6.4.8	Complex IV (CIV) activity assay.....	46
4.6.5	Data analysis.....	47
4.7	Metabolomics investigation.....	50
4.7.1	Introduction.....	50
4.7.2	Materials and instrumentation.....	52
4.7.2.1	Reagents and chemicals	52
4.7.2.2	Consumables and equipment.....	53
4.7.3	Preparation of standard stocks and solutions	54
4.7.4	Methods.....	56
4.7.4.1	Samples and experimental groups.....	56
4.7.4.2	Metabolite extraction.....	56
4.7.4.2.1	Monophasic metabolite extraction.....	59

4.7.4.2.2	Biphasic metabolite extraction	60
4.7.4.3	Preparation of quality control (QC) samples	60
4.7.4.3.1	Preparation of QC samples for GC-TOF analysis	60
4.7.4.3.2	Preparation of QC samples for LC-MS/MS analysis	61
4.7.4.4	Derivatisation.....	64
4.7.4.4.1	Methoximation and trimethylsilylation derivatisation for GC-TOF analysis	64
4.7.4.4.2	Butylation derivatisation for LC-MS/MS analysis.....	65
4.7.4.5	Run order and batch design.....	66
4.7.4.5.1	Run order and batch design for GC-TOF analysis	66
4.7.4.5.2	Run order and batch design for LC-MS/MS analysis.....	67
4.7.4.6	Analytical parameters	70
4.7.4.6.1	Analytical parameters for GC-TOF analysis.....	70
4.7.4.6.2	Analytical parameters for LC-MS/MS Analysis.....	71
4.7.5	Data analysis.....	72
4.7.5.1	Data extraction	72
4.7.5.1.1	Data extraction for GC-TOF analysis	72
4.7.5.1.2	Data extraction for LC-MS/MS analysis	73
4.7.5.2	Data processing and normalisation.....	73
4.7.5.2.1	Processing and normalisation of GC-TOF data.....	75
4.7.5.2.2	Processing and normalisation of LC-MS/MS data.....	76
4.7.5.3	Statistical data analysis	78
4.7.6	Identification of GC-TOF compounds.....	79

CHAPTER 5: BIOCHEMICAL INVESTIGATION OF NDUFS4 KNOCKOUT MOUSE	
BRAIN REGIONS.....	80
5.1 Introduction	80
5.2 The <i>Ndufs4</i> knockout had variable effects on the maximal activities of citrate synthase and respiratory chain enzymes in the various brain regions	81
5.2.1 Maximal citrate synthase activity is generally increased in <i>Ndufs4</i> knockout mice and higher in neurodegeneration-prone brain regions	83
5.2.2 Maximal complex I activity is differentially reduced but not absent across the brain regions of <i>Ndufs4</i> knockout mice	86
5.2.3 Maximal complex II, III and IV activities are not uniquely affected in the neurodegeneration-prone brain regions but are generally higher	89
5.3 Vulnerability to neurodegeneration might be linked to greater OXPHOS dependency or regional differences in OXPHOS organisation ...	94
5.4 Summary of biochemical investigation on <i>Ndufs4</i> knockout brain regions	97
CHAPTER 6: METABOLOMICS INVESTIGATION OF NDUFS4 KNOCKOUT MOUSE	
BRAIN REGIONS.....	98
6.1 Introduction	98
6.2 Metabolomics data quality	99
6.3 The effect of the <i>Ndufs4</i> knockout on metabolic profiles of selected brain regions.....	99
6.3.1 The metabolic profile of each brain region was distinct between the wild-type and knockout mice	99
6.3.2 The <i>Ndufs4</i> knockout affected multiple metabolic pathways in each brain region	104
6.4 The <i>Ndufs4</i> knockout brain regions displayed common and distinct discriminatory metabolites	110

6.4.1	Shared metabolic characteristics of the <i>Ndufs4</i> knockout brain regions.....	115
6.4.1.1	Disturbed energy homeostasis	115
6.4.1.2	Disturbed redox regulation and antioxidant defence	117
6.4.1.3	Common metabolic effect of the <i>Ndufs4</i> knockout on the investigated brain regions	118
6.4.2	Metabolic perturbations that correlated with region-specific neurodegeneration in <i>Ndufs4</i> knockout mice	119
6.4.2.1	BCAA catabolism was more extensively perturbed in the neurodegeneration-prone brain regions.....	119
6.4.2.2	Lysine catabolism was strongly perturbed in the OB.....	123
6.4.2.3	Proline metabolism was less perturbed and arginine metabolism uniquely altered in the resilient AC.....	125
6.4.2.4	Aspartic acid and glutamic acid metabolism were less perturbed, and glutathione metabolism more perturbed in the neurodegeneration-prone brain regions.....	128
6.4.2.5	The provision of TCA cycle-related intermediates was more pronouncedly affected in the neurodegeneration-prone brain regions.....	131
6.4.2.6	Carbohydrate-related metabolism was more perturbed in the neurodegeneration-prone brain regions.....	132
6.4.2.7	Lipid-related metabolism was more perturbed in the neurodegeneration-prone brain regions.....	135
6.4.2.8	One-carbon metabolism was uniquely altered among <i>Ndufs4</i> knockout brain regions.....	138
6.5	Metabolic-related factors that could drive region-specific neurodegeneration in <i>Ndufs4</i> knockout mice	140
6.5.1	The potential role of graded metabolic perturbations in region-specific neurodegeneration	140
6.5.1.1	Greater activation of sub-optimal RC-fuelling and ATP-producing pathways ..	142

6.5.1.2	Greater impairment of RC-fuelling and ATP-producing pathways	143
6.5.1.3	Activation of energetically expensive metabolic pathways	144
6.5.1.4	Increased utilisation of sub-optimal NADH oxidation reactions	145
6.5.1.5	Increased production of reactive species and oxidative damage	145
6.5.1.6	Accumulation of potentially neurotoxic metabolites	146
6.5.1.7	Exacerbation of nucleotide pool imbalances	147
6.5.1.8	Greater metabolic dysregulation of cell signalling pathways	148
6.5.1.9	Aberrant activation or dysregulation of glial cells	149
6.5.1.10	Aberrant inter-cellular signalling and neurotransmitter homeostasis	150
6.5.2	The potential role of inherent metabolic specificity in region-specific neurodegeneration	150
6.5.2.1	Inherent regional differences related to CI activity and/or OXPHOS control	151
6.5.2.2	Inherent regional differences related to NADH oxidation and/or production	151
6.5.2.3	Inherent regional differences related to antioxidant defence and/or production of reactive species	152
6.5.2.4	Inherent regional differences related to metabolic flexibility and/or metabolic switches.....	152
6.5.3	The cumulative metabolic effects of several mechanisms might underlie region-specific neurodegeneration.....	154
6.6	Summary of metabolomics investigation on <i>Ndufs4</i> knockout brain regions	157
CHAPTER 7: SUMMARY, CONCLUSIONS AND RECOMMENDATIONS		158
7.1	Introduction	158
7.2	Objective 1: Verify the genotypes of <i>Ndufs4</i> wild-type and knockout mice	158

7.3	Objective 2: Investigate the biochemical activity of individual respiratory chain complexes I to IV in the selected brain regions.....	159
7.4	Objective 3: Investigate the metabolic profiles of the selected brain regions using a multi-platform metabolomics approach.....	160
7.5	Final conclusions and recommendations.....	165
REFERENCES.....		169
APPENDIX A: GENOTYPING AND ANIMAL INFORMATION		202
A.1.	Introduction	203
A.2.	Genotype verification of experimental mice.....	203
A.3.	Supplementary information of experimental mice	204
APPENDIX B: PREPARATION OF REAGENTS.....		207
B.1.	Introduction	208
B.2.	Preparation of reduced Cytochrome c (Cyt c).....	208
B.3.	Preparation of reduced decylubiquinone / decylubiquinol (DQnoI).....	209
APPENDIX C: STANDARDISATION OF SPECTROPHOTOMETRIC ASSAYS.....		210
C.1.	Introduction	211
C.2.	Standardisation of the bicinchoninic acid (BCA) assay	212
C.3.	Standardisation of the citrate synthase (CS) activity assay	214
C.4.	Standardisation of the respiratory chain enzyme activity assays	217

APPENDIX D: STANDARDISATION OF METABOLOMICS METHODS.....	220
D.1. Introduction	221
D.2. Verification of compound conditions and insertion of time segments for LC-MS/MS method	221
D.3. Evaluation of experimental precision.....	226
APPENDIX E: SUPPLEMENTARY BIOCHEMICAL RESULTS	229
E.1. Introduction	230
E.2. Assumption tests	230
E.2.1. Box-plots for outlier removal and assessment of symmetry	230
E.2.2. Equal variances and sphericity	234
E.3. Maximal enzyme activities normalised to citrate synthase activity	237
APPENDIX F: METABOLOMICS DATA QUALITY	246
F.1. Introduction	247
F.2. Evaluation of experimental precision.....	247
F.3. Evaluation of potential batch effects and overall data integrity.....	250
APPENDIX G: SUPPLEMENTARY METABOLOMICS RESULTS.....	257
G.1. Introduction	258
G.2. PCA of all GC-TOF detected features of the OB.....	258
G.3. Relative abundance of commonly altered discriminatory metabolites.....	259
G.3.1. Relative abundance of the branched-chain amino acids (BCAAs)	260
G.3.2. Relative abundance of lysine-related metabolites	261

G.3.3. Relative abundance of arginine- and proline-related metabolites..... 262

G.3.4. Relative abundance of aspartic acid- and glutamic acid-related metabolites... 263

G.3.5. Relative abundance of TCA cycle-related metabolites 265

G.3.6. Relative abundance of carbohydrate-related metabolites 266

APPENDIX H: LANGUAGE EDITING CERTIFICATE 269

APPENDIX I: ETHICS APPROVAL CERTIFICATE..... 271

APPENDIX REFERENCES..... 273

LIST OF TABLES

MAIN TEXT

Table 4.1:	Primers used for genotyping mice by PCR.....	34
Table 4.2:	Quality control (QC) samples used in GC-TOF and LC-MS/MS analysis of metabolites extracted from mouse brain region tissues.....	62
Table 5.1:	Maximal spectrophotometric enzyme activities in brain regions of <i>Ndufs4</i> wild-type and knockout mice normalised to mg of protein.....	82
Table 5.2:	Maximal respiratory enzyme activities expressed as ratios relative to complex I or complex II within a brain region.....	95
Table 6.1:	Significant metabolites discriminating between the <i>Ndufs4</i> wild-type and knockout mice in the selected brain regions.....	105

APPENDICES

Table A.1:	Information of mice from which samples were obtained and analysed in the metabolomics investigation.....	205
Table A.2:	Information of mice from which samples were obtained and analysed in the biochemical investigation.....	206
Table C.1:	Effective volumes of 700 x g supernatants used and selected for the enzyme activity assays in the various mouse brain regions.....	217
Table D.1:	Optimised source and multiple reaction monitoring (MRM) conditions for each butylated compound and isotope-labelled standard.....	222
Table D.2:	Percentage of features below the QC-CV cut-off value in the GC-TOF and LC-MS/MS metabolomics data sets.....	228
Table E.1:	Statistical processing of maximal enzyme activity data measured in various brain regions of <i>Ndufs4</i> wild-type and knockout mice using a two-way mixed ANOVA.....	236

Table E.2:	Summary of the significance of effects obtained from maximal enzyme activity data measured in various brain regions of <i>Ndufs4</i> wild-type and knockout mice using a two-way mixed ANOVA.	238
Table E.3:	Maximal spectrophotometric enzyme activities in brain regions of <i>Ndufs4</i> wild-type and knockout mice normalised to citrate synthase activity.	238
Table E.4:	Statistically significant differences in CS-normalised maximal enzyme activities when comparing corresponding brain regions from <i>Ndufs4</i> wild-type and knockout mice.	239
Table E.5:	Statistically significant differences in CS-normalised maximal enzyme activities between brain regions of <i>Ndufs4</i> wild-type or knockout mice.	240
Table F.1:	Percentage of features below the QC-CV cut-off value in the GC-TOF and LC-MS/MS metabolomics data sets of the various investigated brain regions.	250

LIST OF FIGURES

MAIN TEXT

Figure 2.1:	Basic structure of the mitochondrion.	4
Figure 2.2:	The oxidative phosphorylation system in the inner mitochondrial membrane.....	6
Figure 2.3:	Structure of mitochondrial complex I.	11
Figure 3.1:	Experimental strategy illustrating the objectives of this study.	28
Figure 4.1:	Schematic diagram of the whole mouse brain and the brain regions used in this study (sagittal view).	32
Figure 4.2:	PCR conditions used for genotyping.	35
Figure 4.3:	Preparation of 700 x g supernatants from selected mouse brain regions.	40
Figure 4.4:	Data processing and analyses of enzyme activity data sets.	49
Figure 4.5:	Schematic summary of the metabolomics experimental workflow.	51
Figure 4.6:	Schematic diagram of the standardised procedure used for metabolite extraction and derivatisation of mouse brain region tissue samples.	58
Figure 4.7:	Run order and batch design of the GC-TOF analysis of derivatised monophasic extracts from <i>Ndufs4</i> wild-type and knockout brain region tissue samples.	68
Figure 4.8:	Run order and batch design of the LC-MS/MS analysis of derivatised polar phase extracts from <i>Ndufs4</i> wild-type and knockout brain region tissue samples.	69
Figure 4.9:	Data processing and normalisation of extracted metabolomics data sets.	74
Figure 5.1:	Maximal citrate synthase activity in the brain regions of <i>Ndufs4</i> wild-type and knockout mice.	83
Figure 5.2:	Maximal complex I activity in the brain regions of <i>Ndufs4</i> wild-type and knockout mice.	86

Figure 5.3:	Maximal complex II activity in the brain regions of <i>Ndufs4</i> wild-type and knockout mice.	89
Figure 5.4:	Maximal complex III activity in the brain regions of <i>Ndufs4</i> wild-type and knockout mice.	91
Figure 5.5:	Maximal complex IV activity in the brain regions of <i>Ndufs4</i> wild-type and knockout mice.	92
Figure 6.1:	The effect of the <i>Ndufs4</i> knockout on the metabolic profiles of various brain regions as detected with GC-TOF and LC-MS/MS analysis.	101
Figure 6.2:	Number of discriminatory metabolites altered in the brain regions of <i>Ndufs4</i> knockout mice compared to wild-type mice.	102
Figure 6.3:	Discriminative power of discriminatory metabolites altered in the brain regions of <i>Ndufs4</i> knockout mice compared to wild-type mice.	104
Figure 6.4:	Discriminatory metabolic alterations in <i>Ndufs4</i> knockout mouse brain regions.	108
Figure 6.5:	Venn diagram of discriminatory metabolites altered in the brain regions of <i>Ndufs4</i> knockout mice compared to wild-type mice.	112
Figure 6.6:	The metabolic pathways associated with the shared and distinct discriminatory metabolites identified across the brain regions of <i>Ndufs4</i> knockout mice.	114
Figure 6.7:	Branched-chain amino acid metabolism and related metabolomic changes in the brain regions of <i>Ndufs4</i> knockout mice.	120
Figure 6.8:	Lysine metabolism and related metabolomics changes in the brain regions of <i>Ndufs4</i> knockout mice.	124
Figure 6.9:	Arginine and proline metabolism and related metabolomics changes in the brain regions of <i>Ndufs4</i> knockout mice.	126
Figure 6.10:	Aspartic acid and glutamic acid metabolism and related metabolomics changes in the brain regions of <i>Ndufs4</i> knockout mice.	129
Figure 6.11:	Carbohydrate metabolism and related metabolomics changes in the brain regions of <i>Ndufs4</i> knockout mice.	133

Figure 6.12:	Lipid metabolism and related metabolomics changes in the brain regions of <i>Ndufs4</i> knockout mice.	136
Figure 6.13:	One-carbon metabolism and related metabolomics changes in the brain regions of <i>Ndufs4</i> knockout mice.	139
Figure 6.14:	Potential mechanisms underlying brain region-specific metabolic alterations of <i>Ndufs4</i> knockout mice.....	156

APPENDICES

Figure A.1:	Example of agarose gel electrophoretogram obtained during genotyping of mice.	204
Figure C.1:	Example of a BSA standard curve utilised during standardisation of the BCA assay.	212
Figure C.2:	Linearity of the BCA assay for different volumes of 700 x g supernatants obtained from various mouse brain regions.....	213
Figure C.3:	Examples of single well CS activity measurement for different volumes of CB supernatant.	215
Figure C.4:	Linearity of the CS assay for different volumes of 700 x g supernatants obtained from various mouse brain regions.....	216
Figure C.5:	Examples of single well CI activity measurements for different volumes of CB supernatant.	218
Figure C.6:	Linearity of the RC enzyme activity assays for different volumes of 700 x g supernatants obtained from various mouse brain regions.....	219
Figure D.1:	Dividing the LC-MS/MS chromatogram into time segments.....	224
Figure D.2:	Examples of extracted peaks from the ion chromatograms acquired with and without time segmentation.....	225
Figure D.3:	Assessment of metabolomics experimental precision.	227

Figure E.1:	Clustered box-plots of maximal enzyme activities for outlier detection and evaluation of symmetry.	234
Figure E.2:	Maximal complex I enzyme activity of <i>Ndufs4</i> wild-type and knockout mice normalised to CS activity.	241
Figure E.3:	Maximal complex II enzyme activity of <i>Ndufs4</i> wild-type and knockout mice normalised to CS activity.	242
Figure E.4:	Maximal complex III enzyme activity of <i>Ndufs4</i> wild-type and knockout mice normalised to CS activity.	243
Figure E.5:	Maximal complex IV enzyme activity of <i>Ndufs4</i> wild-type and knockout mice normalised to CS activity.	244
Figure F.1:	Assessment of experimental precision in final metabolomics analyses.	249
Figure F.2:	Visual assessment of potential batch effects using total signal scatterplots.....	251
Figure F.3:	Evaluation of potential batch effects and overall data integrity of experimental multi-platform metabolomics data sets	254
Figure F.4:	Evaluation of potential batch effects and data integrity of experimental multi-platform metabolomics data sets using principal component analysis on important differential metabolites.	256
Figure G.1:	PCA scores and loadings plot for all GC-TOF detected features of the OB.	259
Figure G.2:	The relative abundance of the branched-chain amino acids in the brain regions of <i>Ndufs4</i> wild-type and knockout mice.....	260
Figure G.3:	The relative abundance of commonly altered lysine-related metabolites in the brain regions of <i>Ndufs4</i> wild-type and knockout mice.	261
Figure G.4:	The relative abundance of commonly altered arginine- and proline-related metabolites in the brain regions of <i>Ndufs4</i> wild-type and knockout mice.	263
Figure G.5:	Relative abundances of aspartic acid- and glutamic acid-related metabolites in the brain regions of <i>Ndufs4</i> wild-type and knockout mice. ...	264

Figure G.6:	The relative abundance of important differential TCA cycle-related metabolites in the brain regions of <i>Ndufs4</i> wild-type and knockout mice. ...	265
Figure G.7:	The relative abundance of commonly altered carbohydrate-related metabolites in the brain regions of <i>Ndufs4</i> wild-type and knockout mice. ...	267
Figure G.8:	The relative abundance of additional carbohydrate-related metabolites in the brain regions of <i>Ndufs4</i> wild-type and knockout mice	268

LIST OF EQUATIONS

MAIN TEXT

Equation 4.1: Calculation of protein concentration.....	41
Equation 4.2: Calculation of specific activity of citrate synthase.....	42
Equation 4.3: Calculation of specific activity of complex I.....	43
Equation 4.4: Calculation of complex I activity normalised to citrate synthase.....	43
Equation 4.5: Calculation of specific activity of complex II.....	45
Equation 4.6: Calculation of complex II activity normalised to citrate synthase.....	45
Equation 4.7: Calculation of specific activity of complex III.....	46
Equation 4.8: Calculation of complex III activity normalised to citrate synthase.....	46
Equation 4.9: Calculation of specific activity of complex IV.....	47
Equation 4.10: Calculation of complex IV activity normalised to citrate synthase.....	47
Equation 4.11: Internal standard normalisation of metabolomics data.....	75
Equation 4.12: Adjustment of LC-MS/MS internal standard area.....	77
Equation 4.13: Calculation of effect size.....	79

APPENDICES

Equation B.1: Calculation of reduced Cytochrome c concentration.....	208
Equation D.1: Calculation of coefficient of variance.....	226

LIST OF SYMBOLS, UNITS, ABBREVIATIONS & LATIN TERMS

Symbols

-	Minus
#	Hashtag; indicates catalogue number
&	And
*	Asterisk
-/-	Homozygous knockout genotype; gene of interest is absent from both alleles
-/+	Heterozygous knockout genotype; gene of interest is present on only one of the two alleles
[]	Concentration
~	Approximately
+/+	Homozygous wild type genotype; gene of interest is present on both alleles
<	Less-than
>	Greater-than
±	Plus-minus
≤	Less-than or equal to
≥	Greater-than or equal to
↑	Relative increase in concentration
↓	Relative decrease in concentration
©	Copyright
®	Registered
♂	Male
I	One (Roman numeral)
II	Two (Roman numeral)
III	Three (Roman numeral)
IV	Four (Roman numeral)
v	Reaction velocity
∅	Diameter
™	Trademark
V	Five (Roman numeral)
x	Times
\bar{x}	Mean or average
α	Alpha
β	Beta
γ	Gamma
Δ	Delta
ΔpH_m	Mitochondrial chemical proton gradient
ΔPMF	Proton motive force
$\Delta \Psi_m$	Mitochondrial electrical membrane potential
ε	Molar extinction coefficient
é	Greenhouse-Geisser's epsilon
ηp^2	Partial eta squared
λ	Wavelength

Units

%	Percentage
°	Degrees
°C	Degrees Celsius
µg	Microgram
µL	Microlitre
µm	Micrometre
µM	Micromolar
µmol	Micromole
Abs	Absorbance
am	Atomic mass unit
cm	Centimetre
eV	Electron volt
g	gram
h	Hour
Hz	Hertz; cycles per second
kb	Kilobase
kDa	Kilodalton
L	Litre
Lux	Unit of illuminance; equal to 1 lumen per square meter
m	Metre
M	Molar or Molarity; moles solute per litre of solvent
m/z	Mass-to-charge ratio
mAbs	Milliabsorbance
mg	Milligram
min	Minute
mL	Millilitre
mm	Millimetre
mM	Millimolar
mol	Mole
Ms	Millisecond
mU	Milli-enzyme unit (nmol/minute or U ÷ 1000)
N	Normality; molar concentration divided by an equivalence factor
ng	Nanogram
nm	Nanometre
nmol	Nanomole
pH	Potential of hydrogen; the negative of the base 10 logarithm of the H ⁺ molar concentration
ppm	Parts per million
psi	Pound-force per square inch; unit of pressure
rpm	Revolutions per minute
s	Seconds
U	Enzyme unit (µmol/min)
V	Volt
v/v	Volume (of solute) per total volume (of solvent)
w/v	Weight (of solute) per volume (of solvent)
w/w	Weight (of solute) per weight (of solution)
x g	Relative centrifugal force

Abbreviations

$^{13}\text{C}_5$	Carbon isotope labelling; number of normal carbon atoms in a compound replaced with carbon-13 e.g. 5
$^{15}\text{N}_2$	Nitrogen isotope labelling; number of normal nitrogen atoms in a compound replaced with carbon-15 e.g. 2
1C	One-carbon
2-AAP	2-acetamidophenol
2-D	Two-dimensional
3'	3-prime end; 3-prime hydroxyl group of the polynucleotide chain
3mH	3-Methylhistidine
3-PBA	3-Phenylbutyric acid
4-PBA	4-Phenylbutyric acid
5'	5-prime end; 5-prime phosphate group of the polynucleotide chain
5' to 3'	Polynucleotide directionality; from the 5-prime end to the 3-prime end of the polynucleotide chain

A

A	Amino acid
AASA	Aminoadipate semialdehyde
AB	Analytical blank
AC	Anterior cortex
ACN	Acetonitrile
ACoA	Acetyl coenzyme A
AD	Acyl-CoA dehydrogenases
ADP	Adenosine diphosphate
Ala	Alanine
ALAT	Alanine aminotransferase
AMDIS	Automated Mass Spectral Deconvolution and Identification System
AMP	Adenosine monophosphate
AMS	Amsterdam
AnimCare	North-West University Animal Care, Health and Safety in Research Ethics Committee
ANOVA	Analysis of variance
ANT	Adenine nucleotide translocase
Ara	Arachidonic acid
Arg	Arginine
ARTs	Adenosine diphosphate-ribose transferases
Asn	Asparagine
Asp	Aspartic acid
ATP	Adenosine triphosphate
AVG	Average

B

BBB	Blood-brain barrier
BCA	Bicinchoninic Acid
BCAA	Branched-chain amino acid
BCKAs	Branched-chain keto acids
BCSFB	Blood-cerebrospinal fluid barrier
bp	Base pairs
BSA	Bovine serum albumin
BST	Brainstem

BSTFA O-bis(trimethylsilyl)trifluoroacetamide)
ButHCl Butanolic hydrochloric acid

C

C Carbohydrates
C0 Free carnitine
C10 Decanoylcarnitine
C12 Dodecanoylcarnitine
C14 Tetradecanoylcarnitine or Myristoylcarnitine
C16 Hexadecanoylcarnitine or Palmitoylcarnitine
C16:0 Palmitic acid
C18 Octadecanoylcarnitine or Stearoylcarnitine
C18:0 Stearic acid
C18:1 Oleic acid
C2 Acetylcarnitine
C3 Propionylcarnitine
C4 Butyrylcarnitine
C5 Isovalerylcarnitine
C57BL/6 C57 black 6 mouse strain
C6 Hexanoylcarnitine
C8 Octanoylcarnitine
CA California
Ca²⁺ Calcium(II) ion
cADPR Cyclic adenosine diphosphate-ribose
Car Carbamic acid
Cat. No. Catalogue Number
CB Cerebellum
CBS Cystathionine β -synthase
CDF Cumulative distribution functions
CE Collision energy
CF Chloroform
cGDH Cytosolic glycerol-3-phosphate dehydrogenase
cHCl Concentrated hydrochloric acid
CI Complex I; NADH:ubiquinone oxidoreductase; NADH dehydrogenase; EC 1.6.5.3 or confidence interval (depending on the context)
CID Collision-induced dissociation
CII Complex II; Succinate:ubiquinone oxidoreductase; succinate dehydrogenase; EC 1.3.5.1
CIII Complex III; ubiquinol:ferricytochrome c oxidoreductase; ubiquinol Cytochrome c reductase; EC 1.10.2.2
Cit Citrulline
CIV Complex IV; ferrocyclochrome-c:oxygen oxidoreductase; Cytochrome c oxidase; EC 1.9.3.1
CNS Central nervous system
Co. Company
CO₂ Carbon dioxide
CoA Coenzyme A
CoA-SH Coenzyme A with a thiol group
-COOH Carboxyl group
CoQ Coenzyme-Q₁₀; Ubiquinone, UQ

C-pool	Cytochrome c pool
CPSI	Carbamoyl phosphate synthetase I
CPT1	Carnitine palmitoyltransferase 1
Crea	Creatinine
Cre-Lox	Site specific recombinase technology
CS	Citrate Synthase; acetyl-CoA:oxaloacetate C-acetyltransferase; E.C. 2.3.3.1
CSF	Cerebral spinal fluid
Cu	Copper(II) sulphate
Cu ⁺	Copper(I) ion
Cu ²⁺	Copper(II) ion
CuSO ₄	Copper(II) sulphate
CV	Complex V; ATP synthase; EC 3.6.1.3. or coefficient of variance (depending on the context)
Cys	Cysteine
Cysta	Cystathionine
Cyt c	Cytochrome c

D

d^3	d -value raised to the third power
d_4	Deuterated; number of normal hydrogen atoms in a compound replaced with deuterium (² H) e.g. 4
DCIP	2,6-Dichloroindophenol
DHAP	Dihydroxyacetone phosphate
DHSA	Dihydroxystearic acid
D-isomer	Right-handed configuration
DMPA	N,N-Dimethyl-L-phenylalanine
DMSO	Dimethyl sulfoxide
DNA	Deoxyribonucleic Acid
DQ	Decylubiquinone
DQnol	Decylubiquinol or reduced decylubiquinone
Dr	Doctor
dSAM	Decarboxylated S-adenosylmethionine
DTNB	2,2'-Dinitro-5,5'-dithiobenzoic acid
d -values	Effect size value of practical significance

E

e ⁻	Electron
e.g.	<i>Exempli gratia</i> (Latin): for example
EC number	Enzyme commission number
EDTA	Ethylenediaminetetraacetic acid
EGTA	Ethylene glycol tetraacetic acid
EMV	Electron multiplier voltage
ER	Endoplasmic reticulum
EryA	Erythronic acid
ESI	Electrospray ionisation
ESI-L	Electrospray ionisation-low concentration tuning mix
et al.	<i>et alii</i> (Latin): for "and others"
EtBr	Ethidium bromide
ETC	Electron transport chain

etc.	<i>Etcetera</i> (Latin): indicates that further, similar items are included
ETF	Electron transfer flavoprotein
ETF/ETF-QO	Electron transfer flavoprotein / electron transfer flavoprotein-ubiquinone oxidoreductase

F

F	Fragmentor or Fatty acids (depending on the context)
<i>F</i>	<i>Fisher</i> -ratio; the ratio of the between group variance to the within group variance
F6P	Fructose-6-phosphate
FA	Formic acid
FAD	Oxidised flavin adenine dinucleotide
FADH ₂	Reduced flavin adenine dinucleotide
FASBMB	Federation of African Societies of Biochemistry and Molecular Biology
FDA	Food and Drug Administration
FDR	False discovery rate
Fe-S	Iron-sulfur
FGly	Formylglycine
FMN	Flavin mononucleotide

G

G1P	Glucose-1-phosphate
G3PDH	Glyceraldehyde-3-phosphate dehydrogenase
G6P	Glucose-6-phosphate
GABA	γ-Aminobutyric acid
GABAergic	γ-Aminobutyric acidergic
GC	Gas chromatography
GC-TOF	Gas chromatography time-of-flight mass spectrometry
GDH	Glutamic acid dehydrogenase
GG	Greenhouse-Geisser
Gln	Glutamine
glog	Generalized logarithm
Glu	Glutamic acid
Gluc	Glucose
Gly	Glycine
Glyc	Glycolic acid
GlyPS	Glycerol-3-phosphate shuttle
GMP	Guanosine monophosphate
GSH	Reduced glutathione
GSSG	Oxidised glutathione; glutathione disulfide
GTP	Guanosine triphosphate

H

H ⁺	Hydrogen ion; proton
H ₂ O	Water
HCh	Hydroxy-cholesterol
HCl	Hydrogen chloride
HEPA	High-efficiency particulate air
HEPES	4-(2-hydroxyethyl)-1-piperazineethanesulfonic Acid
HET	Heterozygous
HIF-1α	Hypoxia-inducible factor 1-alpha

HPLC	High-performance liquid chromatography
HSer	Homoserine
Hyp	Hydroxyproline

I

i.e.	<i>id est</i> : Latin abbreviation for “that is”
IB ₁	Isolation buffer 1
IBM	International Business Machines
ID	Inner diameter or Identification (depending on the context)
Ile	Isoleucine
IMP	Inosine monophosphate
IN	Indiana
Inc.	Incorporated
IS	Internal standard
Iso	isotopically labelled internal standard mix
I th	I th , occurring at position I
IVC	Individually ventilated cage

J

JNB	Johannesburg
-----	--------------

K

K ₂ HPO ₄	Dipotassium hydrogen phosphate
KGDHC	α-Ketoglutarate dehydrogenase complex
KH ₂ PO ₄	Potassium dihydrogen orthophosphate
KNN	K-nearest neighbour
KO	Knockout
KOH	Potassium hydroxide
KPi	Potassium phosphate
KSS	Kearns-Sayre Syndrome

L

L	Length
Lac	Lactic acid
LAT1	Large neutral amino acid transporter 1
LC	Liquid chromatography
LCFA	Long-chain fatty acid
LC-MS/MS	Liquid chromatography-tandem mass spectrometry
LDH	Lactic acid dehydrogenase
LHON	Leber's hereditary optic neuropathy
L-isomer	Left-handed configuration
LMSLR	Least mean squares linear regression
-log ₁₀	Negative logarithm to the base 10
<i>loxP</i>	Locus of X(cross)-over in P1; a site on the bacteriophage P1
LS	Leigh Syndrome
Ltd	Limited
Lys	Lysine
Lyx	Lyxose

M

m/cBCAT	Mitochondrial or cytosolic branched-chain aminotransferase
m/cP5CR	Mitochondrial or cytosolic P5C-reductase
MA	Massachusetts
MAS	Malic acid-aspartic acid redox shuttle
mBCKDH	Mitochondrial branched chain α -ketoacid dehydrogenase complex
MD	Primary mitochondrial disease
ME	Maine
MELAS	Mitochondrial encephalopathy, lactic acidosis, with stroke-like episodes
MeOH	Methanol
MeOX	Methoxime
Met	Methionine
MI	Michigan
mIn	Methylindole
miRNAs	Micro-ribonucleic acids
MO	Missouri
MOX	Methoximation solution
mPTP	Permeability transition pore
MRM	Multiple reaction monitoring
MS	Mass spectrometer
MS/MS	Tandem mass spectrometer
MSUD	Maple syrup urine disease
mtDNA	Mitochondrial DNA
mTOR	Mechanistic/Mammalian target of rapamycin
mTOR1	Mechanistic/Mammalian target of rapamycin complex 1
mt-rRNA	Mitochondrial ribosomal RNA
MTS	Mitochondrial targeting sequence
mt-tRNA	Mitochondrial transfer RNA
MVI	Missing value imputation

N

n	Sample size or number of samples
N ₂ (g)	Nitrogen gas
NAA	N-Acetylaspartic acid
NaCl	Sodium chloride
NAD	Nicotinamide adenine dinucleotide
NAD ⁺	Oxidised nicotinamide adenine dinucleotide
NADH	Reduced nicotinamide adenine dinucleotide
NADP ⁺	Oxidised nicotinamide adenine dinucleotide phosphate
NADPH	Reduced nicotinamide adenine dinucleotide phosphate
NAG	N-Acetylglutamic acid
NAMPT	Nicotinamide phosphoribosyl transferase
NaN ₃	Sodium Azide
nDNA	Nuclear DNA
NDUFS4	NADH dehydrogenase (ubiquinone) iron-sulfur protein 4; NADH:ubiquinone oxidoreductase subunit S4
<i>Ndufs4</i>	NADH dehydrogenase (ubiquinone) iron-sulfur protein 4 gene; NADH:ubiquinone oxidoreductase subunit S4 gene
<i>Ndufs4^{flky/flky}</i>	Mouse model in which the <i>Ndufs4</i> gene was knocked out by aberrant transcript splicing

<i>Ndufs4</i> ^{lox/lox}	Mouse model in which exon 2 of the <i>Ndufs4</i> allele was flagged by <i>loxP</i> sites
<i>Ndufs4</i> ^{PM}	Mouse model in which the <i>Ndufs4</i> gene was knocked out by a heterozygous point mutation
NesKO	Nestin knockout; mouse model in which the <i>Ndufs4</i> gene was knocked out by deleting exon 2 exclusively in brain cells
-NH ₄ ⁺	Ammonium group
NHREC	National Health Research Ethics Council
NIST	National Institute of Standards and Technology
NL	Netherlands
NMN	Nicotinamide mononucleotide
N-module	NADH-oxidising dehydrogenase module
No.	Number
NQO	NAD(P)H:quinone oxidoreductases or diaphorases
NRF	National Research Foundation of South Africa
NWU	North-West University

O

O	Other
O ₂	Oxygen
OAA	Oxaloacetate
OB	Olfactory bulbs
OD	Outer diameter
-OH	Hydroxyl group
OK	Oklahoma
OMIM	Online Mendelian Inheritance in Man
Opa1	Optic Atrophy 1
Orn	Ornithine
OXPPOS	Oxidative phosphorylation

P

P5C	Pyrroline-5-carboxylic acid
P6C	Pyrroline-6-carboxylic acid
PanA	Pantothenic acid
PARPs	Poly(adenosine diphosphate–ribose) polymerases
PBS	Phosphate-buffered saline
PC	Principal component
PCA	Principal component analysis
PCDDP	Preclinical Drug Development Platform
PCR	Polymerase chain reaction
PDH	Pyruvic acid dehydrogenase
PEPK	Phosphoenolpyruvate carboxykinase
PG	Phosphoglycerol
PGe/(2)	Phosphoglycerol enol or phosphoglycerol enol 2
PGK	Phosphoglycerate kinase
PGlu	Pyroglutamic acid
Phe	Phenylalanine
Pi	Inorganic phosphate
Pip	Pipecolic acid
PK	Pyruvate kinase
PLIEM	Potchefstroom Laboratory for Inborn Errors of Metabolism

PMF	Transmembrane electrochemical proton motive force; = $\Delta\Psi_m + \Delta\text{pH}$
P-module	Proton-translocating module
PN	Postnatal day; PN23 means day 23 after birth
PPAR	Peroxisome proliferator-activated receptor
PPP	Pentose phosphate pathway
Pro	Proline
PRODH	Proline dehydrogenase
Pty	Proprietary company
Put	Putrescine
<i>p</i> -value	Probability value; the probability of making a Type I error
Pyr	Pyruvic acid

Q

QC	Quality control
Q-module	Ubiquinone module
Q-pool	Ubiquinone pool
QQQ	Triple quadrupole

R

R	Rest of the brain regions (collective symbol for AC, BST, CB) excluding the OB
R ²	Coefficient of determination; indicated the linearity data
RC	Respiratory chain
Redox	Reduction-oxidation
RET	Reverse electron transport
RGC	Retinal ganglion cells
Rib	Ribitol
RNA	Ribonucleic acid
ROS	Reactive oxygen species
RS	Region-specific
RT	Retention time

S

S/N	Signal-to-noise ratio
SAH	S-adenosylhomocysteine
SAM	S-adenosylmethionine
SASBMB	South African Society of Biochemistry and Molecular Biology
SAVC	South African Veterinary Council
SB	Experimental sample blank
SCD	Stearoyl-CoA desaturase
SCL	Succinyl-CoA ligase
SCoA	Succinyl-CoA
SD	Standard deviation
SDH	Succinate dehydrogenase
Ser	Serine
-SH	Thiol or sulfhydryl group
Si(CH ₃) ₃	Silyl group
SIRT	Sirtuin
SPF	Specific pathogen-free
SPSS	Statistical package for the social sciences

SREBP	Sterol regulatory element binding protein
SSA	Succinic semialdehyde
St.	Saint
Suc	Succinic acid

T

T	TCA cycle
TAG	Triacylglycerol
Tau	Taurine
TCA	Tricarboxylic acid
Thr	Threonine
TIA	Technological Innovation Agency
TIC	Total ion count/chromatogram
T_m	Melting temperature
TMCS	Trimethylchlorosilane
TMG	Trimethylglycine or betaine
TMS	Trimethylsilyl
TNB	2-Nitro-5-thiobenzoic acid
TOF	Time of flight
Trp	Tryptophan
Tukey HSD	Tukey's honest significant difference

U

U	Universal
UMP	Uridine monophosphate
UPS	Uninterrupted power supply
UQ	Oxidised ubiquinone or Coenzyme-Q10, CoQ
UQH ₂	Reduced ubiquinone, ubiquinol
UQ ₁₀	Ubiquinol
USA	United States of America
UV	Ultraviolet

V

v	Version; relating to software
v_1	Initial reaction velocity
Val	Valine
VDAC	Voltage-dependent anion channel
Vice versa	With the main items in the preceding statement the other way around
v_{max}	Maximal initial reaction velocity
VN	Vestibular nucleus
vs	Versus
VT	Vermont
VU	Vrije Universiteit

W

WB	Whole-body
WT	Wild-type; genetically unaltered sample (specific to this study)

Z

ZA South Africa

α

αAAA α-Aminoadipic acid

αHG α-Hydroxyglutaric acid

αKG α-Ketoglutaric acid

β

βAla β-Alanine

Latin terms

Ad libitum According to pleasure; feeding habits are the choice of the animal as food is constantly available

De novo Anew; from the beginning

In vivo In life; a process within a living organism

Post-mortem After death

CHAPTER 1 INTRODUCTION

1.1 Background and rationale for the study

Mitochondria, the small organelles found throughout the cytoplasm of nearly all eukaryotic cells, have many essential cellular functions which have been implicated in the etiology of numerous common metabolic and degenerative diseases. Genetic mutations that affect the energy producing system of mitochondria, namely the oxidative phosphorylation (OXPHOS) system, are the underlying causes of a clinically heterogeneous group of disorders which fall under the umbrella term, primary mitochondrial disease (MD). Collectively, MDs, with an estimated prevalence of one in 5000, are the most common inborn error of metabolism in humans. These diseases generally present with severe, detrimental clinical phenotypes and primarily affect tissues with a high energy demand. A deficiency in the first enzyme complex and primary electron entry point of the OXPHOS system, namely complex I (CI), causes the majority of childhood-onset MDs. Isolated CI deficiencies are often caused by a mutation in the nuclear NADH:ubiquinone oxidoreductase iron-sulfur protein 4 (*Ndufs4*) gene which codes for the NDUFS4 protein subunit of CI. The resulting phenotype, also known as Leigh syndrome, is characterised by neurodegeneration in specific brain regions, which drives disease progression and premature death. The mechanisms underlying the region-specific neurodegeneration are however poorly understood, and as a result, effective treatments are currently lacking.

The whole-body (WB) *Ndufs4* knockout (KO) mouse model faithfully recapitulates the clinical phenotype of humans with a CI deficiency. It has thus been widely utilised to investigate CI-associated pathology. However, the mechanisms that govern region-specific neuropathology remain to be resolved. The rationale behind this study was thus to fill important knowledge gaps by investigating the brain region-specific *in vivo* effects of the *Ndufs4* KO with a holistic experimental approach. A combination of spectrophotometric enzyme activity assays and multiple metabolomics techniques were employed to investigate: 1) the activities of individual mitochondrial enzyme complexes I to IV (CI to CIV) of the OXPHOS system; and 2) the metabolic profiles of the neurodegeneration-prone and -resilient brain regions from *Ndufs4* KO and wild-type (WT) mice. These results could then ultimately be used to determine potential correlations with regional neurodegeneration, as well as to identify potential targets for treatment or for the monitoring of treatment interventions and disease progression in prospective studies.

1.2 Structure of the dissertation

Chapter 1 is the background and rationale of the study. Chapter 2 gives an overview of the concepts relevant to the rationale and motivation for this study and provides the formulated problem statement. The aims, objectives and experimental strategy are summarised in Chapter 3. Thereafter, Chapter 4 gives a detailed description of the methods and materials that were utilised to execute this study. The results of the biochemical and metabolomics investigations of the selected brain regions of *Ndufs4* KO mice are then presented and discussed in Chapter 5 and Chapter 6, respectively. Finally, Chapter 7 summarises the findings and main conclusions according to the objectives formulated for this study. Chapter 7 also provides a few recommendations. Appendices A to I show supplementary information relevant to this study.

1.3 Image disclaimer

All images were generated by the writer. All images excluding those constructed from experimental data are for illustrative purposes only and are intended to convey concepts and do not necessarily represent true and accurate depictions.

1.4 Research output of the study

Although not listed as a specific objective, this study contributed to the field of mitochondrial disease through an oral presentation at an international conference:

Coetzer J., Lindeque J.Z., van der Westhuizen F.H., Louw, R. 2018. *Metabolomics investigation of Ndufs4 knockout mouse brain regions: a step closer to understanding the regional neurodegeneration in mitochondrial complex I deficiency*. Oral presentation: SASBMB-FASBMB 2018, July 8 – 11, Potchefstroom, South Africa.

1.5 Financial support

The work was supported by the National Research Foundation of South Africa (NRF, Grant no. 108146 and 111479), the Technological Innovation Agency of the Department of Science and Technology of South Africa (TIA, Grant no. Metabol. 01), and the North-West University (NWU). Opinions expressed and conclusions arrived at, are those of the authors and are not necessarily to be attributed to the NRF, TIA or NWU.

CHAPTER 2 LITERATURE REVIEW

2.1 Introduction

The goal of this literature review is to provide an overview of the concepts relevant to the rationale and motivation for this study. This review will entail a basic overview of mitochondria, their genetics and their functions. It will primarily focus on energy production via the oxidative phosphorylation (OXPHOS) system. The focus will then be shifted to primary mitochondrial disease (MD) with special attention to an isolated complex I (CI) deficiency. A detailed description will be given of the structure and function of CI as well as the genetics and clinical presentation of a CI deficiency. This will be followed by a brief summary of the metabolic cellular consequences of a mutation in the NADH:ubiquinone oxidoreductase iron-sulfur protein 4 (*Ndufs4*¹) gene, the most common cause of CI deficiency. Emphasis will then be placed on the complexity of the brain and the factors that could contribute to its frequent involvement in mitochondrial disease. An overview will then be given of the important discoveries made on the previously developed *Ndufs4* knockout (KO) mouse model. A brief introduction will be given on the potential of this disease model to expand the current understanding of the global mechanisms underlying the region-specific neurodegeneration in CI deficiency. The chapter will conclude with a brief summary and the problem statement which forms the foundation for this study.

2.2 Mitochondria

2.2.1 Mitochondrial structure and organisation

Mitochondria are small (0.5 μm to 1 μm in diameter, 7 μm in length), rod-like organelles found throughout the cytoplasm of nearly all eukaryotic cells (~800 to 2 500 per cell) (Wallace, 2013; Vasava & Mashiyava, 2016). They are especially abundant in cells with a high energy demand like skeletal muscle, heart, brain and liver. Within a cell, mitochondria are organised into dynamic networks in which the mitochondria's shapes, sizes and positions are continuously altered through the action of protein machinery in response to cellular and environmental cues (Murphy *et al.*, 2016; Murphy & Hartley, 2018). However, the basic structure of mitochondria remains largely conserved (Figure 2.1). The single mitochondrion consists of a double-membrane system in which a smooth outer mitochondrial membrane envelops a highly folded inner mitochondrial membrane (Valsecchi *et al.*, 2012; Zhou *et al.*, 2018). These membranes are separated by the intermembrane space. The folded inner mitochondrial membrane sheets, called cristae, protrude away from the outer mitochondrial membrane into the inner mitochondrial compartment, called

¹ Distinction between acronyms for genes and proteins are made by the use of italics and capitalisation, respectively e.g. *Ndufs4* (gene) and NDUFS4 (protein).

the mitochondrial matrix (Vasava & Mashiyava, 2016). The lipid bilayer of the outer mitochondrial membrane maintains the mitochondrial shape and contains large protein channels, called porin or voltage-dependent anion channel (VDAC), which allow free diffusion of low molecular weight ($\leq 10\,000$ Dalton) molecules (Vasava & Mashiyava, 2016). On the other hand, the lipid bilayer of the inner mitochondrial membrane is impermeable to ions and small molecules. It contains a high percentage of proteins as well as a high percentage of a “double” phospholipid named cardiolipin (Vasava & Mashiyava, 2016). The proteins play a role in oxidative energy metabolism and control the transport of metabolites between the cell cytosol and mitochondrial matrix. Consequently, the matrix contains a highly selected set of molecules under physiological conditions. The matrix also contains numerous enzymes which are involved in the metabolism of nutrient-derived molecules, as well as the mitochondria’s genetic material, called mitochondrial DNA (mtDNA) (Kapnick *et al.*, 2017; Cuperfain *et al.*, 2018).

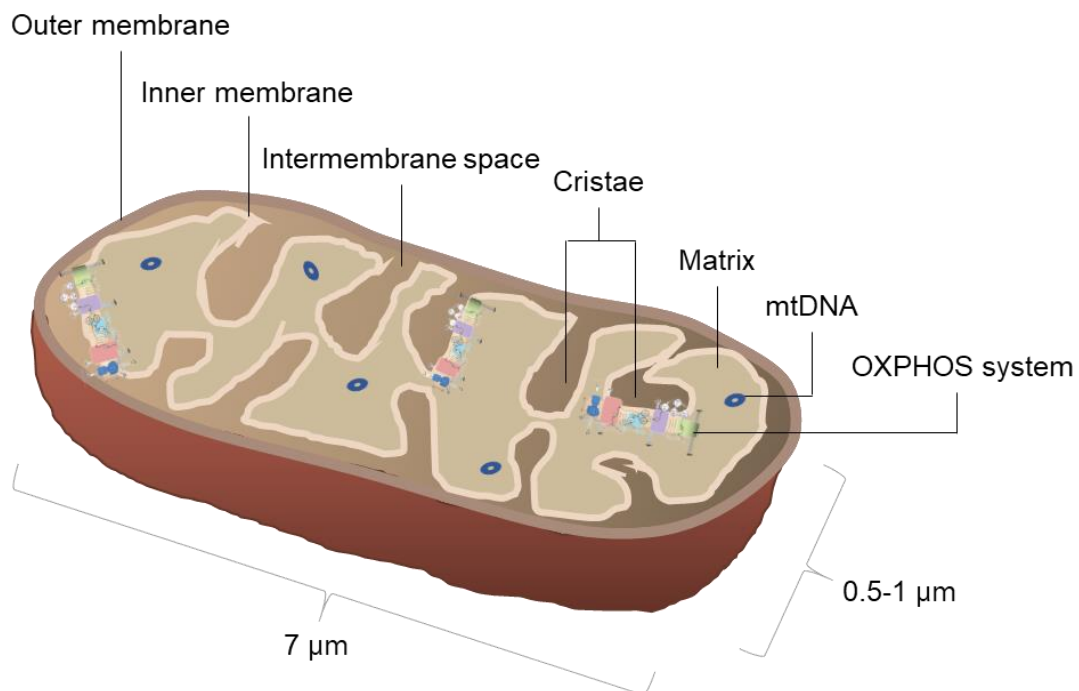


Figure 2.1: Basic structure of the mitochondrion.

The intermembrane space separates the outer- and inner membranes. Cristae are the folded sheets of the inner membrane that protrude into the matrix. The matrix contains a highly selected composition of numerous molecules, ions and enzymes. It also contains multiple copies of circular double-stranded mitochondrial DNA (mtDNA). The main function of mitochondria is to produce energy via the oxidative phosphorylation (OXPHOS) system which is localised in the inner membrane of mitochondria.

2.2.2 Mitochondrial genetics

The mtDNA is small circular, double-stranded DNA of approximately 16.5 kb in length which are present in varying number of copies (1 000 to 100 000) per cell depending on the cell type (Khan *et al.*, 2015; Kapnick *et al.*, 2017; Cuperfain *et al.*, 2018). The maternally inherited mtDNA consists of 37 genes that encode for 13 subunits of the mitochondrial energy generating oxidative phosphorylation (OXPHOS) system, two mitochondrial ribosomal ribonucleic acids (mt-rRNAs) and 22 mitochondrial transfer RNAs (mt-tRNAs) (Chinnery & Hudson, 2013; Koopman *et al.*, 2013; Cuperfain *et al.*, 2018). Collectively, the mitochondrial genes play a role in the synthesis of mitochondrial coded subunits. All other mitochondrial proteins (~1 500 types) are nuclear encoded and are imported typically, but not exclusively, via a mitochondrial targeting sequence to their specific intra-mitochondrial locations after being synthesised on cytosolic ribosomes (Khan *et al.*, 2015; Murphy & Hartley, 2018). The assembly of mitochondria and their components are thus highly dependent on the fine coordination between the nuclear and mitochondrial genomes.

2.2.3 Mitochondrial function and the OXPHOS system

The main function of mitochondria is to produce the majority of the metabolically useful forms of cellular energy, namely adenosine triphosphate (ATP). This occurs primarily through the OXPHOS system in the IMM (Sherratt, 1991). Often referred to as the metabolic hub of a cell, mitochondria additionally play a central role in cellular metabolism and homeostasis. They regulate cellular redox (reduction-oxidation) status, signal transduction and apoptosis; they maintain calcium (Ca^{2+}) homeostasis; they biosynthesise iron-sulfur (Fe-S) clusters, haem and ubiquinone (UQ); and they synthesise and degrade high-energy metabolic intermediates and the one-carbon units required for cell growth and repair (Kruse *et al.*, 2008; Valsecchi *et al.*, 2012; Wallace, 2013; Kapnick *et al.*, 2017; Murphy & Hartley, 2018). Many of these functions are in turn also directly or indirectly dependent on the function of the ATP-producing OXPHOS system.

The OXPHOS system consists of the respiratory chain (RC) and the phosphorylation system. These components function together to oxidise nutrient-derived molecules and create a functional proton (H^+) gradient that drives the phosphorylation of adenosine diphosphate (ADP) to ATP in the mitochondrial matrix (Figure 2.2) (Sherratt, 1991). The RC comprises a series of four multi-protein enzyme complexes I to IV (CI to CIV) and a set of electron carriers, namely UQ and Cytochrome c (Cyt c) (Sarewicz & Osyczka, 2015). The latter respectively constitute the Q-pool and the C-pool of the OXPHOS system. The phosphorylation system in turn, consists of the ATP synthase enzyme (sometimes referred to as complex V) and the transporters, adenine nucleotide translocase (ANT), and the phosphate carrier.

The substrates that drive the RC are obtained from the systematic, oxidative degradation of nutrients (glucose, fatty acids and amino acids). These degradative processes are catalysed by a series of cytosolic and/or mitochondrial enzymes that are organised into metabolic pathways (e.g. glycolysis, fatty acid β -oxidation, and amino acid degradative pathways) that converge at the tricarboxylic acid (TCA) cycle in the mitochondrial matrix (Sharpe & McKenzie, 2018). During these processes, chemical bond energy is transferred in the form of electrons to electron carriers such as the nicotinamide adenine dinucleotide (NAD⁺) co-enzyme and the flavin adenine dinucleotide (FAD) moiety of enzymes, generating the reduced forms of NAD⁺ (NADH) and FAD (FADH₂) (Koopman *et al.*, 2013).

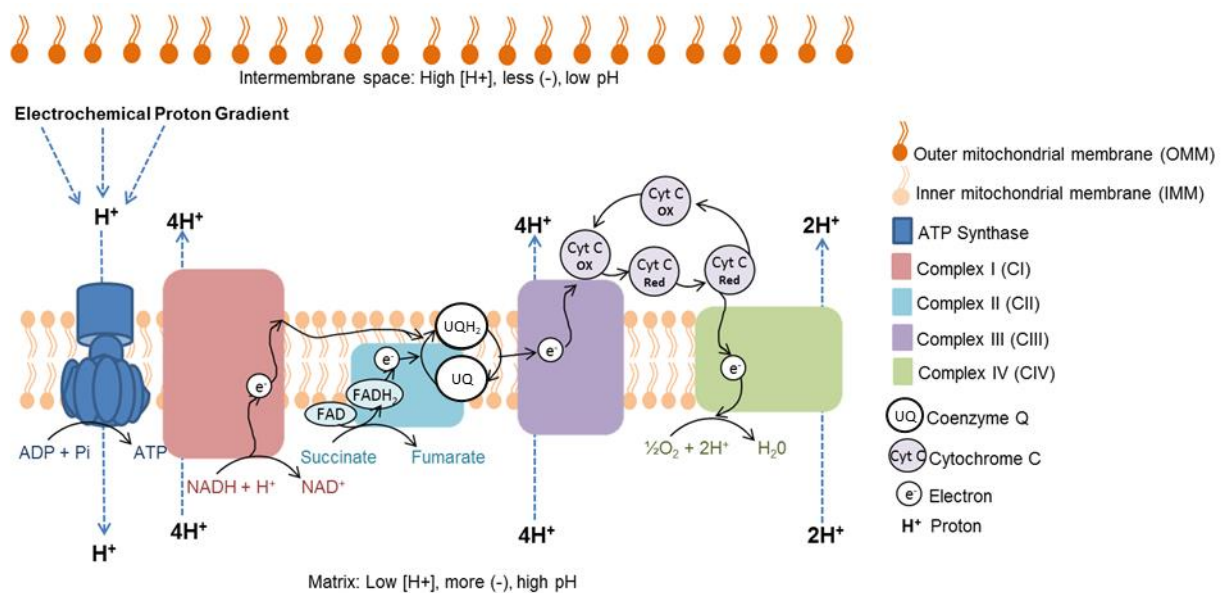


Figure 2.2: The oxidative phosphorylation system in the inner mitochondrial membrane.

Electrons (e⁻) enter the respiratory chain at complex I (CI) via reduced nicotinamide adenine dinucleotide (NADH) or at complex II (CII) when succinate is converted to fumarate to form reduced flavin adenine dinucleotide (FADH₂). As electrons are transferred, energy is liberated in small steps and used to irreversibly pump protons (H⁺) from the matrix to the intermembrane space (IMS). This creates an electrochemical proton gradient across the inner mitochondrial membrane that favours the flow of protons back to the matrix, especially through adenosine triphosphate (ATP) synthase. This then drives reversible ATP synthesis in the matrix from adenosine diphosphate (ADP) and inorganic phosphate (Pi). The adenine nucleotide translocase (ANT) and the phosphate carrier are not shown.

Electrons enter the OXPHOS system during the oxidation of NADH by complex I (CI) or when complex II (CII), which is also a TCA cycle enzyme, oxidises succinate to fumarate (Mailloux, 2015). The oxidation of succinate simultaneously reduces the FAD moiety within CII to FADH₂. Both CI and CII then transfer their electrons to UQ, producing the reduced form of UQ, ubiquinol (UQH₂ or UQ_{inol}). Complex III (CIII) mediates electron transport from UQH₂ to oxidised Cyt c (Valsecchi *et al.*, 2012). Reduced Cyt c, subsequently carries electrons to complex IV (CIV) where

they are utilised to reduce the final electron acceptor, molecular oxygen (O_2), to water (H_2O) (Picard *et al.*, 2016). As a result of its O_2 dependence, this process only occurs under aerobic conditions and is often referred to as mitochondrial respiration, hence the RC. The electron flow through the RC is thermodynamically spontaneous. It liberates energy which in part is utilised by CI, CIII and CIV to irreversibly pump H^+ from the matrix into the IMS (Valsecchi *et al.*, 2012). Due to the impermeability of the IMM to ions, H^+ accumulate in the IMS. This creates an inwardly directed transmembrane electrochemical proton motive force ($\Delta PMF = \Delta \Psi_m$ or mitochondrial electrical membrane potential + ΔpH_m or mitochondrial chemical proton gradient) across the IMM which favours the flow of protons back to the matrix (Mailloux, 2015). Protons re-enter the matrix primarily through the reversible H^+ pump, ATP synthase, which then drives ATP synthesis in the matrix from ADP and inorganic phosphate (Pi) (Brand & Nicholls, 2011; Koopman *et al.*, 2013). This mechanism is known as the Chemiosmotic theory and was first described by Peter Mitchell in 1961. Finally, matrix ATP can then be exchanged for cytosolic ADP by the ANT to drive energy-dependent cellular processes (Demine *et al.*, 2014). In addition to facilitating ATP production, a small percentage of electrons can leak directly to O_2 at any of the RC components, especially CI and CIII, thereby producing reactive oxygen species (ROS) (Grimm & Eckert, 2017; Zhao *et al.*, 2019). Under physiological conditions, ROS function as important signalling molecules and are carefully balanced by ROS scavenging or antioxidant systems (Zhao *et al.*, 2019).

The function and organisation of the OXPHOS system are more intricate than classically described. Effective functioning of the OXPHOS system depends on the proper assembly of each multi-subunit enzyme complex, consisting of between 4 to 45 subunits (Chinnery & Hudson, 2013; Koopman *et al.*, 2013). Nuclear DNA (nDNA) and mtDNA dually control this highly complex, multi-step process. It entails the assembly of various 'core' (catalysing) and 'accessory' (stabilisation) subunits with the help of specific proteins called 'assembly' factors (Koopman *et al.*, 2013). Furthermore, even though RC complexes are independent entities, the organisation of CI, CIII and CIV into super-complex structures have been observed, albeit in varying stoichiometry (Koopman *et al.*, 2013; Mourier *et al.*, 2014; Milenkovic *et al.*, 2017; Signes & Fernandez-Vizarra, 2018). In addition, other non-classical enzyme reactions can contribute to the respiratory capacity of the OXPHOS system by transferring electrons to the Q-pool that supplies electrons to CIII (Lemieux *et al.*, 2017; McDonald *et al.*, 2017). A multitude of factors also tightly regulate the OXPHOS system to meet tissue-specific requirements. In turn, OXPHOS regulates numerous cellular processes that are intimately associated with ATP production, redox reactions and the mitochondrial membrane potential (Wallace, 2005; Hüttemann *et al.*, 2007; Brand & Nicholls, 2011; Ho *et al.*, 2017; Wilson, 2017; Pacheu-Grau *et al.*, 2018). Expectantly, a perturbation in any component of the OXPHOS system could potentially disrupt a plethora of cellular reactions.

2.3 Mitochondrial dysfunction and disease

The vital role of mitochondria is most evident in the diseases that manifest when mitochondrial function is defective. Mitochondrial dysfunction can refer to an abnormality in any of the diverse mitochondrial functions. It is thus implicated in many common diseases such as metabolic, neurodegenerative, cardiovascular and neuromuscular disorders; cancer; and ageing (Brand & Nicholls, 2011; Khan *et al.*, 2015; Niyazov *et al.*, 2016; Picard *et al.*, 2016; Murphy & Hartley, 2018). However, primary mitochondrial disease (MD) refers to a clinically heterogeneous group of disorders caused by a genetically-based (primary) dysfunction (in nDNA or mtDNA) of the OXPHOS system (Reinecke *et al.*, 2012; Chinnery, 2014; Niyazov *et al.*, 2016). Depending on the site of the genetic defect, MD can either be inherited maternally (mtDNA) or in an autosomal dominant, autosomal recessive, or X-linked manner (Kapnick *et al.*, 2017). It is estimated that MD is the most common human inborn metabolic disease. It affects at least one in 5 000 new-borns (Rahman, 2012) or one in 4 300 adults (Gorman *et al.*, 2015) even though one in 200 individuals harbour mtDNA mutations (Khan *et al.*, 2015). This is because copies of mutant and wild-type mtDNA can coexist within a cell (aka heteroplasmy) and the number of mutant mtDNA must exceed a tissue-specific threshold before clinical symptoms ensue (Niyazov *et al.*, 2016).

The heterogeneous clinical features associated with MD are severe in essence, frequently causing progressive degeneration and death in infancy (Scheibye-Knudsen *et al.*, 2015). In general, MDs are characterised by impaired energy metabolism with secondary involvement of tissues, especially those that rely on OXPHOS to a great extent, such as the brain, heart, muscles, liver and eyes (Irwin *et al.*, 2013; Khan *et al.*, 2015). However, symptoms may present at any age, in different degrees of severity and may vary from an isolated tissue involvement to a multi-system disease (Irwin *et al.*, 2013; Khan *et al.*, 2015). Some MDs have a particular disease phenotype (such as Leigh syndrome, LS; Mitochondrial Encephalopathy, Lactic Acidosis, with Stroke-like episodes, MELAS; Leber's Hereditary Optic Neuropathy, LHON; and Kearns-Sayre Syndrome, KSS), while others present with clinical symptoms only suggestive of MD (Khan *et al.*, 2015). Moreover, MDs are pleiotropic and generally exhibit poor genotype-phenotype correlations. The mechanism/s underlying such heterogeneity are complex and not well understood. This is because the clinical symptoms reflect the end product of a multitude of potential contributing factors. This includes the genetic complexity of mitochondria as well as tissue-specific regulation and requirements of OXPHOS at different developmental stages (Rossignol *et al.*, 2000; Rossignol *et al.*, 2003; Dubinsky, 2009; Alston *et al.*, 2017; Frazier *et al.*, 2017).

The variable effects of MDs are also visible on a cellular level in accordance with the multitude of cellular mitochondrial-associated functions and energy-dependent processes. In contrast to most inborn metabolic diseases, in which a few metabolic perturbations are consistently observed, the metabolic effect of an OXPHOS deficiency is widespread and frequently result in a plethora of

cellular perturbations that are discrepantly observed among patients (Esterhuizen *et al.*, 2017). However, some cellular perturbations are more frequently encountered across MD cases and have been utilised for diagnosis or studying potential therapies. These include inadequate ATP production; altered mitochondrial membrane potential; disturbed cellular redox balance (NAD⁺/NADH ratio); increased or disturbed ROS production; aberrant mitochondrial morphology, altered lactic acid/pyruvic acid ratio; as well as alterations in the metabolism of TCA cycle intermediates, amino acids and one-carbon metabolism (Khan *et al.*, 2015; Esterhuizen *et al.*, 2017; Frazier *et al.*, 2017). The accumulation of lactic acid in the biological fluids of patients is considered as a hallmark of MD. Its increased production through lactic acid dehydrogenase (LDH) activity is thought to be stimulated by excess levels of pyruvic acid and NADH. The latter perturbations likely result from increased glycolysis for ATP production via substrate-level phosphorylation, sometimes in concert with impaired oxidation of pyruvic acid by a congested TCA cycle (Smeitink *et al.*, 2006; Falk *et al.*, 2008; Clarke *et al.*, 2013; Johnson *et al.*, 2013; Legault *et al.*, 2015; Ortigoza-Escobar *et al.*, 2016; Feldman *et al.*, 2017; Gaude *et al.*, 2018).

These cellular abnormalities can in turn individually or collectively contribute to, or trigger cell death. This can possibly occur due to a bio-energetic deficiency, aberrant cellular signalling, altered epigenetic and transcriptional changes, impaired transport of metabolites and ions, impaired calcium homeostasis and by damaging cellular components (Frazier *et al.*, 2017). The latter usually results from oxidative stress which occurs when ROS levels exceed the scavenging capacity of cellular antioxidant defence systems (Hoefs *et al.*, 2012; Zhao *et al.*, 2019). In addition, perturbations in redox balance have widespread consequences due to the utilisation of NAD⁺ or NADH as cofactors in a multitude of redox-dependent reactions. This includes the many reactions catalysed by dehydrogenase enzymes which in turn, play an important role in cellular metabolism. Furthermore, NAD⁺ is a co-substrate for enzymes such as sirtuins (SIRTs), ADP-ribose transferases (ARTs), poly (ADP-ribose) polymerases (PARPs) and cyclic ADP-ribose (cADPR) synthases (Verdin, 2015; Goodman *et al.*, 2018). These enzymes play important roles in cellular signalling, metabolism, antioxidant defence, calcium homeostasis, apoptosis, transcription, inflammation and DNA damage repair (Owens *et al.*, 2013; Verdin, 2015; Goodman *et al.*, 2018).

As a result of the genetic, clinic and metabolic complexities associated with MDs, the underlying pathogenic mechanisms are poorly understood (Frazier *et al.*, 2017). Consequently, proper and early diagnosis is difficult and often invasive, treatment is predominantly limited to alleviating symptoms, and no causative cure has yet been developed (Khan *et al.*, 2015; Parikh *et al.*, 2015; Viscomi *et al.*, 2015; Koopman *et al.*, 2016; Niyazov *et al.*, 2016; Wortmann *et al.*, 2017; Finsterer & Zarrouk-Mahjoub, 2018; Rahman & Rahman, 2018; Sorrentino *et al.*, 2018; Sage-Schwaede *et al.*, 2019). Furthermore, early diagnosis and supportive treatment are currently associated with substantial medical and socio-economic costs (McCormack *et al.*, 2017).

2.3.1 Mitochondrial complex I deficiency

The most common childhood-onset MD, accounting for nearly a third of all cases, is caused by alterations in genes that code for proteins that are involved in the structure, function or assembly of CI (Loeffen *et al.*, 2000; Smeitink *et al.*, 2001; Valsecchi *et al.*, 2010; Tucker *et al.*, 2011; Assouline *et al.*, 2012; Torraco *et al.*, 2015; Pacheu-Grau *et al.*, 2018). Most often, an isolated CI deficiency (OMIM 252010) is caused by a genetically-based deficit in the non-enzymatic, ubiquitously expressed, nuclear-coded protein subunit, NDUFS4 (Valsecchi *et al.*, 2012; Lake *et al.*, 2016; Ortigoza-Escobar *et al.*, 2016; Chen *et al.*, 2018a). It has been suggested that the high frequency of CI deficiency compared to deficiencies in the remaining OXPHOS complexes might be related to its genetics, structure and organisation within the OXPHOS system.

2.3.1.1 Complex I structure and function

Mammalian CI (NADH:ubiquinone oxidoreductase; EC 1.6.5.3.) is the largest complex of the RC, consisting of 45 subunits which are assembled into an L-shaped structure with a molecular weight of ~1 000 kDa (Assouline *et al.*, 2012; Guerrero-Castillo *et al.*, 2017) (Figure 2.3). The hydrophobic membrane arm of the L-shaped structure is embedded in the IMM and comprises the proton-translocating module (P-module). The peripheral arm protrudes from the base of the P-module into the matrix and comprises the ubiquinone module (Q-module) and the NADH-oxidising dehydrogenase module (N-module) (Sazanov, 2015). NADH binds at the tip of the N-module where it is oxidised to provide electrons to the flavin mononucleotide (FMN) moiety and a chain of iron-sulfur clusters which transfers the electrons to the Q-module. The Q-module transfers the electrons to UQ and connects the N- and P-modules. Through this connection, the energy released by the redox reactions in the N-module can be utilised by the P-module to pump H⁺ to the IMS (Tucker *et al.*, 2011).

CI therefore functions to re-oxidise the majority of cellular NADH and is a primary entry point of electrons into the RC. It is also a major proton pump that facilitates the maintenance of the electrochemical proton gradient across the IMM which drives ATP production (Luo *et al.*, 2015; Sazanov, 2015; Bilan & Belousov, 2016; Gaude *et al.*, 2018). In addition, CI is also considered to be an important source of ROS (Distelmaier *et al.*, 2009) and have been shown to be closely associated with other enzymes/complexes, especially other dehydrogenases (Sumegi & Srere, 1984; Nsiah-Sefaa & McKenzie, 2016; Sharpe & McKenzie, 2018).

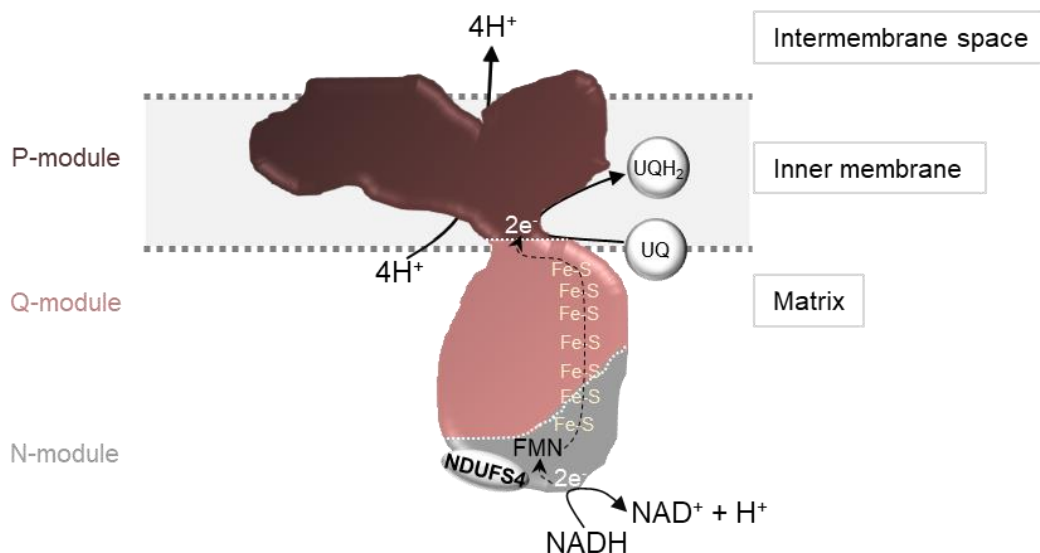


Figure 2.3: Structure of mitochondrial complex I.

The L-shaped structure of complex I (CI) comprises the N-module that binds and oxidises NADH, the Q-module that transfers electrons to ubiquinone (UQ), and the P-module that binds UQ and pumps protons (H⁺). The NDUFS4 subunit frequently mutated in CI deficiency is located at the tip of the N-module.

The assembly of the nuclear (38) and mitochondrial (7) encoded subunits of CI entails the multi-step formation and incorporation of five pre-assembled submodules (Guerrero-Castillo *et al.*, 2017). These submodules are first added to generate a ~830 kDa CI sub-complex constituting the Q- and P-modules. Then follows the addition of the N-module to produce the fully-assembled CI before the onset of super-complex formation (Giachin *et al.*, 2016; Guerrero-Castillo *et al.*, 2017). The NDUFS4 subunit, a small 18 kDa protein, is added as part of the N-module during the later stage of biogenesis. While it does not directly participate in catalytic activity, NDUFS4 is essential for CI assembly and stability and regulates CI activity and abundance through phosphorylation / dephosphorylation (De Rasmio *et al.*, 2008; Valsecchi *et al.*, 2012; Torraco *et al.*, 2015). In addition, NDUFS4 stabilises two iron-sulfur cluster binding sites of the N-module and shields them against O₂ exposure (Kahlhöfer *et al.*, 2017).

It is likely that CI deficiency is the most common MD due to: 1) its greater vulnerability to structural defects; and 2) a greater metabolic flexibility when CI is deficient. CI, compared to other OXPHOS complexes, has a larger size and greater number of subunits that have to be assembled (Irwin *et al.*, 2013; Rodenburg, 2016). It also has more subunits that are encoded by mtDNA which is more susceptible to mutations than nDNA. Moreover, the metabolic function of CI as a source of electrons for the RC can be readily bypassed through electrons entering at alternative sites such as CII and the Q-pool. This is unlike CIII and CIV which function in series (Irwin *et al.*, 2013; Rodenburg, 2016) or CII which is involved in the TCA cycle (Zieliński *et al.*, 2016). Thus, CII to CIV deficiencies might be less often identified due to their embryonic lethality (Rodenburg, 2016).

2.3.1.2 Genetics and clinical presentation

In accordance with other forms of MDs, CI deficiency lacks clear genotype-phenotype correlations and has a wide range of clinical manifestations (Distelmaier *et al.*, 2009; Koene *et al.*, 2012). It is however evident that a CI deficiency, especially when caused by mutations in nuclear-encoded genes like *Ndufs4*, has a great influence on neurodevelopment and patient survival. In most cases (>80%), these patients are diagnosed with a characteristic clinical phenotype known as Leigh syndrome (LS) or Leigh-like syndrome (Distelmaier *et al.*, 2009; Koene *et al.*, 2012; Valsecchi *et al.*, 2012; Lake *et al.*, 2016; Ortigoza-Escobar *et al.*, 2016; Rodenburg, 2016; Chen *et al.*, 2018a).

LS (OMIM 256000) was first described in 1951 (Leigh, 1951) and has more recently been defined as an early-onset (between three to 12 months of age, after a period of normal development), progressive neurodegenerative disorder characterised by focal, bilateral symmetrical lesions in one or more areas of the central nervous system (CNS) (Baertling *et al.*, 2014; Lake *et al.*, 2015; Bonfante *et al.*, 2016; Ortigoza-Escobar *et al.*, 2016; Rodenburg, 2016). These lesions are especially observed in the brainstem and basal ganglia but the thalamus; cerebellum; spinal cord; and optic nerves are also frequently involved. In many cases the rapid clinical deterioration results in fatal respiratory failure and premature death at a median age of 2.4 years (Sofou *et al.*, 2014; Bonfante *et al.*, 2016). Diagnosis of Leigh-like syndrome, is considered when patients exhibit most LS symptoms, but lack typical neuropathology or only partly meet diagnostic criteria (Bonfante *et al.*, 2016; Lake *et al.*, 2016). Even though LS, with a prevalence of at least one in 40 000, is not exclusively caused by a CI deficiency, the correlation between CI deficiency and LS development is much higher than for other causes, such as genetic defects in the remaining OXPHOS components (CII to CV and UQ) or enzymes such as pyruvic acid dehydrogenase (PDH) (Ruhoy & Saneto, 2014; Lake *et al.*, 2015; Gerards *et al.*, 2016; Rodenburg, 2016).

The neuropathological lesions in CI-deficient LS patients are predominantly present in the more ATP-dependent grey matter of the CNS, suggesting a role of a bio-energetic deficit (Lake *et al.*, 2015). The lesions are characterised by reactive gliosis²; demyelination; vascular hypertrophy and proliferation; progressive neuronal deterioration with relative preservation of some neurons; vacuolation³ leading to conspicuous cavitation or spongiosis; and necrosis⁴ (Cavanagh & Harding, 1994; Distelmaier *et al.*, 2009; Lake *et al.*, 2015). The clinical phenotype and disease progression of LS patients largely correlate with lesion topography and development (Ruhoy & Saneto, 2014). Brainstem involvement manifests as swallowing difficulty, persistent vomiting, abnormal

² Proliferation and infiltration of activated non-neuronal cells.

³ Loosening of bundles of astrocytic and neuronal processes in a dense network of brain cells known as the neuropil.

⁴ A dramatic form of cell death which results in the rupturing of the cell membrane and release of intracellular contents into the extracellular environment, which typically induces an inflammatory response (Fricker *et al.*, 2018).

thermoregulation and respiratory abnormalities (Gerards *et al.*, 2016). Neurologic symptoms related to the basal ganglia and cerebellum include deterioration of motor functions, involuntary movements, ataxia, ophthalmologic⁵ abnormalities and progressive cognitive decline (Ruhoy & Saneto, 2014). Encephalopathy⁶ is also expressed with failure to thrive, developmental delay and regression⁷, hypotonia, dystonia and seizures (Ruhoy & Saneto, 2014; Lake *et al.*, 2015; Bonfante *et al.*, 2016; Gerards *et al.*, 2016). Extra-CNS symptoms are variably observed and have also been suggested to be neurologically driven. These include cardiomyopathy, myopathy, renal failure, or gastrointestinal dysfunction to name a few (Quintana *et al.*, 2010; Ruhoy & Saneto, 2014; Lake *et al.*, 2015; Bonfante *et al.*, 2016). The latency of clinical symptom development in LS patients is thought to be related to the protective and supportive gestational environment and energy metabolism of prenatal tissues (Distelmaier *et al.*, 2009). During the postnatal period, OXPHOS requirements of tissues tend to increase along with their susceptibility to an OXPHOS deficiency, especially when subjected to metabolic challenges such as an acute infection or prolonged fasting (Distelmaier *et al.*, 2009; Baertling *et al.*, 2014; Gerards *et al.*, 2016).

As for MDs in general, the characteristic progressive pathophysiology of CI deficiency is not well understood and therapeutic and curative strategies are limited and unsatisfactory (Koopman *et al.*, 2013; Lake *et al.*, 2015; Chen *et al.*, 2018a).

2.3.1.3 Cellular consequences of complex I deficiency due to *Ndufs4* mutations

Depending on the site, genetic mutations can decrease the amount of fully assembled, catalytically active CI (Ugalde *et al.*, 2004). When CI activity decreases beyond a cell-specific threshold, detrimental cellular effects ensue (Rossignol *et al.*, 2000; Rossignol *et al.*, 2003; Pathak & Davey, 2008; Telford *et al.*, 2009). The remainder of this review focuses on the current knowledge concerning a *Ndufs4*-related CI deficiency. This is because *Ndufs4* is a mutational 'hotspot' of CI deficiency and its deficit mostly manifests in the predictable LS phenotype.

Studies have shown that NDUFS4-deficient patient-derived skin fibroblasts have an inactive ~830 kDa CI subcomplex which lacks the N-module (Breuer *et al.*, 2013). However, these CI-deficient models also exhibit residual CI activities of between 15% to 75% of controls which inversely correlates with the severity of disease (Breuer *et al.*, 2013). Most of the measured cellular effects coincide with the immediate function of CI in the OXPHOS system even though correlations between these factors and residual CI activity seem controversial (Breuer *et al.*, 2013). The NDUFS4-deficient fibroblasts typically display decreased ATP levels; depolarised

⁵ Dealing with the structure, function and diseases of the eye.

⁶ A disease affecting brain function.

⁷ Loss of previously acquired skills.

(less negative) inner mitochondrial membrane potential; aberrant mitochondrial morphology; increased or disturbed NADH levels and ROS production; disturbed calcium (Ca²⁺) homeostasis; metabolite imbalances; elevated lactic acid levels; and cell death (Luo *et al.*, 1997; Smeitink *et al.*, 2004; Visch *et al.*, 2004; Visch *et al.*, 2006; Verkaart *et al.*, 2007a; Verkaart *et al.*, 2007b; Distelmaier *et al.*, 2009; Valsecchi *et al.*, 2009; Koopman *et al.*, 2010; Valsecchi *et al.*, 2010; Blanchet *et al.*, 2011; Roostenberg *et al.*, 2012; Rodenburg, 2016; Iannetti *et al.*, 2018). The CI deficiency also affects the activities of other components of the OXPHOS system by disrupting super-complex formation, especially concerning CIII (Budde *et al.*, 2000; Ugalde *et al.*, 2004).

Considering that these findings overlap with the commonly observed perturbations in MDs, it is difficult to discern a CI deficiency. Moreover, it is also challenging to explain its characteristic clinical phenotype solely based on these cellular alterations. The molecular mechanisms underlying the primary involvement of the CNS and of neuropathogenic changes in specific brain regions, despite whole-body CI dysfunction, is only partially understood. Studies on brain tissues have been impeded by the difficulty to procure samples from patients and controls, inadequate sizes of homogeneous patient cohorts and *post-mortem* delays that could influence results e.g. due to ongoing metabolism (Epstein *et al.*, 2013; Ivanisevic *et al.*, 2014). Furthermore, cellular models cannot be easily extrapolated to an *in vivo* context, not to mention its limitations in representing the complexity of an intricate system such as the CNS.

2.3.2 The complexity of the brain and its vulnerability to OXPHOS deficiencies

The mammalian brain, which can be anatomically subdivided into multiple brain regions, functions as a coordinating centre that communicates with organs and tissues. This is done through processing information and controlling motor, sensory, and cognitive functions through electrical and chemical stimuli (Widmaier *et al.*, 2008; Gonzalez-Riano *et al.*, 2016; Zheng *et al.*, 2016b). Each brain region regulates a few specific functions through the interdependent activities of the different cell types within that brain region. Neurons receive and transmit signals, while glial cells (astrocytes, oligodendrocytes and microglia) predominantly function to maintain tissue homeostasis; provide structural and metabolic support to neurons; as well as facilitate neuronal protection and recovery after injury (Widmaier *et al.*, 2008; Jha & Morrison, 2018).

Metabolically, the brain is one of the most active organs in the body, and although it represents a mere 2% of total body weight, it consumes a high fraction of total body O₂ (~20%) and circulating glucose (~25%) (Kety, 1957; Sokoloff, 1960; Gonzalez-Riano *et al.*, 2016; Copley *et al.*, 2018). In accordance, under physiological conditions, the majority of brain energy is derived from glucose by way of glycolysis, the TCA cycle and oxygen-dependent OXPHOS (Dienel, 2018). Of the total energy consumed by the brain, the majority (70% to 80%) is expended by neurons (Harris *et al.*, 2012; Hyder *et al.*, 2013; Camandola & Mattson, 2017; Dienel, 2018). Most of this energy is

utilised on synapses⁸ to maintain and restore electrochemical gradients and for the uptake and recycling of neurotransmitters (Harris *et al.*, 2012; Magistretti & Allaman, 2015). Accordingly, when neuronal ATP production is insufficient, the synapses are the first to degenerate (Harris *et al.*, 2012).

Under non-physiological conditions, the brain can also utilise alternative energy substrates. Under conditions of prolonged fasting or in the brains of milk-fed new-borns, glucose is replaced with ketone bodies as a primary source of energy (Magistretti & Allaman, 2015; Jha & Morrison, 2018). Under conditions of stress or limited O₂, the brain can become more reliant on the metabolism of lactic acid, acetic acid, amino acids and lipids for energy production (Griffin & Bradshaw, 2017; Dienel, 2018; Jha & Morrison, 2018). However, in contrast to other high-energy demand tissues, the brain has limited capacity for utilising these alternative substrates for energy, especially fatty acids via mitochondrial fatty acid β -oxidation (Panov *et al.*, 2014; Dienel, 2018). This is due to tissue-specific expression and regulation of enzymes. Limited fatty acid oxidation in brain cells has been suggested to have a neuroprotective function, as the oxidation of fatty acids promotes mitochondrial ROS production and generates ATP too slowly to meet neuronal energy demands (Schönfeld & Reiser, 2017). Furthermore, the brain also has limited capacity for storing energy; i.e. only small amounts of glycogen are deposited in astrocytes (Koopman *et al.*, 2013; Falkowska *et al.*, 2015; Bonvento *et al.*, 2017; Camandola & Mattson, 2017). As a result, the brain is highly dependent on a continuous, external supply of O₂ and nutrients from the blood. This is also referred to as tight neurovascular- and neurometabolic-coupling (Bélanger *et al.*, 2011). However, the influx of metabolites and ions into the brain is highly regulated and selective due to the presence of the blood-brain barrier (BBB), blood-cerebrospinal fluid barrier (BCSFB) and specific transport mechanisms (Camandola & Mattson, 2017). Together, these components function to keep a stable composition in the brain irrespective of fluctuating substrate concentrations in the blood. The limited influx of non-glucose substrates into the brain therefore also limits the use of these alternative substrates for fuelling the brain (Dienel, 2018).

The O₂ and nutrients which the brain consume are uniquely utilised by each brain cell type, even in different neuron types. As a result, brain cells display differential sensitivities to various insults. Although a controversial matter, it is generally accepted that neurons primarily depend on OXPHOS for energy (oxidative) and contain a large number of mitochondria, whereas astrocytes mainly utilise glycolysis (glycolytic) for energy via substrate-level phosphorylation (Neves *et al.*, 2012; Magistretti & Allaman, 2015; Camandola & Mattson, 2017). A higher OXPHOS capacity also means increased susceptibility to OXPHOS deficiency as well as a higher rate of ROS production and vulnerability to oxidative insults (Grimm & Eckert, 2017). Neurons also have

⁸ The junction between two neurons where electric impulses are transmitted from one neuron to another.

limited glycolysis capacity and primarily metabolise glucose (as glucose-6-phosphate) through the pentose-phosphate-pathway (PPP) for antioxidant defence (Magistretti & Allaman, 2015). Previous studies have suggested that energy production in neurons require the glucose-derived substrates (such as lactic acid) produced by glial cells (Magistretti & Allaman, 2015). The metabolic activity of neurons and glial cells are therefore tightly coupled⁹ and form an interactive metabolic unit within a brain region. This unit depends on a series of shuttling mechanisms between brain cells to transfer metabolic intermediates; e.g. lactic acid; glutamic acid and glutamine; branched-chain amino acids; ketone bodies; and lipids, to name a few (Pellerin & Magistretti, 1994; Dubinsky, 2009; Gimeno-Bayón *et al.*, 2014; Magistretti & Allaman, 2015; Mason *et al.*, 2015; Camandola & Mattson, 2017; Liu *et al.*, 2017; Yudkoff, 2017; Jha & Morrison, 2018). Consequently, perturbations affecting any of the brain cell types within such a metabolic unit are expected to have secondary effects on the surrounding brain cells (Dubinsky, 2009).

The consumption of O₂ and glucose in the brain is not exclusively utilised for energy metabolism, but also for other vital processes. The brain greatly depends on O₂-derived reactive species to perform critical functions through redox signalling (Cobley *et al.*, 2018). It also depends on glucose-derived metabolites as precursors for structural components, amino acids, nucleotides, as well as reduced nicotinamide adenine dinucleotide phosphate (NADPH) for maintaining redox homeostasis and for synthesising neurotransmitters (Camandola & Mattson, 2017; Dienel, 2018). These functions can therefore be influenced by energy metabolism and vice versa. Relative to other tissues, brain cells, especially neurons, are extremely vulnerable to the detrimental effects of oxidative stress, not only in terms of aberrant cell signalling, but also in terms of oxidative damage to cellular components (Cobley *et al.*, 2018). The factors contributing to the vulnerability of the brain to oxidative stress are numerous, and include: i) a high content of unsaturated lipids (susceptible to lipid peroxidation); ii) free radical- and calcium-associated regulation of critical functions (e.g. synaptic plasticity); iii) high neuronal mitochondrial density; iv) neurotransmitter metabolism and auto-oxidation; v) abundance of redox-active transition metals; vi) comparatively low endogenous antioxidant defence; vii) susceptibility to glutamic acid excito-toxicity and glucose induced oxidative stress; as well as viii) the presence of microglia, the resident immune cells of the CNS which generate reactive species as part of their neuroprotective function (Cobley *et al.*, 2018).

Neurons are also post-mitotic cells that rarely undergo mitosis and regeneration. Consequently, they are prone to accumulate damage and genetic mutations over time, especially when autophagy, which has been suggested to be dependent on Cl activity, is defective (Son *et al.*, 2012; Kim *et al.*, 2018; Thomas *et al.*, 2018; Verheijen *et al.*, 2018). Autophagy refers to the

⁹ Also referred to as neuron-glia metabolic coupling.

intracellular degradation of cellular components in lysosomes for normal turnover, adaptation to starvation and/or synapse development (Hara *et al.*, 2006; Son *et al.*, 2012). Other factors that might induce a greater vulnerability of brain cells to degenerate in a CI deficiency might be related to differences in OXPHOS protein expression, inhibition threshold levels and control of the RC and OXPHOS. For instance, it has been reported that CI activity is a major controlling factor of OXPHOS in brain mitochondria, especially in synaptosomes (Rossignol *et al.*, 2000; Pathak & Davey, 2008; Cocco *et al.*, 2009; Telford *et al.*, 2009; Sauerbeck *et al.*, 2011).

In summary, even though information on the exact mechanisms are lacking, there are a few factors that could contribute to the susceptibility of the CNS, particularly neurons, to OXPHOS deficiencies and the high incidence of neuropathological features in MDs: 1) high metabolic requirements; 2) limited metabolic flexibility; 3) limited energy reserve; 4) limited transport of non-glucose nutrients across the BBB; 5) high OXPHOS dependency for ATP production, especially in neurons; 6) complex interdependence of brain cells within a brain region; 7) the reliance of vital, non-energy producing functions on energy substrates; 8) increased susceptibility to oxidative stress; 9) the post-mitotic nature of neurons; and 10) tissue-specific expression and control of OXPHOS.

The potential mechanisms that could underlie the susceptibility of specific brain regions to an OXPHOS or CI deficiency are less obvious. It has for example been reported that regional differences in CI gene expression did not correlate with the regional vulnerability to neurodegeneration in a CI deficiency (Wirtz & Schuelke, 2011). Nevertheless, there are a multitude of other known factors that could collaboratively contribute to the brain regional susceptibility (Dubinsky, 2009). Moreover, region-specific involvement in disease is not a feature that is unique to LS. Brain regional neurodegeneration is also observed in other neurological disorders, albeit at different brain regions. These include neurodegenerative diseases such as Alzheimer's disease, spinocerebellar ataxia type I, Huntington's disease and Parkinson's disease (Lee *et al.*, 2013; Gonzalez-Riano *et al.*, 2016) as well as in excitotoxic injury (Jäger *et al.*, 2015) and in hypoxic-ischemic encephalopathy (Lake *et al.*, 2015). The appearance of selective neuronal- and/or brain regional vulnerability in neurodegenerative disorders is thus a factor of both disease-specific etiology and neuron-specific, or brain region-specific responses to that particular insult (Wang & Michaelis, 2010). Each of these in turn, is extremely complex, being the end product of a multitude of variable factors, both internal (genomic, transcriptomic, proteomic and metabolomic) and external (intercellular, physiological and environmental) (Rossignol *et al.*, 2000; Dubinsky, 2009; Lee *et al.*, 2013). As a result, the mechanisms underlying region-specific vulnerability of the brain to certain insults, including a CI deficiency, is unclear and require further investigation. However, this has previously been impeded by the lack of suitable animal models, as described in Section 2.3.1.3.

2.3.3 The *Ndufs4* knockout mouse model of complex I deficiency

A large number of chemically and genetically induced mouse models have been developed to study an isolated CI deficiency (Ingraham *et al.*, 2009; Breuer *et al.*, 2012; Leong *et al.*, 2012; Irwin *et al.*, 2013; Torraco *et al.*, 2015; Kim *et al.*, 2017; Wang *et al.*, 2017). Of particular interest is Palmiter's (Kruse *et al.*, 2008) whole-body, homozygous *Ndufs4* knockout (KO) mouse model (hereafter referred to as WB *Ndufs4* KO), which to date has been considered the most accurate and well characterised model of LS (Irwin *et al.*, 2013; Ferrari *et al.*, 2017).

In the WB *Ndufs4* KO mice, the *Ndufs4* gene was knocked out by the excision of its second exon which encodes for the last section of the mitochondrial targeting sequence, and first 17 amino acids of the mature NDUFS4 protein (Kruse *et al.*, 2008). It has been shown that by impeding the formation and incorporation of a mature NDUFS4 protein, CI was destabilised. This led to the formation of an inactive 830 kDa CI sub-complex which lacks the N-module and thus also NADH oxidation (Calvaruso *et al.*, 2011; Valsecchi *et al.*, 2012). This was similar to the observation made for *Ndufs4*-deficient patient fibroblasts (Section 2.3.1.3) (Ugalde *et al.*, 2004; Leshinsky-Silver *et al.*, 2009; Valsecchi *et al.*, 2010). Despite the absence of NDUFS4, the WB *Ndufs4* KO mice tissues display variable residual CI activity (9% to 44%) and CI-driven mitochondrial respiration (~50%), resulting from a partially active, fully assembled CI (Kruse *et al.*, 2008; Quintana *et al.*, 2010; Calvaruso *et al.*, 2011; Sterky *et al.*, 2011; Valsecchi *et al.*, 2012; Johnson *et al.*, 2013; Manjeri *et al.*, 2016). While CI lacked the NDUFS4 subunit, it was presumably stabilised through its association with other complexes, especially CIII, into super-complexes. It was subsequently confirmed that NDUFS4 is required for the stabilisation and proper assembly of CI (Kruse *et al.*, 2008).

Similar to LS patients that initially appear asymptomatic, WB *Ndufs4* KO mice seem normal until five weeks of age, when the characteristic neurological and behavioural anomalies start. These anomalies progress until premature death at around seven weeks. Since the mice die before child-bearing age, they are obtained by inter-breeding whole-body heterozygous *Ndufs4* KO mice. The histopathological changes in the WB *Ndufs4* KO mice appear early and prominent in the brainstem, cerebellum and olfactory bulbs, and progress to the striatum (a member of the basal ganglia), while the mid- and forebrain seem to be morphologically unaltered (Kruse *et al.*, 2008; Quintana *et al.*, 2010; Quintana *et al.*, 2012; Song & Cortopassi, 2015). In addition, pathological changes are observed in the retinal ganglion cells (RGC), starting from postnatal day (PN) 16 and ending in RGC death after PN42 (Yu *et al.*, 2015; Song *et al.*, 2017). The brain lesions are characterised by spongiform neurodegeneration, vascular proliferation, gliosis, aberrant mitochondrial morphology (swollen and/or compact cristae) in nerve terminals and necrosis (Kruse *et al.*, 2008; Quintana *et al.*, 2010). Similar to the phenotype of LS, the behavioural changes correlated with the focal damage to the CNS and included progressive encephalopathy,

blindness, ataxia, breathing abnormalities, loss of motor ability, failure to thrive, hypothermia, elevated serum lactic acid levels and death most commonly due to respiratory failure (Kruse *et al.*, 2008).

The initial development of the WB *Ndufs4* KO model from a whole-body conditional *Ndufs4* allele (*Ndufs4*^{lox/lox}), also enabled the generation of cell-specific and time-specific *Ndufs4* KO mice on the same genetic background. Exon 2 in the *Ndufs4*^{lox/lox} mice, which is flanked by loxP sites, can be excised by utilising various Cre-expressor lines or viral inactivation techniques (Kruse *et al.*, 2008). This feature could be utilised to investigate the role of specific tissues or cells in LS pathology. By deleting exon 2 exclusively in brain cells (NesKO mice), it was shown that NesKO mice and WB *Ndufs4* KO mice exhibited very similar phenotypes (Quintana *et al.*, 2010). It was therefore concluded that LS disease pathology is predominantly neurologically driven. When inducing the brain-tissue specific *Ndufs4* KO at a later stage of development (PN60), the mice developed an early-stage phenotype, suggesting that the absence of *Ndufs4* in brain cells prior to PN60 might be more detrimental (Quintana *et al.*, 2010). Subsequent studies have shown that selective deletion of *Ndufs4* in other affected tissues, such as the heart (Sterky *et al.*, 2011; Karamanlidis *et al.*, 2013; Chouchani *et al.*, 2014a), skeletal muscle (Sterky *et al.*, 2011), liver and hematopoietic lineages (Jin *et al.*, 2014), caused milder phenotypes with increased longevity despite severe CI impairment. These findings, together with other studies, showed that while *Ndufs4*-deficient peripheral tissues might contribute to the global LS phenotype, they are not the predominant drivers (Di Meo *et al.*, 2017; Lee *et al.*, 2019). Spectrophotometric measurements of isolated CI activity in different tissues of WB *Ndufs4* KO mice, including the whole-brain, suggested that the vulnerability of the CNS was not related to a more detrimental effect of the *Ndufs4* KO on isolated CI activity, and that other tissue-specific factors are expected to play a role (Calvaruso *et al.*, 2011).

Most LS patients and WB *Ndufs4* KO mice succumb due to respiratory failure. To elucidate the CNS-related factors that ultimately cause death, *Ndufs4* was selectively inactivated in the vestibular nucleus (VN) of the brainstem (Quintana *et al.*, 2012). Specifically, this area regulates breathing and is a prominent site of neurodegeneration in WB *Ndufs4* KO mice. The VN-specific KO mice recapitulated some of the pathological features of the WB *Ndufs4* KO mice. This included local glial activation and neurodegeneration, motor- and breathing-abnormalities as well as premature death. These features could be attenuated by re-expressing *Ndufs4* in the VN (Quintana *et al.*, 2012). Collectively, this suggested that neurodegeneration in the BST has a pivotal role in LS pathology.

Brain regions can differ in their cellular compositions; i.e. varying ratios of neurons to glial cells and various neuronal populations. Relative neuronal preservation in the areas with prominent neurodegeneration are characteristic of LS lesions (Lake *et al.*, 2015). To determine the

contribution of distinct neuronal populations to the LS phenotype of WB *Ndufs4* KO mice, neuron-specific *Ndufs4* KO mice were developed and investigated. Conditional inactivation of the *Ndufs4* gene in glutamatergic¹⁰ or γ -aminobutyric acidergic (GABAergic) neurons of the whole-brain, but not in other distinct classes of neurons (GABAergic striatal medium spiny neurons, dopaminergic neurons, cholinergic neurons or cerebellar Purkinje cells), resulted in neurodegeneration, lesion formation and a lethal phenotype with visible behavioural deficits corresponding with LS symptoms (Quintana *et al.*, 2010; Choi *et al.*, 2011; Kim *et al.*, 2015; Chen *et al.*, 2017a; Choi *et al.*, 2017; Bolea *et al.*, 2019). Mice with *Ndufs4*-deficient glutamatergic neurons most accurately recapitulated the neuro-inflammatory profile of the WB *Ndufs4* KO mice, primarily affecting the brainstem and cerebellum. Whereas mice with *Ndufs4*-deficient GABAergic neurons presented a more restricted neuro-inflammatory profile and primarily affected the basal ganglia and olfactory bulbs (Bolea *et al.*, 2019). The absence of neurodegeneration in the other neuron-specific *Ndufs4*-deficient mice suggested that the degeneration of these neurons (e.g. cerebellar Purkinje cells) in the WB *Ndufs4* KO mice occurred secondary to a CI deficiency. That is to say via non-autonomous mechanisms that require the contribution of other CI-deficient or damaged brain cells (Quintana *et al.*, 2010). Consequently, it was suggested that *Ndufs4*-deficient glutamatergic- and GABAergic-neurons are the primary drivers of the onset and progression of the pathology in a CI deficiency, even though the plethora of symptoms might result from the combined contribution of all affected neuronal populations. The mechanisms driving the neuron-specific loss is unclear.

Over the past few years, studies have aimed to elucidate these mechanisms. The close correlation observed between neurodegeneration, disease severity and degree of gliosis has been proposed to indicate that progressive gliosis might be a major contributing factor that drives neurodegeneration in LS patients and *Ndufs4* KO disease models (Quintana *et al.*, 2010; Lake *et al.*, 2015; Bolea *et al.*, 2019). Furthermore, therapeutic strategies which attenuated neurodegeneration and prolonged lifespan in WB *Ndufs4* KO mice without structurally correcting for the CI defect, also alleviated gliosis in these mice (Johnson *et al.*, 2013; Jain *et al.*, 2016). The signals triggering gliosis and its exact role in neurodegeneration, i.e. whether it is a cause or consequence of neuronal death or perhaps both, is however, uncertain.

Quintana *et al.* (2010) first proposed that a CI deficiency leads to the release of cellular signals that activate glial cells. Activated glial cells in turn, causes oxidative stress, cytokine release and induction of neuronal apoptosis via the extrinsic pathway which, in the presence of an energy deficit, causes necrotic neurodegeneration and lesion formation. By investigating retinas and the retinal innervation of WB *Ndufs4* KO mice, Yu *et al.* (2015) proposed potential 'cellular signals'

¹⁰ The term "ergic" defines a neuron type according to the neurotransmitter released by that particular neuron e.g. glutamatergic neurons release the neurotransmitter glutamic acid.

that might induce an immune response and progressive, detrimental gliosis. That is, the presentation of mutant CI as an antigen on immune cells or perhaps the necrosis of specific cells experiencing a bio-energetic deficit. It was later proposed that the cumulative effects of a bio-energetic deficit and increased oxidative stress, might be the initial cause of apoptosis in a subset of sensitive retinal neurons (Song *et al.*, 2017). The death of these retinal neurons then triggers inflammation and secondarily cause the subsequent death of more cells.

In accordance with NDUFS4-deficient patients, studies on the brains of WB *Ndufs4* KO mice have also suggested that neurodegeneration might be related to the effects of a bio-energetic deficiency, perturbed NAD⁺/NADH ratio, disturbed ROS homeostasis and/or aberrant mitochondrial morphology. Previously, it was shown that maximal CI-dependent ATP production (expressed per tissue mass) was decreased in the brain (Manjeri *et al.*, 2016) and unaltered in the skeletal muscle (Alam *et al.*, 2015) and heart (Karamanlidis *et al.*, 2013; Manjeri, 2017). Moreover, the whole-brain metabolic profile of WB *Ndufs4* KO mice (PN30) indicated perturbations in the main energy producing pathways (Johnson *et al.*, 2013). This was evident by the accumulation of glycolytic intermediates, pyruvic acid and lactic acid; together with decreased levels of free amino acids, free fatty acids, nucleotides, dopamine and GABA. Another independent study on WB *Ndufs4* KO mice, reported significantly increased intracerebral lactic acid levels, an indicator of disturbed energy metabolism, prior to the onset of neurodegeneration (Takahashi *et al.*, 2019). Furthermore, signs of aberrant TCA cycle metabolism, an important source of energy and OXPHOS substrates, has been observed in the brainstem (Piroli *et al.*, 2016).

The WB *Ndufs4* KO mouse brain has also exhibited an increase in energy expensive lipid synthesis in the neurodegeneration-prone brain regions (Liu *et al.*, 2015; Liu *et al.*, 2017). Disturbances in brain energy metabolism was also suggested by the increased activation of the mechanistic Target Of Rapamycin (mTOR) pathway (Johnson *et al.*, 2013). This pathway is a master regulator of mammalian metabolism and growth through sensing of growth factors, energy status, oxygen and amino acids. A study conducted on neurons derived from LS patient cells has suggested that increased mTOR signalling caused neuronal death through ATP depletion (Zheng *et al.*, 2016a). This occurred through a metabolic shift to glycolysis and by inducing energy expensive cellular processes, such as protein- and lipid-synthesis. Also, neuronal mitochondria that were isolated from the neurodegeneration-prone brain regions of WB *Ndufs4* KO mice, showed a progressive reduction in CI-driven respiratory spare capacity with age (Kayser *et al.*, 2016). This was not observed in the degeneration resilient brain regions.

The role of oxidative stress in driving region-specific neurodegeneration is controversial. Abnormally increased oxidative stress markers have been observed in the whole-brain (PN30) (Johnson *et al.*, 2013; Lee *et al.*, 2019), olfactory bulbs (PN26 to PN38) (Quintana *et al.*, 2010; Liu *et al.*, 2015) and cerebellum (>PN42) of WB *Ndufs4* KO mice (de Haas *et al.*, 2017). Conversely, Felici *et al.* (2014) reported that similar oxidative stress markers were unaltered in the olfactory bulbs and motor cortex of mid-stage (PN30) mice, but decreased in the same regions of late stage (PN50) mice presumably due to reduced blood oxygenation (Felici *et al.*, 2014). Furthermore, Kayser *et al.* (2016) showed that brain regional imbalances in ROS homeostasis was unlikely to cause region-specific neurodegeneration. This was because most regions, excluding the olfactory bulbs, did not display abnormal levels of ROS damage, irrespective of age (PN25 to PN30, or PN45 to PN55).

Other studies have shown that chronically elevated ROS levels and aberrant lipid metabolism in the neurodegeneration-prone brain regions of WB *Ndufs4* KO mice disturbed a neuroprotective lipid/lactic acid shuttle mechanism between neurons and glial cells (Liu *et al.*, 2015; Liu *et al.*, 2017). This then induced neuronal death through the accumulation of damaging peroxidated lipids. However, treating WB *Ndufs4* KO mice with various antioxidants, delayed the onset of neurodegeneration but could not enhance survival (Liu *et al.*, 2015; de Haas *et al.*, 2017). Alternatively, attenuation of the lethal phenotype of WB *Ndufs4* KO mice by therapeutic targets such as rapamycin, a mTOR complex 1 (mTORC1)-specific inhibitor, and hypoxia (low oxygen conditions, 11%); have been suggested to at least in part be related to a normalisation in, or more suitable adaptation of the brain to oxidative stress (Johnson *et al.*, 2013; Johnson *et al.*, 2015; Jain *et al.*, 2016; Ferrari *et al.*, 2017; Jain *et al.*, 2019). It was hypothesised that the decreased OXPHOS-related oxygen consumption in brain cells (or the whole body) led to abnormally high brain oxygen levels (hyperoxia) and oxidative stress via either toxic oxidation of intracellular components, aberrant signalling or both (Jain *et al.*, 2019). Collectively, these findings argued that aberrant levels of reactive species might play a role in LS pathogenesis through a complex mechanism, though not a sole or primary contributor.

In accordance with the function of CI as a major consumer of cellular NADH and regenerator of NAD⁺, WB *Ndufs4* KO mice tissues have exhibited perturbed redox balance. Even though redox balance seemed unaltered in the motor cortices of WB *Ndufs4* KO mice at PN30 and PN50 (Koopman *et al.*, 2013), the whole-brain, skeletal muscle, heart, liver and lungs of WB *Ndufs4* KO mice (PN50) (Choi *et al.*, 2011; Schleifer *et al.*, 2018; Lee *et al.*, 2019) and the heart of cardiac-specific *Ndufs4* KO mice (~PN120) (Karamanlidis *et al.*, 2013) displayed significantly increased NADH levels, decreased NAD⁺ levels and a lowered NAD⁺/NADH ratio. It has been suggested that lowered NAD⁺ levels could trigger aberrant metabolic remodelling directly and/or indirectly through the inhibition of the NAD⁺-dependent deacetylase, SIRT 3, and by initiating a discordant

hypoxia response in the presence of an oxygenated environment (Lee *et al.*, 2019). Inhibition of SIRT 3 was evident in the hyperacetylation of proteins in the brain, liver, skeletal muscle and heart of WB *Ndufs4* KO mice (Karamanlidis *et al.*, 2013; Lee *et al.*, 2019). The hyperacetylation decreased bio-energetic fuelling of the TCA cycle via glutamic acid dehydrogenase (GDH) and sensitisation of the permeability transition pore (mPTP) in mitochondria which increases cellular vulnerability to death. Activation of a hypoxia response in the presence of an oxygenated environment in turn, was suggested to cause aberrant metabolic remodelling by increasing glycolysis and LDH activity, thereby exacerbating NAD⁺ shortage and lactic acidosis (Lee *et al.*, 2019).

Interestingly, supplementation with the NAD⁺ precursor, nicotinamide mononucleotide (NMN), doubled the lifespan of WB *Ndufs4* KO mice without improving neurological symptoms (Lee *et al.*, 2019). It was suggested that NMN restored aberrant metabolism and signalling in peripheral tissues but was unable to alter NAD⁺ metabolism in the brain. This is presumably due to mitochondrial dysfunction that prevents the expansion of the NAD⁺-pool by an unclear mechanism. Conversely, supplementation with α -ketoglutaric acid (α KG) improved neurological outcome in addition to a two-fold increase in lifespan (Lee *et al.*, 2019). The improvement was associated with the suppression of hypoxia signalling and augmented support of mitochondrial bio-energetics by maximising compensatory CII-driven respiration via the TCA cycle. In support, when studying mitochondrial respiration in various WB *Ndufs4* KO brain regions, Kayser *et al.* (2016) reported that CI-driven respiration was unaffected when using α KG as a substrate. This was most probably through maximising the contribution of CII to electron transport. The attenuation of hypoxia signalling by NMN and α KG treatment was proposed to block the aberrant metabolic remodelling caused by a CI deficiency.

Additionally, some studies have suggested that aberrant mitochondrial morphology (number, size, and shape) and dynamics contribute to the LS-pathology of WB *Ndufs4* KO mice. Alleviation of the disease phenotype in WB *Ndufs4* KO mice by rapamycin treatment has been proposed to entail a component of improved mitochondrial morphology and autophagy in the brain (Johnson *et al.*, 2013; Felici *et al.*, 2017; Indrieri *et al.*, 2019). Furthermore, phenotypic improvements were observed when the mitochondrial-shaping and -fusion facilitating protein, Optic Atrophy 1 (Opa1), was overexpressed in WB *Ndufs4* KO mice (Civiletto *et al.*, 2015). Similarly, inhibition of NAD⁺-consuming PARP-1 has shown to attenuate neuropathology (Felici *et al.*, 2014). This is most likely through indirectly increasing the expression of RC subunits and mitochondrial biogenesis. Moreover, downregulation of micro-ribonucleic acids (miRNAs) in WB *Ndufs4* KO mice rescued retinal neurons from death and alleviated the disease phenotype by enhancing mitochondrial turnover and partially counteracting the CI defect (Indrieri *et al.*, 2019).

2.3.4 Summary and problem statement

MD is the most common inborn metabolic disease. It generally presents with a severe, detrimental clinical phenotype. Most childhood-onset MD is caused by a deficiency in CI, usually due to a mutation in the *Ndufs4* gene. The resulting phenotype is characterised by neurodegeneration in specific brain regions, which drives disease progression and premature death. Development of appropriate therapeutic strategies has been impeded by the lack of knowledge about the mechanisms underlying the brain regional specificity and neurodegeneration.

Studies on the WB *Ndufs4* KO mouse model illustrated that perturbations on a metabolic level (perturbed metabolism of energy substrates, bio-energetic deficiency, aberrant NAD⁺/NADH ratio, altered ROS levels and disturbed cellular signalling) and ultrastructural level (aberrant mitochondrial morphology and OXPHOS organisation) might contribute to the neuropathology. However, the information on the mechanism/s by which these contributing factors cause region-specific or even neuron-specific degeneration in a CI deficiency, is limited. Furthermore, the biochemical effect of the *Ndufs4* KO on the activities of the individual RC complexes have not been determined in specific brain regions.

Most studies on the *Ndufs4* KO mouse brain were also limited to investigating a selected few known contributing factors. Unfortunately, to the exclusion of other potential, novel mechanisms and without always taking the brain's complexity into account. The latter is necessary as neurodegeneration and regional specificity are multifactorial. Of all the systems biology techniques (including genomics, transcriptomics and proteomics), the 'snapshot' of metabolites provided by metabolomics reflect the final product of all biochemical reactions (Dunn *et al.*, 2011; González-Domínguez *et al.*, 2017). It results from the changes in genetic, transcriptomic, proteomic and environmental interactions and is therefore the closest reflection of the functional phenotype of a cell / tissue. Metabolomics can be defined as the large-scale study of metabolites in cells and tissues using highly selective and sensitive analytical techniques (Dunn *et al.*, 2011; Kolch *et al.*, 2018). However, except for the whole-brain metabolomics analysis conducted on a small group (four per group) of PN30 (prior to onset of neuropathology) WB *Ndufs4* KO mice, holistic investigations are lacking, and have not yet been carried out on specific brain regions.

Consequently, a comprehensive analysis of the metabolic perturbations in specific *Ndufs4* KO brain regions, as well as of the brain region-specific biochemical effect of the *Ndufs4* KO on the activities of individual RC complexes, are required. This could potentially elucidate mechanisms and novel contributors that might drive region-specific neurodegeneration in the WB *Ndufs4* KO mice, and by extension, perhaps also in LS patients.

CHAPTER 3: AIM, OBJECTIVES AND EXPERIMENTAL STRATEGY

3.1 Introduction

As already discussed in Chapter 2, a lack of the NDUFS4 protein subunit of mitochondrial complex I (CI) of the respiratory chain (RC) leads to degeneration in specific brain regions, while other brain regions seem to be unaffected. Importantly, these neuropathological features seem to govern disease progression and premature death. Unfortunately, the lack of knowledge about the underlying pathological mechanisms have impeded the development of satisfactory therapeutic strategies. Also discussed, was the fact that the whole-body (WB) *Ndufs4* knockout (KO) mouse model provides the opportunity to investigate the mechanisms underlying the brain-regional vulnerability to neurodegeneration in a CI deficiency. However, the *in vivo* effect of the *Ndufs4* KO on the biochemical activities of the individual RC complexes, and on the metabolic profiles of the neurodegeneration-prone and -resilient brain regions are currently lacking. It appears important to investigate these factors to better understand the mechanisms that drive region-specific neurodegeneration. This chapter presents the aim and objectives of this study along with an overview of the experimental strategy that was followed to achieve these objectives.

3.2 Aim

The aim of this study was to determine the *in vivo* effect of the *Ndufs4* KO on the activity of individual RC complexes and the metabolic profiles of selected brain regions from *Ndufs4* KO mice; and to investigate potential correlations with neurodegeneration.

The brain regions that were selected for this study included the brain regions of the WB *Ndufs4* KO mice that are most prone to neurodegeneration; namely the brainstem (BST), cerebellum (CB) and olfactory bulbs (OB); as well as a neurodegeneration-resilient brain region, namely the anterior cortex (AC).

3.3 Objectives

The following research objectives were formulated to achieve the above-mentioned aim:

1. To verify the genotypes of the *Ndufs4* wild-type (WT) and KO mouse strains (APPENDIX A).
2. To investigate the biochemical activity of individual RC complexes I to IV (CI to CIV) in the selected brain regions of *Ndufs4* WT and KO mice (Chapter 5) by:
 - 2.1. Standardising existing spectrophotometric assays for measuring the activities of CI to CIV in the selected mouse brain regions (APPENDIX C).
 - 2.2. Measuring the activities of CI to CIV in the selected brain regions of *Ndufs4* WT and KO mice using the standardised assays.

- 2.3. Statistically comparing the activities of CI to CIV between corresponding brain regions of *Ndufs4* WT and KO mice and among the selected brain regions within a genotype.
 - 2.4. Interpreting the biochemical data pertaining to brain region-specific neurodegeneration.
3. To investigate the metabolic profiles of the selected brain regions of *Ndufs4* WT and KO mice using a multi-platform metabolomics approach (Chapter 6) by:
 - 3.1. Standardising an existing gas chromatography time-of-flight mass spectrometry (GC-TOF) method for the untargeted analysis of metabolites in the selected mouse brain regions (APPENDIX D).
 - 3.2. Standardising an existing liquid chromatography-tandem mass spectrometry (LC-MS/MS) method for the targeted analysis of amino acids and acylcarnitines in the selected mouse brain regions (APPENDIX D).
 - 3.3. Measuring metabolites in the selected brain regions of *Ndufs4* WT and KO mice using the standardised multi-platform metabolomics methods.
 - 3.4. Pre-processing and reducing the complexity of the data.
 - 3.5. Statistically determining significant discriminatory metabolites in the selected brain regions between the *Ndufs4* WT and KO mice.
 - 3.6. Interpreting the metabolic data pertaining to brain region-specific neurodegeneration.

3.4 Experimental strategy

Figure 3.1 provides a visual presentation of the experimental strategy. The selected brain regions (AC, BST, CB and OB) were collected from 35 male *Ndufs4* WT (control group) and 33 male *Ndufs4* KO mice (experimental group) which were euthanised as part of a larger study. The mice were euthanised at postnatal day (PN) 45 to PN49 when symptoms of neuropathy are clear and differences between WT and KO mice are more distinct (Kruse *et al.*, 2008; Quintana *et al.*, 2010). Only male mice were used to reduce gender-related variability (especially in metabolomics investigations) and avoid unnecessary complications due to estrous cycles in females (Lovick, 2012; Vasilopoulou *et al.*, 2016b; Zhao *et al.*, 2016). The genotype of each mouse was confirmed before inclusion in the study using the tail tips collected simultaneously with the brain tissues and by using conventional polymerase chain reaction (PCR) for the *Ndufs4* gene (Objective 1).

To investigate the biochemical effect of the *Ndufs4* KO on the maximal activity of individual RC CI to CIV (Objective 2), previously developed microplate-based spectrophotometric assays were standardised for applicability on the mouse brain regions (Objective 2.1). Standardisation was necessary to ensure reliable quantification as the original assays were standardised for human muscle biopsies. It was also essential for obtaining practical experience and to ensure accurate analyses. Spectrophotometric assays for determining protein concentration (bicinchoninic acid / BCA assay) and the maximal activity of the tricarboxylic acid (TCA) cycle enzyme, citrate

synthase (CS), were additionally standardised in order to normalise the measured RC complex activities. Using the standardised assays, the maximal activities of the individual RC complexes, together with protein concentration and CS activity, were measured in the selected brain regions of 12 KO and 10 WT mice (Objective 2.2). Statistical analyses were then performed on the normalised maximal activities of the individual RC complexes (Objective 2.3). The effect of the *Ndufs4* KO on the maximal activity of the individual RC complexes was determined by comparing the activities between the corresponding brain regions of *Ndufs4* WT and KO mice. The maximal activities of the individual RC complexes were also compared inter-regionally within the same genotype. These results were collectively used to interpret the effect of the *Ndufs4* KO and/or differences in isolated RC complex activities among brain regions; and to determine potential correlations with the region-specific neurodegeneration in a CI deficiency (Objective 2.4).

To investigate the effect of the *Ndufs4* KO on the metabolic profiles of the selected brain regions (Objective 3), a multi-platform metabolic approach was used. Since the brain region-specific global metabolic response to a *Ndufs4* KO is unknown, a wide-range of metabolites needed to be measured. This could only be achieved by applying a multi-platform approach as it is currently not possible to cover the entire range of metabolites with a single instrument (Gonzalez-Riano *et al.*, 2016). For this reason, and due to the instruments and existing methods available at the research facility, the metabolomics investigation was carried out using two complementary metabolomics approaches, namely: 1) untargeted analysis with the GC-TOF for broad metabolite coverage; and 2) semi-targeted analysis with the LC-MS/MS for a defined set of compounds that are frequently affected in mitochondrial deficiency. These methods were first standardised for reliable quantification of metabolites in the selected mouse brain regions, and for attaining the skills required for experimental precision (Objective 3.1 & 3.2). Using the standardised methods, the metabolic profiles of the selected brain regions were determined in 21 KO and 25 WT mice (Objective 3.3). Since metabolomics data are highly dimensional and complex, involving many metabolic features (Tugizimana *et al.*, 2016; Dudzik *et al.*, 2017), the data were extracted, pre-processed and normalised prior to statistical analyses (Objective 3.4). Statistical analyses were then used to quantitatively compare the relative concentrations of detected metabolites between the corresponding brain regions of the WT and KO mice and to identify significantly discriminatory metabolites (Objective 3.5). These results were then used to determine if and how the *Ndufs4* KO affected the metabolism of each brain region. The alterations in the levels of discriminatory metabolites were also relatively compared among brain regions to determine metabolic alterations unique to either the neurodegeneration-prone (BST, CB and OB) or the -resilient (AC) brain regions. The metabolic data were then interpreted with regard to potential correlations with the region-specific neurodegeneration in a CI deficiency (Objective 3.6).

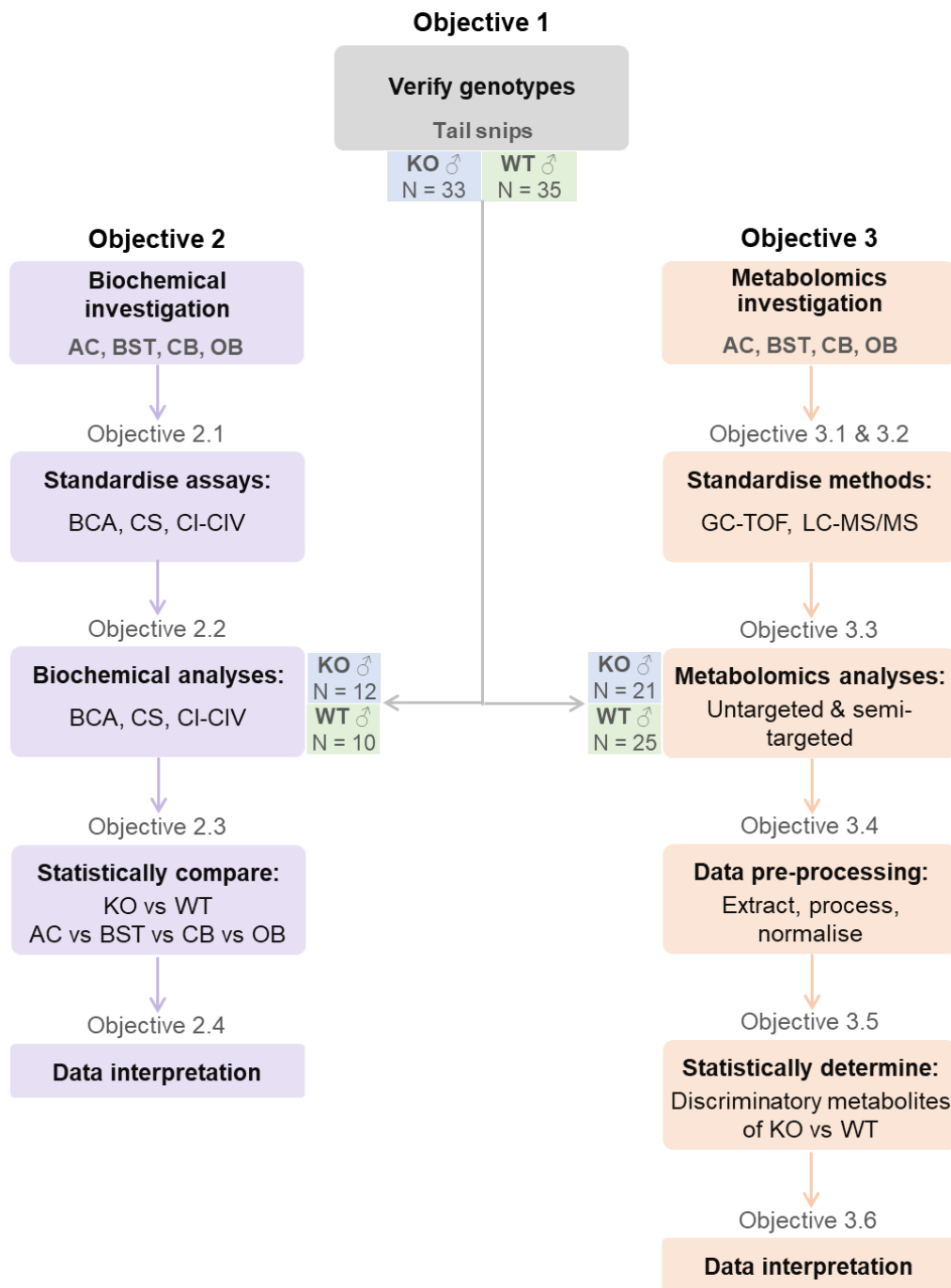


Figure 3.1: Experimental strategy illustrating the objectives of this study.

Objective 1 at the top involved confirming the genotype of the male (♂) knockout (KO) and wild-type (WT) mice, which respectively represent the experimental and control groups. Objective 2 on the left, and Objective 3 on the right depict the biochemical and metabolomics approaches, respectively, and entailed the standardisation of methods, analysis of samples and processing and statistical analysis of the data. *Other abbreviations: AC, anterior cortex; BST, brainstem; CB, cerebellum; OB, olfactory bulbs; BCA, bicinchoninic acid assay for measuring protein concentration; CS, citrate synthase; CI-CIV, complexes I to IV of the respiratory chain.*

CHAPTER 4: MATERIALS AND METHODS

4.1 Introduction

The whole-body inactivation of the mitochondrial respiratory chain (RC) complex I (CI)-subunit gene, *Ndufs4*, in mice results in the development of lesions in specific brain regions, though all regions exhibit a *Ndufs4* knockout (KO). The mechanism governing the regional vulnerability is not fully understood. Understanding the underlying vulnerability of the brainstem (BST), cerebellum (CB) and olfactory bulbs (OB) to the *Ndufs4* KO is important since the clinical phenotype correlate with the progressive neurodegeneration of these regions.

In this study, *Ndufs4* KO and WT mouse brain regions were used to investigate whether regional differences on a biochemical and/or metabolic level of the brain could be correlated with neurodegeneration. For this purpose, the neurodegeneration-prone brain regions (BST, CB and OB) and a neurodegeneration-resilient brain region, the anterior cortex (AC), were investigated. Mice were euthanised and tissue samples collected and stored according to protocol specifications. The genotype of each mouse was confirmed before inclusion in the study (Objective 1). The biochemical characteristics of the selected brain regions and the effect of the KO on these characteristics were evaluated by measuring maximal activities of the mitochondrial marker enzyme, citrate synthase, and RC enzymes on a set of 10 wild-type (WT) and 12 KO mice (Objective 2). The study was concluded by evaluating the effect of the KO on the metabolic profile of the selected brain regions from an additional set of 25 WT and 21 KO mice (Objective 3). The metabolomics investigation was carried out using two complementary metabolomics platforms, namely: 1) untargeted gas chromatography-time of flight spectrometry (GC-TOF); and 2) semi-targeted liquid chromatography-tandem mass spectrometry (LC-MS/MS) analyses of butyl ester derivatives of a defined set of compounds frequently affected in mitochondrial deficiencies. The results were analysed using specific statistical procedures to determine the biochemical and metabolic alterations unique to the vulnerable brain regions.

This chapter gives a detailed explanation of the methods that were used to achieve all the objectives of this study. The methods were based either on pre-existing protocols developed for routine investigations at the Mitochondria Research Laboratory (Centre for Human Metabolomics, North-West University), on in-house methods, or on relevant publications. Brain tissue-specific method modifications and standardisation were required and are provided in APPENDIX C and APPENDIX D, respectively.

4.2 Ethics statement

Animal care and experiments were conducted following the Guide for the Care and Use of Animals for Scientific Purposes of the National Health Research Ethics Council (NHREC), North-West University, and were approved by the North-West University Animal Care, Health and Safety in Research Ethics Committee (AnimCare), ethics number: NWU-00378-16-A5 (see APPENDIX I). The samples used in this study, which is also a sub-study, were obtained from mice that were euthanised for a larger study, ethics number: NWU-00001-15-A1.

4.3 Animals and housing

For this study, mice heterozygous (HET) for the *Ndufs4*-null allele (*Ndufs4*^{+/−}) (B6.129S4-*Ndufs4*^{tm1.1Rpa}/J) were obtained from the Jackson Laboratory (Bar Harbor, ME, USA). These initial breeding pairs were backcrossed to a C57BL/6 genetic background for 20 generations and interbred to generate *Ndufs4* KO (*Ndufs4*^{−/−}) and wild-type (WT) (*Ndufs4*^{+/+}) mice since the KO mice usually die by postnatal day (PN) 55 and are infertile (<https://www.jax.org/strain/027058>). The *Ndufs4* KO was created as described by Kruse *et al.* (2008). In short, the second exon (~800 bp fragment) of the *Ndufs4* gene, which encodes the mitochondrial targeting sequence (MTS) and first 17 amino acids of the NDUF54 protein, was excised by Cre-Lox recombination (Valsecchi *et al.*, 2012 ; <https://www.jax.org/strain/027058>). The excision of exon 2 produces a frameshift that impedes the synthesis of mature NDUF54 subunits in all cells and impairs CI activity. The KO causes a Leigh-like phenotype in the *Ndufs4* KO mouse model that greatly resembles that of patients rendering it useful for studying CI deficiencies.

All mice were propagated under controlled conditions at the Vivarium (SAVC reg. no. FR15/13458) of the Preclinical Drug Development Platform (PCDDP) of the North-West University (ZA¹¹) in the specific pathogen-free (SPF) area. Littermates were group-housed on corn cob chip bedding in 'type ii long' polysulphone individually ventilated cages (IVCs) supplied with 60 air changes of HEPA filtered air per hour. The mice were provided with a standard laboratory rodent diet (Laboratory animal food: Rodent Breeder, #¹²RM1845, purchased from LabChef, Nutritionhub Pty Ltd, Western Cape, ZA) and water access *ad libitum*. Environmental conditions were maintained at controlled conditions of temperature (22 °C ± 2 °C), relative humidity (55% ± 10%), positive air pressure and light (12-hour dark-light cycle) using daylight fluorescent tubes which provide full spectrum white light at 350 lux 1 m above the ground.

¹¹ ZA is an abbreviation for South Africa.

¹² Catalogue numbers follow the # symbol.

Upon weaning (between PN21 and PN23), mice were assigned a unique identification (ID) number by punching holes at specific positions on one or both ears. After identification, the genotypes of the mice born from HET crosses were determined by polymerase chain reaction (PCR) analysis of deoxyribonucleic acid (DNA) isolated from the tail tips. Only samples from male mice were included in this study in order to reduce gender-related variability (especially in metabolomics investigations) and avoid unnecessary complications due to estrous cycles in females (Lovick, 2012; Vasilopoulou *et al.*, 2016b; Zhao *et al.*, 2016).

4.4 Euthanasia and sample collection

The following procedures were performed by, or with the assistance of, the research animal technicians, Mr. Kobus Venter and Mrs. Antoinette Fick, of the Animal Research Centre at the North West University, Potchefstroom Campus. These procedures were selected to obtain, in addition to the brain tissues that were used in this study, all the samples necessary for analysis in concurrent studies. The samples for the biochemical and metabolomics investigations respectively, were collected using similar procedures.

Mice were subjected to an overnight (12-hour) fast in individual metabolic cages with access to drinking water so that urine could be collected (as part of another sub-study). All mice were euthanised via cervical dislocation (to avoid adverse effects of anaesthesia on brain metabolism) at PN45 to PN49 when symptoms of neuropathy are clear and differences between KO and WT mice are more distinct (Quintana *et al.*, 2012; Johnson *et al.*, 2013; Kayser *et al.*, 2016). Blood was collected by cardiac puncture (as part of another sub-study) and after decapitation, the brain was removed, rinsed with ice-cold saline solution (SABAX Pour Saline, PBS, 0.9% NaCl, w/v, #7634, Adcock Ingram Critical Care (Pty) Ltd, ZA) to remove surrounding blood. Brain dissection was then carried out over ice on a metal table, and with dissection tools that were cleaned before each dissection using 70% (v/v) ethanol. This was to avoid sample carryover and contamination. The regions of interest, namely the AC, BST, CB and OB, were distinguished using obvious anatomical markers and known structures. In addition, the Allen Brain Atlas (Lein *et al.*, 2007) for the mouse brain was used to confirm the relevant brain structures. A schematic diagram of the regions of interest is provided in Figure 4.1. The brain tissues were then transferred to individual, pre-labelled 1.5 mL BRAND® microcentrifuge tubes (#Z336769, Sigma-Aldrich, Steinheim, Germany), snap-frozen in liquid nitrogen and stored at -80 °C until analysis. Only brain tissues that were snap-frozen in less than 15 minutes after euthanasia were used for metabolomics studies to prevent adverse changes in metabolites after animal sacrifice due to ongoing enzyme activities (Epstein *et al.*, 2013) (see APPENDIX A for animal information). Hereafter, the tail tip was also collected in a pre-labelled microcentrifuge tube by cutting off ~5 mm of the tail end. The tail tips were stored with the corresponding tissues for genotyping purposes.

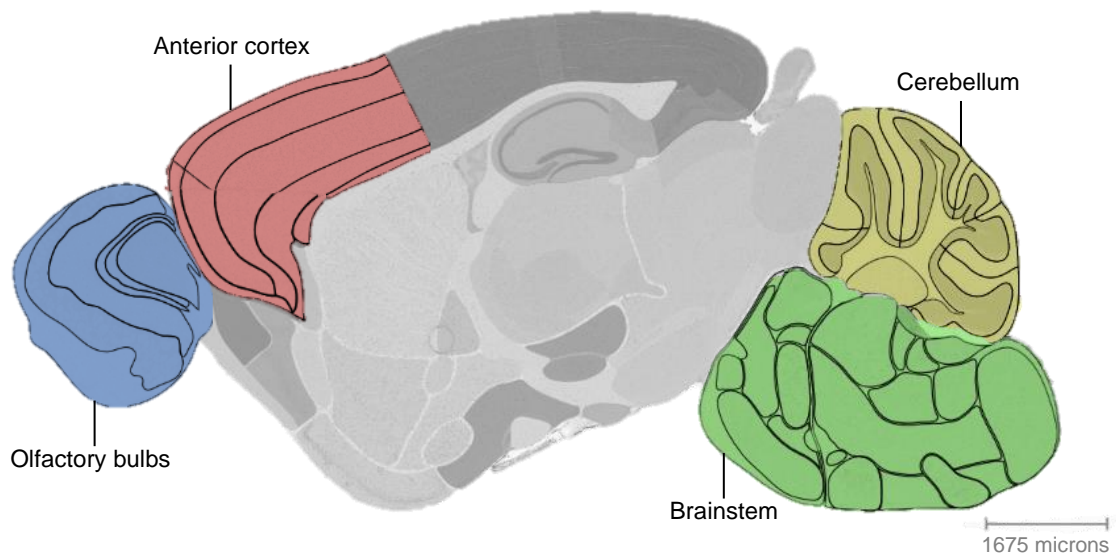


Figure 4.1: Schematic diagram of the whole mouse brain and the brain regions used in this study (sagittal view).

Colour codes show the anterior cortex (AC) in red, brainstem (BST) in green, cerebellum (CB) in yellow and olfactory bulbs (OB) in blue. Each mouse brain was rinsed with ice-cold saline solution (0.9% NaCl, w/v) and subjected to dissection on an ice-cold metal table. The OB was collected first, followed by the CB and BST and the AC was collected last. *Diagram was obtained via the Interactive Atlas Viewer of the Allen Brain Atlas (Lein et al., 2007).*

4.5 Genotyping

4.5.1 Introduction

In addition to being genotyped upon weaning, the mice were genotyped after euthanasia and sample collection to ensure no mix-ups occurred during the initial genotyping process or during the sample collection procedure. The genotype of each mouse was verified using the tail tips collected simultaneously with the brain tissues (Section 4.4) and by using conventional PCR.

4.5.2 Materials and instrumentation

The following reagents were purchased from Inqaba Biotec (Pretoria, ZA): ZR Genomic DNA™ Tissue MiniPrep kit (#D3051), NDUFS4 1060 (forward primer, #532E6) and NDUFS4rev (reverse primer, #53424). A 2x Phire™ Tissue Direct PCR Master Mix (#F170L) and GeneRuler™ 100 bp DNA Ladder (#SM0241) were purchased from Thermo Fisher Scientific™ (Fairland, ZA) while agarose (#8100-CONDA) was purchased via Conda Laboratories from Thermo Fisher Scientific (USA). Bionic™ Buffer (#B6185) and ethidium bromide (EtBr, #46065) were purchased from Sigma-Aldrich® (St. Louis, USA).

The following instrumentation was used: a Thermal Cycler T100™ (#1861096), a Sub-Cell® GT Cell Horizontal Electrophoresis System (#1704401) and a ChemiDoc™ MP system (#17001402) all purchased from Bio-Rad (Pretoria, ZA). The NanoDrop® ND100 Spectrophotometer and Operating Software (v3.8.1) were purchased from NanoDrop® Technologies (Thermo Fisher Scientific™, USA).

4.5.3 Methods

4.5.3.1 DNA isolation and quantification

High quality DNA was isolated from mouse tail tips (Section 4.4) according to the manufacturer's instructions using the ZR Genomic DNA™ Tissue MiniPrep kit and by following the guidelines for solid tissue. A few modifications were implemented at the Mitochondria Research Laboratory for routine genotyping using tail tips. In short, tail tips were cut into similar sizes (± 3 mm) with sterile surgical blades and placed in a sterile 1.5 mL Eppendorf® microcentrifuge tube. Cell lysis or digestion of tail tips was achieved by adding a mixture of 95 μ L nuclease-free water, 95 μ L 2X Digestion Buffer and 10 μ L Proteinase K (all provided with the kit) and then incubating the samples at 55 °C for 2.5 hours using a heating block. Following incubation, 500 μ L Genomic Lysis Buffer were added to the samples to disrupt the nucleic acid-water interaction and allow binding to the silica column. The samples were thoroughly mixed by vortexing and then centrifuged at 10 000 $\times g$ for one minute to remove insoluble debris. The supernatant was transferred to a Zymo-Spin™ IIC column in a Collection Tube and centrifuged at 10 000 $\times g$ for one minute. After discarding the flow-through, 200 μ L DNA Pre-Wash Buffer was added to the spin column in a new collection tube and the column was once again centrifuged at 10 000 $\times g$ for one minute. Contaminants were removed by the addition of 400 μ L genomic-DNA Wash Buffer to the spin column and centrifugation at 10 000 $\times g$ for one minute. The Zymo-Spin™ IIC column was then transferred to a sterile 1.5 mL microcentrifuge tube. The pure DNA was eluted then by carefully adding 25 μ L of pre-warmed (65 °C) DNA Elution Buffer to the silica matrix, incubating the samples at room temperature for five minutes followed by centrifugation at 16 000 $\times g$ for one minute. The elution step was then repeated to increase the DNA yield.

After isolation, the DNA was quantified using the NanoDrop® ND100 Spectrophotometer and Operating Software (v3.8.1). The DNA concentration was determined by measuring maximal absorbance at a wavelength of 260 nm. The purity of each sample was assessed by the Abs_{260}/Abs_{280} ratio and DNA samples within the range of 1.6 to 2.0 were considered as pure. Hereafter, each DNA sample was diluted to 25 ng/ μ L in PCR-grade H₂O.

4.5.3.2 DNA amplification and characterisation

The diluted DNA samples were amplified using conventional PCR (Mullis *et al.*, 1986). To differentiate between the potential genotypes (*Ndufs4* KO, *Ndufs4* WT and *Ndufs4* HET), the deletion in exon 2 of the *Ndufs4* gene can be confirmed by using primer pairs that correspond to the two flanking introns as described previously (Kruse *et al.*, 2008; Valsecchi *et al.*, 2012). The primers used for genotyping and their corresponding sequences and catalogue numbers are shown in Table 4.1. A 1 229 bp fragment is amplified in WT mice, a shorter (429 bp) fragment in KO mice (due to the 800 bp deletion of exon 2) and both fragments are amplified in HET mice (Valsecchi *et al.*, 2012). As controls, isolated DNA with known genotypes (KO, WT and HET) was included in each PCR run.

Table 4.1: Primers used for genotyping mice by PCR.

Primer	Type	Location with regard to deletion	Sequence (5' to 3')	Size (bp)	T _m (°C)	Cat. no.
NDUFS4 1060	Forward	Upstream	AGC CTG TTC TCA TAC CTC GG	20	62.45	#532E6
NDUFS4 Rev	Reverse	Downstream	TTG TGC TTA CAG GTT CAA AGT GA	23	59.2	#53424

Sequences of the forward and reverse primers used for genotyping are listed 5' to 3' together with the corresponding size (in base pairs, bp), melting temperature (T_m) and catalogue number (Cat. no.).

For a 10 µL PCR reaction, the following reagents were added at 0 °C to a PCR tube: 1x Phire™ Tissue Direct PCR Master Mix, premixed with gel loading dye, 0.5 µM of each primer and 25 ng/µL DNA (Section 4.5.3.1). The Phire™ Tissue Direct PCR Master Mix uses the Phire Hot Start II DNA Polymerase which provides a high degree of specificity (Mereis, 2018). This decreases non-specific amplification and allows better distinction between genotypes. As shown in Figure 4.2, PCR was carried out in a Thermal Cycler T100™ under the following conditions: incubation at 98 °C for five minutes for DNA denaturation and activation of the Phire Hot Start II DNA Pol; 35 cycles of 98 °C for five seconds, 57.3 °C for five seconds and 72 °C for 20 seconds; and finally, incubation at 72 °C for one minute. The samples were then held at 4 °C until removal.

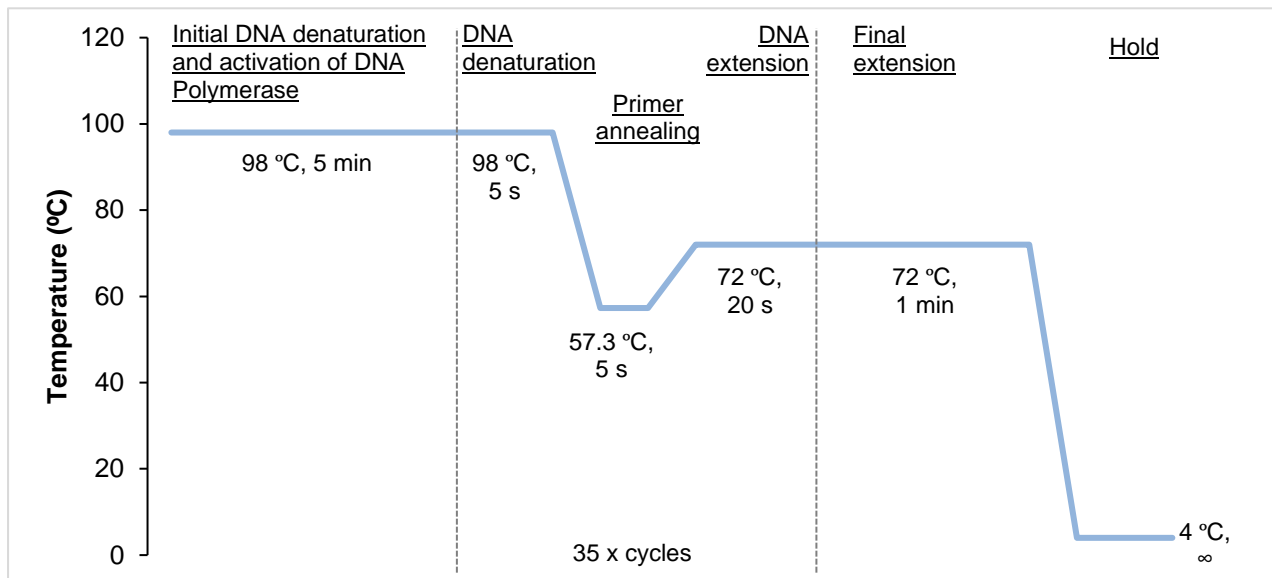


Figure 4.2: PCR conditions used for genotyping.

Initial denaturing of the DNA double strand and activation of the Phire Hot Start II DNA Polymerase occurred at 98 °C for five minutes. DNA was denatured at 98 °C for five seconds, primers annealed at 57.3 °C for five seconds and extension took place at 72 °C for 20 seconds, after which the cycle was repeated 34 times. This was followed by a prolonged extension step (one minute), after which samples were cooled and held at 4 °C until removal from the thermo-cycler. *Note: this figure is for illustrative purposes only and is not necessarily according to scale.*

Differences in amplicon lengths allowed DNA fragments containing a deletion (KO) to be separated by gel electrophoresis from fragments without a deletion (WT). To 10 µL of PCR products, 23.3 µL nuclease-free water was added and 10 µL thereof was loaded onto a 1% (w/v) agarose gel prepared in 1x Bionic™ Buffer containing 0.5 µg/mL ethidium bromide (EtBr) to stain the nucleic acids. As a DNA size marker, a 10 µL mix containing 3 µL GeneRuler™ 100 bp DNA Ladder and 7 µL nuclease-free water was also loaded onto the gel. The samples were analysed at ~8 V/cm in a Sub-Cell® GT Cell Horizontal Electrophoresis System. The gel was photographed under ultraviolet (UV) light with a ChemiDoc™ MP system using Image Lab™ Version 5.2.1 software. The *Ndufs4* WT genotype was identified by the presence of a 1 229 bp band, the *Ndufs4* KO genotype by the presence of a shorter 429 bp band (corresponding with the deletion of exon 2) and the *Ndufs4* HET genotype by the presence of both bands. An example of an agarose gel electrophoretogram for verification of genotypes is provided in APPENDIX A.

4.6 Biochemical investigation

4.6.1 Introduction

Objective 2 of this study was to investigate whether regional differences in mitochondrial respiratory chain (RC) enzyme activities could be correlated with the regional vulnerability to neurodegeneration in *Ndufs4* KO mice. Maximal RC enzyme activities are usually determined spectrophotometrically and are commonly normalised to total protein content or to the activity of the mitochondrial marker enzyme, citrate synthase (CS). This is to account for differences in mitochondrial content and to provide information on the inherent mitochondrial properties (Lanza & Nair, 2009; Spinazzi *et al.*, 2012). These assays are commonly used in clinical diagnostics and research to obtain reliable, sensitive and specific quantitative information on the maximal catalytic activities of the RC complexes. In turn, it can also be used to identify a deficiency or upregulation of RC enzyme activities (Koenig, 2008; Barrientos *et al.*, 2009).

To this end, the brain region-specific maximal activity of CS and of RC complex I (CI), II (CII), III (CIII) and IV (CIV) was measured spectrophotometrically in freeze-thawed 700 x g supernatants prepared from the homogenates of various brain regions (AC, BST, CB and OB) harvested from *Ndufs4* KO and WT mice at postnatal day (PN) 45 to PN49. The maximal enzyme activities were determined in the presence of excess complex-specific substrates according to previously published methods (Shepherd & Garland, 1969; Rahman *et al.*, 1996; Janssen *et al.*, 2007; Luo *et al.*, 2008). These methods were modified and standardised at the Mitochondria Research Laboratory (Centre for Human Metabolomics, North-West University) for routine diagnostic measurements using a microtiter plate system (Du Toit, 2007; Pretorius, 2011). The microplate-based assays allow higher throughput analysis (96 samples simultaneously) and require less sample volume (only 10% to 20%) than cuvette-based assays (Long *et al.*, 2009). It also reduces systematic assay errors by minimising the number of batches in which many samples are analysed (Long *et al.*, 2009; Pretorius, 2011). In these standardised protocols, the enzyme activities for two-substrate reactions are determined colorimetrically by measuring the change in absorbance of a dye and with using initial velocity calculations. These calculations were modified for pseudo-first order reactions since the substrates are added in excess (concentration remains essentially constant during the time the reaction is being monitored) so that the enzyme activity is directly proportional to the change in concentration of the product (Bock & Alberty, 1953). The differences in maximal enzyme activities between KO and WT samples within the same brain region, as well as differences between the four regions of the same genotype, were evaluated using specific statistical analyses.

Notable, the protocols standardised at the Mitochondria Research Laboratory have been optimised for measuring maximal enzyme activities in supernatants obtained from homogenates of human skeletal muscle biopsies. To successfully apply these methods to mouse brain region tissue samples some modifications were necessary. This was to allow good sensitivity and linearity with time, while making provision for small experimental and biological variations. These modifications included adjustments to the loading volumes of the brain region supernatants. Details are provided in APPENDIX C.

4.6.2 Materials and instrumentation

Reagents were purchased from Sigma-Aldrich® (St. Louis, USA) unless specified otherwise. The following reagents were used: acetyl-CoA, trilithium salt (ACoA, #10101907001, Roche, Sigma-Aldrich®), adenosine 5'-triphosphate disodium salt trihydrate (ATP, #A2383, Roche, Sigma-Aldrich®), antimycin A (#A8674), bicinehonic acid (BCA, #B9643), bovine serum albumin fatty acid free (BSA, #10775835001 Roche, Sigma-Aldrich®), BSA protein standard (1 µg/µL, #P0914), cupric sulphate (CuSO₄.5H₂O, #C2284), oxidised Cytochrome c (Cytcox, #C7752), decylubiquinone (DQ, #D7911), 2,6-dichloroindophenol sodium salt hydrate (DCIP, #D1878), dimethyl sulfoxide (DMSO, #C6164), 2,2'-dinitro-5,5'-dithiobenzoic acid (DTNB, #D8130), n-dodecyl β-D-maltoside (#D4641), ethanol (#E7023), ethylenediaminetetraacetic acid disodium salt dihydrate (EDTA, #E1644), ethylene glycol-bis(β-aminoethylether) N,N,N',N'-tetraacetic acid (EGTA, #E4378), HEPES free acid (#H3375), hydrochloric acid (cHCl, #43,557-0), mannitol (#M9546), β-nicotinamide adenine dinucleotide reduced dipotassium salt (NADH, #N4505), oxaloacetate (OAA, #O4126), potassium hydroxide (KOH, #P5958), potassium phosphate dibasic (K₂HPO₄, #P2222), potassium phosphate monobasic (KH₂PO₄, #P5655), rotenone (#R8875), sodium ascorbate (#A4034), sodium azide (NaN₃, #S2002), succinate (#S7501), sucrose (#84100), Triton® X-100 (#T9284), Trizma base (#T1503), Tween® 20 (#822184, Merck Chemicals, MA, USA). Milli-Q®¹³ H₂O was prepared using a Milli-Q® system (Millipore™, Merck, MA, USA).

The following instruments were used: motor driven glass/Teflon® tight fitting Potter Elvehjem homogeniser (Glas-Col, Terre Haute, IN), Heidolph RZR 1 overhead stirrer (#501 11000, Separations, Randburg, ZA), Heraeus™ Multifuge™ X3 Centrifuge (Thermo Fisher Scientific, USA). Spectrophotometric measurements were carried out with a Synergy™ HT Multi-detection microtiter plate reader with Gen5™ Data Analysis Software (both sourced from BioTek® Instruments, VT, USA).

¹³ Milli-Q® H₂O from here on will refer to water that has been purified by the Milli-Q® system (Millipore™, Merck, MA, USA).

4.6.3 Preparation of buffers and reagents

An isolation buffer (IB₁) was prepared by dissolving 210 mM mannitol, 70 mM sucrose, 5 mM HEPES free acid and 0.1 mM EGTA in ultrapure Milli-Q[®] H₂O and adjusting the pH to 7.2 at 37 °C with 1 M KOH. The Tris.HCl solution was prepared by dissolving Trizma base in ultrapure Milli-Q[®] H₂O and by adjusting the pH to 8.0 at 25 °C with concentrated hydrochloric acid (cHCl). A 0.5 M Potassium-phosphate buffer (KPi-buffer, pH 7.4 at 25 °C) was prepared from 0.5 M KH₂PO₄ and 0.5 M K₂HPO₄ in a ~1:4 ratio. Dilutions of the 0.5 M KPi buffer were made with Milli-Q[®] H₂O where necessary. Buffers were aliquoted and stored at -20 °C.

The following reagents were prepared using specific solvents or buffers: DTNB was dissolved in 1 M Tris.HCl solution (pH 8.0), rotenone and antimycin A were prepared in ethanol unless specified otherwise, BSA solutions were made in 0.5 M KPi buffer, and DQ was prepared in DMSO. The rest of the reagents were prepared in Milli-Q[®] H₂O and the pH was adjusted with either potassium hydroxide (KOH) or hydrochloric acid (HCl). Reduced Cyt c and reduced DQ (DQ_{red}) were prepared from their oxidised forms as described by Du Toit (2007) and Luo *et al.* (2008). Details are given in APPENDIX B.

4.6.4 Methods

4.6.4.1 Samples and experimental groups

The brain regions (AC, BST, CB and OB) for the biochemical analyses were collected over time as mice became available and were stored at -80 °C (Section 4.4). The brain regions of 10 WT and 12 KO mice were grouped according to brain region-type. Each region-type was prepared as a separate group; i.e. the 700 x g supernatants of all 22 samples of a specific brain region were prepared together on the same day and then stored until protein and enzyme analyses. Concerning each assay, the different brain region groups were consecutively analysed before moving on to another assay; e.g. the CS assay was carried out for all four brain region groups before continuing with another assay. This was done to minimise the time progressed between the analyses of the different brain regions using a specific assay. In turn, this could ultimately minimise variation and ensure that the results are more comparable.

4.6.4.2 Preparation of homogenates and supernatants

Mitochondrial RC enzyme activities can be measured in crude homogenates (or post-700 x g supernatants) or in an enriched mitochondrial fraction (Thorburn *et al.*, 2004). Preparing homogenates or supernatants from samples rather than isolating enriched mitochondrial fractions, reduces cost, preparation time and the amount of tissue required (Spinazzi *et al.*, 2012). Also, it is known that CS may leak during mitochondrial isolation from frozen tissues. This can cause artefacts when using CS as a mitochondrial marker in preparations of enriched mitochondrial fractions (Thorburn *et al.*, 2004; Janssen *et al.*, 2007). In comparison with homogenates, supernatants provide purer extracts with only a slight loss in enzyme activity while increasing the sensitivity of enzyme activity assays (Janssen *et al.*, 2007; Spinazzi *et al.*, 2012). Taking these factors and study-specific factors, like the unavoidable use of frozen samples and small sample sizes, in to consideration, supernatants were prepared.

Brain region samples were prepared for biochemical analysis by homogenisation and differential centrifugation using an in-house method with slight modification (Pretorius, 2011). All steps were performed on ice with ice-cold buffers to minimise the damage brought about by proteases and phospholipases (Palmer & Bonner, 2007). In short, each brain region sample was weighed and suspended in ice-cold isolation buffer (IB₁) to produce a 10% (w/v) homogenate (5% w/v for the smaller OB). Samples were mechanically homogenised using an overhead stirrer with a motor driven glass/Teflon® tight fitting Potter Elvehjem homogeniser. The glass tube, containing the tissue, was put in melting ice while the tissue was homogenised with 10 slow and controlled up-down strokes at 120 rpm. The homogenate was then transferred to a 2 mL Eppendorf micro-centrifuge tube and centrifuged at 700 x g for 10 minutes (4 °C) using a Heraeus™ Multifuge™ X3 Centrifuge. The resulting supernatant was carefully transferred to a clean 1.5 mL micro-centrifuge tube on ice while taking care not to disturb the pellet. The 700 x g supernatant was then stored at -80 °C for determination of protein concentration (Section 4.6.4.3) and for CS (Section 4.6.4.4) and RC enzyme activity analysis (Section 4.6.4.5 to Section 4.6.4.8). A schematic representation of this procedure can be found in Figure 4.3.

The CS and RC enzyme assays require the disruption of the mitochondrial membranes to allow access of the various substrates to the enzymatic binding sites (Barrientos, 2002). For this reason, the 700 x g supernatants were freeze-thawed three times using liquid nitrogen before being aliquoted for analysis in the respective assays.

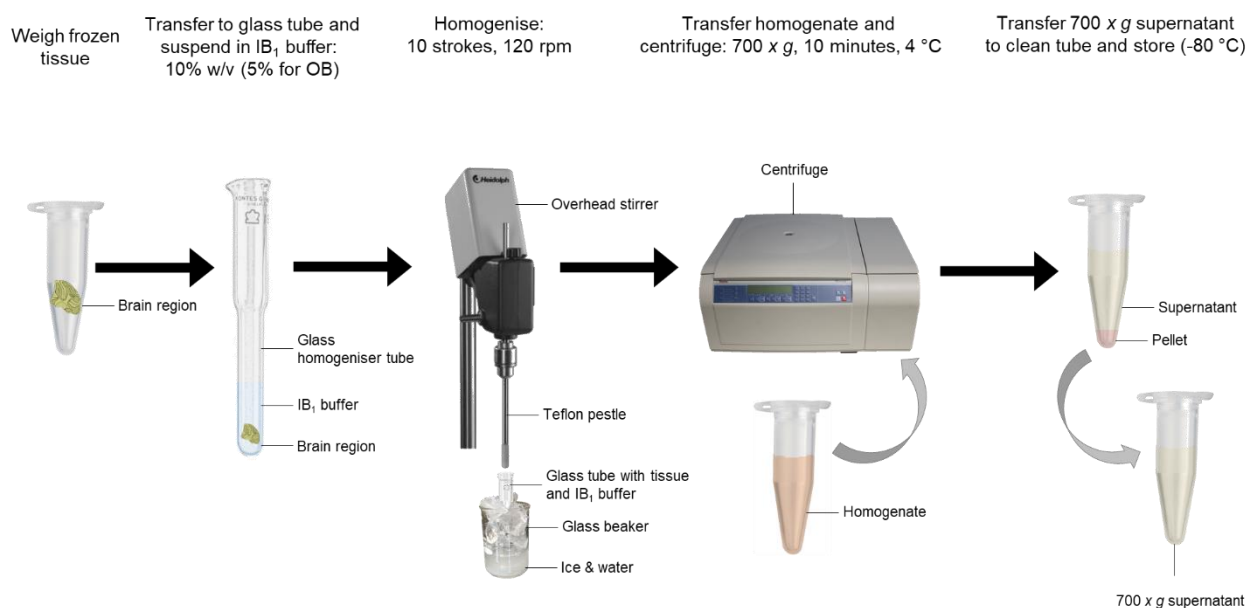


Figure 4.3: Preparation of 700 x g supernatants from selected mouse brain regions.

Samples were grouped according to brain region. Brain region groups were prepared successively as soon as possible. Frozen brain regions were weighed, suspended in IB1 buffer to obtain a 10% (5% for OB) w/v homogenate, homogenised using a Potter Elvehjem homogeniser on ice and centrifuged at 700 x g for 10 minutes at 4 °C. The 700 x g supernatants were stored (-80 °C) until required for protein and enzyme analysis.

4.6.4.3 Bicinchoninic acid (BCA) assay

Protein content of the 700 x g supernatants was determined using the bicinchoninic acid (BCA) assay first described by Smith *et al.* (1985) using bovine serum albumin (BSA) as standard. Under alkaline conditions, the copper(II) ion (Cu^{2+} from CuSO_4) is reduced to the copper(I) ion (Cu^+) when it reacts with peptide bonds. Each Cu^+ in turn reacts with two BCA molecules to form a purple-coloured complex with an absorbance maximum at 562 nm. The absorbance is directly proportional to the protein content (Wilson & Walker, 2010). This assay is simple, more sensitive (0.5 μg protein/mL detection limit) than other protein assays and more tolerant to interferences.

A BSA protein standard series of 0 μg to 20 μg was set up by way of pipetting 1 $\mu\text{g}/\mu\text{L}$ BSA protein standard in increments of 4 μg into a 96-well UV microtiter plate. For each sample, 2 μL (4 μL for the OB) of the 700 x g supernatant was pipetted into the 96-well plate in triplicate. The wells were then topped up with Milli-Q[®] H₂O to a final volume of 20 μL after which 200 μL of the BCA-reagent (BCA: $\text{CuSO}_4 \cdot 5\text{H}_2\text{O}$, 50:1) was added. After incubation (30 minutes, 30 °C) in a Synergy[™] HT Multi-detection microtiter plate reader, the absorbance was measured at 562 nm.

The protein content per well (μg) was determined from the BSA standard curve by using least mean squares linear regression (LMSLR) carried out using the Gen5™ Data Analysis Software. The correlation coefficient (R^2) of the calibration curve had to be >0.99 for acceptable linearity. Protein concentration ($\mu\text{g}/\mu\text{L}$) was then calculated from the protein content by correcting for the sample volume added per well (Equation 4.1).

$$\text{Protein concentration } (\mu\text{g}/\mu\text{L}) = \frac{\text{Protein content } (\mu\text{g})}{\text{Sample volume added } (\mu\text{L})}$$

(Equation 4.1)

4.6.4.4 Citrate synthase (CS) activity assay

Citrate synthase (CS, acetyl-CoA:oxaloacetate C-acetyltransferase, E.C. 2.3.3.1) is an enzyme localised in the matrix of the mitochondria. It catalyses the reaction between oxaloacetate (OAA) and acetyl-coenzyme A (acetyl-CoA) in the tricarboxylic acid (TCA) cycle to form citrate and coenzyme A (CoA) with a thiol group (CoA-SH) (Lanza & Nair, 2009; Garrett & Grisham, 2013). The CS enzyme is commonly used as a single-enzyme mitochondrial marker and its activity is used as an accurate estimate of mitochondrial content and/or mass (Larsen *et al.*, 2012). Maximal enzyme activities are frequently normalised to CS activity to account for differences in mitochondrial content and to identify primary deficiencies in RC enzymes (Thorburn *et al.*, 2004; Porter & Wall, 2012; Spinazzi *et al.*, 2012).

The CS assay was carried out according to the method first described by Shepherd and Garland (1969). In short, the CoA-SH product of CS reacts with added 2,2'-dinitro-5,5'-dithiobenzoic acid (DTNB) to form yellow-coloured 2-nitro-5-thiobenzoate (TNB) with an absorbance maximum at 412 nm. The rate of colour development is directly proportional to CS activity.

The $-80\text{ }^\circ\text{C}$ aliquoted 700 x g supernatant samples (Section 4.6.4.2) were thawed on ice. A 200 μL reaction was prepared in each well and consisted of 0.1 mM DTNB, 0.04% (v/v) Triton® X-100 to further disrupt the mitochondrial membrane, 60 μM acetyl-CoA and 700 x g supernatant (effectively 0.4 μL [0.8 μL for OB] or $\sim 1.7\text{ }\mu\text{g}$ supernatant protein). To avoid inaccurate pipetting of small volumes, each 700 x g supernatant sample was diluted in Milli-Q® H₂O so that 10 μL could be loaded into the 96-well UV microtiter plate per well. The reaction was initiated after incubation of the plate at 30 $^\circ\text{C}$ for 10 minutes by adding pre-heated (30 $^\circ\text{C}$) OAA to a final concentration of 0.5 mM in each 200 μL reaction. Each sample was analysed in triplicate and three blank wells were set up per plate by adding IB₁ buffer instead of sample in each well.

The formation of the coloured product, TNB, at 30 °C was kinetically measured at 412 nm for five minutes with one-minute intervals. The initial velocity (v_1 in mAbs/minute) was determined via linear rate calculations over the first three minutes (first 4 readings) and reported R^2 -values had to be >0.99 for acceptable linearity. The CS activity ($\mu\text{mol}/\text{minute}$ Citrate Synthase, UCS) normalised to protein content (determined in Section 4.6.4.3), was calculated according to Equation 4.2 by using the average v_1 ($AVGv_1$) of the triplicate wells:

$$UCS (\mu\text{mol}/\text{min}/\text{mg}) = \frac{AVGv_1 \div \epsilon_{412} \times 0.2}{\mu\text{L protein} \times \mu\text{g}/\mu\text{L}/1000}$$

ϵ_{412} = molar extinction coefficient for TNB for 200 μL reaction = 7465 Abs/mM (Pretorius, 2011).

(Equation 4.2)

4.6.4.5 Complex I (CI) activity assay

Complex I (CI, NADH:ubiquinone oxidoreductase, NADH dehydrogenase, EC 1.6.5.3) of the RC oxidises NADH to NAD^+ and transfers the electrons to the inner mitochondrial membrane bound electron carrier, ubiquinone (UQ) (Valsecchi *et al.*, 2012). During this process, UQ is converted to ubiquinol (UQ_{ol}) which subsequently transfers electrons to CIII. The energy liberated by the electron flow drives CI to pump protons from the matrix into the inter membrane space thereby contributing to the electrochemical proton gradient necessary for mitochondrial respiration or oxidative phosphorylation (OXPHOS).

The CI assay was based on the method originally described in Janssen *et al.* (2007). The substrates, NADH and decylubiquinone (DQ), a more hydrophilic analogue of UQ, are added in excess (Telford *et al.*, 2010). The reduction of DQ by NAD^+ produces decylubiquinol (DQ_{ol}). DQ_{ol} in turn, reduces the final electron acceptor, the redox dye 2,6-dichloroindophenol (DCIP). The oxidised form of DCIP has a blue colour that absorbs light at 600 nm, but which becomes colourless when DCIP is reduced. Even though DCIP reduction is mostly due to CI activity, other contaminating enzymes may also contribute, such as NADH:cytochrome b_5 reductase (Barrientos, 2002; Long *et al.*, 2009). CI activity can thus be obtained through subtracting the activity measured in the presence of the CI-specific inhibitor, rotenone, from the total activity (activity measured in the absence of rotenone) (Pollard *et al.*, 2016). This is also known as rotenone-sensitive CI activity. Antimycin A is added to prevent reoxidation of DQ_{ol} by CIII and backflow of electrons along the RC (Brooks & Krähenbühl, 2000). The addition of BSA increases the sensitivity and specific activity of CI by solubilising rotenone and DQ (Janssen *et al.*, 2007).

For each sample, a 200 μL reaction was prepared per well of a 96-well microtiter plate. It consisted of 50 μL DMSO or 50 μL 1 mM rotenone (2.5 μM final concentration) prepared in DMSO, 50 mM KPi-buffer, 1 μM antimycin A, 70 μM DQ, 60 μM DCIP, 0.35% (w/v) BSA (prepared in KPi-buffer), 700 x g supernatant (effectively 3 μL for CB and BST [6 μL for OB] or ~12 μg supernatant protein and for AC, effectively 4 μL or ~18 μg supernatant protein). After incubation at 30 $^{\circ}\text{C}$ for 10 minutes, pre-heated (30 $^{\circ}\text{C}$) NADH was added (0.2 mM final concentration) to initiate the reaction. Three blank samples were set up per plate by substituting the volume of sample added per well with IB₁ buffer. Each sample was analysed in triplicate in the presence and absence of rotenone (6 reactions per sample). Analyses were carried out in two batches using two separate plates because the number of reactions exceeded the capacity of the 96-well plate. To correct for batch-to-batch variation, one sample was used as a control by including it on both plates.

The linear rate decrease in absorbance due to DCIP reduction was recorded at 600 nm for five minutes in one-minute intervals. The initial velocity (mAbs/minute) in the absence (v_1) and presence (v_2) of rotenone, was calculated over three minutes starting from the second minute. The reported R²-values had to be >0.99 for acceptable linearity. The average velocity of the triplicate reactions in the presence of rotenone ($AVGv_2$) was then subtracted from the individual reactions in the absence of rotenone (v_1). This was to obtain rotenone-sensitive activity (v_3) (Brooks & Krähenbühl, 2000). CI enzyme activity ($\mu\text{mol}/\text{minute}$ Complex I, UCI), normalised to protein content (Section 4.6.4.3), for each sample was calculated from the average v_3 ($AVGv_3$) of the triplicates according to Equation 4.3. CI activity expressed per units of CS (CI/UCS) was calculated according to Equation 4.4.

$$UCI (\mu\text{mol}/\text{min}/\text{mg}) = \frac{AVGv_3 \div \epsilon_{600} \times 0.2}{\mu\text{L protein} \times \mu\text{g}/\mu\text{L}/1000}$$

ϵ_{600} = molar extinction coefficient for DCIP for 200 μL reaction = 12712 Abs/mM (Pretorius, 2011).

(Equation 4.3)

$$CI/UCS (\text{nmol}/\text{min}/UCS) = \frac{UCI \times 1000}{UCS^{14}}$$

(Equation 4.4)

¹⁴ Calculated in Section 4.6.4.4.

4.6.4.6 Complex II (CII) activity assay

Complex II (CII, Succinate:ubiquinone oxidoreductase; succinate dehydrogenase, EC 1.3.5.1) connects the TCA cycle to the RC in mitochondria. It catalyses the oxidation of mitochondrial matrix succinate to fumarate and the reduction of UQ in the inner mitochondrial membrane (Stepanova *et al.*, 2016). CII transfers electrons from succinate to UQ through covalently bound flavin-adenine dinucleotide (FAD).

The CII assay was based on the method originally described by Janssen *et al.* (2007) and is essentially based on the same principle as the CI assay (Section 4.6.4.5). The CII substrate succinate is added in excess together with DQ which can react with the redox dye DCIP when it is reduced to DQ_{ol} by FAD. Since the CII activity measured with this method is completely inhibited by malonate (CII specific inhibitor), it was not necessary to include malonate control reactions (Pretorius, 2011). The exclusion of replicate reactions in the presence of malonate was especially beneficial for this study considering the limited sample volumes available for all the enzyme assays. ATP is added to activate CII (Stepanova *et al.*, 2016) while rotenone is included to inhibit CI and prevent and backflow of electrons along the RC, as well as any potential contribution of DQ reduction by CI (Barrientos, 2002).

The 200 μ L reaction contained 50 mM KPi-buffer, 1 μ M antimycin A, 2.5 μ M rotenone, 50 μ M DQ, 80 μ M DCIP, 0.1% (w/v) BSA, 0.08% EDTA (pH 7.0), 0.2 mM ATP (pH 7.2), 700 μ g supernatant (effectively 4 μ L or \sim 17 μ g supernatant protein) for all brain regions [9 μ g mitochondrial protein for OB]¹⁵. The reaction was initiated after incubation at 30 °C for 10 minutes, by adding pre-heated (30 °C) succinate (1.5 mM final concentration in 200 μ L). Two blank samples were set up per plate by substituting the volume of sample added per well with IB₁ buffer. Each sample was analysed in duplicate (not in triplicate due to limited sample volume) in the 96-well microtiter plates. The linear rate decrease in absorbance due to DCIP reduction was recorded at 600 nm for five minutes in one-minute intervals. The initial velocity (v_1 in mAbs/minute) was calculated over three minutes starting from the second minute. The reported R²-values had to be >0.99 for acceptable linearity. The CII activity (μ mol/minute Complex II, UCII) for each sample, normalised to protein content (determined in Section 4.6.4.3), was calculated according to Equation 4.5 by using the average v_1 ($_{AVG}v_1$) of the triplicate wells. CII activity expressed per units of CS (CII/UCS) was calculated according to Equation 4.6.

¹⁵ Due to the limited sample volume of the smaller OB, half of the amount of mitochondrial proteins added per well for the BST, CB and AC was added for the OB; i.e. 4 μ L instead of 8 μ L of a 700 \times g supernatant obtained from a 5% w/v homogenate. Even though less mitochondrial proteins were added (lower $_{AVG}v_1$), the rate decrease in absorbance was still linear and therefore reliable and comparable (APPENDIX C).

$$UCII (\mu\text{mol}/\text{min}/\text{mg}) = \frac{AVG v_1 \div \epsilon_{600} \times 0.2}{\mu\text{L protein} \times \mu\text{g}/\mu\text{L}/1000}$$

ϵ_{600} = molar extinction coefficient for DCIP for 200 μL reaction = 12712 Abs/mM (Pretorius, 2011).

(Equation 4.5)

$$CII/UCS (\text{nmol}/\text{min}/UCS) = \frac{UCII \times 1000}{UCS^{16}}$$

(Equation 4.6)

4.6.4.7 Complex III (CIII) activity assay

Complex III (CIII, Ubiquinol:ferricytochrome c oxidoreductase, ubiquinol Cytochrome c reductase, EC 1.10.2.2) receives electrons from UQ_{inol} and then shuttles electrons across the inner mitochondrial membrane to Cytochrome c (Cyt c), the mobile electron carrier located in the intermembrane space (Valsecchi *et al.*, 2012).

CIII activity was measured as described by Luo *et al.* (2008). The 200 μL reaction consisted of 50 μM oxidised Cyt c, 700 $\times g$ supernatant (effectively 0.6 μL or $\sim 2.4 \mu\text{g}$ supernatant protein for all brain regions except the OB [0.5 μL or $\sim 2.3 \mu\text{g}$ supernatant protein]) and, to initiate the reaction after incubation, a reaction mixture was added. The reaction mixture had the following concentrations in the final 200 μL volume: 250 mM KPi buffer, 0.05% BSA, 0.25% (v/v) Tween 20, 0.25 mM DQ_{inol} prepared from DQ (see APPENDIX B) and 20 mM sodium azide (NaN_3). Two blank samples were set up per plate through substituting the volume of sample added per well with IB₁ buffer. Each sample was analysed in duplicate in the 96-well microtiter plates. The assay was performed at 30 °C and the linear rate increase in absorbance due to reduction of Cyt c was recorded spectrophotometrically at 550 nm for five minutes in one-minute intervals. The initial velocity (v_1 in mAbs/minute) was calculated over three minutes starting from the second minute. The reported R^2 -values had to be >0.99 for acceptable linearity. The CIII activity ($\mu\text{mol}/\text{minute}$ Complex III, UCIII) for each sample, normalised to protein content (determined in Section 4.6.4.3), was calculated according to Equation 4.7 using the average v_1 ($AVG v_1$) of the triplicate wells. CIII activity expressed per units of CS (CIII/UCS) was calculated according to Equation 4.8.

¹⁶ Calculated in Section 4.6.4.4.

$$UCIII (\mu\text{mol}/\text{min}/\text{mg}) = \frac{AVG v_1 \div \epsilon_{550} \times 0.2}{\mu\text{L protein} \times \mu\text{g}/\mu\text{L}/1000}$$

ϵ_{550} = molar extinction coefficient for reduced Cyt c for 200 μL reaction = 4180 Abs/mM (Pretorius, 2011).

(Equation 4.7)

$$CIII/UCS (\text{nmol}/\text{min}/\text{UCS}) = \frac{UCIII \times 1000}{UCS^{17}}$$

(Equation 4.8)

4.6.4.8 Complex IV (CIV) activity assay

Complex IV (CIV, Ferrocytochrome-c: oxygen oxidoreductase; cytochrome-c oxidase; EC 1.9.3.1) is the final electron acceptor of the RC. It oxidises reduced Cyt c and uses the electrons to reduce molecular oxygen (O_2) to water (Abdulhag *et al.*, 2014).

CIV activity was measured essentially as described by Rahman *et al.* (1996), but using a higher Cyt c concentration (Pretorius, 2011). The 200 μL reaction contained 12.5 mM KPi-buffer, 700 \times g supernatant (effectively 0.25 μL or ~ 1 μg supernatant protein for all brain regions, except the OB [0.125 μL or ~ 0.6 μg supernatant protein]). The samples were diluted as necessary to obtain a good initial linear reaction rate for at least two to three minutes (Barrientos, 2002). To initiate the reaction after incubation at 30 $^\circ\text{C}$ for 10 minutes, a reaction mixture was added. This mixture had the following concentrations in the final 200 μL volume: 37.5 mM KPi-buffer, 0.5 mM dodecylmaltoside to disturb the super-complex interactions (Lenaz *et al.*, 2016; Baertling *et al.*, 2017) and 25 μM reduced Cyt c (prepared from oxidised Cyt c and sodium ascorbate, see APPENDIX B). Two blank samples were set up per plate by substituting the volume of sample added per well with IB_1 buffer. Each sample was analysed in duplicate. The linear rate decrease in absorbance due to Cyt c oxidation was recorded kinetically at 550 nm for three minutes in 30-second intervals. The initial velocity (v_1 in mAbs/minute) was calculated over three intervals starting from the second 30-second interval. The reported R^2 -values had to be >0.99 for acceptable linearity.

¹⁷ Calculated in Section 4.6.4.4.

The CIV activity ($\mu\text{mol}/\text{minute}$ Complex IV, UCIV) for each sample, normalised to protein content (determined in Section 4.6.4.3), was calculated according to Equation 4.9 by using the average v_1 ($_{AVG}v_1$) of the triplicate wells. CIV activity expressed per units of CS (CIV/UCS) was calculated according to Equation 4.10.

$$UCIV (\mu\text{mol}/\text{min}/\text{mg}) = \frac{_{AVG}v_1 \div \epsilon_{550} \times 0.2}{\mu\text{L protein} \times \mu\text{g}/\mu\text{L}/1000}$$

ϵ_{550} = molar extinction coefficient for reduced Cyt c for 200 μL reaction = 4180 Abs/mM (Pretorius, 2011).

(Equation 4.9)

$$CIV/UCS (\text{nmol}/\text{min}/UCS) = \frac{UCIV \times 1000}{UCS^{18}}$$

(Equation 4.10)

4.6.5 Data analysis

Statistical analyses were carried out as depicted in Figure 4.4 using SPSS Statistics (v.25.0; IBM) and Microsoft Excel[®] 2013. The kinetic measurements of technical replicates (triplicate or duplicate data in the case of limited sample volumes) were examined graphically for obvious outliers. Protein concentration and enzyme activities for each biological replicate were calculated as the mean of minimally two technical replicates (Equation 4.1 to Equation 4.10). Thereafter, the data was statistically evaluated by performing a two-way mixed analysis of variance (ANOVA) for each variable. The genotype was set as the between-subjects factor and brain region as the within-subjects factor. The latter was to account for the fact that the four brain regions were obtained from the same mouse and could be influenced by the same factors (Field, 2009b; Karpinski, 2011; The Open University, 2018). In this way, it could be determined if and how the *Ndufs4* KO affected the enzyme activities in each brain region and whether the enzyme activities displayed brain regional-specificity within a certain genotype. Together, the results were used to determine if regional differences in mitochondrial RC enzyme activities could be correlated with the regional vulnerability to neurodegeneration in *Ndufs4* KO mice.

¹⁸ Calculated in Section 4.6.4.4.

For each analysis the assumptions of: i) no outliers; ii) symmetry; iii) equal variances across genotype levels; and iv) sphericity had to be met (Field, 2009a; The Open University, 2018). Prior to ANOVA analysis, extreme outliers were removed using box-plots based on Tukey's method (Tukey, 1977): outliers were values lying outside three interquartile ranges below the 25th percentile or above the 75th percentile of the data set. Symmetry was assessed based on standardised skewness values. Equal variances across genotype levels and sphericity were assessed as part of the ANOVA model (Field, 2009b; The Open University, 2018). This was done by applying Box's M-test of equality of covariance matrices (Box, 1949), Levene's test of equality of error variances (Levene, 1960), and Mauchly's test of sphericity (Mauchly, 1940).

If the assumption of equal variances was violated ($p < 0.05$), spread-and-level plots were used to assess the severity and to identify the appropriate power transformation. Power transformation was applied for severe violations, and the ANOVA model was reconstructed on the transformed data. Sphericity was assessed based on Greenhouse-Geisser's epsilon (ϵ) (Greenhouse & Geisser, 1959): if $\epsilon \geq 0.9$, sphericity was assumed; if $0.9 > \epsilon \geq 0.7$, Greenhouse-Geisser corrected p -values were considered; if $0.7 > \epsilon \geq 0.5$, multivariate tests were used to establish confidence in the significance of the mixed ANOVA test. In the latter case, if the same conclusions were drawn by both tests, mixed ANOVA results were reported.

Pairwise tests were implemented when interaction effects were significant based on omnibus test p -value and partial eta squared (ηp^2) effect sizes. In other words, enzyme activities of brain regions were compared within a genotype using paired t-tests, and genotypes were compared within each brain region using independent samples t-tests, with Cohen's d -values reported as effect sizes. In the case of insignificant interaction effects and significant main effects, pairwise comparisons based on marginal means were reported together with ηp^2 effect sizes for the effect of genotype and Cohen's d -values for differences between brain regions. Values of $p < 0.05$ were considered statistically significant. Effect sizes were interpreted as follows: $\eta p^2 \geq 0.14$ or $d \geq 0.8$ indicated a large effect; $\eta p^2 \geq 0.06$ or $d \geq 0.5$ indicated a medium effect; and $\eta p^2 \geq 0.01$ or $d \geq 0.3$ indicated a small effect (Kirk, 1996; Ellis & Steyn, 2003).

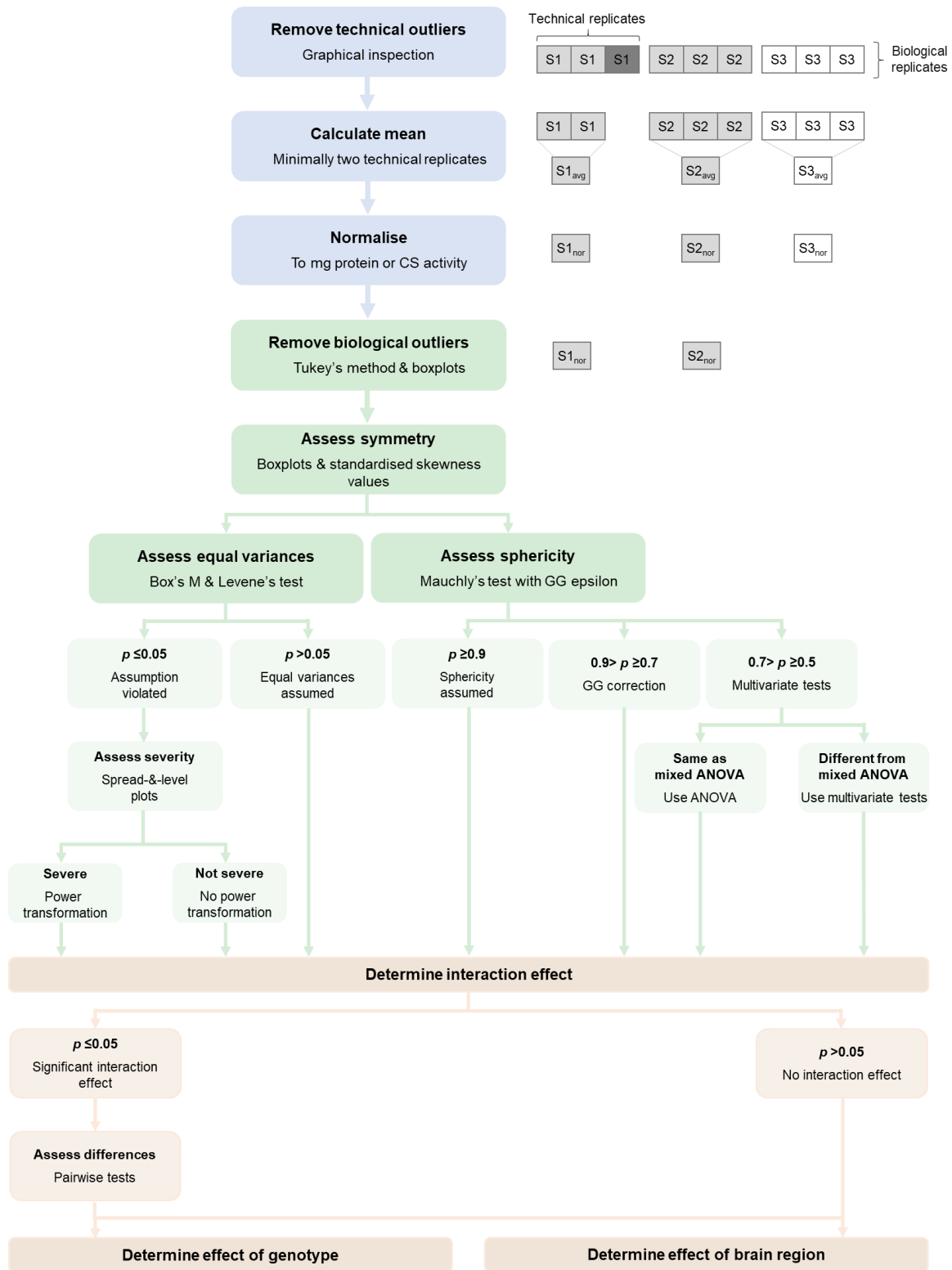


Figure 4.4: Data processing and analyses of enzyme activity data sets.

The data processing of raw data is shown in blue. It included the graphical removal of obvious outliers, calculation of the mean of at least two technical replicates, and normalisation of enzyme activity data according to protein content (in mg) or citrate synthase (CS) activity. Prior to interpreting the mixed ANOVA, assumptions of: i) no outliers; ii) symmetry; iii) equal variances across genotype; and iv) sphericity had to be met. This is depicted in green. Potential interaction effects (between genotype and brain region) were evaluated, followed by assessing the potential effects of genotype and brain region using appropriate tests. *Other abbreviations: GG, Greenhouse-Geisser; S1/2/3, biological sample 1/2/3; S_{avg} , average of technical replicates of a biological sample; S_{nor} , value for a biological sample after normalisation.*

4.7 Metabolomics investigation

4.7.1 Introduction

Objective 3 of this study was to investigate whether regional differences in metabolite levels could be correlated with the regional vulnerability to neurodegeneration in *Ndufs4* knockout (KO) mice. The *Ndufs4* KO disease state causes a response in the metabolism; i.e. in the way metabolites are chemically transformed (Gonzalez-Riano *et al.*, 2016). This can result in changes in the concentrations of metabolites in a brain region. The concentrations of free low molecular weight metabolites can be quantified by metabolomics techniques; i.e. the high-throughput analysis of the metabolic profile. The metabolic profile of each brain region will provide a perspective of the *in vivo* enzymatic activity in a manner which cannot be obtained by transcriptomics or proteomics (Vasilopoulou *et al.*, 2016a) and as a result, can be used to clarify the dynamics of metabolic pathways and reveal the underlying molecular mechanisms of the disorder.

To this end, the metabolic profiles of the vulnerable brain regions (BST, CB and OB) and the more resilient AC harvested from *Ndufs4* WT and KO mice, were analysed using metabolomics techniques. Considering the many functions of mitochondria and the profound changes that can occur in the metabolism when mitochondrial function is altered, metabolomics would be a highly profitable approach to identify metabolic markers, especially in the context of brain region vulnerability to mitochondrial CI dysfunction. However, since a single metabolomics platform cannot cover the heterogeneous range of metabolites in the brain tissue (González-Domínguez *et al.*, 2017), two complementary approaches were used in this study to expand metabolome coverage, namely 1) untargeted gas chromatography-time of flight spectrometry (GC-TOF); and 2) semi-targeted liquid chromatography-tandem mass spectrometry (LC-MS/MS) analyses of butyl ester derivatives of a defined set of compounds that are frequently affected in mitochondrial deficiencies.

The methods used in this study was based on previously developed in-house protocols currently used for metabolomics analyses (Lindeque *et al.*, 2013; Venter *et al.*, 2016; Esterhuizen *et al.*, 2018; Venter *et al.*, 2018). Even though the method specifics differ for the GC-TOF and LC-MS/MS analysis, respectively, the general experimental flow is the same. In short, metabolites were first extracted from the tissue and quality control (QC) samples were prepared. Samples for a given brain region were then divided into batches according to a pre-determined run order and batch design. This was followed by chemical derivatisation and then finally, analysis on a specific metabolomics platform using specific standardised parameters. The metabolic differences between KO and WT samples within the same brain region, as well as differences between the four regions of the same genotype, were evaluated using the specific statistical analyses outlined in this chapter.

Method standardisations were performed to ensure that the in-house methods currently used for metabolomics analysis were applicable on the tissue extracts from the mouse brain region tissue samples. Details are given in APPENDIX D. The experimental workflow for the metabolomics investigation of test samples is summarised schematically in Figure 4.5.

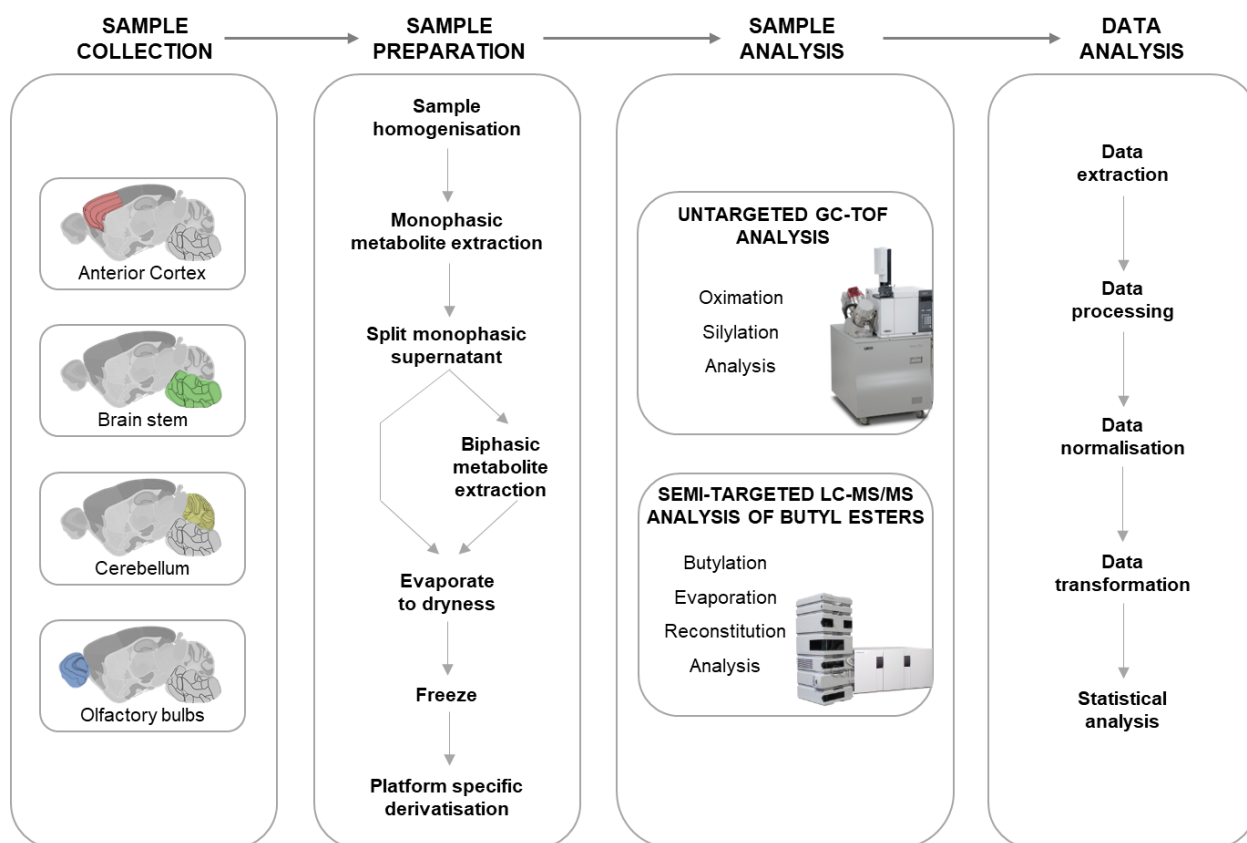


Figure 4.5: Schematic summary of the metabolomics experimental workflow.

The anterior cortex, brainstem, cerebellum and olfactory bulbs were collected and frozen at $-80\text{ }^{\circ}\text{C}$. The brain region tissue samples (from 25 WT mice and 21 KO mice) were then grouped according to brain region and were prepared successively as soon as possible. Each step in the experimental workflow, e.g. sample preparation or sample analysis, was completed for all four brain region-types before moving on to the next step. After platform-specific sample preparation, samples were analysed with the GC-TOF and LC-MS/MS analytical techniques, respectively. Platform-specific sample preparation and analysis with a single analytical platform was completed for all four brain region groups before preparing and analysing samples with the next analytical platform. The data was first subjected to various processing steps followed by statistical analysis and interpretation within the appropriate biological context.

4.7.2 Materials and instrumentation

4.7.2.1 Reagents and chemicals

All chemicals and standard compounds were of analytical-grade purity or higher. High-performance liquid chromatography (HPLC)-grade acetone (#010), acetonitrile (#017), chloroform (#049), isopropyl alcohol (#323), methanol (#230) and water (#365) were purchased from Honeywell Burdick & Jackson® (Muskegon, USA) via Anatech Instruments (Pty) Ltd (Olivedale, ZA). Chemicals and reagents purchased from Sigma-Aldrich (Kempton Park, ZA) included: O-bis(trimethylsilyl)trifluoroacetamide (BSTFA, #33027, Supelco, Bellefonte, USA), 1-butanol (#281549), acetyl chloride (#00990), formic acid (#94318), methoxyamine hydrochloride (#226904), pyridine (#270407) and trimethylchlorosilane (TMCS, #92360). Agilent ESI-L low concentration tuning mix (G1969-85000) were purchased from Chemetrix (Midrand, ZA). SABAX Pour Saline (0.9% NaCl w/v) (PBS, #7634) was purchased from Adcock Ingram Critical Care Pty Ltd, ZA).

Amino acid standards were purchased from Fluka® Analytical, Sigma-Aldrich (St. Louis, MO, USA) and included: L-alanine (#5130), L-arginine (#11010), L-asparagine anhydrous (#11150), L-aspartic acid (#11190), betaine anhydrous (#61962), L-citrulline (#27510), creatinine monohydrate (#27900), L-cystathionine (#30055), L-cysteine (#30090), L-cystine (#30200), L-glutamine (#49419), L-histidine (#53320), L-lysine (#62840), L-methionine (#64320), L-phenylalanine (#78020), L-serine (#84960), taurine (#86330), L-threonine (#89180), L-tryptophan (#93659) and L-tyrosine (#93830). From Sigma-Aldrich (St. Louis, MO, USA) the following standards were purchased: γ -aminobutyric acid (#A5835), L-glutamic acid (#G8415), glycine (#G7126), DL-isoleucine (#298689), L-leucine (#L8000), 1-methyl-L-hystidine (#67520), 3-methyl-L-hystidine (#M9005), L-ornithine hydrochloride (#O8305), L-pipecolic acid (#P2519), L-proline (#P0380), L-pyroglutamic acid (#F3634), L-valine (#V0500) and trans-4-hydroxy-L-proline (#41875) while β -alanine (#37009) was from BDH Biochemicals (Merck NT Laboratory Supplies, JNB, ZA).

The following carnitine and acylcarnitine standards were manufactured by Dr H.J. ten Brink (Organic Synthesis Laboratory, VU Medical Centre, AMS, NL): L-carnitine.HCl (C0), acetyl-L-carnitine.HCl (C2), propionyl-L-carnitine.HCl (C3), butyryl-L-carnitine.HCl (C4), isovaleryl-L-carnitine.HCl (C5), hexanoyl-L-carnitine.HCl (C6), octanoyl-L-carnitine.HCl (C8), decanoyl-L-carnitine.HCl (C10), dodecanoyl-L-carnitine.HCl (C12), tetradecanoyl-L-carnitine.HCl (C14), hexadecanoyl-L-carnitine.HCl (C16) and octadecanoyl-L-carnitine.HCl (C18).

The compounds used as internal standards, namely 2-acetamidophenol (2-AAP, #A7000), N,N-dimethyl-L-phenylalanine (DMPA, #273910), 3-phenylbutyric acid (3-PBA, #116807) and 4-phenylbutyric acid (4-BPA, #P21005) were purchased from Sigma-Aldrich (St. Louis, MO, USA). The stable isotopically labelled standards L-arginine- d_4 .HCl (Arg- d_4 , #DLM-6038), L-asparagine- $^{13}C_4,^{15}N_2$.H₂O (Asn- $^{13}C_4,^{15}N_2$, #CNLM-3819-H), L-citrulline- d_4 (Cit- d_4 , #DLM-6038), L-glutamine- $^{13}C_5,^{15}N_2$ (Gln- $^{13}C_5,^{15}N_2$, #CNLM-1275-H), L-isoleucine- d_{10} (Ile- d_{10} , #DLM-141), L-lysine- d_4 .2HCl (Lys- d_4 , #DLM-2640), L-phenylalanine-(ring- d_5) (Phe- d_5 , #E151P) and L-valine- d_8 (Val- d_8 , #E161P) were purchased from Cambridge Isotope Laboratories Inc. (Andover, MA, USA). The following isotopes were manufactured by Dr H.J. ten Brink (Organic Synthesis Laboratory, VU Medical Centre, AMS, NL): L-carnitine-(methyl- d_3).HCl (C0- d_3), octanoyl-L-carnitine- d_3 .HCl (C8- d_3), dodecanoyl-L-carnitine- d_3 .HCl (C12- d_3) and octadecanoyl-L-carnitine- d_3 .HCl (C18- d_3).

Nitrogen gas, for solvent evaporation, was generated with an NP60 nitrogen generator from Nitralife (Shrewsbury, Sandton, ZA), coupled with a Jemaco AN SPX refrigerated air dryer from Artic Driers International (Benoni, ZA). Instrument-grade helium (baseline 5.0) for use as a carrier gas in GC operations was purchased from African Oxygen Limited (Johannesburg, ZA).

4.7.2.2 Consumables and equipment

Consumables purchased from Sigma-Aldrich (Kempton Park, ZA) included BRAND[®] Microcentrifuge Tubes (1.5 mL, #Z336769), Eppendorf Safe-Lock Microtubes (1.5 mL, #Z606316 and 5 mL, #Z768790), Eppendorf tips (2 μ L to 200 μ L, #Z640093 and 50 μ L to 1000 μ L, #Z640093) and Volac[®] glass Pasteur pipettes (#Z310727). Tungsten Carbide Beads, 3 mm \varnothing (#69997) were purchased via Whitehead Scientific (Pty) Ltd (Brackenfell, ZA) from QIAGEN (Hilden, Germany). The following consumables were purchased from Agilent Technologies (Santa Clara, USA) via Chemetrix (Midrand, ZA) for LC-MS/MS analysis: certified glass vials (#5182-0714), pre-slit vial caps (#5183-2076), pulled point micro-inserts with polymer feet (#5181-1270) and pulled point glass micro-inserts, 250 μ L (#5183-2085) and for GC-TOF analysis: glass vials (#5190-4030), screw vial caps (#5182-0717), manual syringe (#5190-1510) and flat bottom glass micro-inserts, 400 μ L (#5181-3377).

The following consumables were purchased via Separations (Randburg, ZA) from Machete-Nagel GmbH & Co. KG (Düren, Germany): screw vial caps (#702287) and conical glass vials (#702088) for GC-TOF analysis of OB samples, as well as amber vials (#702973 and #702022) with the corresponding vial caps (#702966 and #702061) which were used for temporary storage of prepared solutions. Schott bottles were purchased from Glassworld and Chemical Suppliers CC (Randburg, ZA), as well as via Chemetrix (Midrand, ZA) from Agilent Technologies (Santa Clara, USA).

The following instrumentation were used: AF80 Scotsman ice flaker from Scotsman Ice Systems (Pty) Ltd (Boksburg, ZA), digital Ultrasonic cleaner CD-4820 from Healthcare Technologies (Cape Town, ZA), Eppendorf Pipettes (2-20 μ L, 10-100 μ L, 100-1000 μ L) from Merck Millipore, (Modderfontein, ZA), Heraeus™ Multifuge™ X3 Centrifuge (Thermo Fisher Scientific, USA), MM 400 Mixer Mill (Retsch GmbH & Co. KG, Haan, Germany), Vortex-genie 2 (Scientific Industries, Lasec), Snijders Scientific ultra-low -86 °C freezer and 4 °C refrigerator from United Scientific (Goodwood, ZA) and Techne DB200/3 Dri-Block heater and solvent evaporator (Separation Scientific, Honeydew, ZA).

The GC-TOF system consisted of a LECO® Pegasus® HT TOFMS (LECO® Africa Pty Ltd, Kempton Park, ZA), 7890A GC front-end system and 7693 autosampler both from Agilent Technologies (Santa Clara, USA) as well as a Phenomenex Zebron GC FocusLiner® Inlet Liner for Agilent (#AG0-4680, split/splitless, single taper w/wool, 4 mm ID x 78.5 mm L x 6.3 mm OD) and an Rxi-5Sil MS (30m x 250 μ m x 0.25 μ m) column from Restek (Bellefonte, USA).

The LC-MS/MS system consisted of an Agilent 6410 LC-QQQ system, Agilent 1200 series LC front-end and a C18 Zorbax SB-Aq (150 mm x 2.1 mm x 3.5 μ m) column purchased via Chemetrix (Midrand, ZA) from Agilent Technologies (Santa Clara, USA). The Phenomenex guard pre-column (#AF0-8479, KrudKatcher™ Ultra HPLC In-Line Filter) was purchased from Separations (Randburg, ZA).

4.7.3 Preparation of standard stocks and solutions

Individual standard solutions and mixes of standard solutions were prepared for method standardisation purposes (APPENDIX D), quality control (QC) during analysis, data extraction and for post-analysis normalisation procedures.

Individual internal standard stock solutions of 2-acetamidophenol (2-AAP, 3 333.33 ppm), N,N-dimethyl-L-phenylalanine (DMPA, 10 000 ppm), 3-phenylbutyric acid (3-PBA, 10 000 ppm) and 4-phenylbutyric acid (4-BPA, 10 000 ppm) were prepared in HPLC-grade water.

Isotopically labelled internal standards with at least a +2 amu label were used to avoid significant contamination from naturally occurring isotopes (Boysen *et al.*, 2018). All isotopically labelled internal standard stock solutions were obtained from Potchefstroom Laboratory for Inborn Errors of Metabolism (PLIEM lab, Biochemistry Department, NWU, Potchefstroom Campus) and included: L-carnitine-(methyl- d_3).HCl (C0- d_3 , 73.5 ppm), octanoyl-L-carnitine- d_3 .HCl (C8- d_3 , 77.5-ppm), dodecanoyl-L-carnitine- d_3 .HCl (C12- d_3 , 46 ppm) and octadecanoyl-L-carnitine- d_3 .HCl (C18- d_3 , 59 ppm) prepared in HPLC-grade water and L-valine- d_8 (Val- d_8 , 500 ppm), L-isoleucine- d_{10} (Ile- d_{10} , 500 ppm), L-phenylalanine-(ring- d_5) (Phe- d_5 , 500 ppm), L-lysine- d_4 .2HCl (Lys- d_4 , 500 ppm), L-glutamine- $^{13}C_5, ^{15}N_2$ (Gln- $^{13}C_5, ^{15}N_2$, 153,1 ppm), L-asparagine- $^{13}C_4, ^{15}N_2$.H₂O

(Asn-¹³C₄, ¹⁵N₂, 156,09 ppm), L-citrulline-*d*₄ (Cit-*d*₄, 500 ppm) and L-arginine-*d*₄ (Arg-*d*₄, 500 ppm) prepared in methanol.

Internal standard mix solutions were prepared by using the previously prepared individual internal standard stock solutions and HPLC-grade water. The internal standard mix solutions were made up to concentrations that would ensure identical on-column concentrations for all four brain regions despite the use of different solvent to tissue mass ratios (e.g. a higher solvent to tissue mass ratio was used for OB samples due to the smaller sample size) (see Section 4.7.4.2.1). DMPA and isotopically labelled internal standards were utilised for the LC-MS/MS analysis and were prepared to have final on-column concentrations of 30 ppm and 2.5 ppm respectively. The internal standards 3-PBA, 2-AAP and 4-PBA were utilised for the GC-TOF analysis and were prepared to have final on-column concentrations of respectively 50 ppm, 40 ppm and 40 ppm.

The internal standard (IS) mix solutions for the OB (OB-mixes) were prepared to have the following final concentrations: 1) OB-IS₁: 41.67 ppm DMPA and 92.59 ppm 3-PBA; 2) OB-IS₂: 100 ppm 2-AAP and 100 ppm 4-PBA; and 3) OB-Iso containing all the isotopically labelled internal standards (Iso) to a final concentration of 1.84 ppm.

The following internal standard (IS) mix solutions were prepared in bulk for the remaining brain regions (R-mixes): 1) R-IS₁: 93.75 ppm DMPA and 156.25 ppm 3-PBA; 2) R-IS₂: 200 ppm 2-AAP and 200 ppm 4-PBA; and 3) R-Iso containing all the isotopically labelled internal standards to a final concentration of 3.68 ppm. The R-mixes were aliquoted for AC, BST and CB respectively and used separately.

A standard compound mix solution (S_{SPIKE}) for spiking biological QC samples and for quality control purposes during analysis and data extraction, was prepared in HPLC-grade water. The mix was prepared by adding the individual standard stock solutions (8 ppm final concentration) from the analytes monitored during the LC-MS/MS analysis (analytes are listed in APPENDIX D).

The solutions were prepared in sufficient amounts for all analytical applications. They were sonicated for ~10 minutes at room temperature to ensure complete dissolution and then aliquoted in amber vials to be stored at -20 °C until required.

4.7.4 Methods

4.7.4.1 Samples and experimental groups

For the analysis of metabolite levels in mouse brain region tissue samples, the brain regions were collected over time as mice became available and were stored at -80 °C (Section 4.4). After the regions of all 25¹⁹ WT and 21 KO mice were collected, the samples were grouped according to brain region and each region-type was prepared and analysed as a separate group. However, each step of the experimental procedure was completed for all brain region-types before moving on to the next step. For instance, metabolites were extracted from the samples of all the separate brain region groups before proceeding with derivatisation of all the grouped samples for analysis by a specific metabolomics platform. In this way, the time between analysing the different brain region-types on the same metabolomics platform was minimised to make the data more comparable. To minimise non-biological variation attributed to pre-analytical procedures, all samples underwent the same number of freeze-thaw cycles.

4.7.4.2 Metabolite extraction

The extraction of low molecular weight metabolites from the brain region tissues was carried out using the “stepwise” modified version of Bligh and Dyer’s classic methanol/chloroform/water method (Bligh & Dyer, 1959) as reported by Wu *et al.* (2008). Methanol, water (containing internal standards) and chloroform were added in two steps to give an initial monophasic extract (methanol:chloroform:water, 6:2:2). A fraction of the supernatant was used for the untargeted GC-TOF analysis of polar and nonpolar metabolites. To another fraction, additional chloroform and water were added (methanol:chloroform:water, 2:2:1.8) to give a biphasic separation of polar metabolites in the top methanol/water phase and nonpolar metabolites in the bottom chloroform phase. The top phase (containing polar metabolites) of the biphasic extract was analysed using the LC-MS/MS platform. Details of the metabolite extraction procedures are illustrated in Figure 4.6.

¹⁹The number of samples are given as an approximate value since some samples were deemed unsuitable for use in particular cases due to experimental errors or due to the limited sample volume.

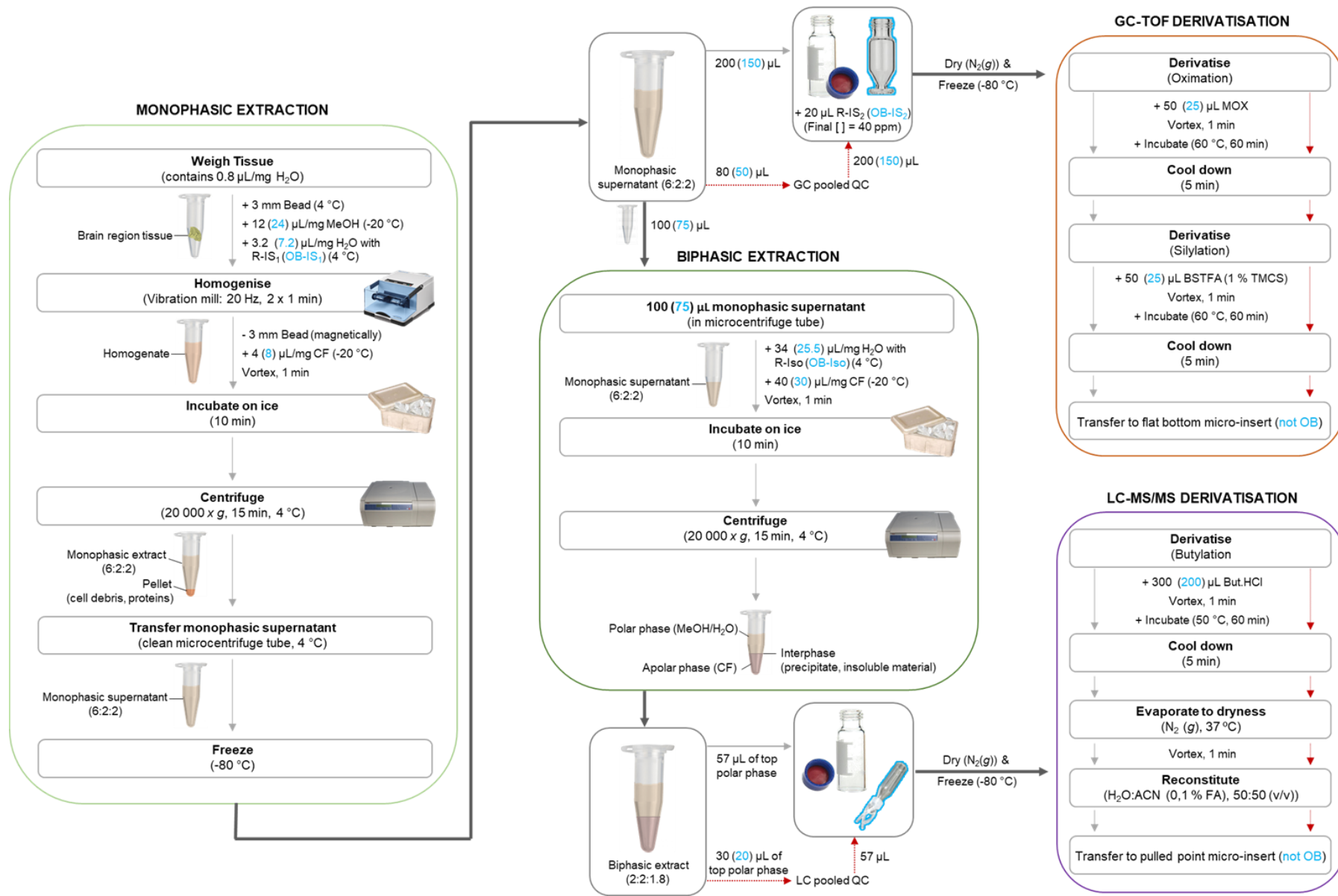


Figure 4.6: Schematic diagram of the standardised procedure used for metabolite extraction and derivatisation of mouse brain region tissue samples.

Brain region tissue samples were grouped according to brain region. Brain region groups were prepared successively as soon as possible. First, all metabolites (polar and nonpolar) were extracted from the tissue into a monophasic solution (6:2:2, MeOH:CF:H₂O) by homogenising the tissue in the presence of a bead, H₂O with internal standards (DMPA for LC-MS/MS and 3-PBA for GC-TOF) and organic solvents (MeOH and CF) using a vibration mill (shown in light green block). After addition of more CF, incubation on ice and centrifugation, the monophasic supernatant of each sample was transferred to a clean tube and divided for analysis by the different analytical platforms (GC-TOF and LC-MS/MS). Of each monophasic supernatant, a fraction was transferred to a vial containing R-IS₂ or OB-IS₂ (a mixture of the internal standards 2-AAP and 4-PBA) for derivatisation and GC-TOF analysis; a fraction was used to prepare a GC QC-pool sample; and a fraction was aliquoted into a clean microcentrifuge tube for biphasic extraction and LC-MS/MS analysis (shown in dark green block). A biphasic separation of the solvent system was induced by adding H₂O containing isotopically labelled internal standards (R-Iso or OB-Iso) and CF to have a final ratio of 2.0:2.0:1.8 (MeOH:CF:H₂O). After the samples were incubated on ice and centrifuged, a fraction of the top polar phase of the biphasic extract was transferred to a vial for derivatisation and LC-MS/MS analysis; while another fraction was used to prepare a LC QC-pool sample. From this point, all QC samples (indicated by red arrows) were treated identically to test samples. The samples were dried under a gentle stream of nitrogen (37 °C) in a fume hood, tightly capped and frozen at -80 °C until required for derivatisation. Samples for GC-TOF analysis were derivatised by oximation and silylation (shown in orange block), while samples for LC-MS/MS analysis was butylated (shown in purple block). The final solution containing the derivatised metabolites were then transferred to a micro-insert except in the case of the OB samples. The latter were either already in an insert (LC-MS/MS analysis) or in a conical vial for smaller sample volumes. Information regarding OB samples is given in light blue. *Other abbreviations: 2-AAP, 2-acetamidophenol; ACN, acetonitrile; 3-PBA, 3-phenylbutyric acid; 4-PBA, 4-phenylbutyric acid; AC, anterior cortex; BST, brainstem; BSTFA, O-bis(trimethylsilyl)trifluoroacetamide; ButHCl, butanolic hydrochloric acid (1-butanol and concentrated acetylchloride in a 4:1 ratio (v/v)); CB, cerebellum; CF, chloroform; DMPA, N,N,-dimethylphenylalanine; FA, formic acid; GC-TOF, gas chromatography time-of-flight mass spectrometry; H₂O, water; LC-MS/MS, liquid chromatography tandem mass spectrometry; MeOH, methanol; MOX, methoximation solution (20 mg/mL methoxyamine hydrochloride in pyridine); N₂(g), stream of nitrogen gas; OB, olfactory bulbs; QC, quality control; R(OB)-IS₁, internal standard mix of DMPA and 3-PBA for the rest of the brain regions (AC, BST, CB) or for OB; R(OB)-IS₂, internal standard mix of 2-AAP and 4-PBA for the rest of the brain regions (AC, BST, CB) or for OB; R(OB)-Iso, isotopically labelled internal standard mix for the rest of the brain regions (AC, BST, CB) or for OB; TMCS, trimethylchlorosilane.*

4.7.4.2.1 Monophasic metabolite extraction

A final monophasic ratio of 6:2:2 (v/v) methanol:chloroform:water, assuming a 80% water content in wet brain tissue (Gonzalez-Riano *et al.*, 2016), was used for all brain regions to ensure a monophasic extract and to avoid solvent partition (Gullberg *et al.*, 2004). Solvent volumes were added according to sample weight (pre-analysis normalisation) to obtain similar concentrations prior to analysis, and thus similar instrumental responses for all samples (Chen *et al.*, 2017b). In this way, variation due to matrix-induced ion suppression was minimised and the optimal amount of sample (concentration of metabolites) could be injected each time (Kapoor & Vaidyanathan, 2016; Boysen *et al.*, 2018). Generally, solvents were added to give a 5% (w/v) final monophasic solution. However, the much smaller OB tissues (wet mass <20 mg) required a higher solvent to tissue mass ratio of 2.5% (w/v) to obtain sufficient volume for sample preparation. Samples were kept on ice where possible and all added solvents were ice-cold (4 °C) unless specified otherwise. From this point, solvent volumes added to the OB tissue samples will follow in parentheses “()” after the volumes given for the R tissue samples.

On the day of extraction, the frozen brain samples were weighed in a clean, pre-cooled 1.5 mL safe-lock microcentrifuge tube and each tube received a cold, single steel bead (3 mm Ø) to increase the extraction efficiency (Gullberg *et al.*, 2004). To the frozen pre-weighed brain tissue, 12 µL/mg (24 µL/mg) methanol (at -20 °C) and 3.2 µL/mg (7.2 µL/mg) water, containing internal standards (R-IS₁ or OB-IS₁), were added to obtain a final concentration (in the final monophasic solution after addition of chloroform) of 25 ppm (16.67 ppm) for 3-PBA and 15 ppm (7.5 ppm) for DMPA. The soft brain regions were then homogenised for two minutes (one minute, rotate milling cups, one minute) at 20 Hz using the high-throughput Retsch MM 400 vibration mill. The vibration mill ensured fast, consistent and complete homogenisation of the soft brain tissue while avoiding sample carryover as each tissue was contained in a separate tube (Wu *et al.*, 2008). Each bead was magnetically removed (carefully to prevent sample loss) after which 4 µL/mg (8 µL/mg) chloroform (at -20 °C) was added to the sample. The samples were then vortexed for one minute, incubated on ice for 10 minutes and centrifuged at 20 000 x g for 15 minutes at 4 °C to pellet the protein and tissue debris.

The monophasic supernatant was then transferred to a clean microcentrifuge tube (being careful not to disturb the pellet) and divided for analysis with the different platforms as shown in Figure 4.6. For GC-TOF analysis, each sample was vortexed and 200 µL (150 µL) of the monophasic supernatant was quickly transferred to a glass vial containing 20 µL R-IS₂ (OB-IS₂ in a conical vial) to a final on-column concentration of 40 ppm. The samples were dried under a gentle stream of nitrogen (37 °C) in a fume hood, tightly capped and frozen at -80 °C until derivatisation. For LC-MS/MS analysis, 100 µL (75 µL) of the monophasic supernatant was transferred to a microcentrifuge tube for the biphasic separation of the metabolites.

4.7.4.2.2 Biphasic metabolite extraction

A biphasic extraction was required to separate the monophasic supernatant into a polar and nonpolar phase so that the former could be analysed with the LC-MS/MS platform. The final ratio of solvents used in the biphasic methanol:chloroform:water extraction was 2.0:2.0:1.8 for all brain regions. To the 100 μL (75 μL) monophasic supernatant (Section 4.7.4.2.1) was added: 34 μL (25.5 μL) cold (4 $^{\circ}\text{C}$) water containing stable isotopically labelled standards (R-Iso or OB-Iso) to a final on-column concentration of 2.5 ppm; and 40 μL (30 μL) chloroform (at -20 $^{\circ}\text{C}$). The samples were then vortexed for one minute, incubated on ice for 10 minutes to allow the partitioning of the solvent system and centrifuged at 20 000 $\times g$ for 15 minutes at 4 $^{\circ}\text{C}$. Due to the higher density of chloroform compared with the water/methanol mixture, the nonpolar (lipid) phase forms at the bottom of the tube. This enables retrieval of the upper polar phase without penetrating the interphase (containing precipitate and insoluble material) or the nonpolar phase. Thus, minimising potential contamination of the polar extract which might compromise analysis or cause unwanted variation (Matyash *et al.*, 2008; Löfgren *et al.*, 2016). Of the top aqueous phase (containing polar metabolites), 57 μL was added to a glass vial (or to a vial with a pulled point micro-insert with polymer feet for the OB). The samples were dried under a gentle stream of nitrogen (37 $^{\circ}\text{C}$) in a fume hood, tightly capped and frozen at -80 $^{\circ}\text{C}$ until required for derivatisation.

4.7.4.3 Preparation of quality control (QC) samples

Quality control (QC) samples were prepared for each analytical platform and included in every analytic batch to monitor analytical performance, and to assess data quality after analysis (Begley *et al.*, 2009; Godzien *et al.*, 2015). Table 4.2 summarises the different types of QC samples that were used in this study and their purpose of inclusion for each analytical platform. In the following sub-sections, the volumes added to the OB tissue samples will follow in parentheses “()” after the volumes given for the R tissue samples.

4.7.4.3.1 Preparation of QC samples for GC-TOF analysis

Biological bulk QC samples of sufficient volume were prepared per brain region-type by pooling ~80 μL (~50 μL) from the remaining monophasic supernatant of each sample. Thereafter, region-specific pooled QC samples for GC-TOF analysis (QC_{GC}) were prepared by transferring 200 μL (150 μL) of the bulk QC-pool to a glass vial containing 20 μL R-IS₂ (or OB-IS₂) (see Figure 4.6). The bulk QC-pool mixture was vigorously vortex mixed before aliquoting to ensure that a homogeneous mixture is transferred to each vial.

The remaining bulk QC-pool sample of each brain region was pooled together to prepare a bulk mixture from the monophasic extracts of all four brain regions samples. Universal²⁰ biological QCs (UQC_{GC}) were then prepared by transferring 200 µL of the bulk monophasic extract mixture of all brain regions to a glass vial containing 20 µL R-IS₂.

In addition, universal GC samples containing standard compounds and internal standards (S/IS_{GC}) with no metabolite extracts were prepared to a final on-column concentration of 15 ppm. These were prepared with the addition of 187.6 µL of S_{SPIKE} to each glass vial containing 20 µL R-IS₂. Samples containing only the internal standard mixture (IS_{GC}) were prepared by adding 32 µL of R-IS₁ (27 µL of OB-IS₁) and 20 µL of R-IS₂ (or OB-IS₂) to each glass vial. The QC_{GC}⁻, UQC_{GC}⁻, S/IS_{GC}⁻, and IS_{GC}⁻-samples, together with empty vials for sample blanks (SB_{GC}), were dried under a gentle stream of nitrogen (37 °C) in a fume hood. Thereafter, the vials were tightly capped and frozen at -80 °C until derivatisation.

4.7.4.3.2 Preparation of QC samples for LC-MS/MS analysis

A biological region-specific bulk QC pool of sufficient volume was prepared from equal volumes (30 µL for R and 20 µL for OB) of the remaining aqueous (polar) phase from the biphasic extract of each sample. From the bulk QC-pool mixture, biological region-specific pooled QC samples for LC-MS/MS analysis (QC_{LC}) were prepared by aliquoting 57 µL thereof into a separate vial (or to a vial with a pulled point micro-insert with polymer feet for the OB). The bulk QC-pool mixture was vigorously vortex before aliquoting to ensure a homogeneous mixture is transferred each time. Spiked biological QC_{LC} samples (QC_{SPIKE}) were prepared for each region by spiking 57 µL of a pooled QC_{LC} sample with S_{SPIKE} to a final on-column concentration of 2.5 ppm.

Universal biological QCs for LC-MS/MS analysis (UQC_{LC}) were prepared by mixing the remaining bulk QC-pool samples of all four brain regions and by aliquoting 57 µL of the bulk mixture into separate glass vials. Universal isotope-mix spiked with internal standard (Iso/IS_{LC}) was prepared by adding R-Iso and DMPA to vials so that a 2.5 ppm final on-column concentration was obtained for all compounds. Similarly, a universal standard solution mix spiked with isotope and internal standard (S/Iso/IS_{LC}) was prepared by adding S_{SPIKE}, R-Iso and DMPA, all to a final on-column concentration of 2.5 ppm. The QC_{LC}⁻, QC_{SPIKE}⁻, UQC_{LC}⁻, Iso/IS_{LC}⁻ and S/Iso/IS_{LC}⁻-samples, together with empty vials for sample blanks (SB_{LC}), were dried under a gentle stream of nitrogen (37 °C) in a fume hood, capped and frozen at -80 °C until derivatisation.

²⁰ From here on "universal" refers to samples that are identical for all brain regions analysed by a specific metabolomics platform.

Table 4.2: Quality control (QC) samples used in GC-TOF and LC-MS/MS analysis of metabolites extracted from mouse brain region tissues.

Quality control sample	Region-specific (RS) or universal* (U)	Symbol	Platform	Constituents	Purpose / Use
Biological QC	RS	QC _{GC} / QC _{LC}	GC / LC	Equal volumes of region-specific brain tissue extracts (monophasic / polar phase).	Equilibration and stabilisation of the system, evaluate analytical performance during the run, method repeatability, data quality, and for batch correction or normalisation (Begley <i>et al.</i> , 2009; Kirwan <i>et al.</i> , 2014; Godzien <i>et al.</i> , 2015; Dudzik <i>et al.</i> , 2017).
Spiked biological QC	RS	QC _{SPIKE}	LC	Biological QC sample (QC _{LC}) with standard compound solution mixture containing all analytes for which MRMs were set up (S _{SPIKE}).	Evaluate matrix effects and retention times, and to discern target compound peaks from other co-eluting peaks (Godzien <i>et al.</i> , 2015; Gika <i>et al.</i> , 2016; Dudzik <i>et al.</i> , 2017).
Universal biological QC	U	UQC _{GC} / UQC _{LC}	GC / LC	Pooled mixture of extracts (monophasic / polar phase) from all brain regions.	Equilibration and stabilisation of the system, evaluate analytical method performance between batches from different regions (Kirwan <i>et al.</i> , 2014; Godzien <i>et al.</i> , 2015; Dudzik <i>et al.</i> , 2017).
Standard compound mix	U	S/IS _{GC} / S/Iso/IS _{LC}	GC / LC	Standard compound solution mixture containing all analytes for which MRMs were set up (S _{SPIKE}) as well as platform specific internal standard mixtures: GC-TOF: DMPA and 3-PBA (R-IS ₁) LC-MS/MS: DMPA and 3-PBA (R-IS ₁) with isotope-mix (R-Iso)	Evaluate analytical performance and sensitivity before and after the analysis of a sample batch (Godzien <i>et al.</i> , 2015; Gika <i>et al.</i> , 2016; Dudzik <i>et al.</i> , 2017).
Internal standard mix	U	IS _{GC} / Iso/IS _{LC}	GC / LC	Platform specific internal standard mixtures: GC-TOF: DMPA and 3-PBA (R(OB)-IS ₁) with 2-AAP and 4-PBA (R(OB)-IS ₂) LC-MS/MS: DMPA and 3-PBA (R(OB)-IS ₁) with isotope-mix (R-Iso)	Control for and filter interferences/artefacts/contaminants present in internal standard solutions.

Experimental sample blank	U*	SB _{GC} / SB _{LC}	GC / LC	Prepared identically to experimental samples and contains only the final solvent/s in which sample metabolites are derivatised (GC-TOF) / reconstituted (LC-MS/MS)	Used as a negative control to test for and filter interferences/artefacts that stem from impurities or contaminations from reagents and/or consumables. Also to test for carry-over and used for cleaning e.g. GC liners and LC needle seat capillary/guard column to prevent sample build-up (Kirwan <i>et al.</i> , 2014; Fiehn, 2016; Dudzik <i>et al.</i> , 2017).
Analytical blank / mobile phase blank	U	AB	LC	Consist of the mobile phase used during the analytical run.	Test for, identify and filter interferences/artefacts that stem from impurities or contamination from reagents and/or consumables used in the analytical method only e.g. mobile phase.

* The term “universal” refers to samples that are identical for all brain regions analysed by a specific metabolomics platform

Other abbreviations: 2-AAP, 2-acetamidophenol; 3-PBA, 3-phenylbutyric acid; 4-PBA, 4-phenylbutyric acid; AC, anterior cortex; BST, brainstem; CB, cerebellum; DMPA, N,N-dimethyl-L-phenylalanine; GC-TOF, gas chromatography time-of-flight mass spectrometry; LC-MS/MS, liquid chromatography tandem mass spectrometry; MRM, multiple reaction monitoring; OB, olfactory bulbs; QC, quality control; R(OB)-IS₁, internal standard mix of DMPA and 3-PBA for the rest of the brain regions (AC, BST, CB) or for OB; R(OB)-IS₂, internal standard mix of 2-AAP and 4-PBA for the rest of the brain regions (AC, BST, CB) or for OB; R(OB)-Iso, isotopically labelled internal standard mix for the rest of the brain regions (AC, BST, CB) or for OB; RT, retention time; RS, region-specific; U, universal.

4.7.4.4 Derivatisation

4.7.4.4.1 Methoximation and trimethylsilylation derivatisation for GC-TOF analysis

GC-TOF analysis of samples can cover a relatively wide range of metabolites. This includes organic acids, amino acids, sugars (usually smaller than three mono-saccharides in length), sugar alcohols, fatty acids, and phosphorylated compounds (Zarate *et al.*, 2016). However, polar low molecular weight metabolites are not sufficiently volatile for GC-TOF analysis and require chemical derivatisation. The current in-house metabolomics derivatisation method for GC-TOF metabolic fingerprinting of a wide range of metabolites in biological samples is based on a two-step derivatisation procedure to convert polar metabolites to their more volatile (methoxime)-trimethylsilyl [(MeOX)-TMS] derivatives (Venter *et al.*, 2016; Esterhuizen *et al.*, 2018). In the first step, carbonyl groups are methoximated to prevent ring formation and reduce the number of stereoisomers. In the second silylation step, a silyl group [-Si(CH₃)₃-] of the trimethylsilyl (TMS) reagent replaces active hydrogens (e.g. -OH, -SH, -NH₄⁺, -COOH) (Zarate *et al.*, 2016).

The sample derivatisation procedure for GC-TOF analysis is illustrated in Figure 4.6. The frozen samples (Section 4.7.4.2.1 and Section 4.7.4.3.1) (the brain region-specific monophasic extracted test samples, together with QC_{GC}, UQC_{GC}, S/IS_{GC}, IS_{GC}, and SB_{GC}) were left to reach room temperature before unscrewing the caps. This was done to avoid condensation of water inside the vials which could render the moisture sensitive BSTFA reagent unsuitable (Fiehn, 2016). In addition, the samples were briefly evaporated to dryness under nitrogen (37 °C) in a fume hood to remove any potential moisture that could have entered the vials.

Methoximation solution (20 mg/mL methoxyamine hydrochloride in pyridine) was freshly prepared each day in an amber vial. It was briefly heated (35 °C) to ensure dissolution and then cooled down before adding 50 µL (25 µL for OB²¹) to each dried sample. Each sample was immediately capped after addition of methoximation solution to prevent evaporation of the organic solution (Fiehn, 2016). The samples were then vortexed for one minute to dissolve the dried compounds and incubated for one hour at 60 °C. Thereafter, samples were left for five minutes to cool to room temperature (to avoid evaporation of volatile compounds when unscrewing the caps) before trimethylsilylation was performed by adding 50 µL (25 µL for OB) freshly prepared BSTFA (containing 1% TMCS as a catalyst) to the methoximated samples. Each sample was immediately capped, and the samples were then vortexed for one minute and incubated again for one hour at 60 °C.

²¹ For clarification sake, “for OB” from here on indicates that while a certain volume was used for all other investigated brain regions, in the case of the OB, a different volume was required due to the limited sample volume, as explained in Section 4.7.4.2.1.

After trimethylsilylation, samples were left to cool to room temperature, and each was transferred to a flat bottom micro-insert using a clean glass Pasteur pipette (except for the OB samples for which micro-inserts were not required due to the use of conical vials). All derivatisation reagents were prepared and transferred with an Agilent manual glass syringe.

4.7.4.4.2 Butylation derivatisation for LC-MS/MS analysis

For LC-MS/MS analysis on a reverse phase chromatographic column, carboxylic acid containing metabolites were derivatised to their corresponding butyl-esters using acidified butanol according to in-house metabolomics protocols (Esterhuizen *et al.*, 2018; Venter *et al.*, 2018). During butylation, the active hydrogen(s) of carboxylic acid group(s) of a metabolite is replaced with a butyl group (m/z 56) to increase lipophilicity (and thus chromatographic retention of polar metabolites). This also promotes ionisation efficiency through the simplification of protonation behaviour by leaving only positively chargeable groups (Harder *et al.*, 2011; Giesbertz *et al.*, 2015). Furthermore, butylation of compounds gives characteristic fragmentation patterns during collision-induced dissociation (CID) which improves selectivity when monitored by tandem MS. Of interest to this study is the common neutral loss of 102 m/z for amino acids and the formation of the common product ion at m/z 85 for acylcarnitines (Santa *et al.*, 2007; Harder *et al.*, 2011).

Sample derivatisation for LC-MS/MS analysis is illustrated in Figure 4.6. The frozen samples (Section 4.7.4.2.2 and Section 4.7.4.3.2) (brain region-specific biphasic extracted test samples, QC_{LC}, QC_{SPIKE}, UQC_{LC}, Iso/IS_{LC}, S/Iso/IS_{LC}, and SB_{LC} samples) were left to reach room temperature and were briefly evaporated to dryness under a gentle stream of nitrogen (37 °C) in a fume hood. This ensured the removal of any moisture that could have entered the vials during storage or after decapping. Any residual moisture that remain in the vials could hinder butylation. Butylation solution (3 N butanolic hydrochloric acid, ButHCl) was prepared by slowly adding concentrated acetylchloride to 1-butanol in a 1:4 ratio (v/v) in a glass reagent bottle kept on ice. After adding 300 μ L (200 μ L for OB) of the butylation solution to each of the vials (or to each vial with a pulled point micro-insert with polymer feet for OB samples) containing the dried sample, the vials were tightly capped, vortexed for one minute. Then followed incubation for one hour at 50 °C. After samples were left to cool to room temperature, the reaction mixture was dried under a gentle stream of nitrogen (37 °C). The dry butylated metabolite residue was reconstituted in a solution corresponding with the mobile phases used during analysis: a 50 μ L (25 μ L for OB) mixture of water:acetonitrile (50:50, v/v) containing 0.1% formic acid. The vials were then capped and vortexed vigorously for one minute to ensure solvation of derivatives. Thereafter, each reconstituted mixture was transferred to a pulled point glass micro-insert (except for the OB samples which were already contained in micro-inserts) using a clean glass Pasteur pipette.

4.7.4.5 Run order and batch design

Factors which could affect instrument reproducibility should be carefully considered. This is because unwanted variation in the metabolomics data may obscure the biological variation of interest. The order and time of sample analysis could cause variability and bias due to run order effects or potential drifts (gradual changes) in peak intensities. These result from drift in instrument performance or in analyte concentrations (Begley *et al.*, 2009; Gika *et al.*, 2016; Zarate *et al.*, 2016). For instance, GC-TOF analytes can continue to derivatise as they remain in the silylation reagent during analysis. To minimise potential drifts in peak intensities with time, samples were analysed in 'batches'; i.e. the number of samples of an entire group (consisting of 46 samples of the same brain region and associated QC samples) was divided into smaller sub-sets (or 'batches') (Begley *et al.*, 2009). Each of these batches was prepared and analysed in a single sequence. Begley *et al.* (2009) recommended that a batch should be completed within 30 hours of derivatisation for TMS derivatives. However, the size of a batch for a given analytical platform can be decided based on previous experience of column performance with a particular sample matrix, as well as MS contamination over time (Gika *et al.*, 2016). The run order of test samples were randomised using the randomisation equation in Microsoft Excel® 2013. This prevents a correlation between biological factors and analysis order (Dudzic *et al.*, 2017).

Prior to analysis, tuning and maintenance activities were carried out to confirm acceptable analytical performance. A sufficient number of samples with a suitable matrix was injected to equilibrate the system (Gika *et al.*, 2016). QC samples were injected at the start and end of each analytical batch and intermittently at regular intervals between samples depending on the analysis time and number of samples per batch (Godzien *et al.*, 2015). Generally, non-matrix solvents or standard solutions used for QC purposes were only injected at the start or end of a batch to prevent partial deconditioning of the system. Exceptions might for example include the injection of the solutions to unblock or prevent blockage of instrument components (Gika *et al.*, 2016).

4.7.4.5.1 Run order and batch design for GC-TOF analysis

The 46 biological samples (25 WT and 21 KO monophasic supernatant extracts) of each brain region-type (AC, BST, CB and OB) were randomised and divided into two batches of similar size to ensure analysis of samples within ~24 hours (Figure 4.7). Before analysis of a batch, the injection needle was cleaned using a mixture of acetone:isopropyl alcohol (50:50, v/v), and the needle wash solution was replaced. The mass and detector calibration and checks were performed according to the instrument manual to ensure optimal system performance. In addition, the starting conditions of the analytical method were loaded, and parameters allowed to equilibrate and stabilise for at least 30 minutes. The inlet liner was only replaced before analysis of a brain region group; i.e. after every two batches.

Each analytical batch was designed to allow evaluation of intra- and inter-batch variation (Kirwan *et al.*, 2014) and consisted of the following samples as determined by the total runtime per sample: four individual QC_{GC}, two individual UQC_{GC}, one S/IS_{GC}, one IS_{GC}, one SB_{GC} and ~23 brain tissue samples. The S/IS_{GC}- and two individual UQC_{GC}-samples were injected at the start and end of most analytical batches. The QC_{GC} samples derived from a single brain region QC-pool were analysed at the beginning and end of each batch and intermittently after every eight biological samples. Fiehn (2016) recommended a QC sample for at least every 11th injection for GC. The first QC sample was injected three times at the start of each batch to allow for equilibration. The second and third QC samples were injected in duplicate for data-processing purposes. The fourth QC sample, IS_{GC}- and SB_{GC}-samples were injected once at the end of each batch. The samples of all four brain regions were analysed consecutively (as practically possible making provision for repairs and cleaning of instruments as required) to limit variation on the instruments, solvents and surrounding conditions (Lindeque *et al.*, 2013).

4.7.4.5.2 Run order and batch design for LC-MS/MS analysis

The ~46 biological samples (25 WT and 21 KO polar phase extracts) of each brain region-type (AC, BST, AC, OB) were divided into two LC-MS/MS analytical batches using the same randomised order as for the GC-TOF analysis (Section 4.7.4.5.1), as illustrated in Figure 4.8. Batches were designed to ensure complete analysis of each batch within ~24 hours by considering the total runtime per sample. Before analysis of a batch, the LC column was flushed at 40 °C for 30 minutes to 60 minutes with 95% of mobile phase B followed by 95% of mobile phase A. The ionisation source was cleaned using a mixture of methanol:isopropyl alcohol in a 3:1 ratio and a lint-free cloth. The accumulation of residue on the source can lead to a significant decrease in sensitivity (Gika *et al.*, 2016). When starting a batch, the column was equilibrated at the starting conditions for at least 30 minutes. Additional maintenance and checks were performed before analysis of a brain region group. An automatic Mass Calibration or Check Tune was performed using the Agilent tuning program and by infusing a reference mix. The MS was cleaned by infusing 100% of mobile phase B for three hours. Finally, the mobile phase and needle wash solution was topped up to a sufficient volume for analysis of two consecutive batches.

Each analytical batch consisted of the following samples: four individual QC_{LC}, one QC_{SPIKE}, two individual UQC_{LC}, one Iso/IS_{LC}, one S/Iso/IS_{LC}, one SB_{LC} and ~23 brain tissue samples. Each batch was initiated by running the mobile phase (water:acetonitrile with 0.1% formic acid) through the column (analytical blank, AB) followed by injection of the experimental blank (SB_{LC}). The QC_{SPIKE}-sample was injected at the start and end of each analytical batch.

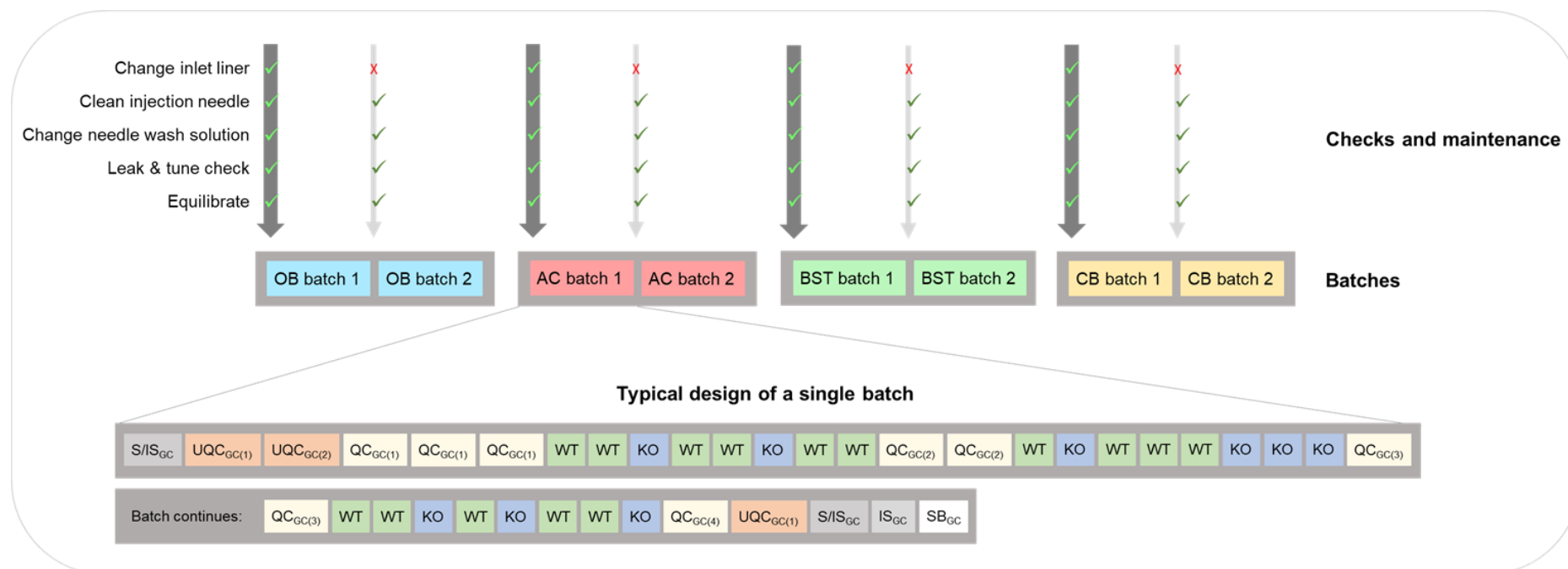


Figure 4.7: Run order and batch design of the GC-TOF analysis of derivatised monophasic extracts from *Ndufs4* wild-type and knockout brain region tissue samples.

Brain region tissue samples were grouped according to brain region and the derivatised tissue extracts of the four brain regions were analysed successively as soon as practically possible. For each brain region-type (olfactory bulbs, OB; anterior cortex, AC; brainstem, BST; and cerebellum, CB), the *Ndufs4* knockout (KO, n = ~21) and wild-type (WT, n = ~25) samples were randomised and divided into two analytical batches of similar size which would ensure batch completion within ~24 hours of derivatisation. In each batch, ~23 biological samples (WT and KO in a randomised order) were analysed intermittently with four equivalent region-specific biological pooled quality control (QC_{GC}) samples. A universal GC sample containing only standard compounds (S/IS_{GC}), two universal QCs (UQC_{GC}) which consisted of a mix of the pooled QCs of all four brain regions, a sample containing only the GC internal standards (IS_{GC}) and an experimental blank sample (SB_{GC}) were also analysed for quality control purposes. The second batch of the same brain region was analysed immediately after the first batch. Checks and maintenance were done before initiating the analysis of a batch.

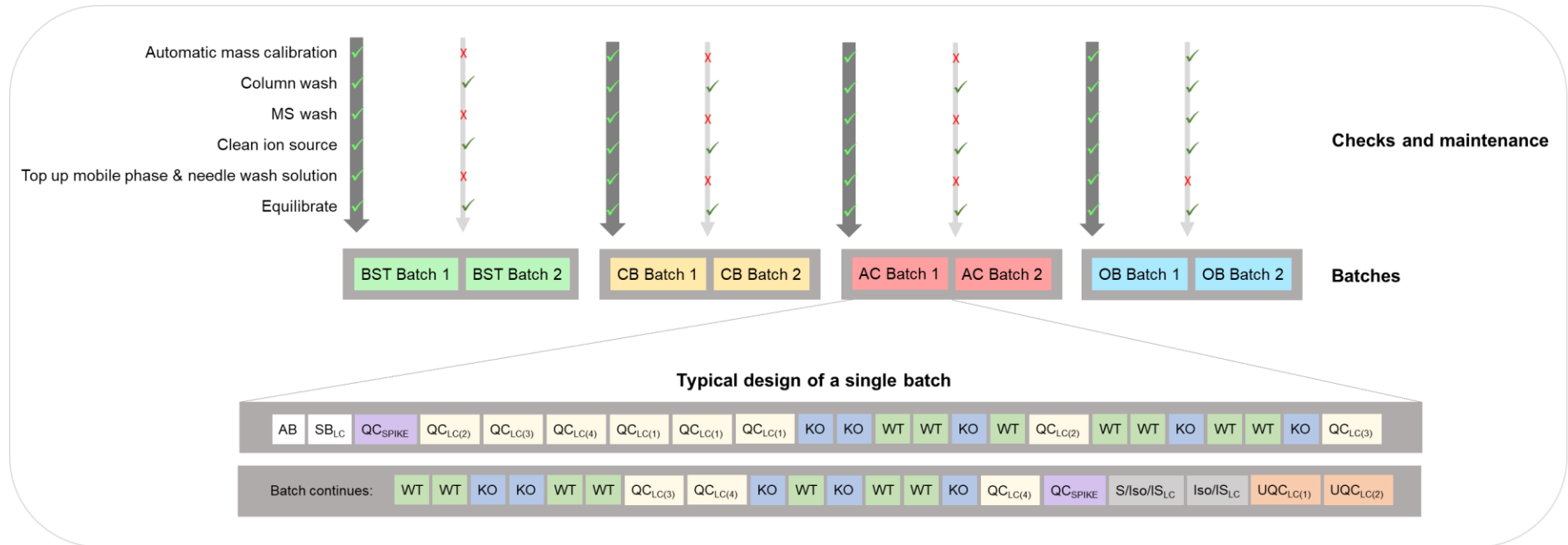


Figure 4.8: Run order and batch design of the LC-MS/MS analysis of derivatised polar phase extracts from *Ndufs4* wild-type and knockout brain region tissue samples.

Brain region tissue samples were grouped according to brain region and the derivatised tissue extracts of the four brain regions were analysed successively as soon as practically possible. For each brain region-type (brainstem, BST; cerebellum, CB; anterior cortex, AC; and olfactory bulbs, OB), the *Ndufs4* knockout (KO, n = ~21) and wild-type (WT, n = ~25) samples were randomised and divided into two analytical batches of similar size which would ensure batch completion within ~24 hours of derivatisation. In each batch, the derivatised polar extracts of ~23 biological samples (WT and KO in a randomised order) were analysed intermittently with four equivalent region-specific biological pooled quality control (QC_{LC}) samples. An analytical blank (AB, analytical mobile phase), an experimental blank (SB_{LC}) containing the final sample reconstitution solution, a QC sample spiked with a mixture of standard compounds (QC_{SPIKE}), a universal standards-mix spiked with isotope and internal standard (S/Iso/IS_{LC}), a universal LC isotope-mix spiked with internal standard (Iso/IS_{LC}) and two universal QCs for LC-MS/MS analysis (UQC_{LC}) which consisted of a mix of the pooled QCs of all four brain regions, were also analysed for quality control purposes. The second batch of the same brain region was analysed immediately after the first batch to minimise variation. Checks and maintenance were done before analysis of a batch was initiated.

The four QC samples, which derived from a single brain region QC-pool, were analysed at the beginning and end of each batch and intermittently after every six biological samples. For HPLC-MS, analysis of a QC sample every five to 10 samples is recommended (Gika *et al.*, 2016). Generally, the LC-column was equilibrated by five injections of QC_{LC} sample. Thereafter, the actual analytical batch commenced with the injection of a QC_{LC} sample followed by the first biological sample. The S/Iso/IS_{LC}, Iso/IS_{LC} and UQC_{LC} samples were injected at the end of each batch. The samples of the four brain regions were analysed consecutively as close to one another as possible (making provision for repairs and cleaning of instruments as required) to limit variation on the instruments, solvents and surrounding conditions (Lindeque *et al.*, 2013).

4.7.4.6 Analytical parameters

4.7.4.6.1 Analytical parameters for GC-TOF analysis

The methoximated/silylated samples (Section 4.7.4.4.1) were analysed on a GC-TOF system which consisted of an Agilent Technologies 7890A GC front-end system coupled with a LECO® Pegasus® HT TOFMS. An Agilent 7693 autosampler was used for the automatic injection of 1 µL sample per run as well as automatic rinsing of the needle between injections using a mixture of acetone:isopropyl alcohol (50:50, v/v). The sample was injected in splitless injector mode and the system was fitted with a Phenomenex Zebron GC FocusLiner® Inlet Liner for Agilent (split/splitless, single taper w/wool, 4 mm ID x 78.5 mm L x 6.3 mm OD). The front inlet temperature was kept at 250 °C throughout the entire run and helium was used as carrier gas at a constant flow rate of 1.5 mL/minute. Chromatography of the volatilised samples was performed on a Restek Rxi-5Sil MS (30m x 250 µm x 0.25 µm) column. The GC oven temperature was initiated at 40 °C for one minute and then increased stepwise to 120 °C at 7 °C/minute after which the temperature was increased to 230 °C at 10 °C/minute and finally to 300°C at 13 °C/minute where it was held for 2.5 minutes before cooling down to the initial temperature. The total run time for each sample was approximately 35 minutes. The transfer line temperature was set constantly to 225 °C. The ion source was maintained at 200 °C, electron ionisation at -70 eV and full scan mass spectra (50 to 950 m/z) were acquired throughout the run at 20 spectra/second and a ~1 500 V detector voltage. A solvent delay of 480 seconds was allowed so that pyridine and BSTFA solvent peaks were not detectable in QC samples, while lactate or pyruvate were detectable (Fiehn, 2016). The LECO® ChromaTOF® Optimised for Pegasus HT Version 4.50.8 software (LECO® Africa Pty Ltd, Kempton Park, ZA) was used for system control and data acquisition.

4.7.4.6.2 Analytical parameters for LC-MS/MS Analysis

Tandem mass spectrometry (MS/MS) of the butylated samples were performed using an Agilent 6410 Triple Quadrupole (QQQ) mass spectrometer (MS) interfaced with an Agilent 1200 series liquid chromatograph (LC) front-end. The autosampler was set at 4 °C and an injection volume of 2 µL was used followed by the initiation of the programmed solvent gradient. The injection needle was washed for 10 seconds in a flush port containing a methanol:isopropanol:water (70:10:20) solution to prevent carryover (Louw *et al.*, 2018). An Agilent C18 Zorbax StableBond-Aqua (150 mm x 2.1 mm x 3.5 µm) column fitted with a Phenomenex guard column (with the same chemistry as the phase in the analytical column) (Gika *et al.*, 2016) was used for reversed phase chromatographic separation at a column temperature of 30 °C.

The chromatographic separation was done with a binary flow. The mobile phases consisted of water with 0.1% formic acid (A) and acetonitrile with 0.1% formic acid (B). The analytical LC gradient started with 5% B at 0 minutes followed by a linear gradient to 20% B at six minutes and another increase to 100% B at 13 minutes. The gradient was kept at 100% B for five minutes and then decreased to 5% within two minutes followed by re-equilibration for eight minutes to maintain reproducibility (Ivanisevic *et al.*, 2014). The flow rate was 0.3 mL/minute for the first 13 minutes after which it was increased to 0.35 mL/minute for the rest of the run. The total run time for each sample was approximately 28 minutes.

The samples were delivered to the QQQ-MS via electrospray ionisation (ESI) in positive mode with the source conditions set as follows: nitrogen drying gas temperature of 300 °C and flow of 7.5 L/minute, a nebuliser pressure of 30 psi and capillary voltage of 3500 V. The first and third quadrupoles served as independent mass analysers while the second quadrupole served as a collision cell to characteristically fragment each analyte. The compounds were analysed in multiple reaction monitoring (MRM) mode using enhanced sensitivity with the multiplier voltage set at 300 Delta EMV and a dwell time of 45 milliseconds for all metabolites. Compound specific transitions (a precursor- and production ion (m/z) transition for each analyte), fragmentor (F) voltages and collision energies (CE) were optimised with Agilent's MassHunter Optimizer software (Version B.04.01) by infusing a standard solution (10 ppm) of each derivatised compound. The parameters for each butylated compound and isotopically labelled standard, are given in APPENDIX D. The overall performance of the acquisition method was improved by dividing the method into a series of time segments each monitoring predefined sets of MRM transitions (APPENDIX D). This decreased the number of MRM transitions during each MS cycle and allowed the acquisition of more data points per peak, and thus better sensitivity. Time segments were switched at retention times where no compounds of interest were eluting, namely at five minutes, 10.1 minutes and 13.4 minutes respectively. The Agilent MassHunter Data Acquisition software (Version B.06) was used for system control and data acquisition.

4.7.5 Data analysis

Metabolomics experiments produce information-rich, high-dimensional and complex data sets that involve many metabolic features (Tugizimana *et al.*, 2016; Dudzik *et al.*, 2017). Consequently, proper data handling steps are crucial to process raw metabolomics data into high quality, biologically relevant results that accurately reflect true differences in concentrations of metabolites in the samples. Therefore, analysis of metabolomics data is performed prior to statistical analysis. Usually, this involves data extraction, data processing and data pre-treatment or normalisation (Tugizimana *et al.*, 2016; Dudzik *et al.*, 2017; Wanichthanarak *et al.*, 2017).

4.7.5.1 Data extraction

Extraction of metabolomics data comprises several steps to: 1) enhance metabolically significant signals by pre-cleaning the raw data (noise reduction, baseline correction, peak picking, deconvolution, alignment and compound identification); and 2) reduce data complexity by extracting the pre-cleaned raw metabolomics data (chromatograms and mass spectra) into rectangular data matrices (relative abundance of each metabolite is organised in a unique column and each sample analysed in a unique row) to facilitate subsequent data processing (Hendriks *et al.*, 2011; Dudzik *et al.*, 2017; Wanichthanarak *et al.*, 2017). Data extraction was performed automatically using platform-specific software packages and guidelines.

4.7.5.1.1 Data extraction for GC-TOF analysis

The GC-TOF data was extracted using LECO® ChromaTOF® Optimised for Pegasus HT Version 4.50.8 software (LECO® Africa Pty Ltd, Kempton Park, ZA) and an in-house protocol. The chromatogram of each sample was inspected manually to detect failure of injection or analysis. This meant that the total ion count (TIC) would have dropped to zero in which case the sample was removed from the data set.

The data extraction procedure included baseline subtraction, peak detection, peak deconvolution and peak alignment. The baseline was removed with the “span” baseline tracking method. The baseline offset was set at one (just above the noise). Automatic smoothing was performed. Peaks were detected using a peak width of three seconds and signal-to-noise (S/N) ratio of 20. Only masses between 100 and 800 m/z were used as model ions and true peaks had to contain five apexing masses. The following masses were omitted as model ions to limit the detection of false positives, since they can originate from the derivatisation reagents: TIC 73, 75 and 147.

Compounds were preliminarily identified using spectral matching to the National Institute of Standards and Technology (NIST) 2011 mass spectral library and an in-house created library (Reinecke et al., 2012). A spectral match of at least 60% similarity (600 in ChromaTOF) was required before a compound was given a tentative identity. Only identities with at least one silyl element in its formula was allowed to avoid spectral matching of non-derivatised compounds or incorrect derivatives (Venter et al., 2016). The add-on package, “Statistical Compare” was used to align the peaks of the remaining samples and to form a data matrix which was exported to Microsoft Excel® 2013 for further data processing.

4.7.5.1.2 Data extraction for LC-MS/MS analysis

The LC-MS/MS data was manually inspected for failure of injection or analysis (i.e. TIC dropped to zero, in which case the sample was removed from the data set). Agilent’s MassHunter Qualitative software (Version B.06) was used to inspect retention time drifts within batches (using QC_{LC}) and between batches (using UQC_{LC}). Thereafter, Agilent’s MassHunter Quantitative software (Version B.06) was used for compound detection and peak alignment (using QC_{LC} and QC_{SPIKE}) as well as for supervised peak integration and the construction of a data matrix which was exported to Microsoft Excel® 2013 for further data processing.

4.7.5.2 Data processing and normalisation

Data was processed and normalised to reduce the data set size and to ensure that only the high-quality peaks of biological origin that were present in most samples, were retained (Kirwan *et al.*, 2014). The main data processing and normalisation steps were based on in-house protocols and relevant literature recommendations (Lindeque *et al.*, 2015; Di Guida *et al.*, 2016; Chen *et al.*, 2017b; Wanichthanarak *et al.*, 2017). These steps are summarised in Figure 4.9 and include: 1) the removal of infrequent features; 2) the removal of contaminant peaks; 3) the removal of unreliable samples; 4) post-analysis normalisation using the internal standards to minimise systematic and technical variations; 5) the removal of unstable or unreliable features using QC samples; and 6) missing value imputation (MVI) to replace missing values with a non-zero value while maintaining the data structure. The latter is important as too many zeroes or missing values cause difficulties in downstream data transformation and statistical analysis. Data transformation was applied to improve the normality of data sets so that the metabolite intensities between and within samples were more comparable before performing statistical analysis. Finally, outlier samples were also removed.

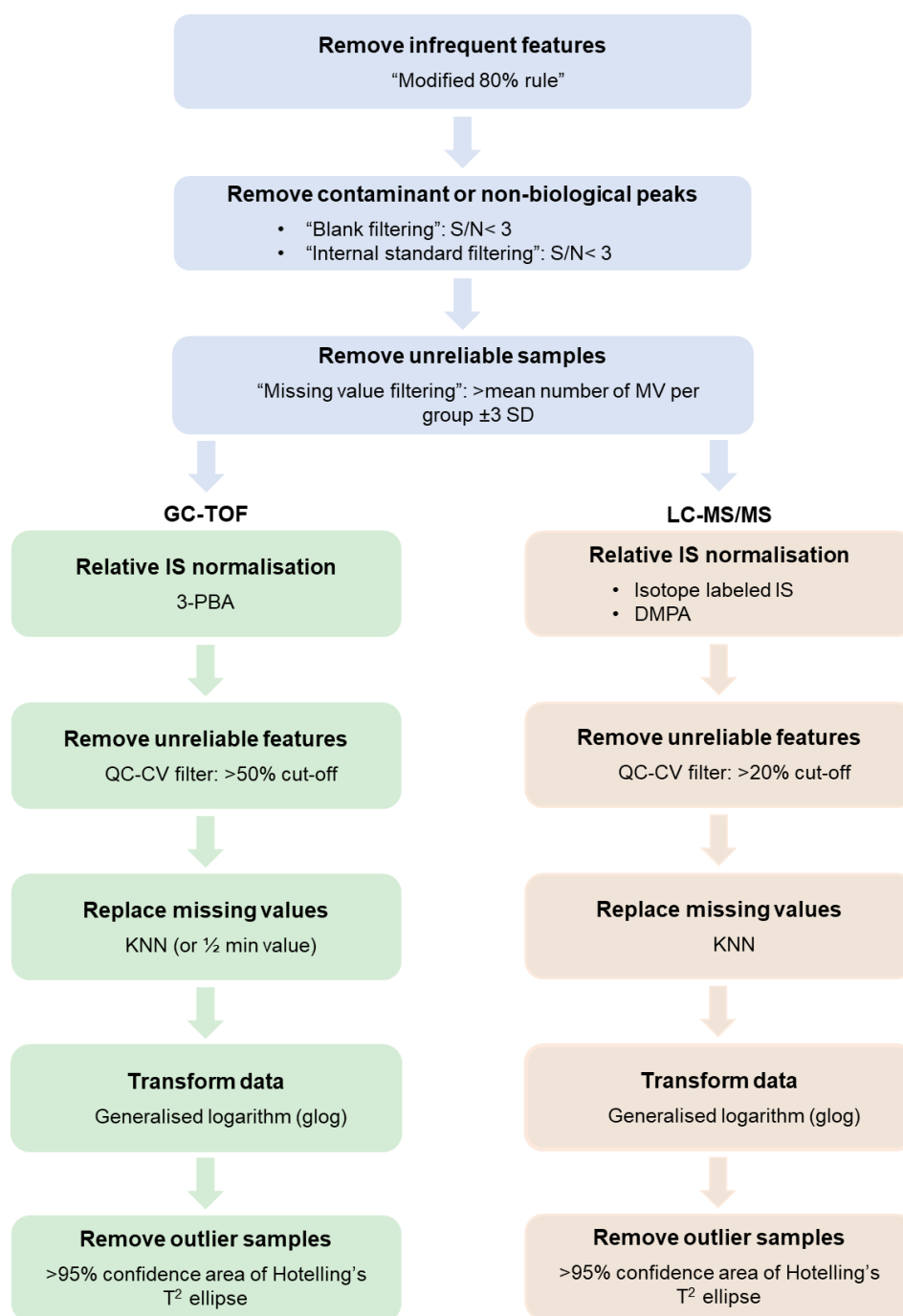


Figure 4.9: Data processing and normalisation of extracted metabolomics data sets.

The data processing steps included the removal of infrequent and contaminant peaks, removal of unreliable samples, post-analysis normalisation using the internal standards to minimise systematic and technical variations, removal of unstable variables using QC samples, replacement of missing values with a non-zero value while maintaining the data, data transformation to improve the normality of data sets so that the metabolite intensities between and within samples were more comparable before performing statistical analysis and the removal of outlier samples. *Other abbreviations: 3-PBA, 3-phenylbutyric acid; DMPA, N,N-dimethylphenylalanine; GC-TOF, gas chromatography-time of flight; IS, internal standards; KNN, k-nearest neighbour; LC-MS/MS, liquid chromatography-tandem mass spectrometer; min, minimum; MV, missing values; SD, standard deviation; S/N, signal to noise ratio.*

4.7.5.2.1 Processing and normalisation of GC-TOF data

Untargeted GC-TOF data sets are prone to contain a large amount of unexpected missing values that may occur during data acquisition or data extraction (Wei *et al.*, 2018). First, the number of missing values were reduced with a group-wise or “supervised” missing value variable filtering procedure. It is also known as the “modified 80% rule”, which states that “a variable is kept if it has a non-zero value for at least 80% in the samples of any one class” (Yang *et al.*, 2015). In this way, potential differentiating metabolites, only detected in one experimental group and not in the other (probably due to concentrations being below the detection limit of the instrument), were not removed from the data set. Contaminant peaks were flagged and removed from the data matrices by applying “blank filtering”. Thus, a peak was considered a contaminant if it had an intensity in the experimental blank samples (SB_{GC}) that was one-third or more of the intensity of the same peak in the biological samples (Kirwan *et al.*, 2014). This type of signal-to-noise ratio cut-off value (< 3) was determined by dividing the average peak area in the samples by the peak area found in the blank samples. Similarly, remaining non-biological compounds (except for internal standards of interest) were flagged and removed by using the samples containing only internal standards (IS_{GC}).

As Kirwan *et al.* (2014) suggested, the data quality was further improved by performing “missing value filtering”. Thus, samples with a high percentage of missing values were identified and removed. Samples excluded in this way had to exceed the acceptability threshold for the number of missing values (mean number of missing values per group plus three standard deviations). In hypothesis-generating or discovery metabolomics (untargeted and semi-targeted approaches), metabolites are relatively quantified; i.e. the relative differences in intensity of an individual metabolite is measured in comparable samples but specific or absolute concentrations are not calculated (Gorrochategui *et al.*, 2016; Wu & Li, 2016; Broadhurst *et al.*, 2018). Also, the focus of this study was to identify only the relative differences in metabolite intensities between KO and WT samples. Therefore, the peaks of the remaining samples were normalised relative to the internal standard, 3-PBA, using Equation 4.11.

$$\text{Relative abundance } (A) = \frac{\text{Peak area } (A)}{\text{Peak area } (IS)}$$

Where A refers to feature A and IS to the internal standard.

(Equation 4.11)

Individual unreliable features were removed from the subset if, in the QC_{GC} samples, it had a $CV_{\text{After normalisation}} > 50\%$ (Dunn *et al.*, 2012; Lindeque *et al.*, 2013). The QC_{GC} samples (prepared separately for brain region types) were used as it had the closest matrix to the samples and was expected to improve the statistical outcome, especially for features unique to one brain region-type (Godzien *et al.*, 2015).

Missing value imputation (MVI) was performed after data normalisation with the webserver, MetaboAnalyst (Version 4.0) (<http://www.metaboanalyst.ca/>) (Chong *et al.*, 2018). Unless specified otherwise, the built-in k-nearest neighbour (KNN) algorithm was utilised for MVI of the metabolomics data (Hrydziuszko & Viant, 2012; Wei *et al.*, 2018). KNN-imputation replaces a missing value by a unique value calculated from the average of the corresponding (feature-specific) non-missing values in the k closest features (peaks that have similar measured signal intensities across the biological samples as compared to the peak for which the missing entry is present) (Troyanskaya *et al.*, 2001; Steuer *et al.*, 2007; Di Guida *et al.*, 2016). In special cases where KNN could not be used (when all the values were missing in one experimental group and not in the other), the missing values were treated as being below the detection limit and were replaced with half of the minimum positive value in the unnormalised data set. The data were then normalised per sample to produce unique values for each sample. After MVI, the data was transformed using the generalised logarithm (glog) transformation function.

Outlier samples in each experimental group (KO and WT) were identified using MetaboAnalyst's principal component analysis (PCA). A sample was considered an outlier if it was located outside the 95% confidence area of the Hotelling's T^2 ellipses in a PCA score plot of the first two principal components (PC) (Gogna *et al.*, 2017). The PCA loadings plot and biplot was also investigated to ensure a sample was not considered an outlier due to a single feature.

4.7.5.2.2 Processing and normalisation of LC-MS/MS data

The LC-MS/MS data was acquired in a semi-targeted manner. Thus, this data set was less prone to contain missing values and non-biological peaks. However, despite measuring target compounds, all target compounds are not necessarily detectable (whether due to the compound being absent in the sample or due to the intensity being below a detection limit (Wei *et al.*, 2018)). Also, each target transition is not guaranteed to be free from co-eluting contaminant peaks that might cause ion suppression of the compound of interest and/or interfere with the software-labelling of the compound of interest. Therefore, unless specified otherwise, the LC-MS/MS data matrices were processed like the GC-TOF data but with LC-MS/MS specific samples (SB_{LC} and QC_{LC}) and internal standards.

The normalisation of LC-MS/MS peak areas was slightly different than for the GC-TOF peak areas. This was because the samples contained, stable isotopically labelled internal standards (added before the biphasic extraction) in addition to the internal standard, DMPA, that was added before the monophasic metabolite extraction. First, each compound was relatively normalised, either with its corresponding stable isotopically labelled internal standard (IS_{iso}) or with the IS_{iso} with the closest retention time to that compound (Bijlsma *et al.*, 2006). This was done by dividing the peak area of each compound by the peak area of the IS_{iso} as shown with Equation 4.11. In this way, the non-uniform responses of individual metabolites, due to different ionisation efficiencies and degrees of ion suppression, could be partially accounted for. This is in contrast to using a single internal standard that do not elute close to the compound of interest (Wu & Li, 2016).

Thereafter, the remaining experimental variability (before biphasic extraction) was accounted for by dividing each IS_{iso} -corrected compound peak area with the peak area of DMPA (added prior to sample extraction), according to Equation 4.11. However, the peak area of DMPA was first corrected as shown in Equation 4.12. This was necessary since the experimental variation after biphasic extraction and the analytical variation were already accounted for by adjusting each compound peak area with the peak area of IS_{iso} . Therefore, the area of DMPA in each sample was divided by the peak area of the IS_{iso} eluting closest to DMPA and the average peak area of DMPA across a batch for each experimental group (KO or WT).

$$Adjusted\ DMPA = \frac{Peak\ area\ (DMPA)}{Peak\ area\ (IS_{iso})} \div AVG\left(\frac{Peak\ area\ (DMPA)}{Peak\ area\ (IS_{iso})}\right)$$

Where the average ration was calculated by averaging the DMPA peak areas batch-wise per experimental group (KO or WT).

(Equation 4.12)

Individual unreliable features were then removed from the subset using a stricter $QC_{LC}\ CV_{After\ normalisation}$ cut-off of >20% as recommended for targeted analyses (FDA, 2001), in comparison with the untargeted GC-TOF analysis (Section 4.7.5.2.1).

4.7.5.3 Statistical data analysis

After the raw metabolomics data was processed into a higher quality data set, the data was subjected to statistical analysis. Unless stated otherwise, all statistical analyses were carried out with MetaboAnalyst (Version 4.0) (<http://www.metaboanalyst.ca/>) (Chong *et al.*, 2018).

The data was examined in two dimensions in accordance with the objectives of this study (Section 3.3; Objective 3.5 and Objective 3.6). First, the data were compared between the corresponding brain regions of the two genotype groups (e.g. KO AC vs WT AC, KO BST vs WT BST, etc.) to identify the most significant discriminatory compounds. This gave an idea of whether and how the metabolism of each brain region had been affected by the *Ndufs4* KO. Second, the altered levels of the most significant discriminatory compounds of each brain region were compared among the four brain regions (AC vs BST vs CB vs OB) to determine metabolic differences that could explain the formation of lesions in some of the brain regions (BST, CB and OB) that are absent in others (AC). Due to the WT-KO comparative study-design, and since different brain regions were prepared and analysed in different blocks, the second dimension of the study was based on: 1) qualitative determination of shared and unique discriminatory metabolites; and 2) relative comparison of the magnitude of change (effect sizes) in the levels of shared discriminatory metabolites.

Unsupervised multivariate statistical PCA was utilised in a qualitative manner for visualisation of the data sets. The PCA scores plots of glog transformed data sets were constructed to: 1) assess data quality (sample and QC clustering and batch effects); 2) identify sample outliers; and 3) visualise the covariance of detected features or significant metabolites. Thereafter, discriminatory metabolites were determined from the GC-TOF and LC-MS/MS data sets. Univariate statistical tests were used on glog-transformed data to identify the compounds that differed most significantly between the two genotypes of each brain region. Student's t-test was carried out to identify features with statistically significant altered intensities. The *p*-value significance scores obtained from the t-test were adjusted for multiple testing and a false discovery rate (FDR)-corrected *p*-value <0.05 was considered significant. Effect sizes (Cohen's *d*-value) were calculated in Microsoft Excel® 2013 (Equation 4.13) and used complementary to the t-test to ensure that only metabolites that also have a 'practical' significance, were labelled as significant. According to Ellis and Steyn (2003) this means a significance that can be understood as a large enough difference to have an effect in practice. Therefore, compounds had to display a *p*-value <0.05 (t-test) and *d*-value ≥0.8 (effect size) to be included in the list of important features. In the case of the untargeted GC-TOF data, the identities of the important features were subsequently determined.

$$Effect\ size\ (d\text{-value}) = \left| \frac{AVERAGE(KO\ range) - AVERAGE(WT\ range)}{MAX(STDEV.S(KO\ range), STDEV.S(WT\ range))} \right|$$

Where MAX refers to maximum and STDEV.S to standard deviation.

(Equation 4.13)

4.7.6 Identification of GC-TOF compounds

Preliminary identities or nomenclature were ascribed to the GC-TOF detected feature during data extraction (Section 4.7.5.1.1) to avoid the laborious process of identifying a great number of features that untargeted data sets contain. Metabolite annotation of the subset of important features, that had statistically and practically significant different intensities between WT and KO samples, was performed by comparing the metadata (intact molecular mass, fragmentation spectra or retention time) to that of known compounds. For this purpose, several in-house, commercial and public libraries/databases were utilised, and an identification confidence level was ascribed to each feature as previously described (Schymanski *et al.*, 2014). Features for which a tentative structure was obtained (based on either matching intact molecular mass or fragmentation spectra), was considered as a Level 3. On the contrary, Level 2 features had a more probable structure identity based on additional evidence. Features for which the structure was identified with spectral and retention time matching with a reference standard, was labelled as Level 1. All unidentified features were excluded since identification of these features are beyond the scope of this study.

CHAPTER 5: BIOCHEMICAL INVESTIGATION OF NDUFS4 KNOCKOUT MOUSE BRAIN REGIONS

5.1 Introduction

Inactivation of the mitochondrial respiratory chain (RC) complex I (CI)-subunit gene, *Ndufs4*, in all tissues leads to lesion development in specific brain regions, namely the brainstem (BST), cerebellum (CB) and olfactory bulbs (OB), but not in other brain regions such as the anterior cortex (AC) (Kruse *et al.*, 2008; Quintana *et al.*, 2010). One of the main objectives (Objective 2) of this study was to investigate whether brain regional differences in RC enzyme activities could be correlated with the regional vulnerability to neurodegeneration in *Ndufs4* knockout (KO) mice.

For this purpose, the brain region-specific maximal activities of the mitochondrial marker, citrate synthase (CS), and of RC complex I (CI), II (CII), III (CIII) and IV (CIV), were measured spectrophotometrically in freeze-thawed 700 x g supernatants prepared from the homogenates of the selected brain regions (AC, BST, CB and OB). The standardisation of the spectrophotometric assays (Objective 2.1) for applicability on mouse brain region samples is shown in APPENDIX C. Using the standardised assays, final analyses (Objective 2.2) were conducted on the selected brain regions harvested from *Ndufs4* WT (n =10) and KO (n =12) mice at postnatal day (PN) 45 to PN49. A detailed description of the experimental methods was given in Section 4.6.4. Data was statistically evaluated and processed as described in Section 4.6.5 (Objective 2.3). Briefly, the maximal enzyme activities were compared between the corresponding brain regions of the *Ndufs4* WT and KO mice to determine the brain region-specific effect of the *Ndufs4* KO. The maximal enzyme activities were also compared among brain regions of the same genotype. This was collectively done by performing a two-way mixed analysis of variance (ANOVA; between-subjects factor = genotype; within-subjects factor = brain region). Only the main results are reported in this section, while the complete set of results is provided in APPENDIX E.

In this chapter (Objective 2.4), the results are presented and discussed with regard to CS activity, CI activity and the activity of the remaining RC complexes (CII, CIII and CIV). Thereafter, potential links between the enzyme profiles of the investigated brain regions and brain region-specific neurodegeneration are considered. Then follows a summary of the main findings. Chapter 7 presents the final conclusions from the results.

5.2 The *Ndufs4* knockout had variable effects on the maximal activities of citrate synthase and respiratory chain enzymes in the various brain regions

The maximal activities determined for citrate synthase (CS) and complex I to IV (CI, CII, CIII and CIV) of the respiratory chain (RC) in the AC, BST, CB and OB from *Ndufs4* wild-type (WT) and knockout (KO) mice, are summarised in Table 5.1. Maximal RC enzyme activities (mean \pm standard deviation) were normalised to protein content (mg of protein) and statistically significant differences between corresponding KO and WT brain regions are indicated by asterisks (* = $p < 0.05$, ** = $p < 0.01$, *** = $p < 0.001$, **** = $p < 0.0001$). Enzyme activities measured in the KO brain regions were also expressed relative to the corresponding activities measured in the cognate WT brain regions (KO/WT) to give an indication of the effect of the *Ndufs4* KO.

A brief overview of the data showed that the activities of some, but not all investigated enzymes were significantly altered by the KO in each brain region. Furthermore, the KO tended to increase the maximal activities of some enzymes, while decreasing the maximal activities of other enzymes. Together, these results suggested that the *Ndufs4* KO had variable effects on the maximal activities of CS and RC enzymes in the various investigated brain regions. The following sections provide an in-depth discussion of these results and the comparison of enzyme activities among the neurodegeneration-prone brain regions and the more resilient AC.

Table 5.1: Maximal spectrophotometric enzyme activities in brain regions of *Ndufs4* wild-type and knockout mice normalised to mg of protein.

v_{max} values	AC			BST			CB			OB		
	WT	KO	KO/ WT	WT	KO	KO/ WT	WT	KO	KO/ WT	WT	KO	KO/ WT
CS (mU/mg)	352 ± 26	398 ± 26 ^{***}	1.13	459 ± 20	467 ± 25	1.02	398 ± 25	485 ± 24 ^{****}	1.22	410 ± 32	450 ± 34 ^{**}	1.10
CI (mU/mg)	27 ± 2	10 ± 1 ^{****}	0.38	35 ± 4	9 ± 3 ^{****}	0.25	37 ± 3	10 ± 1 ^{****}	0.28	23 ± 3	3 ± 1 ^{****}	0.14
CII (mU/mg)	33 ± 3	35 ± 2	1.05	42 ± 5	38 ± 4	0.91	44 ± 4	49 ± 5 [*]	1.10	39 ± 3	38 ± 6	0.97
CIII (mU/mg)	266 ± 30	248 ± 15	0.93	291 ± 27	306 ± 46	1.05	294 ± 18	301 ± 19	1.02	204 ± 30	197 ± 18	0.97
CIV (mU/mg)	647 ± 36	704 ± 31 ^{**}	1.09	925 ± 102	944 ± 101	1.02	893 ± 58	1070 ± 53 ^{***}	1.20	808 ± 53	925 ± 108 ^{**}	1.14

Enzyme activities displayed as the mean activity ± standard deviation. In all cases, wild-type (WT) n ≥ 9 and knockout (KO) n ≥ 11. Statistical significance between KO and corresponding WT regions: * = p < 0.05, ** = p < 0.01, *** = p < 0.001, **** = p < 0.0001. Statistical tests and exact sample sizes are provided in the figure descriptions in the following sections. *Other abbreviations:* v_{max}, maximal activity; AC, anterior cortex; BST, brainstem; CB, cerebellum; OB, olfactory bulbs; CI, complex I; CII, complex II; CIII, complex III; CIV, complex IV; CS, citrate synthase; mU; nmol/minute.

5.2.1 Maximal citrate synthase activity is generally increased in *Ndufs4* knockout mice and higher in neurodegeneration-prone brain regions

Figure 5.1 provides a visual presentation of maximal CS activity (expressed as mean normalised to mg of protein \pm standard deviation) among the investigated brain regions of *Ndufs4* WT and KO mice. Statistical significance (* = $p < 0.05$, ** = $p < 0.01$, *** = $p < 0.001$, **** = $p < 0.0001$) for comparisons between corresponding KO and WT brain regions is given above the data points. Whereas statistical significance obtained for comparisons between the degeneration resilient AC and neurodegeneration-prone brain regions from the same genotype is indicated in grey and red respectively for WT and KO below the neurodegeneration-prone brain region data points.

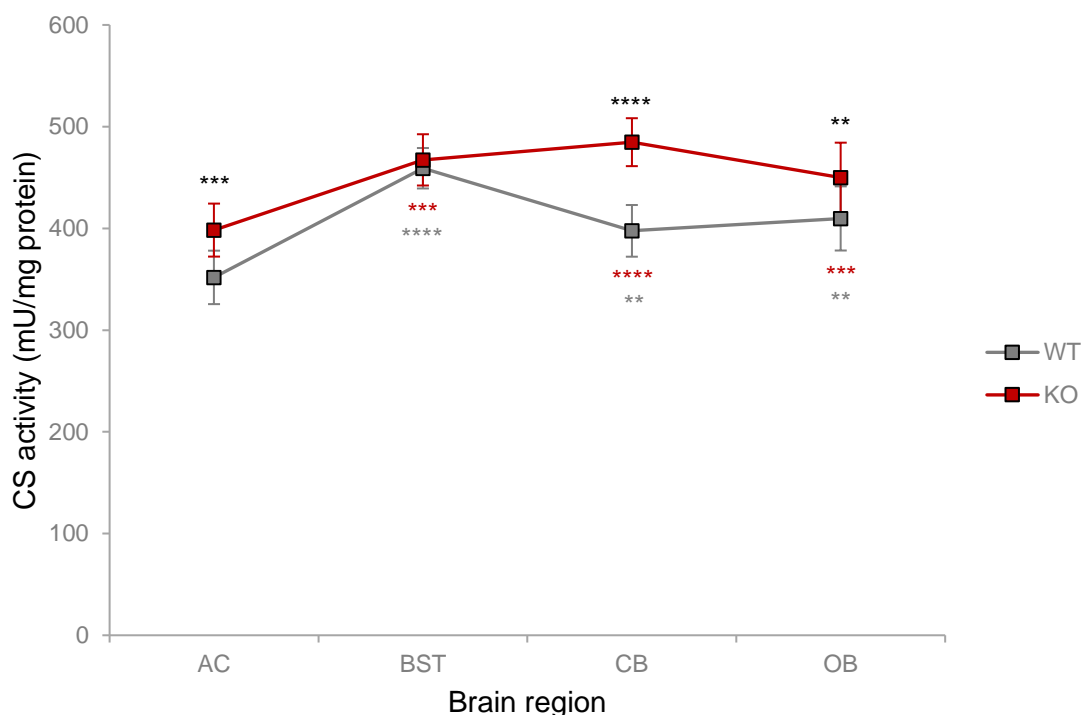


Figure 5.1: Maximal citrate synthase activity in the brain regions of *Ndufs4* wild-type and knockout mice.

The maximal activity of citrate synthase (CS), expressed in mU (nmol/minute) per mg of protein, was measured spectrophotometrically in triplicate in a freeze-thawed 700 x g supernatant of a homogenate of the anterior cortex (AC), brainstem (BST), cerebellum (CB) and olfactory bulbs (OB) from *Ndufs4* wild-type (WT, grey, n =10) and knockout (KO, red, n =12) mice aged PN45 to PN49. Data points display mean activity \pm SD. Statistical significance for comparisons between corresponding KO and WT brain regions is indicated by asterisks (*) above the data points and was determined using the independent samples t-test. Statistical significance obtained for comparisons between the degeneration resilient AC and neurodegeneration-prone brain regions from the same genotype is indicated by grey asterisks (*) for WT and red asterisks (*) for KO below the neurodegeneration-prone brain region data points. This was determined using the paired t-test. Statistical significance: * = $p < 0.05$, ** = $p < 0.01$, *** = $p < 0.001$, **** = $p < 0.0001$.

The two-way mixed ANOVA showed that the interaction between genotype and brain region was significant ($F_{3,60} = 7.3$, $p < 0.0001$, $\eta_p^2 = 0.27$), indicating that the genotype had a different effect on maximal CS activity depending on the brain region analysed. Maximal CS activity was higher in the KO group across all brain regions except in the BST: AC ($p < 0.001$, $d = 1.8$), CB ($p < 0.0001$, $d = 3.4$) and OB ($p < 0.01$, $d = 1.2$). The degeneration resilient AC exhibited low maximal CS activity in both genotypes compared to the neurodegeneration-prone brain regions: AC vs BST in WT ($p < 0.0001$, $d = 4.1$) and in KO ($p < 0.001$, $d = 2.7$), AC vs CB in WT ($p < 0.01$, $d = 1.7$) and in KO ($p < 0.0001$, $d = 3.3$), AC vs OB in WT ($p < 0.01$, $d = 1.8$) and in KO ($p < 0.001$, $d = 1.5$).

When comparing maximal CS activity between the neurodegeneration-prone brain regions (statistical significance not shown in Figure 5.1) of WT mice, the BST displayed higher activity than the CB ($p < 0.0001$, $d = 2.4$) and OB ($p = 0.003$, $d = 1.6$). In KO mice, maximal CS activity of CB was higher than OB ($p < 0.01$, $d = 1.0$), indicating a more significant increase in CS activity of the KO CB. Together, the results showed that the KO generally caused an increase in CS activity (except in the KO BST). However, this effect was not unique to either the more resilient AC or the neurodegeneration-prone brain regions. Nevertheless, the neurodegeneration-prone brain regions had significantly higher CS activities than the AC, regardless of genotype, which might suggest a link to the region-specific neurodegeneration in the *Ndufs4* KO mice.

An increase in the maximal activity of the TCA cycle enzyme, CS, might indicate an increase in mitochondrial content (Lopez-Lluch *et al.*, 2006; Larsen *et al.*, 2012; Porter & Wall, 2012). Indeed, the slightly higher CS activity in the whole-brain of another *Ndufs4* knockout mouse model, generated by a heterozygous point mutation in the *Ndufs4* gene (from here on referred to as *Ndufs4*^{PM}), was proposed to reflect the mitochondrial hyper-proliferation that is seen in a number of Leigh syndrome or MELAS patients (Ingraham *et al.*, 2009). In accordance, mitochondrial biogenesis has been considered to occur in mitochondrial disease to compensate for decreased ATP production per mitochondria (Rodenburg, 2011; Diaz *et al.*, 2012; Uittenbogaard & Chiaramello, 2014; Torraco *et al.*, 2015; Yubero *et al.*, 2016; Manjeri, 2017).

Increased CS activity can alternatively or additionally reflect a modification of the intrinsic properties of CS and/or increased levels or activities of TCA-cycle enzymes in general. This was suggested to occur in the skeletal muscle of *Ndufs4* KO mice to increase CII-mediated fuelling of the OXPHOS system (Alam *et al.*, 2015). In the *Ndufs4* KO mouse brain regions, the increase in CS activity was not accompanied by a parallel increase in CII-, CIII- and CIV-activities (Section 5.2.2 and Section 5.2.3). Thus, mitochondrial biogenesis might also not be the sole mechanism underlying the increased CS activity. As a result, CS activity was not considered to be a reliable measure of mitochondrial mass or content in this study.

Contrary to the results obtained in this study, an independent study on the whole-brain of the *Ndufs4* KO mouse model reported that maximal CS activity was unaltered compared to WT mice at PN35 (Manjeri *et al.*, 2016). CS activity also appeared to be unaltered in cultured neurons and astrocytes derived from mice in which the NDUFS4 protein is absent as a result of aberrant transcript splicing (from here on referred to as *Ndufs4*^{flky/flky} mice) (Bird *et al.*, 2014). These discrepancies might be explained by differences in the age of mice and thus a variable extent of disease severity, experimental procedures employed, tissues utilised and/or the dilution of regional differences in whole-brain preparations. To illustrate the latter, the unaltered CS activity in KO BST might indicate that CS activity is unaltered in some of the remaining untested KO brain regions which, in a whole-brain analysis, might effectively “mask” the increases in CS activity of other brain regions.

Furthermore, while the increase in CS activity in response to the *Ndufs4* KO did not seem to correlate with the regional susceptibility to neurodegeneration, the neurodegeneration-prone brain regions, especially the BST, had higher maximal CS activity than the more resilient AC. This might indicate an increased reliance of the neurodegeneration-prone brain regions on mitochondrial OXPHOS function and thus an increased susceptibility to RC deficiencies, as suggested previously (Pickrell *et al.*, 2011). These results also corresponded with the higher CS activity previously observed in the CB compared to the frontal cortex of rodents (Pickrell *et al.*, 2011; Scaini *et al.*, 2011) and humans (Casademont *et al.*, 2005); as well as with the BST being one of the most severely affected brain regions in the *Ndufs4* KO mice (Quintana *et al.*, 2010; Quintana *et al.*, 2012; Piroli *et al.*, 2016). It is also plausible that the severe vulnerability of the BST to degeneration might be related to its apparent inability to increase CS activity in response to the *Ndufs4* KO.

Additional experimental investigation to elucidate the discrepancies between the results reported here and in independent studies; as well as the mechanism behind the increased maximal CS activity in most, but not all KO brain regions, might hold some promise. However, this was beyond the scope of this study. Consequently, the enzyme activities reported in the remainder of this chapter were mainly normalised to protein content (expressed per mg protein), while relevant and significant CS-normalised data was only mentioned with regard to comparisons among WT brain regions. All CS-normalised data however, is shown and discussed in APPENDIX E for the purpose of completeness. Briefly, normalisation of the data to CS activity did not affect the main conclusions drawn from the protein-normalised data. Besides, normalisation to protein content, which reflected the relative enzyme activities per brain region mass (Lanza & Nair, 2009), corresponded with the metabolomics approach in which data of the same tissue mass was relatively compared between the WT and corresponding KO brain regions.

5.2.2 Maximal complex I activity is differentially reduced but not absent across the brain regions of *Ndufs4* knockout mice

Figure 5.2 provides a visual presentation of the maximal CI activity (expressed as mean normalised to mg protein \pm standard deviation) among brain regions of *Ndufs4* WT and KO mice. The two-way mixed ANOVA showed that the interaction between genotype and brain region was significant ($F_{2,39} = 13.7$, Greenhouse-Geisser $p < 0.0001$, $\eta_p^2 = 0.42$). This indicated that the effect of the KO on maximal CI activity differed depending on the brain region. Maximal CI activity was significantly lower in the KO group across all brain regions: AC ($p < 0.0001$, $d = 8.9$), BST ($p < 0.0001$, $d = 6.3$), CB ($p < 0.0001$, $d = 12.3$) and OB ($p < 0.0001$, $d = 7.2$).

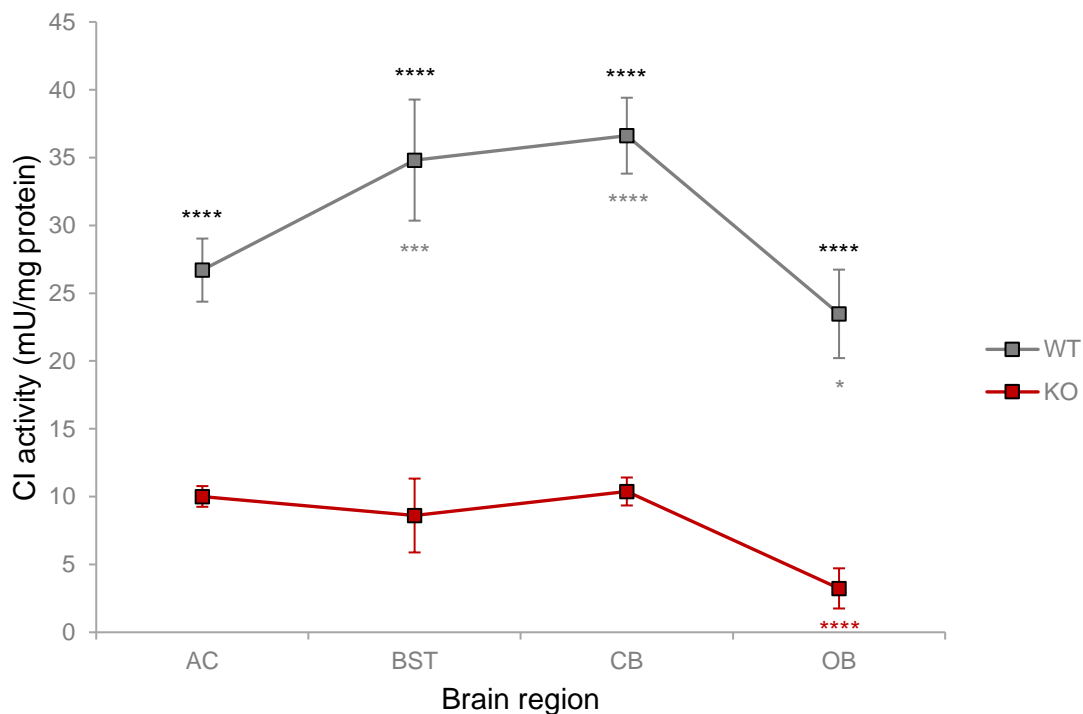


Figure 5.2: Maximal complex I activity in the brain regions of *Ndufs4* wild-type and knockout mice.

The maximal activity of complex I (CI), expressed in mU (nmol/minute) per mg of protein, was measured spectrophotometrically in triplicate in a freeze-thawed 700 x *g* supernatant of a homogenate of the anterior cortex (AC), brainstem (BST), cerebellum (CB) and olfactory bulbs (OB) from *Ndufs4* wild-type (WT, grey, $n = 10$ for all) and knockout (KO, red, $n = 12$ for all except AC $n = 11$) mice aged PN45 to PN49. Data points display mean activity \pm SD. Statistical significance for comparisons between corresponding KO and WT brain regions is indicated by asterisks (*) above the data points and was determined using the independent samples t-test on square-root transformed data. Statistical significance obtained for comparisons between the degeneration resilient AC and neurodegeneration-prone brain regions from the same genotype is indicated by grey asterisks (*) for WTs and red asterisks (*) for KOs below the neurodegeneration-prone brain region data points. This was determined using the paired t-test on square-root transformed data. Statistical significance: * = $p < 0.05$, ** = $p < 0.01$, *** = $p < 0.001$, **** = $p < 0.0001$.

Comparisons of maximal CI activity among brain regions of the same genotype showed significant differences between the resilient AC and neurodegeneration-prone brain regions. Maximal CI activity of WT AC was significantly lower than WT BST ($p=0.001$, $d=1.9$) and WT CB ($p<0.0001$, $d=3.8$), but significantly higher than WT OB ($p<0.05$ and $d=1.0$). In the KO group, the maximal CI activity of the AC was significantly higher than in the OB ($p<0.0001$, $d=3.2$). When comparing among the neurodegeneration-prone brain regions, maximal CI activity was significantly lower in the OB, irrespective of genotype: OB vs BST in WT ($p<0.0001$, $d=2.8$) and in KO ($p<0.0001$, $d=2.5$), OB vs CB in WT ($p<0.0001$, $d=3.7$) and in KO ($p<0.0001$, $d=3.4$).

The significant decrease in, yet not total abolishment of, maximal CI activity in all investigated KO brain regions was in accordance with the formation of an unstable but active CI in the tissues of the *Ndufs4* KO mouse model, as reported previously (Calvaruso *et al.*, 2011). The average residual CI activity in the KO brain regions (calculated as a fraction of the average CI activity of the cognate WT brain region) was 38%, 25%, 28% and 14%, respectively, for the AC, BST, CB and OB (Table 5.1). These results were consistent with previous reports of residual CI activities in the *Ndufs4* KO whole-brain (<50% or 26%) (Quintana *et al.*, 2010; Calvaruso *et al.*, 2011). In addition, these results also corresponded with the residual CI activities reported for the whole-brain (PN40) (between 10% to 20%) (Leong *et al.*, 2012), astrocytes (23%), and neurons (42%) (Bird *et al.*, 2014) of *Ndufs4*^{flky/flky} mice.

Notably, the residual CI activity in the neurodegeneration-prone brain regions was ~1.5-fold to three-fold lower compared to the AC. This finding suggested that a link might exist between residual CI activity and brain regional vulnerability to neurodegeneration. This might especially be relevant considering that even small changes in residual RC enzyme activities can manifest as mitochondrial disease (Spinazzi *et al.*, 2011) and that important cellular factors such as the production of reactive species, mitochondrial membrane potential and ATP production correlate with spectrophotometrically determined residual CI activity in patient cells (Verkaart *et al.*, 2007b; Distelmaier *et al.*, 2009). Moreover, the low levels of absolute (3.1 mU/mg) and residual CI activity in the KO OB might correspond with it being the first and one of the most severely affected brain regions in *Ndufs4* KO mice (Quintana *et al.*, 2010).

Studies have shown that mitochondria generally have a notable amount of excess capacity that could maintain “sufficient” RC function and ATP production in the presence of RC inhibition until a certain “threshold” of inhibition is reached (Pathak & Davey, 2008; Dubinsky, 2009; Alam *et al.*, 2015; Kühn *et al.*, 2015; Chinopoulos & Seyfried, 2018). When this threshold is reached, major detrimental metabolic consequences ensue. The lower residual CI activity in the neurodegeneration-prone brain regions of KO mice, especially in the OB in which maximal CI activity was reduced to only a mere 3.1 mU/mg (14% of WT), might suggest that OXPHOS

capacity in these regions is decreased beyond the relevant threshold. In this case, the cells within the neurodegeneration-prone brain regions would be unable to sustain cellular homeostasis. This in turn could initiate detrimental metabolic effects. At PN35, these metabolic effects might result in cell death and eventually in the dysfunction of these brain regions that support vital physiological processes. Ultimately, this leads to the death of the organism at ~PN50. For instance, the death of cells in the BST result in aberrant breathing and respiratory failure. Conversely, the resiliency of brain regions like the AC might be related to a higher residual CI activity that is still above the threshold of inhibition, having a less severe detrimental impact on cellular homeostasis and survival.

Some studies have suggested that the susceptibility of the brain to degeneration in a CI deficiency was unlikely to be caused by tissue-specific differences in isolated CI activity (Calvaruso *et al.*, 2011; Bird *et al.*, 2014); and that brain regional vulnerability was unrelated to regional differences in CI gene expression (Wirtz & Schuelke, 2011). However, differences in residual CI activity between the neurodegeneration-prone and -resilient brain regions of *Ndufs4* KO mice have according to the best of our knowledge, not been investigated in previous studies and are expected to have important implications. It has been reported that CI activity is a major controlling factor of OXPHOS in brain mitochondria, especially in synaptosomes (Rossignol *et al.*, 2000; Pathak & Davey, 2008; Cocco *et al.*, 2009; Sauerbeck *et al.*, 2011), and that residual CI activity could greatly affect the extent of downstream consequences caused by a CI deficiency (Verkaart *et al.*, 2007b; Pathak & Davey, 2008; Distelmaier *et al.*, 2009; Dubinsky, 2009; Alam *et al.*, 2015; Kühn *et al.*, 2015). In addition, consistent with the findings of this study, it has been reported that CI-driven respiratory capacity was significantly lower in the neurodegeneration-prone brain regions of PN45 to PN55 *Ndufs4* KO mice compared to the rest of the brain that is more resilient (Kayser *et al.*, 2016).

It would seem reasonable to suggest that the higher residual CI activity of the AC might result from more efficient stabilisation of CI in super-complexes (Calvaruso *et al.*, 2011), but previous studies have suggested that this might not be the case (Kayser *et al.*, 2016). Nevertheless, more sensitive experimental procedures or factors other than super-complex formation which could influence or be influenced by residual CI activity might be worth investigating in future studies. This might for example include regional differences in the organisation of OXPHOS systems, energy thresholds or control coefficients among brain regions, and/or in the different brain cells constituting the various brain regions (Rossignol *et al.*, 2003).

5.2.3 Maximal complex II, III and IV activities are not uniquely affected in the neurodegeneration-prone brain regions but are generally higher

The maximal activities of respiratory chain (RC) complexes II (CII), III (CIII) and IV (CIV) were compared among the brain regions of *Ndufs4* WT and KO mice to investigate potential links between brain region-specific vulnerability to neurodegeneration and regional differences in the activities of RC enzymes other than CI. Results (expressed as the mean normalised to mg protein \pm standard deviation) are visualised in Figures 5.3 to 5.5. Two-way mixed ANOVA of maximal CII activities (Figure 5.3) showed that the interaction between genotype and brain region was significant ($F_{2.5,45} = 5.5$, Greenhouse-Geisser $p = 0.004$, $\eta_p^2 = 0.23$), indicating that the effect of the genotype on maximal CII activities differed depending on brain region.

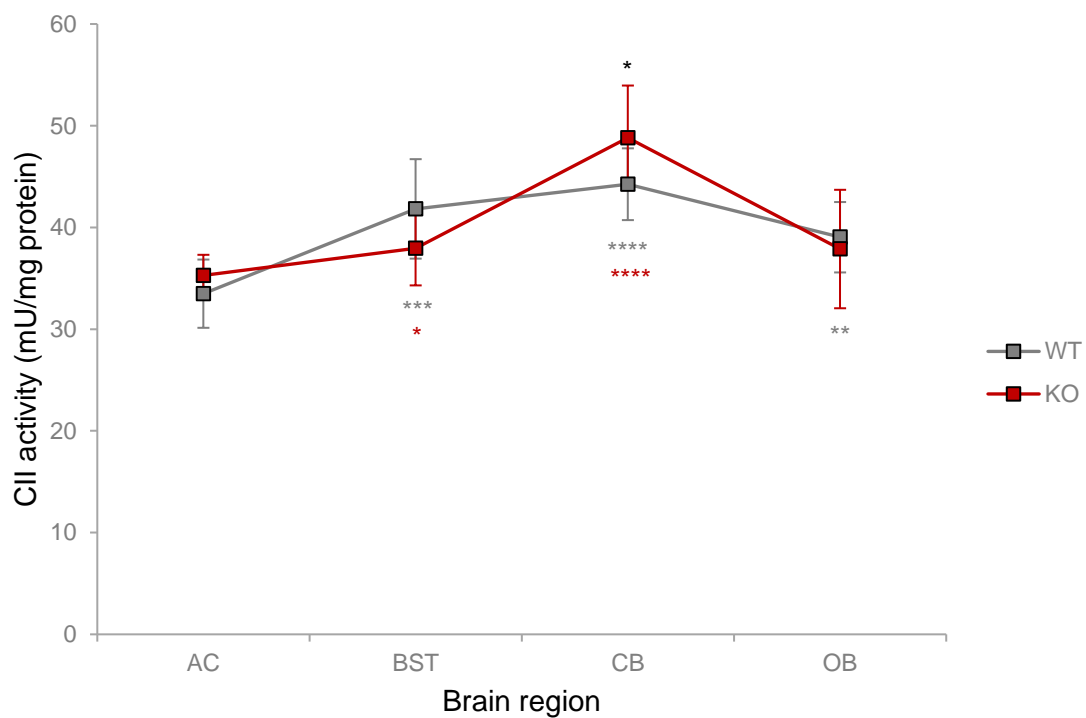


Figure 5.3: Maximal complex II activity in the brain regions of *Ndufs4* wild-type and knockout mice.

Maximal activity of complex II (CII), expressed in mU (nmol/minute) per mg of protein, was measured spectrophotometrically in duplicate in a 700 x *g* supernatant of a homogenate of the anterior cortex (AC), brainstem (BST), cerebellum (CB) and olfactory bulbs (OB) from *Ndufs4* wild-type (WT, grey, $n = 10$ for all, except OB $n = 9$) and knockout (KO, red, $n = 12$ for all, except OB $n = 11$) mice aged PN45 to PN49. Data points display mean activity \pm SD. Statistical significance for comparisons between corresponding KO and WT brain regions is indicated by asterisks (*) above the data points and was determined using the independent samples t-test. Statistical significance obtained for comparisons between the degeneration resilient AC and neurodegeneration-prone brain regions from the same genotype is indicated by grey asterisks (*) for WT and red asterisks (*) for KO below the neurodegeneration-prone data points. This was determined with the paired t-test. Statistical significance: * = $p < 0.05$, ** = $p < 0.01$, *** = $p < 0.001$, **** = $p < 0.0001$.

Maximal CII activity was only significantly higher in the KO CB when compared to WT CB ($p < 0.05$, $d = 0.9$). When comparing maximal CII activities between brain regions of the same genotype, the results showed that the resilient AC exhibited low maximal CII activity compared to the neurodegeneration-prone brain regions, except when compared to KO OB, in which case the KO AC only tended to have lower CII activity: AC vs BST in WT ($p < 0.001$, $d = 1.4$) and in KO ($p < 0.05$, $d = 0.8$), AC vs CB in WT ($p < 0.0001$, $d = 2.3$) and in KO ($p < 0.0001$, $d = 2.4$), AC vs OB in WT ($p < 0.01$, $d = 1.6$).

Among the neurodegeneration-prone brain regions, maximal CII activity of the CB was significantly higher than in the BST and OB for both genotypes: CB vs BST in WT ($p < 0.05$, $d = 0.4$) and in KO ($p < 0.0001$, $d = 1.9$) and CB vs OB in WT ($p < 0.0001$, $d = 1.5$) and in KO ($p < 0.0001$, $d = 1.9$). Overall, the *Ndufs4* KO did not affect CII activity in a manner that coincided with the pattern of brain regional vulnerability to neurodegeneration in the *Ndufs4* KO mice. However, the higher CII activity per brain region mass in the neurodegeneration-prone brain regions than in the degeneration-resilient AC might suggest a potential link with the brain regional vulnerability to neurodegeneration.

When assessing maximal CIII activities (Figure 5.4), the two-way mixed ANOVA showed no significant interaction between genotype and brain region. There was also no significant main effect of genotype. However, maximal CIII activities were significantly affected by brain region ($F_{2,35} = 63$, Greenhouse-Geisser $p < 0.0001$, $\eta_p^2 = 0.79$), indicating differences in maximal CIII activity across brain regions which were similar in both genotypes. Pairwise comparisons showed that CIII activity of the AC was significantly lower than in the BST ($p < 0.01$, $d = 1.1$) and CB ($p < 0.0001$, $d = 1.8$), but significantly higher than in the OB ($p < 0.0001$, $d = 2.3$).

Comparisons among neurodegeneration-prone brain regions showed that CIII activity in the OB was significantly lower than in the BST ($p < 0.0001$, $d = 2.6$) and CB ($p < 0.0001$, $d = 4.2$). Thus, maximal CIII activity of the investigated brain regions was not significantly affected by the *Ndufs4* KO and was not uniquely different in the more resilient AC compared to the neurodegeneration-prone brain regions.

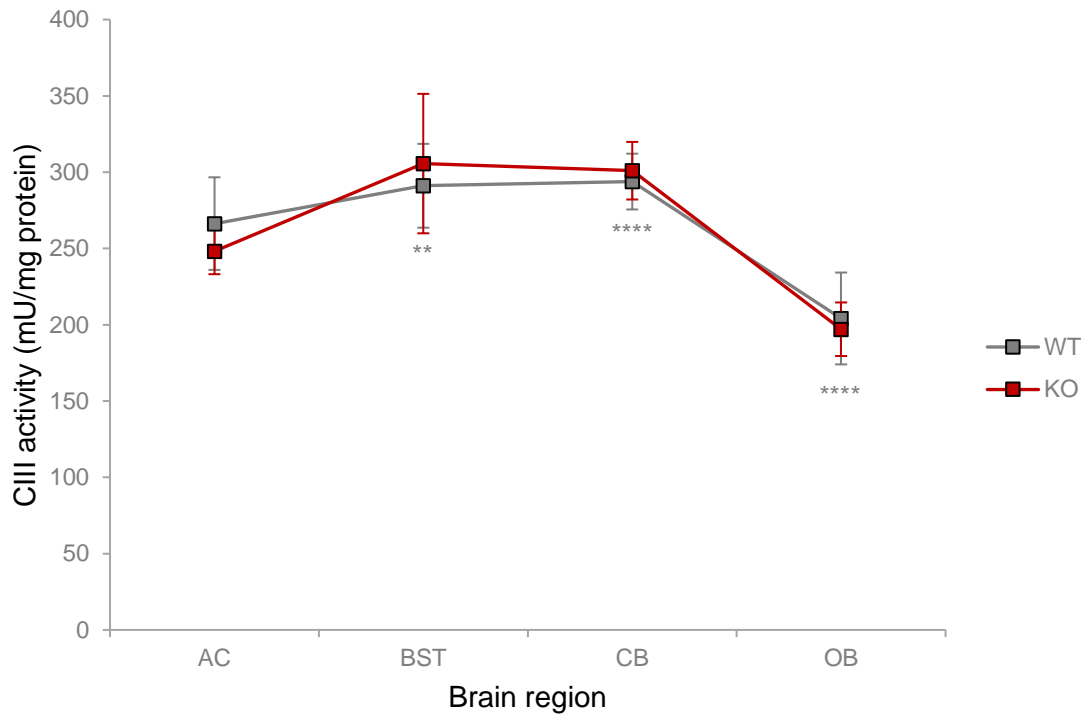


Figure 5.4: Maximal complex III activity in the brain regions of *Ndufs4* wild-type and knockout mice.

Maximal activity of complex III (CIII), expressed in mU (nmol/minute) per mg of protein, was measured spectrophotometrically in duplicate in a freeze-thawed 700 x *g* supernatant of a homogenate of the anterior cortex (AC), brainstem (BST), cerebellum (CB) and olfactory bulbs (OB) from *Ndufs4* wild-type (WT, grey, *n* =10 for AC and CB, *n* =9 for BST and OB) and knockout (KO, red, *n* =12 for all except OB *n* =11) mice aged PN45 to PN49. Data points display mean activity \pm SD. Statistical significance is indicated for pairwise comparisons between the degeneration resilient AC and neurodegeneration-prone brain region data points. Statistical significance: * = $p < 0.05$, ** = $p < 0.01$, *** = $p < 0.001$, **** = $p < 0.0001$.

Two-way mixed ANOVA of maximal CIV activities showed a significant interaction between genotype and brain region ($F_{1,6,29} = 4.5$, Greenhouse-Geisser $p < 0.05$, $\eta_p^2 = 0.20$). This indicated that the effect of the genotype differed depending on the brain region (Figure 5.5). Maximal CIV activity was higher in the KO group across all brain regions, except in the KO BST which only tended to have higher CIV activity: AC ($p < 0.01$, $d = 1.5$), CB ($p < 0.0001$, $d = 2.7$) and OB ($p < 0.01$, $d = 1.1$). Furthermore, the degeneration resilient AC exhibited low maximal CIV activity in both genotypes compared to the neurodegeneration-prone brain regions: AC vs BST in WT ($p < 0.0001$, $d = 2.4$) and in KO ($p < 0.0001$, $d = 2.5$), AC vs CB in WT ($p < 0.0001$, $d = 3.5$) and in KO ($p < 0.0001$, $d = 6.5$), AC vs OB in WT ($p < 0.001$, $d = 3.0$) and in KO ($p < 0.0001$, $d = 2.1$).

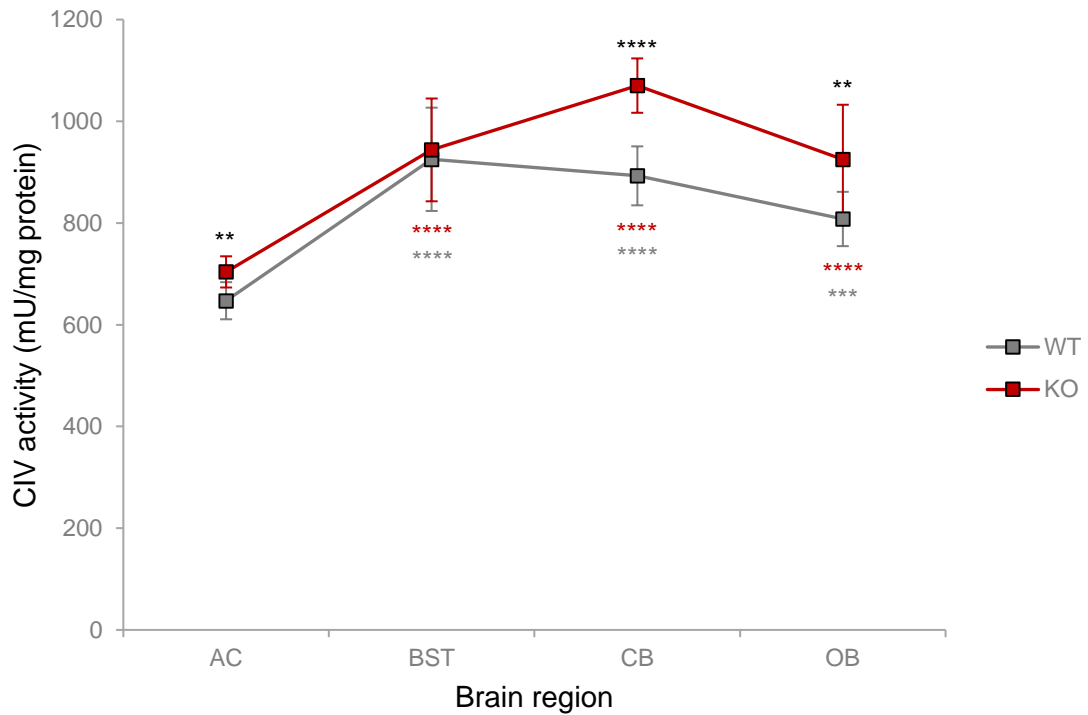


Figure 5.5: Maximal complex IV activity in the brain regions of *Ndufs4* wild-type and knockout mice.

Maximal activity of complex IV (CIV), expressed in mU (nmol/minute) per mg of protein, was measured spectrophotometrically in duplicate in a freeze-thawed 700 x g supernatant of a homogenate of the anterior cortex (AC), brainstem (BST), cerebellum (CB) and olfactory bulbs (OB) from *Ndufs4* wild-type (WT, grey, n =10 for all except OB n =9) and knockout (KO, red, n =12 for all except OB n =11) mice aged PN45 to PN49. Data points display mean activity \pm SD. Statistical significance for comparisons between corresponding KO and WT brain regions is indicated by asterisks (*) above data points. This was determined using the independent samples t-test. Statistical significance obtained for comparisons between the resilient AC and neurodegeneration-prone brain regions from the same genotype is indicated by grey asterisks (*) for WT and red asterisks (*) for KO below the neurodegeneration-prone brain region data points. This was determined using the paired t-test. Statistical significance: * = $p < 0.05$, ** = $p < 0.01$, *** = $p < 0.001$, **** = $p < 0.0001$.

When comparing maximal CIV activity between the neurodegeneration-prone brain regions of the WT group, the results showed a lower activity in the OB than in the BST ($p < 0.05$, $d = 1.2$) and CB ($p < 0.05$, $d = 1.5$). In the KO group, maximal CIV activity of the CB was higher than the BST ($p < 0.001$, $d = 1.3$) and OB ($p < 0.01$, $d = 1.3$). Overall, the *Ndufs4* KO generally increased maximal CIV activity in the investigated brain regions, albeit not uniquely in the more degeneration resilient AC, compared to the neurodegeneration-prone regions. However, the results showed that the neurodegeneration-prone brain regions had significantly higher CIV activity than the AC, regardless of genotype, indicating a possible link to the brain regional-specificity to neurodegeneration.

These results were in accordance with previous reports of unaltered activities of CII and CIII in the whole-brain of *Ndufs4* KO mice when compared to WT mice (Ingraham *et al.*, 2009; Quintana *et al.*, 2010; Calvaruso *et al.*, 2011; Leong *et al.*, 2012; Civiletto *et al.*, 2015; Manjeri *et al.*, 2016; de Haas *et al.*, 2017). However, in contrast with the unaltered CIV activity also reported in these studies, CIV activity was increased in most of the KO brain regions investigated in this study. This discrepancy might once again be caused by differences in the *Ndufs4* KO mouse models used, age of mice, experimental or normalisation procedures, tissues utilised and/or the dilution of regional differences in whole-brain preparations, as mentioned in Section 5.2.1. In contrast, increased levels of CIV complexes have been reported in the whole-brain of PN30 *Ndufs4* KO mice relative to WT mice (Martin-Perez *et al.*, 2019). This might coincide with the increased maximal CIV activity observed in the KO mouse brain regions investigated in this study. An increase in CIV complexes or activity might occur in response to an increased demand for ATP production via OXPHOS (Marczak *et al.*, 2004), oxidative stress or damage (Marczak *et al.*, 2004; Foti *et al.*, 2019), glutamatergic excito-toxicity (Strazielle *et al.*, 2003; Strazielle *et al.*, 2009), post-translational modifications (Martin-Perez *et al.*, 2019), and/or due to its association with CI and other RC enzymes in super-complexes (Li *et al.*, 2007). Nevertheless, the *Ndufs4* KO did not uniquely affect the maximal activities of CII, CIII and CIV per tissue mass in the more resilient AC compared to the neurodegeneration-prone brain regions. These findings suggested that the regional vulnerability is unlikely to result from unique alterations in the isolated RC enzyme activities of the neurodegeneration-prone brain regions in response to the *Ndufs4* KO.

Alternatively, significant differences or trends in enzyme activities per tissue mass that could differentiate between the degeneration-prone and -resilient brain regions within a genotype, might be evident in the activities of CII, perhaps CIII (except when compared to OB) and CIV. These enzyme activities were for the most part higher in the neurodegeneration-prone brain regions. The results corresponded with the higher maximal activity of CS observed in the neurodegeneration-prone brain regions. This also suggested a higher dependency of the neurodegeneration-prone brain regions on the function of OXPHOS and higher susceptibility to RC deficiencies than the AC (Munro *et al.*, 2013). Remarkable, when normalised to CS activity (mitochondrial content) in WT mice, the differences in CII activity among the neurodegeneration-prone and -resilient brain regions disappeared, while the resilient AC showed higher CIII activity in addition to lower CIV activity compared to the neurodegeneration-prone brain regions. These findings indicated that the higher CII activity observed in the neurodegeneration-prone brain regions in WT mice could be ascribed to higher mitochondrial content. Whereas the differences in the activities of CIII and CIV suggested inherent differences in OXPHOS organisation within the mitochondria between the neurodegeneration-prone and -resilient brain regions. The latter might contribute to the brain regional vulnerability to neurodegeneration in *Ndufs4* KO mice.

5.3 Vulnerability to neurodegeneration might be linked to greater OXPHOS dependency or regional differences in OXPHOS organisation

Collectively, the results indicated that it was unlikely that differential effects of the *Ndufs4* KO on the isolated maximal activities of CS and RC enzymes could cause brain regional vulnerability to neurodegeneration. However, the vulnerability of the neurodegeneration-prone brain regions might be related to a lower residual CI activity and/or an inherent greater dependency on the function of mitochondrial OXPHOS. The latter was suggested by the high activities of all investigated CS- and RC-enzymes per tissue mass (except in the case of CI- and CIII-activities of the OB) in the WT neurodegeneration-prone brain regions, compared to the resilient WT AC.

In accordance, it was previously suggested that the vulnerability to neurodegeneration in the BST, CB and OB of *Ndufs4* KO mice might be related to decreased ATP production capacity of the OXPHOS system (Kayser *et al.*, 2016). Furthermore, the vulnerability of the brain to degeneration in the *Ndufs4* KO mouse model has also been suggested to be related to decreased ATP production per tissue mass in the whole-brain (Manjeri, 2017). Such a decrease in ATP capacity might induce a vulnerability of neurons to degeneration since neuronal cells are especially dependent on mitochondria for energy production via OXPHOS. This is due to their high energy demand and low glycolytic capacity (Falkowska *et al.*, 2015; Magistretti & Allaman, 2015). Furthermore, as a source of reactive species, the increased reliance on OXPHOS could potentially also induce a vulnerability to oxidative stress in the neurodegeneration-prone brain regions when CI is deficient (Dubinsky, 2009; Cobley *et al.*, 2018).

The results indicated that the relative maximal activities of the RC enzyme complexes in the neurodegeneration-prone brain regions were distinct from the more resilient AC when expressed per tissue mass and relative to CS activity. The activity ratios between the RC complexes are known to be conserved among cell types (Barrientos, 2002; Chretien & Rustin, 2003; Koenig, 2008; Barrientos *et al.*, 2009) and were briefly evaluated as an additional means of discriminating between the neurodegeneration-prone and -resilient brain regions. The maximal RC enzyme activities of *Ndufs4* WT and KO brain regions, expressed as ratios relative to either CI or CII within a brain region, are shown in Table 5.2.

Table 5.2: Maximal respiratory enzyme activities expressed as ratios relative to complex I or complex II within a brain region.

Genotype	CI : CII : CIII : CIV relative to CI	CI : CII : CIII : CIV relative to CII	
	WT	WT	KO
Brain region			
Anterior cortex	1 : 1.2 : 9.9 : 24.0	0.8 : 1 : 8.0 : 19.6	0.3 : 1 : 7.0 : 19.6
Brainstem	1 : 1.2 : 8.3 : 26.4	0.8 : 1 : 7.0 : 22.0	0.2 : 1 : 8.1 : 24.8
Cerebellum	1 : 1.2 : 8.0 : 24.1	0.8 : 1 : 6.6 : 20.3	0.2 : 1 : 6.2 : 21.8
Olfactory bulbs	1 : 1.7 : 8.9 : 35.1	0.6 : 1 : 5.2 : 20.7	0.1 : 1 : 5.2 : 24.3

Red and green respectively indicates the ratios in the more resilient anterior cortex that are higher and lower compared to the neurodegeneration-prone brain regions.

It was seen that regardless of being expressed as a ratio relative to either CI or CII, the neurodegeneration-prone brain regions of WT mice had a notably lower ratio of CIII activity to the remaining enzyme activities, than the degeneration resilient AC. These regions also generally displayed a higher ratio of CIV activity relative to other RC enzyme activities than the resilient AC, even though these differences were more subtle in WT mice. In accord, a previous study also reported higher maximal activities for CIII in the frontal cortex compared to the CB, but in contrast to the findings reported here, CIV activity was found to be higher in the frontal cortex, indicating some discrepancy (Casademont *et al.*, 2005). The lower residual CI activity in the KO neurodegeneration-prone brain regions compared to the KO AC, was also evident when maximal enzyme activities within a brain region were expressed relative to CII activity. These results might reflect important inherent differences between neurodegeneration-prone and -resilient brain regions with regard to OXPHOS system organisation and function. This might have important implications for the region-specific vulnerability to neurodegeneration.

The imperative function of CIII and CIV in OXPHOS cannot be readily bypassed, in contrast to CI and CII function which converge at the ubiquinone(Q)-pool. Both CIII and CIV are important proton pumps which, in addition to CI, function to maintain the inner mitochondrial membrane (IMM) potential. In addition, CIV is responsible for reducing molecular oxygen, the final electron acceptor in the RC. CIII and CIV function interdependently as they interconvert oxidised and reduced Cytochrome c and associate with other RC enzymes, including CI, in super-complexes (Signes & Fernandez-Vizarra, 2018). Therefore, the organisation and activities of CIII and CIV could potentially affect upstream electron transport processes at CI, CII and the Q-pool, the rate at which reactive species are produced at various sites of the OXPHOS system as well as apoptosis

(Diaz *et al.*, 2012; Lanciano *et al.*, 2013; Guerra-Castellano *et al.*, 2018; Zhao *et al.*, 2019). Moreover, it has been shown that mutations in *Ndufs4* genes decreased the levels and stability of fully-assembled CIII even though it had limited effects on isolated CIII activity (Ugalde *et al.*, 2004). Consequently, differences in the activity or ratios of CIII and CIV enzymes among brain regions might become important in the context of a CI deficiency and could contribute to the region-specific neuropathology in the *Ndufs4* KO mice and Leigh Syndrome-like phenotypes.

For instance, the relative differences in the activity and/or organisation of RC enzyme complexes in the OXPHOS system of the neurodegeneration-prone brain regions might exacerbate the detrimental effects that CI deficiency induced. This might for example be decreased ATP production; decreased IMM potential; increased production of reactive species; as well as subsequent oxidative damage to cellular components, including the RC, when reactive species accumulate to damaging levels. This would be in accordance with the role of ATP depletion and/or excess production of reactive species and disturbances in antioxidant defences that has been implicated in the region-specific neuropathology of the *Ndufs4* KO mice (Quintana *et al.*, 2010; Choi *et al.*, 2011; Quintana *et al.*, 2012; Johnson *et al.*, 2013; Liu *et al.*, 2015; Kayser *et al.*, 2016; Liu *et al.*, 2017). Additionally, the differences in CIII and CIV activities might indicate a unique organisation that allows more effective stabilisation and functioning of CI in the resilient brain regions (Calvaruso *et al.*, 2011; García-Corzo *et al.*, 2012).

The lower CIII activity relative to other RC complexes in the neurodegeneration-prone brain regions compared to the AC, might also indicate a greater control of CIII activity on OXPHOS in the former (Rossignol *et al.*, 2003; Blier *et al.*, 2017). CIII levels, as previously mentioned, might be decreased by the *Ndufs4* KO and could potentially limit the compensatory flux through CIII in response to the effects of a CI deficiency. In support, deficiencies in CIII and CIV, as well as CI deficiencies, have been associated with the development of the Leigh Syndrome phenotype (Lake *et al.*, 2015; Chen *et al.*, 2018a). Also, defects in CIII and ubiquinone in a mouse model have been shown to cause a clinical phenotype similar to that of the *Ndufs4* KO mouse model (Spinazzi *et al.*, 2018). Moreover, therapeutic interventions which alter OXPHOS organisation or capacity, thereby increasing CI-driven respiration (Civiletto *et al.*, 2015) or the activities of CII and CIV (Barrow *et al.*, 2016), had shown to at least partially rescue the phenotype of *Ndufs4* KO mice and CI-deficient cells. Collectively, the results suggested that inherent differences in OXPHOS dependency and/or OXPHOS organisation might be underlying features in the regional neurodegeneration in *Ndufs4* KO mice and therefore worth investigating in future studies.

5.4 Summary of biochemical investigation on *Ndufs4* knockout brain regions

This chapter investigated the brain regional vulnerability to neurodegeneration in the *Ndufs4* KO mice on a biochemical level by evaluating maximal CS and RC enzyme activities in neurodegeneration-prone brain regions (BST, CB and OB) and a degeneration-resilient brain region (AC). The evaluation was carried out on two levels to determine: 1) potential differential effects of the KO on maximal enzyme activities; and 2) unique levels of maximal enzyme activities in the neurodegeneration-prone brain regions when compared to the more resilient AC. While the *Ndufs4* KO had indistinguishable effects on the maximal activity of CS and RC enzymes of the neurodegeneration-prone brain regions compared to the resilient AC, residual CI activity was lower in the former. In WT mice, the activities of CS, CII and CIV were higher in the neurodegeneration-prone brain regions than in the more resilient AC. The activities of CI and CIII were higher in most but not all WT neurodegeneration-prone brain regions than in the AC. Furthermore, it was shown that the relative ratios of maximal RC enzyme activities differed among the neurodegeneration-prone and -resilient brain regions.

Overall, the results suggested that the vulnerability to neurodegeneration in the BST, CB and OB might be linked to: 1) a greater dependency on OXPHOS to meet cellular requirements; 2) a lower residual activity of CI, especially the extremely low residual CI activity (14% of WT, only 3.1 mU/mg absolute CI activity) exhibited by the KO OB; and/or 3) brain regional differences in the relative activities and/or organisation of RC enzymes in the OXPHOS system, especially concerning the CIII and CIV enzyme complexes.

CHAPTER 6: METABOLOMICS INVESTIGATION OF NDUFS4 KNOCKOUT MOUSE BRAIN REGIONS

6.1 Introduction

One of the main objectives (Objective 3) of this study was to investigate if brain regional differences in metabolic responses to the complex I (CI) deficiency could be correlated with the regional vulnerability to neurodegeneration in *Ndufs4* knockout (KO) mice by using a multi-platform metabolomics approach.

The abundances of a wide spectrum of metabolites were measured using untargeted gas chromatography-time of flight (GC-TOF) mass spectrometry as well as semi-targeted liquid chromatography-tandem mass spectrometry (LC-MS/MS) analysis. Sample extracts were prepared from three neurodegeneration-prone brain regions: brainstem (BST), cerebellum (CB) and olfactory bulbs (OB), as well as from the neurodegeneration-resilient anterior cortex (AC). Standardisation of the assays (Objective 3.1 and 3.2) for applicability on mouse brain region samples is shown in APPENDIX D. Using the standardised assays, final analyses (Objective 3.3) were conducted on brain regions harvested from *Ndufs4* wild-type (WT, n =25) and KO (n =21) mice at postnatal day (PN) 45 to PN49. A detailed description of the experimental methods was given in Section 4.7.4. Data was pre-processed (Objective 3.4) and statistically evaluated (Objective 3.5) as described in Section 4.7.5 and Section 4.7.6. Briefly, the metabolic effect of the *Ndufs4* KO on each brain region was evaluated by statistically comparing relative metabolite intensities between the corresponding brain regions of WT and KO mice and by identifying significant discriminatory metabolites. The magnitude of change in the levels of the discriminatory metabolites was then relatively compared among brain regions. The main results are reported in this section, while supplementary results are shown in APPENDIX G.

In this chapter (Objective 3.6), an overview is given on the quality of the metabolomics data. The results concerning the effect of the *Ndufs4* KO on the metabolic profiles of the respective mouse brain regions are then presented followed by a description of discriminatory metabolites that were common and unique between the neurodegeneration-prone and -resilient brain regions. Thereafter, the metabolites and their associated metabolic pathways are evaluated, and an overview is given on the “shared” *in vivo* effects of the *Ndufs4* KO on the mouse brain regions. The metabolic perturbations that could correlate with region-specific neurodegeneration are also discussed. The downstream neurotoxic and neuroprotective effects of the latter are then discussed as well as a few inherent region-specific factors that might contribute to the metabolic correlation with neurodegeneration. The chapter concludes with a summary of the main findings.

6.2 Metabolomics data quality

The reliability and quality of the final metabolomics data sets (after being normalised) were determined by evaluating data repeatability or precision and potential batch-effects. For this purpose, the data of quality control (QC) samples were assessed in terms of the distribution of coefficient of variance (CV) values, distribution of total signal intensity over run-order as well as clustering using principal component analysis (PCA). Details are provided in APPENDIX F. In brief, the reliability of the data was demonstrated in accordance to the standards outlined in the literature. Because non-biological variation did not significantly affect the outcome of the data, the data proved to be of good quality and suitable for further interpretation.

6.3 The effect of the *Ndufs4* knockout on metabolic profiles of selected brain regions

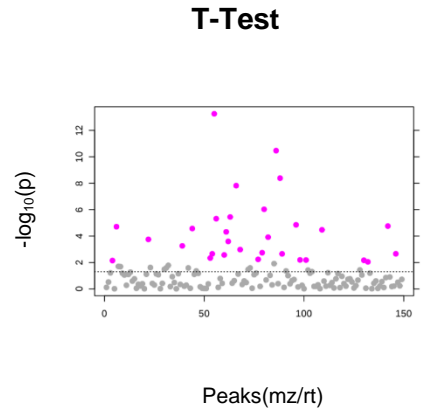
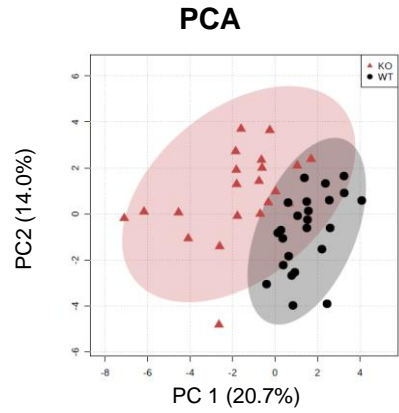
6.3.1 The metabolic profile of each brain region was distinct between the wild-type and knockout mice

Platform-specific data sets were visually evaluated for natural clustering and trends by performing unsupervised PCA on the post-quality control, imputed, generalised (glog) log-transformed data. Figure 6.1 displays the 2-D PCA scores plots for the respective GC-TOF (Figure 6.1.A, left panels) and LC-MS/MS (Figure 6.1.B, left panels) data obtained for the brain regions of *Ndufs4* KO and WT mice. Principal component 1 (PC1, X-axis) and principal component 2 (PC2, Y-axis) represent the two directions of maximum variance in the data set. Student's t-test results are also visualised (Figure 6.1.A and B, right panels). In all brain regions, the samples clustered naturally into the genotype groups (WT and KO) for both the GC-TOF and LC-MS/MS data. This indicated a distinct effect of the KO on the metabolic profiles. While group clustering slightly overlapped in the scores plots of the AC and BST, clear separation was observed in the CB and especially in the OB for both metabolomics platforms. With the exception of the GC-TOF PCA scores plots of the CB, the separation of the genotype groups was mostly in the direction of PC1. This suggested that the maximum variation in the metabolic patterns between samples was mostly due to genotype-related variations. Overall, the WT samples tended to display tighter clustering than the KO samples, demonstrating that the metabolic profiles of mice in the KO group were more variable. This might be reflective of the complexity of the mechanisms underlying mitochondrial disease which can cause variation in tissue-specific cellular responses, even in organisms that are genetically highly homogenous. Furthermore, the LC-MS/MS data exhibited clearer separation of genotype groups compared to the GC-TOF data. This suggested that a higher percentage of detected features had significantly altered levels in the LC-MS/MS data than in the GC-TOF data sets; and/or that more sources of variation in the GC-TOF data obscured natural clustering due to its untargeted nature. This substantiated the need to identify discriminatory metabolites.

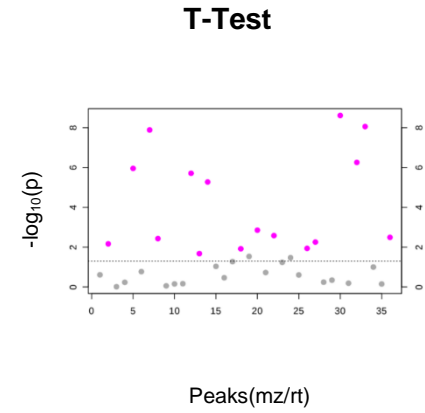
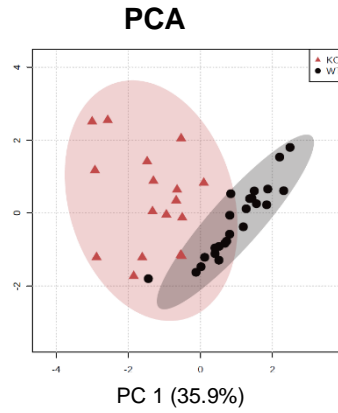
A) GC-TOF Analysis

B) LC-MS/MS Analysis

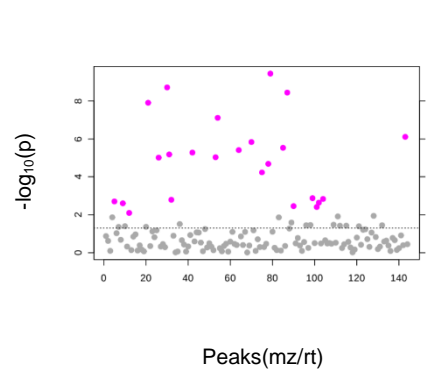
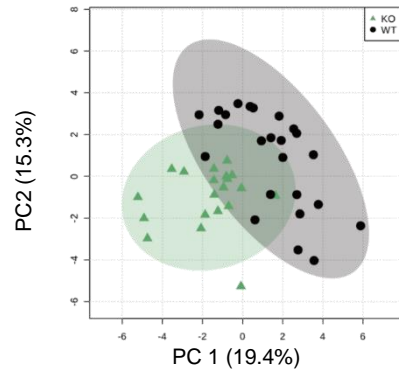
AC



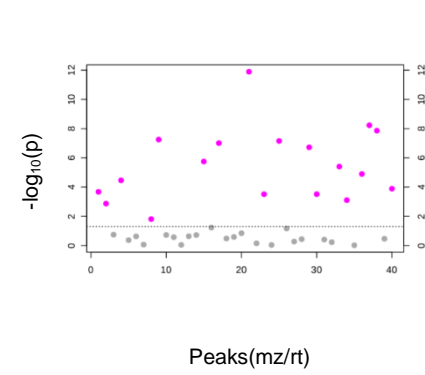
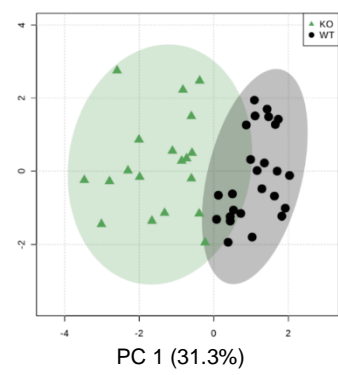
PCA



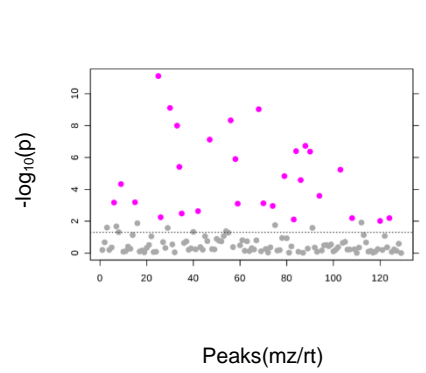
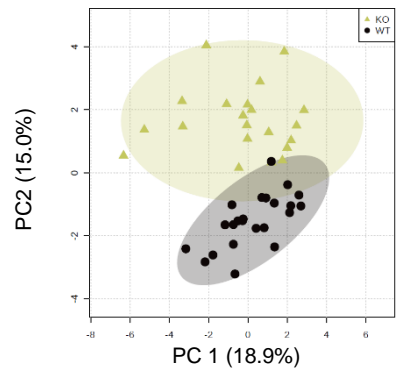
BST



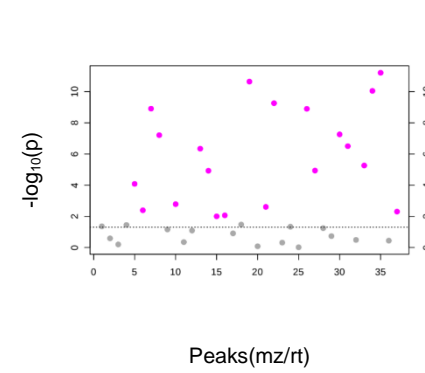
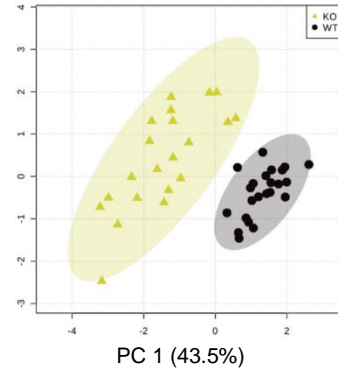
PCA



CB



PCA



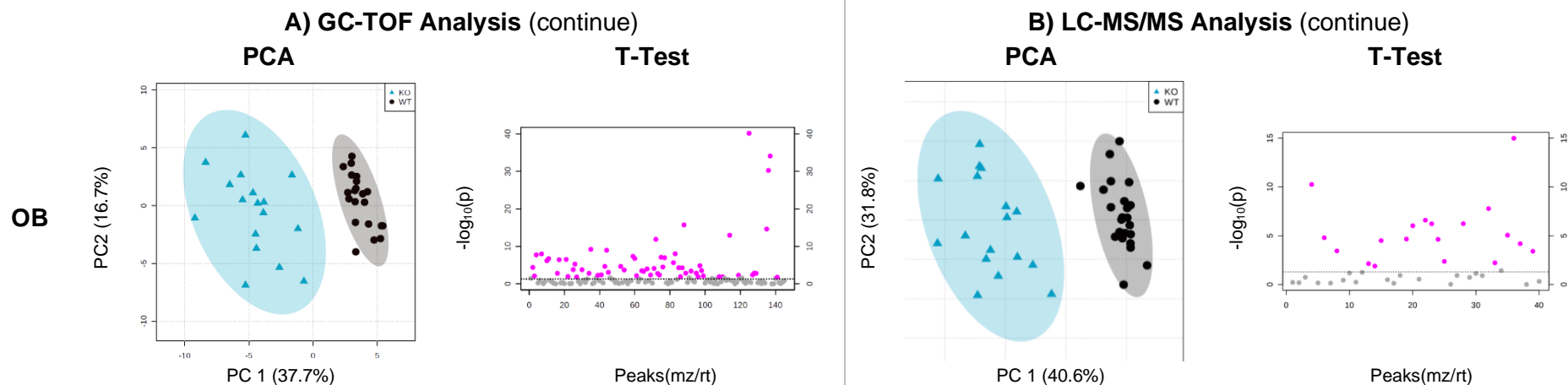


Figure 6.1: The effect of the *Ndufs4* knockout on the metabolic profiles of various brain regions as detected with GC-TOF and LC-MS/MS analysis.

Global metabolite patterns of wild-type (WT, $n = 25$, ●) and *Ndufs4* knockout (KO, $n = 21$, ▲) anterior cortex (AC, red), brainstem (BST, green), cerebellum (CB, yellow) and olfactory bulbs (OB, blue) samples are illustrated using PCA scores plots. Principal component 1 (PC1, X-axis) and Principal component 2 (PC2, Y-axis) represent the two directions of maximum variance in the data set. Shaded ellipses represent the 95% confidence intervals for each experimental group. Significantly altered features were identified using student's t-test and FDR-adjusted $p < 0.05$ (represented by pink circles above the cut-off line). **Note 1:** p -values were transformed by $-\log_{10}$ so that the more significant features (smaller p -values) were plotted higher on the graph. **Note 2:** The GC-TOF scores plot for the OB was constructed without the data of three detected features (see text for details) for proper evaluation of the clustering of sample points. The three features were not detected in any of the WT samples presumably because the intensities were below the detection limit, as these features were detected in both the KO and QC samples. The missing values for the three features in the WT group were therefore replaced with half of the minimum positive value of the entire data set. As a result, when the three features were included in the construction of the PCA scores plots, the separation between the genotype groups overwhelmed the remaining variation in the data set (PC1 and PC2 accounted for 70.7% and 7.0% of variation respectively) (APPENDIX G). **A: GC-TOF analysed samples.** PCA score plots (left panel of left column) and t-test graphs (right panels of left column) show that 30 of the 149 detected features were significantly altered in the AC, 24 of the 144 detected features in the BST, 28 of the 129 detected features in the CB and 65 of the 145 detected features in the OB. **B: LC-MS/MS analysed samples.** PCA score plots (left panel of right column) and t-test graphs (right panel of right column) showing that 16 of the 36 detected features were significantly altered in the AC, 18 of the 40 detected features in the BST, 20 of the 37 detected features in the CB and 19 of the 40 detected features in the OB. *Other abbreviations: mz, mass-to-charge ratio values; rt, retention time.*

In accordance with the PCA scores plots, a number of important features differed significantly (FDR-corrected p -value <0.05) between the corresponding *Ndufs4* KO and WT brain regions (Figure 6.1.A and B, right panels). Of the total features detected by both metabolomics platforms, 46 out of 186 features were significantly altered in the AC, 42 out of 184 features in the BST, 48 out of 166 in the CB, and 84 out of 185 in the OB. The percentage of detected metabolites with significantly altered levels was ~20% higher in the OB than in the other brain regions, in line with the more pronounced separation between genotype groups in the OB PCA scores plot. The alterations in the levels of a few metabolites also seemed more pronounced in the OB (lower p -values) in comparison with the other brain regions. These results suggested that the *Ndufs4* KO caused greater perturbations in the metabolic profile of the OB than in all the remaining brain regions that were investigated.

From the subset of statistically significant features, 44 differential features were also practically significant (d -value ≥ 0.8) in the AC, 40 in the BST, 43 in the CB and 66 in the OB. After removing overlapping metabolites of the two metabolomics platforms, the number of discriminatory metabolites that were identified at an ID level of 1, 2 or 3 (refer to Section 4.7.6) in the data sets of the AC, BST, CB and OB was 31, 29, 32 and 49, respectively. These results are depicted in Figure 6.2.

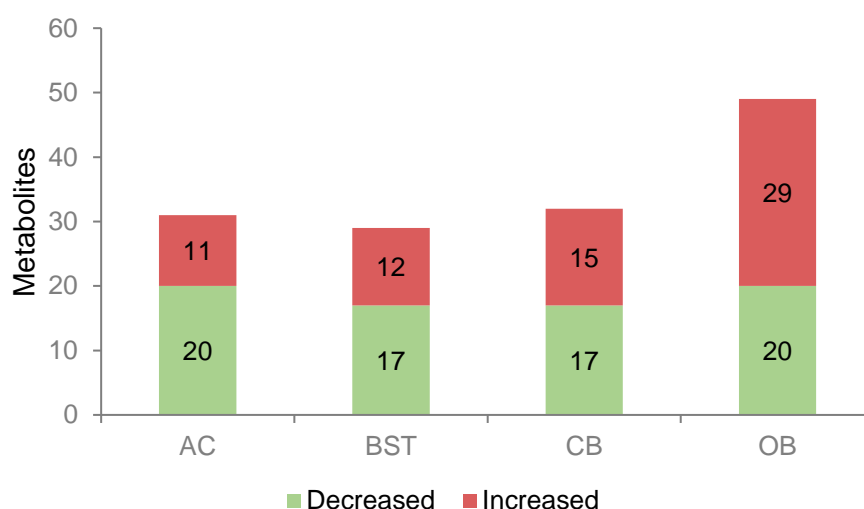


Figure 6.2: Number of discriminatory metabolites altered in the brain regions of *Ndufs4* knockout mice compared to wild-type mice.

In the anterior cortex (AC), brainstem (BST) and cerebellum (CB), most metabolites had decreased levels. A much larger group of significant metabolites was identified in the olfactory bulbs (OB) and the majority of these had significantly increased levels. (KO, $n=21$; WT, $n=25$).

Again, the OB displayed a much greater number of discriminatory metabolites, while the other three brain regions exhibited a similar number of discriminatory metabolites. Most of the important metabolites had decreased levels in the KO AC (20 decreased vs 11 increased), KO BST (17 decreased vs 12 increased) and KO CB (17 decreased vs 15 increased), but increased levels in the KO OB (20 decreased vs 29 increased) when compared to the corresponding WT regions. In addition, the neurodegeneration-prone brain regions exhibited a higher percentage (41% to 59%) of metabolites with significantly increased concentrations than the more resilient AC (35%). This suggested that neurodegeneration might correlate with global, graded perturbations within the brain regions which generally cause metabolites to accumulate.

Multivariate PCA was applied to the discriminatory metabolites obtained from the combined metabolomics approaches to visualise the cumulative discriminative power (Figure 6.3). It was evident that a more pronounced separation were obtained between genotype groups in all brain regions (vs Figure 6.1). These findings substantiated the value of a multi-platform metabolomics approach and the application of statistical processes to identify metabolites that can significantly distinguish between experimental groups. In this way, the data can possibly be utilised to more effectively investigate the regions-specific neurodegeneration in response to the *Ndufs4* KO. Once again it was clear that the *Ndufs4* KO had a significant effect on the metabolic profile of each brain region. The OB and CB exhibited clearer separation in the clustering of *Ndufs4* KO and WT samples than in the BST and the more resilient AC.

Combined, the results showed that the *Ndufs4* KO had a significant effect on the metabolic profiles of the investigated brain regions. It also highlighted the usefulness of utilising genetically homogenous models, statistical analyses and complementary multi-platform metabolomics approaches for investigating mitochondrial disease. Furthermore, it is evident that the *Ndufs4* KO affected the metabolic profile of the OB more severely, compared to other brain regions. This was in accordance with the observations made on the biochemical effect of the *Ndufs4* KO on the activities of individual respiratory chain complexes (Chapter 5) which showed that the absolute and residual CI activity in the OB was dramatically lower compared to the BST, CB and AC (Section 5.2.2). This also corresponded with previous findings, suggesting that the OB may be affected first and to a greater extent when compared to other brain regions in the *Ndufs4* KO mice (Quintana *et al.*, 2010). Lastly, the metabolomics results suggested that the *Ndufs4* KO might cause a gradient of metabolic impairment in all brain regions which correlated with the severity of neuronal damage. Such a phenomenon has also previously been noted in a metabolomics study on the brain regions of Alzheimer's disease patients (Xu *et al.*, 2016).

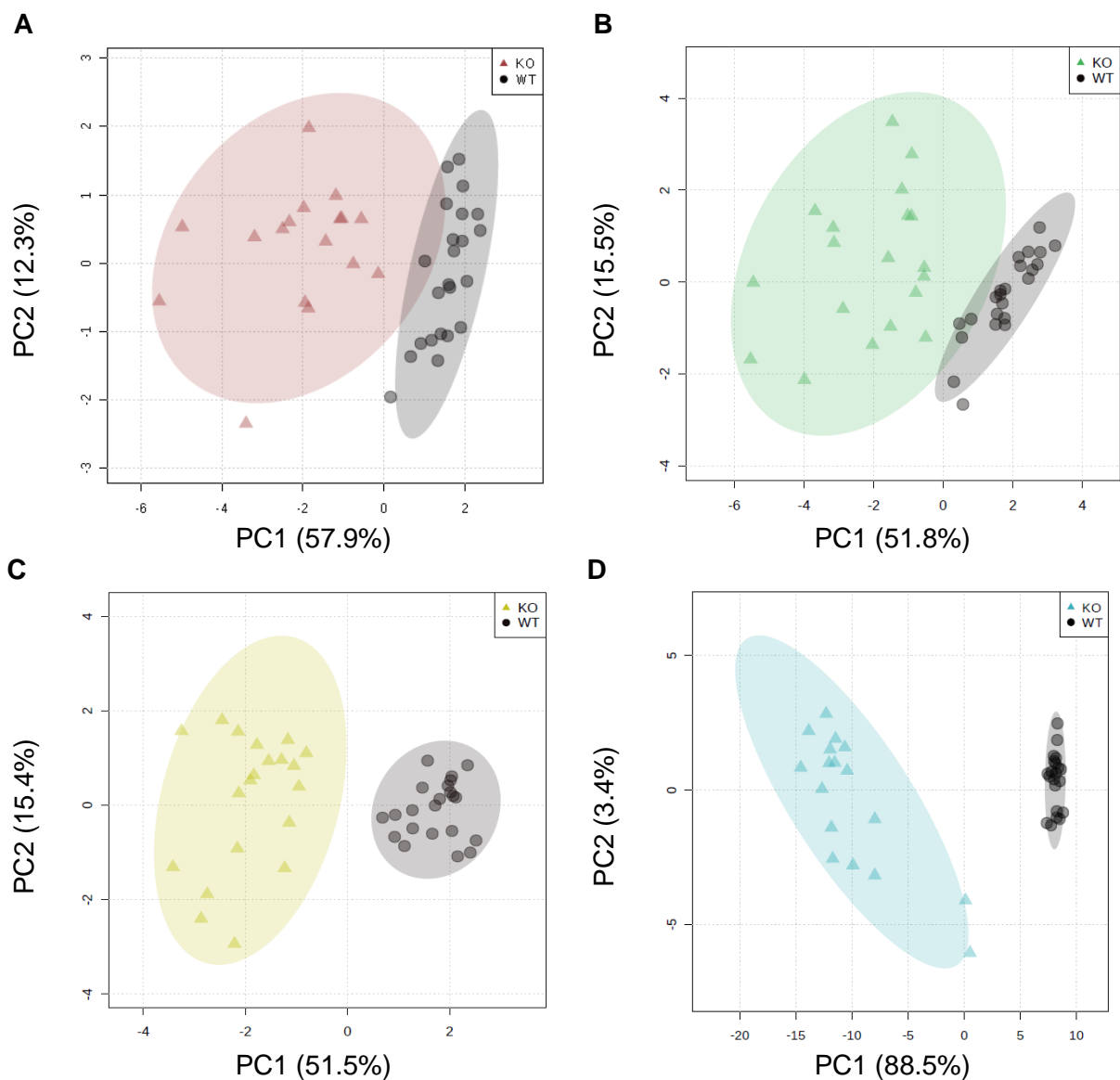


Figure 6.3: Discriminative power of discriminatory metabolites altered in the brain regions of *Ndufs4* knockout mice compared to wild-type mice.

Principle component analysis (PCA) scores plots depicting the data of the metabolites which displayed significantly ($p < 0.05$, $d \geq 0.8$) altered levels when knockout mice (KO, \blacktriangle , $n = 21$) were compared with wild-type (WT, \bullet , $n = 25$) mice in the **A**: anterior cortex (AC), **B**: brainstem (BST), **C**: cerebellum (CB) and **D**: olfactory bulbs (OB).

6.3.2 The *Ndufs4* knockout affected multiple metabolic pathways in each brain region

The important discriminatory metabolites of each brain region were categorized according to their involvement in major energy producing metabolic pathways (amino acid, carbohydrates, fatty acids/lipids and TCA cycle) or in “other” metabolic pathways. A complete list of the discriminatory metabolites together with the statistical information is presented in Table 6.1 and illustrated with volcano plots in Figure 6.4.

Table 6.1: Significant metabolites discriminating between the *Ndufs4* wild-type and knockout mice in the selected brain regions.

The significant discriminatory metabolites with an identification confidence Level of 1, 2 or 3 together with an FDR-corrected *p*-value <0.05 and *d*-value ≥0.8. Compounds are ordered in decreasing statistical (FDR-corrected *p*-value) significance. Arrows indicate an increase (↑) or decrease (↓) relative to the wild-type metabolite levels. The identification (ID) level is given for each metabolite along with a designated metabolite class (amino acid, A; carbohydrates, C; fatty acids, F; TCA cycle, T; or other, O).

Anterior Cortex											
Compound	↑/↓	<i>p</i> -value*	<i>d</i> -value	ID Level	Class	Compound	↑/↓	<i>p</i> -value*	<i>d</i> -value	ID Level	Class
Putrescine	↑	2.56E-09	2.17	3	A	Serine	↓	4.83E-03	1.02	1	A
Aspartic acid	↓	8.73E-09	2.41	1	A	Pipecolic acid	↑	6.33E-03	0.90	1	A
α-Amino adipic acid	↓	1.55E-07	1.67	1	A	N-Acetylglutamic acid	↑	1.17E-02	0.91	1	A
Asparagine	↓	1.55E-07	1.94	1	A	Methylindole	↑	1.42E-02	0.82	3	A
Phosphoglycerol	↓	2.06E-07	2.08	3	C,F	Uridine 5'-monophosphat	↓	1.50E-02	0.95	3	O
α-Hydroxyglutaric acid	↓	5.71E-07	1.58	3	T	5-Oxoproline / pyroglutamic acid	↓	1.50E-02	0.93	3	A
Glutamic acid	↓	4.98E-06	1.89	1	A	(9S,10S)-Dihydroxystearic acid	↓	1.50E-02	0.85	3	F
Arginine	↓	7.97E-06	1.76	1	A	Propionylcarnitine	↓	1.68E-02	0.85	1	A,F
Hydroxy-Proline	↓	1.17E-05	1.66	1	A	Creatinine	↑	1.75E-02	0.78	1	O
Citrulline	↓	2.74E-05	1.37	1	A	Ornithine	↓	1.89E-02	0.87	1	A
Phosphoglycerol (enol) (A)**	↓	2.80E-05	1.24	3	F	Arachidonic acid	↑	1.89E-02	0.78	3	F
Erythronic acid	↑	8.94E-05	1.54	3	C	Methionine	↓	2.86E-02	0.77	1	A
Threose	↓	2.63E-04	1.34	2	C	Proline	↑	2.91E-02	0.80	1	A
Glycolic acid	↓	2.91E-04	1.33	3	F	Carbamic acid	↑	2.91E-02	0.79	3	O
Cysteine	↓	5.50E-04	1.20	1	A	Ribitol	↑	3.44E-02	0.79	3	C
Valine	↑	1.77E-03	1.12	1	A						
Brainstem											
Compound	↑/↓	<i>p</i> -value*	<i>d</i> -value	ID Level	Class	Compound	↑/↓	<i>p</i> -value*	<i>d</i> -value	ID Level	Class
Proline	↑	5.17E-11	2.76	1	A	Leucine	↑	1.06E-04	1.33	1	A
α-Amino adipic acid	↓	1.18E-07	1.56	1	A	3-methyl Histidine	↑	1.25E-04	1.37	1	A
Phosphoglycerol	↓	1.74E-07	1.89	3	C,F	Phosphoglycerol (enol) (A)**	↓	2.10E-04	1.29	3	F
Isovalerylcarnitine	↓	1.83E-07	1.88	1	A,F	N-Acetylglutamic acid	↑	4.29E-04	1.20	1	A
Valine	↑	4.47E-07	2.07	1	A	Ribitol	↑	5.59E-04	1.32	3	C
Asparagine	↓	5.61E-07	1.65	1	A	Taurine	↑	6.51E-04	1.20	1	A
Citrulline	↓	6.52E-07	1.69	1	A	Pipecolic acid	↑	8.16E-04	0.97	1	A
Hydroxy-Proline	↓	8.87E-06	1.49	1	A	Propionylcarnitine	↓	8.16E-04	1.15	1	A,F
Aspartic acid	↓	1.75E-05	1.25	1	A	Butyrylcarnitine	↓	1.95E-03	1.06	1	A,F
25-OH-cholesterol	↓	1.86E-05	1.47	2	F	Ornithine	↓	3.16E-03	1.04	1	A

Brainstem (continue)											
Compound	↑/↓	p-value*	d-value	ID Level	Class	Compound	↑/↓	p-value*	d-value	ID Level	Class
Glutamic acid	↓	5.05E-05	1.14	1	A	Threose	↑	1.21E-02	0.90	2	C
Putrescine	↑	5.25E-05	1.35	3	A	Succinic acid	↓	1.31E-02	0.85	1	T
α-Hydroxyglutaric acid	↓	6.16E-05	1.59	3	T	Glycolic acid	↓	1.51E-02	0.89	3	F
Isoleucine	↑	8.52E-05	1.50	1	A	Glycerol	↑	1.67E-02	0.90	3	C,F
5-Oxoproline / pyroglutamic acid	↓	1.06E-04	1.53	3	A						
Cerebellum											
Compound	↑/↓	p-value*	d-value	ID Level	Class	Compound	↑/↓	p-value*	d-value	ID Level	Class
Isovalerylcarnitine	↓	2.27E-10	2.70	1	A,F	Alanine	↑	3.38E-05	1.25	1	A
Proline	↑	4.20E-10	2.35	1	A	Isoleucine	↑	4.56E-05	1.28	1	A
Valine	↑	1.00E-09	2.25	1	A	Ribitol	↑	1.47E-04	1.33	3	C
α-Aminoadipic acid	↓	1.10E-09	1.86	1	A	Arginine	↓	2.19E-04	1.25	1	A
Asparagine	↓	7.82E-09	1.89	1	A	Phosphoglycerol (enol) (B)**	↑	2.41E-04	0.97	3	F
Leucine	↑	4.03E-08	1.69	1	A	Threose	↓	2.07E-03	1.01	2	C
Erythronic acid	↑	4.03E-08	1.69	3	C	Isothreonine / Homoserine	↓	4.09E-03	0.85	1	A
5-Oxoproline / pyroglutamic acid	↓	1.51E-07	1.85	3	A	2,2-dimethylpropan-1-imine	↑	4.85E-03	0.86	3	O
Aspartic acid	↓	2.87E-07	1.56	1	A	Lactic acid	↑	4.85E-03	0.91	1	C
Serine	↓	2.87E-07	1.58	1	A	α-Hydroxyglutaric acid	↓	5.10E-03	0.88	3	T
Butyrylcarnitine	↓	1.29E-06	1.61	1	A,F	Glycine	↓	8.92E-03	0.89	1	A
Hydroxy-Proline	↓	1.69E-06	1.78	1	A	Pipecolic acid	↑	5.75E-03	0.75	1	A
Putrescine	↑	3.44E-06	0.90	3	A	N-Acetylglutamic acid	↑	1.02E-02	0.76	1	A
Phosphoglycerol	↓	6.13E-06	1.72	3	C,F	Succinic acid	↓	1.84E-02	0.89	1	T
Glutamic acid	↓	1.84E-05	1.19	1	A	Oleic acid	↑	3.17E-02	0.77	1	F
Propionylcarnitine	↓	3.38E-05	1.33	1	A,F	Arachidonic acid	↑	4.55E-02	0.76	3	F
Olfactory Bulbs											
Compound	↑/↓	p-value*	d-value	ID Level	Class	Compound	↑/↓	p-value*	d-value	ID Level	Class
Phosphoglycerol (enol) (B)**	↑	4.37E-34	11.29	3	F	Arginine	↑	7.13E-05	1.38	1	A
Glucose-6-phosphate	↑	2.54E-23	5.47	2	C	Oleic acid	↑	7.36E-05	1.47	1	F
α-Aminoadipic acid	↓	4.24E-14	3.21	1	A	Carnitine	↑	8.57E-05	1.42	1	A,F
Glucose-1-phosphate	↑	3.03E-13	2.71	3	C	Erythronic acid	↑	1.11E-04	1.29	3	C
Adenosine	↓	3.54E-12	3.28	1	O	Isovalerylcarnitine	↓	2.00E-04	1.35	1	A,F
Putrescine	↑	5.02E-12	2.74	3	A	Pyruvic acid	↑	2.10E-04	1.30	2	C
Glucose	↑	2.64E-11	2.46	2	C	α-Hydroxyglutaric acid	↓	2.23E-04	1.11	3	T
Lysine	↑	1.12E-09	2.44	1	A	Threose	↓	2.73E-04	1.14	2	C

Olfactory Bulbs (continue)											
Compound	↑/↓	p-value*	d-value	ID Level	Class	Compound	↑/↓	p-value*	d-value	ID Level	Class
Fructose-6-phosphate	↑	1.32E-09	2.00	3	C	Formylglycine	↑	3.07E-04	1.27	3	A
Aspartic acid	↓	2.24E-07	1.71	1	A	2,5-Pyrazinediol	↓	9.69E-04	1.10	3	O
Leucine	↑	1.07E-06	1.66	1	A	Asparagine	↓	1.03E-03	1.04	1	A
Valine	↑	1.68E-06	1.92	1	A	N-Acetylaspartic acid	↓	1.05E-03	1.03	1	A
Alanine	↑	1.89E-06	1.55	1	A	Threonine	↑	2.14E-03	1.01	1	A
3-((carboxymethyl)(methyl)amino)-3-oxopropanoic acid	↓	2.51E-06	1.47	3	O	Lyxose	↑	2.35E-03	0.96	2	C
Pipecolic acid	↑	2.59E-06	1.76	1	A	Ribitol	↑	2.75E-03	0.96	3	C
Cystathionine	↑	4.01E-06	1.71	1	A	Palmitic acid	↑	2.81E-03	1.08	1	F
Lactic acid	↑	4.05E-06	1.49	1	C	Pantothenic acid	↓	2.97E-03	0.87	3	O
Ethyl-9,10-dihydroxyoctadecanoate	↓	4.05E-06	1.42	3	F	Phosphoglycerol	↓	3.75E-03	0.92	3	C,F
γ-Aminobutyric acid	↑	4.89E-06	1.55	3	A	Xylo-hexos-5-ulose	↓	1.02E-02	0.85	3	C
Proline	↑	5.46E-06	1.60	1	A	Acetylcarnitine	↑	1.06E-02	0.95	1	A,F
2,2-dimethylpropan-1-imine	↑	1.41E-05	1.42	3	O	Succinic acid	↓	1.24E-02	0.89	1	T
D-Mannonic acid, γ-lactone	↑	2.03E-05	1.25	2	C	Butyrylcarnitine	↓	1.40E-02	0.92	1	A,F
Isoleucine	↑	2.50E-05	1.57	1	A	Beta-Alanine	↓	1.61E-02	0.90	1	A
Glutamic acid	↓	4.42E-05	1.25	1	A	Stearic acid	↓	1.81E-02	0.87	1	F
5-Oxoproline / pyroglutamic acid	↓	6.93E-05	1.42	3	A						

*FDR-adjusted

**Phosphoglycerol (enol) (A) of the AC and BST and phosphoglycerol (enol) (B) of the CB and OB are two different metabolites with a tentative Level 3 identity; i.e. overlapping spectral matches but different retention times

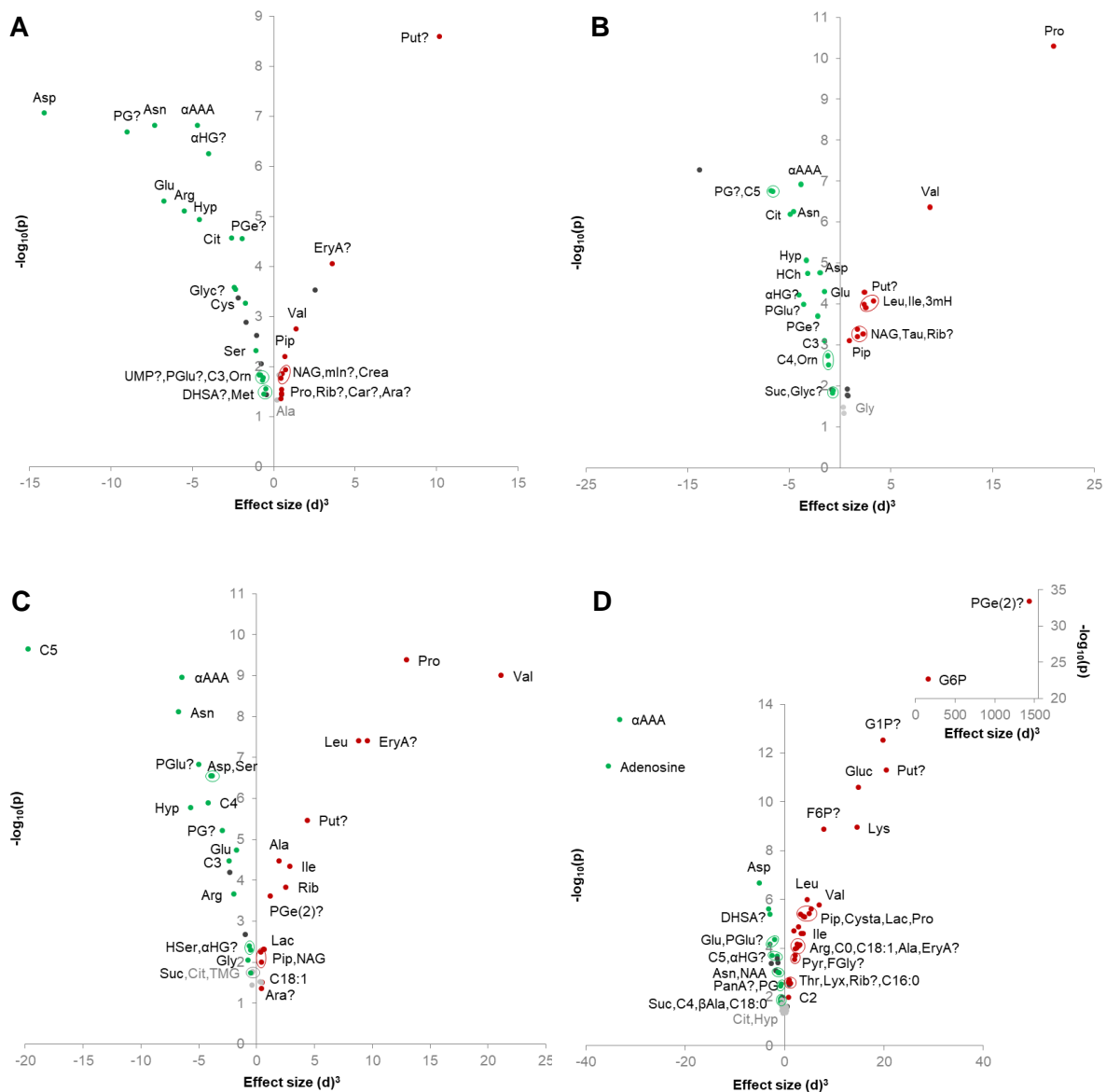


Figure 6.4: Discriminatory metabolic alterations in *Ndufs4* knockout mouse brain regions.

Statistically significant features (FDR-corrected p -value < 0.05) obtained from multi-platform metabolomics data sets of **A:** anterior cortex, **B:** brainstem, **C:** cerebellum and **D:** olfactory bulbs from *Ndufs4* KO ($n = 21$) mice compared to WT ($n = 25$) mice. Statistical significance (Y-axis) depicted as negative logarithm to the base 10 ($-\log_{10}$) of p -values. More significant features plotted higher. Effect sizes (X-axis), calculated using Cohen's d , were raised to the third power (d^3). More significant features plotted wider. Negative and positive d -values respectively represent a decrease or increase in concentrations. Metabolites with significantly ($p < 0.05$ and $d \geq 0.8$) altered levels and reliable identities (ID level 1, 2 and 3) are shown in green (decreased) or red (increased). Practically insignificant ($d < 0.8$) features are shown in grey. Identities of relevant features listed next to symbol. Encircled symbols depict a collection of compounds with identities listed next to the circle. The symbol "?" indicates ID level 3. Other abbreviations: α AAA, α -amino adipic acid; β Ala, β -alanine; Ala, alanine; Ara?, arachidonic acid; Arg, arginine; Asn, asparagine; Asp, aspartic acid; C0, carnitine; C2, acetyl carnitine; C3, propionyl carnitine; C4, butyryl carnitine; C5, isovaleryl carnitine; C16:0, palmitic acid; C18:0, stearic acid; C18:1, oleic acid; Car?, carbamic acid; Cit, citrulline; Crea, creatinine; Cys, cysteine; Cysta, cystathionine; DHSA?, dihydroxystearic acid; EryA?, erythronic acid; FGly?, formylglycine; F6P, fructose-6-phosphate?; G1P, glucose-1-phosphate?; G6P, glucose-6-phosphate; Glu, glutamic acid; Gluc, glucose; Gly, glycine; Glyc?, glycolic acid; HCh, hydroxy-cholesterol; HSer, homoserine; α HG?, α -

hydroxyglutaric acid; Hyp, hydroxyproline; Ile, isoleucine; Lac, lactic acid; Leu, leucine; Lys, lysine; Lyx, lyxose; 3mH, 3-methylhistidine; mIn?, methylindole; Met, methionine; NAA, N-acetylaspartic acid; NAG, N-acetylglutamic acid; Orn, ornithine; PanA?, pantothenic acid; PG?, phosphoglycerol; PGe/(2)?, phosphoglycerol (enol)/2; PGlu?, pyroglutamic acid; Pip, pipercolic acid; Pro, proline; Put?, putrescine; Pyr, pyruvic acid; Rib?, ribitol; Ser, serine; Suc, succinic acid; Tau, taurine; Thr, threonine; Val, valine; UMP?, uridine monophosphate.

The discriminatory metabolites were mostly a combination of amino acids, carbohydrates, lipids and their derivatives, reflecting the involvement of main energy producing pathways. In all brain regions, amino acids and their derivatives comprised the largest group of altered metabolites. The amino acid-associated metabolic alterations were characterised by significantly decreased levels in the KO AC and increased levels in the KO OB. In contrast, the KO BST and KO CB displayed a relatively equal number of increased and decreased levels. These appearances indicated a graded perturbation among brain regions. Alterations in the levels of amino acid-associated metabolites are commonly, yet discrepantly, observed in mitochondrial disease (Legault *et al.*, 2015; Esterhuizen *et al.*, 2017; Frazier *et al.*, 2017). Still, it is important to note that the nature of the metabolomics approaches followed in this study was biased towards detecting and identifying amino acids and their derivatives. The LC-MS/MS method was semi-targeted for amino acids, their derivatives and acylcarnitines and not for other specific carbohydrate- or lipid-related metabolites. Also, the previously developed GC-TOF method utilised in this study and the inclusion of amino acid standard mixes during analysis ensured identification of amino acids at a higher confidence level. Thus, the *Ndufs4* KO undeniably affected amino acid metabolism in all brain regions. In spite of that, it might convey a skewed picture of the global metabolic consequences of the KO.

In comparison with the WT AC, the KO AC (Figure 6.4.A) exhibited the most pronounced decreases in the levels of aspartic acid, α -amino adipic acid, asparagine, phosphoglycerol and the TCA cycle-related derivative, α -hydroxyglutaric acid. However, the strongest increases were observed in the levels of the polyamine, putrescine; followed by the pentose phosphate pathway (PPP) derivative, erythronic acid; valine and pipercolic acid. Other noteworthy changes in this region that were not directly involved in the main energy producing pathways included altered levels of creatinine, carbamic acid and uridine monophosphate.

Relative to the WT BST, the KO BST (Figure 6.4.B) displayed the highest relative decrease in the levels of α -amino adipic acid, phosphoglycerol, isovalerylcarnitine (C5-carnitine), asparagine and citrulline. The highest relative increase was observed in the levels of proline, valine, putrescine, leucine, isoleucine and 3-methylhistidine.

Compared to the WT CB, the KO CB (Figure 6.4.C) exhibited the most pronounced decreases in the levels of C5-carnitine, α -aminoadipic acid, asparagine, pyroglutamic acid, aspartic acid and serine. In contrast, the greatest increases were observed in the levels of proline, valine, leucine, erythronic acid and putrescine.

A different picture arose in the OB when KO mice were compared to WT mice (Figure 6.4.D). The most prominent decreases were observed in the levels of α -aminoadipic acid, adenosine, aspartic acid, dihydroxystearic acid and glutamic acid. The most profound increases were observed in the levels of PGe(2), glucose-6-phosphate, glucose-1-phosphate, glucose, putrescine, fructose-6-phosphate and lysine. Unlike the other brain regions, the KO OB displayed perturbations in a much greater number of carbohydrate and lipid metabolites.

The involvement of numerous metabolic pathways illustrated that the metabolic effect of the *Ndufs4* KO was widespread and complex, especially when considering that only a subset of all possible cellular metabolites was analysed. Also, of these, only metabolites that displayed altered concentrations with the highest significance were selected. This agreed with the typical nature of OXPHOS deficiencies to have extensive cellular consequences instead of localised metabolic perturbations (Reinecke *et al.*, 2012; Esterhuizen *et al.*, 2017). The results also indicated that amino acid metabolism of the brain was especially sensitive to the *Ndufs4* KO.

6.4 The *Ndufs4* knockout brain regions displayed common and distinct discriminatory metabolites

A Venn diagram was used to identify the discriminatory metabolites that were common and unique across the investigated brain regions (Figure 6.5). Of interest to this study was firstly, the metabolites commonly altered in most investigated brain regions, including the AC. This was to determine if the *Ndufs4* KO caused a general response in the brain regions. Also important to this study was the metabolites unique to either the neurodegeneration-prone brain regions or the more resilient AC, reflecting metabolic perturbations which might correlate with region-specific neurodegeneration.

The discriminatory metabolites ($n = 17$, encircled in solid red) that were common to the *Ndufs4* KO brain regions were mostly involved in amino acid metabolism and could be grouped into the metabolism of the branched-chain amino acid (BCAA), valine (valine and propionylcarnitine); lysine (α -aminoadipic acid and pipercolic acid); proline and arginine (proline, hydroxyproline, arginine, putrescine, and N-acetylglutamic acid); as well as in the metabolism of aspartic acid and glutamic acid (aspartic acid, asparagine, glutamic acid, N-acetylglutamic acid and pyroglutamic acid). A few common alterations were also identified in

other metabolic pathways closely related to the TCA cycle (α -hydroxyglutaric acid and propionylcarnitine), in carbohydrate metabolism (phosphoglycerol, ribitol and erythronic acid), in fatty acid/lipid metabolism (phosphoglycerol and propionylcarnitine) and in one-carbon (1C) metabolism (putrescine). These findings showed that the *Ndufs4* KO elicited common metabolic perturbations in the various brain regions, including the AC which was considered to be resilient against neurodegeneration.

A few discriminatory metabolites were exclusive to the neurodegeneration-prone brain regions (n =5) and in the AC (n =6), respectively. The former displayed additional alterations in amino acid- and fatty acid/lipid metabolism as evident by the alterations in the levels of other BCAAs (isoleucine and leucine) and short-chain acylcarnitines (C4- and C5-carnitines). Succinic acid was also significantly decreased in the neurodegeneration-prone brain regions, suggesting that the TCA cycle was differentially affected in these regions. The unique metabolic alterations identified in the resilient AC, on the other hand, were mostly related to 1C-metabolism and nucleotide metabolism (carbamic acid, creatinine, cysteine, methionine and uridine monophosphate). The AC also uniquely displayed changes in the levels of a methylindole of which the origin is unknown but might be related to metabolism in the digestive tract (Ma *et al.*, 2018). Due to the limited information available on the function or metabolism of this metabolite in the brain, further investigation into its role is thus warranted. The unique metabolic alterations confirmed the possibility that region-specific metabolic alterations might contribute to the regional neurodegeneration in *Ndufs4* KO mice.

The shared and unique discriminatory metabolites were evaluated in more detail within the context of their associated metabolic pathways. Figure 6.6 gives a simplified overview of the relevant metabolic pathways. The shared and distinct discriminatory metabolites are shown in red or green to indicate significantly increased or decreased concentrations, respectively. Discriminatory metabolites unique to the neurodegeneration-prone brain regions is indicated by “▲” next to the compound name. The names of the discriminatory metabolites unique to the AC were underlined for emphasis e.g. “UMP”. The relevant affected metabolic pathways were closely linked with one another, with the oxidative phosphorylation (OXPHOS) system and with the γ -glutamyl cycle (glutathione cycle) involved in antioxidant defence and amino acid transport.

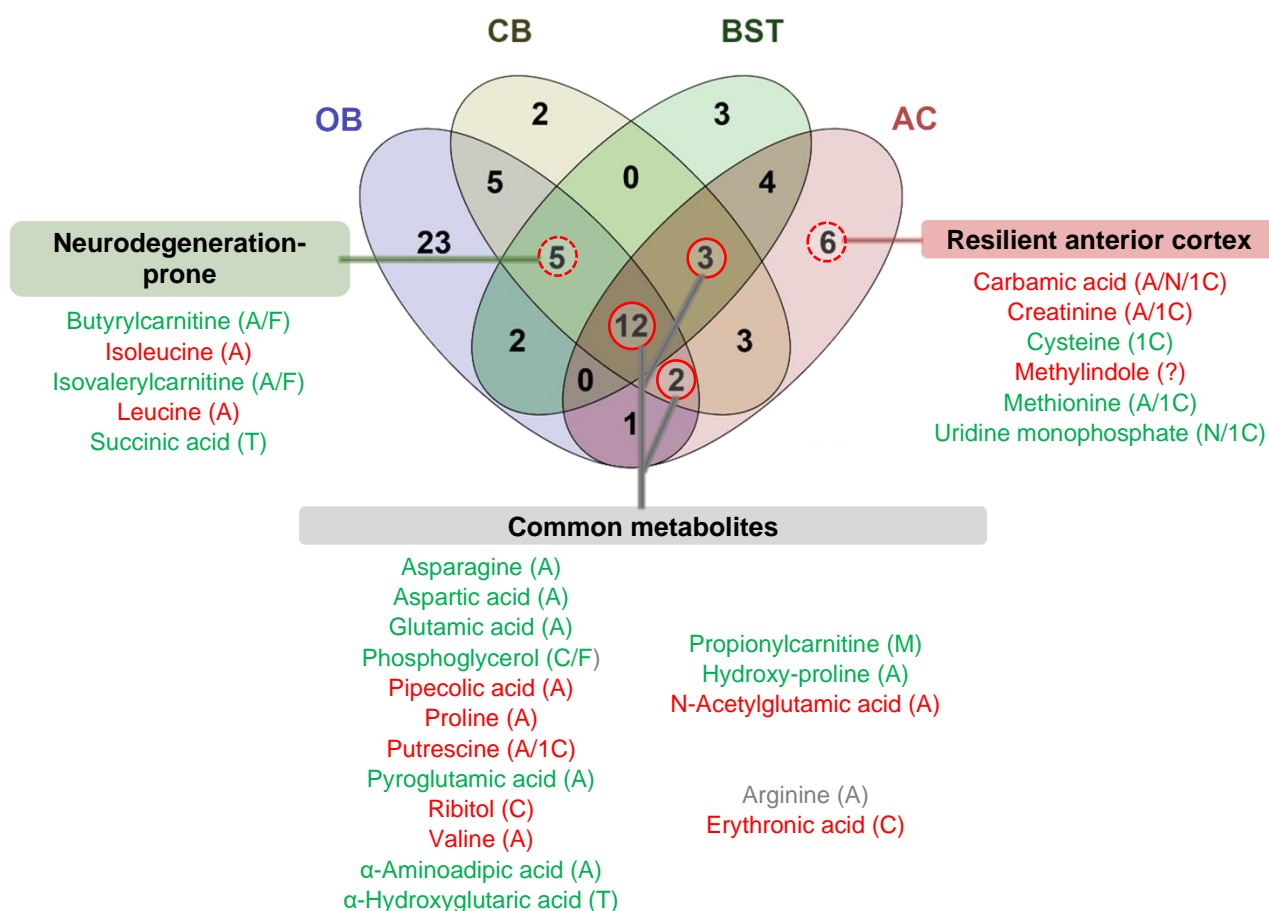


Figure 6.5: Venn diagram of discriminatory metabolites altered in the brain regions of *Ndufs4* knockout mice compared to wild-type mice.

Metabolites listed in green and red respectively indicate a significant ($p < 0.05$, $d \geq 0.8$) decrease and increase in concentration for KO vs WT mice. Metabolites listed in grey indicate that the directionality of change (decrease or increase) in concentrations differed among brain regions. The major metabolic class relevant to each metabolite is given in brackets. Metabolites common to the majority of the investigated brain regions, including the AC is encircled with solid red. The symbol “?” indicates unclear metabolic origin and role in the brain. *Abbreviations:* AC, anterior cortex; BST, brainstem; CB, cerebellum; OB, olfactory bulbs; 1C, one-carbon metabolism; A, amino acid metabolism; C, carbohydrate metabolism; F, fatty acid / lipid metabolism; M, multiple metabolic pathways; N, nucleotide metabolism; T, tricarboxylic acid cycle.

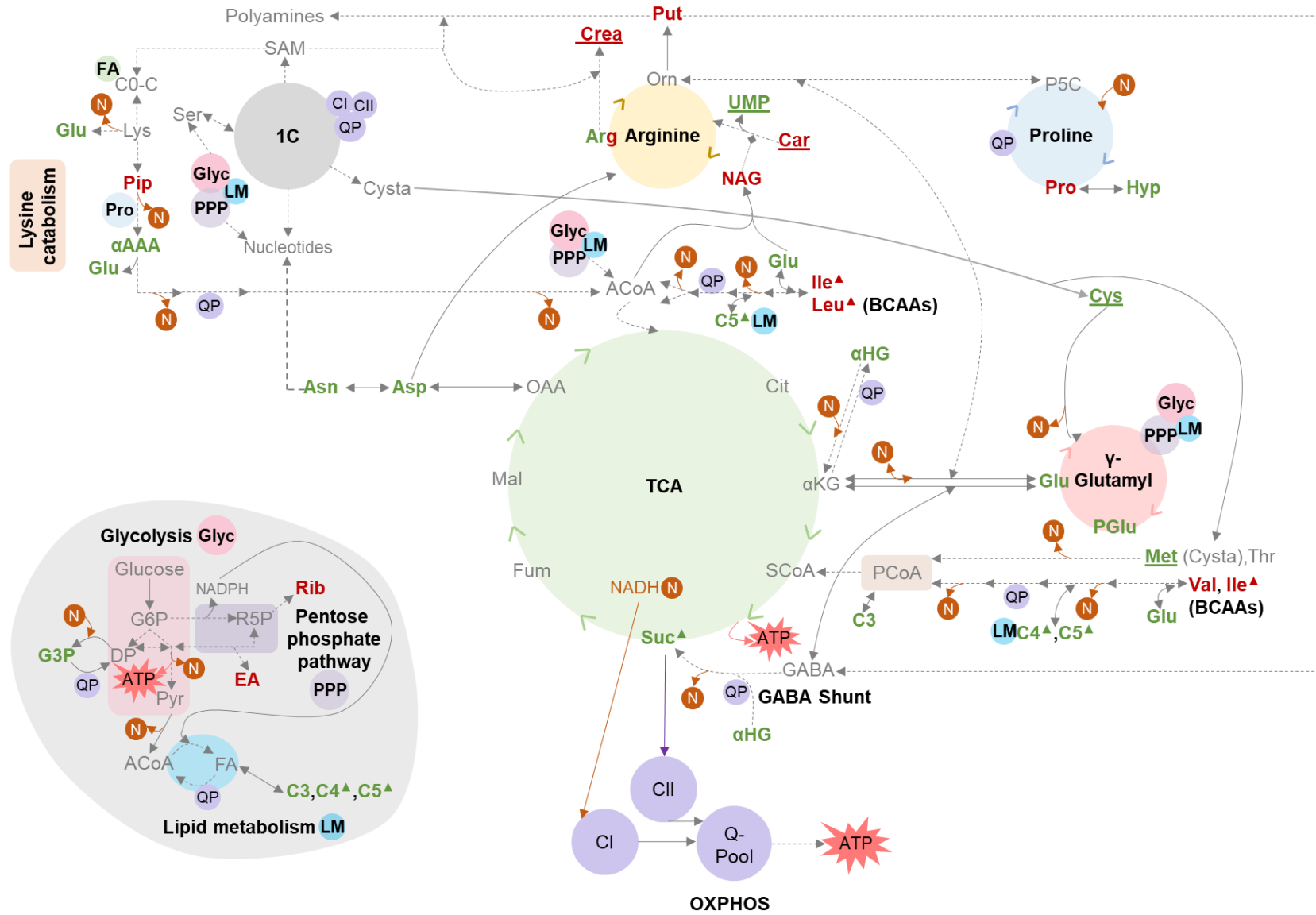


Figure 6.6: The metabolic pathways associated with the shared and distinct discriminatory metabolites identified across the brain regions of *Ndufs4* knockout mice.

Shared and distinct metabolites are shown in **red** and **green** font signifying significantly increased and decreased concentrations, respectively, when KO mice were compared to WT mice. The use of both red and green font for a metabolite name (e.g. Arg) indicates a discrepancy among the investigated brain regions with regards to an increase or decrease in concentration. Metabolites that had significantly altered concentrations in the neurodegeneration-prone brain regions but not in the resilient anterior cortex (AC) are indicated with a [▲], while metabolites with significantly altered concentrations only in the AC are underlined. **Purple**-filled circles indicate the potential destination of metabolites related to the OXPHOS system. **Orange**-filled circles indicate the reduction or oxidation of NADH. **Pink**-filled circles indicate the relation to glycolysis (Glyc), **yellow**-filled circles indicate the relation to the pentose phosphate pathway (PPP) and **blue**-filled circles the relation to lipid metabolism (LM). Dashed arrows represent multiple reaction steps. *Other abbreviations: 1C, one-carbon metabolism; α AAA, α -amino adipic acid; α HG, α -hydroxyglutaric acid; α KG, α -ketoglutaric acid; ACoA, acetyl-CoA; Arg, arginine; Asn, asparagine; Asp, aspartic acid; ATP, adenosine triphosphate; BCAAs, branched-chain amino acids; CI/II, complex I/II; C0-C, free carnitine; C3, propionylcarnitine; C4, butyrylcarnitine; C5, isovalerylcarnitine; Car, carbamic acid; Cit, citric acid; Crea, creatinine; Cys, cysteine; Cysta, cystathionine; DP, dihydroxyacetone phosphate; EA, erythronic acid; FA, fatty acids; Fume, fumaric acid; GABA, γ -aminobutyric acid; Glu, glutamic acid; G3P, glycerol-3-phosphate; G6P, glucose-6-phosphate; Glyc, glycolysis; Hyp, Hydroxyproline; Ile, isoleucine; Leu, leucine; Lys, lysine; Mal, malic acid; Met, methionine; N, NADH; NADH, reduced nicotinamide adenine dinucleotide; NADPH, nicotinamide adenine dinucleotide phosphate; NAG, N-acetylglutamic acid; OAA, oxalic acid; Orn, ornithine; OXPHOS, oxidative phosphorylation; P5C, pyrroline-5-carboxylic acid; PCoA, propionyl-CoA; PGlu, pyroglutamic acid; Pip, pipercolic acid; Pro, proline; Put, putrescine; Pyr, pyruvic acid; Q-pool/QP, quinone-pool; R5P, ribose-5-phosphate; Rib, ribitol; SAM, S-adenosylmethionine; SCoA, succinyl-CoA; Ser, serine; Suc, succinic acid; Thr, threonine; UMP, uridine monophosphate; Val, valine.*

6.4.1 Shared metabolic characteristics of the *Ndufs4* knockout brain regions

The discriminatory metabolites shared across the *Ndufs4* KO brain regions suggested a general or common metabolic response to a mitochondrial CI deficiency. It is important to remember the various functions and roles of CI: i) it operates as a major proton pumping machine that facilitates the maintenance of the mitochondrial membrane potential and the production of ATP via OXPHOS; ii) it provides electrons to the Q-pool; iii) it is a major consumer of cellular NADH; iv) it is a component of the malic acid-aspartic acid redox shuttle (MAS); and v) it is a site for generating reactive species (Sumegi & Srere, 1984; McKenna *et al.*, 2006; Leong *et al.*, 2012; Luo *et al.*, 2015; Bilan & Belousov, 2016; Nsiah-Sefaa & McKenzie, 2016; Gaude *et al.*, 2018; Sharpe & McKenzie, 2018). Accordingly, the shared discriminatory metabolites of the *Ndufs4* KO brain regions are metabolised by classic and non-classic metabolic pathways that are related to the above-mentioned functions of CI. These included the metabolic pathways that can fuel the OXPHOS system at alternative CI-bypassing sites, that can drive OXPHOS-independent ATP production, and that are closely associated with cellular redox status and antioxidant defence.

6.4.1.1 Disturbed energy homeostasis

The involvement of the main energy producing pathways (glucose-, amino acid- and lipid-catabolic pathways as well as the TCA cycle) indicated that energy homeostasis was perturbed in all *Ndufs4* KO brain regions. A clear disturbance was observed in the metabolism of amino acids that eventually catabolise toward acetyl-CoA (ACoA), as well as the TCA cycle at the level of oxaloacetic acid (OAA), α -ketoglutaric acid (α KG), succinyl-CoA (SCoA) and the CII substrate, succinic acid. Importantly, glutamic acid, which had significantly decreased levels in all KO brain regions, is utilised by the brain to supply α KG to the TCA cycle for anaplerotic and/or bio-energetic purposes during an energy deficiency in general (Karaca *et al.*, 2015; Zhang *et al.*, 2016; Divakaruni *et al.*, 2017; Hohnholt *et al.*, 2018) and in OXPHOS deficiencies (Falk *et al.*, 2008; Kiss *et al.*, 2014; Chen *et al.*, 2018b; Chinopoulos, 2018; Lozoya *et al.*, 2018). Furthermore, the altered levels of the non-classical intermediate, α -hydroxyglutaric acid (α HG), as well as the disproportionate changes in the maximal biochemical activity of citrate synthase (CS) (Section 5.2.1) and complex II (CII or succinic acid dehydrogenase) (Section 5.2.3), also supported the notion that TCA cycle metabolism was altered in the KO brain regions. Recall that maximal activity (mU/mg) of CS, the TCA cycle enzyme responsible for generating citric acid from ACoA and OAA, was significantly increased in most KO brain regions (except BST) relative to the WT brain regions, while maximal CII activity (mU/mg) for the most part (excluding CB) was not significantly altered.

Additional alterations related to proline-, arginine- and one-carbon(1C)-metabolism also supported the notion of disturbed energy metabolism. Putrescine, a proline- or arginine-derived polyamine that is also closely associated with 1C-metabolism, can fuel CII-driven ATP production via succinic acid, especially when mitochondrial NADH oxidation is impaired (Lozoya *et al.*, 2018). Moreover, N-acetyl glutamic acid (NAG) is related to the main energy metabolic pathways through its production from acetyl-CoA and glutamic acid, and by stimulating the ATP-dependent activity of carbamoyl phosphate synthetase I (CPSI) of the urea cycle (Thoden *et al.*, 2002; Caldovic & Tuchman, 2003; Mew & Caldovic, 2011). Even though the function of the urea cycle is limited in the brain due to low enzyme activity (Yudkoff *et al.*, 2005; Griffin & Bradshaw, 2017), it can become upregulated to detoxify excess nitrogen and increase polyamine synthesis when energy production is impaired (Caldovic & Tuchman, 2003; Griffin & Bradshaw, 2017; Lozoya *et al.*, 2018).

In addition to driving CII, many of the altered metabolic pathways were directly connected to the OXPHOS system through reactions that produce the CI substrate, NADH, or that could transfer electrons to the quinone(Q)-pool. Recall that electrons can be transferred directly to the Q-pool via the flavin moieties of enzymes, such as proline dehydrogenase in the proline metabolism; as well as choline dehydrogenase, dihydro-orotate dehydrogenase and sulphide-ubiquinone oxidoreductase in one-carbon metabolism (Mailloux, 2015; Lemieux *et al.*, 2017; McDonald *et al.*, 2017). This is also valid for mitochondrial glycerol-3-phosphate dehydrogenase in the glycerol-3-phosphate shuttle (GlyPS). Electrons can also be indirectly transferred to the Q-pool by enzymes that fuel the electron transfer flavoprotein (ETF)/ETF-ubiquinone oxidoreductase (ETF-QO) system, including isovaleryl-CoA dehydrogenase, isobutyryl-CoA dehydrogenase and short/branched-chain acyl-CoA dehydrogenase in branched-chain amino acid and propionyl-CoA catabolism; glutaryl-CoA dehydrogenase in lysine and tryptophan catabolism; α -hydroxyglutarate dehydrogenase which converts α HG to α KG in the mitochondrial matrix; the short-, medium-, long-chain acyl-CoA dehydrogenases in fatty acid β -oxidation; as well as dimethylglycine dehydrogenase and sarcosine dehydrogenase in 1C-metabolism (Watmough & Frerman, 2010; Rzem *et al.*, 2015; Viscomi *et al.*, 2015; McDonald *et al.*, 2017). Clearly, all of these enzymes are implicated in the altered metabolic pathways of the *Ndufs4* KO brain regions.

The affected metabolic pathways were also involved in OXPHOS-independent substrate-level phosphorylation. ATP can be produced through the TCA cycle via succinyl-CoA ligase (SCL) activity; through glucose metabolism via the activities of phosphoglycerate kinase (PGK), pyruvate kinase (PK) and phosphoenolpyruvate carboxykinase (PEPK); and through formate synthesis in the mitochondrial folate cycle of 1C-metabolism (Chinopoulos & Seyfried, 2018).

While upregulation of glycolysis to increase ATP production is considered to be a hallmark of OXPHOS-deficient cells (Smeitink *et al.*, 2006; Koenig, 2008; Clarke *et al.*, 2013; Esterhuizen *et al.*, 2017), some brain cells, particularly neurons, metabolise glucose primarily through the pentose phosphate pathway (PPP) for antioxidant defence (Magistretti & Allaman, 2015). This might suggest that the altered levels of the PPP-derived metabolites in the *Ndufs4* KO brain regions, namely erythronic acid and ribitol, may be linked with altered glycolysis. In fact, it has been shown that the accumulation of erythronic acid and ribitol may result from a bottleneck in the second, non-oxidative phase of the PPP either due to insufficient activities of PPP enzymes (Engelke *et al.*, 2010) and/or as a result of impaired glycolysis in the brain which then shunts glucose to the PPP (Xu *et al.*, 2016).

To summarise, these results suggested that the most significant discriminatory metabolites that were common to all investigated *Ndufs4* KO brain regions, are involved in the major metabolic pathways that fuel: a) the TCA cycle; b) the mitochondrial RC via CII or the Q-pool; and/or c) OXPHOS-independent ATP production via substrate-level phosphorylation.

6.4.1.2 Disturbed redox regulation and antioxidant defence

A few of the common discriminatory metabolites were involved in redox regulation and/or antioxidant defence. In brain cells, the cytosolic NAD⁺/NADH ratio is regulated by the interconversion of pyruvic acid and lactic acid by lactic acid dehydrogenase (LDH) activity as well as through the shuttling of redox equivalents to the mitochondria via the malic acid-aspartic acid redox shuttle (MAS) and glycerol-3-phosphate shuttle (GlyPS) (McKenna *et al.*, 2006). The MAS is believed to primarily occur in neurons and produces mitochondrial NADH while utilising aspartic acid and glutamic acid transport mechanisms (McKenna *et al.*, 2006; Kanunnikova, 2012). In the GlyPS, which predominates in glial cells, cytosolic NADH is utilised to produce glycerol-3-phosphate from dihydroxyacetone phosphate. (McKenna *et al.*, 2006; Kanunnikova, 2012). The former is converted back to dihydroxyacetone phosphate in the inner mitochondrial membrane via mitochondrial glycerol-3-phosphate dehydrogenase which can fuel the Q-pool. The GlyPS thus dually functions to oxidise cytosolic NADH and supply electrons to the Q-pool. Consequently, the decreased levels of aspartic acid, glutamic acid and glycerol-3-phosphate collectively suggested that the *Ndufs4* KO disturbed the regulation of the cytosolic NAD⁺/NADH ratio in all investigated brain regions.

In addition, proline metabolism becomes activated under stress conditions to not only support bio-energetics by supplying electrons to the Q-pool, but also to regulate cellular redox balance and ROS signalling (Wyse & Netto, 2011; Phang *et al.*, 2015; Phang, 2019). The unique metabolism of proline, also called the 'proline cycle', is closely related to the TCA cycle and

the urea cycle. It comprises a mitochondrial and cytosolic cycle in which proline and pyrroline-5-carboxylic acid (P5C) are interconverted through the activity of the ROS-generating, mitochondrial FAD-dependent proline dehydrogenase (PRODH); and the NAD(P)H-dependent activity of mitochondrial and/or cytosolic P5C-reductase (m/cP5CR) isozymes. While mP5CR primarily oxidises excessive mitochondrial NADH, cP5CR has a greater affinity for NADPH and can stimulate glucose metabolism via the PPP (Wyse & Netto, 2011; Zieliński *et al.*, 2016). The PPP can in turn, support antioxidant defence by producing the NADPH required to regenerate the reduced forms of antioxidants such as glutathione, produced by the γ -glutamyl cycle, and thioredoxin (Cooper & Jeitner, 2016). The altered levels of glutamic acid, pyroglutamic acid and metabolites of 1C-metabolism were also indicative of potentially disturbed antioxidant homeostasis through their close association with glutathione metabolism.

6.4.1.3 Common metabolic effect of the *Ndufs4* knockout on the investigated brain regions

The global metabolic disturbances suggested that the *Ndufs4* KO brain regions might attempt to restore cellular homeostasis in the presence of the CI deficiency through classic and non-classic metabolic pathways. Collectively, these affected metabolic pathways have the potential to compensate for the widespread cellular consequences of a CI deficiency by increasing ATP production through CI-bypassing and OXPHOS-independent reactions, and by restoring other imbalances, such as a lowered NAD⁺/NADH ratio or increased production of reactive species.

Previous reports support this notion and demonstrated or proposed the therapeutic potential of metabolic bypassing of CI in the RC via supplementation with succinic acid or succinic acid precursors (Fernandes *et al.*, 2013; Pfeffer *et al.*, 2013; Barrow *et al.*, 2016; Ehinger *et al.*, 2016), short-chain quinones or metabolites fuelling the Q-pool (Haefeli *et al.*, 2011; Barrow *et al.*, 2016) and α KG (Chen *et al.*, 2018b; Lee *et al.*, 2019). Correcting for the cellular consequences of a CI deficiency through the supplementation of antioxidants (Koopman *et al.*, 2016) or NAD⁺-precursors (Iannetti *et al.*, 2018; Lee *et al.*, 2019) have also been considered. In addition, it is not uncommon for cells with RC-complex deficiency to increase the catabolism of energy substrates (glucose, amino acids, fatty acids and/or ketone bodies) to augment the availability of substrates for the TCA cycle, OXPHOS and substrate-level phosphorylation to fuel increased ATP production (Smeitink *et al.*, 2006; Falk *et al.*, 2008; Koenig, 2008; Leong *et al.*, 2012; Kiss *et al.*, 2014; Parikh *et al.*, 2015; Bao *et al.*, 2016; Esterhuizen *et al.*, 2017; Shuvalov *et al.*, 2017; Cabirol-Pol *et al.*, 2018; Lozoya *et al.*, 2018).

6.4.2 Metabolic perturbations that correlated with region-specific neurodegeneration in *Ndufs4* knockout mice

The magnitude of the change²² (effect sizes, *d*-values) in the levels of the shared and distinct discriminatory metabolites were also compared inter-regionally. In short, it was revealed that some metabolic perturbations were completely unique to the AC, e.g. UMP. In addition, it was found that the altered levels of the majority of the shared and distinct discriminatory metabolites reflected a gradient of metabolic disturbance across the brain regions. This seemed to correlate with neurodegeneration. In other words, the metabolite levels were altered in all brain regions, but either the neurodegeneration-prone brain regions or resilient brain region were more severely affected. The following sections show and discuss these findings. The relative abundance of metabolite levels are illustrated in APPENDIX G.

6.4.2.1 BCAA catabolism was more extensively perturbed in the neurodegeneration-prone brain regions

Figure 6.7 shows the detailed BCAA catabolic pathways, the relevant intermediates and bar graphs of the magnitude of change in concentrations (effect size, *d*-values) across the various brain regions. Positive values (red bars) indicate a relative increase in metabolite levels, while effect sizes were given negative values (green bars) to indicate a relative decrease in metabolite levels. The data of a brain region was only displayed when levels between KO and WT mice differed with at least practical visible ($d \geq 0.5$) significance.

The neurodegeneration-prone brain regions displayed a significant increase in the relative abundance of all BCAAs, especially of valine (BST: $d = 1.3$ for leucine, $d = 1.5$ for isoleucine, and $d = 2.1$ for valine; CB: $d = 1.7$ for leucine, $d = 1.3$ for isoleucine, and $d = 2.3$ for valine; OB: $d = 1.7$ for leucine; $d = 1.5$ for isoleucine; and $d = 1.9$ for valine). The KO AC also exhibited a significant increase in the levels of valine ($d = 1.1$) and a tendency towards increased levels of leucine ($d = 0.4$) and isoleucine ($d = 0.7$). Thus, all investigated brain regions displayed the same tendency of increased concentrations of BCAAs with the most profound increase observed for the concentrations of valine. However, the effect of the KO on the levels of each BCAA was generally more than two-fold larger in the neurodegeneration-prone brain regions than in the AC.

²² Effect sizes or *d*-values differing ≥ 1.5 -fold when comparing brain regions were considered to indicate significant differences since different classes of effect sizes; i.e. practical visible/medium effect ($d = 0.5$) vs practical significant/large effect ($d = 0.8$) differs in magnitude of 0.3 (1.5-fold) from one another.

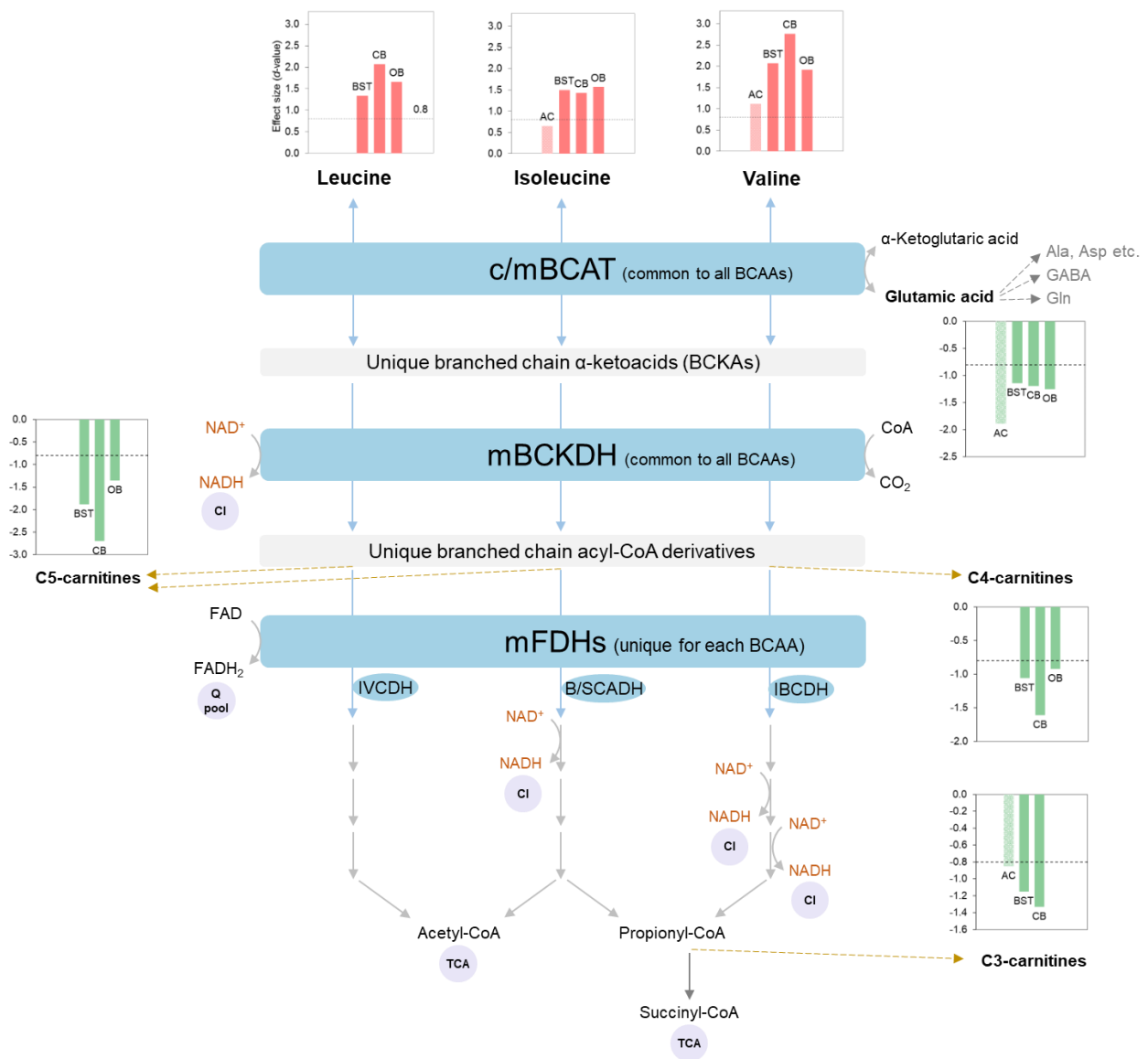


Figure 6.7: Branched-chain amino acid metabolism and related metabolomic changes in the brain regions of *Ndufs4* knockout mice.

Inserted graphs display the practical significance (Cohen's *d*-value, effect size) obtained for each metabolite given in **bold** when its relative abundance was compared between KO and WT mice in each brain region; i.e. the anterior cortex (AC), brainstem (BST), cerebellum (CB) and olfactory bulbs (OB). Data shown are only for brain regions which displayed at least a practical visible ($d \geq 0.5$) difference between metabolite levels. Positive values (red bars) indicate a relative increase in metabolite levels while negative values (green bars) were allocated to *d*-values to indicate a relative decrease. The dotted line indicates the level set for practical significance ($d \geq 0.8$). The names of relevant enzymes are given in ovals next to the reaction it catalyses. Purple-filled circles: relation to the TCA cycle and OXPHOS system. Branched-chain amino acids (BCAAs) are catabolised via a common three-step pathway (in blue) after which each BCAA follows a unique pathway. Other abbreviations: Ala, alanine; Asp, aspartic acid; BCKAs, branched-chain α -ketoacids (BCKAs); B/SCADH, branched/short-chain acyl-CoA dehydrogenase; C3-carnitines, propionyl-carnitines; C4-carnitines, butyrylcarnitines; C5-carnitines, isovalerylcarnitines; CI, complex I; CoA, coenzyme-A; GABA, gamma-aminobutyric acid; Gln, glutamine; Glu, glutamic acid; IBCDH, isobutyryl-CoA dehydrogenase; IVCDH, isovaleryl-CoA dehydrogenase; mBCKDH, mitochondrial branched-chain α -ketoacid dehydrogenase complex; m/cBCAT, mitochondrial or cytosolic branched-chain aminotransferase; m-FDHs, mitochondrial flavoprotein dehydrogenases; Q-pool, quinone-pool.

As shown in Figure 6.7, the levels of a few BCAA catabolic by-products (glutamic acid, propionyl(C3)-, butyryl(C4)- and isovaleryl(C5)-carnitine) were also decreased in some of the KO brain regions. The relative decrease in the levels of glutamic acid and C3-carnitines are discussed in Section 6.4.2.4 and Section 6.4.2.5, respectively, as these metabolites are products and branch points of numerous converging metabolic pathways. Conversely, C4- and C5-carnitines (a collection of isomers) are derived from BCAA catabolism or fatty acid metabolism (Arany & Neinast, 2018). Therefore, they are more exclusive to and reflective of the alterations in BCAA catabolism, especially considering that fatty acid oxidation is limited in the brain (Panov *et al.*, 2014; Dienel, 2018). Short-chain acylcarnitines are formed by the condensation of acyl-CoA derivatives with free carnitine (C0-carnitine) and are usually in equilibrium with the acyl-CoA derivatives (Arany & Neinast, 2018).

Inter-regional comparison of these metabolites showed that in addition to the significantly decreased levels of C4- and C5-carnitines previously noted in the neurodegeneration-prone brain regions (BST: $d=1.1$ for C4 and $d=1.9$ for C5; CB: $d=1.6$ for C4 and $d=2.7$ for C5; OB: $d=0.9$ for C4 and $d=1.4$ for C5), a tendency towards decreased levels was also observed in the resilient AC ($d=0.4$ for C4 and $d=0.5$ for C5). Thus, while all brain regions displayed the same tendency of decreased concentrations of BCAA-catabolic by-products, the effect was more than two-fold larger in the neurodegeneration-prone brain regions, in accordance with the perturbations in BCAA levels.

It was interesting that the KO had the most significant effect on the concentrations of C5-carnitines, and not C4-carnitines, as the latter is related to the catabolism of valine, the BCAA whose levels were most perturbed in the KO brain regions (Figure 6.7). This phenomenon might be attributed to the combined effects of the perturbed catabolism of leucine and isoleucine which are both sources of C5-carnitines, but not C4-carnitines. Nevertheless, this combination of accumulated BCAAs and decreased levels of BCAA catabolic by-products suggested a perturbation in BCAA catabolism. This perturbation seemed to reflect a bottleneck effect at or upstream of the second reaction catalysed by the mitochondrial branched-chain α -ketoacid dehydrogenase complex (mBCKDH). The fact that the perturbation in BCAA catabolism was of a similar nature between the neurodegeneration-prone brain regions and resilient AC, but more pronounced in the former, suggested that the *Ndufs4* KO caused graded perturbations in BCAA catabolism across the various brain regions. The severity of the perturbations seemed to correlate with neurodegeneration.

Regarding the nature or cause of the metabolic perturbations, the evidence strongly suggested that a disturbance in redox balance might play a major role, in accordance with the global metabolic disturbances conveyed by the KO brain regions (Section 6.4.1.2). CI is known as the major consumer of cellular NADH and its dysfunction generally results in a lowered NAD⁺/NADH ratio in affected tissues. The mBCKDH-catalysed reaction is an irreversible, rate-controlling step that requires NAD⁺ and which could greatly perturb BCAA catabolism when impaired (Cole *et al.*, 2012; Lynch & Adams, 2014; Esterhuizen *et al.*, 2017). In fact, a genetic deficiency in this enzyme causes maple syrup urine disease (MSUD, OMIM #248600) which is characterised by metabolic perturbations in the brain similar to those observed in the KO mouse brain regions (Yudkoff *et al.*, 2005; Yudkoff, 2017).

In MSUD, the insufficient decarboxylation of branched-chain keto acids (BCKAs) leads to a decreased formation of the downstream acyl-CoA products and presumably their acylcarnitine derivatives. The accumulation of BCKAs causes a shift in the equilibrium of the reaction catalysed by mitochondrial or cytosolic branched-chain aminotransferase (m/cBCAT) isozymes so that BCAAs accumulate due to their regeneration from the cognate BCKAs and glutamic acid (Bifari & Nisoli, 2017; Yudkoff, 2017; Arany & Neinast, 2018). This, by implication, impairs glutamic acid biosynthesis in the brain, which is greatly dependent on BCAAs as sources of amino groups, and could cause a secondary depletion in aspartic acid levels (Yudkoff *et al.*, 2005; Kanunnikova, 2012). Furthermore, a lowered NAD⁺/NADH ratio in the KO brain regions would not only impair mBCKDH, but also other NAD⁺-dependent dehydrogenases in BCAA catabolism. The catabolic pathway of valine that contains the most NAD⁺-dependent reactions would be most sensitive, which is consistent with the metabolic findings in the KO brain regions. All together the results suggested a disturbance in the NAD⁺/NADH ratio that manifested more in the neurodegeneration-prone brain regions. The accumulation of BCAAs due to a decreased NAD⁺/NADH ratio is in line with mitochondrial disease studies, especially CI deficiencies (Falk *et al.*, 2008; Clarke *et al.*, 2013; Vergano *et al.*, 2014; Esterhuizen *et al.*, 2017; Lozoya *et al.*, 2018).

It is, however, plausible that the perturbed BCAA metabolic profile could additionally or alternatively result from a deficit in m/cBCAT transamination reactions, perhaps due to insufficient levels of α -ketoglutaric acid or pyridoxal phosphate. The latter is a cofactor in all transamination reactions which requires energy for activation, and which might be impeded by the lack of energy in CI-deficient cells (Wilson *et al.*, 2019). However, this hypothesis did not correlate with the more dramatic perturbations in valine metabolism or the absence of dramatic changes in the levels of many other amino acids in the investigated brain regions. Furthermore, the metabolic profiles of the *Ndufs4* KO brain regions also indicated that the

elevated levels of BCAAs did not result from their increased transport into the brain. Increased plasma concentrations of BCAAs, as in MSUD, or increased activity or expression of the large neutral amino acid transporter 1 (LAT1), can result in elevated brain BCAAs since BCAAs are nutritionally essential and indispensable for the brain (Manoli & Venditti, 2016; Bifari & Nisoli, 2017). However, the relative concentrations of most large neutral amino acids, which compete for LAT1 transport, were unaltered in most KO brain regions, including histidine, phenylalanine, tryptophan and tyrosine (Bifari & Nisoli, 2017). Furthermore, the transport system generally has a much greater affinity for leucine (Yudkoff, 2017), while valine levels were most dramatically increased in all investigated KO brain regions.

In summary, the metabolic findings of the *Ndufs4* KO brain regions indicated graded perturbations in BCAA-related intermediates across brain regions, being more pronounced in the neurodegeneration-prone brain regions than in the resilient AC. Furthermore, it is most likely that a decreased NAD^+/NADH ratio caused these perturbations. This also suggested that the redox balance was more dramatically affected in the neurodegeneration-prone brain regions and that BCAAs might be considered as markers for perturbed redox balance.

6.4.2.2 Lysine catabolism was strongly perturbed in the OB

Lysine is a nutritional-essential amino acid which is catabolised via either the pipecolic acid pathway or saccharopine pathway as depicted in Figure 6.8 (Hallen *et al.*, 2013; Rzem *et al.*, 2015). Both these pathways converge in the synthesis of aminoadipate semialdehyde (AASA). AASA is then oxidised to α -aminoadipic acid and eventually to acetyl-CoA. In the mature brain, lysine is mainly degraded via the pipecolic acid pathway which is also the major source of pipecolic acid as the latter is poorly transported into the brain (Hallen *et al.*, 2013; Posset *et al.*, 2015). However, the saccharopine pathway contributes significantly to the levels of AASA and α -aminoadipic acid in the brain (Pena *et al.*, 2017). The fact that all KO brain regions exhibited significantly increased levels of pipecolic acid ($d=0.9$ for AC, $d=1.0$ for BST, $d=0.8$ for CB and $d=1.8$ for OB) and decreased levels of α -aminoadipic acid ($d=1.7$ for AC, $d=1.6$ for BST, $d=1.9$ for CB and $d=3.2$ for OB) suggested a common perturbation in lysine metabolism regardless of brain region.

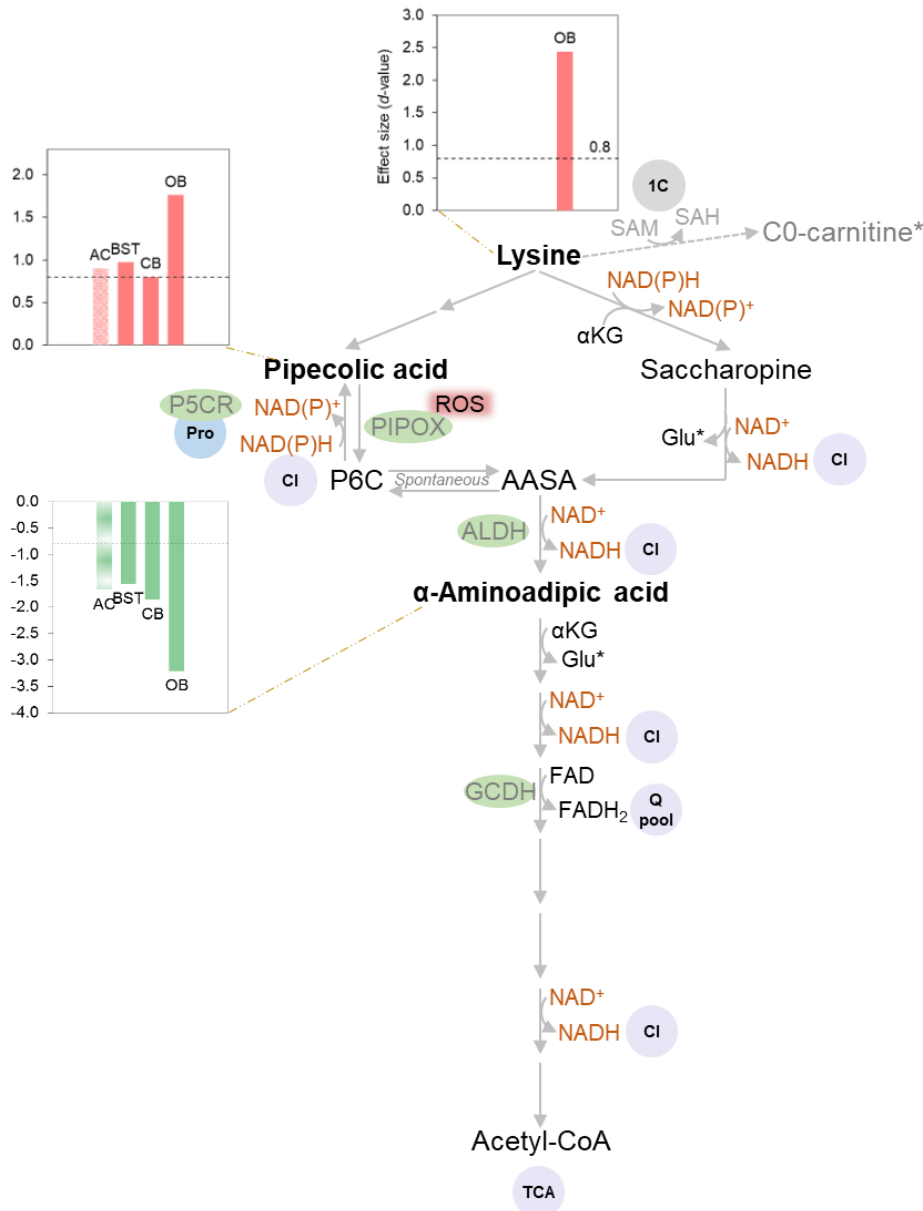


Figure 6.8: Lysine metabolism and related metabolomics changes in the brain regions of *Ndufs4* knockout mice.

Refer to Figure 6.7 for detail on *inserted graphs*. The names of relevant enzymes are given in ovals next to the reaction it catalyses. Purple-filled circles: relation the TCA cycle and OXPHOS system. Grey-filled circle: relation to one-carbon (1C) metabolism. Blue-filled circle: relation to proline (Pro) metabolism. Dashed arrows represent multiple reaction steps. *Compound also affected in some/all KO brain regions, but results are discussed elsewhere (Section 6.4.2.7 and Section 6.4.2.8). Lysine is metabolised via either the pipepicolic acid pathway (top left) or the saccharopine pathway (top right) or can be used to synthesise free carnitine (C0-carnitine) required for fatty acid oxidation after its methylation using SAM (made from methionine in one-carbon (1C) metabolism). *Other abbreviations:* AASA, α -aminoadipic semialdehyde; ALDH, α -aminoadipic semialdehyde dehydrogenase; Cl, complex I; FAD/FADH₂, oxidised/reduced form of flavin adenine dinucleotide; GCDH, glutaryl-CoA dehydrogenase; Glu, glutamic acid; α KG, α -ketoglutarate; P5CR, pyrroline-5-carboxylate reductase; P6C, piperidine-6-carboxylate; PIPOX, pipepicolic acid oxidase; Q-pool, quinone pool; ROS, reactive oxygen species; SAH, S-adenosylhomocysteine; SAM, S-adenosylmethionine; NAD⁺/NADH, oxidised/reduced form of nicotinamide adenine dinucleotide; NADP⁺/NADPH, oxidised/reduced form of nicotinamide adenine dinucleotide phosphate.

This perturbation was characterised by a “block” downstream of pipercolic acid and upstream of α -aminoadipic acid. These perturbations corresponded with the effect of a decreased NAD⁺/NADH ratio (Figure 6.8 in orange) which is expected to impair the saccharopine pathway, the metabolism of AASA (formed from saccharopine and/or pipercolic acid) to α -aminoadipic acid and perhaps favour the formation of pipercolic acid from pyrroline-6-carboxylic acid (P6C). Interestingly, in the BCAA- (Section 6.4.2.1) and lysine-catabolic pathways, the accumulated amino acids (or amino acid derivatives) were followed by: 1) at least one irreversible NAD⁺-dependent reaction that cannot be bypassed by alternative metabolic pathways; and 2) at least one downstream Q-pool-reducing reaction. Proline, on the other hand, is produced by an NADH-oxidising reaction and catabolised through a Q-pool-reducing reaction (Section 6.4.2.3). Conversely, the metabolic pathways of amino acids with decreased or unaltered levels either had no NAD⁺-dependent or Q-pool-reducing step, or had bypassing pathways (Esterhuizen *et al.*, 2018).

While the magnitude of the lysine-related perturbations was similar among the AC, BST and CB, the effect was nearly two-fold greater in the OB. The OB additionally displayed a significant accumulation of lysine ($d=2.4$) which did not tend to occur in other brain regions. This phenomenon supported the notion of a graded perturbation across the brain regions of *Ndufs4* KO mice. In this case, it might have occurred beyond a region-specific threshold for lysine catabolism in the OB, causing more pronounced metabolic perturbations. Considering that the OB is one of the first and most affected brain regions in *Ndufs4* KO mice, the perturbation in lysine catabolism could potentially correlate with the severity of neurodegeneration and/or perturbed redox balance.

6.4.2.3 Proline metabolism was less perturbed and arginine metabolism uniquely altered in the resilient AC

Figure 6.9 depicts the magnitude of the relative changes in concentrations of proline- and arginine-related intermediates in the investigated brain regions of the *Ndufs4* KO mice, together with the relevant metabolic pathways. Recall that proline metabolism entails a unique mitochondrial and cytosolic cycle (Figure 6.9, bottom right). The increase in the levels of proline in the KO BST ($d=2.8$), KO CB ($d=2.4$) and KO OB ($d=1.6$) was more than two-fold higher than in the KO AC ($d=0.8$). The levels of hydroxy-proline, a post-translational, hydroxylated derivative and precursor of proline that is liberated from collagen under stress conditions (Phang *et al.*, 2015), were similarly decreased among brain regions ($d=1.7$ for AC, $d=1.5$ for BST and $d=1.8$ for CB), with the exception of the OB ($d=0.7$) in which hydroxy-proline levels only tended to be decreased.

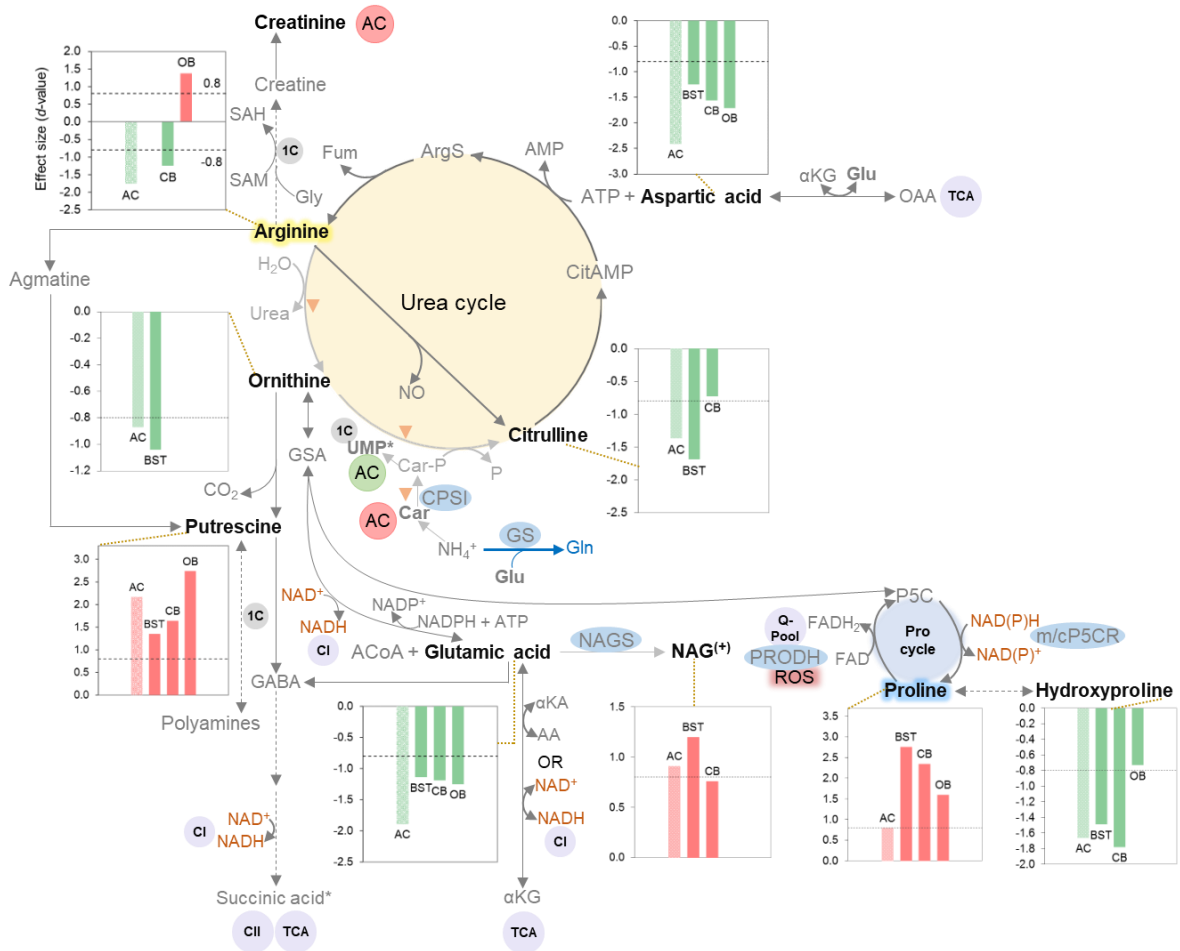


Figure 6.9: Arginine and proline metabolism and related metabolomics changes in the brain regions of *Ndufs4* knockout mice.

Refer to Figure 6.7 for detail on *inserted graphs*. Names of relevant enzymes are given in ovals next to relevant reactions. Purple-filled circles: indicate relation to the TCA cycle and OXPPOS system. Grey-filled circles: relation to one-carbon (1C). Red- and green-filled circles respectively indicate a significant increase or decrease in the concentration of compounds in **bold** which were uniquely altered in the KO anterior cortex (AC). Urea cycle (yellow-filled circle), proline (Pro) cycle (blue-filled circle), 1C-metabolism (grey filled circles) and glutamine (Gln) synthesis (blue arrows). The low activity of urea cycle enzymes in the brain is indicated with “▼”. Dashed arrows represent multiple reaction steps. *Compound also affected in some/all KO brain regions, but results are discussed in Section 6.4.2.8. Arginine (Arg) can be metabolised either into urea and ornithine (Orn), into nitric oxide (NO) and citrulline (Cit), into agmatine and/or into creatine. The polyamine putrescine (Put) can be produced from Orn and agmatine and N-acetylglutamic acid (NAG) can stimulate Arg metabolism via the urea cycle. In the proline cycle, Pro and P5C are interconverted through the activity of FAD-dependent proline dehydrogenase/ oxidase (PRODH/POX) and mitochondrial P5C reductase (P5CR). *Other abbreviations*: AC, anterior cortex; BST, brainstem; CB, cerebellum; OB, olfactory bulbs; α KG, α -ketoglutarate, α KA, α -ketoacid; AA, amino acid; ACoA, acetyl-CoA; AMP, adenosine monophosphate; ArgS, argininosuccinate; ATP, adenosine triphosphate; CI/II, complex I/II; Car, carbamic acid; Car-P, carbamoyl-phosphate; citAMP, citrullyl-AMP; CO₂, carbon dioxide; FAD/FADH₂, oxidised/reduced form of flavin adenine dinucleotide; Fum, fumarate; GABA, γ -aminobutyric acid; Gln, glutamine; Glu, glutamic acid; GSA, glutamyl-gamma-semialdehyde; H₂O, water; NAD⁺/NADH, oxidised/reduced form of nicotinamide adenine dinucleotide; NADP⁺/NADPH, oxidised/reduced form of nicotinamide adenine dinucleotide phosphate; NAGS, NAG-synthase; NH₄⁺, ammonium; NO, nitric oxide; OAA, oxaloacetate; P, phosphate; P5C, pyrroline-5-carboxylic acid; P5CR, pyrroline-5-carboxylate reductase; Q-pool, quinone pool; ROS, reactive oxygen species; SAH, S-adenosylhomocysteine; SAM, S-adenosylmethionine; UMP, uridine monophosphate.

Arginine is a precursor for various bio-active molecules produced by the activity of cytosolic and mitochondrial enzymes, including those associated with the urea cycle (Jing *et al.*, 2013; Gonzalez-Riano *et al.*, 2017). The concentrations of arginine (Figure 6.9, top left) were slightly (>1.3-fold) more affected in the KO AC when compared to the KO BST, KO CB and KO OB. Then again, the directionality of change differed among the brain regions. Arginine levels were decreased in the KO AC ($d=1.8$) and KO CB ($d=1.3$), unaltered in the KO BST and increased in the KO OB ($d=1.4$). The levels of putrescine were significantly increased in all brain regions ($d=2.2$ for AC, $d=1.4$ for BST, $d=1.3$ for CB and $d=2.7$ for OB), especially the OB, but did not clearly differentiate the more resilient AC. Furthermore, the significantly increased concentrations in NAG, the co-factor that stimulates the urea cycle via carbamoyl phosphate synthetase I (CPSI) activity, were similar among all brain regions, except for the OB which did not display a tendency towards altered levels ($d=1.0$ for AC, $d=1.2$ for BST and $d=0.8$ for CB).

The perturbations in proline- and arginine-metabolism in the KO brain regions were also substantiated by disturbances in the levels of other closely-related metabolic intermediates. One of the pathways leading to arginine synthesis also requires aspartic acid. However, the levels of aspartic acid was significantly decreased in all the investigated KO brain regions, especially in the AC (see also Section 6.4.2.4). Ornithine concentrations were found to be significantly decreased in the KO AC ($d=0.9$) and KO BST ($d=1.0$), but no conclusions about ornithine concentrations in the CB could be made due to its removal from the data set during data filtering. The levels of citrulline were also significantly decreased in the KO AC ($d=1.4$) and KO BST ($d=1.7$) with a tendency towards decreased levels observed in the KO CB ($d=0.7$). The latter might have important therapeutic considerations. For instance, citrulline supplementation has previously been considered as treatment for the stroke-like episodes in mitochondrial disease patients with MELAS (Jing *et al.*, 2013; El-Hattab *et al.*, 2017) and might have potential for treating related symptoms in *Ndufs4* KO mice (Quintana *et al.*, 2010).

The significantly increased concentrations of the CPSI substrate, carbamic acid ($d=0.8$) and of the downstream arginine-derivative, creatinine ($d=0.8$), in the KO AC were not observed in the neurodegeneration-prone brain regions. Creatinine is generated from the spontaneous, irreversible, non-enzymatic degradation of creatine and creatine phosphate. The latter had been suggested to play a role in maintaining energy homeostasis in the brain (Wyss & Kaddurah-Daouk, 2000; Allen, 2012; Hanna-El-Daher & Braissant, 2016; Gonzalez-Riano *et al.*, 2017). These perturbations suggested that arginine metabolism might be differentially affected in the AC.

Collectively, the findings supported the notion of graded metabolic perturbations across the investigated brain regions. Proline metabolism was more pronouncedly affected in the neurodegeneration-prone brain regions, suggesting a greater disturbance in energy-, redox- and/or antioxidant-homeostasis. Furthermore, the arginine-related metabolic alterations in especially the KO AC and KO OB seemed to imply that regional differences in arginine metabolism might also play a role in region-specific neurodegeneration. In addition, the metabolic perturbations in the OB of *Ndufs4* KO mice might occur beyond a region-specific threshold for arginine-related metabolism, causing a differential metabolic picture. Finally, the metabolic perturbations observed in arginine metabolism should be explored in future studies as targets for therapeutic interventions.

6.4.2.4 Aspartic acid and glutamic acid metabolism were less perturbed, and glutathione metabolism more perturbed in the neurodegeneration-prone brain regions

Both aspartic acid and glutamic acid are non-essential amino acids that are poorly transported across the blood-brain barrier. Nevertheless, they are found in high concentrations in the brain where they are endogenously synthesised and function as metabolic intermediates and excitatory neurotransmitters (Cooper & Jeitner, 2016; Griffin & Bradshaw, 2017). Both also partake in transamination reactions and can be directly interconverted with one another as well as with the TCA cycle intermediates, oxaloacetate (OAA) and α -ketoglutaric acid (α KG), respectively. Asparagine is a direct product and precursor of aspartic acid, while pyroglutamic acid is a cyclised derivative and immediate precursor of glutamic acid in the γ -glutamyl cycle. The latter produces glutathione, the main antioxidant of the brain. Figure 6.10 depicts the metabolic pathways of aspartic acid and glutamic acid (indicated with blue highlight and font in bold), along with closely related intermediates and the magnitude of the relative change in concentrations when KO mice were compared with WT mice.

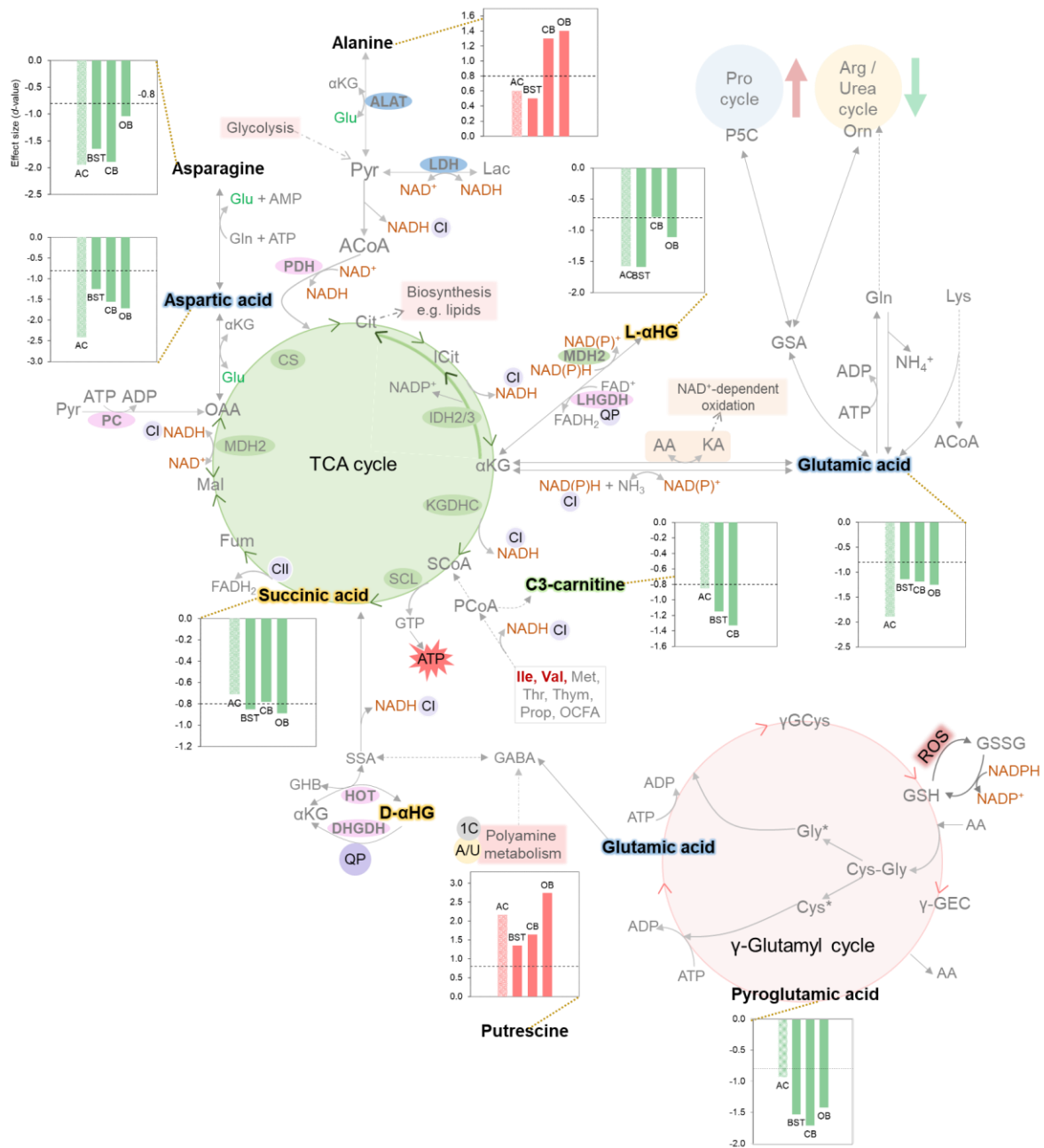


Figure 6.10: Aspartic acid and glutamic acid metabolism and related metabolomics changes in the brain regions of *Ndufs4* knockout mice.

Refer to Figure 6.7 for detail on *inserted graphs*. The names of relevant enzymes are given in ovals next to relevant reactions. Purple-filled circles: relation to the OXPHOS system. Grey-filled circles: relation to one-carbon (1C). Yellow filled circles: relation to arginine/urea (A/U) metabolism. Proline (Pro) cycle (blue-filled circle), γ -glutamyl cycle (light pink-filled circle) and TCA cycle (green-filled circle). Dashed arrows represent multiple reaction steps. *Compounds also affected in some/all KO brain regions, but results are discussed in Section 6.4.2.8. Metabolism of aspartic acid (Asp) and glutamic acid (Glu) is closely associated with transamination reactions, the TCA cycle as well as arginine (Arg) / ornithine (Orn), proline (Pro), Lys and asparagine (Asn) metabolism. Glu, together with pyroglutamic acid/5-oxoproline (PGlu), are involved in the metabolism of the potent antioxidant glutathione (GSH) in the γ -glutamyl cycle. Reductive (anti-clockwise) flux through the TCA cycle is possible via the conversion of α -ketoglutarate (α KG) to isocitrate (ICit) and citrate (Cit). *Other abbreviations:* α KA, α -ketoacid; AA, amino acid; ACoA, acetyl-CoA; C3-carnitine, propionylcarnitine; Cys, cysteine; Fum, fumarate; GABA, γ -aminobutyric acid; γ GEC, γ -glutamyl enzyme complex; γ G-Cys, γ -glutamylcysteine;

Gln, glutamine; *GHB*, γ -hydroxybutyric acid; *Gly*, glycine; *GSA*, glutamyl-gamma-semialdehyde; *GSH/GSSH*, reduced/oxidised form of glutathione; *GTP*, guanosine triphosphate; *L/DHGDH*, L- or D- α -hydroxyglutaric acid dehydrogenase; *HOT*, hydroxyacid-oxoacid transhydrogenase; *IDH2*, NADP⁺-dependent mitochondrial isocitrate dehydrogenase; *IDH3*, NAD⁺ dependent mitochondrial isocitrate dehydrogenase; *Ile*, isoleucine; *KGDHC*, α -ketoglutarate dehydrogenase complex; *Leu*, leucine; *MDH2*, mitochondrial malate dehydrogenase; *Met*, methionine; *NH₃⁺*, ammonia; *NH₄⁺*, ammonium; *OAA*, oxaloacetate; *OCFA*, odd-chain fatty acids; *P5C*, pyrroline-5-carboxylic acid; *PC*, pyruvate carboxylase; *PCoA*, propionyl CoA; *Prop*, propionic acid; *QP*, quinone pool; *SCL*, succinyl-CoA ligase; *SCoA*, succinyl-CoA; *SSA*, succinic semialdehyde; *Thr*, threonine; *Thym*, thymine.

All brain regions displayed significantly decreased levels in asparagine ($d=1.9$ for AC, $d=1.7$ for BST, $d=1.9$ for CB and $d=1.0$ for OB), aspartic acid ($d=2.4$ for AC, $d=1.3$ for BST, $d=1.6$ for CB and $d=1.7$ for OB), glutamic acid ($d=1.9$ for AC, $d=1.1$ for BST, $d=1.2$ for CB and $d=1.3$ for OB) and pyroglutamic acid ($d=0.9$ for AC, $d=1.5$ for BST, $d=1.7$ for CB and $d=1.4$ for OB). The KO AC had the greatest decrease in the levels of aspartic acid (>1.4-fold) and glutamic acid (>1.5-fold). It also had the least affected levels of pyroglutamic acid by 1.6-fold. In contrast, the perturbations were generally similar among the KO BST, KO CB and KO OB.

Once again, these findings supported the notion of graded perturbations in the metabolic profiles across the *Ndufs4* KO brain regions. The regional vulnerability to neurodegeneration might be correlated with the degree of change in pyroglutamic acid levels and inversely correlated with the degree of alterations in aspartic acid and glutamic acid levels. The former might indicate a greater disturbance in glutathione metabolism and thus in the antioxidant status of the neurodegeneration-prone brain regions. Yet, the latter might indicate less efficient utilisation of aspartic acid- and glutamic acid-related intermediates within the TCA cycle for bio-energetic and anaplerotic or “filling up” purposes. This in turn, corresponded with a more perturbed redox balance in the neurodegeneration-prone brain regions, since the TCA cycle and catabolism of glutamic acid to α KG by glutamic acid dehydrogenase is NAD⁺-dependent. Additionally, these alterations might also indicate more efficient redox-shuttling in the AC due to the involvement of aspartic acid and glutamic acid transport in the MAS.

It is noteworthy to mention that while the alterations in the levels of aspartic acid and glutamic acid in the *Ndufs4* KO brain regions could also be related to the disturbances in amino acid transamination, the metabolic findings indicated additional contributing factors. The more resilient AC, which had the most significant decrease in aspartic acid and glutamic acid levels, also displayed the least dramatic perturbations in the amino acids involved in glutamic acid-linked transamination (isoleucine, leucine, valine and alanine) and for that matter in the perturbation of other glutamic acid-related metabolites (lysine, proline, N-acetylglutamic acid and pyroglutamic acid). The relative abundance of these amino acids was also not uniquely different in the WT AC compared to the other investigated WT brain regions (APPENDIX G).

6.4.2.5 The provision of TCA cycle-related intermediates was more pronouncedly affected in the neurodegeneration-prone brain regions

In addition to the perturbations observed in the metabolism of amino acids supplying the TCA cycle, the altered levels of propionyl(C3)-carnitine, succinic acid and α -hydroxyglutaric acid may suggest a disturbance in the TCA cycle of the *Ndufs4* KO brain regions. The TCA cycle, along with closely related metabolic pathways and the magnitude of the relative change in concentrations of the relevant intermediates (indicated with a yellow highlight and font in bold), are shown in Figure 6.10. C3-carnitine is derived from propionyl-CoA, a precursor of succinyl-CoA, while succinic acid is simultaneously a TCA cycle intermediate and mitochondrial complex II (CII) substrate. α -Hydroxyglutaric acid (α HG) on the other hand, exists in two enantiomeric forms (L and D) in eukaryotes of which the metabolic origins and fates are not entirely clear. Nevertheless, both have been shown to be generated from and reconverted to the TCA cycle intermediate α -ketoglutaric acid (α KG) and to be linked with the Q-pool of the respiratory chain (Rzem *et al.*, 2007; Engqvist *et al.*, 2014; Rzem *et al.*, 2015; Ravasz *et al.*, 2017). In addition, D- α HG is also a precursor of succinic semialdehyde (SSA) and ultimately of succinic acid.

Comparison of the magnitude of the perturbations among brain regions revealed that the alterations in C3-carnitine levels were more pronouncedly affected in the BST ($d=1.2$) and CB ($d=1.3$) than in the resilient AC ($d=0.9$), with no tendency towards altered levels observed in the OB. On the other hand, succinic acid levels were similarly decreased in all investigated KO brain regions ($d=0.7$ for AC, $d=0.9$ for BST, $d=0.8$ for CB and $d=0.9$ for OB). Furthermore, the significantly decreased levels of α HG in the investigated brain regions did not correlate with neurodegeneration ($d = 1.6$ for AC; $d = 1.6$ for BST; $d = 0.8$ for CB; and $d = 1.1$ for OB).

As a result, the *Ndufs4* KO brain regions displayed graded perturbations in C3-carnitine levels that suggested a greater disturbance in the supply of propionyl-CoA to the TCA cycle in the majority of neurodegeneration-prone brain regions. In addition, the findings supported a differential metabolic profile in the OB of *Ndufs4* KO mice. Finally, the metabolomics data seemed to indicate that the *Ndufs4* KO generally caused a decrease in the levels of closely linked TCA cycle-fuelling metabolites. This phenomenon might be related to an alteration in the metabolic pathways supplying intermediates to the TCA cycle and/or in the metabolism of compounds within the TCA cycle itself.

6.4.2.6 Carbohydrate-related metabolism was more perturbed in the neurodegeneration-prone brain regions

Erythronic acid and ribitol are derived from the pentose phosphate pathway (PPP) by an unclear mechanism (Engelke *et al.*, 2010; Xu *et al.*, 2016). Bear in mind that the PPP is closely linked to energy-, redox-, and antioxidant homeostasis. On the other hand, glycerol-3-phosphate can be produced from the glycolysis intermediate, dihydroxyacetone phosphate (DHAP), via the NADH-dependent reaction catalysed by cytosolic glycerol-3-phosphate dehydrogenase (cGDH) of the GlyPS. Figure 6.11 shows the relevant carbohydrate-related metabolic pathways and the inter-regional comparison of the magnitude of the effect of the KO on the relative abundance of the associated intermediates. Of note, erythronic acid was not reliably detected in the KO BST and was excluded from the final data set. The significantly increased levels of erythronic acid ($d=1.5$ for AC, $d=2.1$ for CB and $d=1.3$ for OB) in the KO brain regions did not correlate with neurodegeneration. Alternatively, the dramatic increase in ribitol in all investigated brain regions ($d=0.8$ for AC, $d=1.3$ for BST, $d=1.4$ for CB and $d=1.0$ for the OB) was more profound (>1.3 -fold) in the neurodegeneration-prone brain regions. The decrease in the levels of glycerol-3-phosphate in the investigated brain regions ($d=2.1$ for AC, $d=1.9$ for BST, $d=1.4$ for CB and $d=0.9$ for OB) was more dramatic (>1.5 -fold) in the KO AC than in the KO CB and KO OB, but only slightly more (1.1-fold) than in the KO BST.

Even though other carbohydrate metabolism-related compounds such as pyruvic acid, lactic acid and alanine were not identified as important distinct or shared discriminatory metabolites, their frequent involvement or accumulation in mitochondrial disease (Esterhuizen *et al.*, 2017) warranted a more in-depth evaluation. Pyruvic acid is the end-product of glycolysis. It links the main energy producing pathways; i.e. glycolysis, the TCA cycle and OXPHOS system. Its accumulation exacerbates its conversion to lactic acid and alanine by shifting the equilibrium of the reactions catalysed respectively by lactic acid dehydrogenase (LDH) and alanine aminotransferase (ALAT). Moreover, LDH is also stimulated to regenerate the NAD^+ required to support ongoing glycolysis when the cytosolic NAD^+/NADH ratio decreases (McKenna *et al.*, 2006; Handy & Loscalzo, 2012; Esterhuizen *et al.*, 2017).

Generally, the KO brain regions displayed a tendency towards increased levels of pyruvic acid ($d=0.6$ for AC, $d=0.4$ for BST, $d=0.7$ for CB and $d=1.3$ for OB) and alanine ($d=0.6$ for AC, $d=0.5$ for BST, $d=1.3$ for CB and $d=1.4$ for OB). These alterations were not unique between the neurodegeneration-prone brain regions and resilient AC but were more pronounced in the OB (and CB for alanine). Then again, all the neurodegeneration-prone brain regions, especially the OB, displayed a tendency towards lactic acid levels that was not observed in the AC ($d=0.6$ for BST, $d=0.9$ for CB and $d=1.5$ for OB).

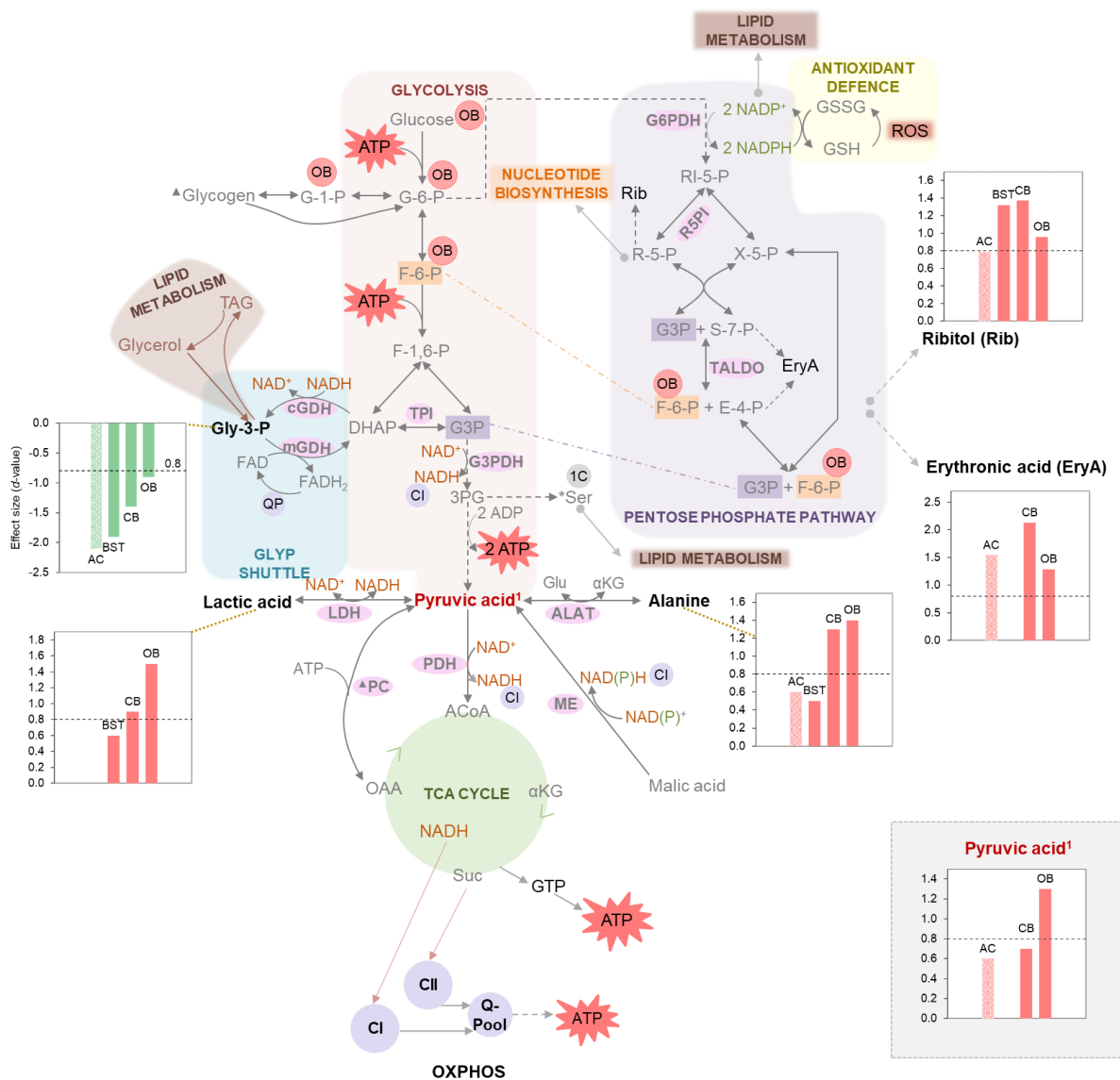


Figure 6.11: Carbohydrate metabolism and related metabolomics changes in the brain regions of *Ndufs4* knockout mice.

Refer to Figure 6.7 for detail on *inserted graphs*. Glycerol-3-phosphate (GLYP) shuttle (blue block), glycolysis (light red block), pentose-phosphate pathway (purple block) and lipid metabolism (brown shapes). Names of relevant enzymes are given in ovals next to reactions. Purple-filled circles: relation to the OXPHOS system. Grey-filled circles: relation to one-carbon (1C) metabolism. Red-filled circles: accumulation of carbohydrate intermediates in the KO OB. Dashed arrows represent multiple reaction steps. ▲ Compound or enzyme primarily found in astrocytes. *Compound also affected in some/all KO brain regions, but results are discussed in Section 6.4.2.8. The precise reactions forming erythronic acid (EryA) and ribitol (Rib) are unclear (grey dashed arrows). Other abbreviations: ACoA, acetyl-CoA; Ala, alanine; ALAT, alanine aminotransferase; α KG, α -ketoglutaric acid; DHAP, dihydroxyacetone phosphate; E-4-P, erythrose-4-phosphate; F-1,6-P, fructose-1,6-bisphosphate; G-3-P, glyceraldehyde-3-phosphate; G3PDH, glyceraldehyde-3-phosphate dehydrogenase; G6PDH, glucose-6-phosphate dehydrogenase; c/mGDH, cytosolic/mitochondrial Gly-3-P dehydrogenase; Glu, glutamic acid; Gly-3-P, glycerol-3-phosphate; GSSG / GSH, oxidised / reduced glutathione; GTP, guanosine triphosphate; Lac, lactic acid; LDH, lactic acid dehydrogenase; ME, malic enzyme; OAA, oxaloacetate; 3PG, 3-phosphoglycerate; Pyr, pyruvic acid; Q-pool, quinone pool; R-5-P, ribose-5-phosphate; RI-5-P, ribulose-5-phosphate; S-7-P, sedoheptulose-7-phosphate; Ser, serine; Suc, succinic acid; TAG, triacylglycerol; TALDO, transaldolase; TPI, triosephosphate isomerase; X-5-P, xylulose-5-phosphate.

These findings suggested that even though not so prominent, pyruvic acid metabolism was affected in the KO brain regions and pyruvic acid seemed to be more extensively converted to lactic acid in the neurodegeneration-prone brain regions, especially in the KO OB, than in the KO AC. Of note, the KO OB also displayed dramatically increased levels of other PPP- and glycolysis-related intermediates (fructose-6-phosphate, glucose, glucose-1-phosphate, glucose-6-phosphate, $d \geq 2$ for KO vs WT for all). However, these metabolites could not be detected in other samples so that prospective alterations in the levels of these metabolites in the KO AC, KO BST and KO CB remain ambiguous and warrant further investigation.

In general, the perturbations in carbohydrate-, glucose- and pyruvic acid-metabolism reflected graded metabolic perturbations across the investigated *Ndufs4* KO brain regions that were generally characterised by the accumulation of the carbohydrate-related intermediates. Furthermore, accumulation of ribitol, lactic acid and presumably glycolytic intermediates pointed towards greater disturbances in energy metabolism, redox balance and antioxidant status of the neurodegeneration-prone brain regions. This was especially evident in the KO OB which displayed the greatest perturbations in the levels of pyruvic acid, lactic acid and alanine, least pronounced decrease in glycerol-3-phosphate levels and an accumulation of many other glucose-related intermediates upstream of glyceraldehyde-3-phosphate dehydrogenase (G3PDH). The latter catalyses the first redox step in glycolysis. This was consistent with previous notions (Section 6.4.2.2 and Section 6.4.2.3) which suggested that the metabolic perturbations in the OB of *Ndufs4* KO mice might occur beyond a region-specific threshold.

Of note, activated glial cells upregulate glycolysis to produce ATP, lactic acid and NADPH, of which the latter is utilised for rapid superoxide production via NADPH oxidases as part of microglial immune defence (Dienel, 2012; Magistretti & Allaman, 2015; Camandola & Mattson, 2017; Ghosh *et al.*, 2018). Therefore, it is possible that the perturbed carbohydrate-related metabolism exhibited by the neurodegeneration-prone brain regions might be related to the glial activation observed in these regions (Quintana *et al.*, 2010). It might therefore also contribute to increased production of reactive species and/or perturbed antioxidant homeostasis in the neurodegeneration-prone regions.

6.4.2.7 Lipid-related metabolism was more perturbed in the neurodegeneration-prone brain regions

The significantly decreased concentrations of short-chain acyl carnitines (Section 6.4.2.1 and Section 6.4.2.5) and glycerol-3-phosphate (Section 6.4.2.6) in the brain regions, could reflect a disturbance in lipid metabolism. This was reinforced by the unique lipid metabolism-related alterations exhibited by each KO brain region when compared to its corresponding WT brain region. Figure 6.12 shows a schematic representation of various lipid-related metabolic pathways and related metabolites which had significantly altered levels in some or all of the investigated KO brain regions. The KO AC additionally displayed a profound decrease in the levels of dihydroxystearic acid (DHSA, $d = 0.9$) and increase in the levels of the polyunsaturated fatty acid, arachidonic acid ($d = 0.8$). The KO BST also displayed a decrease in the levels of oxysterol ($d = 1.5$). Furthermore, the KO CB displayed significantly increased levels of arachidonic acid ($d = 0.8$) and the long-chain fatty acid (LCFA), oleic acid (C18:1, $d = 0.8$). Lastly, the KO OB exhibited a decrease in the levels of DHSA ($d = 1.4$) and stearic acid (C18:0, $d = 0.9$), increased concentrations of C18:1 ($d = 1.5$), palmitic acid (C16:0, $d = 1.1$), carnitine ($d = 1.4$) and acetyl(C2)-carnitine ($d = 1.0$); as well as a tendency towards increased levels of arachidonic acid ($d = 0.7$).

Overall, the investigated KO brain regions displayed a combination of altered levels of lipid synthesis-related metabolites (LCFAs, LCFA-derivatives, oxysterol, arachidonic acid and glycerol-3-phosphate) and fatty acid oxidation-related intermediates (LCFAs, carnitine and acylcarnitines), suggesting a global disturbance in lipid metabolism. These findings were also in accordance with the alterations in carbohydrate metabolism (Section 6.4.2.6) which supplies the NADPH and DHAP or glycerol-3-phosphate required for lipid metabolism. In addition, the marked decrease in the levels of C18:0 and accumulation of C18:1 suggested that the desaturation of stearoyl-CoA (CoA derivative of C18:0) to oleoyl-CoA (CoA derivative of C18:1) by stearoyl-CoA desaturase (SCD) activity was increased at the surface of the endoplasmic reticulum (ER). Since this reaction can regenerate NAD^+ , it might support the notion that redox balance was more perturbed in the neurodegeneration-prone brain regions. Furthermore, the elevated levels of C2-carnitine in the KO OB could potentially reflect a surplus of acetyl-CoA, which is a product of fatty acid oxidation, amino acids, glycolysis and ketone bodies (if mice have become ketotic) as well as a key building block and stimulus for fatty acid synthesis (Liu *et al.*, 2017; Tracey *et al.*, 2018).

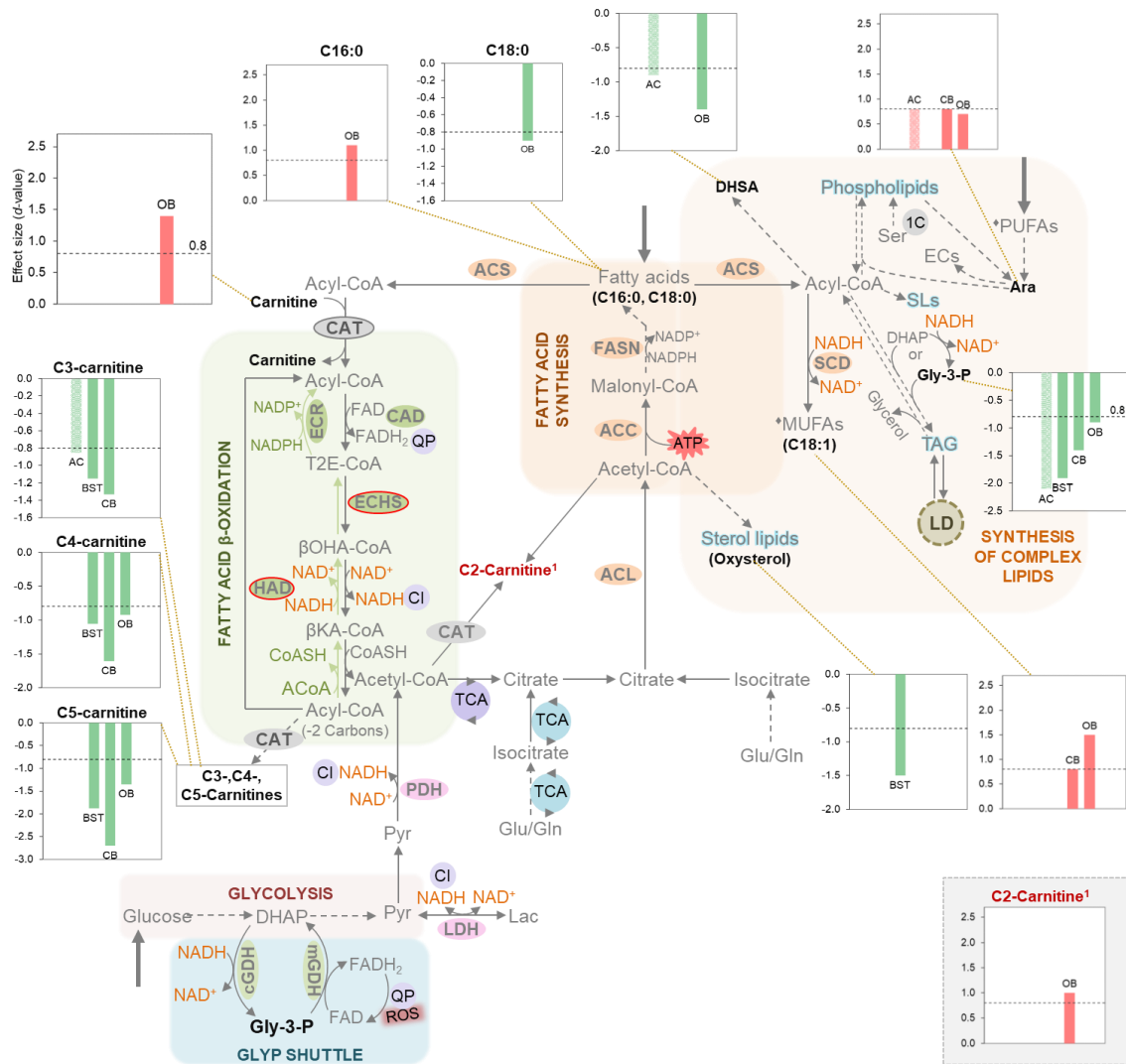


Figure 6.12: Lipid metabolism and related metabolomics changes in the brain regions of *Ndufs4* knockout mice.

Refer to Figure 6.7 for detail on *inserted graphs*. Fatty acid oxidation (FAO, green block), fatty acid synthesis (dark orange block), synthesis of complex lipids (light orange block), glycolysis (light red block) and glycerol-3-phosphate (GLYP) shuttle (blue block). Names of relevant enzymes are given in ovals next to the reaction it catalyses. Purple-filled circles: relation to the TCA cycle and OXPHOS system. Grey-filled circles: relation to one-carbon (1C) metabolism. Purple/blue TCA cycle indicate oxidative-clockwise / reductive-anticlockwise direction. Green arrows indicate reversal of mitochondrial β-oxidation for fatty acid synthesis. Red-encircled enzymes indicate those that are physically closely associated with mitochondrial complex I (CI). Dashed arrows indicate multiple steps and thick arrows indicate transport into the cell. ♦ Indicate origin from the diet or cell membrane. **Fatty acid metabolism.** Free fatty acids are kept in the cell through condensation with coenzyme A (CoA) to form fatty acyl CoAs (FACoAs) of various lengths which are substrates for both fatty acid oxidation and lipid synthesis. The former primarily occurs in the mitochondria, except for long-chain fatty acids (>18C) which are usually oxidised in peroxisomes and are associated with the formation of acylcarnitines to allow transport across membranes. Acylcarnitines can also be formed as part of an overflow mechanism when organellar concentrations of acyl groups are high. Lipid synthesis occurs in the cytosol and endoplasmic reticulum. Palmitic acid is the first end-product of fatty acid elongation in the cytosol. Further elongation of 16-carbon fatty acids occurs primarily at the surface of the ER even though it can also take place in the mitochondria by reversing β-oxidation and substituting the acyl-CoA

dehydrogenase (AD) step with enoyl-CoA reductase (ECR) (indicated by green arrows). Dehydrogenation of fatty acids is catalysed at the ER membrane by NADH-dependent stearoyl-CoA desaturase (SCD). Palmitic acid and stearic acid are both end-products of peroxisomal β -oxidation. Polyunsaturated fatty acids (PUFAs) are obtained from the diet. *Other abbreviations: -2 Carbons, 2 carbons shorter; ACC, acetyl-CoA carboxylase; ACL, acetyl-CoA-citrate lyase; ACoA, acetyl-CoA; ACS, acyl-CoA synthetase; Ara, arachidonic acid; ATP, adenosine triphosphate; β KA-CoA, β -ketoacyl CoA; β OHA-CoA, β -hydroxyacyl CoA; C2-carnetine, acetylcarnitine; C16:0, palmitic acid; C18:0, stearic acid; C18:1, oleic acid; CAD, (short/medium/long)-chain acyl-CoA dehydrogenase; CAT, carnitine acyltransferase; CoASH, coenzyme A; DHAP, dihydroxyacetone phosphate; DHSAs, dihydroxystearic acid; ECHS, enoyl-CoA hydratase; ECs, eicosanoids; FAD/FADH₂, oxidised/reduced form of flavin adenine dinucleotide; FASN, fatty acid synthase; c/mGDH, cytosolic/mitochondrial glycerol-3-phosphate dehydrogenase; Gln, glutamine; Glu, glutamic acid; Gly-3-P, glycerol-3-phosphate; GLYP, glycerolphosphate; HAD, hydroxyacyl-CoA dehydrogenase; Lac, lactic acid; LD, lipid droplets; MUFAs, mono-unsaturated fatty acids; Pyr, pyruvic acid; SCD, stearoyl-CoA desaturase; Ser, serine; SLs, sphingolipids; T2E-CoA, trans-2-enoyl CoA; TAG, triacylglycerols.*

In comparison with the neurodegeneration-prone brain regions, the KO AC did not display elevated levels of the detected LCFAs or LCFA-derivatives. It also had a less perturbed carnitine / acylcarnitine profile. In addition, the OB displayed the most distinct and extensive disturbance in lipid metabolism. The latter two findings supported a graded perturbation in lipid metabolism that was more pronounced in the neurodegeneration-prone brain regions and beyond a certain metabolic threshold in the OB. Consequently, a relation between regional differences in lipid metabolic profiles and the region-specific neurodegeneration of the *Ndufs4* KO mice might be plausible. Finally, the disturbances in lipid metabolism also supported a greater perturbation in global energy metabolism and redox balance in the neurodegeneration-prone brain regions. It is also plausible that the more significantly impaired mitochondrial β -oxidation in the neurodegeneration-prone brain regions might exacerbate ROS production in the mitochondria and peroxisomes (Tracey *et al.*, 2018).

6.4.2.8 One-carbon metabolism was uniquely altered among *Ndufs4* knockout brain regions

Figure 6.13 depicts the 1C-metabolic pathways, together with closely associated metabolic pathways and the related metabolites that were altered in some or all of the *Ndufs4* KO brain regions. 1C-metabolism comprises a series of interconnected metabolic pathways, including the methyl/methionine cycle (Figure 6.13, blue), the folate cycle (Figure 6.13, orange) and the trans-sulfuration pathway (Figure 6.13, green). These function together to transfer the 1C-units required for various cellular processes such as biosynthesis (purines and thymidine), amino acid homeostasis, epigenetic regulation, redox regulation, energy production and glutathione synthesis (Ducker & Rabinowitz, 2017; Clare *et al.*, 2019). Also, the supply of decarboxylated S-adenosylmethionine (dSAM) from 1C-metabolism is the rate-limiting factor for the synthesis of higher polyamines from putrescine (Lozoya *et al.*, 2018; Clare *et al.*, 2019).

Putrescine levels were significantly increased in all investigated brain regions (Section 6.4.2.3). Conversely, the levels of other 1C-metabolism-related intermediates were inconsistently altered among brain regions. Overall, the investigated KO brain regions displayed aberrations in the levels of potential 1C-unit donors; i.e. serine in the AC ($d=1.0$) and CB ($d=1.6$), glycine in the BST ($d=0.7$) and CB ($d=0.9$), trimethylglycine in the CB (TMG / betaine, $d=0.7$) and threonine in the OB ($d=1.0$). Additional perturbations related to methyl/methionine metabolism included putrescine in all brain regions, creatinine ($d=0.8$) and methionine ($d=0.8$) in the AC, as well as carnitine ($d=1.4$) and adenosine ($d=3.3$) in the OB. Additional perturbations related to the trans-sulfuration pathway included cysteine ($d=1.2$) in the AC, taurine ($d=1.2$) in the BST and cystathionine ($d=1.7$) in the OB. A disturbance in the closely-associated *de novo* nucleotide metabolism was also observed. The AC displayed altered levels of pyrimidine-related intermediates, namely carbamic acid ($d=0.8$) and uridine monophosphate (UMP, $d=1.0$). This was also evident in the OB which displayed altered levels of the purine-related intermediate, adenosine.

Collectively, these findings suggested that the cellular perturbations resulting from a CI deficiency might trigger a complex response in 1C-metabolism of the *Ndufs4* KO brain regions. The unique 1C-metabolic perturbations in the KO AC (carbamic acid, UMP, creatinine, methionine and cysteine) were implicated in all three 1C-metabolic pathways, perhaps indicating a unique alteration or adaptation in global 1C-metabolism in response to the *Ndufs4* KO. This might play a role in the resiliency of the AC to neurodegeneration. Finally, these results also supported the notion of altered energy metabolism and antioxidant status in the *Ndufs4* KO brain regions due to the close association of 1C-metabolism with energy- and glutathione-metabolism.

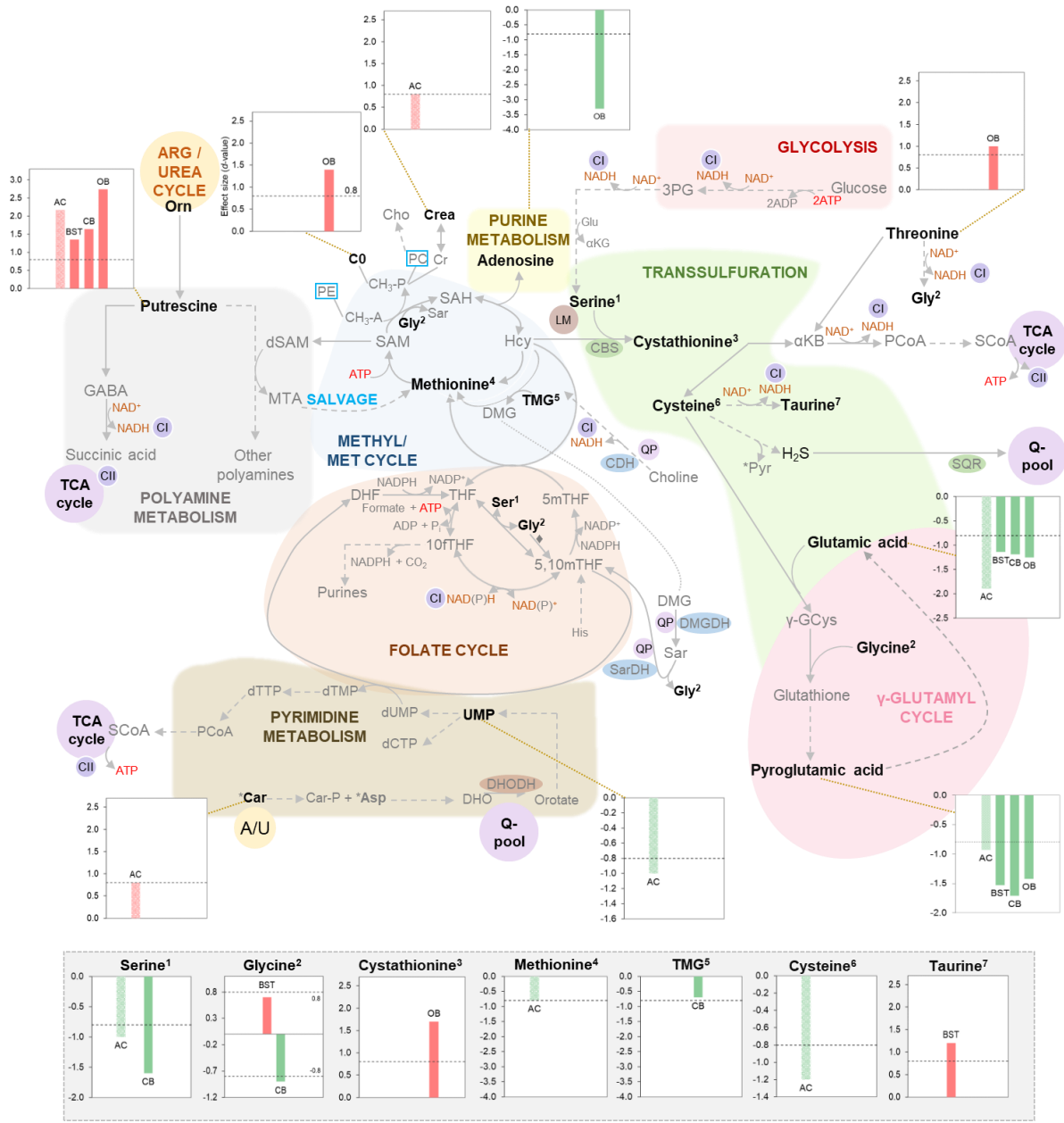


Figure 6.13: One-carbon metabolism and related metabolomics changes in the brain regions of *Ndufs4* knockout mice.

Refer to Figure 6.7 for detail on *inserted graphs*. Polyamine metabolism (grey block), purine metabolism (yellow block), glycolysis (light red block), methyl/methionine cycle (light blue shape), trans-sulfuration pathway (light green shape), folate cycle (orange shape), pyrimidine metabolism (brown shape) and γ -glutamyl/glutathione cycle (pink oval). Names of relevant enzymes are given in ovals next to the reaction it catalyses. Purple-filled circles: relation to the TCA cycle and OXPHOS system. Brown-filled circle: relation to lipid metabolism (LM). Blue rectangles: phospholipids. Dashed arrows indicate multiple reaction steps. One-carbon (1C) metabolism comprises a series of interconnected metabolic pathways compartmentalised between the cytoplasm, nucleus and mitochondria, and include the methyl/methionine cycle, the folate cycle and the trans-sulfuration pathway, which together function to transfer 1C units required for synthesis of various other metabolites. Folate cycle: 1C units are loaded onto THF from serine (Ser), glycine (Gly, via the mitochondrial glycine cleavage system (\blacklozenge)), formate, histidine (His) and choline-derived methyl-glycine species such as sarcosine (Sar) and dimethylglycine (DMG). Methyl/methionine cycle: methionine (Met) is converted to the 1C unit donor S-adenosylmethionine (SAM). The 1C unit required for Met synthesis from Hcy is obtained from either

trimethylglycine (TMG)/betaine, a catabolic product of choline (Cho) in the mitochondria, or 5mTHF from the folate cycle. Trans-sulfuration pathway: the sulfur of Met is transferred to Ser via Hcy to yield cystathionine and other intermediates, including glutathione. *Other abbreviations*: 3PG, 3-phosphoglycerate (3PG); 5mTHF, 5-methyl THF; 5,10mTHF, 5,10-methylene THF; 10fTHF, 10-formyl THF; C0, carnitine; CDH, choline dehydrogenase; CH₃-A/P, methyl group acceptor/product; CoA, coenzyme A; Cr, creatine; Crea, creatine; dCTP, deoxycytidine triphosphate; DHF, dihydrofolate (DHF); DHO, dihydroorotate; DHODH, dihydroorotate dehydrogenase; DMGDH, dimethylglycine dehydrogenase; dSAM, decarboxylated S-adenosylmethionine; dTMP, deoxythymidine monophosphate; dTTP, deoxythymidine triphosphate; dUMP, deoxyuridine monophosphate; γ -GCys, γ -glutamylcysteine; GABA, γ -aminobutyric acid; Glu, glutamic acid; H₂S, hydrogen sulphide; Hcy, homocysteine; α KB, α -ketobutyric acid; α KG, α -ketoglutaric acid; MTA, 5'-methylthiodenosine; Orn, ornithine; PC, phosphatidylcholine; PCoA, propionyl-CoA; PE, phosphatidylethanolamine; P_i, inorganic phosphate; Pyr, pyruvic acid; QP, quinone-pool; SAH, S-adenosylhomocysteine; SarDH, sarcosine dehydrogenase; SCoA, succinyl-CoA; SQR, sulfide-ubiquinone oxidoreductase; THF, tetrahydrofolate; UMP, uridine monophosphate.

6.5 Metabolic-related factors that could drive region-specific neurodegeneration in *Ndufs4* knockout mice

The metabolomics' findings that differentiated between the neurodegeneration-prone and -resilient brain regions suggested that region-specific neurodegeneration was related to: 1) graded perturbations in global metabolism that reached a detrimental threshold in the neurodegeneration-prone brain regions, especially the OB; and 2) inherent regional specificity in metabolism.

6.5.1 The potential role of graded metabolic perturbations in region-specific neurodegeneration

Recall that the shared metabolic perturbations of the investigated brain regions of *Ndufs4* KO mice pointed towards global cellular compensatory responses in classic and non-classic metabolic pathways, to counteract the widespread cellular consequences of a CI deficiency (Section 6.4.1.3). However, these compensatory metabolic pathways were generally more pronouncedly affected in the neurodegeneration-prone brain regions. These findings showed that compared to the resilient AC, the neurodegeneration-prone brain regions had greater disturbances in: 1) energy metabolism and in metabolic pathways fuelling the RC at CI-bypassing sites (Section 6.4.1.1 and Section 6.4.2.1 to Section 6.4.2.7); 2) mechanisms maintaining the cellular redox status under conditions of perturbed redox balance (see Section 6.4.1.2, the proline cycle in Section 6.4.2.3 and LDH in Section 6.4.2.6); and 3) antioxidant homeostasis (Section 6.4.1.2 and Section 6.4.2.3 to Section 6.4.2.4). The impairment of redox-sensitive reactions was also more prominent in these regions (see Section 6.4.2.1 to Section 6.4.2.7). The latter suggested that the regional vulnerability to the CI deficiency could to a large extent be linked to the detrimental effect/s of a more pronounced disturbance in

redox balance. Collectively, the results suggested that the metabolic effects of a CI deficiency was more pronounced in the neurodegeneration-prone brain regions. Conversely, a few metabolic perturbations were more dramatic in the KO AC. This included the disturbances in the levels of aspartic acid, glutamic acid, and glycerol-3-phosphate (Section 6.4.2.4 and Section 6.4.2.6). Taken together, these findings suggested that more efficient fuelling of the TCA cycle and maintenance of the cytosolic NAD⁺/NADH ratio under physiological conditions (refer to MAS and GlyPS in Section 6.4.1.2) might confer neurons in the AC with a resiliency to degeneration. It therefore seemed that the *Ndufs4* KO caused common disturbances in global metabolism across the brain regions that displayed a gradient of severity. This gradient of severity also correlated with the severity of neurodegeneration. Interestingly, such a phenomenon has also been noted previously in the brain region metabolic profiles of Alzheimer's disease patients (Xu *et al.*, 2016).

Compatible with this notion of graded metabolic perturbations, the biochemical investigation of the *Ndufs4* KO brain regions conducted during this study, showed that the neurodegeneration-prone brain regions had lower residual CI activity than the KO AC (Section 5.2.2). It is important to remember that all KO brain regions had significantly decreased, but not diminished maximal CI activity (expressed in mU/mg protein) when compared with WT brain regions. However, remarkable differences were observed in the residual CI activities (calculated as a fraction of the CI activity of the corresponding WT region) among the various KO brain regions. The more resilient KO AC had a residual CI activity of 38%; whereas the KO CB, KO BST and KO OB had residual activities of 28%, 25% and 14%, respectively. In accordance, the KO OB which displayed the lowest absolute (expressed in mU/mg protein) and residual CI activity, also had the most profoundly altered metabolic profile. This was in accordance with a previous study which reported that the OB was the earliest and most affected brain region in *Ndufs4* KO mice (Quintana *et al.*, 2010). It is noteworthy to mention that neurogenesis, which has been associated with high CI-gene expression levels, continually occurs in the OB; and might play a role in the more dramatic metabolic alterations and vulnerability to neurodegeneration (Wirtz & Schuelke, 2011; Liu *et al.*, 2015).

It is thus tempting to speculate that CI activity in the neurodegeneration-prone brain regions might be deficient beyond a threshold at which metabolic consequences become detrimental; and neurodegenerative processes become activated. Some of the metabolic perturbations that differentiated between the neurodegeneration-prone and -resilient brain regions have the potential to induce neurodegenerative processes. These factors will be discussed in the following sections to illustrate how the metabolic perturbations identified in the metabolomics investigation could contribute to neurodegeneration. Of note, these mechanisms are not

suggested to reflect the only or true potential neurodegenerative mechanisms, but were primarily considered since: 1) these mechanisms were related to the most significant metabolic alterations in the *Ndufs4* KO brain regions and could clearly differentiate between the neurodegeneration-prone brain regions and more resilient AC, be it based on degree of alteration or exclusivity; and/or 2) these mechanisms corresponded with findings previously reported in *Ndufs4* KO mice, CI-deficient experimental models and/or Leigh syndrome patients.

6.5.1.1 Greater activation of sub-optimal RC-fuelling and ATP-producing pathways

Unlike the previously proposed therapeutic supplementation strategies (Section 6.4.1.3), endogenous compensatory metabolic pathways utilise several ATP-consuming and/or NADH- and ROS-producing reactions to metabolise the energy substrates into the precursors that provide electrons to CI-bypassing sites or drive non-OXPHOS ATP production. Apart from glutamine and glutamic acid that can be catabolised through α -ketoglutarate dehydrogenase complex (KGDHC) activity, all other metabolic pathways that converge towards succinyl-CoA entail the consumption of at least one ATP molecule (Figure 6.6) (Bui *et al.*, 2019). In addition, the first part of glycolysis preceding NAD⁺-dependent glyceraldehyde-3-phosphate dehydrogenase (G3PDH), consume two ATP molecules per glucose molecule (Figure 6.11). Some affected metabolic pathways also irreversibly produce NADH (and utilise NAD⁺) (see Figure 6.7 to Figure 6.11) and contain a few sites that are prone to produce ROS such as the CI-bypassing sites (CII, CIII and ETF/ETF-QO system) (Mráček *et al.*, 2014; Holzerová & Prokisch, 2015; Morris & Berk, 2015; Vasava & Mashiyava, 2016; Stepanova *et al.*, 2017). This is also true for the enzymes involved in non-OXPHOS ATP production, namely branched-chain alpha-ketoacid dehydrogenase (BCKDH, Figure 6.7), KGDHC (Figure 6.10), pyruvic acid dehydrogenase (PDH, Figure 6.11) and acyl-CoA dehydrogenases (AD, Figure 6.12) (Verkaart *et al.*, 2007b; Holzerová & Prokisch, 2015; Richard *et al.*, 2018; Tracey *et al.*, 2018).

In addition, a greater reliance on multiple pathways that utilise a limited Q-pool (Figure 6.6) could prevent CII from transferring electrons to the Q-pool. This could result in extensive ROS generation by reverse electron transport (RET) at CI (Kluckova *et al.*, 2015; Stepanova *et al.*, 2017). This phenomenon has been noted in neurons derived from *Ndufs4* KO mice (Bird *et al.*, 2014) and in the development of brain lesions in hypoxia-ischemic encephalopathy, a condition that shares features with Leigh syndrome (Chouchani *et al.*, 2014b; Lake *et al.*, 2015). It is also noteworthy to mention that while CII-driven respiration might compensate for some aspects of a CI deficiency, it is unable to pump protons across the inner mitochondrial membrane. Consequently, a higher electron flow through CII and the Q-pool to drive CIII would be required to maintain the mitochondrial membrane potential. This in turn, could exacerbate

the leakage of electrons and production of reactive species. Consequently, the metabolic pathways that can bypass CI are expected to produce more ROS than the classic brain energy metabolic pathways.

Considering that the CI-bypassing and OXPHOS-independent ATP producing metabolic pathways of the neurodegeneration-prone brain regions were more pronouncedly affected by the KO than the resilient AC (Figure 6.7 to Figure 6.12 and Section 6.5.1), along with the lower residual CI activity observed in the former (Section 5.2.2), it might be that the neurodegeneration-prone brain regions not only had greater or earlier requirements for the compensatory metabolic pathways, but also that the “side effects” of these pathways were augmented. This meant that even though such reactions would also be active in the more resilient AC, the chronically more prominent requirements of these pathways in the neurodegeneration-prone brain regions could exacerbate the disturbances in redox balance, ROS production and energy metabolism. In this regard, the metabolic dysregulation in the neurodegeneration-prone brain regions could have reached a threshold that triggered neurodegeneration.

6.5.1.2 Greater impairment of RC-fuelling and ATP-producing pathways

The more pronounced disturbance in energy metabolism (amino acid-, TCA cycle-, glycolysis- and lipid metabolism; Section 6.4.2.1 to Section 6.4.2.7) of the neurodegeneration-prone brain regions, provided evidence to suggest that an energy deficit might play a role in Leigh syndrome neuropathology. This is in agreement with previous studies (Quintana *et al.*, 2010; Lake *et al.*, 2015; Kayser *et al.*, 2016). The energy deficit might reflect the combined effects of greater cellular energy requirements and a greater disturbance in redox balance due to a lower residual CI activity. The latter is because most of the classic and “compensatory” RC-fuelling and ATP-producing metabolic pathways that were more vigorously impaired in the neurodegeneration-prone brain regions, are redox sensitive (see Figure 6.6 to Figure 6.12). This would imply a more severe impairment of the residual function of the RC by inducing a state of low electron entry or flow. Incidentally, deficiencies causing decreased electron flow through CIII, due to CIII- and/or ubiquinone-deficiency, are common causes of Leigh syndrome (Lake *et al.*, 2015; Spinazzi *et al.*, 2018), suggesting a possible relation. Importantly, this also includes the NAD⁺-dependent entry of glutamic acid into the TCA cycle via oxidative deamination by glutamic acid dehydrogenase (GDH) (Figure 6.10). The collective impairment of these pathways could result in energy depletion and cell death, especially in neurons. This is because neurons have high energy requirements especially during depolarisation. To fulfil these requirements, the neurons depend mostly on the functioning of the OXPHOS system and TCA cycle. In addition, as part of the BCAA-glutamic acid shuttle between glia and

neurons, mBCKDH is primarily restricted to neurons and might be an important energy source under stress conditions (Falk *et al.*, 2008; Bifari & Nisoli, 2017). The prominent impairment of mBCKDH in the neurodegeneration-prone brain regions (Figure 6.7), could thus contribute to an energy deficit within neurons in these regions.

The metabolomics data provided some additional insights as to why neurons in the BST, CB and OB might be particularly vulnerable to an energy deficiency and degeneration in a CI deficiency. The *Ndufs4* KO especially in glutamatergic neurons, and in GABAergic neurons, are considered to be the primary cause of the neuropathological features observed in whole-body *Ndufs4* KO mice (Bolea *et al.*, 2019). Glutamatergic- and GABAergic neurons are respectively the main excitatory and inhibitory neurotransmitters in the brain and account for a large proportion of the CNS synapses (Dubinsky, 2009) especially within the BST, CB and OB (Bolea *et al.*, 2019). The metabolomics perturbations in the *Ndufs4* KO brain regions call to mind that putrescine (Section 6.4.2.3) and glutamic acid (Section 6.4.2.4), which are both GABA precursors, might be extensively utilised to support the TCA cycle and CII-driven respiration. These neurons might be rendered more vulnerable to death in *Ndufs4* KO mice because of: 1) competitive utilisation of intermediates for bio-energetic and neurotransmitter purposes; and 2) a lowered NAD⁺/NADH ratio that perturbed metabolism. This in turn, can induce secondary neurodegeneration and glial activation (Dubinsky, 2009; Bolea *et al.*, 2019).

6.5.1.3 Activation of energetically expensive metabolic pathways

The metabolic perturbations in the neurodegeneration-prone brain regions have the potential to exacerbate an energy deficit by stimulating energetically expensive metabolic pathways. The presumably more pronounced decrease in the NAD⁺/NADH ratio in these brain regions (e.g. Section 6.4.2.1 to Section 6.4.2.7 and Section 6.5.1) could stimulate ATP-dependent NAD⁺-synthesis (Owens *et al.*, 2013; Srivastava, 2016). Moreover, the accumulation of nutrients, such as BCAAs (Section 6.4.2.1), arginine (Section 6.4.2.3) and acetyl-CoA (Section 6.4.2.7) in the neurodegeneration-prone brain regions, could induce energetically expensive processes such as protein- and lipid-synthesis (Zheng *et al.*, 2016a; Griffin & Bradshaw, 2017; Chen *et al.*, 2018b; Chinopoulos & Seyfried, 2018). The greater deficiency in CI and impairment of RC-fuelling metabolic pathways (refer to Section 6.5.1 and Section 6.5.1.2) might also lead to the dissipation of the proton gradient across the inner mitochondrial membrane and subsequent reversal of ATP synthase (Kiss *et al.*, 2014; Chinopoulos & Seyfried, 2018). ATP synthase would then hydrolyse ATP to pump protons out of the matrix. A severe deficit in OXPHOS-related ATP production together with an impairment of TCA cycle substrate-level phosphorylation could also lead to reversal of the adenine nucleotide translocase (ANT) (Kiss *et al.*, 2014). This in turn, might exhaust cytosolic ATP reserves.

6.5.1.4 Increased utilisation of sub-optimal NADH oxidation reactions

Cells contain several mechanisms to maintain redox homeostasis and which become important at different stages depending on the size of NAD⁺/NADH pools and degree of lowered NAD⁺/NADH ratio (Goodman *et al.*, 2018). The more decreased NAD⁺/NADH ratio in the neurodegeneration-prone brain regions can thus lead to a greater dependence of cells on the relative contribution of non-classical, sub-optimal NADH-oxidising mechanisms to restore redox balance. For example, the metabolomics results indicated an involvement of the Cl-independent proline cycle (Section 6.4.2.3) and GlyPS (Section 6.4.2.6). Other metabolic pathways that were more pronouncedly affected in the neurodegeneration that could also enable sub-optimal NADH-oxidation, include the reversal of mitochondrial NAD⁺-dependent fatty acid β -oxidation reactions (Figure 6.12); and the glycolysis reaction catalysed by G3PDH (Figure 6.11). Additional mechanisms that could compensate for the lowered NAD⁺/NADH ratio in OXPHOS deficiencies might also be more active in the neurodegeneration-prone brain regions. These might include the reductive carboxylation of glutamine (or glutamic acid, Figure 6.10) (Gaude *et al.*, 2018) and the NADH-oxidation activity of mitochondrial NAD(P)H:quinone oxidoreductases (NQO) (aka diaphorases) (Kiss *et al.*, 2014). These reactions are sub-optimal in that they are prone to produce ROS and/or exacerbate cellular energy deficiency by impairing energy production and/or by driving energy-consuming anabolic processes when chronically activated (Kiss *et al.*, 2014; Karlsson *et al.*, 2016; Martano *et al.*, 2016; Zieliński *et al.*, 2016; Gaude *et al.*, 2018; Tracey *et al.*, 2018; Phang, 2019). Importantly, the C57BL/6J mice do not express the gene encoding for the proton translocating transhydrogenase which catalyses the reversible exchange of NADP⁺ and NAD⁺ for NADH and NADPH, respectively (Kiss *et al.*, 2014). Therefore, it is not a viable NAD⁺-generating mechanism in the *Ndufs4* KO mice.

6.5.1.5 Increased production of reactive species and oxidative damage

The neurodegeneration-prone brain regions displayed more pronounced perturbations in antioxidant homeostasis (refer to Section 6.4.1.2 and Section 6.4.2.4). One possible explanation could be that the antioxidants were utilised to scavenge the excess reactive species that result from the effects of a lower residual Cl activity (Section 5.2.2). For instance, Rodenburg (2016) reported that ROS production inversely correlated with residual Cl activity. This might also be exacerbated through the increased ROS production of sub-optimal “compensatory” metabolic pathways (Section 6.5.1.1 and Section 6.5.1.4), of neurotoxic metabolites (Section 6.5.1.6) and of aberrantly activated or dysregulated glial cells (Section 6.5.1.9). It is also noteworthy to mention that some antioxidants can even behave as pro-oxidants under certain circumstances i.e. they produce ROS (Carocho & Ferreira, 2013;

Bouchez & Devin, 2019). Excessive ROS in turn can cause oxidative damage to cellular components, dysregulate cell signalling or perhaps affect mitochondrial biogenesis and thus energy production (Bouchez & Devin, 2019). It is therefore possible that oxidative stress might play a role in the region-specific neurodegeneration of *Ndufs4* KO mice.

6.5.1.6 Accumulation of potentially neurotoxic metabolites

A few of the detected compounds which accumulated more pronouncedly in the neurodegeneration-prone brain regions can induce neuropathology or have neurotoxic potential when chronically elevated. These included the BCAAs (Section 6.4.2.1) (Yudkoff *et al.*, 2005; Lynch & Adams, 2014; Richard *et al.*, 2018), pipercolic acid (Section 6.4.2.2) (Hallen *et al.*, 2013), proline (Section 6.4.2.3) (Wyse & Netto, 2011; Phang *et al.*, 2015; Kori *et al.*, 2016; Cappelletti *et al.*, 2018), ribitol (Section 6.4.2.6) (Huck *et al.*, 2004; Klusmann *et al.*, 2005; Jäger *et al.*, 2015; Xu *et al.*, 2016), glycolytic intermediates (Section 6.4.2.6) (Johnson *et al.*, 2013; Xu *et al.*, 2016), free fatty acids (Tracey *et al.*, 2018), palmitic acid (C16:0) (Lee & Wolfgang, 2012; Ng & Say, 2018), oleic acid (C18:1) (Palladini *et al.*, 2019) and altered activity of SCD (Section 6.4.2.7) (Ntambi *et al.*, 2002; Liu *et al.*, 2009; Astarita *et al.*, 2011; Liu *et al.*, 2011; Ackerman *et al.*, 2018; Fanning *et al.*, 2019; Qin & Kojima, 2019). The neurotoxic effects of many of these metabolites have been attributed to increased ROS production, oxidative stress, lipid peroxidation, oxidative damage and apoptosis. Incidentally, these are all features of the neurodegeneration-prone brain regions of *Ndufs4* KO mice, especially the OB (Quintana *et al.*, 2010; Liu *et al.*, 2015; Kayser *et al.*, 2016; Liu *et al.*, 2017).

Some of these metabolites have additional neuropathological effects. Chronically elevated BCAA levels can inhibit pyruvic acid dehydrogenase (PDH) (Li *et al.*, 2017). The accumulation of proline can induce excessive activation of excitatory receptors which leads to excitotoxic cell death (Wyse & Netto, 2011). Furthermore, elevated levels of C16:0 and/or the altered activity of SCD can dysregulate neuro-inflammation (Liu *et al.*, 2009; Liu *et al.*, 2011; Ng & Say, 2018) and lipid metabolism/homeostasis (Astarita *et al.*, 2011; Ackerman *et al.*, 2018; Fanning *et al.*, 2019; Qin & Kojima, 2019). In addition, the more dramatic alterations in lipid metabolism of the neurodegeneration-prone brain regions (Section 6.4.2.7) could induce aberrant metabolic regulation. This can occur through the direct action of lipid-intermediates on enzymes such as carnitine palmitoyltransferase 1 (CPT1) which transports long chain fatty acids (LCFAs) across organelle membranes (Ntambi *et al.*, 2002; Lee & Wolfgang, 2012). The two CPT1 isoforms localised in the brain, CPT1A and CPT1C, had been shown to respectively regulate oxidation and storage of LCFAs in the form of triacylglycerols (TAGs). The latter is perturbed in Leigh syndrome patients and in the OB of *Ndufs4* KO mice (Legault *et al.*, 2015; Casals *et al.*, 2016; Liu *et al.*, 2017).

The neurodegeneration-prone regions also uniquely exhibited increased concentrations of lactic acid (Section 6.4.2.6). The effect of lactic acid accumulation in the brain is controversial and might have neurotoxic or neuroprotective functions depending on the cellular context and concentration (Cater *et al.*, 2003; Bird *et al.*, 2014; Lake *et al.*, 2015; Mason *et al.*, 2015; Mason, 2017). Elevated levels of lactic acid might contribute to neuronal injury and lesion formation by inducing local pH changes and/or vessel hypertrophy (Bird *et al.*, 2014; Lake *et al.*, 2015) and have been considered as a biomarker for mitochondrial disease progression in the *Ndufs4* KO mouse brain (Takahashi *et al.*, 2019).

The fact that glutamic acid levels were significantly decreased in all investigated *Ndufs4* KO brain regions, but less so in the neurodegeneration-prone brain regions (Section 6.4.2.4) might also be significant in the light of its potential as a neurotoxic metabolite. As the main excitatory neurotransmitter in the brain, glutamic acid excito-toxicity have been implicated in many neurodegenerative disorders, including Leigh syndrome (Kanunnikova, 2012). In fact, it is evident that CI deficiencies can result in the release of large amounts of potentially excito-toxic glutamic acid (Pathak & Davey, 2008). The more dramatic decline in the levels of glutamic acid (and perhaps aspartic acid) in the resilient AC, might thus be neuroprotective in itself (Kanunnikova, 2012; Divakaruni *et al.*, 2017). Conversely, increased glutamic acid levels at the synapses of the neurodegeneration-prone brain regions might contribute to neuronal cell death (Lake *et al.*, 2015). This is perhaps due to impaired NAD⁺-dependent oxidation and decreased neuronal uptake of glutamic acid.

Together, these findings suggested that the accumulation of neurotoxic metabolites in the neurodegeneration-prone brain regions secondary to a CI deficiency might play a role in the progression of neuropathology. Notably, the induction of oxidative stress seemed to be a common mechanism driving the neurotoxicity associated with many of these accumulating metabolites. This might explain why antioxidant supplementation is beneficial in CI deficiencies but does not rescue the clinical phenotype.

6.5.1.7 Exacerbation of nucleotide pool imbalances

The presumably more decreased NAD⁺/NADH ratio (e.g. Section 6.4.2.1 to Section 6.4.2.7 and Section 6.5.1) could drive greater nucleotide pool imbalances in the neurodegeneration-prone brain regions. In addition to its role in substrate-level phosphorylation, the NAD⁺-dependent mitochondrial folate cycle plays a role in *de novo* nucleotide synthesis. This suggests that redox- and energy-associated perturbation of the folate cycle might be responsible for the perturbation observed in nucleotide metabolism of the KO brain regions (Section 6.4.2.8). Moreover, the more perturbed redox balance could also impede the NAD⁺-

dependent synthesis of the purine, guanosine monophosphate (GMP), from inosine monophosphate (IMP) (Kimoloi, 2018). Such nucleotide imbalances might especially become exacerbated in OB which displays continuous neurogenesis. While imbalanced nucleotide pools and folate-dependent biosynthetic pathways have not explicitly been associated with Leigh syndrome phenotypes, other mitochondrial disease studies have suggested that it might be a major contributor to the mitochondrial disease progression in affected tissues (Bao *et al.*, 2016; Nikkanen *et al.*, 2016).

6.5.1.8 Greater metabolic dysregulation of cell signalling pathways

The direct neurotoxic effects of some metabolites that accumulated in the neurodegeneration-prone brain regions and/or their impaired metabolism, might induce neuronal vulnerability to degeneration by affecting cellular signalling pathways. For instance, the neurodegeneration-prone brain regions exhibited more pronounced accumulation of mTOR activating amino acids, such as BCAAs (Section 6.4.2.1) and arginine (Section 6.4.2.3) (Boulton *et al.*, 2013; Zheng *et al.*, 2016a; Bifari & Nisoli, 2017; Griffin & Bradshaw, 2017; Arany & Neinstadt, 2018). These regions also seemingly displayed greater perturbations in other mTOR regulators, such as redox status (e.g. Section 6.4.2.1 to Section 6.4.2.7 and Section 6.5.1) and oxidative stress (Section 6.4.2.4 and Section 6.5.1) (Krug *et al.*, 2014; Bao *et al.*, 2016; Ben-Sahra *et al.*, 2016; Karuppagounder *et al.*, 2016; Khan *et al.*, 2017; Kimoloi, 2018). In accordance with these findings, previous studies proposed a role of aberrant activation of the mTOR signalling pathway in the neurodegeneration of *Ndufs4* KO mice.

Additionally, the more noticeable disturbances in carbohydrate metabolism (Section 6.4.2.6) and lipid metabolism (Section 6.4.2.7) of the neurodegeneration-prone brain regions could induce neurodegeneration. These metabolic perturbations may result in dysregulated cellular signalling in glial cells (Liu *et al.*, 2017; Ghosh *et al.*, 2018) and lipid-sensing transcription factors; such as peroxisome proliferator-activated receptor (PPAR) transcription factors and sterol regulatory element binding protein (SREBP) (Ntambi *et al.*, 2002; Hall *et al.*, 2008; Clarke *et al.*, 2013; Liu *et al.*, 2015). Aberrant PPAR pathway signalling has the potential to trigger global metabolic perturbations, inflammation and oxidative damage (Hall *et al.*, 2008; Nakamura *et al.*, 2014; D'Angelo *et al.*, 2018). This pathway has been also been considered as a potential therapeutic target in RC deficiency and neurodegeneration (Hall *et al.*, 2008; Falk *et al.*, 2011; Clarke *et al.*, 2013; Corona & Duchon, 2016; Chen *et al.*, 2018a; D'Angelo *et al.*, 2018).

In addition to impeding many redox-dependent reactions, apparently the greater perturbation in the NAD⁺/NADH ratio (e.g. Section 6.4.2.1 to Section 6.4.2.7 and Section 6.5.1) can inhibit cellular signalling enzymes such as SIRT6 and PARPs. These enzymes utilise NAD⁺ as a primary substrate to regulate metabolism, energy homeostasis, antioxidant defence, calcium homeostasis, apoptosis, transcription, inflammation and DNA damage repair (Owens *et al.*, 2013; Verdin, 2015; Goodman *et al.*, 2018). In support, the less dramatic decreases in glutamic acid levels (Section 6.4.2.4) and more pronounced perturbations in glycolysis and lactic acid levels (Section 6.4.2.6) in the neurodegeneration-prone brain regions corresponded with the signs of decreased SIRT3 activity, and subsequently increased activation of HIF-1 α (Lee *et al.*, 2019). Moreover, the effects of NAD⁺ depletion might be aggravated in the neurodegeneration-prone brain regions if PARPs become activated due to greater oxidative DNA damage (Section 6.5.1.5), and/or in neurons which have low expression of the rate-limiting factor in the NAD⁺ salvage pathway, nicotinamide phosphoribosyl transferase (NAMPT) (Verdin, 2015).

The greater disturbance in antioxidant homeostasis of the neurodegeneration-prone brain regions (Section 6.4.2.4 and Section 6.5.1) has the potential to induce neurodegeneration by modulating epigenetic alterations, redox-sensitive proteins, cell death pathways, inflammation, hypoxia signalling, DNA damage response and activation of mTORC1 (Handy & Loscalzo, 2012; Shaughnessy *et al.*, 2014; Holzerová & Prokisch, 2015; Morris & Berk, 2015; Vasava & Mashiyava, 2016; Ye *et al.*, 2016). Lastly, ATP and acetyl-CoA levels, which might be more pronouncedly perturbed in the neurodegeneration-prone brain regions (see Section 6.5.1.1 to Section 6.5.1.3 and Section 6.4.2.7), are co-substrates required for various transcriptional and epigenetic processes (Shaughnessy *et al.*, 2014).

6.5.1.9 Aberrant activation or dysregulation of glial cells

Recall that the presence of activated glial cells are considered to be a major contributing factor in neurodegeneration in Leigh syndrome patients and in *Ndufs4* KO mice (Quintana *et al.*, 2010). Some metabolomic perturbations unique to or more pronounced in the neurodegeneration-prone brain regions, such as altered antioxidant metabolism (Section 6.4.1.2 and Section 6.4.2.4), diminished OXPHOS (Section 6.5.1.2) as well as increased glucose levels, glycolysis (Section 6.4.2.6) and NADH levels (see Section 6.4.2.1 to Section 6.4.2.7 and Section 6.5.1), can activate and/or interfere with microglial inflammatory responses, causing secondary neuronal injury (Owens *et al.*, 2013; Ye *et al.*, 2016; Angelini & Di Stadio, 2018; Ghosh *et al.*, 2018). Furthermore, the more pronouncedly elevated levels of BCAAs (Section 6.4.2.1) can augment microglial phagocytotic activity and free radical production while simultaneously impairing neuroprotective functions (De Simone *et al.*, 2013).

Microglial activation, can also trigger the activation of astrocytes and vice versa, causing progressive damage to surrounding tissue and neurons when persistently activated (Block *et al.*, 2007; Rose *et al.*, 2017; Ignatenko *et al.*, 2018). In addition, more astrocytes can become activated in response to a more severe RC deficiency (Bolaños *et al.*, 2010). A greater perturbation in the energy metabolic pathways of glial cells can also alter their neuroprotective functions. This can ultimately impede or dysregulate neuronal nutrient supply, the maintenance of neurotransmitter homeostasis, shuttling mechanisms, the provision of neuronal antioxidant or glutathione precursors, as well as the oxidation of potentially damaging peroxidated lipids (Vásquez *et al.*, 2001; Prabakaran *et al.*, 2004; Kanunnikova, 2012; Lei *et al.*, 2014; Panov *et al.*, 2014; Mason *et al.*, 2015; Schreiner *et al.*, 2015; Cooper & Jeitner, 2016; Lopez-Fabuel *et al.*, 2016; Camandola & Mattson, 2017; Griffin & Bradshaw, 2017; Liu *et al.*, 2017; Rose *et al.*, 2017; Yudkoff, 2017; Cabirol-Pol *et al.*, 2018). Failure of these functions could exacerbate an energy deficit and oxidative stress. Thus, the more pronounced metabolic perturbations in the neurodegeneration-prone brain regions could persistently activate and/or dysregulate glial cells to be less neuroprotective and to produce more neurotoxic factors. This might contribute to the progressive neuronal cell death, necrosis and damage to surrounding vasculature in the *Ndufs4* KO mice.

6.5.1.10 Aberrant inter-cellular signalling and neurotransmitter homeostasis

The pronounced metabolic perturbations in the neurodegeneration-prone brain regions can individually or collectively disturb inter-cellular signalling and neurotransmitter homeostasis to such a degree that it might induce neuronal death. This could for example, include the disturbances in central carbon metabolism (i.e., glycolysis, OXPHOS and PPP; see Section 6.4.2.6 and Section 6.5.1.2) and lipid metabolism (Section 6.4.2.7) and the perturbations in the levels of neurotransmitters, such as aspartic acid and glutamic acid (Section 6.4.2.4) (Tracey *et al.*, 2018). The latter can disturb the ratio of excitatory and inhibitory processes and/or trigger excitotoxicity which can cause neuronal injury (Kanunnikova, 2012; Lei *et al.*, 2014).

6.5.2 The potential role of inherent metabolic specificity in region-specific neurodegeneration

There is a plethora of inherent brain region-specific factors that could also mediate the differential metabolic profiles between the neurodegeneration-prone and -resilient brain regions of the *Ndufs4* KO mice (Dubinsky, 2009; Koopman *et al.*, 2010). Some components relevant to the main biochemical and metabolomics findings that could contribute to either the graded metabolic response or unique metabolic alterations, will briefly be mentioned.

6.5.2.1 Inherent regional differences related to CI activity and/or OXPHOS control

The biochemical (Section 5.2.2) and metabolomics (Section 6.5.1) data of the *Ndufs4* KO brain regions suggested that brain regional vulnerability could be related to regional differences in maximal residual CI activity. In other words, the more vulnerable brain regions have a lower residual CI activity. Previous studies have excluded regional differences in CI stability (Bird *et al.*, 2014; Kayser *et al.*, 2016), in isolated CI activity (Bird *et al.*, 2014) and in CI gene expression (Wirtz & Schuelke, 2011) as major factors in regional neurodegeneration in a CI deficiency. However, differences in the threshold of CI-inhibition or -deficiency (Leong *et al.*, 2012); in the molar ratios of components of the OXPHOS system (Koopman *et al.*, 2010), especially concerning CI, UQ and CIII; and their association into higher order super-complexes (García-Corzo *et al.*, 2012; Spinazzi *et al.*, 2018), might play a role. Furthermore, the direct interaction of CI with enzymes that, when deficient also lead to the development of a Leigh syndrome-like phenotype, might also differ among the neurodegeneration-prone and -resilient brain regions. This includes the enzymes in BCAA catabolism and fatty acid oxidation (Peters *et al.*, 2014; Nsiah-Sefaa & McKenzie, 2016; Sharpe & McKenzie, 2018; Uchino *et al.*, 2019), as well as other NADH dehydrogenases (Sharpe & McKenzie, 2018). This is plausible given that these metabolic pathways were more pronouncedly affected in the neurodegeneration-prone brain regions than in the AC (Section 6.4.2.1 and Section 6.4.2.7).

6.5.2.2 Inherent regional differences related to NADH oxidation and/or production

Factors other than a lower residual CI activity can also lead to the presumably lowered NAD⁺/NADH ratio in the neurodegeneration-prone brain regions (see Section 6.4.2.1 to Section 6.4.2.3 and Section 6.5.1). This might for instance include regional differences in the expression and regulation of NADH-oxidising mechanisms and NADH-producing pathways together with the relative contribution and properties of their constituents. For example, the NADH-oxidising proline cycle (Section 6.4.2.3) and GlyPS (Section 6.4.2.6) that were affected by the *Ndufs4* KO, produce less energy and more ROS in comparison with the MAS (Wyse & Netto, 2011; Martano *et al.*, 2016; Cappelletti *et al.*, 2018). Whereas NADH diaphorases might limit the availability of endogenous ubiquinones (Kiss *et al.*, 2014). In this light, the more resilient brain regions might have superior NADH-oxidation mechanisms. On the other hand, the NADH-producing pathways in the neurodegeneration-prone brain regions might be regulated in a way that exacerbates the disturbance of redox balance in a CI deficiency. Another contributing factor might be the relative distribution of NAD⁺ pools in the different brain regions under normal and CI-deficient states. This is because compartmentalisation ensures different ratios of NAD⁺/NADH within organelles and cells that can affect the threshold at which redox-dependent reactions become affected (Owens *et al.*, 2013; Goodman *et al.*, 2018).

6.5.2.3 Inherent regional differences related to antioxidant defence and/or production of reactive species

In a similar manner, the more pronounced alterations in antioxidant homeostasis of the neurodegeneration-prone brain regions (refer to Section 6.4.1.2 and Section 6.4.2.4) might be associated with differential expression and regulation of antioxidant defence, metabolic pathways that could contribute to the production of reactive species, and/or the cellular structures susceptible to oxidative damage (Dubinsky, 2009). As an example, the content of uric acid and carnosine, which function as free radical scavengers and have antioxidant and neuroprotective functions, has been shown to be significantly higher in the AC than in other brain regions (Ivanisevic *et al.*, 2014). Whereas heavy metals that are prone to exacerbate the production of reactive species, are abundant in the basal ganglia (Dubinsky, 2009; Lake *et al.*, 2015). This is one of the brain regions that is often affected in Leigh syndrome.

6.5.2.4 Inherent regional differences related to metabolic flexibility and/or metabolic switches

The metabolomics findings suggested that regional vulnerability to neurodegeneration might be related to regional differences in metabolic flexibility (Section 6.4.2.3 and Section 6.4.2.8). This refers to the expression, regulation and requirements of various metabolic pathways that determine the ability of cells to “respond or adapt to conditional changes in metabolic demand” (Goodpaster & Sparks, 2017). This in turn, goes hand in hand with the cellular composition of a brain region (Dubinsky, 2009; Sauerbeck *et al.*, 2011; Rose *et al.*, 2017; Kleinridders *et al.*, 2018) as well as regional differences in substrate availability (Dubinsky, 2009; Kleinridders *et al.*, 2018). Important is that previous studies suggested that the neuron:glia ratio in the relevant brain regions does not account for the regional vulnerability to a CI deficiency (Azevedo *et al.*, 2009; Sauerbeck *et al.*, 2011; Lent *et al.*, 2012). However, the metabolomics’ findings showed regional vulnerability and that especially amino acid metabolism in the neurodegeneration-prone brain regions was more severely perturbed than in the resilient AC (Section 6.4.2.1 to Section 6.4.2.4). A previous study has shown that the CB synaptosomes (neuronal mitochondria) had a limited reserve glycolytic capacity and relied much more on amino acids and polyamines under stress conditions, compared to other brain regions such as the cortex, hippocampus and striatum (Lee *et al.*, 2013). Consequently, it can be proposed that a perturbation in amino acid metabolism might be more detrimental to neurons in this region. Also, as mentioned previously, the glutamatergic- and GABAergic-neurons, which are abundant in the affected areas of the neurodegeneration-prone brain regions (Bolea 2019), might be more vulnerable to the persistent fuelling of the TCA cycle in response to the *Ndufs4* KO (refer to Section 6.5.1.2).

The metabolic alterations in the *Ndufs4* KO brain regions also suggested that regional differences related to arginine- (Section 6.4.2.3) and 1C-metabolism (Section 6.4.2.8) might correlate with region-specific neurodegeneration. In accordance, the expression and activities of enzymes related to arginine metabolism (Yu *et al.*, 2001; Liu *et al.*, 2003; Liu *et al.*, 2004; Jing *et al.*, 2013; Peters *et al.*, 2013) and 1C-metabolism (Robert *et al.*, 2003; Sontag *et al.*, 2008; Bronowicka-Adamska *et al.*, 2011) varies among brain regions. Notably, the activity of arginase, the enzyme that hydrolyses arginine to urea and ornithine, has been shown to be consistently high in the BST (Yu *et al.*, 2001), but increases with age in the frontal cortex and in regions of the hippocampus (Liu *et al.*, 2003; Liu *et al.*, 2004; Jing *et al.*, 2013). Furthermore, the levels of cystathionine, cysteine and the antioxidant glutathione have been found to be distinctly different in the human CB than in the hypothalamus, thalamus, subcortical nuclei, hippocampus, frontal cortex and parietal cortex (Bronowicka-Adamska *et al.*, 2011). In general, the expression of cystathionine β -synthase (CBS), the enzyme that catalyses the first step of the trans-sulfuration pathway, was also found to be particularly high in the CB, OB and hippocampus (Robert *et al.*, 2003).

Lastly, developmental or metabolic switches might also predispose certain brain regions to degeneration in a CI deficiency. The neuropathology in *Ndufs4* KO mice is triggered at PN35. This could either be due to the accumulation of detrimental effects that reaches a certain threshold (Quintana *et al.*, 2010; Liu *et al.*, 2015; Liu *et al.*, 2017), and/or perhaps certain metabolic events or “switches” that occurred at a certain time point (Mattson *et al.*, 2018). The metabolomics data provided evidence to support a role of progressive detrimental processes, such as bio-energetic decline (Section 6.5.1.1 to Section 6.5.1.3), progressive glial activation (Section 6.5.1.9) and/or accumulation of ROS (Section 6.5.1.5) and NADH (Section 6.5.1.1 and Section 6.5.1.4). In accordance, these factors have also been suggested by previous studies (Quintana *et al.*, 2010; Liu *et al.*, 2015; Liu *et al.*, 2017). In addition, these factors might be exacerbated in the neurodegeneration-prone brain regions due to the metabolic changes initiated after weaning.

During brain development, ketone bodies obtained from the maternal milk are crucial for energy and biosynthesis of amino acids and lipids (Nehlig, 2004; Camandola & Mattson, 2017). After weaning (PN21 for rodents) however, the brain progressively switches to glucose metabolism at rates that show regional heterogeneity related to the acquisition of sensory-motor functions (Nehlig, 2004). If the capacity for glucose metabolism is different or limited in the neurodegeneration-prone brain regions (Lee *et al.*, 2013; Goyal *et al.*, 2014), this “metabolic switch” from ketones to glucose as primary energy source during an energy crisis, might infer susceptibility to neuronal death and/or glial activation (Baertling *et al.*, 2014; Parikh

et al., 2015). In accordance, a ketotic state has been shown to spare glucose for NADPH synthesis, suppress microglial activation and promote neuroprotective microglia phenotypes (Nehlig, 2004; Theunissen *et al.*, 2017; Ghosh *et al.*, 2018). Moreover, milk contains various forms of vitamin B3 that have been shown to increase intracellular NAD⁺ levels and be neuroprotective (Verdin, 2015; Ummarino *et al.*, 2017). The latter might suppress the perturbation in redox balance in the brain regions until weaning.

6.5.3 The cumulative metabolic effects of several mechanisms might underlie region-specific neurodegeneration

Overall, the metabolic alterations in the KO brain regions could be related to various factors that might render neurons in the BST, CB and OB more vulnerable to degeneration in a CI deficiency, than the neurons in the AC. It is likely that cumulative effects of a few mechanisms in the neurodegeneration-prone brain regions trigger the regional neurodegeneration. This is because regional-specificity: a) might be mediated at different levels (effects of graded cellular consequences and inherent metabolic specificity); and b) entail different aspects (energy metabolism, redox balance, antioxidant defence and metabolite induced neurotoxicity). It is important to mention that over time; the cumulative effects can ultimately reach a certain detrimental threshold in the neurodegeneration-prone brain regions that triggers neurodegenerative processes. Figure 6.14 summarises this proposed mechanism. Notably, regional differences in redox balance (NAD⁺/NADH ratio) might be a key player in inducing region-specific neurodegeneration.

One can speculate that the more severe effects of the *Ndufs4* KO on the activity of CI in the neurodegeneration-prone brain regions (Section 5.2.2) aggravated the compensatory responses in classic and non-classic metabolic pathways. While initially beneficial in a CI deficiency, some of the adaptive metabolic pathways (which might be inherently region-specific) seemed sub-optimal and unsustainable in the long run, potentially entailing maladaptive features. A CI deficiency causes chronic imbalances, especially a lowered NAD⁺/NADH ratio and increased ROS production, which can impair these adaptive mechanisms. In turn, the adaptive mechanisms have the potential to exacerbate these metabolic imbalances in CI-deficient cells. In this way, chronic activation of sub-optimal compensatory metabolic pathways might activate a vicious detrimental cycle that ultimately triggered neurotoxicity via secondary mechanisms. These might for example include an energy deficiency, oxidative stress or damage, accumulation of neurotoxic metabolites and other mechanisms related to dysregulated cellular metabolism.

This phenomenon of sub-optimal adaptation is also supported by previous studies of OXPHOS deficiencies which observed similar metabolic alterations (Smeitink *et al.*, 2006; Falk *et al.*, 2008; Koenig, 2008; Leong *et al.*, 2012; Kiss *et al.*, 2014; Parikh *et al.*, 2015; Bao *et al.*, 2016; Esterhuizen *et al.*, 2017; Shuvalov *et al.*, 2017; Cabirol-Pol *et al.*, 2018; Lozoya *et al.*, 2018). These alterations were ascribed to the disruption of activated compensatory metabolic responses by the chronic imbalances brought about by the OXPHOS deficiency.

Notably, the findings also corresponded with the hypothetical mechanism of neuronal cell death in *Ndufs4* KO mice as Quintana *et al.* (2010) proposed. It was hypothesised that cellular signals caused by CI dysfunction could activate glial cells. This in turn, leads to oxidative stress, cytokine release by microglia, and activation of the extrinsic apoptotic pathway in neurons. The insufficient ATP levels in neurons then induce necrotic cell death. It could be added that the differential metabolic alterations identified in this study could reflect these “cellular signals”; explain the nature of the energy deficit in neurons; and perhaps also the mechanism governing the cell-autonomous death of glutamatergic and GABAergic neurons.

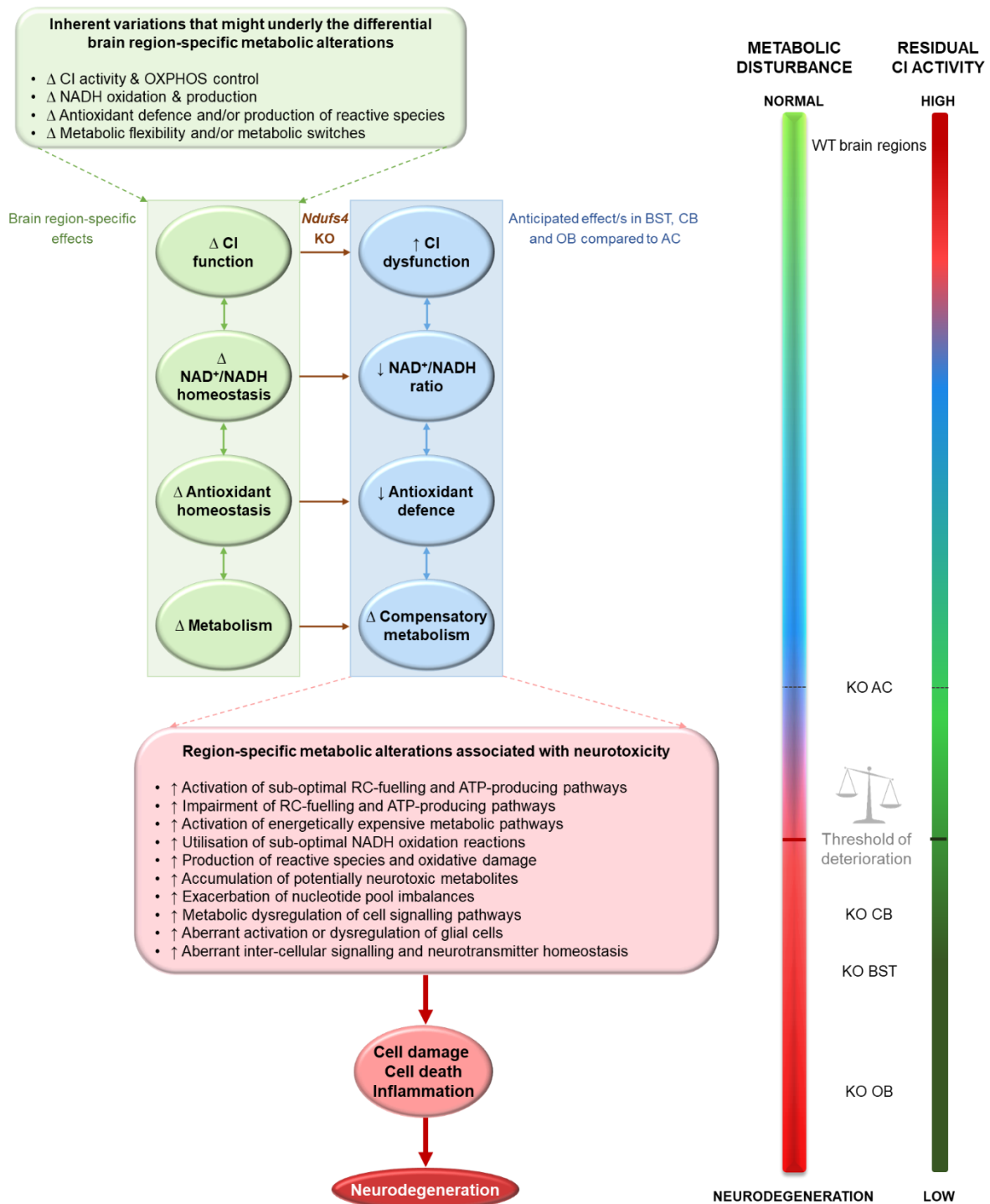


Figure 6.14: Potential mechanisms underlying brain region-specific metabolic alterations of *Ndufs4* knockout mice.

Potential inherent factors that might drive the brain region-specific metabolic alterations differentiating between the more resilient AC and the neurodegeneration-prone brain regions (BST, CB and OB) are shown at the top in green. Mechanisms potentially responsible for the vulnerability of the knockout neurodegeneration-prone brain regions, as revealed by the metabolic perturbations and biochemical investigation, are shown in blue. Potential mechanisms by which the differential or graded metabolic perturbations could hypothetically contribute to neurodegeneration are shown in red. Two-way arrows depict an interdependence of events, e.g. a more pronounced CI deficiency might also cause depletion of antioxidant defence via direct production of reactive species, which in turn could damage CI. Dashed

arrows indicate that the collective or individual effects of the preceding shape/s, from which the arrows originate, could contribute to or exacerbate the changes listed in the succeeding shape/s. Symbols within shapes respectively indicate a decrease (↓), an increase (↑), brain regional variability (Δ) and alteration (▲). Bars on the right illustrate the gradient-effect of the *Ndufs4* KO on the metabolic profiles and residual CI activity in the investigated brain regions. *Other abbreviations: ATP, adenosine triphosphate; CI, complex I; NAD⁺/NADH, oxidised/reduced form of nicotinamide adenine dinucleotide; OXPHOS, oxidative phosphorylation; RC, respiratory chain.*

6.6 Summary of metabolomics investigation on *Ndufs4* knockout brain regions

The *Ndufs4* KO had a significant and wide-ranging effect, affecting multiple metabolic pathways in the investigated brain regions. The discriminatory metabolites that were commonly altered among all investigated brain regions, reflected a general or common *in vivo* effect of the CI deficiency. This was marked by perturbations in energy-, redox-, and antioxidant-metabolism. It was also shown that the regional vulnerability to neurodegeneration might be related to graded metabolic perturbations across the investigated brain regions. It seemed that these perturbations reached a detrimental threshold in the neurodegeneration-prone brain regions, especially in the OB, that triggered maladaptive and potentially neurotoxic features. The metabolic perturbations in all brain regions conveyed a global picture which suggested that a perturbed redox balance might play a major part in the gradual metabolic dysfunction. The fact that the brain regions displayed a graded decline in CI activity that correlated with the severity of neurodegeneration, supported this notion. Then again, the metabolic perturbations also revealed potential brain region-specific inherent factors that might exacerbate the detrimental metabolic consequences of a CI deficiency in the neurodegeneration-prone brain regions. Together, these findings can guide future studies that aim to elucidate the exact underlying pathological mechanisms of the *Ndufs4* KO, or that aims to investigate potential therapeutic targets.

The metabolomics investigation also revealed that metabolic alterations such as the accumulation of BCAAs, proline, lysine-derived pipecolic acid and lactic acid could potentially be used to monitor redox balance and/or progression of neurodegeneration. Therefore, these metabolic alterations might be considered as metabolic biomarkers of a CI deficiency. Finally, the perturbations in arginine metabolism of the *Ndufs4* KO brain regions, especially with regard to citrulline, could be explored in future studies to alleviate pathological symptoms such as seizures.

CHAPTER 7: SUMMARY, CONCLUSIONS AND RECOMMENDATIONS

7.1 Introduction

Mitochondria play a vital role in a plethora of cellular functions. Mitochondrial dysfunction has been widely recognised in the pathology of numerous common metabolic and degenerative diseases. The clinically heterogeneous group of disorders known as primary mitochondrial disease (MD), are caused by a genetically based dysfunction of the oxidative phosphorylation (OXPHOS) system. An isolated complex I (CI) deficiency, often due to a mutation in the nuclear coded *Ndufs4* gene, is the cause of the majority of childhood-onset MDs. Patients with a CI deficiency typically present with Leigh syndrome which is characterised by progressive focal neurodegeneration and premature death. To date, therapeutic strategies are unsatisfactory. This study was therefore driven by the recognised necessity to obtain a better understanding of the neuropathological consequences of an isolated CI deficiency using the whole-body (WB) *Ndufs4* knockout (KO) mouse model (Kruse *et al.*, 2008). The aim was to combine biochemical (Chapter 5) and multi-platform metabolomics (Chapter 6) strategies to determine the *in vivo* effect of the *Ndufs4* KO on neurodegeneration-prone and -resilient brain regions from *Ndufs4* KO mice; and to investigate potential correlations with neurodegeneration. To this end, the neurodegeneration-prone brainstem (BST), cerebellum (CB) and olfactory bulbs (OB); as well as the resilient anterior cortex (AC) of WB *Ndufs4* KO mice were investigated. This chapter summarises the main results. Also, conclusions that were drawn according to the formulated objectives (Chapter 3) are presented. This chapter concludes with a few recommendations for prospective studies.

7.2 Objective 1: Verify the genotypes of *Ndufs4* wild-type and knockout mice

As a quality control measure, the genotype of each mouse from which brain tissues were sourced, was re-confirmed prior to experimentation. Genotyping was carried out on the tail tips collected simultaneously with the brain tissues. Conventional PCR was used to determine the absence or presence of exon 2 of the *Ndufs4* gene (APPENDIX A). From these results, the genotypes of 35 wild-type (WT) and 33 KO mice were successfully verified. It was then concluded that the corresponding brain region tissues could be used in subsequent experiments to accurately represent the respective genotype groups.

7.3 Objective 2: Investigate the biochemical activity of individual respiratory chain complexes I to IV in the selected brain regions

The second main objective of this study was formulated to address the lack of information regarding the activities of individual respiratory chain (RC) complexes in the neurodegeneration-prone and -resilient brain regions of *Ndufs4* WT and KO mice. To achieve this objective, the relevant methods for spectrophotometric determination of citrate synthase (CS) and RC complex activities had to be standardised (Objective 2.1). This was required to ensure applicability on the supernatants obtained from the tissue homogenates of the various mouse brain regions. Minor modifications to the concentrations of the supernatants (obtained from homogenised tissues) analysed per well were sufficient to ensure linear ($R^2 > 0.99$) quantification while accommodating for slight experimental or biological variation (APPENDIX C). It was thus concluded that the standardised methods were sufficiently reliable, and that the subsequent experimental data would accurately reflect biological differences. In addition, the skills gained during method standardisation ensured that analyses could be conducted with better precision.

The standardised methods were subsequently used to determine the maximal activities of CS and the individual mitochondrial RC complexes in the selected brain regions of *Ndufs4* KO (n = 12) and WT (n = 10) mice. This was to investigate whether brain regional differences could be correlated with the regional vulnerability to neurodegeneration (Objective 2.2 to Objective 2.4). Consequently, the results were evaluated on two levels to determine: 1) brain region-specific differences in the effect of the KO on the maximal enzyme activities; as well as 2) brain region-specific differences in maximal enzyme activities among brain regions within a genotype.

The *Ndufs4* KO had variable effects on the maximal activities of CS and the respective RC complexes of the investigated brain regions. As a result, the reliability of CS as a mitochondrial marker in the KO brain regions was deemed questionable. Thus, main conclusions were drawn from protein-normalised data. As expected, the *Ndufs4* KO significantly lowered CI activity (between 60% and 85%). This suggested that CI-related functions had to be severely impaired across brain regions. Surprisingly, the neurodegeneration-prone brain regions displayed notably lower residual CI activity than the resilient AC. Moreover, the OB, which is the first and most affected brain region in *Ndufs4* KO mice (Quintana *et al.*, 2010), displayed the lowest residual CI activity. The OB also exhibited dramatically lower absolute CI- and CIII-activity compared to other brain regions of the same genotype. These results suggested a causal relationship between lower residual CI activity and vulnerability to neurodegeneration.

The findings was in contrast to a previous study which suggested that tissue vulnerability in *Ndufs4* KO mice did not correlate with residual CI activity (Calvaruso *et al.*, 2011).

No clear correlation could be identified between region-specific neurodegeneration and the effect of the KO on the activities of CII, CIII or CIV. However, the WT neurodegeneration-prone brain regions displayed significantly higher activities of CS and RC complexes per tissue mass (except in the case of CI- and CIII-activities of the OB). This indicated a greater dependency on OXPHOS to meet cellular requirements and thus, a greater vulnerability to an OXPHOS deficiency. Compared to the resilient AC, the respective neurodegeneration-prone brain regions also displayed a notably lower ratio of CIII activity and higher ratio of CIV activity, relative to the other RC complexes within that region.

Overall, it was concluded that the vulnerability of the BST, CB and OB to neurodegeneration in a CI deficiency might be linked to: 1) a lower residual activity of CI; 2) a greater dependency on OXPHOS to meet cellular requirements; and/or 3) brain regional differences in the relative activities and/or organisation of RC enzymes in the OXPHOS system, especially concerning CIII and CIV. The latter was consistent with previous reports which have proposed: i) a correlation between residual CI activity and super-complex formation with CIII (Calvaruso *et al.*, 2011); ii) a concurrent deficiency in CIII when *NDUFS4* is absent (Budde *et al.*, 2000; Ugalde *et al.*, 2004); and iii) a frequent involvement of CIII and CIV-deficiencies in causing the Leigh syndrome phenotype (Lake *et al.*, 2015; Chen *et al.*, 2018a; Spinazzi *et al.*, 2018). In other words, it seemed that the “same” *Ndufs4* KO in all brain regions had brain region-specific effects due to inherent differences related to the OXPHOS system. The more prominent relative decrease in CI activity in the neurodegeneration-prone brain regions, could then trigger or exacerbate detrimental cellular processes, especially if CI activity had been decreased beyond a threshold of deficiency, which ultimately induce neurodegeneration.

7.4 Objective 3: Investigate the metabolic profiles of the selected brain regions using a multi-platform metabolomics approach

The third main objective of this study was formulated due to a recognised necessity to investigate the *in vivo* metabolic profiles of the neurodegeneration-prone and -resilient brain regions of *Ndufs4* KO mice with an explorative, hypothesis-generating, multi-platform metabolomics approach. This objective was achieved by first standardising the previously developed laboratory metabolomics methods (Objective 3.1 and Objective 3.2) for applicability on the metabolite extracts from the selected mouse brain regions (APPENDIX D). Slight modifications to on-column sample and internal standard (IS) concentrations were sufficient to enable reliable quantification of the relative abundances of the extracted compounds.

The identities of the compounds targeted by the multiple reaction monitoring (MRM) conditions of the previously developed LC-MS/MS method were verified. The addition of appropriate time segments to the LC-MS/MS acquisition method increased the analytical sensitivity and precision. Repeated analysis of replicate brain region samples, with both analytical methods, demonstrated that the instrument-, intra- and inter-batch precision of the standardised methods were well within the generally accepted criteria for untargeted and semi-targeted metabolomics analytical methods, respectively. As expected, the semi-targeted LC-MS/MS data sets displayed better precision than the untargeted GC-TOF data sets. Even though analyses of the limited OB sample volumes resulted in less precision compared to the analyses of other brain region samples, the data still displayed sufficient precision. These results also demonstrated that analyst precision was acceptable. It was therefore concluded that the standardised methods were sufficiently repeatable to generate good quality data.

The standardised metabolomics methods were subsequently used to measure the abundances of compounds in the selected brain regions of *Ndufs4* KO (n =21) and WT (n =25) mice to investigate whether brain regional metabolic differences could be correlated with the regional vulnerability to neurodegeneration (Objective 3.3 to Objective 3.6). Even though not a specific objective of this study, it was considered good practice to evaluate the quality of the final experimental metabolomics data sets (APPENDIX F) prior to statistical determination of discriminatory metabolites. By using the data of quality control (QC) samples that were analysed intermittently with the biological samples, it was demonstrated that the data displayed sufficient precision without profound batch effects. Consequently, the data was deemed reliable and of good quality according to standards outlined in the literature.

Visualisation of the experimental metabolic data using principle component analysis (PCA) indicated that the *Ndufs4* KO had a significant and widespread metabolic effect on all investigated brain regions. This was true even in the resilient AC which has been considered to be relatively resilient to degeneration. The most prominent effect was observed in the OB, in accordance with the biochemical findings. It was demonstrated that by combining the GC-TOF and LC-MS/MS statistically determined differential metabolites, the power of the data sets to discriminate between the genotype groups could be greatly increased. These findings underscored the value of a multi-platform metabolomics approach and statistical identification of differential metabolites.

Several metabolic pathways were prominently affected in the KO brain regions, including amino acid-, carbohydrate-, lipid-, TCA cycle-, and one-carbon (1C)-metabolism. The involvement of various metabolic pathways or a global metabolic perturbation was consistent with the complex and extensive metabolic effects expected from an OXPHOS deficiency.

Furthermore, the results suggested that energy metabolism, especially amino acid metabolism, of the brain regions was particularly sensitive to the effects of the *Ndufs4* KO, even though the possibility existed that the analytical methods were inherently biased towards detecting amino acid-related intermediates.

Important discriminatory metabolites with levels that statistically and practically differ between corresponding KO and WT mouse brain regions were subsequently determined (Objective 3.5). This was followed by the identification of the discriminatory metabolites that were common and unique between the neurodegeneration-prone and -resilient brain regions. The commonly altered metabolites indicated that the KO brain regions shared general disturbances in energy-, redox- and antioxidant-related metabolic pathways. These findings were consistent with the role of CI in metabolism and with previous reports of CI deficiencies. It therefore seemed that the global metabolic perturbations in the *Ndufs4* KO brain regions could reflect a compensatory cellular response in classic and non-classic metabolic pathways to counteract or alleviate the cellular consequences of a CI deficiency.

The metabolic data were then evaluated and interpreted regarding potential association with brain region-specific neurodegeneration (Objective 3.6). Closer inspection of the discriminatory metabolic perturbations revealed that a few metabolites related to arginine- and 1C-metabolism (carbamic acid, creatinine, cysteine, methylindole, methionine and uridine monophosphate) were uniquely altered in the more resilient AC. These results demonstrated that differential metabolic responses to the *Ndufs4* KO might contribute to the regional neurodegeneration in a CI deficiency. Additionally, the metabolic data demonstrated that the severity of the shared or common metabolic disturbances could notably differentiate between the neurodegeneration-prone and -resilient brain regions. Some of the metabolic perturbations were more profound in the neurodegeneration-prone brain regions than in the AC. These included the disturbances in branched-chain amino acid (BCAA) and lysine catabolism; proline levels; pyroglutamic acid levels; propionylcarnitine levels; the levels of carbohydrate-related intermediates, including lactic acid; and in global lipid metabolism. Together, these findings implied that the neurodegeneration-prone brain regions had greater disturbances in: 1) the main energy producing metabolic pathways and in CI-bypassing reactions that are involved in fuelling the quinone (Q)-pool, the TCA cycle and CII; 2) mechanisms that maintain cellular redox status under conditions of perturbed redox balance (proline cycle and lactic acid production); and 3) antioxidant homeostasis. Thus, it seemed that the metabolic pathways that might compensate for the direct consequences of a CI deficiency (like decreased energy production, RC fuelling and NADH oxidation as well as increased ROS production) were more pronouncedly affected in the neurodegeneration-prone brain regions. Accordingly, the

perturbations in a few metabolic pathways reflected an impairment of one or more redox-sensitive reactions that was more prominent in the neurodegeneration-prone brain regions. These results implied that redox balance was more perturbed in the neurodegeneration-prone brain regions, consistent with the notion that these regions had lower residual activity of CI, the major consumer of cellular NADH, than the resilient AC. Conversely, a few metabolic perturbations were more dramatic in the resilient AC, such as the perturbations observed in the levels of aspartic acid, glutamic acid and glycerol-3-phosphate. These results suggested that the resilient AC might have more efficient utilisation of energy sources and of mechanisms that maintain the cytosolic NAD⁺/NADH ratio under physiological conditions, such as the malic acid-aspartic acid shuttle (MAS) and the glycerol-3-phosphate shuttle (GlyPS).

Taking all the findings into consideration, it seemed that the *Ndufs4* KO caused common disturbances in global metabolism across the brain regions. This was characterised by a gradient of severity which correlated with the severity of neurodegeneration. In other words, the more resilient AC with the highest residual CI activity and “less affected” metabolic profile was situated on the one end of a hypothetical spectrum. Then, BST and CB followed with lower residual CI activities and more pronouncedly affected metabolic profiles situated further towards the other end of the spectrum. Finally, the OB with the lowest residual CI activity and most severely affected metabolic profile was situated at the end of the spectrum furthest away from the AC. The notion of graded metabolic perturbations across brain regions was consistent with a previous study on Alzheimer’s disease patients (Xu *et al.*, 2016). The graded perturbations in the *Ndufs4* KO brain regions then presumably reached a detrimental threshold in the neurodegeneration-prone brain regions, especially in the OB, that triggered maladaptive and potentially neurotoxic features. For instance, by surveying the literature it could be demonstrated how the: 1) more decreased CI activity; 2) lower NAD⁺/NADH ratio; and 3) gradient of metabolic disturbances in the neurodegeneration-prone brain regions could potentially exert direct or indirect neurotoxic effects. These in turn, could individually or cumulatively further contribute to neurodegeneration and thus to the pathogenesis in *Ndufs4* KO mice.

Some of the neurotoxic effects of the graded metabolic perturbations in the neurodegeneration-prone brain regions were for instance associated with the exacerbation of an energy deficit. This could result from the more dramatic activation of sub-optimal RC-fuelling and ATP-producing pathways, greater impairment of classic and sub-optimal RC-fuelling and ATP-producing pathways, and/or activation of ATP-consuming cellular processes. Moreover, the more dramatic activation of sub-optimal metabolic pathways was also suggested to augment the disturbances in redox balance, the utilisation of sub-optimal

NADH-oxidation reactions, and the increased production of reactive species. Many of the accumulating metabolites were also shown to have direct neurotoxic properties. In addition, the more severe metabolic disturbances in the neurodegeneration-prone brain regions were shown to have the potential to aggravate nucleotide pool imbalances, dysregulate cell signalling pathways, cause aberrant activation or dysregulation of glial cells, as well as disturb inter-cellular signalling and neurotransmitter homeostasis.

A few inherent brain region-specific factors that could mediate the differential metabolic profiles were also considered. This was because these factors, together with their end-point neurotoxic effects, could potentially serve as therapeutic targets in prospective studies. The potential brain region-specific factors could be related to regional differences in: 1) CI activity and OXPHOS control (also in accordance with the biochemical findings); 2) NADH-oxidising and -producing processes; 3) ROS-scavenging or -producing processes; as well as 4) metabolic flexibility or the vulnerability of brain regions to metabolic switches. Together these findings could also provide some insight into the vulnerability of glutamatergic- and GABAergic neurons to degeneration when *NDUFS4* is absent. This is important as these neurons primarily drive the neuropathogenesis in *Ndufs4* KO mice.

Taking these factors into consideration, it seemed that the graded global metabolic perturbations in classic and non-classic compensatory metabolic pathways are unsustainable and sub-optimal in the long run. This is because they are susceptible to being impaired by the consequences of a CI deficiency and potentially entail maladaptive features. This notion was in accordance with previous reports on OXPHOS deficiencies. These studies also attributed similar metabolic alterations to a disturbance in compensatory metabolic responses due to chronic imbalances in energy status, redox status, ROS levels and/or metabolite levels (Smeitink *et al.*, 2006; Falk *et al.*, 2008; Koenig, 2008; Leong *et al.*, 2012; Kiss *et al.*, 2014; Parikh *et al.*, 2015; Bao *et al.*, 2016; Esterhuizen *et al.*, 2017; Shuvalov *et al.*, 2017; Cabiro-Pol *et al.*, 2018; Lozoya *et al.*, 2018). Accordingly, the greater relative CI dysfunction in the neurodegeneration-prone brain regions would activate these sub-optimal compensatory pathways more vigorously, while simultaneously exacerbating their maladaptive features or “side effects” which then ultimately triggers neurodegeneration.

It was therefore concluded that the regional vulnerability to neurodegeneration in *Ndufs4* KO mice and by extension, perhaps also in CI-deficient and/or Leigh syndrome patients, might be related to: 1) graded global metabolic perturbations that could compensate for CI dysfunction, but which were sub-optimal and reached a detrimental threshold in the neurodegeneration-prone brain regions; and/or 2) inherent regional specificity in metabolism. Further evaluation of the metabolic alterations additionally revealed that the accumulation of BCAAs, proline,

lysine-derived pipercolic acid as well as lactic acid could potentially be used as sensitive biomarkers for a perturbed redox balance and/or progression of neurodegeneration in a CI deficiency. Moreover, it was suggested that the perturbations in arginine metabolism, especially with regards to citrulline, should be explored in future studies as it might have played a role in the seizures of *Ndufs4* KO mice.

7.5 Final conclusions and recommendations

As stated in the title of this study, the selected brain regions of *Ndufs4* KO mice were investigated with a biochemical and metabolomics approach. The three main objectives of this study were attained by first verifying the genotypes of the experimental mice. Thereafter, the biochemical activity of individual RC complexes I to IV and the metabolic profiles of the selected brain regions of *Ndufs4* WT and KO mice were also investigated with standardised methods. It was hypothesised that regional differences in residual CI activity, OXPHOS requirements and organisation of CI within the OXPHOS system underlie the regional vulnerability to a CI deficiency. As a result, the *Ndufs4* KO caused graded global metabolic perturbations across all brain regions that are more prominent in the neurodegeneration-prone brain regions. It was further hypothesised that the metabolic disturbances might occur beyond a certain threshold in the neurodegeneration-prone brain regions. This then triggered several potential neurodegenerative processes. Consequently, the *in vivo* effect of the *Ndufs4* KO on the activity of the individual RC complexes and the metabolic profiles of the selected brain regions was successfully determined. Furthermore, potential correlations with neurodegeneration were identified, thereby successfully attaining the aim of this study. In addition, this study contributed to the standardisation of analytical techniques for applicability on mouse brain region tissues. This study also revealed potential pathogenic mechanisms, therapeutic targets as well as potential biomarkers for monitoring disease progression and therapeutic interventions. Thus, the methods and the results obtained during this study facilitated a better understanding of region-specific neurodegeneration in *Ndufs4* KO mice; and could aid and guide future experimental studies on the brain regions of *Ndufs4* KO mice and/or other mouse models.

To further facilitate the investigation on region-specific neurodegeneration in *Ndufs4* KO mice, prospective studies utilising validated, targeted metabolomics methods are required to confirm the preliminary metabolomics results and hypotheses generated in this study. By targeting the affected metabolic pathways, the validated methods could also be utilised to gain better understanding of the nature of the metabolic perturbations across brain regions. In addition, more information could be obtained by way of: 1) utilising alternative complimentary metabolomics techniques to increase metabolite coverage; 2) including more than one control

(neurodegeneration-resilient) brain region; 3) including female mice in experiments; and 4) conducting brain region-specific analyses at different time points of the disease.

Future studies can also focus on re-analysing the metabolomics data generated during this study. Such studies could maximise the extraction of relevant information and discovery of novel insights by using alternative strategies that were beyond the scope of this study. This can for example include investigating the less significantly altered metabolites or applying different data analysis pipelines, additional identification efforts and more complex multivariate analyses which consider the simultaneous contribution or interaction of multiple dependent variables (Long, 2013; Hervé *et al.*, 2018). Furthermore, the presumable correlation between the severity of a perturbed redox balance and region-specific neurodegeneration warrants the measurement of the relative ratios of NAD⁺/NADH across brain regions, and even in different brain cell types or organelles. In addition, the effects of the discriminatory metabolites in neuronal cell culture models should be studied to determine whether and which of the metabolic perturbations might contribute to neurodegeneration in *Ndufs4* KO mice.

With regard to the biochemical investigation, future work is warranted to elucidate the mechanism/s underlying the increased maximal CS activity observed in most KO brain regions. This will lead to a better understanding of how different brain regions respond to a CI deficiency. It would also be helpful to include additional or alternative markers of mitochondrial content (e.g. cardiolipin and voltage-dependent anion channels [VDAC]) in future studies on KO brain regions (Larsen *et al.*, 2012; Burtscher *et al.*, 2015). Furthermore, information on region-specific perturbations related to the Q-pool should be obtained. This can be done for example through measuring the combined function of CI/CIII and CII/CIII which were omitted in this study due to limited sample volumes (Spinazzi *et al.*, 2012; Spinazzi *et al.*, 2018). Importantly, the isolated maximal activities of RC enzymes did not necessarily reflect their absolute concentration, nor the flux through the RC enzymes as part of the OXPHOS system or the contribution of each RC enzyme to controlling OXPHOS function (coefficient of control) (Rossignol *et al.*, 2003; Benard *et al.*, 2006). Therefore, it is recommended that alternative or supplementary experimental techniques should be utilised to elucidate the causal relationship between these factors and regional vulnerability to neurodegeneration. This can be accomplished for example by way of monitoring metabolic effects and cell death in different brain regions or brain cells by titrating the effects of a CI deficiency with appropriate CI inhibitors. Furthermore, mitochondrial respiration or flux measurements in various brain regions can be carried out using high-resolution respirometry techniques together with different mitochondrial substrates that were identified as discriminatory metabolites during the metabolomics investigation. This might for example

include succinic acid precursors, α -ketoglutaric acid, glutamic acid and other Q-pool-fuelling substrates. Specific reagents can also be utilised to evaluate the sequential flow of electrons through the RC complexes within the OXPHOS system of *Ndufs4* KO mice compared to WT mice (Rogers *et al.*, 2011; Burtscher *et al.*, 2015). This can determine whether and how the changes in the maximal activities of individual RC enzymes affected the overall OXPHOS function.

While valuable information could be obtained from the biochemical and metabolomics approaches, the results of both these techniques are limited when trying to ascertain the exact mechanisms that underlie the significant alterations. For instance, the biochemical experimental procedures could not account for the effects of altered cellular conditions on the maximal activity or abundances of the RC complexes (Rossignol *et al.*, 2003; Dubinsky, 2009; Mirandola *et al.*, 2010). On the other hand, the metabolomics approach provided only a snapshot of metabolite levels which are actually the end-product and substrates of various dynamic processes (Griffin & Bradshaw, 2017). Therefore, future studies should focus on obtaining complementary information that more formally focusses on testing for causation by means of investigating the affected metabolic pathways. The associated enzymes should also be examined as well as the various OXPHOS components. An example in this regard involves the utilisation of a combination of enzyme activity assays, transcriptomic and proteomic techniques or perhaps isotope-assisted metabolic flux analyses (Wei *et al.*, 2017; Yang *et al.*, 2018). The latter measures the levels of metabolites implicated in a particular metabolic pathway over time. Furthermore, the heterogenous nature of the cellular composition of brain regions complicated the interpretation of the *in vivo* results. Especially when considering that the neurodegeneration-prone brain regions are characterised by the infiltration of glial cells. Considering this notion and the fact that cellular specificity might play a role in the region-specific neurodegeneration, future studies are advised to utilise experimental procedures that could evaluate cell-specific biochemical enzyme activities or metabolic profiles, or that take in to account the contribution of the different cells per brain region to the overall biochemical or metabolic picture.

In terms of therapeutic approaches, the findings in this study pointed towards at least two levels of therapeutic intervention, namely: 1) targeting inherent regional differences in OXPHOS structure, OXPHOS requirements, and constituent metabolic responses; and 2) counteracting or managing neurotoxic metabolic perturbations (disturbances in energy metabolism, redox balance, antioxidant defence, cellular regulation, altered levels of neurotoxic metabolites etc.). Future studies are therefore recommended to pursue a holistic approach that targets several aspects simultaneously. For instance, single- or multi-

component, multi-factorial therapeutic interventions that could perhaps support RC-fuelling via CI-bypassing sites directly or by recruiting CI-independent metabolic pathways. At the same time, future research could focus on therapies that also increase NAD⁺ levels, facilitate NADH oxidation in appropriate compartments, and scavenge excessive ROS. By this means, the accumulation of neurotoxic metabolites, oxidative stress, cellular dysregulation and cell death could ultimately be prevented. In addition, it is recommended that the monitoring of disease progression and/or the therapeutic efficacy of interventions should also be multi-factorial and be addressed at the cell type-specific level.

Overall, this study substantiated the value of using distinct, yet complementary analytical techniques (biochemical and multi-platform metabolomics techniques) when trying to understand the consequences of mitochondrial disease or a CI deficiency. It also underscored the potential of metabolomics as an investigatory tool and the necessity of using multiple metabolomics platforms when trying to explore the wide-ranging metabolic effects of a mitochondrial deficiency. These results also substantiated the usefulness of mouse models to study tissues that are scarcely available for experimental studies, such as the brain. Finally, the correspondence of these alterations with previous reports of CI deficiencies and/or neurodegeneration highlighted the validity of the *Ndufs4* KO mouse model as a model for CI deficiency and Leigh syndrome.

In conclusion, the results from this study provided new insights on the potential role of OXPHOS structure and function, as well as of neurotoxic metabolites, in brain region-specific neurodegeneration. This study also revealed exciting avenues for prospective studies that aims to understand the neuropathological mechanisms underlying the destructive and progressive nature of a CI deficiency. The results further provide a foundation to develop effective therapeutic approaches. Filling the proposed knowledge gaps can result in a more concrete understanding of the exact neuropathological mechanisms in a CI deficiency.

REFERENCES

- Abdulhag, U.N., Soiferman, D., Schueler-Furman, O., Miller, C., Shaag, A., Elpeleg, O., Edvardson, S. & Saada, A. 2014. Mitochondrial complex IV deficiency, caused by mutated COX6B1, is associated with encephalomyopathy, hydrocephalus and cardiomyopathy. *European Journal of Human Genetics*, 23:159-164.
- Ackerman, D., Tumanov, S., Qiu, B., Michalopoulou, E., Spata, M., Azzam, A., Xie, H., Simon, M.C. & Kamphorst, J.J. 2018. Triglycerides promote lipid homeostasis during hypoxic stress by balancing fatty acid saturation. *Cell Reports*, 24(10):2596-2605.
- Alam, M.T., Manjeri, G.R., Rodenburg, R.J., Smeitink, J.A., Notebaart, R.A., Huynen, M., Willems, P.H. & Koopman, W.J. 2015. Skeletal muscle mitochondria of NDUFS4^{-/-} mice display normal maximal pyruvate oxidation and ATP production. *Biochimica et Biophysica Acta (BBA)-Bioenergetics*, 1847(6-7):526-533.
- Allen, P.J. 2012. Creatine metabolism and psychiatric disorders: does creatine supplementation have therapeutic value? *Neuroscience and Biobehavioral Reviews*, 36(5):1442-1462.
- Alston, C.L., Rocha, M.C., Lax, N.Z., Turnbull, D.M. & Taylor, R.W. 2017. The genetics and pathology of mitochondrial disease. *The Journal of Pathology*, 241(2):236-250.
- Angelini, C. & Di Stadio, A. 2018. Metabolites-mitochondria-microglia (Mmma): therapeutic strategy for treatment of neural inflammation and neurodegeneration. *Journal of Molecular Biomarkers and Diagnosis*, 9(1), art. #376. doi:10.4172/2155-9929.1000376
- Arany, Z. & Neinast, M. 2018. Branched chain amino acids in metabolic disease. *Current Diabetes Reports*, 18(10), art. #76. <https://doi.org/10.1007/s11892-018-1048-7>
- Assouline, Z., Jambou, M., Rio, M., Bole-Feysot, C., De Lonlay, P., Barnerias, C., Desguerre, I., Bonnemains, C., Guillermet, C. & Steffann, J. 2012. A constant and similar assembly defect of mitochondrial respiratory chain complex I allows rapid identification of NDUFS4 mutations in patients with Leigh syndrome. *Biochimica et Biophysica Acta (BBA)-Molecular Basis of Disease*, 1822(6):1062-1069.
- Astarita, G., Jung, K.-M., Vasilevko, V., DiPatrizio, N.V., Martin, S.K., Cribbs, D.H., Head, E., Cotman, C.W. & Piomelli, D. 2011. Elevated stearoyl-CoA desaturase in brains of patients with Alzheimer's disease. *Public Library of Science (PloS) One*, 6(10), e24777. doi:10.1371/journal.pone.0024777
- Azevedo, F.A.C., Carvalho, L.R.B., Grinberg, L.T., Farfel, J.M., Ferretti, R.E.L., Leite, R.E.P., Jacob Filho, W., Lent, R. & Herculano-Houzel, S. 2009. Equal numbers of neuronal and nonneuronal cells make the human brain an isometrically scaled-up primate brain. *The Journal of Comparative Neurology*, 513(5):532-541.
- Baertling, F., Al-Murshedi, F., Sánchez-Caballero, L., Al-Senaidi, K., Joshi, N.P., Venselaar, H., van den Brand, M.A., Nijtmans, L.G. & Rodenburg, R.J. 2017. Mutation in mitochondrial complex IV subunit COX5A causes pulmonary arterial hypertension, lactic acidemia, and failure to thrive. *Human Mutation*, 38(6):692-703.
- Baertling, F., Rodenburg, R.J., Schaper, J., Smeitink, J.A., Koopman, W.J., Mayatepek, E., Morava, E. & Distelmaier, F. 2014. A guide to diagnosis and treatment of Leigh syndrome. *Journal of Neurology, Neurosurgery and Psychiatry*, 85(3):257-265.

- Bao, X.R., Ong, S.-E., Goldberger, O., Peng, J., Sharma, R., Thompson, D.A., Vafai, S.B., Cox, A.G., Marutani, E. & Ichinose, F. 2016. Mitochondrial dysfunction remodels one-carbon metabolism in human cells. *Elifesciences*, 5, e10575. doi:10.7554/eLife.10575
- Barrientos, A. 2002. In vivo and in organello assessment of OXPHOS activities. *Methods*, 26(4):307-316.
- Barrientos, A., Fontanesi, F. & Díaz, F. 2009. Evaluation of the mitochondrial respiratory chain and oxidative phosphorylation system using polarography and spectrophotometric enzyme assays. *Current Protocols in Human Genetics*, 63(1):19.13.11-19.13.14.
- Barrow, J.J., Balsa, E., Verdeguer, F., Tavares, C.D., Soustek, M.S., Hollingsworth IV, L.R., Jedrychowski, M., Vogel, R., Paulo, J.A. & Smeitink, J. 2016. Bromodomain inhibitors correct bioenergetic deficiency caused by mitochondrial disease complex I mutations. *Molecular Cell*, 64(1):163-175.
- Begley, P., Francis-McIntyre, S., Dunn, W.B., Broadhurst, D.I., Halsall, A., Tseng, A., Knowles, J., HUSERMET Consortium, Goodacre, R. & Kell, D.B. 2009. Development and performance of a gas chromatography-time-of-flight mass spectrometry analysis for large-scale nontargeted metabolomic studies of human serum. *Analytical Chemistry*, 81(16):7038-7046.
- Bélanger, M., Allaman, I. & Magistretti, P.J. 2011. Brain energy metabolism: focus on astrocyte-neuron metabolic cooperation. *Cell Metabolism*, 14(6):724-738.
- Ben-Sahra, I., Hoxhaj, G., Ricoult, S.J., Asara, J.M. & Manning, B.D. 2016. mTORC1 induces purine synthesis through control of the mitochondrial tetrahydrofolate cycle. *Science*, 351(6274):728-733.
- Benard, G., Faustin, B., Passerieux, E., Galinier, A., Rocher, C., Bellance, N., Delage, J.-P., Casteilla, L., Letellier, T. & Rossignol, R. 2006. Physiological diversity of mitochondrial oxidative phosphorylation. *American Journal of Physiology-Cell Physiology*, 291(6):C1172-C1182.
- Bifari, F. & Nisoli, E. 2017. Branched-chain amino acids differently modulate catabolic and anabolic states in mammals: a pharmacological point of view. *British Journal of Pharmacology*, 174(11):1366-1377.
- Bijlsma, S., Bobeldijk, I., Verheij, E.R., Ramaker, R., Kochhar, S., Macdonald, I.A., van Ommen, B. & Smilde, A.K. 2006. Large-scale human metabolomics studies: a strategy for data (pre-) processing and validation. *Analytical Chemistry*, 78(2):567-574.
- Bilan, D.S. & Belousov, V.V. 2016. Genetically encoded probes for NAD⁺/NADH monitoring. *Free Radical Biology and Medicine*, 100:32-42.
- Bird, M.J., Wijeyeratne, X.W., Komen, J.C., Laskowski, A., Ryan, M.T., Thorburn, D.R. & Frazier, A.E. 2014. Neuronal and astrocyte dysfunction diverges from embryonic fibroblasts in the Ndufs4fky/fky mouse. *Bioscience Reports*, 34(6), e00151. <https://doi.org/10.1042/BSR20140151>
- Blanchet, L., MC Buydens, L., AM Smeitink, J., HGM Willems, P. & JH Koopman, W. 2011. Isolated mitochondrial complex I deficiency: explorative data analysis of patient cell parameters. *Current Pharmaceutical Design*, 17(36):4023-4033.

Blier, P.U., Abele, D., Munro, D., Degletagne, C., Rodriguez, E. & Hagen, T. 2017. What modulates animal longevity? Fast and slow aging in bivalves as a model for the study of lifespan. *Seminars in Cell and Developmental Biology*, 70:130-140.

Bligh, E.G. & Dyer, W.J. 1959. A rapid method of total lipid extraction and purification. *Canadian Journal of Biochemistry and Physiology*, 37(8):911-917.

Block, M.L., Zecca, L. & Hong, J.-S. 2007. Microglia-mediated neurotoxicity: uncovering the molecular mechanisms. *Nature Reviews Neuroscience*, 8(1):57-69.

Bock, R.M. & Alberty, R.A. 1953. Studies of the enzyme fumarase I: kinetics and equilibrium. *Journal of the American Chemical Society*, 75(8):1921-1925.

Bolaños, J.P., Almeida, A. & Moncada, S. 2010. Glycolysis: a bioenergetic or a survival pathway? *Trends in Biochemical Sciences*, 35(3):145-149.

Bolea, I., Gella, A., Sanz, E., Prada-Dacasa, P., Menardy, F., Machuca-Marquez, P., Bard, A.M., Kalume, F. & Quintana, A. 2019. Defined neuronal populations drive fatal phenotype in Leigh Syndrome. *Elifesciences*, 8, e47163. doi:10.7554/eLife.47163.

Bonfante, E., Koenig, M.K., Adejumo, R.B., Perinjelil, V. & Riascos, R.F. 2016. The neuroimaging of Leigh syndrome: case series and review of the literature. *Pediatric Radiology*, 46(4):443-451.

Bonvento, G., Valette, J., Flament, J., Mochel, F. & Brouillet, E. 2017. Imaging and spectroscopic approaches to probe brain energy metabolism dysregulation in neurodegenerative diseases. *Journal of Cerebral Blood Flow and Metabolism*, 37(6):1927-1943.

Bouchez, C. & Devin, A. 2019. Mitochondrial biogenesis and mitochondrial reactive oxygen species (ROS): a complex relationship regulated by the camp/pka signaling pathway. *Cells*, 8(4), art. #287. doi:10.3390/cells8040287

Boultonwood, J., Yip, B.H., Vuppusetty, C., Pellagatti, A. & Wainscoat, J.S. 2013. Activation of the mTOR pathway by the amino acid L-leucine in the 5q-syndrome and other ribosomopathies. *Advances in Biological Regulation*, 53(1):8-17.

Box, G.E. 1949. A general distribution theory for a class of likelihood criteria. *Biometrika*, 36(3-4):317-346.

Boysen, A.K., Heal, K.R., Carlson, L.T. & Ingalls, A.E. 2018. Best-matched internal standard normalization in liquid chromatography–mass spectrometry metabolomics applied to environmental samples. *Analytical Chemistry*, 90(2):1363-1369.

Brand, M.D. & Nicholls, D.G. 2011. Assessing mitochondrial dysfunction in cells. *Biochemical Journal*, 435(2):297-312.

Breuer, M.E., Willems, P.H., Russel, F.G., Koopman, W.J. & Smeitink, J.A. 2012. Modeling mitochondrial dysfunctions in the brain: from mice to men. *Journal of Inherited Metabolic Disease*, 35(2):193-210.

Breuer, M.E., Willems, P.H., Smeitink, J.A., Koopman, W.J. & Nooteboom, M. 2013. Cellular and animal models for mitochondrial complex I deficiency: a focus on the NDUFS4 subunit. *International Union of Biochemistry and Molecular Biology (IUBMB) Life*, 65(3):202-208.

- Broadhurst, D., Goodacre, R., Reinke, S.N., Kuligowski, J., Wilson, I.D., Lewis, M.R. & Dunn, W.B. 2018. Guidelines and considerations for the use of system suitability and quality control samples in mass spectrometry assays applied in untargeted clinical metabolomic studies. *Metabolomics*, 14(6), art. #72. <https://doi.org/10.1007/s11306-018-1367-3>
- Bronowicka-Adamska, P., Zagajewski, J., Czubak, J. & Wróbel, M. 2011. RP-HPLC method for quantitative determination of cystathionine, cysteine and glutathione: an application for the study of the metabolism of cysteine in human brain. *Journal of Chromatography B*, 879(21):2005-2009.
- Brooks, H. & Krähenbühl, S. 2000. Development of a new assay for complex I of the respiratory chain. *Clinical Chemistry*, 46(3):345-350.
- Budde, S., Van den Heuvel, L., Janssen, A., Smeets, R., Buskens, C., DeMeirleir, L., Van Coster, R., Baethmann, M., Voit, T. & Trijbels, J. 2000. Combined enzymatic complex I and III deficiency associated with mutations in the nuclear encoded NDUFS4 gene. *Biochemical and Biophysical Research Communications*, 275(1):63-68.
- Bui, D., Ravasz, D. & Chinopoulos, C. 2019. The effect of 2-ketobutyrate on mitochondrial substrate-level phosphorylation. *Neurochemical Research*, 44(10):2301-2306.
- Burtscher, J., Zangrandi, L., Schwarzer, C. & Gnaiger, E. 2015. Differences in mitochondrial function in homogenated samples from healthy and epileptic specific brain tissues revealed by high-resolution respirometry. *Mitochondrion*, 25:104-112.
- Cabirol-Pol, M.J., Khalil, B., Rival, T., Faivre-Sarrailh, C. & Besson, M.T. 2018. Glial lipid droplets and neurodegeneration in a Drosophila model of complex I deficiency. *Glia*, 66(4):874-888.
- Caldovic, L. & Tuchman, M. 2003. N-acetylglutamate and its changing role through evolution. *Biochemical Journal*, 372(2):279-290.
- Calvaruso, M.A., Willems, P., van den Brand, M., Valsecchi, F., Kruse, S., Palmiter, R., Smeitink, J. & Nijtmans, L. 2011. Mitochondrial complex III stabilizes complex I in the absence of NDUFS4 to provide partial activity. *Human Molecular Genetics*, 21(1):115-120.
- Camandola, S. & Mattson, M.P. 2017. Brain metabolism in health, aging, and neurodegeneration. *The European Molecular Biology Organisation (EMBO) Journal*, 36(11):1474-1492.
- Cappelletti, P., Tallarita, E., Rabattoni, V., Campomenosi, P., Sacchi, S. & Pollegioni, L. 2018. Proline oxidase controls proline, glutamate, and glutamine cellular concentrations in a U87 glioblastoma cell line. *Public Library of Science (PloS) One*, 13(4), e0196283. <https://doi.org/10.1371/journal.pone.0196283>
- Carocho, M. & Ferreira, I.C.F.R. 2013. A review on antioxidants, prooxidants and related controversy: natural and synthetic compounds, screening and analysis methodologies and future perspectives. *Food and Chemical Toxicology*, 51:15-25.
- Casademont, J., Rodriguez-Santiago, B., Miró, O., Beato, A., López, S., Nunes, V. & Cardellach, F. 2005. Mitochondrial respiratory chain in brain homogenates: activities in different brain areas in patients with Alzheimer's disease. *Aging Clinical and Experimental Research*, 17(1):1-7.

- Casals, N., Zammit, V., Herrero, L., Fadó, R., Rodriguez-Rodriguez, R. & Serra, D. 2016. Carnitine palmitoyltransferase 1C: from cognition to cancer. *Progress in Lipid Research*, 61:134-148.
- Cater, H.L., Chandratheva, A., Benham, C.D., Morrison III, B. & Sundstrom, L.E. 2003. Lactate and glucose as energy substrates during, and after, oxygen deprivation in rat hippocampal acute and cultured slices. *Journal of Neurochemistry*, 87(6):1381-1390.
- Cavanagh, J. & Harding, B. 1994. Pathogenic factors underlying the lesions in Leigh's disease: Tissue responses to cellular energy deprivation and their clinico-pathological consequences. *Brain*, 117(6):1357-1376.
- Chen, B., Hui, J., Montgomery, K.S., Gella, A., Bolea, I., Sanz, E., Palmiter, R.D. & Quintana, A. 2017a. Loss of Mitochondrial Ndufs4 in Striatal Medium Spiny Neurons Mediates Progressive Motor Impairment in a Mouse Model of Leigh Syndrome. *Frontiers in Molecular Neuroscience*, 10, art. #265. doi:10.3389/fnmol.2017.00265
- Chen, J., Zhang, P., Lv, M., Guo, H., Huang, Y., Zhang, Z. & Xu, F. 2017b. Influences of normalization method on biomarker discovery in gas chromatography–mass spectrometry-based untargeted metabolomics: what should be considered? *Analytical Chemistry*, 89(10):5342-5348.
- Chen, L., Cui, Y., Jiang, D., Ma, C.Y., Tse, H.F., Hwu, W.L. & Lian, Q. 2018a. Management of Leigh syndrome: current status and new insights. *Clinical Genetics*, 93(6):1131-1140.
- Chen, Q., Kirk, K., Shurubor, Y.I., Zhao, D., Arreguin, A.J., Shahi, I., Valsecchi, F., Primiano, G., Calder, E.L. & Carelli, V. 2018b. Rewiring of glutamine metabolism is a bioenergetic adaptation of human cells with mitochondrial DNA mutations. *Cell Metabolism*, 27(5):1007-1025.
- Chinnery, P.F. 2014. *Mitochondrial disorders overview*. <https://www.ncbi.nlm.nih.gov/books/NBK1224/> Date of Access: 27 Feb. 2019.
- Chinnery, P.F. & Hudson, G. 2013. Mitochondrial genetics. *British Medical Bulletin*, 106(1):135-159.
- Chinopoulos, C. 2018. OXPHOS defects due to mtDNA mutations: glutamine to the rescue! *Cell Metabolism*, 27(6):1165-1167.
- Chinopoulos, C. & Seyfried, T.N. 2018. Mitochondrial substrate-level phosphorylation as energy source for glioblastoma: review and hypothesis. *American Society for Neurochemistry (ASN Neuro)*, 10:1-27.
- Choi, W.-S., Kim, H.-W., Tronche, F., Palmiter, R.D., Storm, D.R. & Xia, Z. 2017. Conditional deletion of Ndufs4 in dopaminergic neurons promotes Parkinson's disease-like non-motor symptoms without loss of dopamine neurons. *Scientific Reports*, 7, art. #44989. doi:10.1038/srep44989
- Choi, W.-S., Palmiter, R.D. & Xia, Z. 2011. Loss of mitochondrial complex I activity potentiates dopamine neuron death induced by microtubule dysfunction in a Parkinson's disease model. *The Journal of Cell Biology*, 192(5):873-882.
- Chong, J., Soufan, O., Li, C., Caraus, I., Li, S., Bourque, G., Wishart, D.S. & Xia, J. 2018. MetaboAnalyst 4.0: towards more transparent and integrative metabolomics analysis. *Nucleic Acids Research*, 46(W1):W486-W494.

- Chouchani, E.T., Methner, C., Buonincontri, G., Hu, C.-H., Logan, A., Sawiak, S.J., Murphy, M.P. & Krieg, T. 2014a. Complex I deficiency due to selective loss of Ndufs4 in the mouse heart results in severe hypertrophic cardiomyopathy. *Public Library of Science (PloS) One*, 9(4), e94157. doi:10.1371/journal.pone.0094157
- Chouchani, E.T., Pell, V.R., Gaude, E., Aksentijević, D., Sundier, S.Y., Robb, E.L., Logan, A., Nadtochiy, S.M., Ord, E.N. & Smith, A.C. 2014b. Ischaemic accumulation of succinate controls reperfusion injury through mitochondrial ROS. *Nature*, 515(7527), art. #431. doi:10.1038/nature13909
- Chretien, D. & Rustin, P. 2003. Mitochondrial oxidative phosphorylation: pitfalls and tips in measuring and interpreting enzyme activities. *Journal of Inherited Metabolic Disease*, 26(2-3):189-198.
- Civiletto, G., Varanita, T., Cerutti, R., Gorletta, T., Barbaro, S., Marchet, S., Lamperti, C., Viscomi, C., Scorrano, L. & Zeviani, M. 2015. Opa1 overexpression ameliorates the phenotype of two mitochondrial disease mouse models. *Cell Metabolism*, 21(6):845-854.
- Clare, C.E., Brassington, A.H., Kwong, W.Y. & Sinclair, K.D. 2019. One-carbon metabolism: linking nutritional biochemistry to epigenetic programming of long-term development. *Annual Review of Animal Biosciences*, 7:263-287.
- Clarke, C., Xiao, R., Place, E., Zhang, Z., Sondheimer, N., Bennett, M., Yudkoff, M. & Falk, M.J. 2013. Mitochondrial respiratory chain disease discrimination by retrospective cohort analysis of blood metabolites. *Molecular Genetics and Metabolism*, 110(1):145-152.
- Cobley, J.N., Fiorello, M.L. & Bailey, D.M. 2018. 13 reasons why the brain is susceptible to oxidative stress. *Redox Biology*, 15:490-503.
- Cocco, T., Pacelli, C., Sgobbo, P. & Villani, G. 2009. Control of OXPHOS efficiency by complex I in brain mitochondria. *Neurobiology of Aging*, 30(4):622-629.
- Cole, J.T., Sweatt, A.J. & Hutson, S.M. 2012. Expression of mitochondrial branched-chain aminotransferase and α -keto-acid dehydrogenase in rat brain: implications for neurotransmitter metabolism. *Frontiers in Neuroanatomy*, 6, art. #18. doi:10.3389/fnana.2012.00018
- Cooper, A.J. & Jeitner, T.M. 2016. Central role of glutamate metabolism in the maintenance of nitrogen homeostasis in normal and hyperammonemic brain. *Biomolecules*, 6(2), art. #16. doi:10.3390/biom6020016
- Corona, J.C. & Duchon, M.R. 2016. PPAR γ as a therapeutic target to rescue mitochondrial function in neurological disease. *Free Radical Biology and Medicine*, 100:153-163.
- Cuperfain, A.B., Zhang, Z.L., Kennedy, J.L. & Gonçalves, V.F. 2018. The complex interaction of mitochondrial genetics and mitochondrial pathways in psychiatric disease. *Molecular Neuropsychiatry*, 4(1):52-69.
- D'Angelo, M., Antonosante, A., Castelli, V., Catanesi, M., Moorthy, N., Iannotta, D., Cimini, A. & Benedetti, E. 2018. PPARs and energy metabolism adaptation during neurogenesis and neuronal maturation. *International Journal of Molecular Sciences*, 19(7), art. #1869. <https://doi.org/10.3390/ijms19071869>

- de Haas, R., Das, D., Garanto, A., Renkema, H.G., Greupink, R., van den Broek, P., Pertjjs, J., Collin, R.W., Willems, P. & Beyrath, J. 2017. Therapeutic effects of the mitochondrial ROS-redox modulator KH176 in a mammalian model of Leigh Disease. *Scientific Reports*, 7(1), art. #11733. <https://doi.org/10.1038/s41598-017-09417-5>
- De Rasmio, D., Panelli, D., Sardanelli, A.M. & Papa, S. 2008. cAMP-dependent protein kinase regulates the mitochondrial import of the nuclear encoded NDUFS4 subunit of complex I. *Cellular Signalling*, 20(5):989-997.
- De Simone, R., Vissicchio, F., Mingarelli, C., De Nuccio, C., Visentin, S., Ajmone-Cat, M.A. & Minghetti, L. 2013. Branched-chain amino acids influence the immune properties of microglial cells and their responsiveness to pro-inflammatory signals. *Biochimica et Biophysica Acta (BBA) - Molecular Basis of Disease*, 1832(5):650-659.
- Demine, S., Reddy, N., Renard, P., Raes, M. & Arnould, T. 2014. Unraveling biochemical pathways affected by mitochondrial dysfunctions using metabolomic approaches. *Metabolites*, 4(3):831-878.
- Di Guida, R., Engel, J., Allwood, J.W., Weber, R.J., Jones, M.R., Sommer, U., Viant, M.R. & Dunn, W.B. 2016. Non-targeted UHPLC-MS metabolomic data processing methods: a comparative investigation of normalisation, missing value imputation, transformation and scaling. *Metabolomics*, 12(5), 93. <https://doi.org/10.1007/s11306-016-1030-9>
- Di Meo, I., Marchet, S., Lamperti, C., Zeviani, M. & Viscomi, C. 2017. AAV9-based gene therapy partially ameliorates the clinical phenotype of a mouse model of Leigh syndrome. *Gene Therapy*, 24(10):661-667.
- Diaz, F., Garcia, S., Padgett, K.R. & Moraes, C.T. 2012. A defect in the mitochondrial complex III, but not complex IV, triggers early ROS-dependent damage in defined brain regions. *Human Molecular Genetics*, 21(23):5066-5077.
- Dienel, G.A. 2012. Brain lactate metabolism: the discoveries and the controversies. *Journal of Cerebral Blood Flow and Metabolism*, 32(7):1107-1138.
- Dienel, G.A. 2018. Brain glucose metabolism: integration of energetics with function. *Physiological Reviews*, 99(1):949-1045.
- Distelmaier, F., Koopman, W.J., van den Heuvel, L.P., Rodenburg, R.J., Mayatepek, E., Willems, P.H. & Smeitink, J.A. 2009. Mitochondrial complex I deficiency: from organelle dysfunction to clinical disease. *Brain*, 132(4):833-842.
- Divakaruni, A.S., Wallace, M., Buren, C., Martyniuk, K., Andreyev, A.Y., Li, E., Fields, J.A., Cordes, T., Reynolds, I.J. & Bloodgood, B.L. 2017. Inhibition of the mitochondrial pyruvate carrier protects from excitotoxic neuronal death. *The Journal of Cell Biology*, 216(4):1091-1105.
- Du Toit, H. 2007. *Biochemical analyses of deficiencies in the oxidative phosphorylation system in human muscle*. Potchefstroom: North-West University. (Dissertation - MSc).
- Dubinsky, J.M. 2009. Heterogeneity of nervous system mitochondria: location, location, location! *Experimental Neurology*, 218(2):293-307.
- Ducker, G.S. & Rabinowitz, J.D. 2017. One-carbon metabolism in health and disease. *Cell Metabolism*, 25(1):27-42.

- Dudzik, D., Barbas-Bernardos, C., García, A. & Barbas, C. 2017. Quality assurance procedures for mass spectrometry untargeted metabolomics: a review. *Journal of Pharmaceutical and Biomedical Analysis*, 147:149-173.
- Dunn, W.B., Broadhurst, D.I., Atherton, H.J., Goodacre, R. & Griffin, J.L. 2011. Systems level studies of mammalian metabolomes: the roles of mass spectrometry and nuclear magnetic resonance spectroscopy. *Chemical Society Reviews*, 40(1):387-426.
- Dunn, W.B., Wilson, I.D., Nicholls, A.W. & Broadhurst, D. 2012. The importance of experimental design and QC samples in large-scale and MS-driven untargeted metabolomic studies of humans. *Bioanalysis*, 4(18):2249-2264.
- Ehinger, J.K., Piel, S., Ford, R., Karlsson, M., Sjövall, F., Frostner, E.Å., Morota, S., Taylor, R.W., Turnbull, D.M. & Cornell, C. 2016. Cell-permeable succinate prodrugs bypass mitochondrial complex I deficiency. *Nature Communications*, 7(1):1-8.
- El-Hattab, A.W., Almannai, M. & Scaglia, F. 2017. Arginine and citrulline for the treatment of MELAS syndrome. *Journal of Inborn Errors of Metabolism and Screening*, 5:1-5.
- Ellis, S. & Steyn, H. 2003. Practical significance (effect sizes) versus or in combination with statistical significance (p-values): research note. *Management Dynamics: Journal of the Southern African Institute for Management Scientists*, 12(4):51-53.
- Engelke, U.F., Zijlstra, F.S., Mochel, F., Valayannopoulos, V., Rabier, D., Kluijtmans, L.A., Perl, A., Verhoeven-Duif, N.M., De Lonlay, P. & Wamelink, M.M. 2010. Mitochondrial involvement and erythronic acid as a novel biomarker in transaldolase deficiency. *Biochimica et Biophysica Acta (BBA)-Molecular Basis of Disease*, 1802(11):1028-1035.
- Engqvist, M.K., Eßer, C., Maier, A., Lercher, M.J. & Maurino, V.G. 2014. Mitochondrial 2-hydroxyglutarate metabolism. *Mitochondrion*, 19:275-281.
- Epstein, A.A., Narayanasamy, P., Dash, P.K., High, R., Bathena, S.P.R., Gorantla, S., Poluektova, L.Y., Alnouti, Y., Gendelman, H.E. & Boska, M.D. 2013. Combinatorial assessments of brain tissue metabolomics and histopathology in rodent models of human immunodeficiency virus infection. *Journal of Neuroimmune Pharmacology*, 8(5):1224-1238.
- Esterhuizen, K., Lindeque, J.Z., Mason, S., van der Westhuizen, F.H., Suomalainen, A., Hakonen, A.H., Carroll, C.J., Rodenburg, R.J., de Laat, P.B. & Janssen, M.C. 2018. A urinary biosignature for mitochondrial myopathy, encephalopathy, lactic acidosis and stroke like episodes (MELAS). *Mitochondrion*, 45:38-45.
- Esterhuizen, K., van der Westhuizen, F.H. & Louw, R. 2017. Metabolomics of mitochondrial disease. *Mitochondrion*, 35:97-110.
- Falk, M., Zhang, Z., Rosenjack, J., Nissim, I., Daikhin, E., Sedensky, M., Yudkoff, M. & Morgan, P. 2008. Metabolic pathway profiling of mitochondrial respiratory chain mutants in *C. elegans*. *Molecular Genetics and Metabolism*, 93(4):388-397.
- Falk, M.J., Polyak, E., Zhang, Z., Peng, M., King, R., Maltzman, J.S., Okwuego, E., Horyn, O., Nakamaru-Ogiso, E. & Ostrovsky, J. 2011. Probucol ameliorates renal and metabolic sequelae of primary CoQ deficiency in Pdss2 mutant mice. *European Molecular Biology Organisation (EMBO) Molecular Medicine*, 3(7):410-427.

- Falkowska, A., Gutowska, I., Goschorska, M., Nowacki, P., Chlubek, D. & Baranowska-Bosiacka, I. 2015. Energy metabolism of the brain, including the cooperation between astrocytes and neurons, especially in the context of glycogen metabolism. *International Journal of Molecular Sciences*, 16(11):25959-25981.
- Fanning, S., Haque, A., Imberdis, T., Baru, V., Barrasa, M.I., Nuber, S., Termine, D., Ramalingam, N., Ho, G.P. & Noble, T. 2019. Lipidomic analysis of α -synuclein neurotoxicity identifies stearyl CoA desaturase as a target for Parkinson treatment. *Molecular Cell*, 73(5):1001-101.
- FDA (Food and Drug Administration). 2018. Guidance for industry: bioanalytical method validation. <https://www.fda.gov/files/drugs/published/Bioanalytical-Method-Validation-Guidance-for-Industry.pdf> Date of access: 3 Sept. 2018.
- Feldman, A.G., Sokol, R.J., Hardison, R.M., Alonso, E.M., Squires, R.H., Narkewicz, M.R. & Group, P.A.L.F.S. 2017. Lactate and lactate: pyruvate ratio in the diagnosis and outcomes of pediatric acute liver failure. *The Journal of Pediatrics*, 182:217-222.
- Felici, R., Buonvicino, D., Muzzi, M., Cavone, L., Guasti, D., Lapucci, A., Pratesi, S., De Cesaris, F., Luceri, F. & Chiarugi, A. 2017. Post onset, oral rapamycin treatment delays development of mitochondrial encephalopathy only at supramaximal doses. *Neuropharmacology*, 117:74-84.
- Felici, R., Cavone, L., Lapucci, A., Guasti, D., Bani, D. & Chiarugi, A. 2014. PARP inhibition delays progression of mitochondrial encephalopathy in mice. *Neurotherapeutics*, 11(3):651-664.
- Fernandes, J., Saudubray, J.-M. & van den Berghe, G. 2013. *Inborn Metabolic Diseases: Diagnosis and Treatment*. Heidelberg: Springer Science and Business Media. p. 207.
- Ferrari, M., Jain, I.H., Goldberger, O., Rezoagli, E., Thoonen, R., Cheng, K.-H., Sosnovik, D.E., Scherrer-Crosbie, M., Mootha, V.K. & Zapol, W.M. 2017. Hypoxia treatment reverses neurodegenerative disease in a mouse model of Leigh syndrome. *Proceedings of the National Academy of Sciences*, 114(21):E4241-E4250.
- Fiehn, O. 2016. Metabolomics by gas chromatography–mass spectrometry: combined targeted and untargeted profiling. *Current Protocols in Molecular Biology*, 114(1):30.34.31-30.34.32.
- Field, A. 2009a. *Discovering statistics using SPSS*. 3rd ed. London: SAGE. p. 131 - 165.
- Field, A. 2009b. *Discovering statistics using SPSS*. 3rd ed. London: SAGE. p. 506 - 538.
- Finsterer, J. & Zarrouk-Mahjoub, S. 2018. Biomarkers for detecting mitochondrial disorders. *Journal of Clinical Medicine*, 7(2), art. #16. <https://doi.org/10.3390/jcm7020016>
- Foti, S.C., Hargreaves, I., Carrington, S., Kiely, A.P., Houlden, H. & Holton, J.L. 2019. Cerebral mitochondrial electron transport chain dysfunction in multiple system atrophy and Parkinson's disease. *Scientific Reports*, 9(1), art. #6559. <https://doi.org/10.1038/s41598-019-42902-7>
- Frazier, A.E., Thorburn, D.R. & Compton, A.G. 2017. Mitochondrial energy generation disorders: genes, mechanisms and clues to pathology. *Journal of Biological Chemistry (JBC)*, 294(14):5386-5395.

- Fricker, M., Tolkovsky, A.M., Borutaite, V., Coleman, M. & Brown, G.C. 2018. Neuronal cell death. *Physiological Reviews*, 98(2):813-880.
- García-Corzo, L., Luna-Sánchez, M., Doerrier, C., García, J.A., Guarás, A., Acín-Pérez, R., Bullejos-Peregrín, J., Lopez, A., Escames, G. & Enríquez, J.A. 2012. Dysfunctional Coq9 protein causes predominant encephalomyopathy associated with CoQ deficiency. *Human Molecular Genetics*, 22(6):1233-1248.
- Garrett, R.H. & Grisham, C.M. 2013. *Biochemistry*. 5th ed. Belmont, CA: Brooks/Cole, Cengage Learning.
- Gaude, E., Schmidt, C., Gammage, P.A., Dugourd, A., Blacker, T., Chew, S.P., Saez-Rodriguez, J., O'Neill, J.S., Szabadkai, G. & Minczuk, M. 2018. NADH shuttling couples cytosolic reductive carboxylation of glutamine with glycolysis in cells with mitochondrial dysfunction. *Molecular Cell*, 69(4):581-593.
- Gerards, M., Sallevelt, S.C. & Smeets, H.J. 2016. Leigh syndrome: resolving the clinical and genetic heterogeneity paves the way for treatment options. *Molecular Genetics and Metabolism*, 117(3):300-312.
- Ghosh, S., Castillo, E., Frias, E.S. & Swanson, R.A. 2018. Bioenergetic regulation of microglia. *Glia*, 66(6):1200-1212.
- Giachin, G., Bouverot, R., Acajjaoui, S., Pantalone, S. & Soler-López, M. 2016. Dynamics of human mitochondrial complex I assembly: implications for neurodegenerative diseases. *Frontiers in Molecular Biosciences*, 3, art. #43. doi:10.3389/fmolb.2016.00043
- Giesbertz, P., Ecker, J., Haag, A., Spanier, B. & Daniel, H. 2015. An LC-MS/MS method to quantify acylcarnitine species including isomeric and odd-numbered forms in plasma and tissues. *Journal of Lipid Research (JLR)*, 56(10):2029-2039.
- Gika, H.G., Zisi, C., Theodoridis, G. & Wilson, I.D. 2016. Protocol for quality control in metabolic profiling of biological fluids by U(H)PLC-MS. *Journal of Chromatography B*, 1008:15-25.
- Gimeno-Bayón, J., López-López, A., Rodríguez, M. & Mahy, N. 2014. Glucose pathways adaptation supports acquisition of activated microglia phenotype. *Journal of Neuroscience Research*, 92(6):723-731.
- Godzien, J., Alonso-Herranz, V., Barbas, C. & Armitage, E.G. 2015. Controlling the quality of metabolomics data: new strategies to get the best out of the QC sample. *Metabolomics*, 11(3):518-528.
- Gogna, N., Sharma, R., Gupta, V., Dorai, K. & Prasad, N. 2017. Evolution of the metabolome in response to selection for increased immunity in populations of *Drosophila melanogaster*. *Public Library of Science (PloS) One*, 12(11), e0188089. doi:10.1371/journal.pone.0188089
- González-Domínguez, R., Sayago, A. & Fernández-Recamales, Á. 2017. Metabolomics in Alzheimer's disease: the need of complementary analytical platforms for the identification of biomarkers to unravel the underlying pathology. *Journal of Chromatography B*, 1071:75-92.
- Gonzalez-Riano, C., Garcia, A. & Barbas, C. 2016. Metabolomics studies in brain tissue: a review. *Journal of Pharmaceutical and Biomedical Analysis*, 130:141-168.

- Gonzalez-Riano, C., Tapia-González, S., García, A., Muñoz, A., DeFelipe, J. & Barbas, C. 2017. Metabolomics and neuroanatomical evaluation of post-mortem changes in the hippocampus. *Brain Structure and Function*, 222(6):2831-2853.
- Goodman, R.P., Calvo, S.E. & Mootha, V.K. 2018. Spatiotemporal compartmentalization of hepatic NADH and NADPH metabolism. *Journal of Biological Chemistry*, 293(20):7508-7516.
- Goodpaster, B.H. & Sparks, L.M. 2017. Metabolic Flexibility in Health and Disease. *Cell Metabolism*, 25(5):1027-1036.
- Gorman, G.S., Schaefer, A.M., Ng, Y., Gomez, N., Blakely, E.L., Alston, C.L., Feeney, C., Horvath, R., Yu-Wai-Man, P. & Chinnery, P.F. 2015. Prevalence of nuclear and mitochondrial DNA mutations related to adult mitochondrial disease. *Annals of Neurology*, 77(5):753-759.
- Gorrochategui, E., Jaumot, J., Lacorte, S. & Tauler, R. 2016. Data analysis strategies for targeted and untargeted LC-MS metabolomic studies: overview and workflow. *Trends in Analytical Chemistry*, 82:425-442.
- Goyal, Manu S., Hawrylycz, M., Miller, Jeremy A., Snyder, Abraham Z. & Raichle, Marcus E. 2014. Aerobic glycolysis in the human brain is associated with development and neotenus gene expression. *Cell Metabolism*, 19(1):49-57.
- Greenhouse, S.W. & Geisser, S. 1959. On methods in the analysis of profile data. *Psychometrika*, 24(2):95-112.
- Griffin, J.W. & Bradshaw, P.C. 2017. Amino acid catabolism in Alzheimer's disease brain: friend or foe? *Oxidative Medicine and Cellular Longevity*, 201, art. #5472792. <https://doi.org/10.1155/2017/5472792>
- Grimm, A. & Eckert, A. 2017. Brain aging and neurodegeneration: from a mitochondrial point of view. *Journal of Neurochemistry*, 143(4):418-431.
- Guerra-Castellano, A., Díaz-Quintana, A., Pérez-Mejías, G., Elena-Real, C.A., González-Arzola, K., García-Mauriño, S.M., Miguel, A. & Díaz-Moreno, I. 2018. Oxidative stress is tightly regulated by cytochrome c phosphorylation and respirasome factors in mitochondria. *Proceedings of the National Academy of Sciences*, 115(31):7955-7960.
- Guerrero-Castillo, S., Baertling, F., Kownatzki, D., Wessels, H.J., Arnold, S., Brandt, U. & Nijtmans, L. 2017. The assembly pathway of mitochondrial respiratory chain complex I. *Cell Metabolism*, 25(1):128-139.
- Gullberg, J., Jonsson, P., Nordström, A., Sjöström, M. & Moritz, T. 2004. Design of experiments: an efficient strategy to identify factors influencing extraction and derivatization of Arabidopsis thaliana samples in metabolomic studies with gas chromatography/mass spectrometry. *Analytical Biochemistry*, 331(2):283-295.
- Haefeli, R.H., Erb, M., Gemperli, A.C., Robay, D., Fruh, I.C., Anklin, C., Dallmann, R. & Gueven, N. 2011. NQO1-dependent redox cycling of idebenone: effects on cellular redox potential and energy levels. *Public Library of Science (PloS) One*, 6(3), e17963. doi:10.1371/journal.pone.0017963
- Hall, M., Quignodon, L. & Desvergne, B. 2008. Peroxisome proliferator-activated receptor in the brain: facts and hypothesis. *PPAR Research*, 2008, art. #780452. doi:10.1155/2008/780452

- Hallen, A., Jamie, J.F. & Cooper, A.J. 2013. Lysine metabolism in mammalian brain: an update on the importance of recent discoveries. *Amino Acids*, 45(6):1249-1272.
- Handy, D.E. & Loscalzo, J. 2012. Redox regulation of mitochondrial function. *Antioxidants and Redox Signaling*, 16(11):1323-1367.
- Hanna-El-Daher, L. & Braissant, O. 2016. Creatine synthesis and exchanges between brain cells: what can be learned from human creatine deficiencies and various experimental models? *Amino Acids*, 48(8):1877-1895.
- Hara, T., Nakamura, K., Matsui, M., Yamamoto, A., Nakahara, Y., Suzuki-Migishima, R., Yokoyama, M., Mishima, K., Saito, I. & Okano, H. 2006. Suppression of basal autophagy in neural cells causes neurodegenerative disease in mice. *Nature*, 441(7095):885-889.
- Harder, U., Koletzko, B. & Peissner, W. 2011. Quantification of 22 plasma amino acids combining derivatization and ion-pair LC-MS/MS. *Journal of Chromatography B*, 879(7):495-504.
- Harris, J.J., Jolivet, R. & Attwell, D. 2012. Synaptic energy use and supply. *Neuron*, 75(5):762-777.
- Hendriks, M.M., van Eeuwijk, F.A., Jellema, R.H., Westerhuis, J.A., Reijmers, T.H., Hoefsloot, H.C. & Smilde, A.K. 2011. Data-processing strategies for metabolomics studies. *Trends in Analytical Chemistry*, 30(10):1685-1698.
- Hervé, M.R., Nicolè, F. & Lê Cao, K.-A. 2018. Multivariate analysis of multiple datasets: a practical guide for chemical ecology. *Journal of Chemical Ecology*, 44(3):215-234.
- Ho, H.-Y., Lin, Y.-T., Lin, G., Wu, P.-R. & Cheng, M.-L. 2017. Nicotinamide nucleotide transhydrogenase (NNT) deficiency dysregulates mitochondrial retrograde signaling and impedes proliferation. *Redox Biology*, 12:916-928.
- Hoefs, S.J., Rodenburg, R.J., Smeitink, J.A. & van den Heuvel, L.P. 2012. Molecular base of biochemical complex I deficiency. *Mitochondrion*, 12(5):520-532.
- Hohnholt, M.C., Andersen, V.H., Andersen, J.V., Christensen, S.K., Karaca, M., Maechler, P. & Waagepetersen, H.S. 2018. Glutamate dehydrogenase is essential to sustain neuronal oxidative energy metabolism during stimulation. *Journal of Cerebral Blood Flow and Metabolism*, 38(10):1754-1768.
- Holzerová, E. & Prokisch, H. 2015. Mitochondria: much ado about nothing? How dangerous is reactive oxygen species production? *The International Journal of Biochemistry and Cell Biology*, 63:16-20.
- Hrydziuszko, O. & Viant, M.R. 2012. Missing values in mass spectrometry based metabolomics: an undervalued step in the data processing pipeline. *Metabolomics*, 8(1):161-174.
- Huck, J.H., Verhoeven, N.M., Struys, E.A., Salomons, G.S., Jakobs, C. & van der Knaap, M.S. 2004. Ribose-5-phosphate isomerase deficiency: new inborn error in the pentose phosphate pathway associated with a slowly progressive leukoencephalopathy. *The American Journal of Human Genetics*, 74(4):745-751.

- Hüttemann, M., Lee, I., Samavati, L., Yu, H. & Doan, J.W. 2007. Regulation of mitochondrial oxidative phosphorylation through cell signaling. *Biochimica et Biophysica Acta (BBA)-Molecular Cell Research*, 1773(12):1701-1720.
- Hyder, F., Rothman, D.L. & Bennett, M.R. 2013. Cortical energy demands of signaling and nonsignaling components in brain are conserved across mammalian species and activity levels. *Proceedings of the National Academy of Sciences*, 110(9):3549-3554.
- Iannetti, E.F., Smeitink, J.A., Willems, P.H., Beyrath, J. & Koopman, W.J. 2018. Rescue from galactose-induced death of Leigh syndrome patient cells by pyruvate and NAD⁺. *Cell death and Disease*, 9(11), art. #1135. doi:10.1038/s41419-018-1179-4
- Ignatenko, O., Chilov, D., Paetau, I., de Miguel, E., Jackson, C.B., Capin, G., Paetau, A., Terzioglu, M., Euro, L. & Suomalainen, A. 2018. Loss of mtDNA activates astrocytes and leads to spongiform encephalopathy. *Nature Communications*, 9(1), art. #70. doi: 10.1038/s41467-017-01859-9
- Indrieri, A., Carrella, S., Romano, A., Spaziano, A., Marrocco, E., Fernandez-Vizarra, E., Barbato, S., Pizzo, M., Ezhova, Y. & Golia, F.M. 2019. miR-181a/b downregulation exerts a protective action on mitochondrial disease models. *European Molecular Biology Organisation (EMBO) Molecular Medicine*, 11(5), e8734. doi:10.15252/emmm.201708734
- Ingraham, C.A., Burwell, L.S., Skalska, J., Brookes, P.S., Howell, R.L., Sheu, S.-S. & Pinkert, C.A. 2009. NDUFS4: creation of a mouse model mimicking a Complex I disorder. *Mitochondrion*, 9(3):204-210.
- Irwin, M.H., Parameshwaran, K. & Pinkert, C.A. 2013. Mouse models of mitochondrial complex I dysfunction. *The International Journal of Biochemistry and Cell Biology*, 45(1):34-40.
- Ivanisevic, J., Epstein, A.A., Kurczyk, M.E., Benton, P.H., Uritboonthai, W., Fox, H.S., Boska, M.D., Gendelman, H.E. & Siuzdak, G. 2014. Brain region mapping using global metabolomics. *Chemistry and Biology*, 21(11):1575-1584.
- Jäger, C., Glaab, E., Michelucci, A., Binz, T.M., Köglberger, S., Garcia, P., Trezzi, J.-P., Ghelfi, J., Balling, R. & Buttini, M. 2015. The mouse brain metabolome: region-specific signatures and response to excitotoxic neuronal injury. *The American Journal of Pathology*, 185(6):1699-1712.
- Jain, I.H., Zazzeron, L., Goldberger, O., Marutani, E., Wojtkiewicz, G.R., Ast, T., Wang, H., Schleifer, G., Stepanova, A. & Brepoels, K. 2019. Leigh syndrome mouse model can be rescued by interventions that normalize brain hyperoxia, but not HIF activation. *Cell Metabolism*, 30(4):824-832.
- Jain, I.H., Zazzeron, L., Goli, R., Alexa, K., Schatzman-Bone, S., Dhillon, H., Goldberger, O., Peng, J., Shalem, O. & Sanjana, N.E. 2016. Hypoxia as a therapy for mitochondrial disease. *Science*, 352(6281):54-61.
- Janssen, A.J., Trijbels, F.J., Sengers, R.C., Smeitink, J.A., Van den Heuvel, L.P., Wintjes, L.T., Stoltenberg-Hogenkamp, B.J. & Rodenburg, R.J. 2007. Spectrophotometric assay for complex I of the respiratory chain in tissue samples and cultured fibroblasts. *Clinical Chemistry*, 53(4):729-734.

- Jha, M.K. & Morrison, B.M. 2018. Glia-neuron energy metabolism in health and diseases: New insights into the role of nervous system metabolic transporters. *Experimental Neurology*, 309:23-31.
- Jin, Z., Wei, W., Yang, M., Du, Y. & Wan, Y. 2014. Mitochondrial complex I activity suppresses inflammation and enhances bone resorption by shifting macrophage-osteoclast polarization. *Cell Metabolism*, 20(3):483-498.
- Jing, Y., Fleete, M., Collie, N., Zhang, H. & Liu, P. 2013. Regional variations and age-related changes in arginine metabolism in the rat brain stem and spinal cord. *Neuroscience*, 252:98-108.
- Johnson, S.C., Yanos, M., Sangesland, M., Bitto, A., Castanza, A., Gagnidze, A., Cordoba, J., Gonzalez, B., Gupta, K. & Hui, J. 2015. Dose-dependent effects of mTOR inhibition on weight and mitochondrial disease in mice. *Frontiers in Genetics*, 6, art. #247. doi:10.3389/fgene.2015.00247
- Johnson, S.C., Yanos, M.E., Kayser, E.-B., Quintana, A., Sangesland, M., Castanza, A., Uhde, L., Hui, J., Wall, V.Z. & Gagnidze, A. 2013. mTOR inhibition alleviates mitochondrial disease in a mouse model of Leigh syndrome. *Science*, 342(6165):1524-1528.
- Kahlhöfer, F., Kmita, K., Wittig, I., Zwicker, K. & Zickermann, V. 2017. Accessory subunit NUYM (NDUFS4) is required for stability of the electron input module and activity of mitochondrial complex I. *Biochimica et Biophysica Acta (BBA)-Bioenergetics*, 1858(2):175-181.
- Kanunnikova, N.P. 2012. Role of brain glutamic acid metabolism changes in neurodegenerative pathologies. *Journal of Biology and Earth Sciences*, 2(1):1-10.
- Kapnick, S.M., Pacheco, S.E. & McGuire, P.J. 2017. The emerging role of immune dysfunction in mitochondrial diseases as a paradigm for understanding immunometabolism. *Metabolism*, 81:97-112.
- Kapoor, R.V. & Vaidyanathan, S. 2016. Towards quantitative mass spectrometry-based metabolomics in microbial and mammalian systems. *Philosophical Transactions of the Royal Society A: Mathematical, Physical and Engineering Sciences*, 374(2079), art. #20150363. <http://dx.doi.org/10.1098/rsta.2015.0363>
- Karaca, M., Frigerio, F., Migrenne, S., Martin-Levilain, J., Skytt, D.M., Pajacka, K., Martin-del-Rio, R., Gruetter, R., Tamarit-Rodriguez, J. & Waagepetersen, H.S. 2015. GDH-dependent glutamate oxidation in the brain dictates peripheral energy substrate distribution. *Cell Reports*, 13(2):365-375.
- Karamanlidis, G., Lee, C.F., Garcia-Menendez, L., Kolwicz Jr, S.C., Suthammarak, W., Gong, G., Sedensky, M.M., Morgan, P.G., Wang, W. & Tian, R. 2013. Mitochondrial complex I deficiency increases protein acetylation and accelerates heart failure. *Cell Metabolism*, 18(2):239-250.
- Karlsson, M., Ehinger, J.K., Piel, S., Sjövall, F., Henriksnäs, J., Höglund, U., Hansson, M.J. & Elmér, E. 2016. Changes in energy metabolism due to acute rotenone-induced mitochondrial complex I dysfunction: an in vivo large animal model. *Mitochondrion*, 31:56-62.

- Karpinski, A. 2011. Graduate statistics and data analysis. Chapter 7: factorial ANOVA: two-way ANOVA. Unpublished lecture notes, Psych 8011/8021. Temple University: https://astro.temple.edu/~andykarp/Graduate_Statistics/Graduate_Statistics_files/Ch%2007%20Lecture%20Notes.pdf Date of access: 23 October 2018.
- Karuppagounder, S.S., Alim, I., Khim, S.J., Bourassa, M.W., Sleiman, S.F., John, R., Thinnis, C.C., Yeh, T.-L., Demetriades, M. & Neitemeier, S. 2016. Therapeutic targeting of oxygen-sensing prolyl hydroxylases abrogates ATF4-dependent neuronal death and improves outcomes after brain hemorrhage in several rodent models. *Science Translational Medicine*, 8(328):328ra329-328ra329.
- Kayser, E.-B., Sedensky, M.M. & Morgan, P.G. 2016. Region-specific defects of respiratory capacities in the *Ndufs4* (KO) mouse brain. *Public Library of Science (PloS) One*, 11(1), e0148219. doi:10.1371/journal.pone.0148219
- Kety, S.S. 1957. The general metabolism of the brain in vivo. In: Richter, D., eds. *Metabolism of the nervous system*. London: Pergamon. p. 221-237.
- Khan, N.A., Govindaraj, P., Meena, A.K. & Thangaraj, K. 2015. Mitochondrial disorders: challenges in diagnosis and treatment. *Indian Journal of Medical Research*, 141(1):13-26.
- Khan, N.A., Nikkanen, J., Yatsuga, S., Jackson, C., Wang, L., Pradhan, S., Kivelä, R., Pessia, A., Velagapudi, V. & Suomalainen, A. 2017. mTORC1 regulates mitochondrial integrated stress response and mitochondrial myopathy progression. *Cell Metabolism*, 26(2):419-428.
- Kim, C., Potluri, P., Khalil, A., Gaut, D., McManus, M., Compton, S., Wallace, D.C. & Yadava, N. 2017. An X-chromosome linked mouse model (*Ndufa1S55A*) for systemic partial complex I deficiency for studying predisposition to neurodegeneration and other diseases. *Neurochemistry International*, 109:78-93.
- Kim, H.-W., Choi, W.-S., Sorscher, N., Park, H.J., Tronche, F., Palmiter, R.D. & Xia, Z. 2015. Genetic reduction of mitochondrial complex I function does not lead to loss of dopamine neurons in vivo. *Neurobiology of Aging*, 36(9):2617-2627.
- Kim, Y., Zheng, X., Ansari, Z., Bunnell, M.C., Herdy, J.R., Traxler, L., Lee, H., Paquola, A.C., Blithikioti, C. & Ku, M. 2018. Mitochondrial aging defects emerge in directly reprogrammed human neurons due to their metabolic profile. *Cell Reports*, 23(9):2550-2558.
- Kimoloi, S. 2018. Modulation of the de novo purine nucleotide pathway as a therapeutic strategy in mitochondrial myopathy. *Pharmacological Research*, 138:37-42.
- Kirk, R.E. 1996. Practical significance: a concept whose time has come. *Educational and Psychological Measurement*, 56(5):746-759.
- Kirwan, J.A., Weber, R.J.M., Broadhurst, D.I. & Viant, M.R. 2014. Direct infusion mass spectrometry metabolomics dataset: a benchmark for data processing and quality control. *Scientific Data*, 1, art. #140012. doi:10.1038/sdata.2014.12
- Kiss, G., Konrad, C., Pour-Ghaz, I., Mansour, J.J., Németh, B., Starkov, A.A., Adam-Vizi, V. & Chinopoulos, C. 2014. Mitochondrial diaphorases as NAD⁺ donors to segments of the citric acid cycle that support substrate-level phosphorylation yielding ATP during respiratory inhibition. *The Federation of American Societies for Experimental Biology (FASEB) Journal*, 28(4):1682-1697.

- Kleinridders, A., Ferris, H.A., Reyzer, M.L., Rath, M., Soto, M., Manier, M.L., Spraggins, J., Yang, Z., Stanton, R.C., Caprioli, R.M. & Kahn, C.R. 2018. Regional differences in brain glucose metabolism determined by imaging mass spectrometry. *Molecular Metabolism*, 12:113-121.
- Kluckova, K., Sticha, M., Cerny, J., Mracek, T., Dong, L., Drahota, Z., Gottlieb, E., Neuzil, J. & Rohlena, J. 2015. Ubiquinone-binding site mutagenesis reveals the role of mitochondrial complex II in cell death initiation. *Cell Death and Disease*, 6(5), e1749. doi:10.1038/cddis.2015.110
- Klusmann, A., Fleischer, W., Waldhaus, A., Siebler, M. & Mayatepek, E. 2005. Influence of D-arabitol and ribitol on neuronal network activity. *Journal of Inherited Metabolic Disease*, 28(6):1181-1183.
- Koene, S., Rodenburg, R., Van Der Knaap, M., Willemsen, M., Sperl, W., Laugel, V., Ostergaard, E., Tarnopolsky, M., Martin, M. & Nesbitt, V. 2012. Natural disease course and genotype-phenotype correlations in Complex I deficiency caused by nuclear gene defects: what we learned from 130 cases. *Journal of Inherited Metabolic Disease*, 35(5):737-747.
- Koenig, M.K. 2008. Presentation and diagnosis of mitochondrial disorders in children. *Pediatric Neurology*, 38(5):305-313.
- Kolch, W., Fey, D., Ryan, C.J., Tavassoly, I., Goldfarb, J. & Iyengar, R. 2018. Systems biology primer: the basic methods and approaches. *Essays in Biochemistry*, 62(4):487-500.
- Koopman, W.J., Beyrath, J., Fung, C.W., Koene, S., Rodenburg, R.J., Willems, P.H. & Smeitink, J.A. 2016. Mitochondrial disorders in children: toward development of small-molecule treatment strategies. *European Molecular Biology Organisation (EMBO) Molecular Medicine*, 8(4):311-327.
- Koopman, W.J., Distelmaier, F., Smeitink, J.A. & Willems, P.H. 2013. OXPHOS mutations and neurodegeneration. *The European Molecular Biology Organization (EMBO) Journal*, 32(1):9-29.
- Koopman, W.J., Nijtmans, L.G., Dieteren, C.E., Roestenberg, P., Valsecchi, F., Smeitink, J.A. & Willems, P.H. 2010. Mammalian mitochondrial complex I: biogenesis, regulation, and reactive oxygen species generation. *Antioxidants and Redox signaling*, 12(12):1431-1470.
- Kori, M., Aydın, B., Unal, S., Arga, K.Y. & Kazan, D. 2016. Metabolic biomarkers and neurodegeneration: a pathway enrichment analysis of Alzheimer's disease, Parkinson's disease, and amyotrophic lateral sclerosis. *Omics: A Journal of Integrative Biology*, 20(11):645-661.
- Krug, A.K., Gutbier, S., Zhao, L., Pörtl, D., Kullmann, C., Ivanova, V., Förster, S., Jagtap, S., Meiser, J. & Leparc, G. 2014. Transcriptional and metabolic adaptation of human neurons to the mitochondrial toxicant MPP+. *Cell Death and Disease*, 5(5):e1222.
- Kruse, S.E., Watt, W.C., Marcinek, D.J., Kapur, R.P., Schenkman, K.A. & Palmiter, R.D. 2008. Mice with mitochondrial complex I deficiency develop a fatal encephalomyopathy. *Cell Metabolism*, 7(4):312-320.
- Kühn, K., Obata, T., Feher, K., Bock, R., Fernie, A.R. & Meyer, E.H. 2015. Complete mitochondrial complex I deficiency induces an up-regulation of respiratory fluxes that is abolished by traces of functional complex I. *Plant Physiology*, 168(4):1537-1549.

- Lake, N.J., Bird, M.J., Isohanni, P. & Paetau, A. 2015. Leigh syndrome: neuropathology and pathogenesis. *Journal of Neuropathology and Experimental Neurology*, 74(6):482-492.
- Lake, N.J., Compton, A.G., Rahman, S. & Thorburn, D.R. 2016. Leigh syndrome: one disorder, more than 75 monogenic causes. *Annals of Neurology*, 79(2):190-203.
- Lanciano, P., Khalfaoui-Hassani, B., Selamoglu, N., Ghelli, A., Rugolo, M. & Daldal, F. 2013. Molecular mechanisms of superoxide production by complex III: a bacterial versus human mitochondrial comparative case study. *Biochimica et Biophysica Acta (BBA)-Bioenergetics*, 1827(11-12):1332-1339.
- Lanza, I.R. & Nair, K.S. 2009. Functional assessment of isolated mitochondria in vitro. *Methods in Enzymology*, 457:349-372.
- Larsen, S., Nielsen, J., Hansen, C.N., Nielsen, L.B., Wibrand, F., Stride, N., Schroder, H.D., Boushel, R., Helge, J.W. & Dela, F. 2012. Biomarkers of mitochondrial content in skeletal muscle of healthy young human subjects. *The Journal of Physiology*, 590(14):3349-3360.
- Lee, C.F., Caudal, A., Abell, L., Gowda, G.N. & Tian, R. 2019. Targeting NAD⁺ metabolism as interventions for mitochondrial disease. *Scientific Reports*, 9(1), art. #3073. <https://doi.org/10.1038/s41598-019-39419-4>
- Lee, D.Y., Xun, Z., Platt, V., Budworth, H., Canaria, C.A. & McMurray, C.T. 2013. Distinct pools of non-glycolytic substrates differentiate brain regions and prime region-specific responses of mitochondria. *Public Library of Science (PloS) One*, 8(7), e68831. doi:10.1371/journal.pone.0068831
- Lee, J. & Wolfgang, M.J. 2012. Metabolomic profiling reveals a role for CPT1c in neuronal oxidative metabolism. *BioMed Central (BMC) Biochemistry*, 13(1), art. #23. doi:10.1186/1471-2091-13-23
- Legault, J.T., Strittmatter, L., Tardif, J., Sharma, R., Tremblay-Vaillancourt, V., Aubut, C., Boucher, G., Clish, C.B., Cyr, D. & Daneault, C. 2015. A metabolic signature of mitochondrial dysfunction revealed through a monogenic form of Leigh syndrome. *Cell Reports*, 13(5):981-989.
- Lei, Y., Li, D., Deng, J., Shao, W.-h., Fan, S.-h., Wang, X., Huang, H., Chen, S.-g., Zhang, H.-z., Zhang, L., Zhang, Y., Li, W.-j., Huang, R.-z., Liu, X., Zhou, C.-j., Chen, J.-j. & Xie, P. 2014. Metabolomic profiling of three brain regions from a postnatal infected Borna disease virus Hu-H1 rat model. *Metabolomics*, 10(3):484-495.
- Leigh, D. 1951. Subacute necrotizing encephalomyelopathy in an infant. *Journal of Neurology, Neurosurgery, and Psychiatry*, 14(3):216-221.
- Lein, E.S., Hawrylycz, M.J., Ao, N., Ayres, M., Bensinger, A., Bernard, A., Boe, A.F., Boguski, M.S., Brockway, K.S. & Byrnes, E.J. 2007. Genome-wide atlas of gene expression in the adult mouse brain. *Nature*, 445(7124):168-176.
- Lemieux, H., Blier, P.U. & Gnaiger, E. 2017. Remodeling pathway control of mitochondrial respiratory capacity by temperature in mouse heart: electron flow through the Q-junction in permeabilized fibers. *Scientific Reports*, 7(1), art. #2840. doi:10.1038/s41598-017-02789-8
- Lenaz, G., Tioli, G., Falasca, A.I. & Genova, M.L. 2016. Complex I function in mitochondrial supercomplexes. *Biochimica et Biophysica Acta (BBA)-Bioenergetics*, 1857(7):991-1000.

- Lent, R., Azevedo, F.A.C., Andrade-Moraes, C.H. & Pinto, A.V.O. 2012. How many neurons do you have? Some dogmas of quantitative neuroscience under revision. *The European Journal of Neuroscience*, 35(1):1-9.
- Leong, D.W., Komen, J.C., Hewitt, C.A., Arnaud, E., McKenzie, M., Phipson, B., Bahlo, M., Laskowski, A., Kinkel, S.A. & Davey, G.M. 2012. Proteomic and metabolomic analyses of mitochondrial complex I-deficient mouse model generated by spontaneous B2 short interspersed nuclear element (SINE) insertion into NADH dehydrogenase (ubiquinone) Fe-S protein 4 (Ndufs4) gene. *Journal of Biological Chemistry*, 287(24):20652-20663.
- Leshinsky-Silver, E., Lebre, A.-S., Minai, L., Saada, A., Steffann, J., Cohen, S., Rötig, A., Munnich, A., Lev, D. & Lerman-Sagie, T. 2009. NDUFS4 mutations cause Leigh syndrome with predominant brainstem involvement. *Molecular Genetics and Metabolism*, 97(3):185-189.
- Levene, H. 1960. *Contributions to probability and statistics: essays in honor of Harold Hotelling*. Heidelberg: Springer Science and Business Media.
- Li, T., Zhang, Z., Kolwicz Jr, S.C., Abell, L., Roe, N.D., Kim, M., Zhou, B., Cao, Y., Ritterhoff, J. & Gu, H. 2017. Defective branched-chain amino acid catabolism disrupts glucose metabolism and sensitizes the heart to ischemia-reperfusion injury. *Cell Metabolism*, 25(2):374-385.
- Li, Y., D'Aurelio, M., Deng, J.-H., Park, J.-S., Manfredi, G., Hu, P., Lu, J. & Bai, Y. 2007. An assembled complex IV maintains the stability and activity of complex I in mammalian mitochondria. *Journal of Biological Chemistry*, 282(24):17557-17562.
- Lindeque, J.Z., Hidalgo, J., Louw, R. & van der Westhuizen, F.H. 2013. Systemic and organ specific metabolic variation in metallothionein knockout mice challenged with swimming exercise. *Metabolomics*, 9(2):418-432.
- Lindeque, J.Z., van Rensburg, P.J.J., Louw, R., van der Westhuizen, F.H., Florit, S., Ramirez, L., Giralt, M. & Hidalgo, J. 2015. Obesity and metabolomics: metallothioneins protect against high-fat diet-induced consequences in metallothionein knockout mice. *Omics: A Journal of Integrative Biology*, 19(2):92-103.
- Liu, L., MacKenzie, K.R., Putluri, N., Maletić-Savatić, M. & Bellen, H.J. 2017. The glia-neuron lactate shuttle and elevated ROS promote lipid synthesis in neurons and lipid droplet accumulation in glia via APOE/D. *Cell Metabolism*, 26(5):719-737.
- Liu, L., Zhang, K., Sandoval, H., Yamamoto, S., Jaiswal, M., Sanz, E., Li, Z., Hui, J., Graham, B.H. & Quintana, A. 2015. Glial lipid droplets and ROS induced by mitochondrial defects promote neurodegeneration. *Cell*, 160(1):177-190.
- Liu, P., Smith, P.F., Appleton, I., Darlington, C.L. & Bilkey, D.K. 2003. Regional variations and age-related changes in nitric oxide synthase and arginase in the sub-regions of the hippocampus. *Neuroscience*, 119(3):679-687.
- Liu, P., Smith, P.F., Appleton, I., Darlington, C.L. & Bilkey, D.K. 2004. Age-related changes in nitric oxide synthase and arginase in the rat prefrontal cortex. *Neurobiology of Aging*, 25(4):547-552.

- Liu, X., Miyazaki, M., Flowers, M.T., Sampath, H., Zhao, M., Chu, K., Paton, C.M., Joo, D.S. & Ntambi, J.M. 2009. Loss of stearoyl-coa desaturase-1 attenuates adipocyte inflammation: effects of adipocyte-derived oleate. *Arteriosclerosis, Thrombosis and Vascular Biology*, 30(1):31-38.
- Liu, X., Strable, M.S. & Ntambi, J.M. 2011. Stearoyl CoA desaturase 1: role in cellular inflammation and stress. *Advances in Nutrition*, 2(1):15-22.
- Loeffen, J., Smeitink, J., Trijbels, J., Janssen, A., Triepels, R., Sengers, R. & Van den Heuvel, L. 2000. Isolated complex I deficiency in children: clinical, biochemical and genetic aspects. *Human Mutation*, 15(2):123-134.
- Löfgren, L., Forsberg, G.-B. & Ståhlman, M. 2016. The BUME method: a new rapid and simple chloroform-free method for total lipid extraction of animal tissue. *Scientific Reports*, 6, art. #27688. doi:10.1038/srep27688
- Long, F.H. 2013. Multivariate analysis for metabolomics and proteomics data. In Issaq, H.J. & Veenstra, T.D., eds. *Proteomic and metabolomic approaches to biomarker discovery*. Boston: Academic Press. p. 299-311.
- Long, J., Ma, J., Luo, C., Mo, X., Sun, L., Zang, W. & Liu, J. 2009. Comparison of two methods for assaying complex I activity in mitochondria isolated from rat liver, brain and heart. *Life Sciences*, 85(7-8):276-280.
- Lopez-Fabuel, I., Le Douce, J., Logan, A., James, A.M., Bonvento, G., Murphy, M.P., Almeida, A. & Bolaños, J.P. 2016. Complex I assembly into supercomplexes determines differential mitochondrial ROS production in neurons and astrocytes. *Proceedings of the National Academy of Sciences*, 113(46):13063-13068.
- Lopez-Lluch, G., Hunt, N., Jones, B., Zhu, M., Jamieson, H., Hilmer, S., Cascajo, M., Allard, J., Ingram, D. & Navas, P. 2006. Calorie restriction induces mitochondrial biogenesis and bioenergetic efficiency. *Proceedings of the National Academy of Sciences*, 103(6):1768-1773.
- Louw, R., Smuts, I., Wilsenach, K.-L., Jonck, L.-M., Schoonen, M. & van der Westhuizen, F.H. 2018. The dilemma of diagnosing coenzyme Q10 deficiency in muscle. *Molecular Genetics and Metabolism*, 125(1-2):38-43.
- Lovick, T.A. 2012. Estrous cycle and stress: influence of progesterone on the female brain. *Brazilian Journal of Medical and Biological Research*, 45(4):314-320.
- Lozoya, O.A., Martinez-Reyes, I., Wang, T., Grenet, D., Bushel, P., Li, J., Chandel, N., Woychik, R.P. & Santos, J.H. 2018. Mitochondrial nicotinamide adenine dinucleotide reduced (NADH) oxidation links the tricarboxylic acid (TCA) cycle with methionine metabolism and nuclear DNA methylation. *Public Library of Science (PLoS) Biology*, 16(4), e2005707. <https://doi.org/10.1371/journal.pbio.2005707>
- Luo, C., Long, J. & Liu, J. 2008. An improved spectrophotometric method for a more specific and accurate assay of mitochondrial complex III activity. *Clinica Chimica Acta*, 395(1-2):38-41.
- Luo, X., Li, R. & Yan, L.-J. 2015. Roles of pyruvate, NADH, and mitochondrial complex I in redox balance and imbalance in β cell function and dysfunction. *Journal of Diabetes Research*, 2015, art. #512618. <https://doi.org/10.1155/2015/512618>

- Luo, X., Pitkänen, S., Kassovska-Bratinova, S., Robinson, B.H. & Lehotay, D.C. 1997. Excessive formation of hydroxyl radicals and aldehydic lipid peroxidation products in cultured skin fibroblasts from patients with complex I deficiency. *The Journal of Clinical Investigation*, 99(12):2877-2882.
- Lynch, C.J. & Adams, S.H. 2014. Branched-chain amino acids in metabolic signalling and insulin resistance. *Nature Reviews Endocrinology*, 10(12):723-736.
- Ma, Q., Zhang, X. & Qu, Y. 2018. Biodegradation and biotransformation of indole: advances and perspectives. *Frontiers in Microbiology*, 9, art. #2625. doi:10.3389/fmicb.2018.02
- Magistretti, P.J. & Allaman, I. 2015. A cellular perspective on brain energy metabolism and functional imaging. *Neuron*, 86(4):883-901.
- Mailloux, R.J. 2015. Teaching the fundamentals of electron transfer reactions in mitochondria and the production and detection of reactive oxygen species. *Redox Biology*, 4:381-398.
- Manczak, M., Park, B.S., Jung, Y. & Reddy, P.H. 2004. Differential expression of oxidative phosphorylation genes in patients with Alzheimer's disease. *Neuromolecular Medicine*, 5(2):147-162.
- Manjeri, G. 2017. *Characterization of the Ndufs4-/- model to evaluate a novel therapeutic strategy towards mitochondrial dysfunction*. Nijmegen: Radboud University. (Thesis - PhD).
- Manjeri, G.R., Rodenburg, R.J., Blanchet, L., Roelofs, S., Nijtmans, L.G., Smeitink, J.A., Driessen, J.J., Koopman, W.J. & Willems, P.H. 2016. Increased mitochondrial ATP production capacity in brain of healthy mice and a mouse model of isolated complex I deficiency after isoflurane anesthesia. *Journal of Inherited Metabolic Disease*, 39(1):59-65.
- Manoli, I. & Venditti, C. 2016. Disorders of branched chain amino acid metabolism. *Translational Science of Rare Diseases*, 1(2):91-110.
- Martano, G., Murru, L., Moretto, E., Gerosa, L., Garrone, G., Krogh, V. & Passafaro, M. 2016. Biosynthesis of glycerol phosphate is associated with long-term potentiation in hippocampal neurons. *Metabolomics*, 12(8), art. #133. doi:10.1007/s11306-016-1083-9
- Martin-Perez, M., Ito, T.K., Grillo, A.S., Valente, A.S., Han, J., Entwisle, S.W., Huang, H.Z., Kim, D., Yajima, M. & Kaeberlein, M. 2019. Protein kinase C is a key target for attenuation of Leigh syndrome by rapamycin. *BioRxiv*, art. #562207. <https://doi.org/10.1101/562207>
- Mason, S. 2017. Lactate shuttles in neuroenergetics—homeostasis, allostasis and beyond. *Frontiers in Neuroscience*, 11, art. #43. doi:10.3389/fnins.2017.00043
- Mason, S., van Furth, A.M., Mienie, L.J., Engelke, U.F., Wevers, R.A., Solomons, R. & Reinecke, C.J. 2015. A hypothetical astrocyte–microglia lactate shuttle derived from a 1 H NMR metabolomics analysis of cerebrospinal fluid from a cohort of South African children with tuberculous meningitis. *Metabolomics*, 11(4):822-837.
- Mattson, M.P., Moehl, K., Ghena, N., Schmaedick, M. & Cheng, A. 2018. Intermittent metabolic switching, neuroplasticity and brain health. *Nature Reviews Neuroscience*, 19(2):63-80.
- Matyash, V., Liebisch, G., Kurzchalia, T.V., Shevchenko, A. & Schwudke, D. 2008. Lipid extraction by methyl-tert-butyl ether for high-throughput lipidomics. *Journal of Lipid Research*, 49(5):1137-1146.

- Mauchly, J.W. 1940. Significance test for sphericity of a normal n-variate distribution. *The Annals of Mathematical Statistics*, 11(2):204-209.
- McCormack, S.E., Xiao, R., Kilbaugh, T.J., Karlsson, M., Ganetzky, R.D., Cunningham, Z.Z., Goldstein, A., Falk, M.J. & Damrauer, S.M. 2017. Hospitalizations for mitochondrial disease across the lifespan in the US. *Molecular Genetics and Metabolism*, 121(2):119-126.
- McDonald, A.E., Pichaud, N. & Darveau, C.-A. 2017. "Alternative" fuels contributing to mitochondrial electron transport: importance of non-classical pathways in the diversity of animal metabolism. *Comparative Biochemistry and Physiology Part B: Biochemistry and Molecular Biology*, 224:185-194.
- McKenna, M.C., Waagepetersen, H.S., Schousboe, A. & Sonnewald, U. 2006. Neuronal and astrocytic shuttle mechanisms for cytosolic-mitochondrial transfer of reducing equivalents: current evidence and pharmacological tools. *Biochemical Pharmacology*, 71(4):399-407.
- Mereis, M. 2018. *Evaluating the involvement of metallothionein I in complex I deficiency: an in vitro study*. Potchefstroom: North-West University. (Dissertation - MSc).
- Mew, N.A. & Caldovic, L. 2011. N-acetylglutamate synthase deficiency: an insight into the genetics, epidemiology, pathophysiology, and treatment. *The Application of Clinical Genetics*, 4:127-135.
- Milenkovic, D., Blaza, J.N., Larsson, N.-G. & Hirst, J. 2017. The enigma of the respiratory chain supercomplex. *Cell Metabolism*, 25(4):765-776.
- Mirandola, S.R., Melo, D.R., Saito, Â. & Castilho, R.F. 2010. 3-nitropropionic acid-induced mitochondrial permeability transition: comparative study of mitochondria from different tissues and brain regions. *Journal of Neuroscience Research*, 88(3):630-639.
- Mitchell, P. 1961. Coupling of phosphorylation to electron and hydrogen transfer by a chemi-osmotic type of mechanism. *Nature*, 191(4784):144-148.
- Morris, G. & Berk, M. 2015. The many roads to mitochondrial dysfunction in neuroimmune and neuropsychiatric disorders. *BioMed Central (BMC) Medicine*, 13(1), art. #68. doi:10.1186/s12916-015-0310-y
- Mourier, A., Matic, S., Ruzzenente, B., Larsson, N.-G. & Milenkovic, D. 2014. The respiratory chain supercomplex organization is independent of COX7a2l isoforms. *Cell Metabolism*, 20(6):1069-1075.
- Mráček, T., Holzerová, E., Drahota, Z., Kovářová, N., Vrbacký, M., Ješina, P. & Houštěk, J. 2014. ROS generation and multiple forms of mammalian mitochondrial glycerol-3-phosphate dehydrogenase. *Biochimica et Biophysica Acta (BBA)-Bioenergetics*, 1837(1):98-111.
- Mullis, K., Faloona, F., Scharf, S., Saiki, R., Horn, G. & Erlich, H. 1986. Specific enzymatic amplification of DNA in vitro: the polymerase chain reaction. *Cold Spring Harbor Symposia on Quantitative Biology*, 51:263-273.
- Munro, D., Pichaud, N., Paquin, F., Kemeid, V. & Blier, P.U. 2013. Low hydrogen peroxide production in mitochondria of the long-lived *Arctica islandica*: underlying mechanisms for slow aging. *Aging Cell*, 12(4):584-592.

- Murphy, E., Ardehali, H., Balaban, R.S., DiLisa, F., Dorn, G.W., Kitsis, R.N., Otsu, K., Ping, P., Rizzuto, R. & Sack, M.N. 2016. Mitochondrial function, biology, and role in disease: a scientific statement from the American Heart Association. *Circulation Research*, 118(12):1960-1991.
- Murphy, M.P. & Hartley, R.C. 2018. Mitochondria as a therapeutic target for common pathologies. *Nature Reviews Drug Discovery*, 17(12), art. #865. doi:10.1038/nrd.2018.174
- Nakamura, M.T., Yudell, B.E. & Loor, J.J. 2014. Regulation of energy metabolism by long-chain fatty acids. *Progress in Lipid Research*, 53(1):124-144.
- Nehlig, A. 2004. Brain uptake and metabolism of ketone bodies in animal models. *Prostaglandins, Leukotrienes and Essential Fatty Acids*, 70(3):265-275.
- Neves, A., Costalat, R. & Pellerin, L. 2012. Determinants of brain cell metabolic phenotypes and energy substrate utilization unraveled with a modeling approach. *Public Library of Science (PLoS) Computational Biology*, 8(9), e1002686. doi:10.1371/journal.pcbi.1002686
- Ng, Y.-W. & Say, Y.-H. 2018. Palmitic acid induces neurotoxicity and gliotoxicity in SH-SY5Y human neuroblastoma and T98G human glioblastoma cells. *PeerJ*, 6, e4696. doi:10.7717/peerj.4696
- Nikkanen, J., Forsström, S., Euro, L., Paetau, I., Kohnz, R.A., Wang, L., Chilov, D., Viinamäki, J., Roivainen, A. & Marjamäki, P. 2016. Mitochondrial DNA replication defects disturb cellular dNTP pools and remodel one-carbon metabolism. *Cell Metabolism*, 23(4):635-648.
- Niyazov, D.M., Kahler, S.G. & Frye, R.E. 2016. Primary mitochondrial disease and secondary mitochondrial dysfunction: importance of distinction for diagnosis and treatment. *Molecular Syndromology*, 7(3):122-137.
- Nsiah-Sefaa, A. & McKenzie, M. 2016. Combined defects in oxidative phosphorylation and fatty acid β -oxidation in mitochondrial disease. *Bioscience Reports*, 36(2), e00313. doi:10.1042/BSR20150295
- Ntambi, J.M., Miyazaki, M., Stoehr, J.P., Lan, H., Kendzioriski, C.M., Yandell, B.S., Song, Y., Cohen, P., Friedman, J.M. & Attie, A.D. 2002. Loss of stearoyl-CoA desaturase-1 function protects mice against adiposity. *Proceedings of the National Academy of Sciences*, 99(17):11482-11486.
- Ortigoza-Escobar, J.D., Oyarzabal, A., Montero, R., Artuch, R., Jou, C., Jiménez, C., Gort, L., Briones, P., Muchart, J., López-Gallardo, E., Emperador, S., Pesini, E.R., Montoya, J., Pérez, B., Rodríguez-Pombo, P. & Pérez-Dueñas, B. 2016. Ndufs4 related Leigh syndrome: a case report and review of the literature. *Mitochondrion*, 28:73-78.
- Owens, K., Park, J.H., Schuh, R. & Kristian, T. 2013. Mitochondrial dysfunction and NAD⁺ metabolism alterations in the pathophysiology of acute brain injury. *Translational Stroke Research*, 4(6):618-634.
- Pacheu-Grau, D., Rucktäschel, R. & Deckers, M. 2018. Mitochondrial dysfunction and its role in tissue-specific cellular stress. *Cell Stress*, 2(8):184-199.
- Palladini, G., Di Pasqua, L.G., Berardo, C., Siciliano, V., Richelmi, P., Mannucci, B., Croce, A.C., Rizzo, V., Perlini, S. & Vairetti, M. 2019. Fatty Acid desaturase involvement in non-alcoholic fatty liver disease rat models: oxidative stress versus metalloproteinases. *Nutrients*, 11(4), art. #799. <https://doi.org/10.3390/nu11040799>

- Palmer, T. & Bonner, P.L. 2007. *Enzymes: biochemistry, biotechnology, clinical chemistry*. 2nd ed. Cambridge: Woodhead Publishing Limited.
- Panov, A., Orynbayeva, Z., Vavilin, V. & Lyakhovich, V. 2014. Fatty acids in energy metabolism of the central nervous system. *BioMed Research International*, 2014, art. #472459. <https://doi.org/10.1155/2014/472459>
- Parikh, S., Goldstein, A., Koenig, M.K., Scaglia, F., Enns, G.M., Saneto, R., Anselm, I., Cohen, B.H., Falk, M.J. & Greene, C. 2015. Diagnosis and management of mitochondrial disease: a consensus statement from the Mitochondrial Medicine Society. *Genetics in Medicine*, 17(9):689-701.
- Pathak, R.U. & Davey, G.P. 2008. Complex I and energy thresholds in the brain. *Biochimica et Biophysica Acta (BBA)-Bioenergetics*, 1777(7-8):777-782.
- Pellerin, L. & Magistretti, P.J. 1994. Glutamate uptake into astrocytes stimulates aerobic glycolysis: a mechanism coupling neuronal activity to glucose utilization. *Proceedings of the National Academy of Sciences*, 91(22):10625-10629.
- Pena, I.A., Marques, L.A., Laranjeira, Â.B., Yunes, J.A., Eberlin, M.N., MacKenzie, A. & Arruda, P. 2017. Mouse lysine catabolism to amino adipate occurs primarily through the saccharopine pathway: implications for pyridoxine dependent epilepsy (PDE). *Biochimica et Biophysica Acta (BBA)-Molecular Basis of Disease*, 1863(1):121-128.
- Peters, D., Berger, J., Langnaese, K., Derst, C., Madai, V.I., Krauss, M., Fischer, K.-D., Veh, R.W. & Laube, G. 2013. Arginase and arginine decarboxylase: where do the putative gate keepers of polyamine synthesis reside in rat brain? *Public Library of Science (PloS) One*, 8(6), e66735. doi:10.1371/journal.pone.0066735
- Peters, H., Buck, N., Wanders, R., Ruiten, J., Waterham, H., Koster, J., Yapfite-Lee, J., Ferdinandusse, S. & Pitt, J. 2014. ECHS1 mutations in Leigh disease: a new inborn error of metabolism affecting valine metabolism. *Brain*, 137(11):2903-2908.
- Pfeffer, G., Horvath, R., Klopstock, T., Mootha, V.K., Suomalainen, A., Koene, S., Hirano, M., Zeviani, M., Bindoff, L.A. & Yu-Wai-Man, P. 2013. New treatments for mitochondrial disease—no time to drop our standards. *Nature Reviews Neurology*, 9(8):474-482.
- Phang, J.M. 2019. Proline metabolism in cell regulation and cancer biology: recent advances and hypotheses. *Antioxidants and Redox Signaling*, 30(4):635-649.
- Phang, J.M., Liu, W., Hancock, C.N. & Fischer, J.W. 2015. Proline metabolism and cancer: emerging links to glutamine and collagen. *Current Opinion in Clinical Nutrition and Metabolic Care*, 18(1):71-77.
- Picard, M., Wallace, D.C. & Burrell, Y. 2016. The rise of mitochondria in medicine. *Mitochondrion*, 30:105-116.
- Pickrell, A.M., Fukui, H., Wang, X., Pinto, M. & Moraes, C.T. 2011. The striatum is highly susceptible to mitochondrial oxidative phosphorylation dysfunctions. *Journal of Neuroscience*, 31(27):9895-9904.
- Piroli, G.G., Manuel, A.M., Clapper, A.C., Walla, M.D., Baatz, J.E., Palmiter, R.D., Quintana, A. & Frizzell, N. 2016. Succination is increased on select proteins in the brainstem of the NADH dehydrogenase (ubiquinone) Fe-S protein 4 (Ndufs4) knockout mouse, a model of leigh syndrome. *Molecular and Cellular Proteomics*, 15(2):445-461.

- Pollard, A.K., Craig, E.L. & Chakrabarti, L. 2016. Mitochondrial complex 1 activity measured by spectrophotometry is reduced across all brain regions in ageing and more specifically in neurodegeneration. *Public Library of Science (PloS) One*, 11(6), e0157405. doi:10.1371/journal.pone.0157405
- Porter, C. & Wall, B.T. 2012. Skeletal muscle mitochondrial function: is it quality or quantity that makes the difference in insulin resistance? *The Journal of Physiology*, 590(23):5935-5936.
- Posset, R., Opp, S., Struys, E.A., Völkl, A., Mohr, H., Hoffmann, G.F., Kölker, S., Sauer, S.W. & Okun, J.G. 2015. Understanding cerebral L-lysine metabolism: the role of L-pipecolate metabolism in Gcdh-deficient mice as a model for glutaric aciduria type I. *Journal of Inherited Metabolic Disease*, 38(2):265-272.
- Prabakaran, S., Swatton, J., Ryan, M., Huffaker, S., Huang, J.-J., Griffin, J., Wayland, M., Freeman, T., Dudbridge, F. & Lilley, K. 2004. Mitochondrial dysfunction in schizophrenia: evidence for compromised brain metabolism and oxidative stress. *Molecular Psychiatry*, 9(7):684-697.
- Pretorius, M. 2011. *Evaluation of metallothionein involvement in the modulation of mitochondrial respiration in mice*. Potchefstroom: North-West University. (Dissertation - MSc).
- Qin, X.-Y. & Kojima, S. 2019. Inhibition of stearyl-CoA desaturase-1 activity suppressed SREBP signaling in colon cancer cells and their spheroid growth. *Gastrointestinal Disorders*, 1(1):191-200.
- Quintana, A., Kruse, S.E., Kapur, R.P., Sanz, E. & Palmiter, R.D. 2010. Complex I deficiency due to loss of Ndufs4 in the brain results in progressive encephalopathy resembling Leigh syndrome. *Proceedings of the National Academy of Sciences*, 107(24):10996-11001.
- Quintana, A., Zanella, S., Koch, H., Kruse, S.E., Lee, D., Ramirez, J.M. & Palmiter, R.D. 2012. Fatal breathing dysfunction in a mouse model of Leigh syndrome. *The Journal of Clinical Investigation*, 122(7):2359-2368.
- Rahman, J. & Rahman, S. 2018. Mitochondrial medicine in the omics era. *The Lancet*, 391(10139):2560-2574.
- Rahman, S. 2012. Mitochondrial disease and epilepsy. *Developmental Medicine and Child Neurology*, 54(5):397-406.
- Rahman, S., Blok, R., Dahl, H.H., Danks, D., Kirby, D., Chow, C., Christodoulou, J. & Thorburn, D. 1996. Leigh syndrome: clinical features and biochemical and DNA abnormalities. *Annals of Neurology*, 39(3):343-351.
- Ravasz, D., Kacso, G., Fodor, V., Horvath, K., Adam-Vizi, V. & Chinopoulos, C. 2017. Catabolism of GABA, succinic semialdehyde or gamma-hydroxybutyrate through the GABA shunt impair mitochondrial substrate-level phosphorylation. *Neurochemistry International*, 109:41-53.
- Reinecke, C.J., Koekemoer, G., Van der Westhuizen, F.H., Louw, R., Lindeque, J.Z., Mienie, L.J. & Smuts, I. 2012. Metabolomics of urinary organic acids in respiratory chain deficiencies in children. *Metabolomics*, 8(2):264-283.

- Richard, E., Gallego-Villar, L., Rivera-Barahona, A., Oyarzábal, A., Pérez, B., Rodríguez-Pombo, P. & Desviat, L.R. 2018. Altered redox homeostasis in branched-chain amino acid disorders, organic acidurias, and homocystinuria. *Oxidative Medicine and Cellular Longevity*, 2018, art. #1246069. <https://doi.org/10.1155/2018/1246069>
- Robert, K., Vialard, F., Thiery, E., Toyama, K., Sinet, P.-M., Janel, N. & London, J. 2003. Expression of the cystathionine beta synthase (CBS) gene during mouse development and immunolocalization in adult brain. *The Journal of Histochemistry and Cytochemistry*, 51(3):363-371.
- Rodenburg, R.J. 2011. Biochemical diagnosis of mitochondrial disorders. *Journal of Inherited Metabolic Disease*, 34(2):283-292.
- Rodenburg, R.J. 2016. Mitochondrial complex I-linked disease. *Biochimica et Biophysica Acta (BBA)-Bioenergetics*, 1857(7):938-945.
- Roestenberg, P., Manjeri, G.R., Valsecchi, F., Smeitink, J.A., Willems, P.H. & Koopman, W.J. 2012. Pharmacological targeting of mitochondrial complex I deficiency: the cellular level and beyond. *Mitochondrion*, 12(1):57-65.
- Rogers, G., Murphy, A., Elorza, A. & Brand, M. 2011. *Analyzing microgram quantities of isolated mitochondria in the XF24 Analyzer*. <https://www.agilent.com/cs/library/applications/5991-7145EN.pdf> Date of access: 29 Jun. 2019.
- Rose, J., Brian, C., Woods, J., Pappa, A., Panayiotidis, M.I., Powers, R. & Franco, R. 2017. Mitochondrial dysfunction in glial cells: implications for neuronal homeostasis and survival. *Toxicology*, 391:109-115.
- Rossignol, R., Faustin, B., Rocher, C., Malgat, M., Mazat, J.-P. & Letellier, T. 2003. Mitochondrial threshold effects. *Biochemical Journal*, 370(3):751-762.
- Rossignol, R., Letellier, T., Malgat, M., Rocher, C. & Mazat, J.-P. 2000. Tissue variation in the control of oxidative phosphorylation: implication for mitochondrial diseases. *Biochemical Journal*, 347(1):45-53.
- Ruhoy, I.S. & Saneto, R.P. 2014. The genetics of Leigh syndrome and its implications for clinical practice and risk management. *The Application of Clinical Genetics*, 7:221-234.
- Rzem, R., Achouri, Y., Marbaix, E., Schakman, O., Wiame, E., Marie, S., Gailly, P., Vincent, M.-F., Veiga-da-Cunha, M. & Van Schaftingen, E. 2015. A mouse model of L-2-hydroxyglutaric aciduria, a disorder of metabolite repair. *Public Library of Science (PloS) One*, 10(3), e0119540. doi:10.1371/journal.pone.0119540
- Rzem, R., Vincent, M.F., Van Schaftingen, E. & Veiga-da-Cunha, M. 2007. L-2-Hydroxyglutaric aciduria, a defect of metabolite repair. *Journal of Inherited Metabolic Disease*, 30(5):681-689.
- Sage-Schwaede, A., Engelstad, K., Salazar, R., Curcio, A., Khandji, A., Garvin Jr, J.H. & De Vivo, D.C. 2019. Exploring mTOR inhibition as treatment for mitochondrial disease. *Annals of Clinical and Translational Neurology*, 6(9):1877-1881.
- Santa, T., Al-Dirbashi, O.Y. & Fukushima, T. 2007. Derivatization reagents in liquid chromatography/electrospray ionization tandem mass spectrometry for biomedical analysis. *Drug Discoveries and Therapeutics*, 1(2):108-118.

Sarewicz, M. & Osyczka, A. 2015. Electronic connection between the quinone and cytochrome C redox pools and its role in regulation of mitochondrial electron transport and redox signaling. *Physiological Reviews*, 95(1):219-243.

Sauerbeck, A., Pandya, J., Singh, I., Bittman, K., Readnower, R., Bing, G. & Sullivan, P. 2011. Analysis of regional brain mitochondrial bioenergetics and susceptibility to mitochondrial inhibition utilizing a microplate based system. *Journal of Neuroscience Methods*, 198(1):36-43.

Sazanov, L.A. 2015. A giant molecular proton pump: structure and mechanism of respiratory complex I. *Nature Reviews Molecular Cell Biology*, 16(6):375-388.

Scaini, G., Rochi, N., Benedet, J., Ferreira, G.K., Teodorak, B.P., Comim, C.M., Constantino, L.d.S., Vuolo, F., Constantino, L.C. & Quevedo, J. 2011. Inhibition of brain citrate synthase activity in an animal model of sepsis. *Revista Brasileira de Terapia Intensiva*, 23(2):158-163.

Schleifer, G., Marutani, E., Ferrari, M., Sharma, R., Skinner, O., Goldberger, O., Grange, R.M.H., Peneyra, K., Malhotra, R. & Wepler, M. 2018. Impaired hypoxic pulmonary vasoconstriction in a mouse model of Leigh syndrome. *American Journal of Physiology Lung Cellular and Molecular Physiology*, 316(2):L391-L399.

Schönfeld, P. & Reiser, G. 2017. Brain energy metabolism spurns fatty acids as fuel due to their inherent mitotoxicity and potential capacity to unleash neurodegeneration. *Neurochemistry International*, 109:68-77.

Schreiner, B., Romanelli, E., Liberski, P., Ingold-Heppner, B., Sobottka-Brillout, B., Hartwig, T., Chandrasekar, V., Johannssen, H., Zeilhofer, Hanns U., Aguzzi, A., Heppner, F., Kerschensteiner, M. & Becher, B. 2015. Astrocyte depletion impairs redox homeostasis and triggers neuronal loss in the adult CNS. *Cell Reports*, 12(9):1377-1384.

Schymanski, E.L., Jeon, J., Gulde, R., Fenner, K., Ruff, M., Singer, H.P. & Hollender, J. 2014. Identifying small molecules via high resolution mass spectrometry: communicating confidence. *Environmental Science and Technology*, 48(4):2097-2098.

Sharpe, A.J. & McKenzie, M. 2018. Mitochondrial fatty acid oxidation disorders associated with short-chain enoyl-CoA hydratase (ECHS1) deficiency. *Cells*, 7(46):1-13.

Shaughnessy, D.T., McAllister, K., Worth, L., Haugen, A.C., Meyer, J.N., Domann, F.E., Van Houten, B., Mostoslavsky, R., Bultman, S.J. & Baccarelli, A.A. 2014. Mitochondria, energetics, epigenetics, and cellular responses to stress. *Environmental Health Perspectives*, 122(12):1271.

Shepherd, D. & Garland, P. 1969. The kinetic properties of citrate synthase from rat liver mitochondria. *Biochemical Journal*, 114(3):597-610.

Sherratt, H. 1991. Mitochondria: structure and function. *Revue Neurologique*, 147(6-7):417-430.

Shuvalov, O., Petukhov, A., Daks, A., Fedorova, O., Vasileva, E. & Barlev, N.A. 2017. One-carbon metabolism and nucleotide biosynthesis as attractive targets for anticancer therapy. *Oncotarget*, 8(14):23955-23977.

Signes, A. & Fernandez-Vizarra, E. 2018. Assembly of mammalian oxidative phosphorylation complexes I–V and supercomplexes. *Essays in Biochemistry*, 62(3):255-270.

- Smeitink, J., van den Heuvel, L. & DiMauro, S. 2001. The genetics and pathology of oxidative phosphorylation. *Nature Reviews Genetics*, 2(5):342-352.
- Smeitink, J.A., van den Heuvel, L.W., Koopman, W.J., Nijtmans, L.G., Ugalde, C. & Willems, P.H. 2004. Cell biological consequences of mitochondrial NADH: ubiquinone oxidoreductase deficiency. *Current Neurovascular Research*, 1(1):29-40.
- Smeitink, J.A., Zeviani, M., Turnbull, D.M. & Jacobs, H.T. 2006. Mitochondrial medicine: a metabolic perspective on the pathology of oxidative phosphorylation disorders. *Cell Metabolism*, 3(1):9-13.
- Smith, P.K., Krohn, R.I., Hermanson, G., Mallia, A., Gartner, F., Provenzano, M., Fujimoto, E., Goeke, N., Olson, B. & Klenk, D. 1985. Measurement of protein using bicinchoninic acid. *Analytical Biochemistry*, 150(1):76-85.
- Sofou, K., De Coo, I.F.M., Isohanni, P., Ostergaard, E., Naess, K., De Meirleir, L., Tzoulis, C., Uusimaa, J., De Angst, I.B., Lönnqvist, T., Pihko, H., Mankinen, K., Bindoff, L.A., Tulinius, M. & Darin, N. 2014. A multicenter study on Leigh syndrome: disease course and predictors of survival. *Orphanet Journal of Rare Diseases*, 9(52):1-16.
- Sokoloff, L. 1960. The metabolism of the central nervous system in vivo. In: Field, J., Magoun, H.W., Hall, V.E., eds *Handbook of Physiology, Section 1, Neurophysiology*. Washington, DC: American Physiological Society. p.1843-1864.
- Son, J.H., Shim, J.H., Kim, K.-H., Ha, J.-Y. & Han, J.Y. 2012. Neuronal autophagy and neurodegenerative diseases. *Experimental and Molecular Medicine*, 44(2):89-98.
- Song, L. & Cortopassi, G. 2015. Mitochondrial complex I defects increase ubiquitin in substantia nigra. *Brain Research*, 1594:82-91.
- Song, L., Yu, A., Murray, K. & Cortopassi, G. 2017. Bipolar cell reduction precedes retinal ganglion neuron loss in a complex 1 knockout mouse model. *Brain Research*, 1657:232-244.
- Sontag, J.-M., Nunbhakdi-Craig, V., Montgomery, L., Arning, E., Bottiglieri, T. & Sontag, E. 2008. Folate deficiency induces in vitro and mouse brain region-specific downregulation of leucine carboxyl methyltransferase-1 and protein phosphatase 2A B(alpha) subunit expression that correlate with enhanced tau phosphorylation. *Journal of Neuroscience*, 28(45):11477-11487.
- Sorrentino, V., Menzies, K.J. & Auwerx, J. 2018. Repairing mitochondrial dysfunction in disease. *Annual Review of Pharmacology and Toxicology*, 58:353-389.
- Spinazzi, M., Casarin, A., Pertegato, V., Ermani, M., Salviati, L. & Angelini, C. 2011. Optimization of respiratory chain enzymatic assays in muscle for the diagnosis of mitochondrial disorders. *Mitochondrion*, 11(6):893-904.
- Spinazzi, M., Casarin, A., Pertegato, V., Salviati, L. & Angelini, C. 2012. Assessment of mitochondrial respiratory chain enzymatic activities on tissues and cultured cells. *Nature Protocols*, 7(6):1235-1247.
- Spinazzi, M., Radaelli, E., Horre, K., Arranz, A., Gounko, N., Agostinis, P., Impens, F., Morais, V., Lopez-Lluch, G. & Serneels, L. 2018. Parl deficiency in mouse causes coenzyme q depletion, complex iii defects, and Leigh-like syndrome. *BioRxiv*, art. #368654. <https://doi.org/10.1101/368654>

Srivastava, S. 2016. Emerging therapeutic roles for NAD⁺ metabolism in mitochondrial and age-related disorders. *Clinical and Translational Medicine*, 5(25):1-11.

Stepanova, A., Kahl, A., Konrad, C., Ten, V., Starkov, A.S. & Galkin, A. 2017. Reverse electron transfer results in a loss of flavin from mitochondrial complex I: potential mechanism for brain ischemia reperfusion injury. *Journal of Cerebral Blood Flow and Metabolism*, 37(12):3649-3658.

Stepanova, A., Shurubor, Y., Valsecchi, F., Manfredi, G. & Galkin, A. 2016. Differential susceptibility of mitochondrial complex II to inhibition by oxaloacetate in brain and heart. *Biochimica et Biophysica Acta (BBA)-Bioenergetics*, 1857(9):1561-1568.

Sterky, F.H., Hoffman, A.F., Milenkovic, D., Bao, B., Paganelli, A., Edgar, D., Wibom, R., Lupica, C.R., Olson, L. & Larsson, N.-G. 2011. Altered dopamine metabolism and increased vulnerability to MPTP in mice with partial deficiency of mitochondrial complex I in dopamine neurons. *Human Molecular Genetics*, 21(5):1078-1089.

Steuer, R., Morgenthal, K., Weckwerth, W. & Selbig, J. 2007. A gentle guide to the analysis of metabolomic data. *Methods in Molecular Biology*, 358:105-126.

Strazielle, C., Jazi, R., Verdier, Y., Qian, S. & Lalonde, R. 2009. Regional brain metabolism with cytochrome c oxidase histochemistry in a PS1/A246E mouse model of autosomal dominant Alzheimer's disease: correlations with behavior and oxidative stress. *Neurochemistry International*, 55(8):806-814.

Strazielle, C., Sturchler-Pierrat, C., Staufenbiel, M. & Lalonde, R. 2003. Regional brain cytochrome oxidase activity in β -amyloid precursor protein transgenic mice with the Swedish mutation. *Neuroscience*, 118(4):1151-1163.

Sumegi, B. & Srere, P.A. 1984. Complex I binds several mitochondrial NAD-coupled dehydrogenases. *Journal of Biological Chemistry*, 259(24):15040-15045.

Takahashi, Y., Kioka, H., Shintani, Y., Ohki, A., Takashima, S., Sakata, Y., Higuchi, T. & Saito, S. 2019. Detection of increased intracerebral lactate in a mouse model of Leigh syndrome using proton MR spectroscopy. *Magnetic resonance imaging*, 58:38-43.

Telford, J.E., Kilbride, S.M. & Davey, G.P. 2009. Complex I is rate-limiting for oxygen consumption in the nerve terminal. *Journal of Biological Chemistry*, 284(14):9109-9114.

Telford, J.E., Kilbride, S.M. & Davey, G.P. 2010. Decylubiquinone increases mitochondrial function in synaptosomes. *Journal of Biological Chemistry*, 285(12):8639-8645.

The Open University. 2018. *SPSS statistics tutorial: two-way mixed ANOVA*. <http://www.open.ac.uk/socialsciences/spsstutorial/files/tutorials/two-way-mixed-ANOVA.pdf>
Date of access: 3 Oct. 2018.

Theunissen, T.E.J., Gerards, M., Hellebrekers, D.M.E.I., van Tienen, F.H., Kamps, R., Sallevelt, S.C.E.H., Hartog, E.N.M.M.D., Scholte, H.R., Verdijk, R.M., Schoonderwoerd, K., de Coo, I.F.M., Szklarczyk, R. & Smeets, H.J.M. 2017. Selection and characterization of palmitic acid responsive patients with an oxphos complex I defect. *Frontiers in Molecular Neuroscience*, 10:336-336.

Thoden, J.B., Huang, X., Raushel, F.M. & Holden, H.M. 2002. Carbamoyl-phosphate synthetase creation of an escape route for ammonia. *Journal of Biological Chemistry*, 277(42):39722-39727.

- Thomas, H.E., Zhang, Y., Stefely, J.A., Veiga, S.R., Thomas, G., Kozma, S.C. & Mercer, C.A. 2018. Mitochondrial complex I activity is required for maximal autophagy. *Cell Reports*, 24(9):2404-2417.
- Thorburn, D., Chow, C. & Kirby, D. 2004. Respiratory chain enzyme analysis in muscle and liver. *Mitochondrion*, 4(5):363-375.
- Torraco, A., Peralta, S., Iommarini, L. & Diaz, F. 2015. Mitochondrial diseases part I: mouse models of OXPHOS deficiencies caused by defects in respiratory complex subunits or assembly factors. *Mitochondrion*, 21:76-91.
- Tracey, T.J., Steyn, F.J., Wolvetang, E.J. & Ngo, S.T. 2018. Neuronal lipid metabolism: multiple pathways driving functional outcomes in health and disease. *Frontiers in Molecular Neuroscience*, 11, art. #10. doi:10.3389/fnmol.2018.00010
- Troyanskaya, O., Cantor, M., Sherlock, G., Brown, P., Hastie, T., Tibshirani, R., Botstein, D. & Altman, R.B. 2001. Missing value estimation methods for DNA microarrays. *Bioinformatics*, 17(6):520-525.
- Tucker, E.J., Compton, A.G., Calvo, S.E. & Thorburn, D.R. 2011. The molecular basis of human complex I deficiency. *International Union of Biochemistry and Molecular Biology (IUBMB) Life*, 63(9):669-677.
- Tugizimana, F., Steenkamp, P., Piater, L. & Dubery, I. 2016. A conversation on data mining strategies in LC-MS untargeted metabolomics: pre-processing and pre-treatment steps. *Metabolites*, 6, art. #40. doi:10.3390/metabo6040040
- Tukey, J.W. 1977. Some thoughts on clinical trials, especially problems of multiplicity. *Science*, 198(4318):679-684.
- Uchino, S., Iida, A., Sato, A., Ishikawa, K., Mimaki, M., Nishino, I. & Goto, Y.-i. 2019. A novel compound heterozygous variant of ECHS1 identified in a Japanese patient with Leigh syndrome. *Human Genome Variation*, 6(19):1-4.
- Ugalde, C., Janssen, R.J., van den Heuvel, L.P., Smeitink, J.A. & Nijtmans, L.G. 2004. Differences in assembly or stability of complex I and other mitochondrial OXPHOS complexes in inherited complex I deficiency. *Human Molecular Genetics*, 13(6):659-667.
- Uittenbogaard, M. & Chiaramello, A. 2014. Mitochondrial biogenesis: a therapeutic target for neurodevelopmental disorders and neurodegenerative diseases. *Current Pharmaceutical Design*, 20(35):5574-5593.
- Ummarino, S., Mozzon, M., Zamporlini, F., Amici, A., Mazzola, F., Orsomando, G., Ruggieri, S. & Raffaelli, N. 2017. Simultaneous quantitation of nicotinamide riboside, nicotinamide mononucleotide and nicotinamide adenine dinucleotide in milk by a novel enzyme-coupled assay. *Food Chemistry*, 221:161-168.
- Valsecchi, F., Esseling, J.J., Koopman, W.J. & Willems, P.H. 2009. Calcium and ATP handling in human NADH: ubiquinone oxidoreductase deficiency. *Biochimica et Biophysica Acta (BBA)-Molecular Basis of Disease*, 1792(12):1130-1137.
- Valsecchi, F., Koopman, W.J., Manjeri, G.R., Rodenburg, R.J., Smeitink, J.A. & Willems, P.H. 2010. Complex I disorders: causes, mechanisms, and development of treatment strategies at the cellular level. *Developmental Disabilities Research Reviews*, 16(2):175-182.

- Valsecchi, F., Monge, C., Forkink, M., de Groof, A.J., Benard, G., Rossignol, R., Swarts, H.G., van Emst-de Vries, S.E., Rodenburg, R.J. & Calvaruso, M.A. 2012. Metabolic consequences of NDUFS4 gene deletion in immortalized mouse embryonic fibroblasts. *Biochimica et Biophysica Acta (BBA)-Bioenergetics*, 1817(10):1925-1936.
- Vasava, A. & Mashiyava, P. 2016. Electron transport chain: role in reactive oxygen species production and aging. *Scholars Journal of Agriculture and Veterinary Sciences*, 3(5):378-388.
- Vasilopoulou, C.G., Margarity, M. & Klapa, M.I. 2016a. Metabolomic analysis in brain research: opportunities and challenges. *Frontiers in Physiology*, 7, art. #183. doi:10.3389/fphys.2016.00183
- Vasilopoulou, C.G., Margarity, M. & Klapa, M.I. 2016b. Metabolomics and network biology: sex comparative analysis of mouse brain regional metabolic physiology. *International Federation of Automatic Control (IFAC) PapersOnLine*, 49(26):283-285.
- Vásquez, O.L., Almeida, Á. & Bolaños, J.P. 2001. Depletion of glutathione up-regulates mitochondrial complex I expression in glial cells. *Journal of Neurochemistry*, 76(5):1593-1596.
- Venter, L., Mienie, L.J., van Rensburg, P.J.J., Mason, S., Vosloo, A. & Lindeque, J.Z. 2018. Uncovering the metabolic response of abalone (*Haliotis midae*) to environmental hypoxia through metabolomics. *Metabolomics*, 14, art. #49. doi.org/10.1007/s11306-018-1346-8
- Venter, L., van Rensburg, P.J., Vosloo, A. & Lindeque, J.Z. 2016. Untargeted metabolite profiling of abalone using gas chromatography mass spectrometry. *Food Analytical Methods*, 9(5):1254-1261.
- Verdin, E. 2015. NAD⁺ in aging, metabolism, and neurodegeneration. *Science*, 350(6265):1208-1213.
- Vergano, S.S., Rao, M., McCormack, S., Ostrovsky, J., Clarke, C., Preston, J., Bennett, M.J., Yudkoff, M., Xiao, R. & Falk, M.J. 2014. In vivo metabolic flux profiling with stable isotopes discriminates sites and quantifies effects of mitochondrial dysfunction in *C. elegans*. *Molecular Genetics and Metabolism*, 111(3):331-341.
- Verheijen, B.M., Vermulst, M. & van Leeuwen, F.W. 2018. Somatic mutations in neurons during aging and neurodegeneration. *Acta Neuropathologica*, 135(6):811-826.
- Verkaart, S., Koopman, W.J., Cheek, J., Van Emst-de Vries, S.E., Van den Heuvel, L.W., Smeitink, J.A. & Willems, P.H. 2007a. Mitochondrial and cytosolic thiol redox state are not detectably altered in isolated human NADH: ubiquinone oxidoreductase deficiency. *Biochimica et Biophysica Acta (BBA)-Molecular Basis of Disease*, 1772(9):1041-1051.
- Verkaart, S., Koopman, W.J., Van Emst-de Vries, S.E., Nijtmans, L.G., Van den Heuvel, L.W., Smeitink, J.A. & Willems, P.H. 2007b. Superoxide production is inversely related to complex I activity in inherited complex I deficiency. *Biochimica et Biophysica Acta (BBA)-Molecular Basis of Disease*, 1772(3):373-381.
- Visch, H.-J., Koopman, W.J., Leusink, A., van Emst-de Vries, S.E., van den Heuvel, L.W., Willems, P.H. & Smeitink, J.A. 2006. Decreased agonist-stimulated mitochondrial ATP production caused by a pathological reduction in endoplasmic reticulum calcium content in human complex I deficiency. *Biochimica et Biophysica Acta (BBA)-Molecular Basis of Disease*, 1762(1):115-123.

- Visch, H.-J., Rutter, G.A., Koopman, W.J., Koenderink, J.B., Verkaart, S., de Groot, T., Varadi, A., Mitchell, K.J., van den Heuvel, L.P. & Smeitink, J.A. 2004. Inhibition of mitochondrial Na⁺-Ca²⁺ exchange restores agonist-induced ATP production and Ca²⁺ handling in human complex I deficiency. *Journal of Biological Chemistry*, 279(39):40328-40336.
- Viscomi, C., Bottani, E. & Zeviani, M. 2015. Emerging concepts in the therapy of mitochondrial disease. *Biochimica et Biophysica Acta (BBA)-Bioenergetics*, 1847(6-7):544-557.
- Wallace, D.C. 2005. A mitochondrial paradigm of metabolic and degenerative diseases, aging, and cancer: a dawn for evolutionary medicine. *Annual Review of Genetics*, 39(1):359-407.
- Wallace, D.C. 2013. A mitochondrial bioenergetic etiology of disease. *The Journal of Clinical Investigation*, 123(4):1405-1412.
- Wang, M., Huang, Y.-P., Wu, H., Song, K., Wan, C., Chi, A.-N., Xiao, Y.-M. & Zhao, X.-Y. 2017. Mitochondrial complex I deficiency leads to the retardation of early embryonic development in Ndufs4 knockout mice. *PeerJ*, 5, e3339. <https://doi.org/10.7717/peerj.3339>
- Wang, X. & Michaelis, E.K. 2010. Selective neuronal vulnerability to oxidative stress in the brain. *Frontiers in Aging Neuroscience*, 2, art. #12. <https://doi.org/10.3389/fnagi.2010.00012>
- Wanichthanarak, K., Fan, S., Grapov, D., Barupal, D.K. & Fiehn, O. 2017. Metabox: a toolbox for metabolomic data analysis, interpretation and integrative exploration. *Public Library of Science (PloS) One*, 12(1), e0171046. doi:10.1371/journal.pone.0171046
- Watmough, N.J. & Frerman, F.E. 2010. The electron transfer flavoprotein: ubiquinone oxidoreductases. *Biochimica et Biophysica Acta (BBA)-Bioenergetics*, 1797(12):1910-1916.
- Wei, R., Wang, J., Su, M., Jia, E., Chen, S., Chen, T. & Ni, Y. 2018. Missing value imputation approach for mass spectrometry-based metabolomics data. *Scientific Reports*, 8(1), art. #663. doi:10.1038/s41598-017-19120-0
- Wei, X., Shi, B., Koo, I., Yin, X., Lorkiewicz, P., Suhail, H., Rattan, R., Giri, S., McClain, C.J. & Zhang, X. 2017. Analysis of stable isotope assisted metabolomics data acquired by GC-MS. *Analytica Chimica Acta*, 980:25-32.
- Widmaier, E.P., Raff, H., Strang, K.T. & Vander, A.J. 2008. *Vander's Human physiology: the mechanisms of body function*. 14th ed. New York, NY: McGraw-Hill Higher Education.
- Wilson, D.F. 2017. Oxidative phosphorylation: regulation and role in cellular and tissue metabolism. *The Journal of Physiology*, 595(23):7023-7038.
- Wilson, K. & Walker, J. 2010. *Principles and techniques of biochemistry and molecular biology*. 7th ed. New York, NY: Cambridge University Press.
- Wilson, M.P., Plecko, B., Mills, P.B. & Clayton, P.T. 2019. Disorders affecting vitamin B6 metabolism. *Journal of Inherited Metabolic Disease*, 42(4):629-646.
- Wirtz, S. & Schuelke, M. 2011. Region-specific expression of mitochondrial complex I genes during murine brain development. *Public Library of Science (PloS) One*, 6(4), e18897. doi:10.1371/journal.pone.0018897

- Wortmann, S.B., Mayr, J.A., Nuoffer, J.M., Prokisch, H. & Sperl, W. 2017. A guideline for the diagnosis of pediatric mitochondrial disease: the value of muscle and skin biopsies in the genetics era. *Neuropediatrics*, 48(4):309-314.
- Wu, H., Southam, A.D., Hines, A. & Viant, M.R. 2008. High-throughput tissue extraction protocol for NMR-and MS-based metabolomics. *Analytical Biochemistry*, 372(2):204-212.
- Wu, Y. & Li, L. 2016. Sample normalization methods in quantitative metabolomics. *Journal of Chromatography A*, 1430:80-95.
- Wyse, A.T. & Netto, C.A. 2011. Behavioral and neurochemical effects of proline. *Metabolic Brain Disease*, 26(3):159-172.
- Wyss, M. & Kaddurah-Daouk, R. 2000. Creatine and creatinine metabolism. *Physiological Reviews*, 80(3):1107-1213.
- Xu, J., Begley, P., Church, S.J., Patassini, S., Hollywood, K.A., Jüllig, M., Curtis, M.A., Waldvogel, H.J., Faull, R.L. & Unwin, R.D. 2016. Graded perturbations of metabolism in multiple regions of human brain in Alzheimer's disease: snapshot of a pervasive metabolic disorder. *Biochimica et Biophysica Acta (BBA)-Molecular Basis of Disease*, 1862(6):1084-1092.
- Yang, J., Cheng, J., Sun, B., Li, H., Wu, S., Dong, F. & Yan, X. 2018. Untargeted and stable isotope-assisted metabolomic analysis of MDA-MB-231 cells under hypoxia. *Metabolomics*, 14, art. #40. <https://doi.org/10.1007/s11306-018-1338-8>
- Yang, J., Zhao, X., Lu, X., Lin, X. & Xu, G. 2015. A data preprocessing strategy for metabolomics to reduce the mask effect in data analysis. *Frontiers in Molecular Biosciences*, 2, art. #4. <https://doi.org/10.3389/fmolb.2015.00004>
- Ye, J., Jiang, Z., Chen, X., Liu, M., Li, J. & Liu, N. 2016. Electron transport chain inhibitors induce microglia activation through enhancing mitochondrial reactive oxygen species production. *Experimental Cell Research*, 340(2):315-326.
- Yu, A.K., Song, L., Murray, K.D., Van Der List, D., Sun, C., Shen, Y., Xia, Z. & Cortopassi, G.A. 2015. Mitochondrial complex I deficiency leads to inflammation and retinal ganglion cell death in the *Ndufs4* mouse. *Human Molecular Genetics*, 24(10):2848-2860.
- Yu, H., Iyer, R.K., Kern, R.M., Rodriguez, W.I., Grody, W.W. & Cederbaum, S.D. 2001. Expression of arginase isozymes in mouse brain. *Journal of Neuroscience Research*, 66(3):406-422.
- Yubero, D., Adin, A., Montero, R., Jou, C., Jiménez-Mallebrera, C., García-Cazorla, A., Nascimento, A., O'Callaghan, M.M., Montoya, J., Gort, L., Navas, P., Ribes, A., Ugarte, M.D. & Artuch, R. 2016. A statistical algorithm showing coenzyme Q10 and citrate synthase as biomarkers for mitochondrial respiratory chain enzyme activities. *Scientific Reports*, 6, art. #15. <https://doi.org/10.1038/s41598-016-0008-1>
- Yudkoff, M. 2017. Interactions in the Metabolism of glutamate and the branched-chain amino acids and ketoacids in the CNS. *Neurochemical Research*, 42(1):10-18.
- Yudkoff, M., Daikhin, Y., Nissim, I., Horyn, O., Luhovyy, B., Lazarow, A. & Nissim, I. 2005. Brain amino acid requirements and toxicity: the example of leucine. *The Journal of Nutrition*, 135(6):1531S-1538S.

- Zarate, E., Boyle, V., Rupprecht, U., Green, S., Villas-Boas, S.G., Baker, P. & Pinu, F.R. 2016. Fully automated trimethylsilyl (TMS) derivatisation protocol for metabolite profiling by GC-MS. *Metabolites*, 7(1), art. #1. doi:10.3390/metabo7010001
- Zhang, T., Wang, W., Huang, J., Liu, X., Zhang, H. & Zhang, N. 2016. Metabolomic investigation of regional brain tissue dysfunctions induced by global cerebral ischemia. *BioMed Central (BMC) Neuroscience*, 17(1), art. #25. doi:10.1186/s12868-016-0256-9
- Zhao, L., Mao, Z., Woody, S.K. & Brinton, R.D. 2016. Sex differences in metabolic aging of the brain: insights into female susceptibility to Alzheimer's disease. *Neurobiology of Aging*, 42:69-79.
- Zhao, R.Z., Jiang, S., Zhang, L. & Yu, Z.B. 2019. Mitochondrial electron transport chain, ROS generation and uncoupling. *International Journal of Molecular Medicine*, 44(1):3-15.
- Zheng, X., Boyer, L., Jin, M., Kim, Y., Fan, W., Bardy, C., Berggren, T., Evans, R.M., Gage, F.H. & Hunter, T. 2016a. Alleviation of neuronal energy deficiency by mTOR inhibition as a treatment for mitochondria-related neurodegeneration. *Elifesciences*, 5, e13378. doi:10.7554/eLife.13378
- Zheng, X., Chen, T., Zhao, A., Wang, X., Xie, G., Huang, F., Liu, J., Zhao, Q., Wang, S. & Wang, C. 2016b. The brain metabolome of male rats across the lifespan. *Scientific Reports*, 6, art. #24125. <https://doi.org/10.1038/srep24125>
- Zhou, Z., Austin, G.L., Young, L.E., Johnson, L.A. & Sun, R. 2018. Mitochondrial metabolism in major neurological diseases. *Cells*, 7(12), art. #229. doi:10.3390/cells7120229
- Zieliński, Ł.P., Smith, A.C., Smith, A.G. & Robinson, A.J. 2016. Metabolic flexibility of mitochondrial respiratory chain disorders predicted by computer modelling. *Mitochondrion*, 31:45-55.

APPENDIX A

Genotyping and animal information

A.1. Introduction

In this section, a typical example is shown of the genotype verification results for the mice from which samples were obtained and analysed in this study. Additional information of these mice are also provided in this section.

A.2. Genotype verification of experimental mice

In addition to being genotyped upon weaning, the mice used in this study (n =68) were genotyped after euthanasia and sample collection. This was done to ensure no mix-ups occurred during the initial genotyping process or during the sample collection procedure. The genotype of each mouse was verified using the tail tips collected simultaneously with the brain tissues (Section 4.4). Conventional polymerase chain reaction (PCR) amplification and electrophoresis were carried out as described in Section 4.5. To differentiate between the potential genotypes (*Ndufs4* knockout [KO], *Ndufs4* wild-type [WT] and *Ndufs4* heterozygous [HET]), the deletion in exon 2 of the *Ndufs4* gene can be confirmed by using primer pairs that correspond to the two flanking introns as described previously (Kruse *et al.*, 2008; Valsecchi *et al.*, 2012). Isolated DNA with known genotypes (KO, WT and HET) was included as controls in each PCR run, together with a 100 bp DNA ladder as a DNA size marker. The presence of a 1 229 bp band identified the *Ndufs4* WT genotype, while the presence of a shorter 429 bp band (corresponding with the 800 bp deletion of exon 2) identified the *Ndufs4* KO genotype. In addition, the presence of both bands distinguished the *Ndufs4* HET genotype. An example of an agarose gel electrophoretogram for verification of genotypes is provided in Figure A.1.

APPENDIX A: Animal information

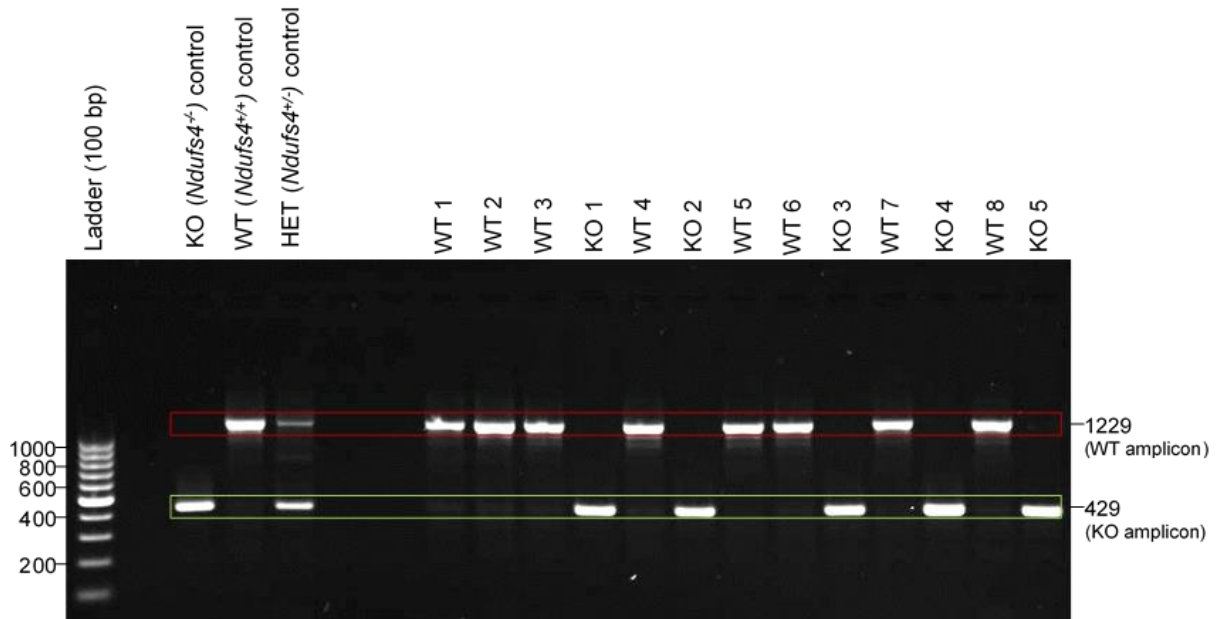


Figure A.1: Example of agarose gel electrophoretogram obtained during genotyping of mice.

A 100 base pair (bp) DNA size marker (ladder) was loaded in the first lane followed by three control samples (knockout/KO: *Ndufs4*^{-/-}, wild-type/WT: *Ndufs4*^{+/+} and heterozygote/HET: *Ndufs4*^{+/-}) and test samples. Ladder sizes are indicated to the far left and DNA amplicon sizes to the far right. Sizes of the PCR products are given in base pairs (bp).

A.3. Supplementary information of experimental mice

In the metabolomics investigation, the brain regions of interest were obtained from a total of 46 mice, 25 *Ndufs4* wild-type (WT) mice and 21 *Ndufs4* knockout (KO) mice. In addition, brain region samples from 22 mice, 10 WT mice and 12 KO mice, were used for the biochemical investigation. Information of these mice are provided in Table A.1 and Table A.2, with identification- and litter-numbers; age of euthanasia; and the time taken until samples were snap frozen after removal. Take into consideration that only samples from male mice were included in this study. This was done in order to reduce gender-related variability (especially in metabolomics investigations) and avoid unnecessary complications due to estrous cycles in females (Lovick, 2012; Vasilopoulou *et al.*, 2016b; Zhao *et al.*, 2016).

APPENDIX A: Animal information

Table A.1: Information of mice from which samples were obtained and analysed in the metabolomics investigation.

Genotype	ID no.	Litter no.	Age (PN) euthanised	Time (minutes) until frozen after removal
WT	95	1t	48	11:30
	2	1u	46	11:18
	14	1w	48	10:50
	8	1v	48	09:50
	27	1x	47	10:17
	54	2c	47	13:00
	59	2e	46	12:15
	61	2e	47	12:59
	80	2g	48	12:10
	81	2g	48	13:49
	82	2g	48	12:17
	62	2t	48	11:36
	2	3c	47	11:50
	9	3d	47	12:00
	42	3k	46	09:00
	57	3l	46	09:50
	83	3p	49	09:35
	88	3q	49	10:15
	9	3t	49	08:00
	19	3u	49	09:15
	35	3x	49	09:06
	40	3y	49	08:18
	48	3z	46	08:07
	62	4b	46	08:30
	63	4b	46	07:50
TOTAL WT: 25				
KO	10	1f	46	10:43
	68	1o	46	13:00
	70	1o	46	11:20
	89	1r	46	12:05
	4	1v	48	09:30
	10	1v	48	10:30
	15	1w	48	11:10
	56	2d	46	14:40
	69	2f	48	11:24
	44	3k	46	10:00
	45	3k	46	09:40
	2	3s	49	10:43
	86	3q	49	10:15
	54	4a	46	09:00
	1	4i	48	09:25

APPENDIX A: Animal information

2	4i	48	09:06
8	4j	48	09:08
34	4o	47	08:37
42	4q	49	08:50
50	4s	45	08:07
37	3j	48	11:03

TOTAL KO: 21

Abbreviations: ID, identification; KO, knockout; no., number; PN, postnatal day; WT, wild-type

Table A.2: Information of mice from which samples were obtained and analysed in the biochemical investigation.

Genotype	ID no.	Litter no.	Age (PN) euthanised	Time (minutes) until frozen after removal
WT	93	5o	46	06:07
	73	5z	47	07:24
	67	5x	46	06:26
	25	5r	46	06:30
	75	5z	47	06:33
	67	5j	48	10:15
	69	5x	46	06:40
	34	5s	46	06:26
	42	5t	46	06:13
	65	5j	48	08:33

TOTAL WT: 10

KO	48	5h	48	07:06
	2	5p	46	06:11
	39	5g	48	07:30
	90	5o	46	05:51
	3	5s	46	06:14
	91	6b	46	06:10
	43	5t	46	05:30
	44	5t	46	06:50
	14	5q	46	04:55
	52	5v	46	06:53
	17	5q	46	05:08
	74	5z	47	06:19

TOTAL KO: 12

Abbreviations: ID, identification; KO, knockout; no., number; PN, postnatal day; WT, wild-type.

APPENDIX B

Preparation of reagents

B.1. Introduction

This section outlines the steps to prepare the reduced Cytochrome c and reduced decylubiquinol from their oxidised forms for use in the spectrophotometric assay of mitochondrial complex III and complex IV activities. The preparation procedures of Du Toit (2007) and Luo *et al.* (2008) that were routinely implemented at the Mitochondrial Research Laboratory, NWU, were applied.

B.2. Preparation of reduced Cytochrome c (Cyt c)

To prepare (500 μ M):

- Add 10 mM sodium ascorbate (Sigma-Aldrich[®], #A4034) to 2 mM oxidised Cyt c (Sigma-Aldrich[®], #C7752).
- Incubate at room temperature for five minutes (dark red colour changes to light red colour).
- Remove ascorbate by dialysing (Pierce Slide-A-Lyzer Mini Dialysis unit, Sigma-Aldrich[®], # 69570) for 5 x 2 hrs in 200 mL 5 mM potassium-phosphate (KPi) buffer at 4 °C.
- Change buffer at each interval.

To check reduction:

- Pipette 5 μ L to 9995 μ L KPi buffer (50 mM) into a cuvette.
- Scan 500-600 nm.
- If A550/A565 >8, it is sufficiently reduced.

To calculate the reduced Cyt c concentration, Equation B.1 was used:

$$\text{Reduced Cyt c (mM)} = \frac{A_{550}}{29.5 \text{ mM}^{-1} \cdot \text{cm}^{-1}} \times 200 \text{ (dilution)}$$

(Equation B.1)

Dilute the reduced Cyt c with KPi (50 mM) buffer to 500 μ M, aliquot 200 μ L volumes into micro-centrifuge tubes and store at -20 °C.

B.3. Preparation of reduced decylubiquinone / decylubiquinol (DQnol)

Prepare the following reagents:

- 10 mM oxidised decylubiquinone (DQ) (Sigma-Aldrich®, #D7911), in ethanol.
- 0.1 N HCl in ethanol.
- 0.1 M potassium-phosphate (KPi) buffer (pH7.4) and 0.25 M sucrose (Sigma-Aldrich®, #84100). Add 2 mL 0.5 M KPi buffer to 0.8558 g sucrose and top up to 10 mL.

To prepare 9.62 mM DQnol:

- a) To 100 μ L DQ, add 6 mL of buffer/sucrose mix.
- b) Add 1 mL cyclohexane and 0.7 g of solid sodium dithionite.
- c) Vortex until colourless.
- d) Transfer upper cyclohexane layer to separate vial and repeat step b, without dithionite.
- e) Combine the organic phases and evaporate *in vacuo* until a light-yellow syrup is left.
- f) Dissolve this in 90 μ L ethanol and 10 μ L of 0.1 mol/L HCl.
- g) Store in aliquots at -80 °C.

APPENDIX C

Standardisation of spectrophotometric assays

C.1. Introduction

In this section, the standardisation of the spectrophotometric assays utilised in this study will be discussed (Objective 2.1); i.e. measurement of protein content (bicinchoninic acid / BCA assay) as well as the maximal activities of citrate synthase (CS) and mitochondrial respiratory chain (RC) enzyme (complexes I, II, III and IV) in the supernatants obtained from homogenates of brain region samples. These assays were based on protocols previously standardised at the Mitochondria Research Laboratory (North-West University) for analysis of human skeletal muscle biopsies using a Synergy™ HT Multi-detection microtiter plate reader. To ensure reliable quantification within the linear range of the instrument (response measured is directly proportional to the concentration of the protein or enzyme activity in the sample) when applied to mouse brain region tissue samples, minor adjustments to sample volumes were required. This was necessary since the relative concentration of proteins and the activities of enzymes may differ substantially according to species, tissue type and even brain region (Rossignol *et al.*, 2000; Pathak & Davey, 2008; Dubinsky, 2009).

The aim was therefore to determine the volumes of the brain region-specific tissue preparations required for each assay to enable quantification within the linear range of the instrument. For this purpose, the anterior cortex (AC), brainstem (BST), cerebellum (CB) and olfactory bulbs (OB) of male mice heterozygous for the *Ndufs4* knockout (KO) were prepared by first producing 10% (w/v) homogenates (or 5% w/v for the OB due to limited sample). These were then centrifuged to obtain 700 x *g* supernatants (from here on referred to as 'supernatant/s'). For each assay, a series of supernatant volumes (effectively representing different concentrations of enzyme) were analysed in replicate. Of note, working dilutions were prepared from the supernatants to ensure accurate pipetting volumes. However, all results are expressed as the effective volume of supernatant added per well; i.e. after dilution factors were accounted for. The standardisation was also essential for obtaining practical experience to ensure accurate analyses.

C.2. Standardisation of the bicinchoninic acid (BCA) assay

Smith *et al.* (1985) first described the bicinchoninic acid (BCA) assay, and it was standardised at the Mitochondria Research Laboratory to quantify the protein content of the mouse brain region supernatants. The protein concentration ($\mu\text{g}/\mu\text{L}$) of the supernatants and standard supernatant volume required for quantification within the limits of a standard BSA curve were determined. Different volumes (effectively representing 1 μL , 2 μL and 3 μL for the AC, BST, CB and 2 μL , 4 μL and 6 μL for the OB) of the supernatants were pipetted into the wells of a 96-well UV microtiter plate and analysed in triplicate as described in Section 4.6.4.3. In each case, the protein content was determined from a BSA standard curve which exhibited sufficient linearity ($R^2 > 0.99$) as illustrated in Figure C.1.

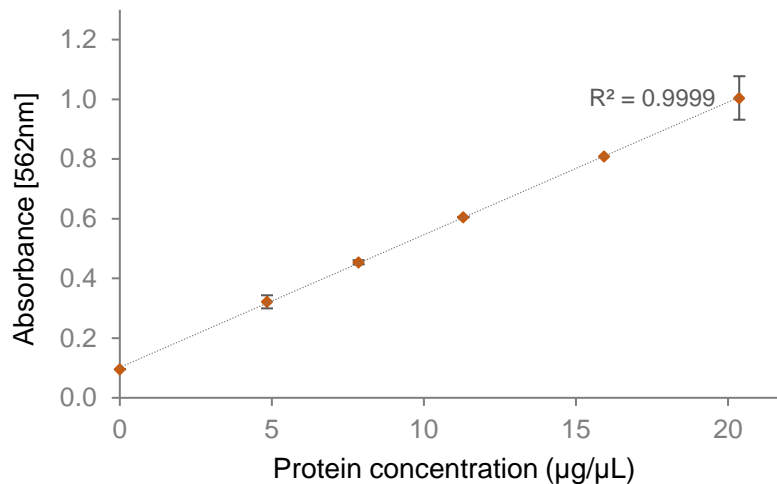


Figure C.1: Example of a BSA standard curve utilised during standardisation of the BCA assay.

Absorbance values were obtained for a BSA protein standard series of 0 μg to 20 μg prepared by pipetting 1 $\mu\text{g}/\mu\text{L}$ BSA protein standard in increments of 4 μg into the 96-well UV microtiter plate. Data points represent the average absorbance \pm SD vs the average protein concentration obtained from duplicate wells. The linear regression of the data showed that the absorbance increased linearly with protein concentration ($R^2 > 0.99$), indicating that a reliable curve was utilised for quantification.

The results for the different supernatant volumes are shown in Figure C.2 for each brain region. Each data point represents the average protein content per well \pm SD determined for each supernatant volume analysed in triplicate. The supernatant protein concentrations of the various brain regions, after accounting for the fact that a 5% and not 10% (w/v) homogenate was prepared for the smaller OB, were roughly in the same range ($\sim 5 \mu\text{g}/\mu\text{L}$). For each brain

APPENDIX C: Standardisation of spectrophotometric assays

region, the protein content of the different supernatant volumes was within the range of the standard BSA curve ($0 \mu\text{g}$ and $<20 \mu\text{g}$). These results indicated that any one of the three volumes could be used in subsequent assays for reliable quantification. Consequently, to ensure accurate protein quantification within these linear ranges while accommodating for potential experimental and biological variation, the mid-volumes of effectively $2 \mu\text{L}$ per well were selected as a standard volume for BCA analysis of AC, BST and CB supernatants and effectively $4 \mu\text{L}$ per well in the case of the OB supernatants.

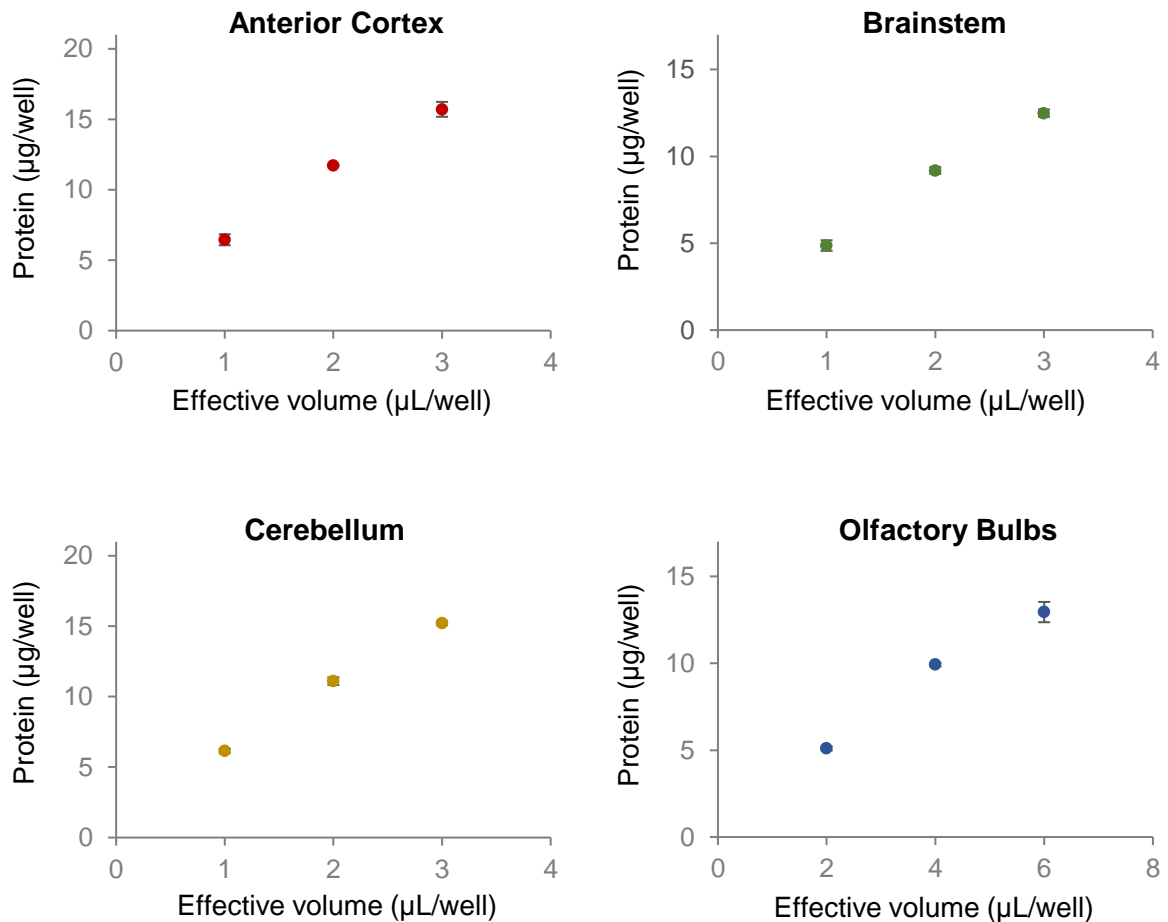


Figure C.2: Linearity of the BCA assay for different volumes of $700 \times g$ supernatants obtained from various mouse brain regions.

The protein content of different volumes (effectively representing $1 \mu\text{L}$, $2 \mu\text{L}$ and $3 \mu\text{L}$ for the anterior cortex, brainstem and cerebellum; and $2 \mu\text{L}$, $4 \mu\text{L}$ and $6 \mu\text{L}$ for the olfactory bulbs) of the supernatants were measured spectrophotometrically in triplicate. Each data point represents the average amount of protein per well \pm SD as determined from the BSA standard curve (Figure C.1). In each case, the protein content was within the range of the standard BSA curve ($0 \mu\text{g}$ and $<20 \mu\text{g}$). The intermediate volumes ($2 \mu\text{L}$ for the anterior cortex, brainstem and cerebellum; and $4 \mu\text{L}$ for the olfactory bulbs) were selected to ensure protein quantification in the linear range of the BSA standard curve while accommodating for potential variation.

C.3. Standardisation of the citrate synthase (CS) activity assay

Shepherd and Garland (1969) first described the citrate synthase (CS) assay, and it was standardised at the Mitochondria Research Laboratory to be used as a marker for mitochondrial content in tissue supernatants. In this assay, CS activity is measured kinetically over five minutes and the average initial velocity (v_1) calculated over the first three minutes. To evaluate the linearity, different volumes (effectively representing 0.25 μL , 0.33 μL and 0.50 μL for the AC, BST, CB and 0.5 μL , 0.66 μL and 1.0 μL for the OB) of the supernatants were analysed in triplicate as described in Section 4.6.4.4. The linearity of the kinetic measurements was evaluated over the entire period of measurement to ensure that the standard volumes selected for experimental assays displayed sufficient linearity to accommodate slight experimental or biological variation. An example of the raw kinetic measurements is shown for the analysis of three different CB supernatant volumes in Figure C.3. For all three volumes, the change in absorbance was linear over the first three minutes ($R^2 > 0.99$). However, for the largest volume (Figure C.3.C) a slight deviation from linearity was seen as equilibrium was slowly being reached after a few minutes. This indicated that effective volumes greater than 0.50 μL might not allow linear quantification over the first three minutes as a plateau will possibly be reached before then. In this case, volumes $< 0.50 \mu\text{L}$ were more reliable.

The calculated v_1 results for the CS linearity assays are shown in Figure C.4 for the different brain regions. Each data point represents the average v_1 per well \pm SD obtained for the respective volumes of supernatant added per well. For each brain region, v_1 increased linearly ($R^2 > 0.99$) with the effective volume added per well, indicating linear quantification over the three volumes used. To ensure accurate quantification in these linear ranges, effectively 0.4 μL per well was selected for the AC, BST and CB supernatants and effectively 0.8 μL per well in the case of the OB supernatants.

APPENDIX C: Standardisation of spectrophotometric assays

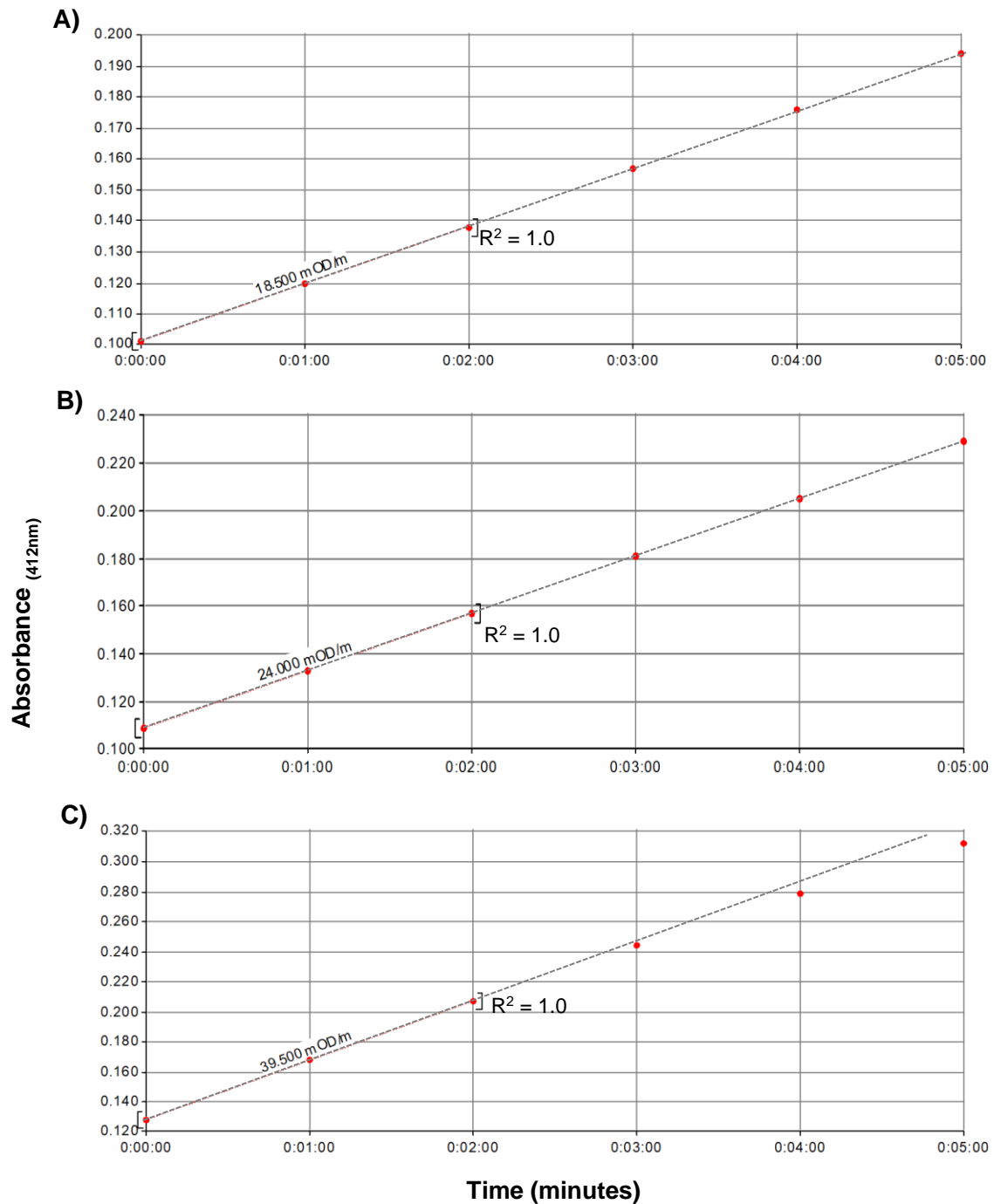


Figure C.3: Examples of single well CS activity measurement for different volumes of CB supernatant.

The linear rate increase in absorbance was recorded at 412 nm over five minutes in one-minute intervals in respective wells containing effectively **A)** 0.25 µL; **B)** 0.33 µL; and **C)** 0.50 µL of a 700 x g CB supernatant. The first three data points were used to determine the average initial velocity (v_1) of CS activity per well or per replicate. For each volume, the absorbance increased linearly ($R^2 > 0.99$) over the first three minutes. The largest volume (Figure C.3.C) displayed a slight deviation from linearity after four minutes, indicating that equilibrium is slowly being reached. In this case, volumes <0.50 µL were more reliable.

APPENDIX C: Standardisation of spectrophotometric assays

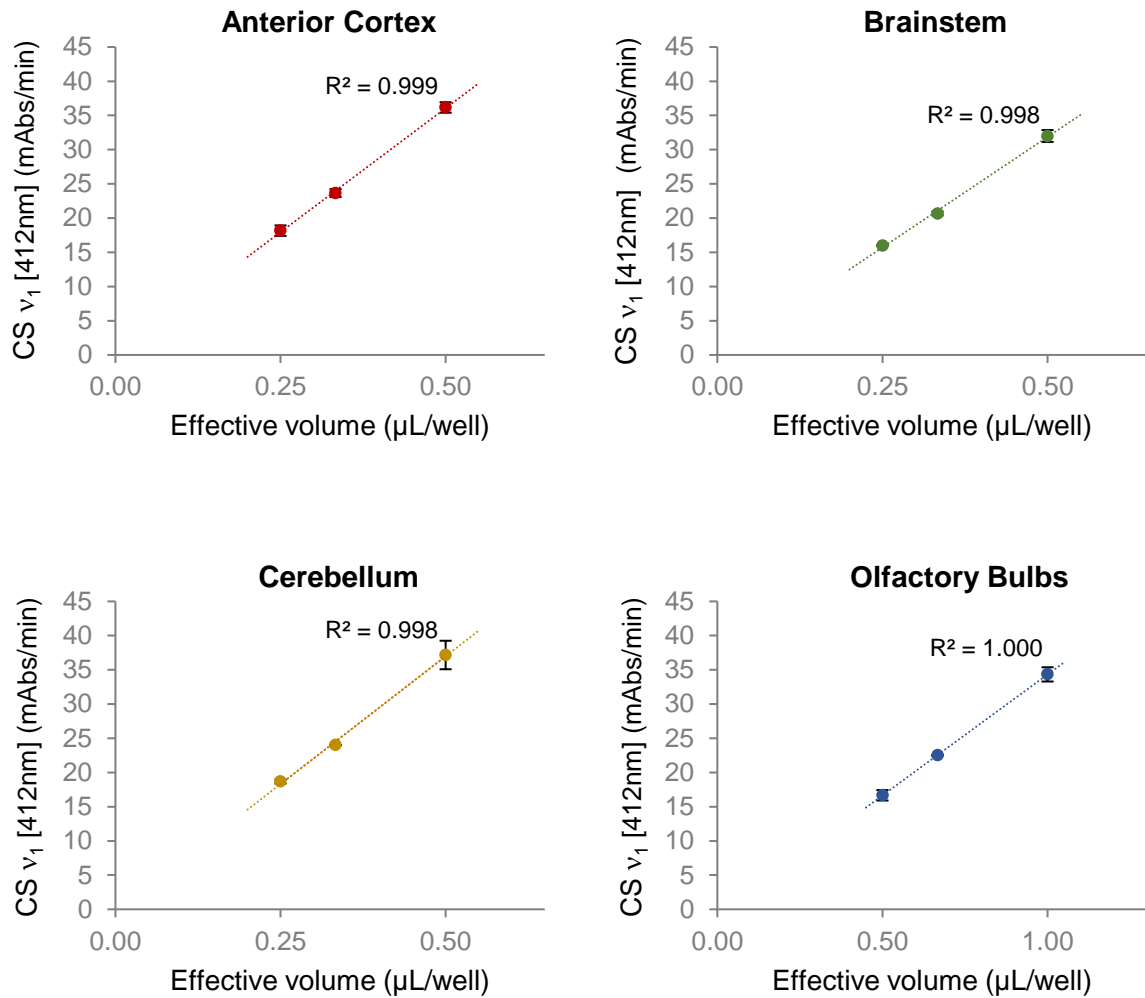


Figure C.4: Linearity of the CS assay for different volumes of 700 x g supernatants obtained from various mouse brain regions.

The initial velocity (v_1) of different volumes (effectively representing 0.25 μL , 0.33 μL and 0.50 μL for the anterior cortex, brainstem and cerebellum; and 0.5 μL , 0.66 μL and 1.0 μL for the olfactory bulbs) of supernatants, were measured spectrophotometrically in triplicate. Each data point represents the average $v_1 \pm \text{SD}$ as determined over the first three minutes (e.g. Figure C.3). In each case, v_1 of CS activity increased linearly ($R^2 > 0.99$) with the effective volume of supernatant added per well. Intermediate volumes (0.4 μL for the anterior cortex, brainstem and cerebellum; and 0.8 μL for the olfactory bulbs) were selected to ensure quantification in the linear range while accommodating for potential variation.

C.4. Standardisation of the respiratory chain enzyme activity assays

In this study, the activities of complexes I, II, III and IV (CI-CIV) were measured kinetically as previously described (Rahman *et al.*, 1996; Janssen *et al.*, 2007; Luo *et al.*, 2008; Pretorius, 2011) and standardised at the Mitochondria Research Laboratory. In these assays, the average initial velocity (v_1) of the enzyme activities was measured kinetically and calculated over an initial time period as described in Section 4.6.4.5 to Section 4.6.4.8. The different supernatant volumes given in Table C.1 were used to evaluate the linearity of each assay for the various mouse brain regions. The linearity of each kinetic measurement was also evaluated over the entire period of measurement to ensure that the standard volumes selected for experimental assays displayed sufficient linearity to accommodate slight experimental or biological variation. A proof of principle is given for the analysis of the four different CB supernatant volumes used in the CI enzyme activity assay Figure C.5 For all four volumes, the change in absorbance was linear over the first four minutes ($R^2 > 0.99$). However, a slight deviation from linearity can be seen when 4 μL or 5 μL are used. In this case, volumes $< 4 \mu\text{L}$ were more reliable.

Figure C.6 shows the calculated v_1 results for the linearity assays for the different brain regions. Each data point represents the average v_1 per well \pm SD obtained for the respective volume of supernatant added per well. For each brain region, v_1 increased linearly ($R^2 > 0.99$) with the effective volume added per well, indicating linear quantification over the volumes used. Table C.1 presents the standard volumes selected for accurate quantification in the linear ranges.

Table C.1: Effective volumes of 700 x g supernatants used and selected for the enzyme activity assays in the various mouse brain regions.

Enzyme Activity Assay	Effective volumes ($\mu\text{L}/\text{well}$) used		Effective volumes($\mu\text{L}/\text{well}$) selected		
	AC, BST, CB	OB	AC	BST, CB	OB
CI	2, 3, 4, 5	4, 6, 8, 10	4	3	6
CII	2, 4, 6	2, 4, 6	4	4	4
CIII	0.4, 0.6, 0.8	0.5, 1.0, 1.5	0.6	0.6	1
CIV	0.1, 0.2, 0.3	0.1, 0.2, 0.3	0.25	0.25	0.125

CI-CIV, complexes I – CIV; AC, anterior cortex; BST, brainstem; CB, cerebellum; OB, olfactory bulbs

APPENDIX C: Standardisation of spectrophotometric assays

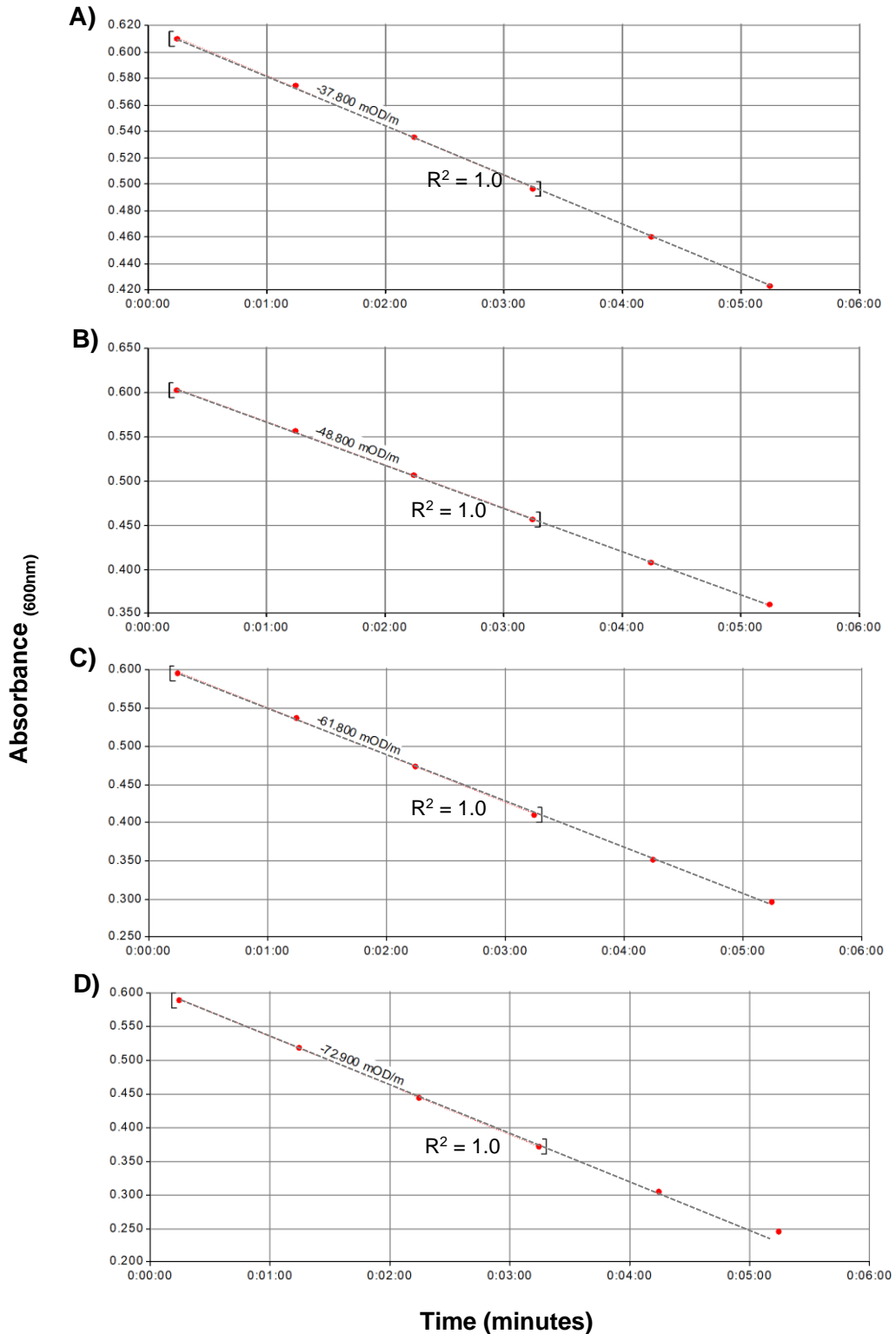


Figure C.5: Examples of single well CI activity measurements for different volumes of CB supernatant.

The linear rate decrease in absorbance was recorded at 600 nm for five minutes in one-minute intervals in in respective wells containing effectively **A)** 2 μL ; **B)** 3 μL ; **C)** 4 μL ; and **D)** 5 μL of a 700 x g CB supernatant. First few data points were used to calculate the average initial velocity (v_1) of the CI activity per well or replicate. For each volume, the absorbance decreased linearly ($R^2 > 0.99$) over the first four minutes. The largest volumes (C and D) displayed a slight deviation from linearity after four minutes, indicating that equilibrium is slowly being reached. In this case, volumes $< 4 \mu\text{L}$ were more reliable.

APPENDIX C: Standardisation of spectrophotometric assays

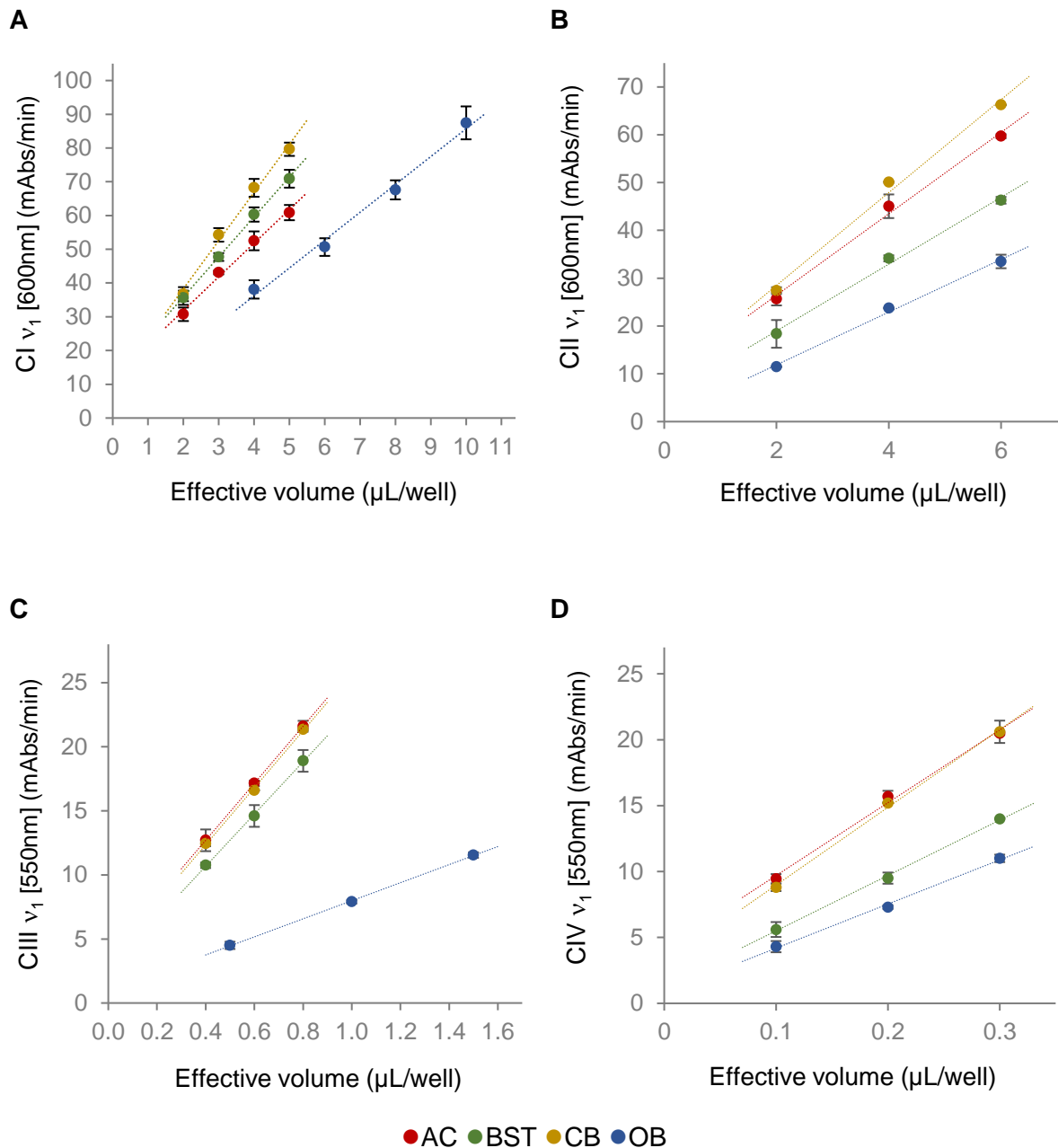


Figure C.6: Linearity of the RC enzyme activity assays for different volumes of 700 x g supernatants obtained from various mouse brain regions.

A) Complex I (CI); **B)** Complex II (CII); **C)** Complex III (CIII); and **D)** Complex IV (CIV). The initial velocity (v_1) of different volumes of the supernatants of the anterior cortex (AC), brainstem (BST), cerebellum (CB) and olfactory bulbs (OB) were respectively measured spectrophotometrically in duplicate due to limited sample. Each data point represents the average $v_1 \pm \text{SD}$ as determined over the first few minutes (e.g. Figure C.5). In each case, v_1 increased linearly ($R^2 > 0.99$, not shown on figures) with the volume of supernatant added per well. Intermediate effective volumes were selected to ensure quantification in the linear range while accommodating for potential variation.

APPENDIX D

Standardisation of metabolomics methods

D.1. Introduction

This section provides a summary of the standardisation of the: 1) Untargeted gas chromatography-time of flight spectrometry (GC-TOF) method (Objective 3.1); and 2) Semi-targeted liquid chromatography-tandem mass spectrometry (LC-MS/MS) method (Objective 3.2). Standardisation was carried out to ensure reliable and reproducible quantification of metabolites in the limited volumes of tissue extracts obtained from the selected mouse brain region samples. In addition, the standardisation realised the skills required for experimental precision. These methods were based on protocols previously standardised at the Mitochondria Research Laboratory (North-West University) (Lindeque *et al.*, 2013; Venter *et al.*, 2016; Esterhuizen *et al.*, 2018; Venter *et al.*, 2018). The standardisation entailed determining the adequate on-column sample and internal standard (IS) concentration for each analysis via a sample dilution series (data not shown). In addition, for the LC-MS/MS method, the conditions for the measurement of each targeted compound were verified. Also, time segments were inserted to improve analytical precision. Lastly, repeatability studies were performed to determine the instrument-, intra- and inter-batch precision of the standardised methods. The latter two points are discussed in this section.

D.2. Verification of compound conditions and insertion of time segments for LC-MS/MS method

As a precautionary measure, and to develop necessary analytical skills, the identities of the compounds targeted in the LC-MS/MS analytical method was confirmed by preparing and derivatising 5 ppm mixtures (Section 4.7.4.4.2) of the corresponding standards and analysing the mixture using the previously developed method. The verified compounds and their corresponding optimised conditions are provided in Table D.1.

Table D.1: Optimised source and multiple reaction monitoring (MRM) conditions for each butylated compound and isotope-labelled standard.

Butylated compounds and isotope-labelled standards of interest, sorted according to retention time and divided into the time segments used in the analytical method, are detailed together with their respective precursor- and product ions, fragmentor (F) voltages and collision energy (CE) voltages.

Compound	Abbreviation	Retention Time (minutes)	Precursor Ion (MS1) (m/z)	Product Ion (MS2) (m/z)	F (V)	CE (V)
Time Segment 1 (0 to 5 minutes)						
Taurine	Tau	1.37	126.0	107.9	93	10
L-Ornithine	Orn	1.50	189.2	70.2	74	20
L-Histidine	His	1.62	212.1	110.1	89	16
L-Lysine- <i>d</i> ₄	Lys- <i>d</i> ₄	1.65	207.2	88.2	118	16
3-Methyl-L-Histidine	3-Mhis	1.65	226.4	96.2	130	25
L-Lysine	Lys	1.65	203.2	84.1	89	20
1-Methyl-L-Histidine	1-Mhis	1.80	226.4	124.2	120	15
L-Arginine	Arg	1.85	231.2	70.1	103	40
L-Arginine- <i>d</i> ₄	Arg- <i>d</i> ₄	1.85	235.2	74.2	108	32
L-Asparagine- ¹³ C ₄ , ¹⁵ N ₂	Asn- ¹³ C ₄ , ¹⁵ N ₂	2.50	195.2	148.1	89	8
L-Asparagine	Asn	2.51	189.1	144.1	89	8
L-Glycine	Gly	2.52	132.1	76.1	65	4
L-Serine	Ser	2.66	162.1	60.1	94	12
L-Glutamine	Gln	3.22	203.1	84.1	89	20
L-Glutamine- ¹³ C ₅ , ¹⁵ N ₂	Gln- ¹³ C ₅ , ¹⁵ N ₂	3.22	210.2	89.1	89	20
L-Isothreonine / L-Homoserine	Iso-Thr	3.43	176.1	74.1	94	12
β-Alanine	β-Ala	3.70	146.2	72.1	90	10
L-Threonine	Thr	3.70	176.1	74.1	94	12
L-Threonine*	Thr	3.70	176.1	158.1	94	5
L-Alanine	Ala	3.91	146.1	44.2	80	15
L-Hydroxy-Proline	Hyp	3.93	188.1	68.1	120	35
L-Citrulline- <i>d</i> ₄	Cit- <i>d</i> ₄	4.52	236.2	74.1	108	28
L-Citrulline	Cit	4.58	232.2	70.1	89	32
Time Segment 2 (5 to 10.1 minutes)						
Trimethylglycine / Betaine	TMG	5.39	174.2	58.2	130	45
γ-Aminobutyric acid	GABA	5.94	160.1	87.1	79	8
L-Carnitine-(methyl- <i>d</i> ₃)	C0- <i>d</i> ₃	6.28	221.2	103.1	127	16
L-Carnitine	C0	6.31	218.2	103.0	132	16
L-Proline	Pro	6.48	172.1	70.2	94	20
Creatine	Cr	6.57	188.1	90.1	104	16
L-Pipecolic acid	Pip	7.85	186.1	84.1	108	16
L-Cystine	Cys	8.43	353.0	130.0	118	16
L-Cystathionine	Cysta	8.52	335.2	190.1	127	16
L-Valine- <i>d</i> ₈	Val- <i>d</i> ₈	8.60	182.2	80.2	103	12

APPENDIX D: Standardisation of metabolomics methods

Table D.1 (continue)						
L-Valine	Val	8.65	174.2	72.2	89	12
L-Methionine	Met	9.08	206.1	104.1	94	8
Acetyl-L-Carnitine	C2	9.11	260.2	85.1	122	24
L-Tyrosine	Tyr	9.46	238.2	136.1	94	12
Time Segment 3 (10.1 to 13.4 minutes)						
L-Isoleucine- <i>d</i> ₁₀	Ile- <i>d</i> ₁₀	10.66	198.2	96.2	108	12
L-Isoleucine	Ile	10.93	188.2	86.2	89	8
L-Leucine	Leu	10.93	188.2	86.2	89	8
Propionyl-L-Carnitine	C3	11.18	274.2	85.1	127	20
L-Pyroglutamic acid	pGlu	11.46	186.1	84.1	108	16
L-Phenylalanine- (ring- <i>d</i> ₅)	Phe- <i>d</i> ₅	11.85	227.2	125.1	108	16
L-Phenylalanine	Phe	11.88	222.2	120.1	108	16
L-Aspartic acid	Asp	12.20	246.2	144.1	98	12
Butyryl-L-Carnitine	C4	12.31	288.2	85.1	110	20
L-Tryptophan	Trp	12.34	261.2	244.1	94	8
N,N-Dimethyl-L-Phenylalanine	DMPA	12.42	250.1	148.1	103	20
L-Glutamic acid	Glu	12.43	260.2	84.1	89	24
L- α -Aminoadipic acid	α -AAA	12.69	274.2	98.1	113	24
Isovaleryl-L-Carnitine	C5	12.81	302.2	85.1	105	24
Hexanoyl-L-carnitine	C6	13.23	316.2	85.1	137	24
Time Segment 4 (13.4 minutes to end of run)						
Octanoyl-L-Carnitine- <i>d</i> ₃	C8- <i>d</i> ₃	13.74	347.3	85.1	136	24
Octanoyl-L-Carnitine	C8	13.75	344.3	85.1	115	28
N-Acetylaspartic acid	NAA	14.10	288.2	144.1	98	16
N-Acetylglutamic acid	NAG	14.17	302.2	186.1	113	12
Dodecanoyl-L-Carnitine- <i>d</i> ₃	C12- <i>d</i> ₃	14.54	403.4	85.1	160	32
Dodecanoyl-L-Carnitine	C12	14.55	400.3	85.1	155	28
Tetradecanoyl-L-Carnitine	C14	14.91	428.4	85.1	150	28
Palmitoyl-L-Carnitine	C16	15.27	456.4	85.1	160	36
Octadecanoyl-L-Carnitine- <i>d</i> ₃	C18- <i>d</i> ₃	15.63	487.5	85.1	160	36
Octadecanoyl-L-Carnitine	C18	15.64	484.0	85.1	155	36

*Due to the co-elution of threonine and isothreonine, another set of MRM conditions were used for threonine to discriminate between threonine and iso-threonine peaks.

Compounds in grey represents conditions for internal standards.

MS1, first quadrupole mass spectrometer; MS2, third quadrupole and second mass spectrometer; m/z, mass to charge ratio; V, Voltage.

APPENDIX D: Standardisation of metabolomics methods

During visual inspection of the standard compound analyte peaks, some peaks appeared somewhat blunted at the top and/or varied in height or area after repeated injection. Interference of a matrix via ion suppression and experimental variability were ruled out as the analysed standard mix was matrix-free and a single sample was repeatedly injected. These results suggested that analytical acquisition was the source of variance and that there were not enough data points per peak for accurate peak integration. This problem can be addressed with a relatively simple technique, without making drastic alterations to the analytical method and still using the available software. The technique requires adding time segments to the acquisition method. In this way, the chromatogram is divided into a series of time segments in which a predefined set of transitions are monitored for analytes that elute in that segment. This reduces the number of transitions during each scan, allowing longer dwell time on each transition and/or a reduction of the overall cycle time (total time required to scan once through an entire transition list), effectively increasing the data points that can be detected per peak (Stone *et al.*, 2009). Time segments are typically inserted at time points where no peaks elute from the LC column (a chromatographic quiet zone between peaks). Subsequently, switching to another time segment with other transitions does not compromise the data quality. The time segments added to the LC-MS/MS method are indicated in Table D.1 and illustrated in Figure D.1. This reduced overall cycle time and increased the number of scans per peak.

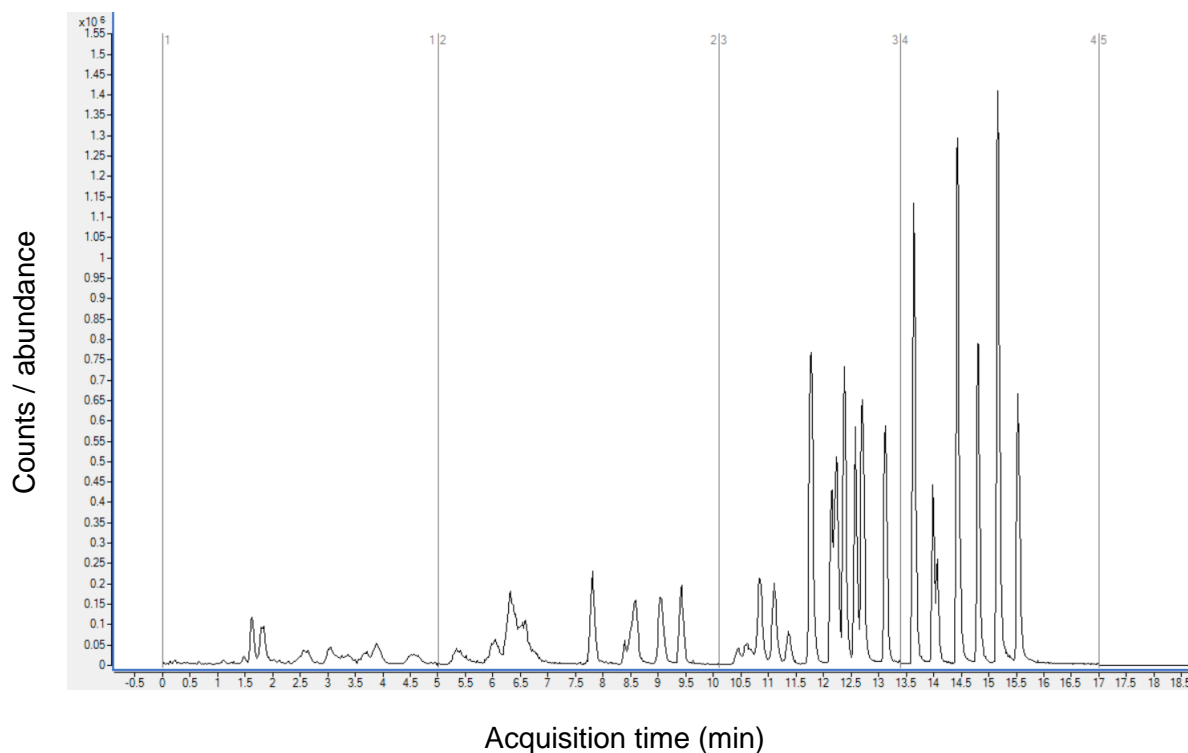


Figure D.1: Dividing the LC-MS/MS chromatogram into time segments.

Total ion chromatogram (TIC) of a standard compound mixture as analysed with the LC-MS/MS after adding time segments to the acquisition method.

APPENDIX D: Standardisation of metabolomics methods

As observed in Figure D.2, time segmentation greatly improved peak shapes and repeatability of the peak area. In fact, without time segments, triplicate measurements of the standard compound mix resulted in only 68% of standard compounds having a coefficient of variance (CV) (see Equation D.1 in Section D.3) below 20% when calculated from the quantified peak areas. However, with time segments, triplicate measurements of the same standard mix sample resulted in 100% of compounds having a CV <20% (data not shown).

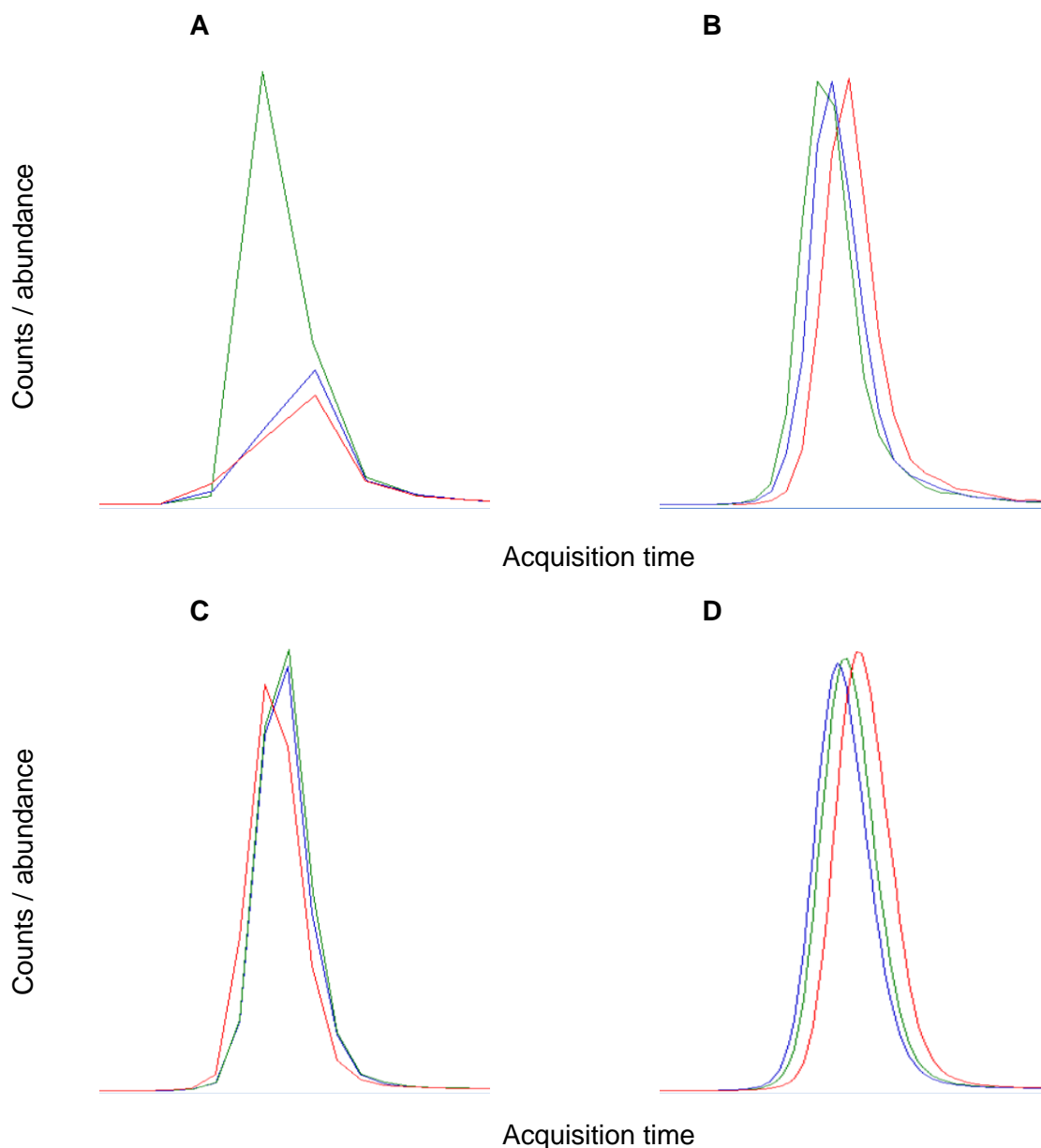


Figure D.2: Examples of extracted peaks from the ion chromatograms acquired with and without time segmentation.

Peaks extracted from ion chromatograms of three repeated analyses of a single standard compound mixture without time segmentation (A & C) and three repeated analyses with time segmentation (B & D). **A:** The valine isotopic internal standard without time segments; and **B:** After adding time segments and for phenylalanine; **C:** Without time segments; and **D:** After adding time segments.

D.3. Evaluation of experimental precision

Prior to GC-TOF and LC-MS/MS analyses, metabolites had to be extracted and derivatised to enhance detection (see Section 4.7.4.2 and Section 4.7.4.4). These procedures were identical for three of the four brain regions, namely the anterior cortex (AC), brainstem (BST) and cerebellum (CB). However, the limited sample size (<20 mg) of the olfactory bulbs (OB) necessitated a higher solvent to tissue mass ratio during extraction to obtain sufficient volumes. For this reason, the precision of the methods were separately evaluated for the OB, and collectively for the rest (R) of the brain regions.

In short, experimental precision refers to the closeness of agreement between a series of repeated measurements. For this study, precision was evaluated on three levels, namely intra-batch/assay precision (repeatability), inter-batch/assay precision (intermediate precision) and instrumental precision. For each analytical method, precision was evaluated by first preparing a single pooled, homogenous sample of the R and OB tissues, respectively. The pooled sample of each was then divided into aliquots of similar mass representative of the average mass of the particular brain region/s. Five replicates were then separately prepared (as described in Section 4.7.4.2 to Section 4.7.4.4) and analysed (as described in Section 4.7.4.6) together on the same day to determine the intra-batch precision for each detected metabolite. Another two replicate samples were separately prepared and analysed on the second and third day, respectively. The data of the replicates over three days were used to determine the inter-batch precision of each detected metabolite. In addition, a single replicate was also repeatedly (five times) injected to quantify instrument precision.

Precision was evaluated by assessing the cumulative distribution functions (CDFs) of the coefficient of variance (CV) of each feature detected with the GC-TOF and LC-MS/MS metabolomics platforms, respectively (Quintás *et al.*, 2018) and are depicted in Figure D.3. The CV for each feature was calculated from the relative abundances of each metabolite across the relevant sample replicates using Equation D.1.

$$\text{Coefficient of variance (CV)} = \frac{\text{Standard deviation (SD)}}{\text{Mean } (\bar{x})} \times 100$$

(Equation D.1)

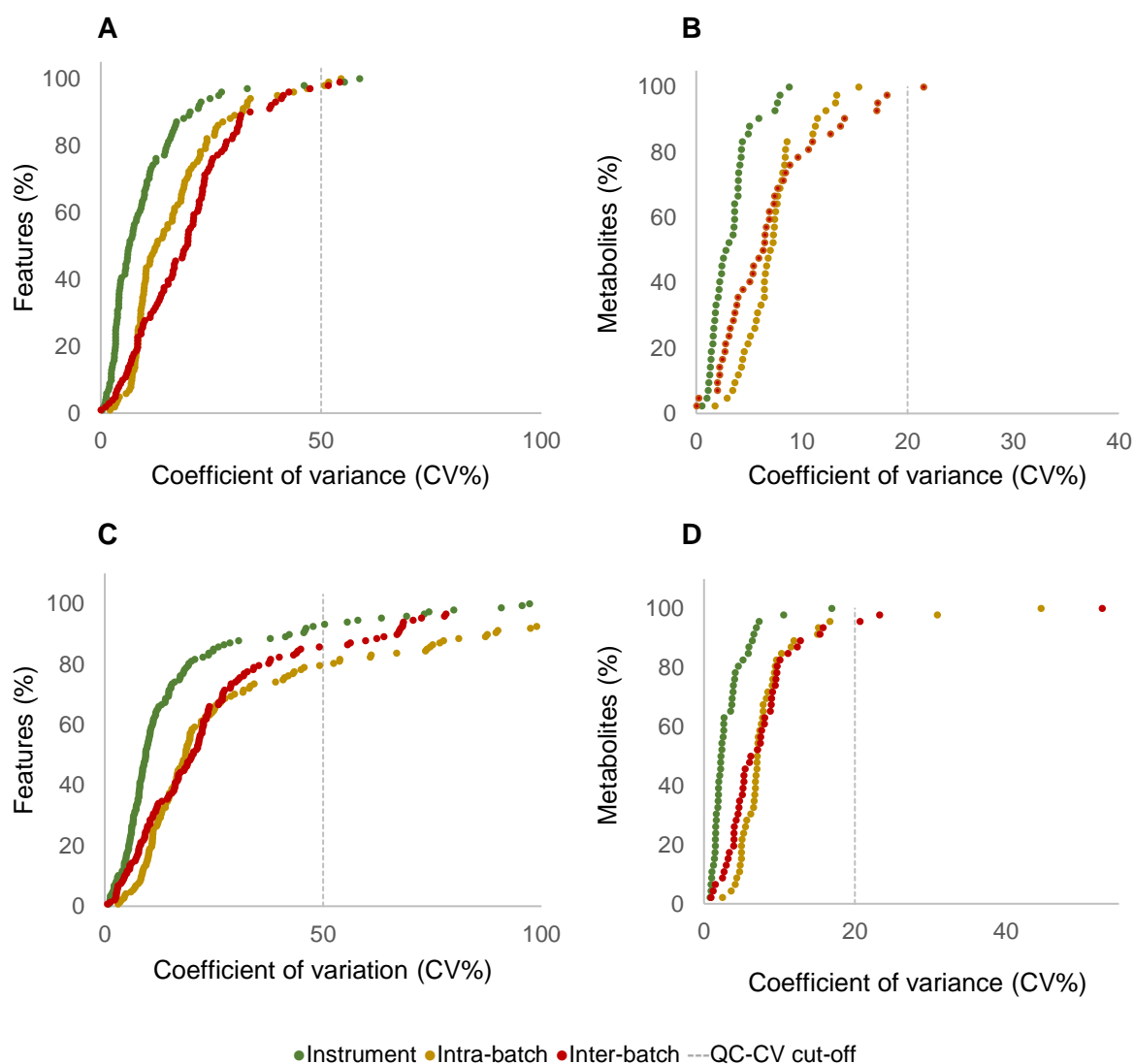


Figure D.3: Assessment of metabolomics experimental precision.

Scatter plots depict the percentage of features in replicate samples at a certain level of coefficient of variance (CV) as detected by the GC-TOF (graphs on the left, A & C) and LC-MS/MS (graphs on the right, B & D) metabolomics platforms, respectively. **A&B:** Rest of the brain (R) and **C&D:** Olfactory bulbs (OB). Instrument precision (5x replicates) is shown in green, intra-batch precision (5x replicates) in yellow and inter-batch precision (3x replicates) is depicted in red. Vertical dashed lines indicate the quality control (QC)-CV cut-off value for removing unreliable features. Plots were constructed from post-normalised data.

For untargeted metabolomics approaches, features with a quality control (QC)-CV value >50% are typically deemed unreliable (Dunn *et al.*, 2012; Lindeque *et al.*, 2013). Whereas features with a QC-CV value >20% (FDA, 2001) are removed from data sets obtained from targeted metabolomics approaches. A summary of the percentage of features below the QC-CV cut-off line in the GC-TOF and LC-MS/MS metabolomics data sets are provided in Table D.2.

Table D.2: Percentage of features below the QC-CV cut-off value in the GC-TOF and LC-MS/MS metabolomics data sets.

	GC-TOF			LC-MS/MS		
	Instrument	Intra-batch	Inter-batch	Instrument	Intra-batch	Inter-batch
R	98	97	97	100	100	98
OB	93	80	86	100	96	96

QC-CV cut-off value for unreliable features is >50% for GC-TOF and >20% for LC-MS/MS detected features. Abbreviations: R, rest; OB, olfactory bulbs; QC, quality control; CV, coefficient of variance.

In all cases, the precision of the instrument and acquisition method using the brain region samples proved to be sufficient with more than 90% of compounds having CV-values below the respective QC-CV cut-off values for the untargeted GC-TOF method. Furthermore, 100% of compounds had CV-values less than 20% when detected with the LC-MS/MS method. As expected, the semi-targeted LC-MS/MS data sets displayed better precision than the untargeted GC-TOF data sets. This could be due to the fact that many unknown factors, which might also include unreliable artefacts, are measured in the untargeted approach and that samples continuously derivatise and degrade due to the final reconstitution in derivatisation reagent. Furthermore, unlike for the LC-MS/MS method, time segments could not be added to the GC-TOF method to increase precision and the auto-sampler could not be kept at a controlled or cooler temperature. Instrument precision was generally superior to that of intra- and inter-batch precision. This is in line with the fact that the former considers analytical variation of, and perhaps ongoing derivatisation, but not variation due to experimental errors.

In all cases of intra- and inter-batch precision, >80% of the detected features had CV-values below the respective QC-CV cut-off values and were deemed reliable. The precision of the methods used to prepare and analyse the OB samples, displayed less precision (~10% to 15%) than when analysing R samples, most probably due to the small sample volumes of the latter. In addition, even though samples are mixed prior to injection by the auto-sampler, the utilisation of sharp point vials might still cause a slight concentration gradient within the samples that might cause a drift in the detected signals over time. Nevertheless, even with the additional variation, the data still displayed sufficient precision and was of good quality.

Collectively, these results showed that instrument precision and both intra- and inter-batch/day precision of the standardised experimental and analytical techniques were well within the generally accepted criteria for each untargeted and semi-targeted metabolomics analytical methods. This suggested that the methods had sufficient repeatability and had generated good quality data. These methods were subsequently used to measure the concentrations of analytes in the experimental and control mouse brain regions.

APPENDIX E

Supplementary biochemical results

E.1. Introduction

One of the main objectives (Objective 2) of this study was to investigate whether brain regional differences in the maximal activities of the mitochondrial marker citrate synthase (CS), and of RC complex I (CI), II (CII), III (CIII) and IV (CIV) could be correlated with the regional vulnerability to neurodegeneration in *Ndufs4* KO mice. The measured enzyme activities were compared between brain regions of similar genotypes, as well as between corresponding brain regions of KO and WT mice. This was done by performing a two-way mixed analysis of variance (ANOVA) with genotype as the between-subjects factor and brain region as the within-subjects factor. Only the most relevant results were reported in the main text. In this section additional information is reported on the statistical procedures employed for each variable as well as the outcome for when the data was normalised to CS activity.

E.2. Assumption tests

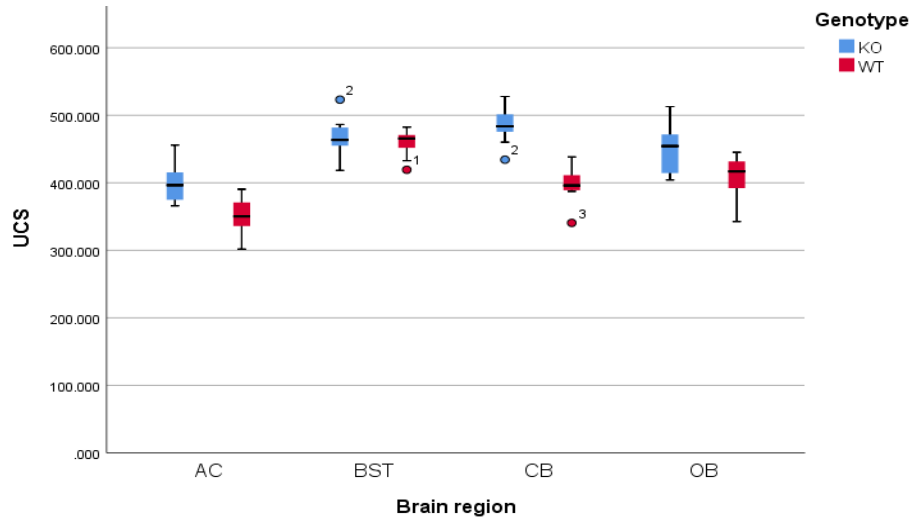
Prior to a mixed ANOVA analysis, the assumptions of (i) no outliers; (ii) symmetry; (iii) equal variances across genotype levels; and (iv) sphericity had to be met (Field, 2009a; Field, 2009b; The Open University, 2018). Table E.1 in Section E.2.2 provides a summary.

E.2.1. Box-plots for outlier removal and assessment of symmetry

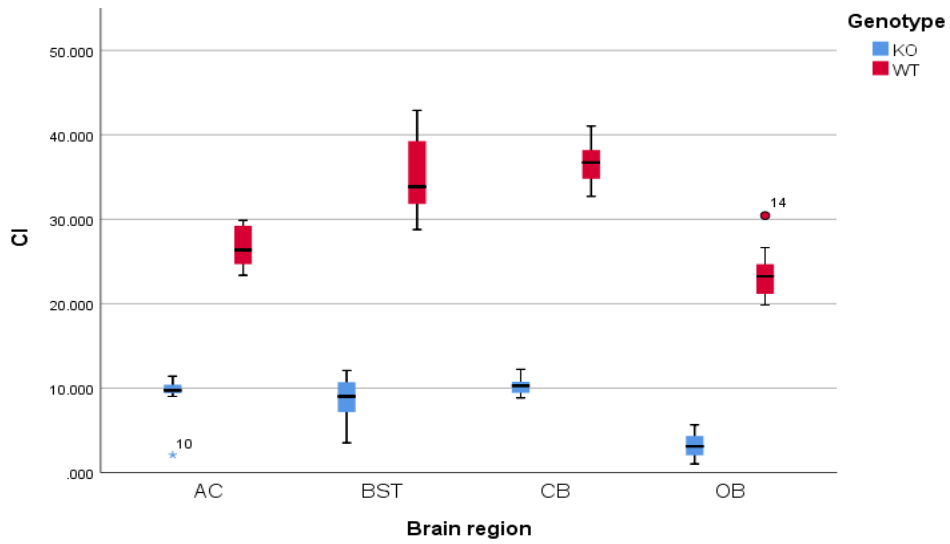
Box-plots constructed for maximal enzyme activities normalised to either protein content (mg of protein) or mitochondrial content (CS activity) are shown in Figure E.1 for the brain regions of *Ndufs4* wild-type (WT) and knockout (KO) mice. Only extreme outliers were removed: values lying outside three interquartile ranges below the 25th percentile or above the 75th percentile of the data set (indicated by asterisks, *). Symmetry was assessed based on standardised skewness values and was achieved for all variables.

APPENDIX E: Supplementary biochemical results

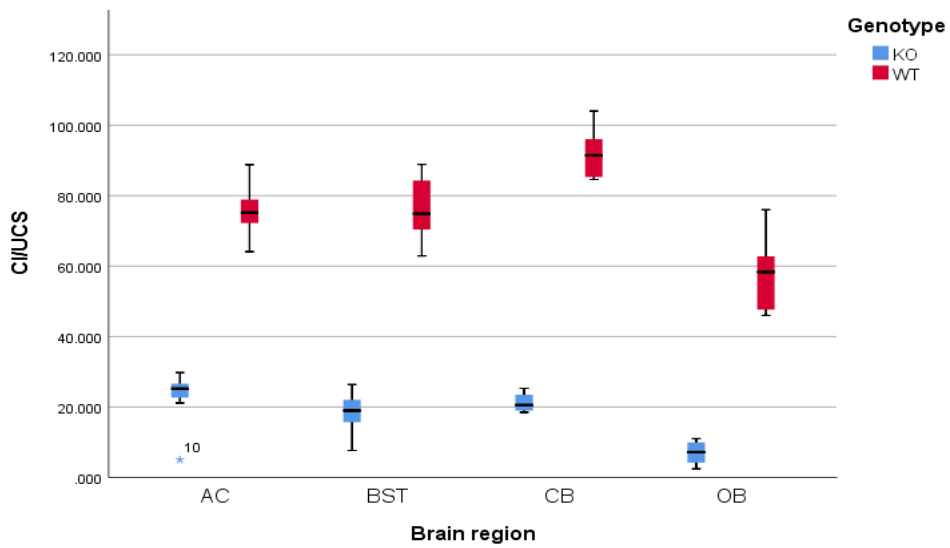
A



B

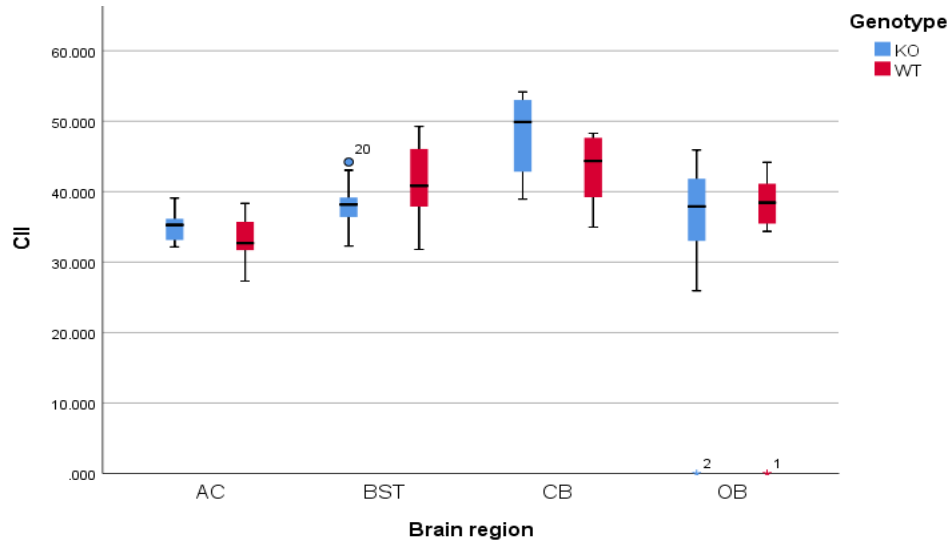


C

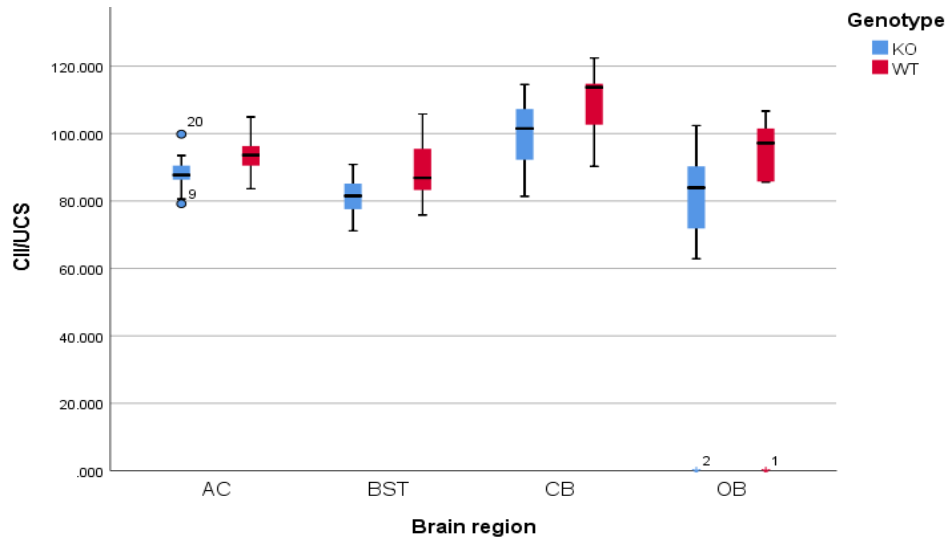


APPENDIX E: Supplementary biochemical results

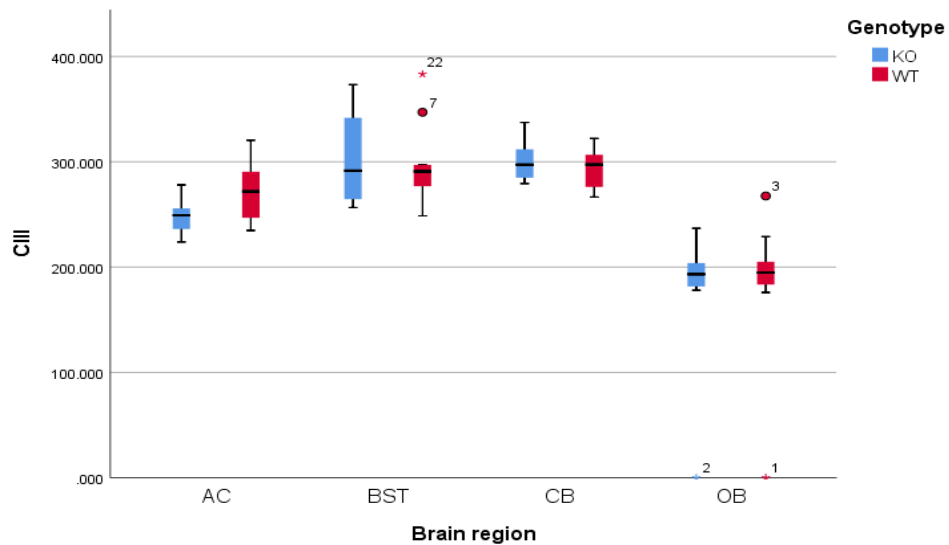
D



E

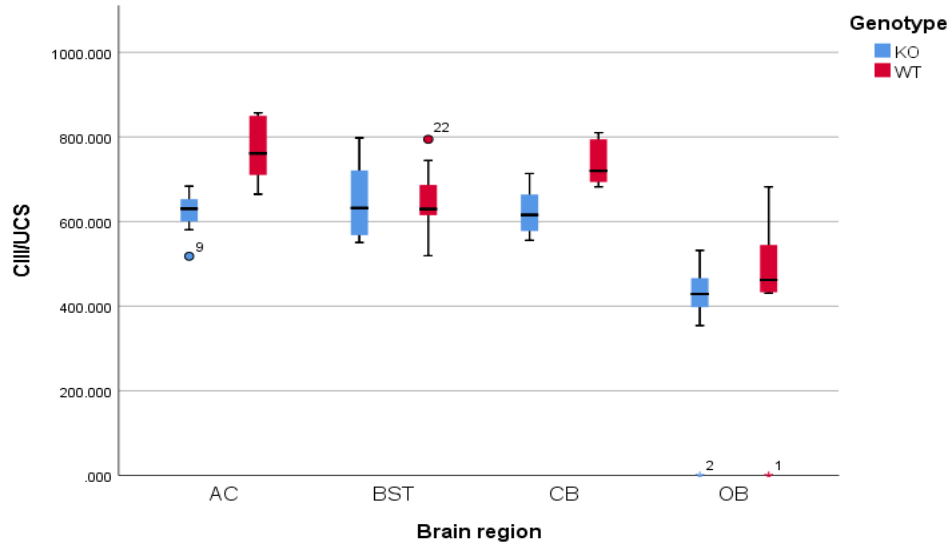


F

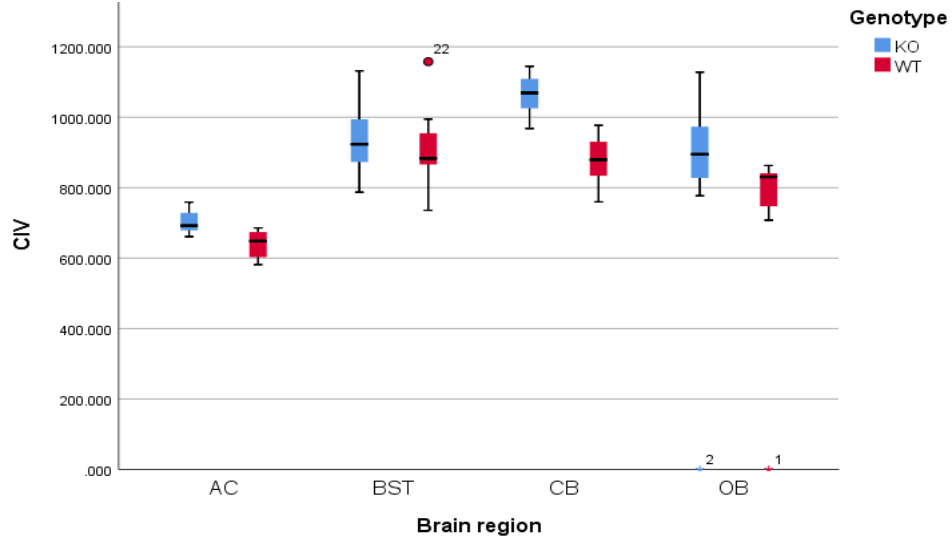


APPENDIX E: Supplementary biochemical results

G



H



I

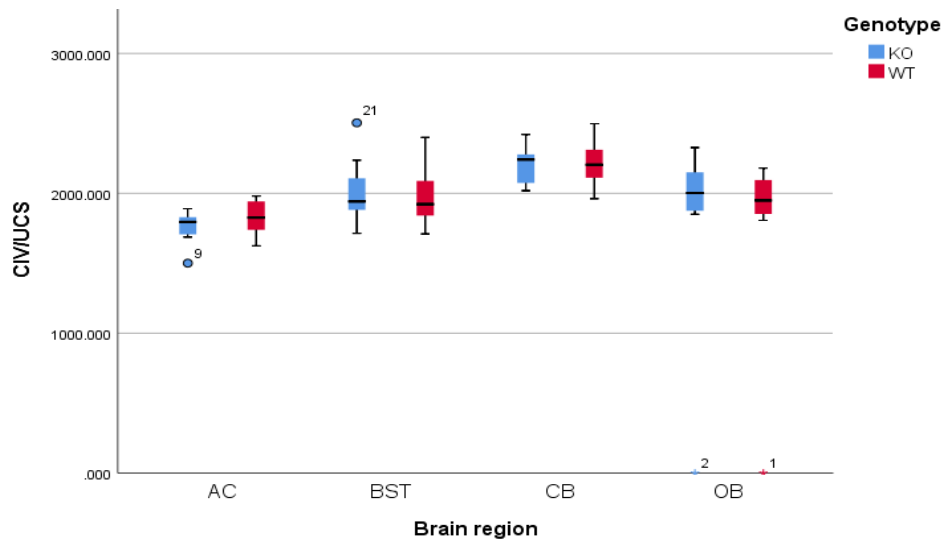


Figure E.1: Clustered box-plots of maximal enzyme activities for outlier detection and evaluation of symmetry.

Plots were constructed from the maximal enzyme activities measured spectrophotometrically in freeze-thawed 700 x g supernatants prepared from the homogenates of the anterior cortex (AC), brainstem (BST), cerebellum (CB) and olfactory bulbs (OB) harvested from *Ndufs4* WT (n =10 in red) and KO (n =12 in blue) mice at PN45 to PN49. Potential outliers are indicated above the top whiskers and extreme outliers (depicted by asterisks) were removed; i.e. those that lie outside three interquartile ranges below the 25th percentile or above the 75th percentile of the data set. Symmetry was assessed based on standardised skewness values and was achieved for all variables. **A**: Maximal citrate synthase activity (UCS); **B, D, F & H**: maximal activity of complex I to IV (CI, CII, CIII and CIV) normalised to protein content; and **C, E, G & I**: Maximal activity of CI, CII, CIII and CIV normalised to mitochondrial content (UCS).

E.2.2. Equal variances and sphericity

In addition to the assumptions of (i) no outliers and (ii) symmetry required to perform a mixed ANOVA analysis, assumptions of (iii) equal variances across genotype levels; and (iv) sphericity also had to be met. Equal variances and sphericity were assessed as part of the ANOVA model (Field, 2009a; Field, 2009b; The Open University, 2018). The following tests were applied, namely Box's M-test of equality of covariance matrices (Box, 1949), Levene's test of equality of error variances (Levene, 1960), and Mauchly's test of sphericity (Mauchly, 1940). If the assumption of equal co-variances/variances was violated ($p < 0.05$), spread-and-level plots were used to assess the severity and identify the appropriate power transformation. Power transformation was applied for severe violations, and the ANOVA model reconstructed on the transformed data. Sphericity was assessed based on Greenhouse-Geisser's epsilon (ϵ) (Greenhouse & Geisser, 1959): if $\epsilon \geq 0.9$, sphericity was assumed; if $0.9 > \epsilon \geq 0.7$, Greenhouse-Geisser corrected p -values were considered; if $0.7 > \epsilon \geq 0.5$, multivariate tests were used to establish confidence in the significance of the mixed ANOVA test. In the latter case, if both tests came to the same conclusions, mixed ANOVA results were reported. Table E.1 summarises the statistical outcome for each variable.

The assumption of equal variance was violated in the case of the CI and CI/UCS data sets which required a square-root transformation. However, the transformation of the CI data set in turn resulted in a violation of the sphericity assumption with a Greenhouse-Geisser estimate of 0.69. That said, the violation was not severe as multivariate test p -values were comparable to ANOVA p -values (corrected and not correct for sphericity). In addition, Box's M was not significant ($p = 0.67$) for the transformed data set. Hence ANOVA results were reported for the transformed CI data set. Transformation of the CI/UCS data set was successful in that the variances were acceptable, and the sphericity assumption was met with a Greenhouse-Geisser estimate of 0.75. Consequently, ANOVA results were reported.

APPENDIX E: Supplementary biochemical results

The assumption of sphericity was met in the cases of maximal CII-, CII/UCS- and CIII/UCS- activity data sets with Greenhouse-Geisser estimates of 0.83, 0.82 and 0.79, respectively, but required a Greenhouse-Geisser correction for p -values. The assumption of sphericity was violated in the data sets of maximal CIII- and CIV-activities with Greenhouse-Geisser estimates of 0.68 and 0.53, respectively. For these data sets, multivariate tests were evaluated. In each case the violation was not severe as multivariate test p -values were comparable to ANOVA p -values (corrected and not correct for sphericity) and yielded similar results. Hence ANOVA results were reported.

APPENDIX E: Supplementary biochemical results

Table E.1: Statistical processing of maximal enzyme activity data measured in various brain regions of *Ndufs4* wild-type and knockout mice using a two-way mixed ANOVA.

Enzyme activity	Outliers	Symmetry	Equal variances (Genotype) Box's M / Levene's test			Sphericity (Brain region) (Mauchly's test using GG estimate)			
			Significance	Equal	Correction	Significance	Sphericity	Action	Stats reported
UCS	X	✓	$p=1.0 / p>0.05$	✓	X	$\epsilon > 0.9$	✓	X	Sphericity As.
CI	KO AC (1)	✓	$p=0.04 / p<0.05$	X	SQRT	$\epsilon = 0.69$	X	Multivariate vs GG corrected	GG corrected
CI/UCS	KO AC (1)	✓	$p<0.05 / p<0.05$	X	SQRT	$\epsilon = 0.75$	✓	GG corrected	GG corrected
CII	KO OB (1) WT OB (1)	✓	$p=0.5 / p>0.05$	✓	X	$\epsilon = 0.83$	✓	GG corrected	GG corrected
CII/UCS	KO OB (1) WT OB (1)	✓	$p=0.9 / p>0.05$	✓	X	$\epsilon = 0.82$	✓	GG corrected	GG corrected
CIII	WT BST (1) KO OB (1) WT OB (1)	✓	$p=0.3 / p>0.05$	✓	X	$\epsilon = 0.68$	X	Multivariate vs GG corrected	GG corrected
CIII/UCS	KO OB (1) WT OB (1)	✓	$p=0.6 / p>0.05$	✓	X	$\epsilon = 0.79$	✓	GG corrected	GG corrected
CIV	KO OB (1) WT OB (1)	✓	$p=0.3 / p>0.05$	✓	X	$\epsilon = 0.53$	X	Multivariate vs GG corrected	GG corrected
CIV/UCS	KO OB (1) WT OB (1)	✓	$p=0.2 / p>0.05$	✓	X	$\epsilon > 0.9$	✓	X	Sphericity As.

Values in brackets indicate the number of outliers removed from the designated group using the box-plots in Section E.2.1. Equal co-variances/variances and sphericity were assessed as part of the analysis of variance (ANOVA) model. If the assumption of equal variances was violated ($p < 0.05$), spread-and-level plots were used to assess the severity and identify the appropriate power transformation. Power transformation was applied for severe violations, and the ANOVA model reconstructed on the transformed data. Sphericity was assessed based on Greenhouse-Geisser's (GG) epsilon (ϵ): if $\epsilon \geq 0.9$, sphericity assumed; if $0.9 > \epsilon \geq 0.7$, GG corrected p -values were used; if $0.7 > \epsilon \geq 0.5$, multivariate tests were used to establish confidence in the significance of the mixed ANOVA test. In the latter case, if the same conclusions were drawn by both tests, mixed ANOVA results were reported. *Other abbreviations:* AC, anterior cortex; As, assumed; BST, brainstem; CI-CIV, complex I to IV; KO, knockout; OB, olfactory bulbs; stats, statistics; SQRT, square root transformation; UCS, maximal citrate synthase activity; WT, wild-type.

E.3. Maximal enzyme activities normalised to citrate synthase activity

A parallel increase in the maximal activities of all the mitochondrial RC enzymes did not accompany the increase in maximal citrate synthase (CS) activity observed in most, though not all KO brain regions. This suggested that the alterations in CS activity might be related to factors other than mitochondrial content. Besides, CS activity could be an unreliable measure of mitochondrial content in *Ndufs4* KO mice (Alam *et al.*, 2015). Thus, the enzyme activities reported in Chapter 5 were mainly normalised to protein content (expressed per mg protein), while relevant and significant CS-normalised data was only briefly mentioned with regard to comparisons among WT brain regions. The statistical significance of interaction effects and main effects are given for the protein- and CS-normalised data in Table E.2. The complete set of CS-normalised data is shown in Table E.3. Pairwise test results for the CS-normalised data are given for comparisons between corresponding brain regions of the two genotypes in Table E.4 and for comparisons between brain regions of the same genotype in Table E.5.

The results of maximal CI activity that were normalised to unit CS activity (CI/UCS) are illustrated in Figure E.2. The genotype affected CI/UCS differentially depending on the brain region (Greenhouse-Geisser $p < 0.0001$, $\eta_p^2 = 0.31$). Also, CI/UCS was significantly lower in the KO group across all brain regions ($p < 0.0001$ for WT vs KO for all regions with $d = 9.3$ for AC, $d = 6.5$ for BST, $d = 15.2$ for CB and $d = 7.8$ for OB). Comparing brain regions within genotype, results showed that CI/UCS of WT AC was significantly lower than WT CB ($p < 0.0001$, $d = 2.2$) and significantly higher than WT OB ($p = 0.001$ and $d = 1.9$). CI/UCS of KO AC was significantly higher than in all other KO brain regions: AC vs CB ($p = 0.006$, $d = 1.4$), AC vs BST ($p = 0.002$, $d = 1.2$) and AC vs OB ($p < 0.0001$, $d = 3.7$). Moreover, residual CI activity was higher in the KO AC (33%) compared to the KO neurodegeneration-prone brain regions (24%, 23% and 13% for BST, CB and OB respectively) (Table E.3). Comparison of CI/UCS between the neurodegeneration-prone brain regions showed lower activity in the OB, regardless of genotype: OB vs BST in WT ($p = 0.001$, $d = 1.8$) and KO ($p < 0.0001$, $d = 2.5$), and OB vs CB in WT ($p < 0.0001$, $d = 3.3$) and KO ($p < 0.0001$, $d = 3.2$). Additionally, WT BST had significantly lower CI/UCS than WT CB ($p < 0.0001$, $d = 1.8$).

APPENDIX E: Supplementary biochemical results

Table E.2: Summary of the significance of effects obtained from maximal enzyme activity data measured in various brain regions of *Ndufs4* wild-type and knockout mice using a two-way mixed ANOVA.

Enzyme Activity	Interaction effect				Effect of genotype				Effect of brain region			
	Significance	Effect	Effect size		Significance	Effect	Effect size		Significance	Effect	Effect size	
UCS	$p < 0.001$	✓	$\eta p^2 = 0.3$	Large	$p < 0.0001$	✓	$\eta p^2 = 0.8$	Large	$p < 0.0001$	✓	$\eta p^2 = 0.7$	Large
CI	$p < 0.0001$	✓	$\eta p^2 = 0.4$	Large	$p < 0.0001$	✓	$\eta p^2 = 1.0$	Large	$p < 0.0001$	✓	$\eta p^2 = 0.8$	Large
CI/UCS	$p < 0.001$	✓	$\eta p^2 = 0.3$	Large	$p < 0.0001$	✓	$\eta p^2 = 1.0$	Large	$p < 0.0001$	✓	$\eta p^2 = 0.8$	Large
CII	$p < 0.01$	✓	$\eta p^2 = 0.2$	Large	$p > 0.05$	✗			$p < 0.0001$	✓	$\eta p^2 = 0.7$	Large
CII/UCS	$p > 0.05$	✗			$p < 0.01$	✓	$\eta p^2 = 0.4$	Large	$p < 0.0001$	✓	$\eta p^2 = 0.6$	Large
CIII	$p > 0.05$	✗			$p > 0.05$	✗			$p < 0.0001$	✓	$\eta p^2 = 0.9$	Large
CIII/UCS	$p < 0.01$	✓	$\eta p^2 = 0.3$	Large	$p < 0.001$	✓	$\eta p^2 = 0.5$	Large	$p < 0.0001$	✓	$\eta p^2 = 0.8$	Large
CIV	$p < 0.05$	✓	$\eta p^2 = 0.2$	Large	$p < 0.0001$	✓	$\eta p^2 = 0.6$	Large	$p < 0.0001$	✓	$\eta p^2 = 0.8$	Large
CIV/UCS	$p > 0.05$	✗			$p > 0.05$	✗			$p < 0.0001$	✓	$\eta p^2 = 0.6$	Large

Abbreviations: CI-CIV, complex I to IV; UCS, maximal citrate synthase activity.

Table E.3: Maximal spectrophotometric enzyme activities in brain regions of *Ndufs4* wild-type and knockout mice normalised to citrate synthase activity.

V_{max} values	AC			BST			CB			OB		
	WT	KO	KO/WT	WT	KO	KO/WT	WT	KO	KO/WT	WT	KO	KO/WT
CI (mU/UCS)	76 ± 7	25 ± 3 ^{****}	0.33	76 ± 9	18 ± 6 ^{****}	0.24	92 ± 6	21 ± 3 ^{****}	0.23	58 ± 9	7 ± 3 ^{****}	0.13
CII (mU/UCS)	95 ± 5	88 ± 6	0.93	90 ± 9	82 ± 6	0.91	111 ± 8	100 ± 11	0.90	96 ± 7	84 ± 12	0.87
CIII (mU/UCS)	761 ± 72	620 ± 47 ^{****}	0.81	650 ± 82	660 ± 87	1.02	744 ± 55	616 ± 52 ^{****}	0.83	506 ± 85	437 ± 50 [*]	0.86
CIV (mU/UCS)	1835 ± 123	1759 ± 112	0.96	1996 ± 200	2041 ± 196	1.02	2245 ± 170	2189 ± 129	0.98	1996 ± 137	2037 ± 154	1.02

Enzyme activities were measured in a freeze-thawed 700 x g supernatant of a homogenate of each brain region and are displayed as the mean activity ± standard deviation. In all cases, wild-type (WT) n ≥ 9 and knockout (KO) n ≥ 11. Tests for statistical significance between KO and corresponding WT regions (* = $p < 0.05$, ** = $p < 0.01$, *** = $p < 0.001$, **** = $p < 0.0001$). Other abbreviations: v_{max} , maximal activity; AC, anterior cortex; BST, brainstem; CB, cerebellum; OB, olfactory bulbs; CI, complex I; CII, complex II; CIII, complex III; CIV, complex IV; UCS, unit citrate synthase activity in $\mu\text{mol}/\text{minute}/\text{mg}$; mU, nmol/minute.

Table E.4: Statistically significant differences in CS-normalised maximal enzyme activities when comparing corresponding brain regions from *Ndufs4* wild-type and knockout mice.

Variable	Region	<i>p</i> -value	ES	↓ or ↑
C1/UCS	AC	<0.0001	9.3	↓
	BST	<0.0001	6.5	↓
	CB	<0.0001	15.2	↓
	OB	<0.0001	7.8	↓
CII/UCS	All	<0.01	0.4*	↓
CIII/UCS	AC	<0.0001	2.0	↓
	BST			
	CB	<0.0001	2.1	↓
	OB	<0.05	0.8	↓

*Partial Eta Squared. Abbreviations: AC, anterior cortex; BST, brainstem; CB, cerebellum; OB, olfactory bulbs; C1, complex I; CII, complex II; CIII, complex III; CIV, complex IV; UCS, unit citrate synthase activity in $\mu\text{mol}/\text{minute}/\text{mg}$; ES, effect size; KO, knockout; WT, wild-type.

APPENDIX E: Supplementary biochemical results

Table E.5: Statistically significant differences in CS-normalised maximal enzyme activities between the brain regions of *Ndufs4* wild-type or knockout mice.

Variable	Genotype	Comparison	p-value	ES	↓ or ↑
C1/UCS	WT	AC vs BST			
		AC vs CB	0.0002	2.2	↓
		AC vs OB	0.0009	1.9	↑
		BST vs CB	<0.0001	1.8	↓
		BST vs OB	0.0009	1.8	↑
		CB vs OB	<0.0001	3.3	↑
	KO	AC vs BST	0.002	1.2	↑
		AC vs CB	0.006	1.4	↑
		AC vs OB	<0.0001	3.7	↑
		BST vs CB			
		BST vs OB	<0.0001	2.5	↑
		CB vs OB	<0.0001	3.2	↑
C2/UCS	WT/KO	AC vs BST	0.031	0.7	↑
		AC vs CB	<0.0001	1.3	↓
		AC vs OB			
		BST vs CB	<0.0001	1.7	↓
		BST vs OB			
		CB vs OB	<0.0001	1.3	↑
C3/UCS	WT	AC vs BST	0.011	1.6	↑
		AC vs CB			
		AC vs OB	<0.0001	3.0	↑
		BST vs CB	0.006	1.2	↓
		BST vs OB	0.012	1.7	↑
		CB vs OB	<0.0001	2.8	↑
	KO	AC vs BST			
		AC vs CB			
		AC vs OB	<0.0001	3.7	↑
		BST vs CB			
		BST vs OB	<0.0001	2.6	↑
		CB vs OB	<0.0001	3.4	↑
C4/UCS	WT/KO	AC vs BST	0.002	1.2	↓
		AC vs CB	<0.0001	2.9	↓
		AC vs OB	0.001	1.6	↓
		BST vs CB	0.008	1	↓
		BST vs OB			
		CB vs OB	0.002	1.3	↑

Abbreviations: AC, anterior cortex; BST, brainstem; CB, cerebellum; OB, olfactory bulbs; C1, complex I; C2, complex II; C3, complex III; C4, complex IV; UCS, unit citrate synthase activity in $\mu\text{mol}/\text{minute}/\text{mg}$; ES, effect size; KO, knockout; WT, wild-type.

In accordance with the protein-normalised data, the results showed that maximal CI activity in the KO brain regions was significantly decreased but was not diminished. It was further evident that CI activity was not uniquely different in the AC compared to the neurodegeneration-prone brain regions of WT mice. Moreover, the OB had significantly lower CI activity than all other brain regions, regardless of genotype. However, CI activity per tissue mass only tended to be higher in the AC than in the neurodegeneration-prone brain regions, but reached significance when expressed per unit of CS. The higher residual CI capacity per unit of CS in the AC might correlate with it being less susceptible to the degeneration in a CI deficiency.

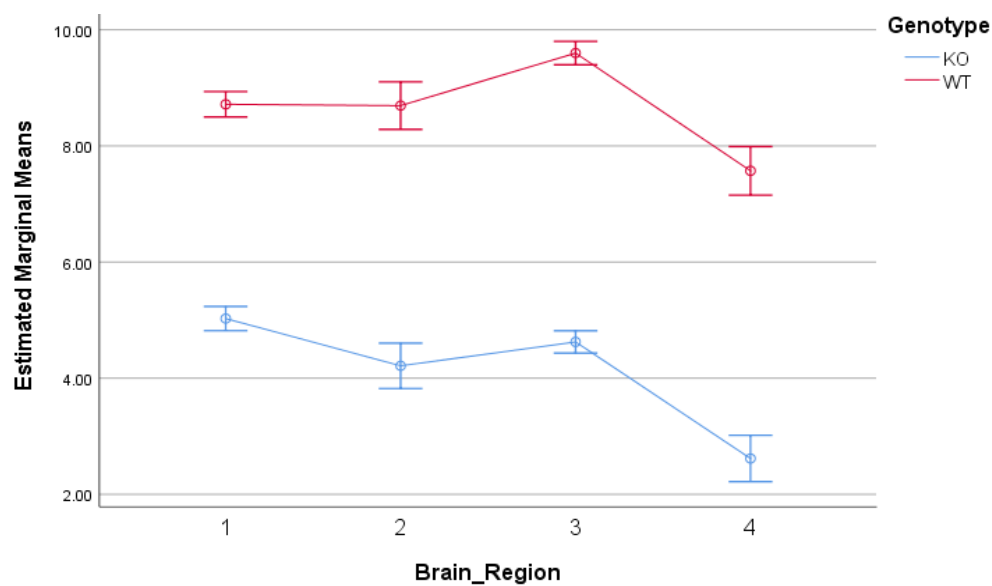


Figure E.2: Maximal complex I enzyme activity of *Ndufs4* wild-type and knockout mice normalised to CS activity.

Plots represent the estimated marginal means \pm standard error of maximal CI activity measured spectrophotometrically in triplicate. This was done in 700 x g supernatants prepared from the homogenates of the anterior cortex (1), brainstem (2), cerebellum (3) and olfactory bulbs (4) harvested from *Ndufs4* WT (red, n=10) and KO (blue, n=12 except for AC n=11) mice at PN45 to PN49.

Results of maximal CII activity normalised to CS activity (CII/UCS) are shown in Figure E.3. No significant interaction was observed between genotype and brain region. However, CII/UCS was lower in all KO brain regions compared to the corresponding WT regions ($p=0.002$, $\eta_p^2=0.42$). Also, a significant effect was observed for brain region (Greenhouse-Geisser $p<0.0001$, $\eta_p^2=0.63$). For both genotypes, CII/UCS of the AC was significantly higher compared to BST ($p=0.03$, $d=0.7$) and lower compared to CB ($p<0.0001$, $d=1.3$). Among the neurodegeneration-prone brain regions, CII/UCS of CB was significantly higher, regardless of genotype: CB vs BST ($p<0.0001$, $d=1.7$) and CB vs OB ($p<0.0001$, $d=1.3$).

APPENDIX E: Supplementary biochemical results

In accordance with the protein-normalised data, CII/UCS differed among brain regions and was the highest in CB, regardless of genotype. In contrast to the protein-normalised data, CII/UCS was significantly and equally reduced by the KO in all brain regions and not significantly lower in the AC compared to the neurodegeneration-prone brain regions. Collectively, these results suggested that the KO decreased CII activity relative to CS activity, but not per tissue mass, in all investigated brain regions. In other words, the *Ndufs4* KO differentially affected CII and CS activity. Moreover, while CII activity relative to CS activity was not unique in the AC compared to the neurodegeneration-prone brain regions within a genotype, the lower CII activity per tissue mass in the former might be due to its lower mitochondrial content (lower maximal CS activity in WT) per tissue mass.

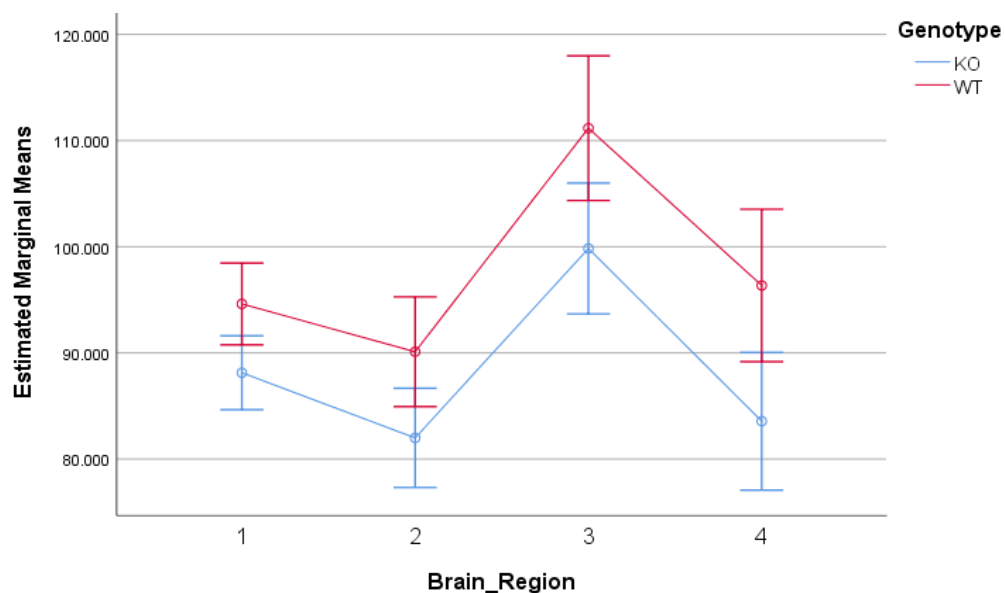


Figure E.3: Maximal complex II enzyme activity of *Ndufs4* wild-type and knockout mice normalised to CS activity.

Plots represent the estimated marginal means \pm standard error of maximal CII activity measured spectrophotometrically in triplicate. This was done in 700 \times g supernatants prepared from the homogenates of the anterior cortex (1), brainstem (2), cerebellum (3) and olfactory bulbs (4) harvested from *Ndufs4* WT (red, n =10) and KO (blue, n =12 except for OB n =11) mice at PN45 to PN49.

Figure E.4 shows maximal CIII activity normalised to CS activity (CIII/UCS) for the various brain regions. Two-way mixed ANOVA of CIII/UCS showed a significant interaction between genotype and brain region ($p = 0.003$, $\eta_p^2 = 0.26$). Also evident was the significantly lower CIII/UCS in all KO brain regions compared to corresponding WT brain regions (AC, $p < 0.0001$, $d = 2.0$; CB, $p < 0.0001$, $d = 2.1$ and OB, $p < 0.05$, $d = 0.8$). In the WT group, the CIII/UCS of the

APPENDIX E: Supplementary biochemical results

AC was significantly higher when compared to BST ($p = 0.011$, $d = 1.6$) and OB ($p < 0.0001$, $d = 3.0$) but only tended to be higher compared to CB. In the KO group, CIII/UCS of the AC was significantly higher compared to the OB ($p < 0.0001$, $d = 3.7$). The comparison between the neurodegeneration-prone brain regions, showed that CIII/UCS was significantly lower in the OB, regardless of genotype: OB vs BST in WT ($p = 0.012$, $d = 1.7$) and in KO ($p < 0.0001$, $d = 2.6$), OB vs CB in WT ($p < 0.0001$, $d = 2.8$) and in KO ($p < 0.0001$, $d = 3.4$). Furthermore, a significantly lower CIII/UCS was observed in WT BST than in WT CB ($p = 0.006$, $d = 1.2$).

In accordance with the protein-normalised data, CIII/UCS was significantly lower in the OB, regardless of genotype. Contrary to the protein-normalised data, CIII/UCS was decreased in most KO brain regions and was generally higher in the WT AC than in the remaining WT brain regions, except for the CB. Together, the data suggested that the KO differentially affected CIII and CS activity. In addition, the more resilient AC has a higher capacity for CIII activity relative to CS in comparison with the neurodegeneration-prone brain regions.

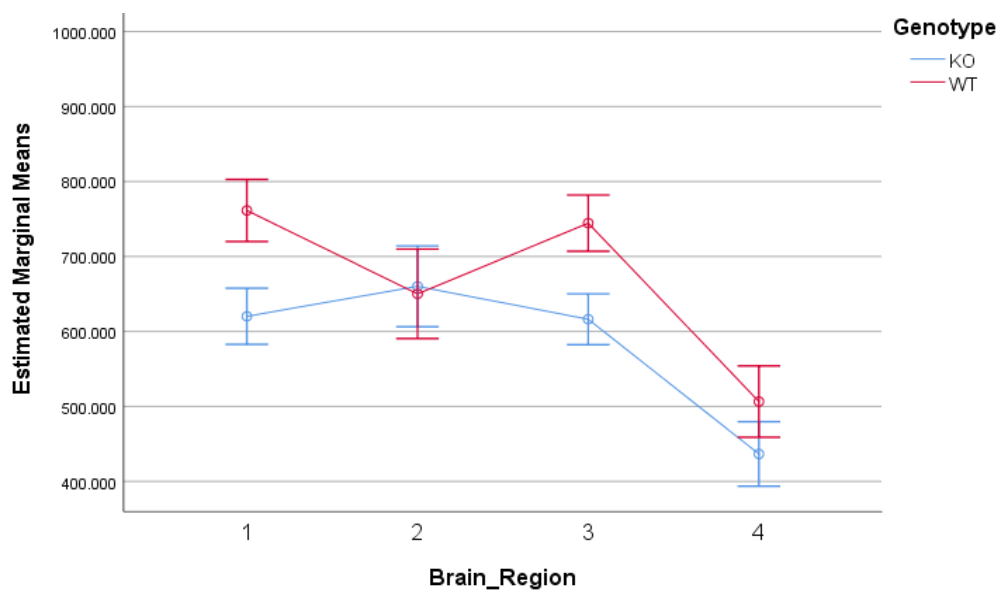


Figure E.4: Maximal complex III enzyme activity of *Ndufs4* wild-type and knockout mice normalised to CS activity.

Plots represent the estimated marginal means \pm standard error of maximal CIII activity measured spectrophotometrically in triplicate. This was done in 700 \times g supernatants prepared from the homogenates of the anterior cortex (1), brainstem (2), cerebellum (3) and olfactory bulbs (4) harvested from *Ndufs4* WT (red, $n = 10$ except for OB $n = 9$) and KO (blue, $n = 12$ except for OB $n = 11$) mice at PN45 to PN49.

APPENDIX E: Supplementary biochemical results

The results of maximal CIV activity normalised to CS activity (CIV/UCS) are illustrated in Figure E.5. The two-way mixed ANOVA showed no significant interaction between genotype and brain region, neither any effect of genotype when CIV was expressed per unit of CS (CIV/UCS). However, a significant effect of brain region on CIV/UCS ($p < 0.0001$, $\eta_p^2 = 0.57$) was observed which indicated that CIV/UCS differed across brain regions in a similar manner in both genotypes. Pairwise comparisons showed that CIV/UCS was significantly lower in the more resilient AC compared to all other regions: AC vs BST ($p = 0.002$, $d = 1.2$), AC vs CB ($p < 0.0001$, $d = 2.9$) and AC vs OB ($p = 0.001$, $d = 1.6$). Furthermore, CIV/UCS was also significantly higher in the CB than in the BST ($p = 0.008$, $d = 1.0$) and OB ($p = 0.002$, $d = 1.3$).

The significantly lower CIV/UCS in the AC and higher CIV/UCS in the CB compared to all other brain regions were in accordance with the protein-normalised data. Unlike the protein-normalised data, the KO did not affect CIV/UCS. These results suggested that the KO affected maximal CIV and CS activity in a similar manner in all brain regions. In addition, the more resilient AC has lower CIV-activity relative to the neurodegeneration-prone brain regions.

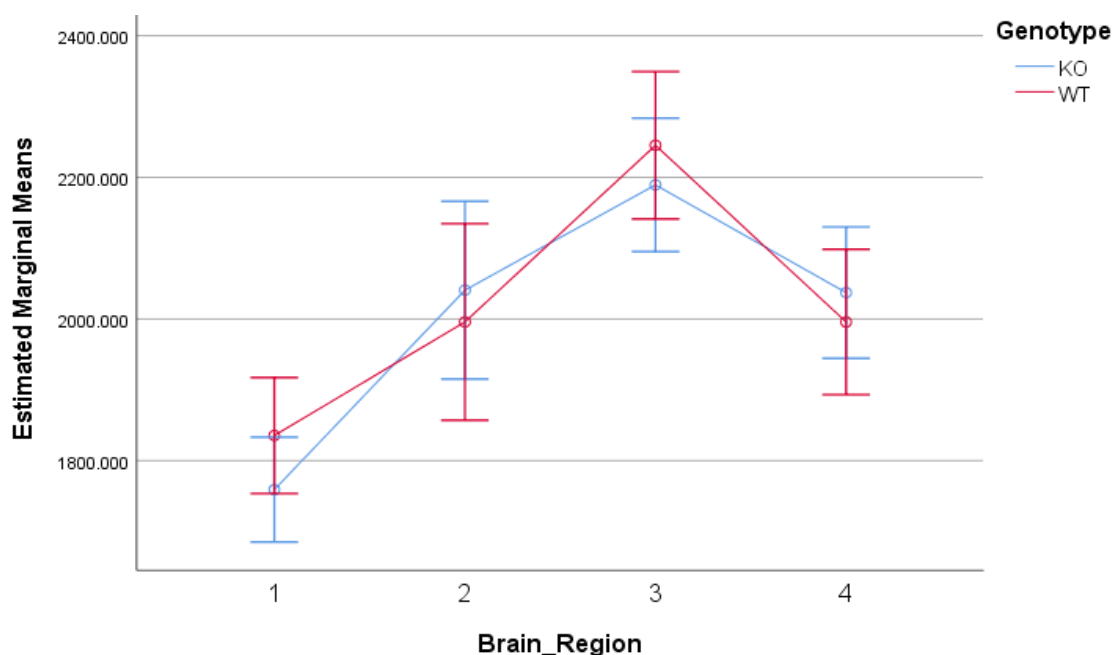


Figure E.5: Maximal complex IV enzyme activity of *Ndufs4* wild-type and knockout mice normalised to CS activity.

Plots represent the estimated marginal means \pm standard error of maximal CIV activity measured spectrophotometrically in triplicate. This was done in 700 x g supernatants prepared from the homogenates of the anterior cortex (1), brainstem (2), cerebellum (3) and olfactory bulbs (4) harvested from *Ndufs4* WT (red, n = 10 except for OB n = 9) and KO (blue, n = 12 except for OB n = 11) mice at PN45 to PN49.

APPENDIX E: Supplementary biochemical results

In summary, the results of the CS-normalised data were generally in accordance with the protein-normalised data. Some exceptions worth mentioning include: 1) The effect of the KO to cause significantly lower maximal activities of CII and CIII relative to CS activity which was mostly unaltered when expressed per tissue mass; 2) The unaltered activity of CIV in KO brain regions relative to CS activity compared to the generally higher CIV activity in KO regions when expressed per tissue mass; 3) In the WT AC the activity of CII relative to CS activity was comparable to that of the neurodegeneration-prone brain regions, while CII activities in WT AC were significantly lower when expressed per tissue mass; and 4) In the WT AC, the activity of CIII relative to CS activity was higher than in the neurodegeneration-prone brain regions, while CIII activities expressed per tissue mass were not uniquely different in the WT AC. Together, these results confirmed that within a brain region, the KO differentially affected the activities of CS and RC enzymes. Furthermore, that inherent differences in the relative activities of CS and RC enzymes might exist between neurodegeneration-prone and -resilient brain regions of WT mice.

With regard to brain regional differences in enzyme activities that could be correlated with the region-specific neurodegeneration in *Ndufs4* KO mice, it was shown that relative to CS, the more resilient WT AC had greater residual CI activities than the neurodegeneration-prone brain regions. In addition, it was evident that the more resilient WT AC had comparable CII activities, high maximal CIII activities, and lower CIV activities relative to CS activity than the neurodegeneration-prone brain regions. This corresponded with the protein-normalised data which suggested that regional vulnerability to neurodegeneration in the *Ndufs4* KO mice might be related to residual CI activities and/or inherent differences in OXPHOS organisation within mitochondria (or relative to CS activity) that might exist between the neurodegeneration-resilient and -prone brain regions. Consequently, the normalisation of the data to CS activity supported the main conclusions drawn from the protein-normalised data, even though CS might not be a reliable marker of mitochondrial content in the *Ndufs4* KO mouse brain regions.

APPENDIX F

Metabolomics data quality

F.1. Introduction

Metabolomics analyses entail the generation of large amounts of data that could be influenced on many levels by non-biological factors that may obscure biologically relevant variation. Even though the repeatability or precision of the standardised analytical methods proved to be sufficient across batches (APPENDIX D), variation might still arise from uncontrolled factors or unexpected variation during preparation and/or analysis. Consequently, the quality of the experimental data sets had to be verified to warrant that the data was reproducible and suitable for its further use. These verifications were primarily based on the assessment of quality control (QC) samples which represent technical replicates that were intermittently analysed with experimental samples and which is expected to give a good approximation of complete technical variance.

F.2. Evaluation of experimental precision

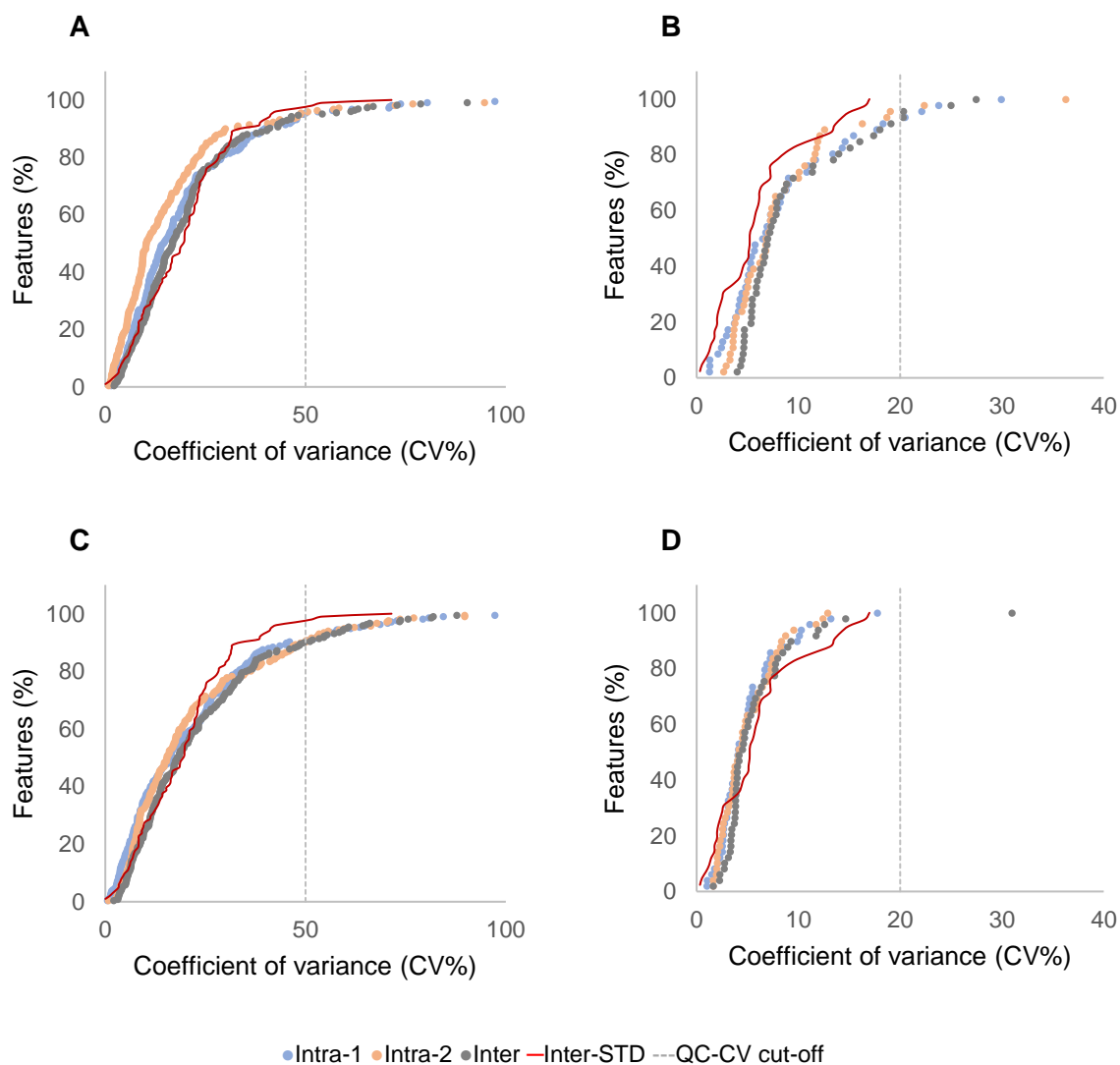
Experimental precision and/or instrument performance were evaluated by assessing the cumulative distribution functions (CDFs) of the coefficient of variance (CV) of all features detected in the experimental QC samples with the GC-TOF and LC-MS/MS metabolomics platforms, respectively (Quintás *et al.*, 2018). Results are shown in Figure F.1. The CV-value for each feature was calculated using Equation D.1 on post-normalised data sets before features with high QC-CV values were removed; i.e. before applying QC-CV filtering (see Chapter 4). For untargeted metabolomics approaches, features with a QC-CV value >50% are typically deemed unreliable (Dunn *et al.*, 2012; Lindeque *et al.*, 2013), while features with a QC-CV value >20% (FDA, 2001) are removed from data sets obtained from targeted metabolomics approaches. A summary of the percentage of features below the QC-CV cut-off line in the GC-TOF and LC-MS/MS metabolomics data sets are provided in Table F.1 for the various investigated brain regions.

In each case, >80 % of the detected features had CV values below the respective QC-CV cut-off values and were deemed reliable. As expected, the semi-targeted LC-MS/MS data sets displayed much greater precision than the untargeted GC-TOF data sets. Furthermore, the inter-batch precision of the experimental data sets was very similar to that obtained for the standardised methods (represented by a red line in Figure F.1), indicating acceptable method and/or instrument performance.

APPENDIX F: Metabolomics data quality

Notably, a somewhat higher inter-batch variance was observed in the experimental LC-MS/MS data set of the OB when compared to that of the standardised method. This was partly due to an unforeseen failure of the uninterrupted power supply (UPS) during power cuts. Nevertheless, even with the additional variation, the data still displayed sufficient precision to be considered as good quality data.

Together, these findings showed that experimental variation was, in all cases, within acceptable limits and instrument performance was satisfactory. The experimental data therefore displayed sufficient repeatability, confirming the suitability of the various data sets for further use.



APPENDIX F: Metabolomics data quality

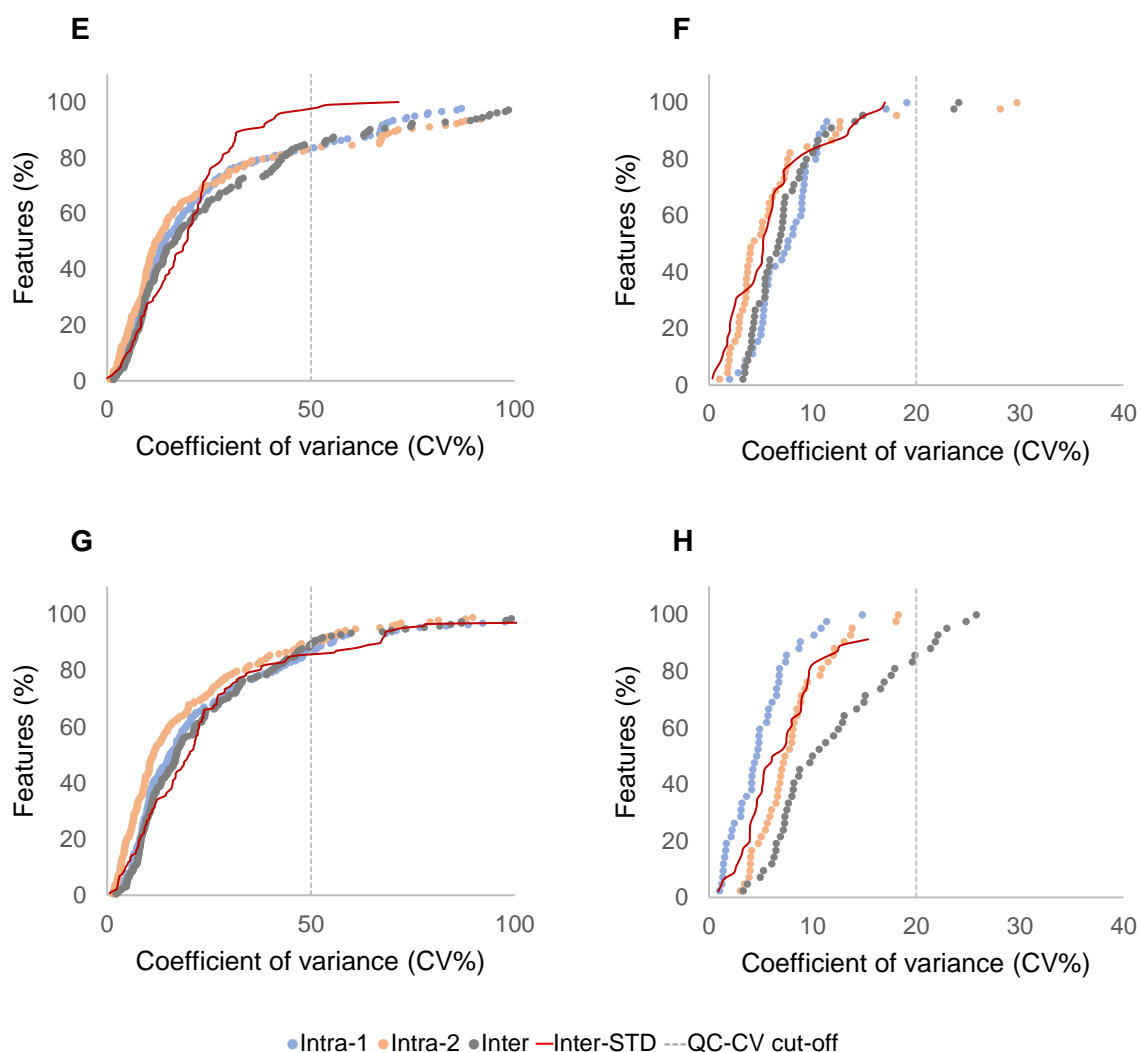


Figure F.1: Assessment of experimental precision in final metabolomics analyses.

Scatter plots depict the percentage of features in replicate quality control (QC) samples at a certain level of coefficient of variance (CV) as detected by the GC-TOF (graphs on the left, A, C, E & G) and LC-MS/MS (graphs on the right, B, D, F & H) metabolomics platforms, respectively. **A&B:** anterior cortex, **C&D:** brainstem, **E&F:** cerebellum and **G&H:** olfactory bulbs. Intra-batch precision (4x QCs) is depicted in blue and orange, while inter-batch precision (8x QCs) is depicted in grey. The inter-batch precision determined during method standardisation was included for comparison purposes and is represented by a red line. Vertical dashed lines indicate the QC-CV cut-off value for removing unreliable features. Plots were constructed from post-normalised data of QC samples analysed intermittently during each experimental batch consisting of ~23 samples. The precision of the methods during analyses of experimental samples proved to be acceptable in all cases. *Other abbreviations: GC-TOF, gas chromatography-time-of-flight mass spectrometry; LC-MS/MS liquid chromatography-tandem mass spectrometry.*

Table F.1: Percentage of features below the QC-CV cut-off value in the GC-TOF and LC-MS/MS metabolomics data sets of the various investigated brain regions.

	GC-TOF			LC-MS/MS		
	Intra-batch 1	Intra-batch 2	Inter-batch	Intra-batch 1	Intra-batch 2	Inter-batch
AC	95	95	95	91	96	91
BST	90	90	90	100	100	98
CB	83	84	85	100	96	96
OB	87	90	89	100	100	86

QC-CV cut-off value for unreliable features is >50 % for GC-TOF and >20 % for LC-MS/MS detected features. Abbreviations: AC, anterior cortex; BST, brainstem; CB, cerebellum; OB, olfactory bulbs; GC-TOF, gas chromatography-time-of-flight mass spectrometry; LC-MS/MS liquid chromatography-tandem mass spectrometry; QC, quality control; CV, coefficient of variance.

F.3. Evaluation of potential batch effects and overall data integrity

The large number of samples (~46) and run-time per sample necessitated that samples be divided into two smaller sub-sets or 24h-‘batches’. This was to minimise the potential variability and bias caused by run order effects or potential drifts (gradual changes) in instrument performance or in analyte concentrations. Especially for the unquenched TMS derivatives analysed by the GC-TOF metabolomics platform. To minimise variation between batches, precautionary measures were implemented: sample randomisation, balanced experimental design, the preparation of samples by a single analyst and analysing batches of the same brain regions within the shortest time frame from one another. However, despite these measures, the separate preparation and analysis of each batch, as well as potential unforeseen instrumental or external interruptions, might also have contributed to non-biological variation between analysed batches. Since substantial systematic, non-biological variation between batches; i.e. “batch effect” (Salerno Jr *et al.*, 2017), can have dramatic effects on the outcome and accuracy of the results, the final data sets were visually or qualitatively inspected for batch-related effects or grouping.

Figure F.2 and Figure F.3 illustrate the visual assessment of the changes in the total signal or response (Y-axis) of each sample over the order (X-axis) in which the samples of two batches were analysed. The total signal of each sample represents the sum of all peak intensities measured within that sample. Two batches are presented on each side of the vertical dashed line by plots of experimental samples (represented by coloured ○) and quality control (QC) samples (represented by ●).

APPENDIX F: Metabolomics data quality

Figure F.2 illustrates how batch effects can be visually identified. In the case of insignificant or small batch effects (Figure F.2.A), the global total intensities of samples are similar within and between batches. This can be seen in a horizontal distribution of QC samples throughout the run-order in each batch and distribution on the same vertical plane between the two batches. Substantial inter- or between-batch effects would cause clear differences in the global intensities of samples in one batch compared to the other, resulting in the horizontal alignment of the QCs of the two batches on distinctly different intensity or vertical planes (Figure F.2.B). Gradual changes in the global intensities of experimental and QC samples analysed in the same batch represented the intra- or within-batch effects (Figure F.2.C).

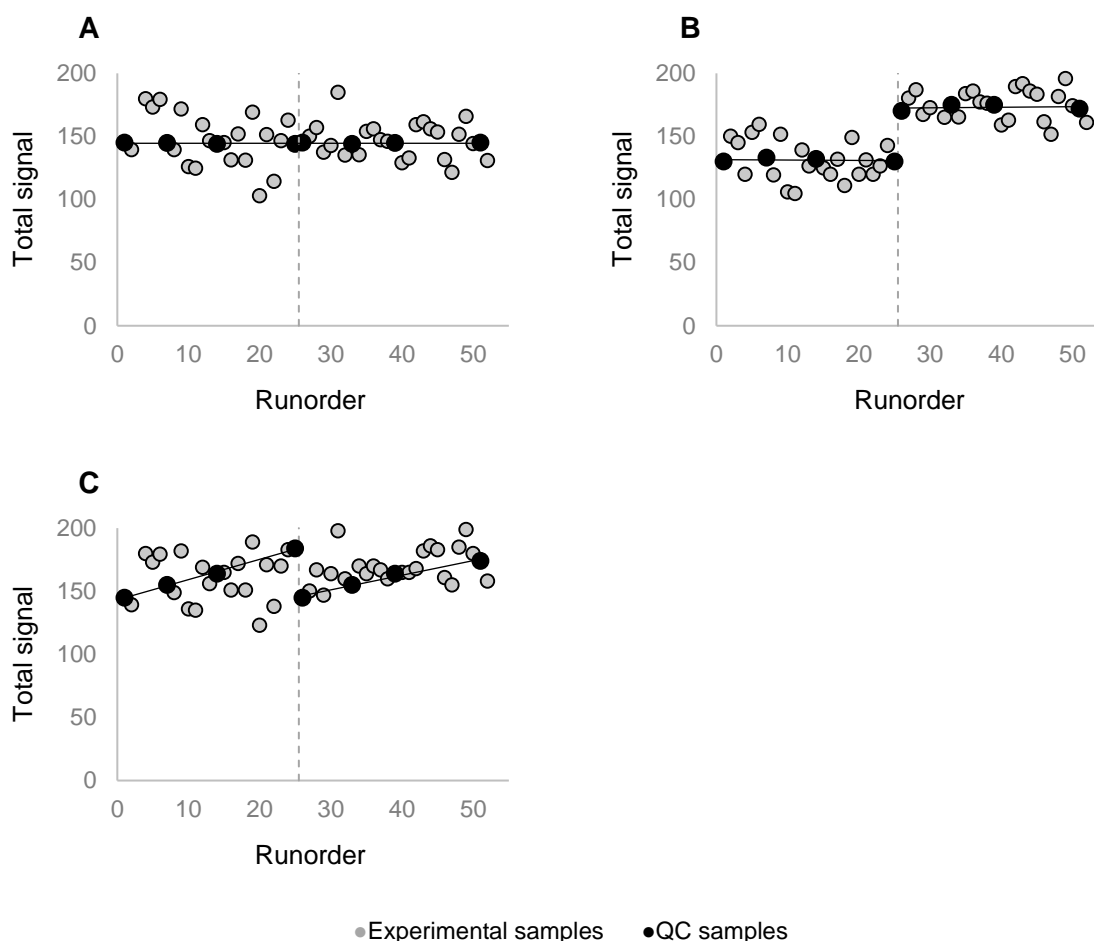


Figure F.2: Visual assessment of potential batch effects using total signal scatterplots.

A: No batch effect/s, **B:** inter- or between-batch effects and **C:** intra- or within-batch effects. Plots were constructed from a fictitious dataset. Experimental samples are represented by ○ in grey and quality control (QC) samples are represented by ●.

APPENDIX F: Metabolomics data quality

Figure F.3 shows the visual assessment applied to the samples of each brain region analysed in two batches with the GC-TOF (graphs on the left) and LC-MS/MS (graphs on the right) metabolomics platforms, respectively. The total signal of each sample was calculated using the datasets obtained after processing, internal standard normalisation and missing value-imputation.

Overall, the QC samples were distributed in a horizontal line within batches as well as in horizontal lines on the same intensity level across batches. This illustrated an absence of substantial differences in global intensities of samples which indicated that no significant batch effects occurred. A slight gradual increase was observed in the total intensity of the OB samples measured with the LC-MS/MS platform. As mentioned previously, this might be ascribed to the unfortunate series of events which included failure of the UPS during power cuts and an increase in column pressure caused by the gradual build-up of sample residue that precipitated in the small volume of the OB samples. Nevertheless, the gradual increase in total signal intensity of OB QC samples was minimal and were also not clearly observed in the distribution of the experimental samples. Considering the practical limitations that prevented re-analysis, such as limited sample volume, scarcity of samples and other technical problems, together with the fact that this was a minor within-batch effect that did not necessitate intensive corrective procedures that might have their own built-in bias and disadvantages, it was concluded that the data was of sufficient quality to use as is.

Altogether, it was shown that batch-related technical variability was minimal, that additional post-run batch correction was unnecessary, and that the data was expected to accurately reflect biological differences between samples.

APPENDIX F: Metabolomics data quality

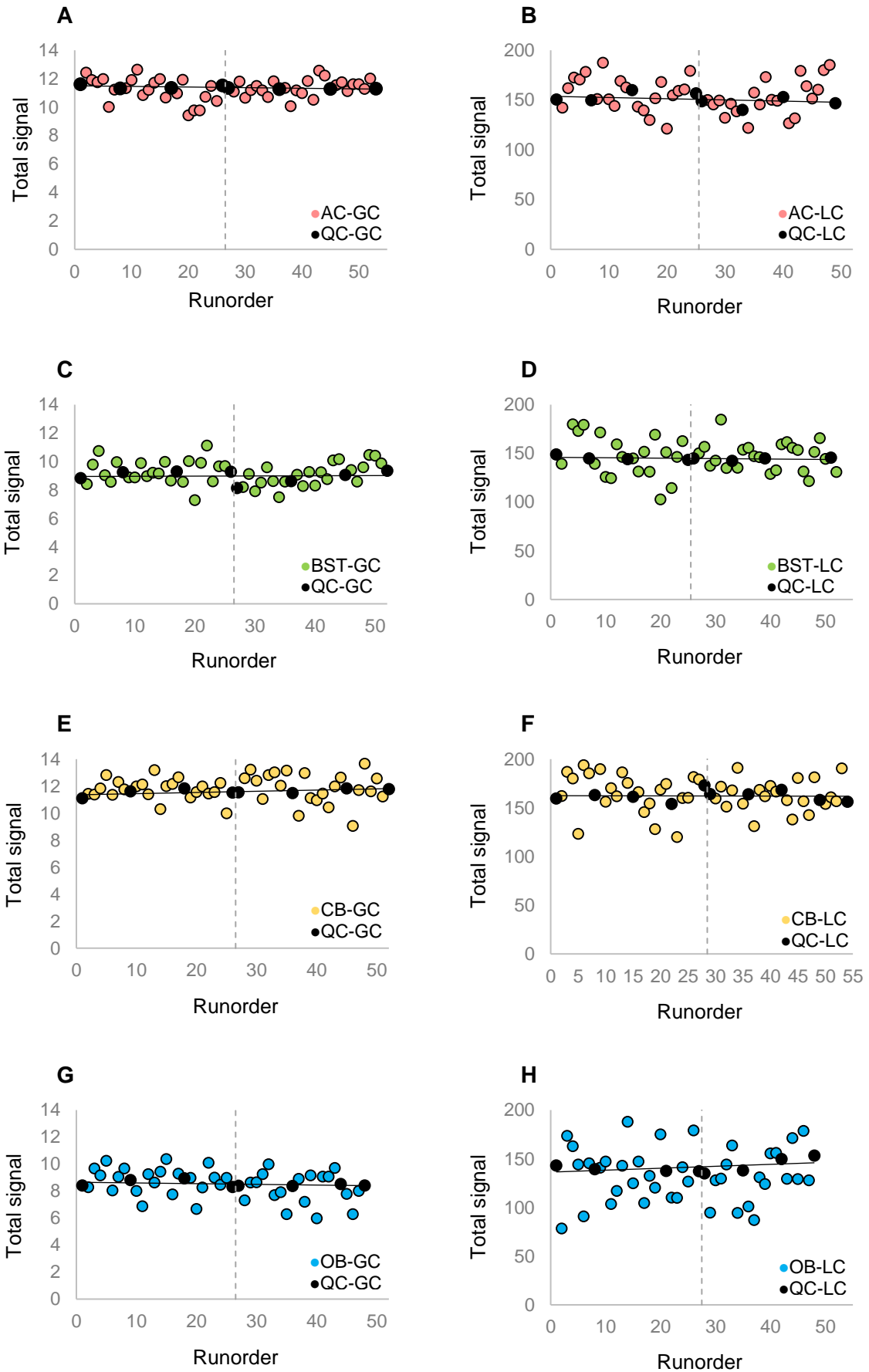


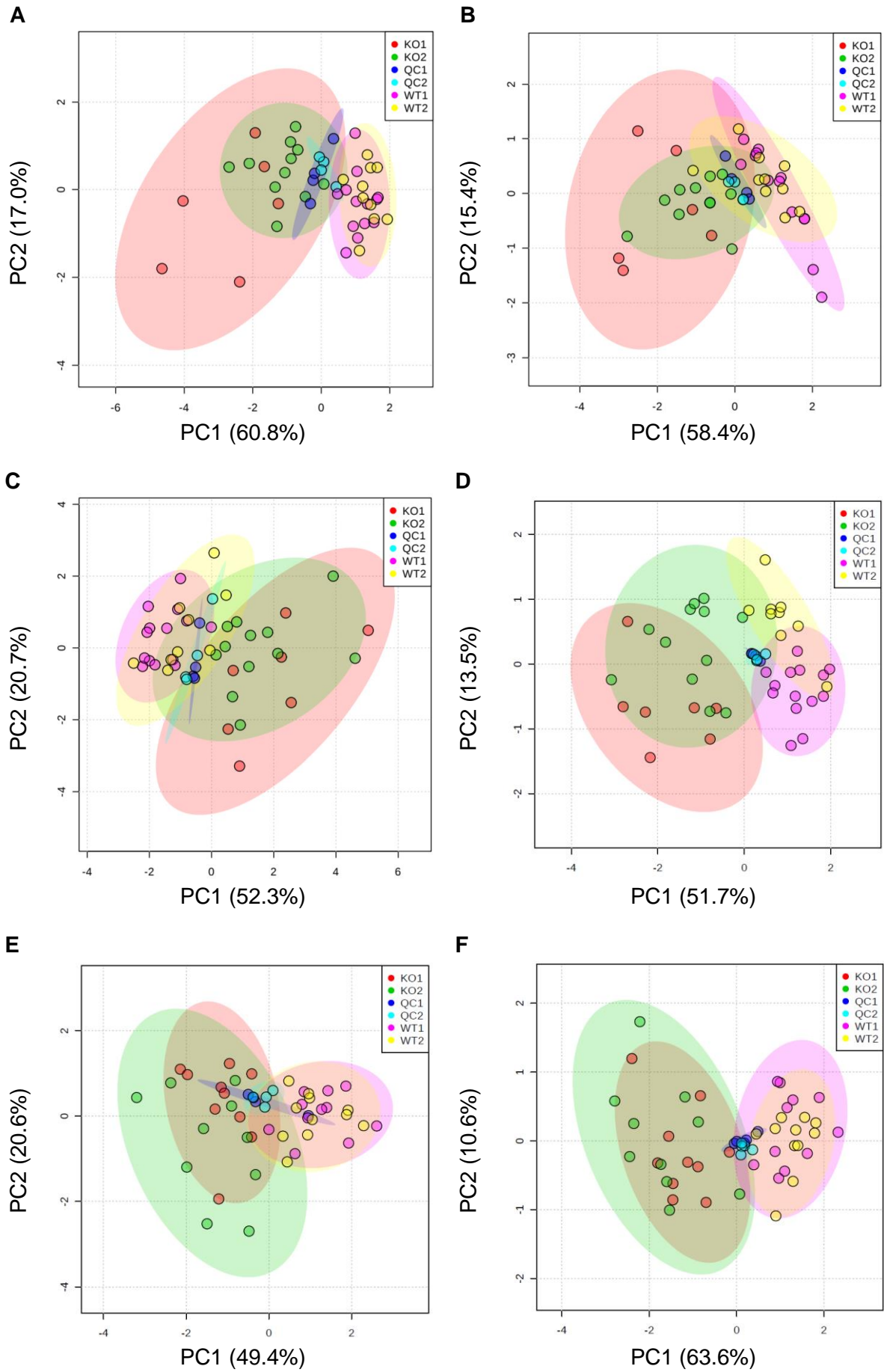
Figure F.3: Evaluation of potential batch effects and overall data integrity of experimental multi-platform metabolomics data sets

Scatter plots depict the total signal (calculated as the sum of all peak intensities within a sample obtained from processed normalised data) of each sample over the order in which samples were analysed using the GC-TOF (graphs on the left, A, C, E & G) and LC-MS/MS (graphs on the right, B, D, F & H) metabolomics platforms, respectively. **A&B**: anterior cortex (AC), **C&D**: brainstem (BST), **E&F**: cerebellum (CB) and **G&H**: olfactory bulbs (OB). Two batches are presented on both sides of the vertical dashed line by plots of experimental samples (represented by coloured ○) consisting of *Ndufs4* wild-type (n =~25) and knockout (n =~21) samples as well as quality control (QC) samples (represented by ●). Evaluation of potential batch effects and general quality of the data was primarily based on the distribution of QC samples. No clear overall difference in total intensities was observed within or between any of the batches. A slight, gradual, but insignificant drift in total intensities was noted in the second batch of the OB samples analysed with the LC-MS/MS. *Other abbreviations: GC-TOF, gas chromatography-time-of-flight mass spectrometry; LC-MS/MS liquid chromatography-tandem mass spectrometry.*

Potential batch-effects and overall platform-specific data quality were also evaluated after the identification of important metabolites through visualising the distribution and clustering of sample groups with an unsupervised principle component analysis (PCA). Figure F.4 displays the two-dimensional (2-D) PCA score plots obtained from the respective GC-TOF (graphs on the left) and LC-MS/MS (graphs on the right) data sets of each of the four investigated brain regions. These plots were generated from the post-processed, generalised log (glog) transformed data of *Ndufs4* KO (represented by ● in red, green, yellow or blue) and WT mice (represented by ● in black) as well as of QC samples (represented by ● in shades of purple). The first two principal components (PC1, X-axis and PC2, Y-axis) of the PCA score plots represent the coordinate axes of the uncorrelated maximum variance direction of the data, while the shaded ellipses represent the 95% confidence intervals of each experimental group. Important to note, the GC-TOF PCA score plot of the OB was constructed without the data of three features which caused a separation between the genotype groups that overwhelmed the remaining variation in the data set and consequently impeded proper visual evaluation.

In all cases, the QC samples clustered tightly together (generally in the middle) in the PCA, indicating the reproducibility of the experimental procedures and an absence of significant batch effects. The close grouping of samples according to genotype, and the strong overlap of sample groups (KO or WT samples) analysed in different batches also confirmed the reproducibility and absence of significant batch effects. The most significant variation (separation in principal component 1) was seen between experimental groups and clear separation between experimental samples that could be attributed to strong batch-specific factors not being visible. These findings confirmed that analytical variation within and between batches were relatively small in comparison to the biological variation. Similar results were also obtained when PCAs were applied to the data sets containing all features (data not shown).

APPENDIX F: Metabolomics data quality



APPENDIX F: Metabolomics data quality

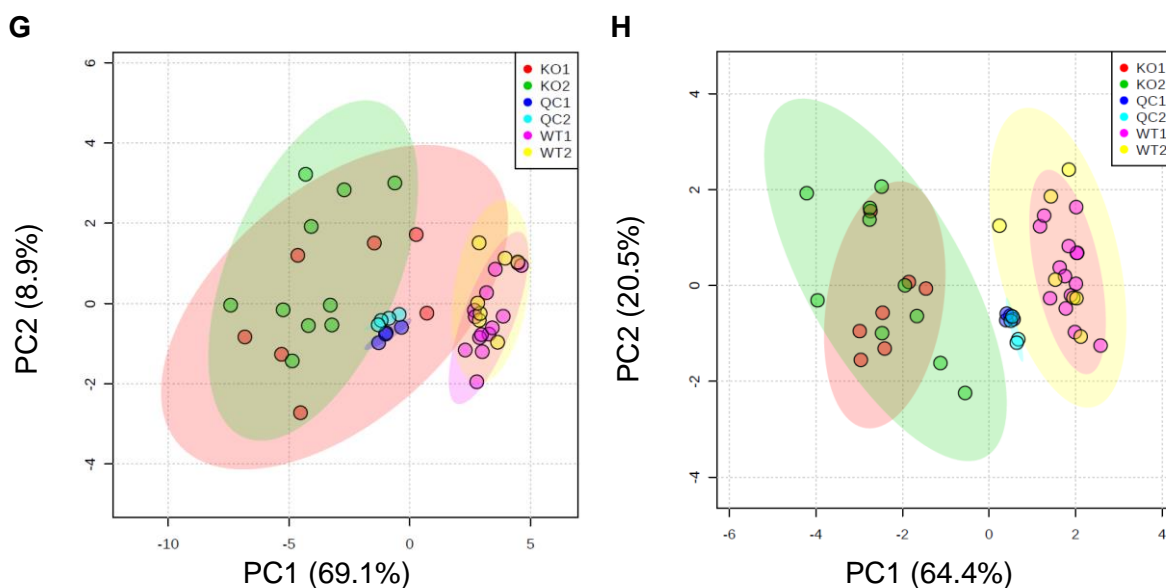


Figure F.4: Evaluation of potential batch effects and data integrity of experimental multi-platform metabolomics data sets using principal component analysis on important differential metabolites.

Principal component analysis (PCA) score plots of post-processed, post-normalised (by internal standards) and post-transformed (generalised logarithmic transformation) quality control (QC, $n=8$, ● in dark and light blue), wild-type (WT, $n=25$, ● in purple and yellow) and *Ndufs4* knockout (KO, $n=21$, ● in red and green) samples analysed with the GC-TOF (graphs on the left, A, C, E & G) and LC-MS/MS (graphs on the right, B, D, F & H) metabolomics platforms, respectively. Principal component 1 (PC1, X-axis) and 2 (PC2, Y-axis) represent the two directions of maximum uncorrelated variance in the data set. Shaded ellipses represent the 95% confidence intervals for each experimental group. **A&B:** anterior cortex, **C&D:** brainstem, **E&F:** cerebellum and **G&H:** olfactory bulbs. Samples analysed in the first batch (indicated by “1” in the legend) is represented in red, dark blue and purple, while samples analysed in the second batch (indicated by “2” in the legend) is represented in green, light blue and yellow. **Note:** The GC-TOF score plot for the OB was constructed without three of the detected features for proper evaluation of the clustering of sample points. No significant overall separation was observed in either QC- or experimental samples-based on batch-specific factors. Close clustering of QC samples indicated good quality data, while clustering of experimental samples according to genotype suggested that biological variation greatly exceeded analytical variation. *Other abbreviations: GC-TOF, gas chromatography-time-of-flight mass spectrometry; LC-MS/MS liquid chromatography-tandem mass spectrometry.*

To summarise, the reliability and quality of the final metabolomics data sets (after being normalised) were determined by evaluating data repeatability or precision and potential batch-effects. Collectively, the experimental data sets showed acceptable precision and the absence of visible or strong batch-related effects that would otherwise have required correction. It was confirmed that the level of experimental variation in all data sets were sufficiently low and were greatly overshadowed by biological variation, indicating good quality data that was suitable for further interpretation.

APPENDIX G

Supplementary metabolomics results

G.1. Introduction

One of the main objectives (Objective 3) of this study was to investigate whether brain regional differences in metabolic responses to the CI deficiency could be correlated with the regional vulnerability to neurodegeneration in *Ndufs4* knockout (KO) mice by using a multi-platform metabolomics approach. The most important results were reported in the main text (see Chapter 6). In this section, supplementary results are provided with regard to the principal component analysis (PCA) of all detected GC-TOF features of the olfactory bulbs (OB) and a visual comparison of the relative abundance of commonly altered discriminatory metabolites via box-plots.

G.2. PCA of all GC-TOF detected features of the OB

Recall that the platform-specific data sets were visually evaluated for general and natural clustering and trends by performing unsupervised PCA on the post-quality control, imputed, generalised (glog) log transformed data. In the main text, the GC-TOF PCA scores plot of the OB was constructed without the data of three features: glucose-1-phosphate (G1P), glucose-6-phosphate (G6P) and phosphoglycerol enol (PGe(2)) (refer to Figure 6.1). These three features were not detected in any of the WT samples. In all probability, this is because the intensities were below the detection limit as these features were detected in both the KO and QC samples. The missing values for the three features in the WT group were therefore replaced with half of the minimum positive value of the entire data set. As a result, when the three features were included in the construction of the PCA scores plot, the separation between the genotype groups overwhelmed the remaining variation in the data set. Figure G.1 displays the two-dimensional (2-D) PCA scores plot (left panel) and loadings plot (right panel) generated from all GC-TOF detected features of the OB. Figure G.1 not only illustrated the previous point, but also justified the exclusion of the three features from Figure 6.1. The first two principal components (PC1, X-axis and PC2, Y-axis) of the PCA scores plots represent the coordinate axes of the maximum variance direction of the data, while the shaded ellipses represent the 95% confidence intervals of each experimental group. PC1 and PC2 accounted for 70.7% and 7.0% of variation, respectively, compared to 37.7% and 16.7%, respectively when constructed without the three features. The loadings plot illustrated that the contribution of the features to the created components caused severe separation between genotype groups that overwhelmed the remaining variation in the data set.

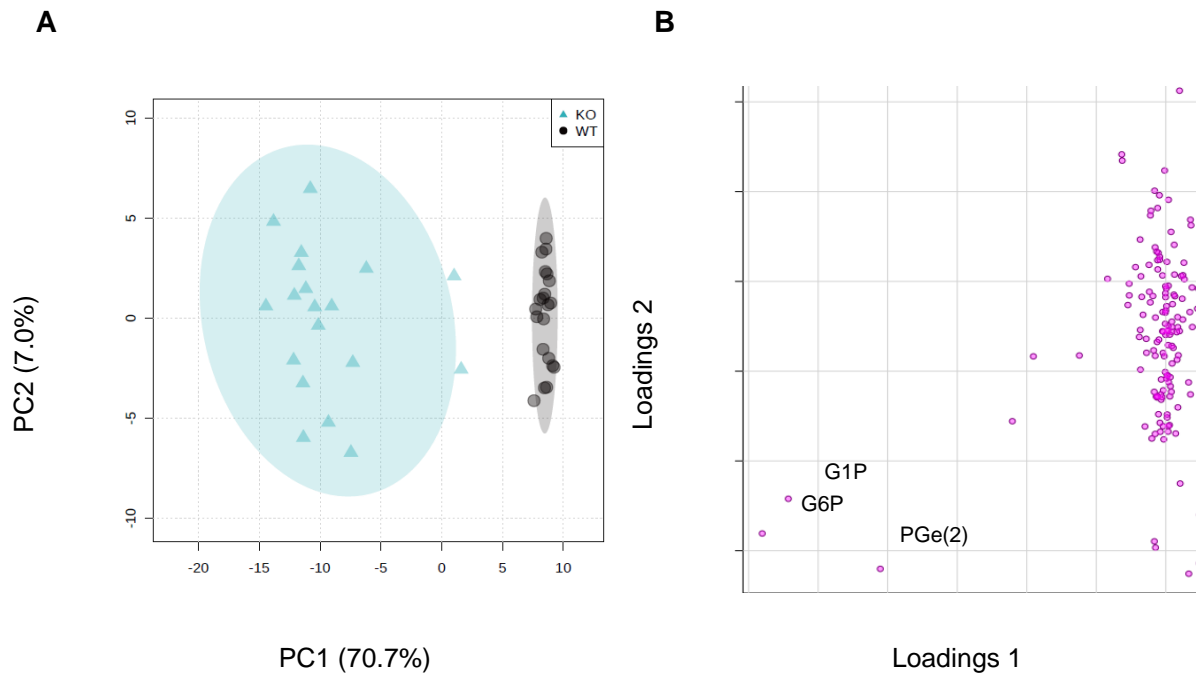


Figure G.1: PCA scores and loadings plot for all GC-TOF detected features of the OB.

Wild-type (WT, $n = 21$, ●) and *Ndufs4* knockout (KO, $n = 19$, ▲).

G.3. Relative abundance of commonly altered discriminatory metabolites

The metabolic effect of the *Ndufs4* KO on each brain region was evaluated by statistically comparing relative metabolite intensities between the corresponding brain regions of wild-type (WT, $n = 25$) and KO mice ($n = 21$) and by identifying significant discriminatory metabolites. That is to say metabolites whose concentrations differed with statistical (Student's *t*-test, FDR-adjusted $p < 0.05$) and practical (Effect size, d -value ≥ 0.8) significance when KO mice were compared to WT mice and which could be identified at an ID level of 1, 2 or 3 (Section 4.7.6). In this chapter, an additional visual comparison of the relative abundance of these discriminatory metabolites is given via box-plots. In each case, the box-plots were constructed from normalised, untransformed data sets of the anterior cortex (AC, red), brainstem (BST, green), cerebellum (CB, yellow) and olfactory bulbs (OB, blue) from wild-type (WT, $n = 25$) and knockout (KO, $n = 21$) mice. These box-plots display a median (central horizontal line), 25th and 75th percentiles (horizontal border lines), and 95% confidence intervals (CI, errors bars). The data points falling outside the CI are represented as dots. Statistical and practical significance of altered concentrations when KO mice were compared to WT mice, are indicated above the box-plots and were in all cases calculated from log-transformed data.

G.3.1. Relative abundance of the branched-chain amino acids (BCAAs)

Figure G.2 shows a comparison of the relative abundance of the BCAAs between KO and WT brain regions. The KO AC exhibited a significant increase in the levels of valine (Val) compared to WT AC ($p < 0.001$, $d = 1.1$). However, a tendency towards increased levels of leucine (Leu) and isoleucine (Ile) was also observed in the KO AC. In the KO BST, the relative abundance of all BCAAs was significantly increased in comparison with the WT BST, with the most profound increase observed for valine ($p < 0.0001$ for KO vs WT for all BCAAs, $d = 1.3$ for Leu; $d = 1.5$ for Ile; and $d = 2.1$ for Val). A similar pattern was also evident in the KO CB ($p < 0.0001$ for KO vs WT for all BCAAs, $d = 1.7$ for Leu; $d = 1.3$ for Ile; and $d = 2.3$ for Val) and KO OB ($p < 0.0001$ for KO vs WT for all BCAAs, $d = 1.7$ for Leu; $d = 1.5$ for Ile; and $d = 1.9$ for Val).

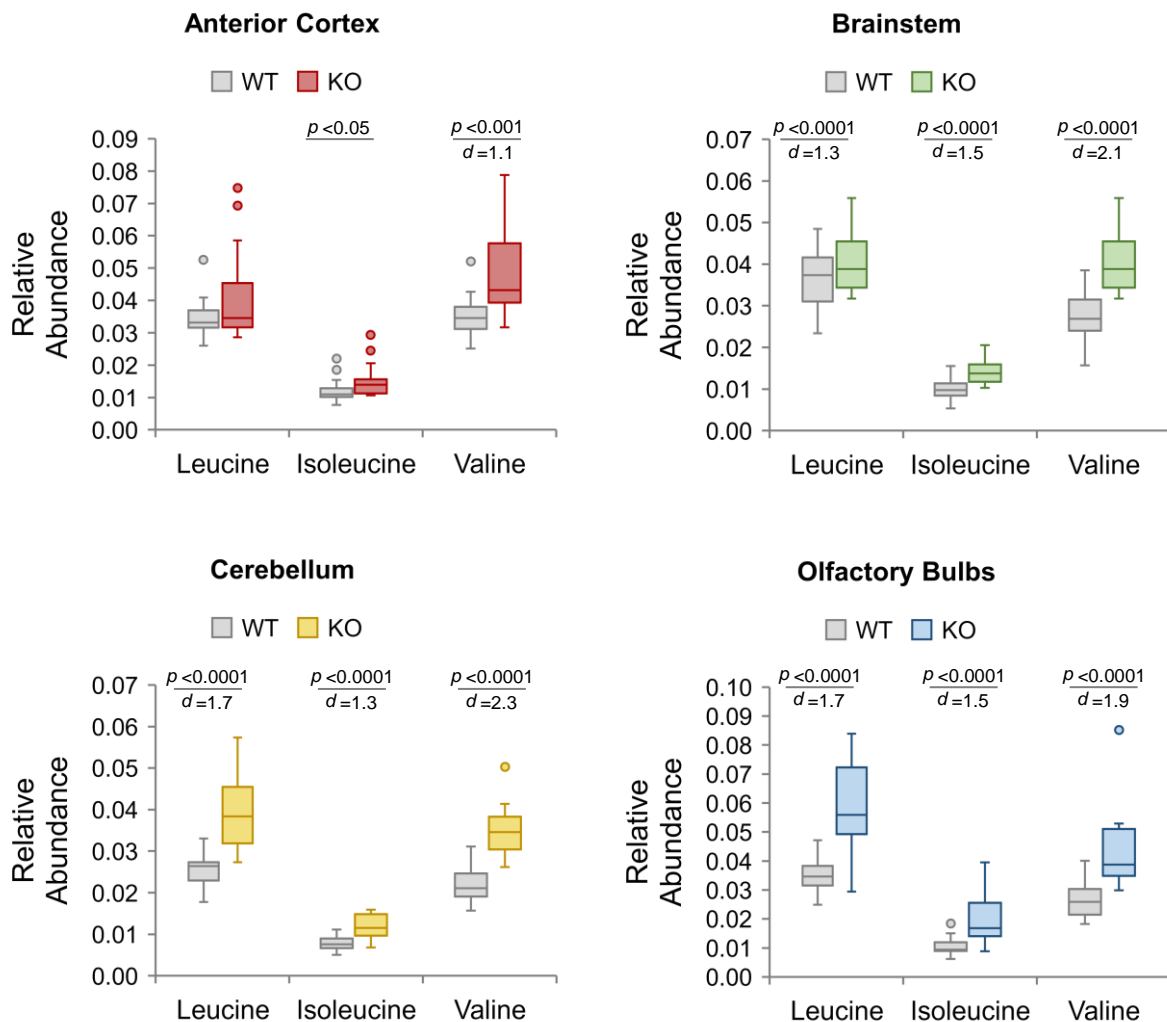


Figure G.2: The relative abundance of the branched-chain amino acids in the brain regions of *Ndufs4* wild-type and knockout mice.

G.3.2. Relative abundance of lysine-related metabolites

Figure G.3 shows a comparison of the relative abundance of the significantly altered lysine catabolic products in the investigated brain regions of KO and WT mice. The KO brain regions exhibited significant decreases in the levels of α -aminoadipic acid ($p < 0.0001$ for all KO vs WT, $d=1.7$ for AC; $d=1.6$ for BST; $d=1.9$ for CB and $d=3.2$ for OB) and dramatically increased levels of pipecolic acid ($p < 0.01$, $d=0.9$ for AC; $p < 0.001$, $d=1.0$ for BST; $p < 0.01$, $d=0.8$ for CB and $p < 0.0001$, $d=1.8$ for OB), suggesting a common perturbation in lysine metabolism.

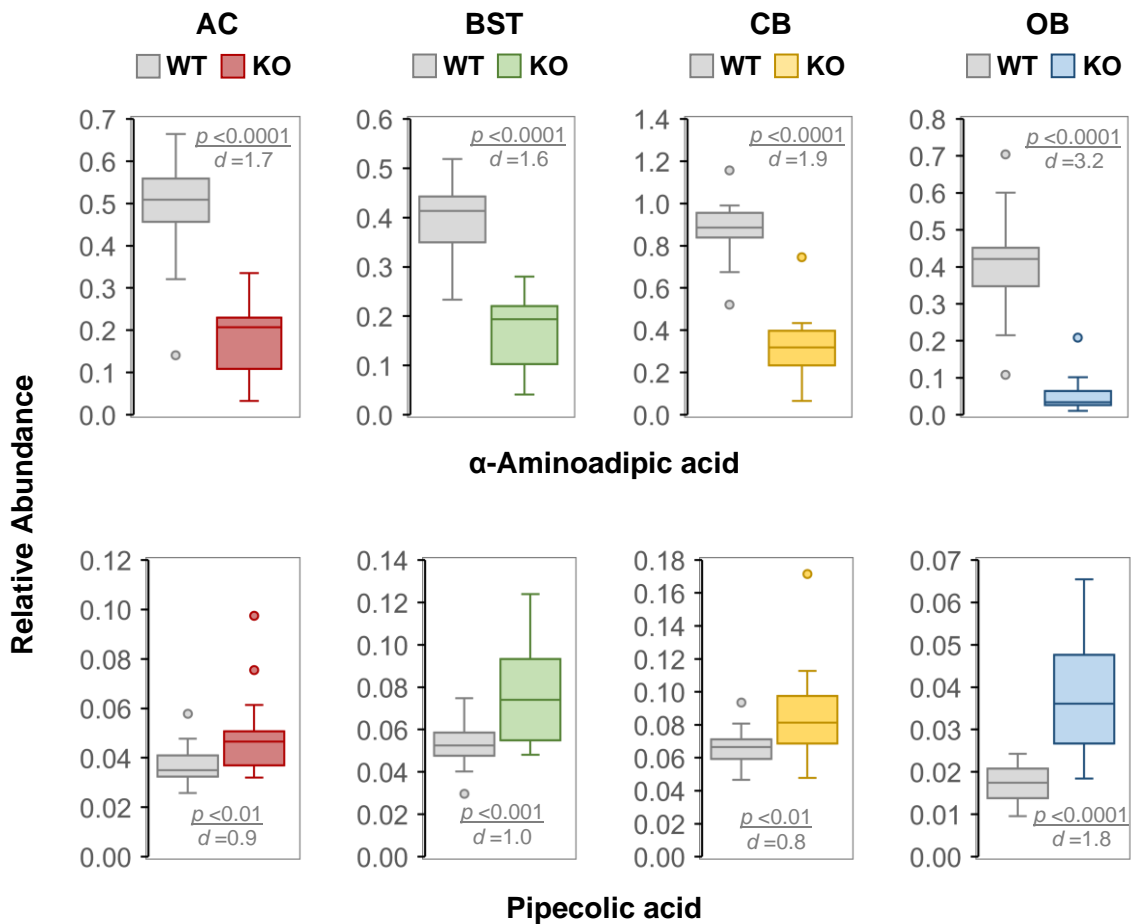
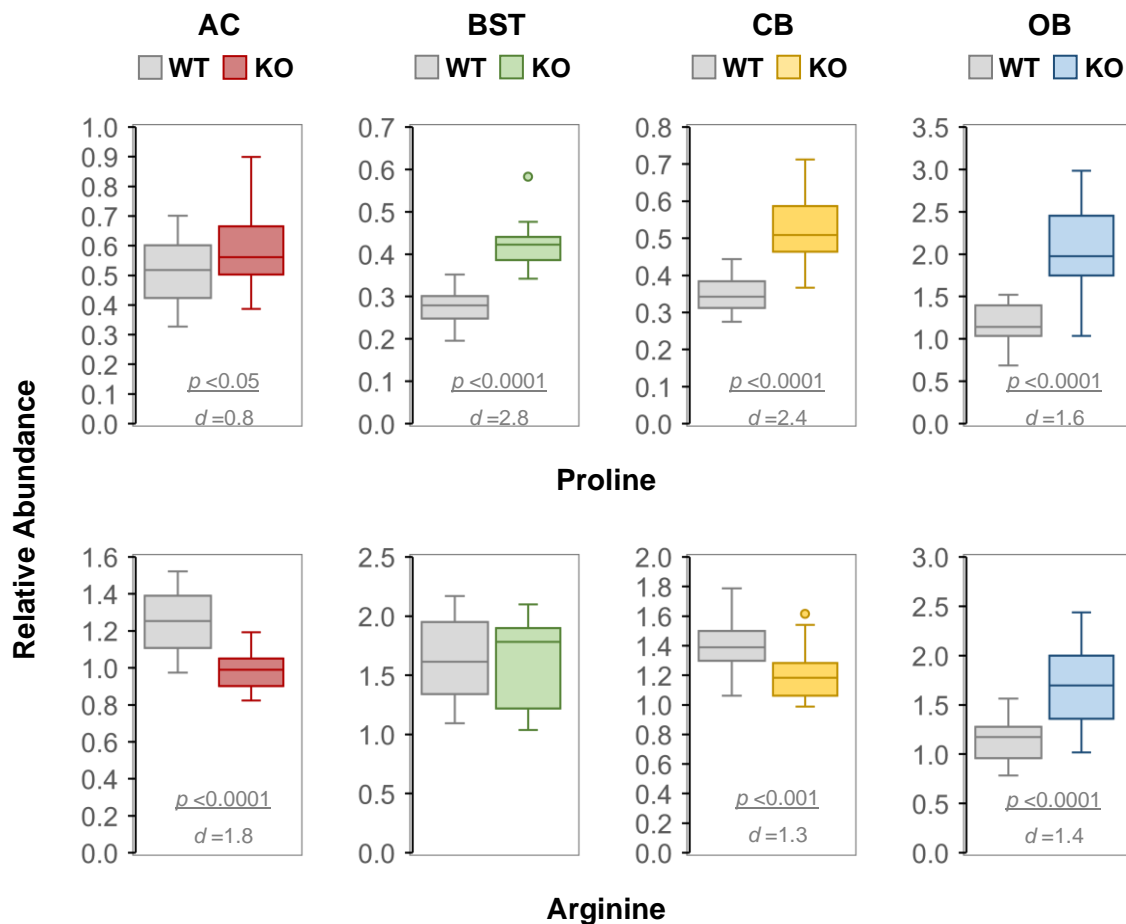


Figure G.3: The relative abundance of commonly altered lysine-related metabolites in the brain regions of *Ndufs4* wild-type and knockout mice.

G.3.3. Relative abundance of arginine- and proline-related metabolites

Figure G.4 shows a comparison of the relative abundance of arginine- and proline-related metabolites between KO and WT mice in the investigated brain regions. Compared to the WT AC, the KO AC displayed a significant increase in the levels of proline (Pro; $p < 0.05$, $d = 0.8$) and putrescine (Put; $p < 0.0001$, $d = 2.2$) together with a dramatic decrease in arginine (Arg; $p < 0.0001$, $d = 1.8$) and hydroxy-proline (Hyp; $p < 0.0001$, $d = 1.7$) levels. In comparison with the WT regions, similar results were obtained for the KO BST ($p < 0.0001$ for KO vs WT for all, $d = 2.8$ for Pro, $d = 1.5$ for Hyp and $d = 1.4$ for Put), except for the unaltered levels of Arg, and the KO CB ($p < 0.0001$ for KO vs WT for all except $p < 0.001$ for Arg, $d = 2.4$ for Pro; $d = 1.8$ for Hyp, $d = 1.6$ for Put and $d = 1.3$ for Arg). On the other hand, the KO OB displayed dramatic increases in the concentrations of Pro, Arg and Put ($p < 0.0001$ for KO vs WT for all, $d = 1.6$ for Pro, $d = 1.4$ for Arg and $d = 2.7$ for Put) and only a tendency towards decreased Hyp levels when compared to the WT OB.



APPENDIX G: Supplementary metabolomics results

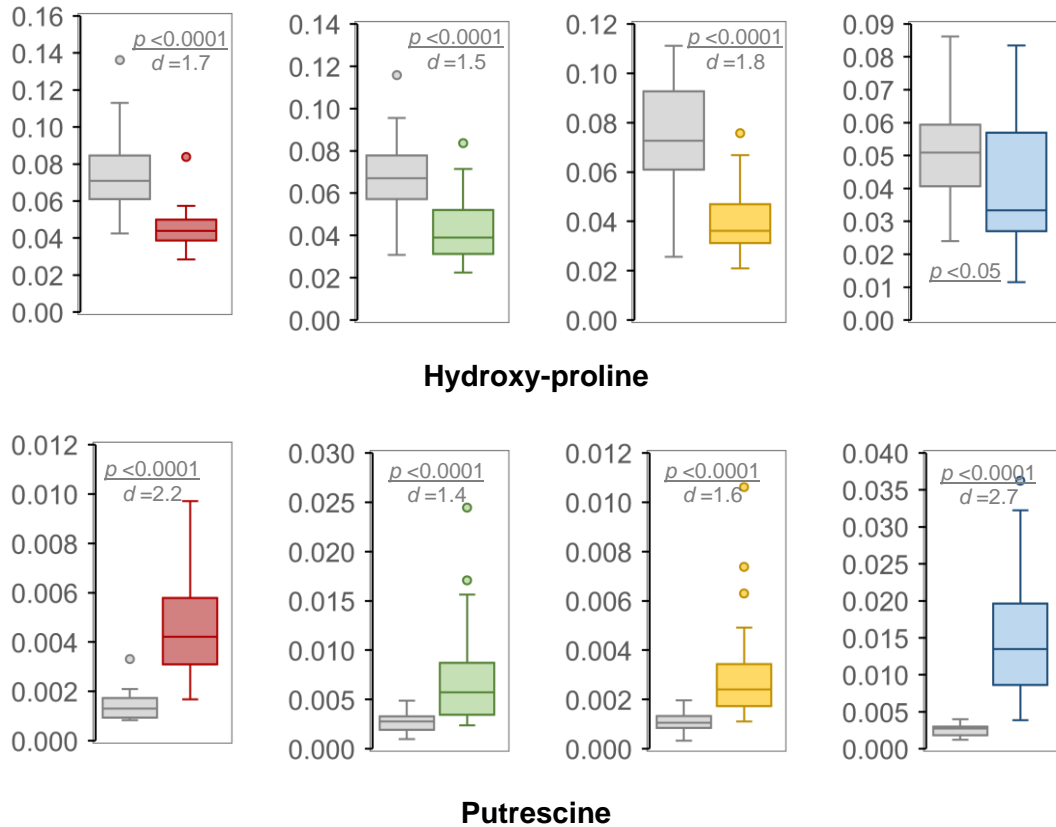


Figure G.4: The relative abundance of commonly altered arginine- and proline-related metabolites in the brain regions of *Ndufs4* wild-type and knockout mice.

G.3.4. Relative abundance of aspartic acid- and glutamic acid-related metabolites

Figure G.5 shows a comparison of the relative abundance of aspartic acid- and glutamic acid-related metabolites between KO and WT mice in the investigated brain regions. Compared to the WT AC, the KO AC displayed a dramatic decrease in the levels of aspartic acid (Asp), glutamic acid (Glu), asparagine (Asn) ($p < 0.0001$ for KO vs WT for all, $d = 2.4$ for Asp; $d = 1.9$ for Glu and $d = 1.9$ for Asn) and pyroglutamic acid (PGLu; $p < 0.05$, $d = 0.9$). In comparison with their corresponding WT regions, similar results were observed in the KO BST ($p < 0.0001$ for KO vs WT for all except $p < 0.001$ for PGLu, $d = 1.3$ for Asp; $d = 1.1$ for Glu; $d = 1.7$ for Asn; and $d = 1.5$ for PGLu), KO CB ($p < 0.0001$ for KO vs WT for all, $d = 1.6$ for Asp; $d = 1.2$ for Glu; $d = 1.9$ for Asn; and $d = 1.7$ for PGLu) and KO OB ($p < 0.0001$ for KO vs WT for all except for $p < 0.01$ for Asn, $d = 1.7$ for Asp; $d = 1.3$ for Glu; $d = 1.0$ for Asn; and $d = 1.4$ for PGLu). Interestingly, the extent of the alteration in the levels of aspartic acid and glutamic acid were comparable (similar d -values) within a brain region, suggesting a close relation.

APPENDIX G: Supplementary metabolomics results

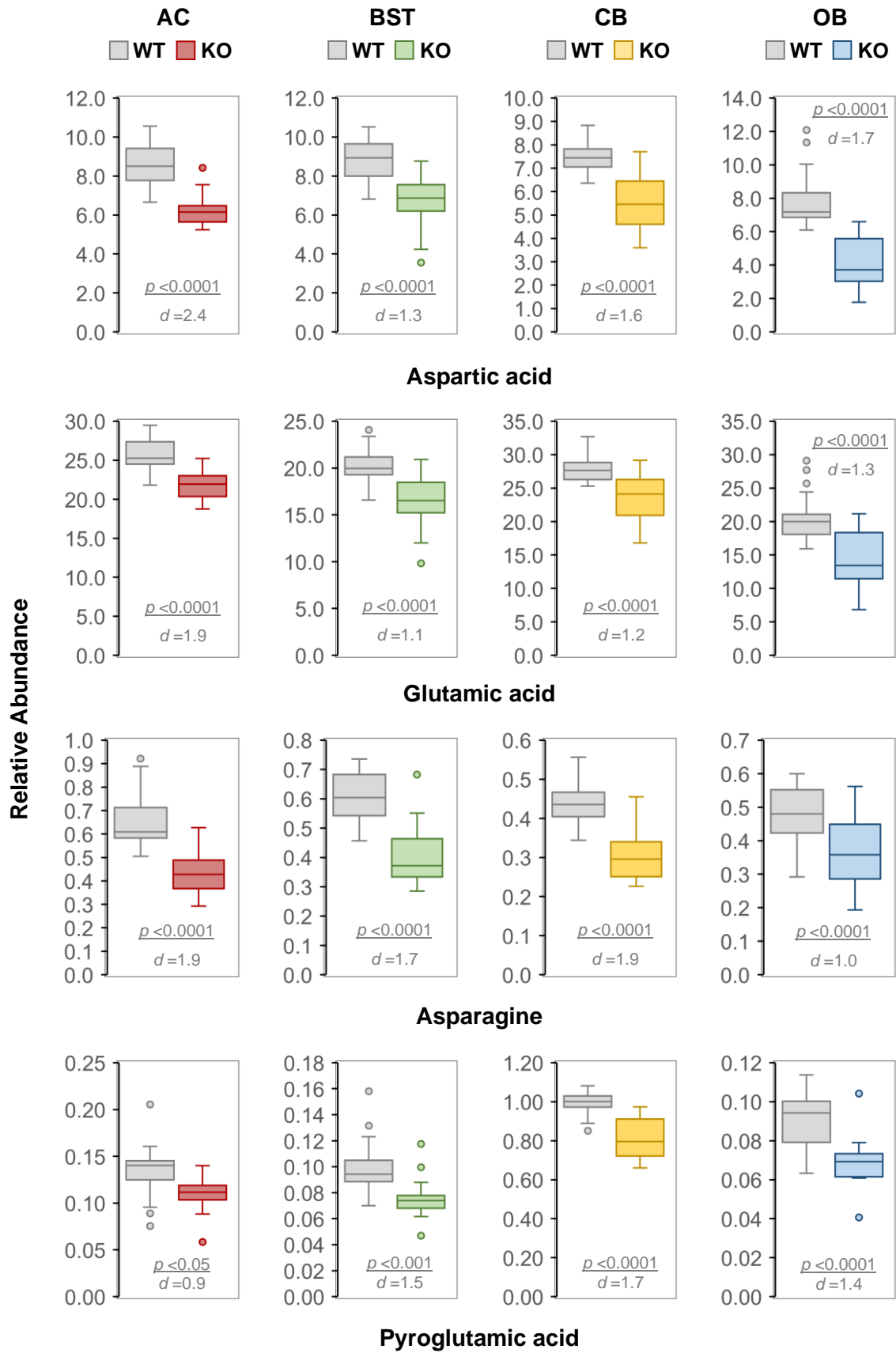


Figure G.5: Relative abundances of aspartic acid- and glutamic acid-related metabolites in the brain regions of *Ndufs4* wild-type and knockout mice.

G.3.5. Relative abundance of TCA cycle-related metabolites

Figure G.6 shows a comparison of the relative abundance of succinic acid and α -hydroxyglutaric acid metabolites between KO and WT mice in the investigated brain regions. Succinic acid was significantly decreased in all investigated KO brain regions ($p < 0.05$ for KO vs WT for all, $d = 0.9$ for BST and OB; and $d = 0.8$ for CB) except in the KO AC which only showed a tendency towards decreased levels. The levels of α -hydroxyglutaric acid were also significantly decreased in all investigated brain regions in response to the *Ndufs4* KO ($p < 0.0001$ for AC, BST, OB and $p < 0.01$ for CB for KOs vs WTs, $d = 1.6$ for AC; $d = 1.6$ for BST; $d = 0.8$ for CB; and $d = 1.1$ for OB).

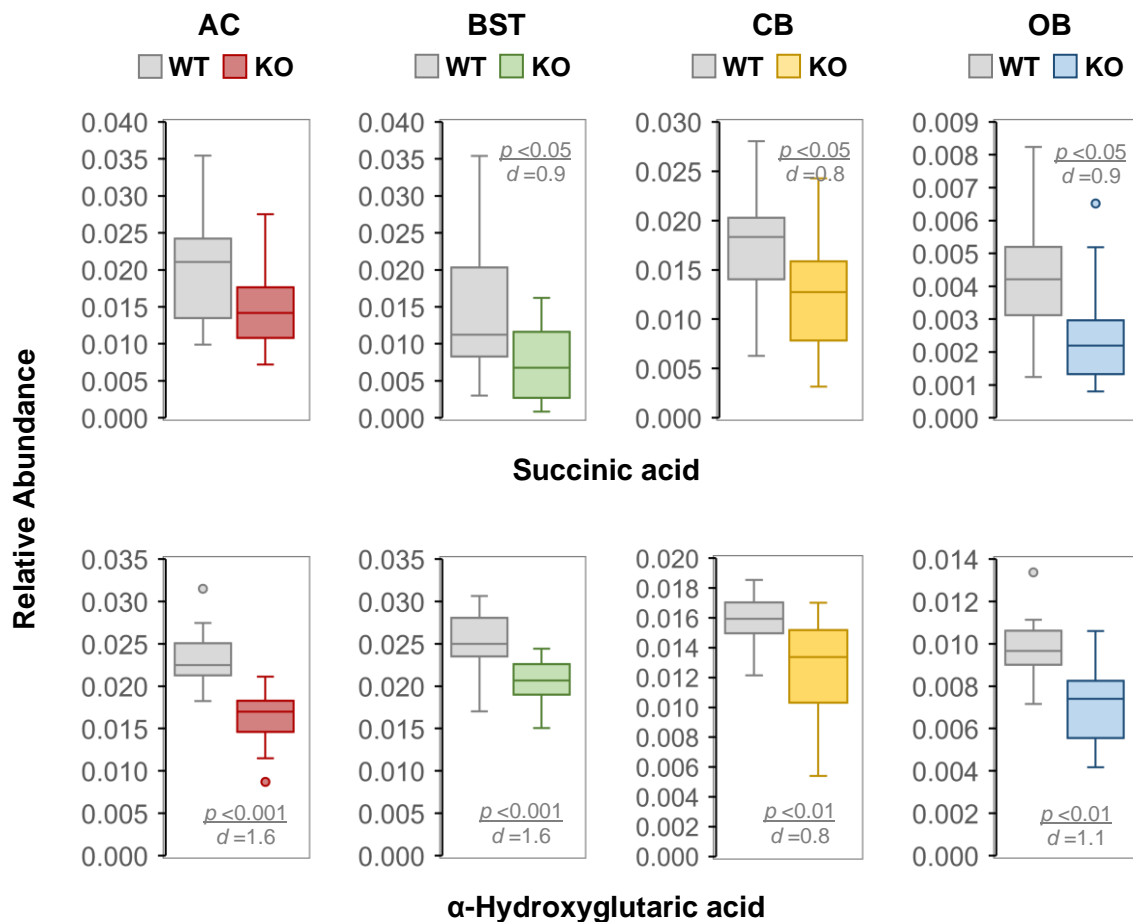
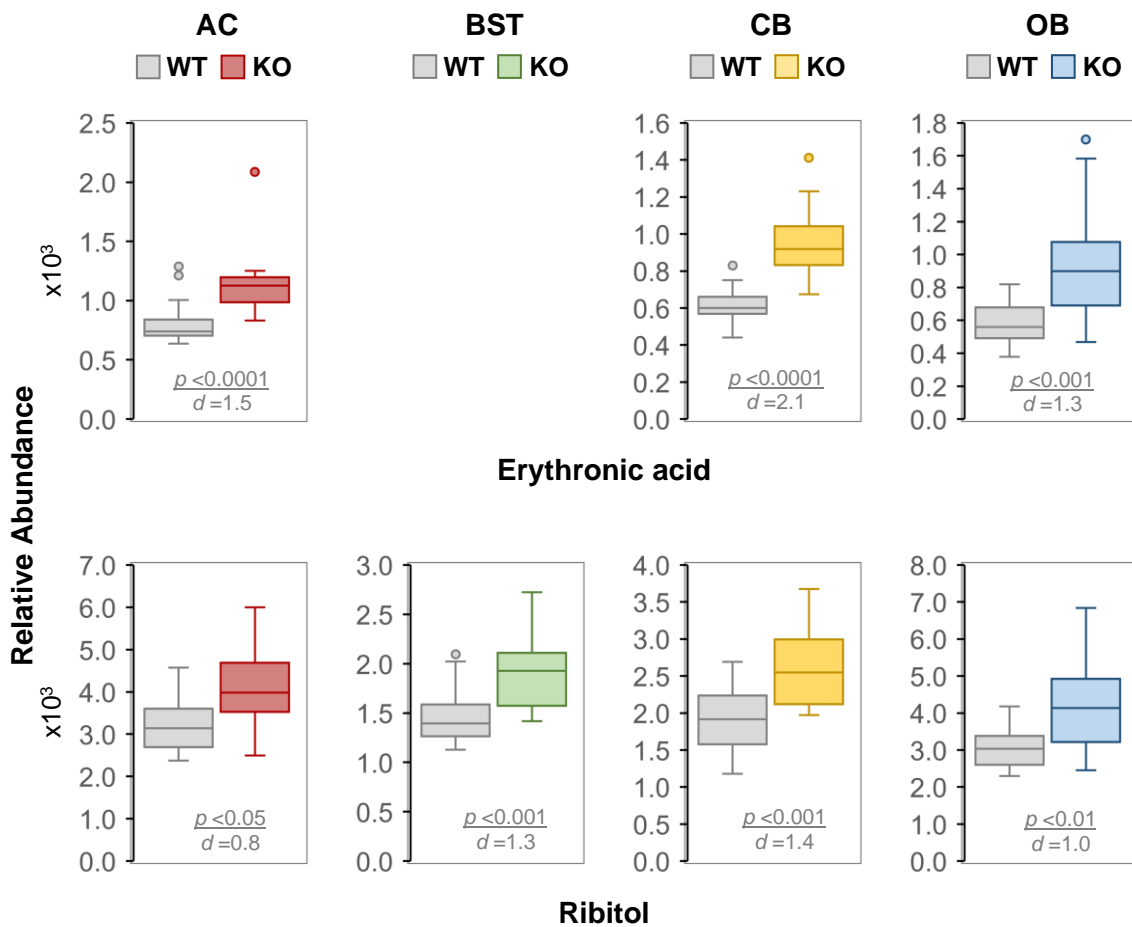


Figure G.6: The relative abundance of important differential TCA cycle-related metabolites in the brain regions of *Ndufs4* wild-type and knockout mice.

G.3.6. Relative abundance of carbohydrate-related metabolites

Figure G.7 shows a comparison of the relative abundance of erythronic acid, ribitol and glycerol-3-phosphate between KO and WT mice in the investigated brain regions. Of note, erythronic acid was not reliably detected in the KO BST and was excluded from the final data set. Most of the investigated KO brain regions displayed a profound increase in the levels of erythronic acid ($p < 0.0001$, $d = 1.5$ for the AC; $p < 0.0001$, $d = 2.1$ for the CB; and $p < 0.001$, $d = 1.3$ for the OB) and ribitol ($p < 0.05$, $d = 0.8$ for the AC; $p < 0.001$, $d = 1.3$ for the BST; $p < 0.001$, $d = 1.4$ for the CB; and $p < 0.01$, $d = 1.0$ for the OB) when compared with the corresponding WT brain regions, which indicated a disturbance in the pentose phosphate pathway. Although not exclusively associated with carbohydrate metabolism, phosphoglycerol (presumably glycerol-3-phosphate) was to a great extent decreased in all investigated KO brain regions when compared to the cognate WT brain regions ($p < 0.0001$ for KO vs WT for all except $p < 0.01$ for OB, $d = 2.1$ for AC; $d = 1.9$ for BST; $d = 1.4$ for CB and $d = 0.9$ for OB).



APPENDIX G: Supplementary metabolomics results

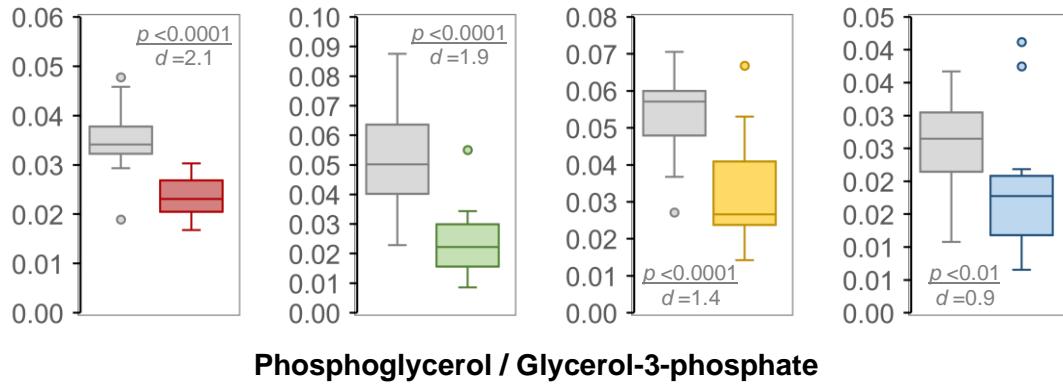


Figure G.7: The relative abundance of commonly altered carbohydrate-related metabolites in the brain regions of *Ndufs4* wild-type and knockout mice.

Even though other carbohydrate metabolism-related compounds such as pyruvic acid (the end-product of glycolysis), as well as lactic acid and alanine, which can be directly interconverted with pyruvic acid, were not identified as important distinct or common metabolites among the investigated brain regions, their frequent involvement/accumulation in mitochondrial disease warranted a more in-depth evaluation. A comparison of the relative abundance of these compounds between KO and WT mice in the investigated brain regions are depicted in Figure G.8. Generally, in comparison with the WT brain regions, the KO brain regions displayed a tendency towards increased levels of all three metabolites. However, statistical and practical significance was only obtained for pyruvic acid in the KO OB ($p < 0.001$, $d = 1.3$) and for lactic acid (Lac) and alanine (Ala) in both the KO CB ($p < 0.01$, $d = 0.9$ for Lac; $p < 0.0001$, $d = 1.3$ for Ala) and KO OB ($p < 0.0001$, $d = 1.5$ for Lac; $p < 0.001$, $d = 1.4$ for Ala).

APPENDIX G: Supplementary metabolomics results

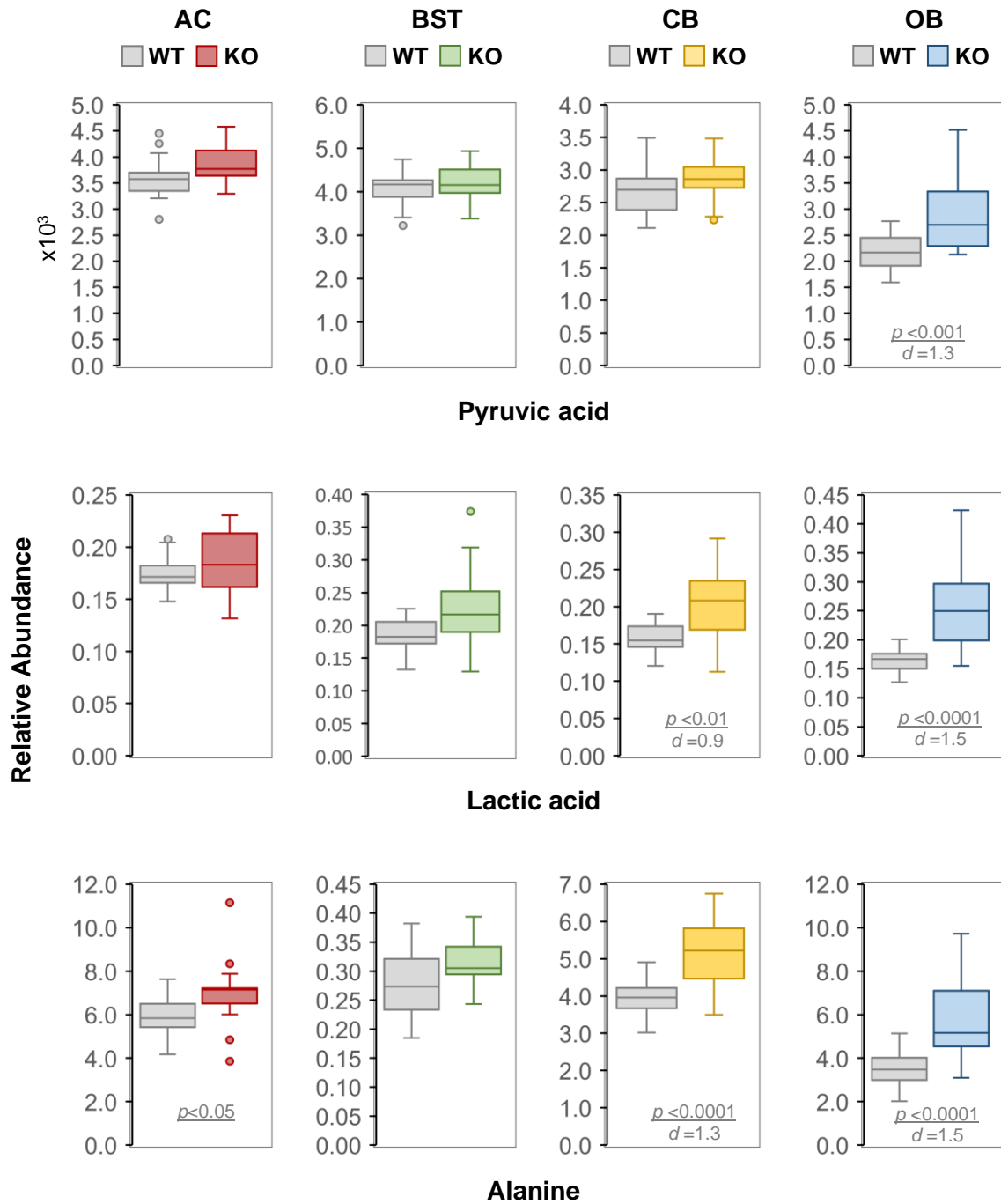


Figure G.8: The relative abundance of additional carbohydrate-related metabolites in the brain regions of *Ndufs4* wild-type and knockout mice

APPENDIX H

Language editing certificate

CERTIFICATE OF CONFIRMATION: LANGUAGE EDITING AND PROOFREADING

This certificate confirms the proofreading and language editing of:

**A metabolomics and biochemical investigation of
selected brain regions from *Ndufs4* knockout mice**

Author: Janeé Coetzer

Student number: 23509805

 **orcid.org 0000-0002-9269-3777**

The language editing involved:

- Spelling;
- Grammar;
- Academic style; and
- In text referencing.



CM Snoer
Signature of provider

18/11/2019
Date signed

*For any enquiries regarding the language editing contact Elmarie Snoer at
elsnoer13@gmail.com*

APPENDIX I

Ethics approval certificate

APPENDIX I: Ethics approval certificate



NORTH-WEST UNIVERSITY
YUNIBESITI YA BOKONE-BOPHIRIMA
NOORDWES-UNIVERSITEIT

Private Bag X6001, Potchefstroom,
South Africa, 2520

Tel: (018) 299-4900

Faks: (018) 299-4910

Web: <http://www.nwu.ac.za>

Institutional Research Ethics Regulatory Committee

Tel: +27 18 299 4849

Email: Ethics@nwu.ac.za

ETHICS APPROVAL CERTIFICATE OF STUDY

Based on approval by **AnimCare Animal Research Ethics Committee (AREC-130913-015)** on **27/10/2016** after the meeting held on **27/10/2016**, the North-West University Institutional Research Ethics Regulatory Committee (NWU-IRERC) hereby **approves** your study as indicated below. This implies that the NWU-IRERC grants its permission that provided the special conditions specified below are met and pending any other authorisation that may be necessary, the study may be initiated, using the ethics number below.

Study title: Biological investigations in NDUFS4-MT1 genetically modified mice.														
Study Leader/Supervisor: Prof Francois van der Westhuizen														
Student: Miss K Terburgh & Miss J Coetzer														
Ethics number:														
N	W	U	-	0	0	3	7	8	-	1	6	-	A	5
Institution			Study Number					Year		Status				
Status: S = Submission; R = Re-Submission; P = Provisional Authorisation; A = Authorisation														
Application Type: New Application - Category 0														
Commencement date: 2016-10-27										Category: <input type="text" value="0"/>				
Continuation of the study is dependent on receipt of the annual (or as otherwise stipulated) monitoring report and the concomitant issuing of a letter of continuation up to a maximum period of three years.														

Special conditions of the approval (if applicable):

- Any research at governmental or private institutions, permission must still be obtained from relevant authorities and provided to the AnimCare. Ethics approval is required BEFORE approval can be obtained from these authorities.

General conditions:

While this ethics approval is subject to all declarations, undertakings and agreements incorporated and signed in the application form, please note the following:

- The study leader (principle investigator) must report in the prescribed format to the NWU-IRERC via AnimCare:
 - annually (or as otherwise requested) on the monitoring of the study, and upon completion of the study
 - without any delay in case of any adverse event or incident (or any matter that interrupts sound ethical principles) during the course of the study.
- Annually a number of studies may be randomly selected for an external audit.
- The approval applies strictly to the proposal as stipulated in the application form. Would any changes to the proposal be deemed necessary during the course of the study, the study leader must apply for approval of these amendments at the AnimCare, prior to implementation. Would there be deviated from the study proposal without the necessary approval of such amendments, the ethics approval is immediately and automatically forfeited.
- The date of approval indicates the first date that the study may be started.
- In the interest of ethical responsibility the NWU-IRERC and AnimCare retains the right to:
 - request access to any information or data at any time during the course or after completion of the study;
 - to ask further questions, seek additional information, require further modification or monitor the conduct of your research or the informed consent process.
 - withdraw or postpone approval if:
 - any unethical principles or practices of the study are revealed or suspected,
 - it becomes apparent that any relevant information was withheld from the AnimCare or that information has been false or misrepresented,
 - the required amendments, annual (or otherwise stipulated) report and reporting of adverse events or incidents was not done in a timely manner and accurately,
 - new institutional rules, national legislation or international conventions deem it necessary.
- AnimCare can be contacted for further information or any report templates via Ethics-AnimCare@nwu.ac.za or 018 299 2197.

The IRERC would like to remain at your service as scientist and researcher, and wishes you well with your study. Please do not hesitate to contact the IRERC or AnimCare for any further enquiries or requests for assistance.

Yours sincerely

Prof LA

Digitally signed by
Prof LA Du Plessis

Du Plessis

Date: 2016.11.08
10:53:35 +02'00'

Prof Linda du Plessis

Chair NWU Institutional Research Ethics Regulatory Committee (IRERC)

APPENDIX REFERENCES

APPENDIX REFERENCES

- Alam, M.T., Manjeri, G.R., Rodenburg, R.J., Smeitink, J.A., Notebaart, R.A., Huynen, M., Willems, P.H. & Koopman, W.J. 2015. Skeletal muscle mitochondria of NDUFS4^{-/-} mice display normal maximal pyruvate oxidation and ATP production. *Biochimica et Biophysica Acta (BBA)-Bioenergetics*, 1847(6-7):526-533.
- Box, G.E. 1949. A general distribution theory for a class of likelihood criteria. *Biometrika*, 36(3/4):317-346.
- Du Toit, H. 2007. *Biochemical analyses of deficiencies in the oxidative phosphorylation system in human muscle*. Potchefstroom: North-West University. (Dissertation - MSc).
- Dubinsky, J.M. 2009. Heterogeneity of nervous system mitochondria: location, location, location! *Experimental Neurology*, 218(2):293-307.
- Dunn, W.B., Wilson, I.D., Nicholls, A.W. & Broadhurst, D. 2012. The importance of experimental design and QC samples in large-scale and MS-driven untargeted metabolomic studies of humans. *Bioanalysis*, 4(18):2249-2264.
- Esterhuizen, K., Lindeque, J.Z., Mason, S., van der Westhuizen, F.H., Suomalainen, A., Hakonen, A.H., Carroll, C.J., Rodenburg, R.J., de Laat, P.B. & Janssen, M.C. 2018. A urinary biosignature for mitochondrial myopathy, encephalopathy, lactic acidosis and stroke like episodes (MELAS). *Mitochondrion*, 45:38-45.
- FDA (Food and Drug Administration). 2018. Guidance for industry: bioanalytical method validation. <https://www.fda.gov/files/drugs/published/Bioanalytical-Method-Validation-Guidance-for-Industry.pdf> Date of access: 3 Sept. 2018.
- Field, A. 2009a. *Discovering statistics using SPSS*. 3rd ed. London: SAGE. p. 131 - 165.
- Field, A. 2009b. *Discovering statistics using SPSS*. 3rd ed. London: SAGE. p. 506 - 538.
- Greenhouse, S.W. & Geisser, S. 1959. On methods in the analysis of profile data. *Psychometrika*, 24(2):95-112.
- Janssen, A.J., Trijbels, F.J., Sengers, R.C., Smeitink, J.A., Van den Heuvel, L.P., Wintjes, L.T., Stoltenborg-Hogenkamp, B.J. & Rodenburg, R.J. 2007. Spectrophotometric assay for complex I of the respiratory chain in tissue samples and cultured fibroblasts. *Clinical chemistry*, 53(4):729-734.
- Kruse, S.E., Watt, W.C., Marcinek, D.J., Kapur, R.P., Schenkman, K.A. & Palmiter, R.D. 2008. Mice with mitochondrial complex I deficiency develop a fatal encephalomyopathy. *Cell metabolism*, 7(4):312-320.
- Levene, H. 1960. *Contributions to probability and statistics: essays in honor of Harold Hotelling*. Heidelberg: Springer Science and Business Media.
- Lindeque, J.Z., Hidalgo, J., Louw, R. & van der Westhuizen, F.H. 2013. Systemic and organ specific metabolic variation in metallothionein knockout mice challenged with swimming exercise. *Metabolomics*, 9(2):418-432.
- Lovick, T.A. 2012. Estrous cycle and stress: influence of progesterone on the female brain. *Brazilian Journal of Medical and Biological Research*, 45(4):314-320.
- Luo, C., Long, J. & Liu, J. 2008. An improved spectrophotometric method for a more specific and accurate assay of mitochondrial complex III activity. *Clinica Chimica Acta*, 395(1-2):38-41.
- Mauchly, J.W. 1940. Significance test for sphericity of a normal n-variate distribution. *The Annals of Mathematical Statistics*, 11(2):204-209.

APPENDIX REFERENCES

- Pathak, R.U. & Davey, G.P. 2008. Complex I and energy thresholds in the brain. *Biochimica et Biophysica Acta (BBA)-Bioenergetics*, 1777(7-8):777-782.
- Pretorius, M. 2011. *Evaluation of metallothionein involvement in the modulation of mitochondrial respiration in mice*. Potchefstroom: North-West University. (Dissertation - MSc).
- Quintás, G., Sánchez-Ilana, Á., Piñeiro-Ramos, J.D. & Kuligowski, J. 2018. Data quality assessment in untargeted LC-MS metabolomics. *Comprehensive Analytical Chemistry*, 82:137-164.
- Rahman, S., Blok, R., Dahl, H.H., Danks, D., Kirby, D., Chow, C., Christodoulou, J. & Thorburn, D. 1996. Leigh syndrome: clinical features and biochemical and DNA abnormalities. *Annals of Neurology*, 39(3):343-351.
- Rossignol, R., Letellier, T., Malgat, M., Rocher, C. & Mazat, J.-P. 2000. Tissue variation in the control of oxidative phosphorylation: implication for mitochondrial diseases. *Biochemical Journal*, 347(1):45-53.
- Salerno Jr, S., Mehrmohamadi, M., Liberti, M.V., Wan, M., Wells, M.T., Booth, J.G. & Locasale, J.W. 2017. RRMix: A method for simultaneous batch effect correction and analysis of metabolomics data in the absence of internal standards. *Public Library of Science (PloS) One*, 12(6), e0179530. <https://doi.org/10.1371/journal.pone.0179530>
- Shepherd, D. & Garland, P. 1969. The kinetic properties of citrate synthase from rat liver mitochondria. *Biochemical Journal*, 114(3):597-610.
- Smith, P.K., Krohn, R.I., Hermanson, G., Mallia, A., Gartner, F., Provenzano, M., Fujimoto, E., Goeke, N., Olson, B. & Klenk, D. 1985. Measurement of protein using bicinchoninic acid. *Analytical Biochemistry*, 150(1):76-85.
- Stone, P., Glauner, T., Kuhlmann, F., Schlabach, T. & Miller, K. 2009. *New dynamic MRM mode improves data quality and triple quad quantification in complex analyses*. https://www.agilent.com/cs/library/technicaloverviews/Public/5990-3595en_lo%20CMS.pdf Date of access: 11 Jun. 2018.
- The Open University. 2018. *SPSS statistics tutorial: two-way mixed ANOVA*. <http://www.open.ac.uk/socialsciences/spsstutorial/files/tutorials/two-way-mixed-ANOVA.pdf> Date of access: 3 Oct. 2018.
- Valsecchi, F., Monge, C., Forkink, M., de Groof, A.J., Benard, G., Rossignol, R., Swarts, H.G., van Emst-de Vries, S.E., Rodenburg, R.J. & Calvaruso, M.A. 2012. Metabolic consequences of NDUFS4 gene deletion in immortalized mouse embryonic fibroblasts. *Biochimica et Biophysica Acta (BBA)-Bioenergetics*, 1817(10):1925-1936.
- Vasilopoulou, C.G., Margarity, M. & Klapa, M.I. 2016. Metabolomics and network biology: sex comparative analysis of mouse brain regional metabolic physiology. *International Federation of Automatic Control (IFAC) PapersOnLine*, 49(26):283-285.
- Venter, L., Mienie, L.J., van Rensburg, P.J.J., Mason, S., Vosloo, A. & Lindeque, J.Z. 2018. Uncovering the metabolic response of abalone (*Haliotis midae*) to environmental hypoxia through metabolomics. *Metabolomics*, 14, art. #49. doi.org/10.1007/s11306-018-1346-8
- Venter, L., van Rensburg, P.J., Vosloo, A. & Lindeque, J.Z. 2016. Untargeted metabolite profiling of abalone using gas chromatography mass spectrometry. *Food Analytical Methods*, 9(5):1254-1261.

APPENDIX REFERENCES

Zhao, L., Mao, Z., Woody, S.K. & Brinton, R.D. 2016. Sex differences in metabolic aging of the brain: insights into female susceptibility to Alzheimer's disease. *Neurobiology of Aging*, 42:69-79.